

**Development of Laser Based Plasma Diagnostics
for Fusion Research on NSTX-U**

By

ROBERT ADAM BARCHFELD

B.S. (California State University, Sacramento) 2009

DISSERTATION

Submitted to partially fulfill the requirements for the degree of

DOCTOR OF PHILOSOPHY

in

APPLIED SCIENCE

in the

OFFICE OF GRADUATE STUDIES

of the

UNIVERSITY OF CALIFORNIA

DAVIS

Approved:

Neville C. Luhmann, Jr.

Jonathan P. Heritage

David Hwang

Committee in Charge

2017

for Leilani

Acknowledgements

There are numerous people who made these projects possible, and I would like to extend my deepest gratitude for their contributions to my research. First I would like to thank my dissertation committee, Professors Luhmann, Heritage, and Hwang. As my final adjudicators, it is with their cooperation and support that I can complete my studies. The staff and fellow graduate students of Professor Luhmann's research group provided invaluable support for my tenure at UC Davis. From group work in classroom assignments, mutual support for numerous posters and presentations, and the fellowship exhibited during trying times were essential to my successes. Among the staff, I would first like to thank Dr. Calvin Domier. His knack for making the complex, understandable, was a great benefit to comprehend the vast assortment of science and technologies that must be integrated to construct plasma diagnostics instruments. His knowledge, experience, and kind nature kept the tasks at hand in perspective. Dr. Christopher Muscatello provided the initial guidance to get these projects underway, set goals, and provided feedback to keep progress moving ahead. He also spent an undisclosed number of hours writing proposals and reports on my behalf. Lynette Lombardo routinely performed beyond any reasonable measure to ensure our official affairs were in order, and she always made time to solve my personal predicaments. My first foray into graduate research was to operate the NN1000 "nano mill". I would like to thank *Digital Technology Laboratory* for allowing me access to their prototype machine, and in particular to Adam Hansel, Zachary Piner, and Jongsoo Kim. Their extreme generosity was a boon to our research efforts, and to my personal achievements. I thank Dr. Diana Gamzina for her contributions for the "nano mill" applications, and to the HiFIVE design team. I would like to thank Logan Himes for assuming the nano-machining duties, which allowed me to focus on plasma physics and fusion technology, and for his assistance in the laboratory and machine shop. My primary goal of constructing plasma diagnostic instruments would not have been possible without the support of *Princeton Plasma Physics Laboratory* and the *U.S. Department of Energy*. I offer sincere appreciation for the support and

collaboration of Dr. Robert Kaita and Dr. Yang Ren. Their support was essential to provide the applications for the instruments described in this dissertation, and they provided counsel and refinements to facilitate the development of these instruments. I would like to acknowledge, and offer appreciation, to the *U.S. Department of Energy* for funding this project through grant number, DE-FG02-99ER54518. I am grateful for the advice received from Dr. Edward Danielewicz and Dr. Alain Semet. Their knowledge of gas lasers was a tremendous help to me. I thank Paul Riemenscheider for his help of various component designs, and the numerous CAD drawings that were drawn, and redrawn. I also need to thank my wife, family, and friends for their support and understanding. They allowed me to set my schoolwork as my first priority. For them, my venture into higher education started long before my graduate work. Many events and gatherings were delayed or cancelled so I could concentrate on completing my studies. My most heartfelt gratitude for the greatest contribution to my education is extended to Professor Neville C. Luhmann, Jr. His knowledge and generosity knows no bounds. He bestowed upon me knowledge, skill, and confidence. His wisdom and guidance kept my course true, and he deserves all possible credit for any success I enjoy. He shall always be, the *Professor*.

"What men are poets who can speak of Jupiter if he were a man, but if he is an immense spinning sphere of methane and ammonia must be silent?"

-Richard P. Feynman

Table of Contents

Abstract.....	.ix
I Introduction.....	1
I.1 World Energy Supply and Demand.....	1
I.2 Fusion Solution.....	10
I.3 Fusion Science.....	11
I.4 Tokamaks	15
I.5 NSTX-U.....	20
I.6 Anomalous Transport	24
I.7 Drift Waves and ETG Modes.....	26
I.8 Instrumentation.....	30
I References.....	31
II Plasma Diagnostics	36
II.1 Types of Plasma Diagnostics	37
II.2 FIReTIP System.....	40
II.3 Interferometry.....	42
II.4 High-k Scattering System	48
II.5 Collective Thomson Scattering	54
II References	60
III FIReTIP Design.....	63
III.1 FIReTIP Laser System	64
III.1.1 FIReTIP CO ₂ Laser	66
III.1.2 FIReTIP FIR Lasers	80
III.1.3 FIR Laser Performance.....	98

III.2	FIReTIP Waveguide.....	105
III.3	FIReTIP Launch Optics.....	124
III.4	Vibration Monitor	139
III.5	FIReTIP Receiver Table.....	143
III.6	FIReTIP IF Electronics	148
III	References	152
IV	High- k_θ Scattering System Design	156
IV.1	High- k_θ Scattering Laser System	157
IV.1.1	PL-6 CO ₂ Laser.....	158
IV.1.2	Formic Acid Laser.....	171
IV.2	High- k_θ Scattering Corrugated Waveguide	183
IV.3	High- k_θ Scattering Launching Optics	192
IV.4	High- k_θ Scattering Receiving Optics	201
IV.5	High- k_θ Scattering Receiver	211
IV.6	High- k_θ Scattering Reference Channel.....	216
IV.7	High- k_θ Scattering IF Electronics	223
IV	References	225
V	Future Work	229
V.1	FIReTIP System Improvements.....	229
V.2	High- k_θ Scattering System Improvements.....	235
V.3	Microfabrication Techniques	239
V.3.1	DRIE.....	240
V.3.2	Ultra Violet LIGA	241
V.3.3	EDM	243
V.3.4	Nano-CNC-Machining.....	244

V.4	Vacuum Electronic Devices.....	246
V.4.1	Slow Wave Structures.....	248
V.4.2	Electron Guns	249
V.4.3	Collector.....	251
V.4.4	Magnetic Focusing	252
V.4.5	Cooling	253
V.5	Design and Fabrication of the 346 GHz BWO and 220 GHz TWT	253
V.5.1	220 GHz TWT.....	254
V.5.2	346 GHz BWO	261
V	References	270
VI	Conclusions.....	276
VI.1	Installation	276
VI.1.1	FIReTIP Installation	277
VI.1.2	High- k_0 Scattering Installation.....	283
VI.2	Diagnostic Operation	287
VI.2.1	FIReTIP Operation	288
VI.2.2	High- k_0 Scattering Operation.....	292
VI.3	LabView Control Program	296
VI.4	Fusion Power Legacy.....	301
VI	References.....	303
Appendix A	Laser Maintenance and Overhauls.....	304
A.A.1	Laser Maintenance.....	304
A.A.1.1	FIReTIP CO ₂ Laser Maintenance	305
A.A.1.2	FIReTIP FIR Laser Maintenance.....	312
A.A.1.3	High- k_0 Scattering PL-6 Laser Maintenance	318
A.A.1.4	High- k_0 Scattering FIR Laser Maintenance.....	321

A.A.2	Laser Overhauls.....	328
A.A.2.1	FIReTIP CO ₂ Laser Overhaul.....	328
A.A.2.2	FIReTIP FIR Laser Overhaul	337
A.A.2.3	FIReTIP FIR Laser Alignment	342
A.A.2.4	High-k ₀ Scattering PL-6 Laser Overhaul	344
A.A.2.5	High-k ₀ Scattering FIR Laser Overhaul	347
Appendix B	Nano-CNC-Machining	356
A.B.1	Machining Fundamentals	356
A.B.1.1	Conventional Machining	358
A.B.1.2	Nano-CNC-Machining	360
A.B.2	Machining Techniques	363
A.B.2.1	Materials.....	367
A.B.2.2	Tooling	370
A.B.2.3	Tool Setting	378
A.B.2.4	Surfacing	381
A.B.2.5	Milling.....	385
A.B.2.6	Part Assembly Alignments	391
A.B.3	NN1000 Details	393
A.B.4	Nano-CNC-Machining Conclusion	399

Abstract

Worldwide demand for power, and in particular electricity, is growing. Increasing population, expanding dependence on electrical devices, as well as the development of emerging nations, has created significant challenges for the power production. Compounding the issue are concerns over pollution, natural resource supplies, and political obstacles in troubled parts of the world. Many believe that investment in renewable energy will solve the expected energy crisis; however, renewable energy has many shortfalls. Consequently, additional sources of energy should be explored to provide the best options for the future. Electricity from fusion power offers many advantages over competing technologies. It can potentially produce large amounts of clean energy, without the serious concerns of fission power plant safety and nuclear waste. Fuel supplies for fusion are plentiful. Fusion power plants can be operated as needed, without dependence on location, or local conditions. However, there are significant challenges before fusion can be realized.

Many factors currently limit the effectiveness of fusion power, which prevents a commercial power plant from being feasible. Scientists in many countries have built, and operate, experimental fusion plants to study the fusion process. The leading examples are magnetic confinement reactors known as tokamaks. At present, reactor gain is near unity, where the fusion power output is nearly the same as the power required to operate the reactor. A tenfold increase in gain is what reactors such as ITER hope to achieve, where ~ 50 MW will be used for plasma heating, magnetic fields, and so forth, with a power output of ~ 500 MW. Before this can happen, further research is required. Loss of particle and energy confinement is a principal cause of low performance; therefore, increasing confinement time is key. There are many causes of thermal and particle transport that are being researched, and the prime tools for conducting this research are plasma diagnostics.

Plasma diagnostics collect data from fusion reactors in a number of different ways. Among these are far infrared (FIR) laser based systems. By probing a fusion plasma with FIR lasers, many properties can be measured, such as density and density fluctuations. This dissertation discusses the theory and design of two laser based diagnostic instruments: 1) the Far Infrared Tangential Interferometer and Polarimeter (FIReTIP) systems, and 2) the High- k_θ Scattering System. Both of these systems have been designed and fabricated at UC Davis for use on the National Spherical Torus Experiment - Upgrade (NSTX-U), located at Princeton Plasma Physics Laboratory (PPPL). These systems will aid PPPL scientists in fusion research. The FIReTIP system uses 119 μm methanol lasers to pass through the plasma core to measure a chord averaged plasma density through interferometry. It can also measure the toroidal magnetic field strength by the way of polarimetry. The High- k_θ Scattering System uses a 693 GHz formic acid laser to measure electron scale turbulence. Through collective Thomson scattering, as the probe beam passes through the plasma, collective electron motion will scatter power to a receiver with the angle determined by the turbulence wavenumber. This diagnostic will measure k_θ from 7 to 40 cm^{-1} with a 4-channel receiver array. The High- k_θ Scattering system was designed to facilitate research on electron temperature gradient (ETG) modes, which are believed to be a major contributor to anomalous transport on NSTX-U.

The design and testing of these plasma diagnostics are described in detail. There are a broad range of components detailed including: optically pumped gas FIR lasers, overmoded low loss waveguide, launching and receiving optical designs, quasi-optical mixers, electronics, and monitoring and control systems. Additionally, details are provided for laser maintenance, alignment techniques, and the fundamentals of nano-CNC-machining.

I. Introduction

The prospects of fusion power motivate an exciting and technically challenging field. To understand why research into fusion is a worthy scientific pursuit, one should understand the state of current and future world energy demand, and the various proposals of how to meet this demand together with the associated problems with various energy sources. Fusion power is one of many methods in current development around the world, and offers many attractive benefits. There are certainly many challenges to overcome. It is important to address these challenges, and offer strategies to research them.

I.1 World Energy Supply and Demand

Ever increasing demand for power production is likely to continue for the foreseeable future; however, there has been much debate over the best method for power generation. Increasing global population, coupled with greater energy demand per capita, will drive energy consumption to unprecedented levels. The U.S. Energy Information Administration projects that energy demand will increase by 48% by 2040 [1]. While there are efforts to reduce carbon based energy in favor of renewable sources, all types of power production are expected to increase over the next few decades. The United States Clean Power Plan (CPP) is estimated to reduce fossil fuel use, while increasing renewable energy. However, on a global scale, nations such as China and India offset the CCP gains to only a few percent [1]. Figure 1 shows the projected world energy consumption by energy source. The EIA did not originally include the CPP in this plot; however, the dotted lines show a marginal effect when the CCP is included. There are significant concerns whether this power demand can be met with our current methods of power production. A massive energy shortfall would be a crisis with many negative outcomes probable.

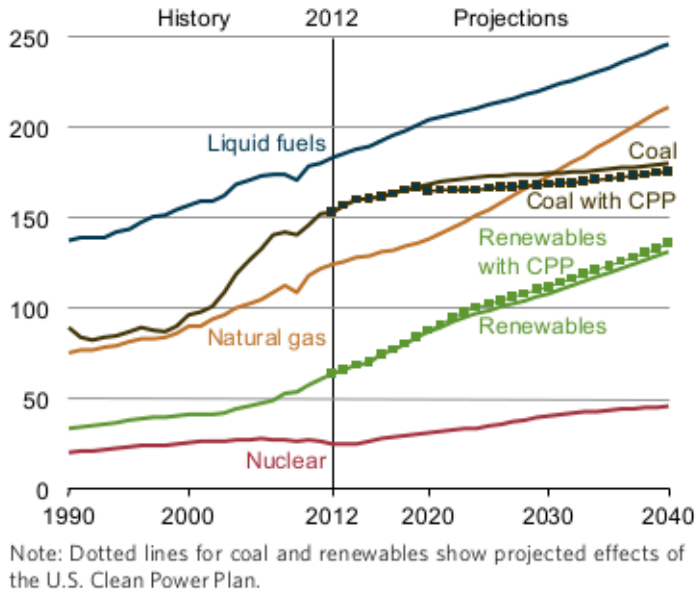


Figure 1. EIA projections for energy consumption by energy source in quadrillion BTUs. By 2040, a 48% increase in demand is predicted. Source: U.S. Energy Information Administration [1].

Coal power plants have been under considerable public pressure over pollution concerns. The EIA reports that coal provides 43% of electricity in the United States; however, it is responsible for 76% of carbon dioxide production [2]. In 1990, amendments to the Clean Air Act of 1970 increased regulations on many sources of pollution, including oil, coal, and ground and air transportation. This act identifies carbon dioxide as a pollutant with significant risk, and provides guidelines to study its effects, and suggests methods to prevent and reduce.

*"...pollutants which pose a significant risk to human health and the environment,... preventing or reducing multiple air pollutants, including sulfur oxides, nitrogen oxides, heavy metals, PM-10 (particulate matter), carbon monoxide, and **carbon dioxide**, from stationary sources, including fossil fuel power plants. "[3]*

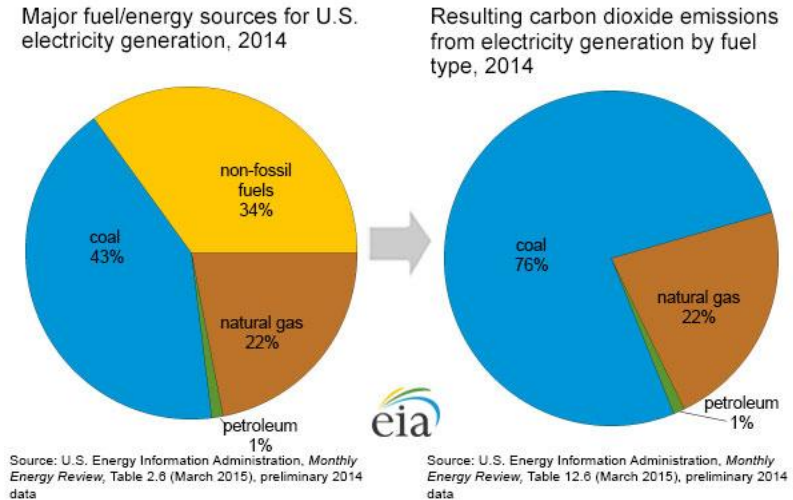


Figure 2. EIA shows that coal is a major source of carbon dioxide pollution, disproportionate to its energy contribution. Source: U.S. Energy Information Administration [2].

The CAA encourages cleaner technologies, such as "clean coal"; however, the recent political environment has turned against coal power of any type. President Obama recently authorized the Environmental Protection Agency to further increase regulations on coal-fired plants. This has sparked heated debates on regulation versus economic concerns. In 2016, the Supreme Court ruled against the President's regulations with a temporary injunction [4]. This topic continued to be a topic of debate in the 2016 U.S. elections [5].

Oil supply and usage is frequently a topic of controversy, both politically and environmentally. To increase oil production to meet future needs, additional sources are needed. This is further complicated by uncertainty in traditional sources. Venezuela was one of the largest oil exporters in the world. They are currently in political upheaval, resulting in diminished production to a 13 year low in 2016 [6]. The Deepwater Horizon oil spill in 2010 caused international concern over the safety of water based oil drilling. Federal and State moratoria on new leases for offshore drilling have fluctuated many times in the past few decades [7]. There have been debates regarding drilling in the Arctic National Wildlife Refuge (ANWR) in Alaska since 1977, and continue to present times [8]. The Keystone pipeline transports oil

from Canada across the United States to various locations and first began operations in 2010. However, Phase IV of the project proposed a route through the Sandhills of Nebraska, which created great concerns over the possibility of a spill in the refuge [9]. Ultimately, Phase IV of the Keystone project was rejected by President Obama in 2015 [10]. War in the Middle East has created turmoil over oil exports for the past decade. The practice of "Fracking" has alleviated some of the concerns for a stable oil supply, and fuel costs have dropped accordingly [11]; however, the process is controversial. Fracking uses hydraulic pressure deep underground to fracture the Earth, thereby releasing trapped shale oil and gas. Efforts have been made to curtail "fracking" over environmental and safety concerns. Among these concerns are that the oil companies have not disclosed what "fracking" fluids they employ, citing trade secrets essential to the process [12]. Should environmental concerns reduce or eliminate "fracking", uncertainty in future oil production would be reintroduced. The volatility of oil has motivated investments in electric transportation. However, this increases demand on electrical production which is largely dependent on fossil fuels. The debate on how to advance the U.S. energy policy continues, and has increased in volatility since the 2016 presidential election [13]. Competition between oil production and alternative sources of energy are not likely to be settled soon.

Solar power plants, both commercially and individually owned, represent a growing market offering independence from fossil fuels and no recurring fuel costs; however, their actual economic efficiency is quite poor. Solar power plants are significantly more expensive to build than competing technologies. The EIA reports that the average solar plant in 2014 cost \$3,492 per kilowatt, while natural gas was \$965 per kilowatt [14]. However, costs for solar generator construction are decreasing, with a ~6% reduction between 2013 and 2014 [14, 15]. While there are no fuel costs for solar power, and maintenance is relatively light, it could be argued that their long term economy should prevail. However, analysis from the EIA shows that the high initial cost dominates the cost of the power over the lifetime of the power plant. The "levelized cost of electricity" (LCOE) is the cost per megawatt-hour including the total cost to build and operate a power plant divided by its expected output over its lifetime. Solar varies wildly

depending on the plant's location and local conditions with a LOCE of \$85 to \$190 per megawatt-hour.

Nuclear power compares with a LCOE of \$90 to \$100 per megawatt-hour [16].

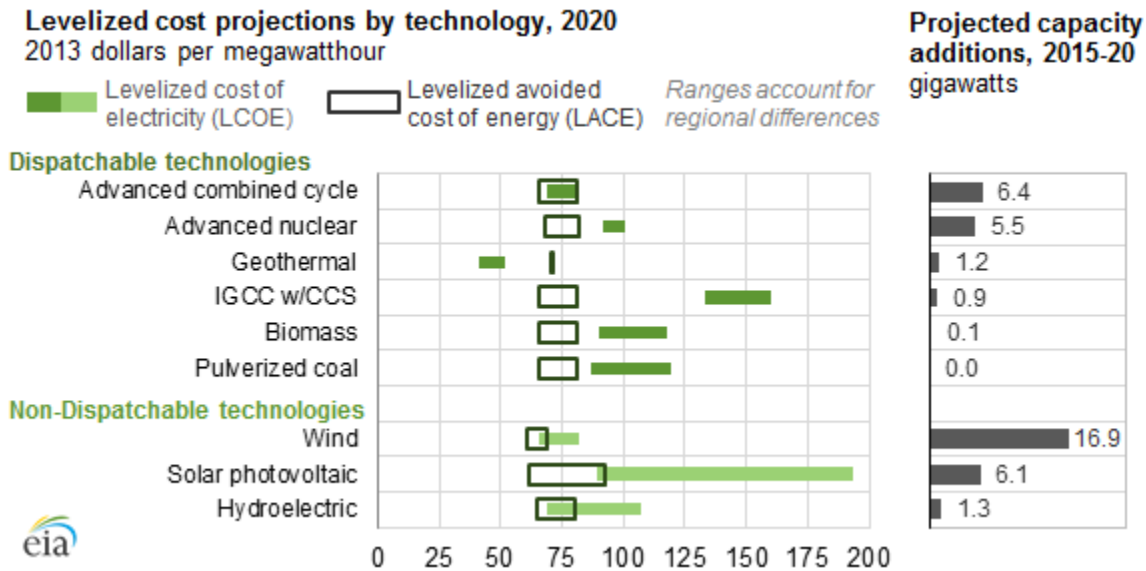


Figure 3. Levelized cost projections for various types of power production by 2020. The high cost of building solar power plants drives their cost per megawatt-hour to the most expensive technology available. Location and other factors cause a large spread in costs, indicating that solar is not suitable everywhere. When LCOE (green) costs are higher than LACE (open box) costs, the technology is considered economically uncompetitive. Source: U.S. Energy Information Administration [16].

Solar power also suffers from low power conversion rates, ~10% to 20% for commonly used silicon photovoltaic cells [17]. Many other factors reduce their potential power output, such as latitude, cloud cover, night time, inclement weather, and temperature. Solar cells function better when they are cool; however, the bright, sunny areas also tend to be the hottest. Solar power is ultimately limited by the energy intensity received from the sun; therefore, the common method of increasing output is to cover a larger area. Steerable panels can improve performance, but add to the already expensive installation. Not all places are suitable for efficient operation, economically or electrically, and there are too many factors that prevent a true on-demand power generation. Solar power plants are an expensive option.

Improvements to solar technology may make them more viable in the future, but it cannot be a standalone source, and will always need supplemental power generation. An alternative, or supplemental, form of solar power has been proposed that involves building extensive solar panels in orbit. These would collect solar energy, convert it to microwaves, and beam the power down to receiving stations on Earth [18, 19]. It remains to be seen; however, if any nations are willing to commit to a project of this scope. In addition, there are a number of concerns ranging from cost, stray microwaves, and potential environmental issues.

Wind power rivals solar for the preferred source of renewable energy; however, it possesses many of the same setbacks. Economical operation depends on operating in a region with sufficient wind. The California Energy Commission notes that wind farms are typically located in places where the annual average wind speed exceeds 13 miles per hour [20]. Many locations have variable or seasonal wind; therefore, power production depends on local weather, rather than demand from the population. Large windmills can produce on the order of 1 megawatt each. To supply power on the scale of a typical coal plant (~1 GW), about a thousand windmills are needed. This occupies a large swath of land, which could be developed for other purposes. Many people have complained that windmills are unsightly and hazardous to migratory birds and raptors [21], and in particular to endangered species [22]. These concerns could cause significant obstacles when choosing locations for wind farms. One solution is to move wind farms offshore, where they are out of sight, and wind is more consistent. The U.S. Department of Energy has released a report for offshore wind strategy [22]. In this report, they acknowledge that "...the cost of offshore wind energy is too high to compete in most U.S. markets..." [22]. The sea has proven to be a harsher environment than engineers predicted. The failure rate of offshore wind turbines contributes to very high maintenance costs [23]. Recently, Vattenfall's Ytre Stengrund wind farm off the coast of Sweden has been decommissioned [24]. The company cited excessive maintenance problems. After 15 years of operation, only one out of five turbines was operational. Upgrading to newer designs was deemed economically and technically infeasible.

Other types of renewable energy have their benefits and shortfalls. Hydro-electric power requires building dams and using the stored water to drive turbines. Many people oppose the flooding of valleys dams require. Environmentalists are at odds with themselves since the power created is clean and renewable, but the local wildlife, and sometimes protected species can be devastated [25]. Hydro-electric power also depends on steady water supply. Regions with periodic drought conditions, such as California, can find their water flow insufficient to meet power demand. California has experienced ~50% reduction in hydro-electric power since the current drought began in 2012 [26]. There are limited successes for some types of renewable energy where conditions are ideal. Tidal generators in Nova Scotia have provided a reliable 20 megawatts since 1984 [27], and there are plans to expand to 50 megawatts by 2019 [28]. While this is heralded as a great achievement, 50 MW is relatively small, and Nova Scotia benefits from the largest tides in the world at 16.3 m [29]. In certain regions, geothermal power makes sense. Iceland has long since used geothermal power directly for heating, and for electricity generation [30]. Iceland is able to exploit this natural resource due to its unique location in one of the most tectonically active regions in the world, with more than 200 volcanoes [30].

Clean, renewable energy is an attractive proposition for its lessened impact on the environment. They share many serious shortfalls, not the least of which is cost. So long as cheaper sources of power are available, it will be difficult to convince populations to switch to more expensive power. Innovation may improve the outlook of these technologies; however, most of them have a fundamental flaw of generating power in response to the environment, rather than meeting the demands of the people. Energy storage technology is not in a state to support a power system founded on renewable energy. As such, it is employed as supplemental power, with fossil fuels continuing to provide a foundation for our energy needs [31].

Nuclear power has the potential to provide abundant clean power; however, there are concerns over their radioactive fuel. Under normal operations, concerns revolve around what to do with spent fuel which is

still dangerously radioactive. The general public has greater fears about a potential catastrophic failure, exposing the core to the environment [32]. Concerns for public safety were first realized from the near disaster at *Three Mile Island* in 1979 [33]. Even though the health impact proved to be minimal, public opinion was forever wary of nuclear power [34]. In 1986, the *Chernobyl Nuclear Power Plant* experienced the catastrophe many people feared when excessive steam destroyed the reactor containment [35]. Dozens of workers were exposed to lethal radiation, and hundreds more were exposed to various levels of radiation on a short time scale. Thousands more were exposed when radioactive material spread through the atmosphere. There are many cases of cancer linked to the Chernobyl disaster, but the full impact will probably never be known [36]. The accident was ultimately blamed on a flawed design and inappropriate procedures [37]; however, this was not very reassuring to the general public. In 2011, an earthquake, and tsunami, struck Japan resulting in damage to the nuclear power plant in Fukushima [38]. The fear of worldwide contamination has not come to fruition; however, this disaster has shown that nuclear power is susceptible to dangers beyond human control [39]. Immediately after the *Fukushima* disaster, all nuclear plants in Japan were taken off-line to assess their safety. After five years of inactivity, only three plants have been restored to operational status to provide 2.5 gigawatts of power. Other plants are either shut down or still under review, leaving Japan nearly 45 gigawatts short of their previous nuclear power capacity [40].

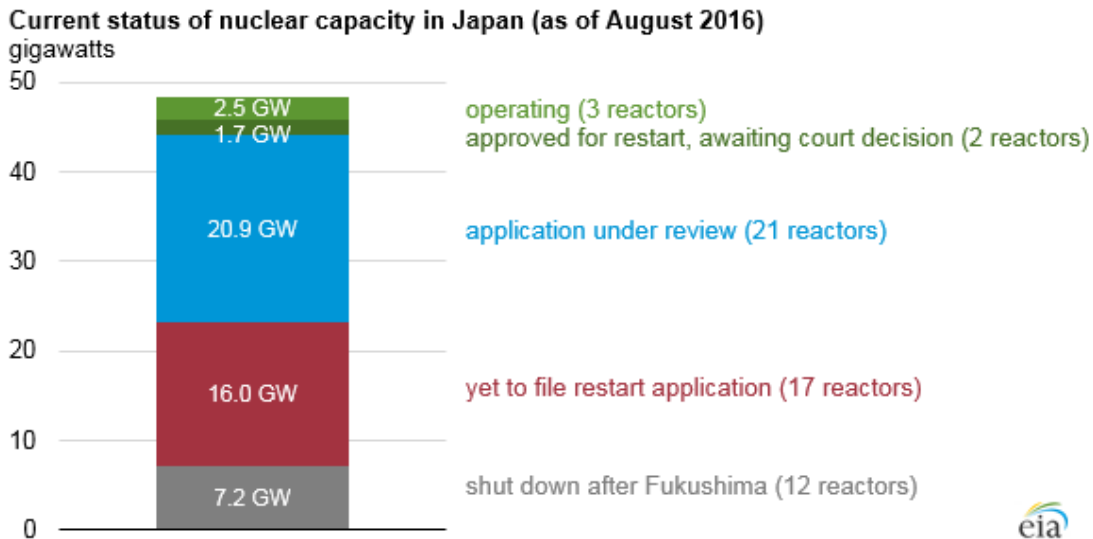


Figure 4. All 54 of Japan's nuclear reactors were shut down after the 2011 earthquake. Of these, only 3 are back on-line. 12 have been shut down permanently, 17 have not filed to restart, 21 are under review (including 1 new plant), and 2 more are expected to restart soon. Source: U.S. Energy Information Administration [40].

These few accidents have eroded public trust in nuclear power [41]. When coupled with resistance to fossil fuels, the demand on renewable energy is tremendous. However, renewable energy is laden with problems that make it impractical as a foundation for energy policy. The *Fukushima* disaster has underscored this dilemma, not only for Japan, but for most of the world. Germany has invested heavily in renewable energy, and has seen stark increases in prices to the consumer [42]. Apart from the cost, heavy dependency on renewable sources has created problems with their back-up systems. When renewable power exceeds 40% of a power grid's potential, there are problems with excess power on days with good conditions for renewable energy, and problems with how to fill in for power deficiency on poor days [43]. These issues could be solved with carbon capture and storage (CCS) to limit pollution from fossil fuels, or more sophisticated energy storage to store renewable energy during peak generation, and expend it on days when needed. These technologies need much further progress before they could be implemented in a meaningful manner [42]. Nuclear power appears to be in decline with stiffer regulations and waning

public support. China is expected to focus on nuclear power in the coming decades, but the western world favors renewable energy. It is uncertain if nuclear will ever regain public support [44]. In Japan the subject of whether or not to reopen their nuclear power plants has been a key topic in their politics. In October of 2016, Ryuichi Yoneyama was elected governor of Niigata (near Tokyo), who campaigned in favor of keeping Japan's nuclear power plants closed [46], despite facing massive energy shortfalls.

The current nuclear dilemma in Japan can serve as a model for nuclear policies worldwide [42]. Japan had depended on a combination of nuclear, renewable, and fossil fuels, with upwards of 80% fossil fuel dependence in 2012 [42]. Policies to reduce fossil fuel use to ~ 15% by 2050 will vastly increase demand on renewable and nuclear power. Due to the *Fukushima Disaster*, nuclear power appears to be rejected as a future power source. Over-reliance on renewable energy could cause severe energy supply fluctuations [43]. The absence of nuclear power could create energy shortfalls of 20% by 2070 [47]. To prevent an energy crisis, more options are needed. In the coming decades the world should explore new technologies. Chief among the options are twofold. First, develop better methods of storing energy for long terms. This will provide a safety cushion for renewable energy to provide excess power, and deliver it on demand. Second, a new source of power should be developed, fusion [42]. Fusion power offers an option that could potentially solve the foreseeable energy needs. Experts believe that fusion could be realized in about 30 or more years; however, it is relatively poorly funded, and could be greatly accelerated if it were given a priory for development. Renewable power is funded by a factor of 200 times greater than current fusion research [42]. If fusion power can be developed before the expected energy crisis, then it can provide clean and abundant energy for centuries [45].

I.2 Fusion Solution

Fusion power has been undergoing continuous research and development for more than five decades [45, 48, 49]; however, a commercially viable power plant remains elusive. The potential for fusion to provide

bountiful power generation, with a seemingly endless fuel supply, all the while presenting minimal risk to the environment makes for an attractive endeavor for scientists and engineers around the world. The complexity of such a device has spurred new applications in many fields, such as vacuum electronics, quasi-optical components, and microfabrication. As technologies develop, their application towards fusion technology promotes increased understanding of the fusion process and its limitations.

Experimental reactors have been built around the world to facilitate fusion research, which in turn helps to design the next generation of reactors. At the time of this writing, construction is underway on the first fusion reactor that will demonstrate the feasibility of commercial fusion power, ITER (*International thermonuclear experimental reactor*). This reactor promises to provide a power gain of 10, with sustainable power generation of 500 MW [50]. If successful, the future of fusion power will be assured. ITER is being constructed in southern France through international cooperation. Development will continue through the next decade at an estimated cost of 20 billion Euro to achieve first plasma by 2026. Research critical to ITER's success is ongoing. There are many gaps in fusion knowledge which reduce fusion output. To better understand the dynamics of fusion reactors, diagnostic instruments are needed to collect data, and visualize internal processes. Since all experimental reactors are unique in the size, scope, and configuration, plasma diagnostic instruments must be custom designed and fabricated for the desired tasks at hand. Experimental results may motivate additional instruments for further understanding, as well as improved technologies may prompt upgrading existing instruments.

I.3 Fusion Science

Fusion power is the process whereby low Z atomic nuclei are brought together, and then fuse into a heavier nucleus. The products of fusion are slightly less massive than the reactants. The lost mass is converted into energy via Einstein's equation $E=mc^2$. The released energy is captured and used to heat water to drive steam turbines, and in turn, produce electricity. The preferred reactants are isotopes of hydrogen, namely deuterium (D) and tritium (T). In a D-T reaction, equal portions of deuterium and

tritium are brought together to make helium-4, and a very high energy neutron (≈ 14 MeV). D-D reactions have less energy output, but produce either helium-3 and a proton, or tritium and a neutron, each with roughly equal probability. Secondary reactions between deuterium and either tritium or helium-3 can produce additional energy. Overall, D-D reactions produce less energy (43.15 MeV for 6 deuterium) than D-T (52.8 MeV for 3 deuterium and 3 tritium) [1]. D-T also has a larger collision cross section, and higher reaction rates than D-D. Therefore, D-T is the high performance fuel that future reactors such as ITER will use [50, 51]; however, experimental reactors such as NSTX-U will use all deuterium fuel [49]. Neutrons cannot be contained by magnetic or electrostatic means; therefore, neutron flux is omnidirectional. D-D reactions have a smaller collisional cross-section than D-T, and require higher temperature to sustain fusion reactions according to the Lawson criterion [52]. Consequently, D-D reactions require temperatures of ~ 100 MK, while D-T can operate at ~ 30 MK. Lower power output from D-D reactions is expected, and correspondingly less neutron flux. This results in fewer issues from material activation. Furthermore, using deuterium exclusively has no concerns from tritium breeding and storage. This permits a more favorable working environment where frequent access to the reactor is needed to facilitate the variety of experiments. However, it should be noted that tritium is a possible product from D-D reactions, so there may be small amounts created that can be hazardous during maintenance periods.

Table 1. D-D and D-T Fusion Reactions [48]

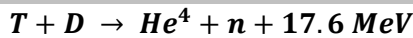
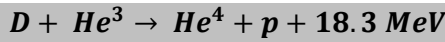
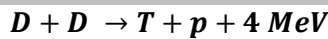
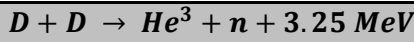


Table 1 shows the energy released from various fusion reactions. These figures exclude the initial kinetic energy of the reactants. The energy produced will be divided among the products as kinetic energy inversely proportional to the mass of each product.

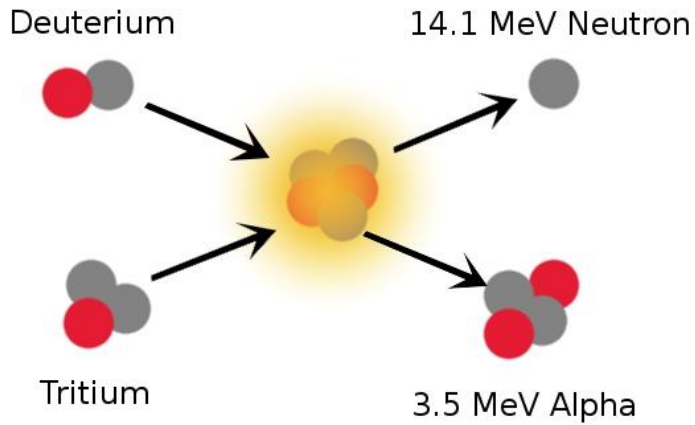
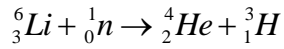


Figure 5. Deuterium-Tritium reaction yielding a neutron and α -particle (helium). 17.6 MeV is released in this reaction as kinetic energy is split between the products. The neutron being the lighter product receives 80% of the energy.

In a D-T reaction, the 14 MeV neutrons are both problematic and beneficial. They are problematic since they are extremely high energy. They can erode materials, and activate materials surrounding the reactor. The biological danger in the reactor room is serious. Heavy neutron shielding is needed around the reactor room. Even with D-D reactions, there are enough secondary reactions creating high energy neutrons to be of concern. A beneficial aspect to high energy neutrons is they can exit the magnetic confinement, and can carry energy out of the reactor. Special blankets will line the reactor to absorb high energy neutrons [53]. Their energy is then converted to heat for steam turbines. They can also be used to breed tritium, which serves as the moderator and breeder.

Fuel can be drawn from the ocean in large parts to obtain deuterium, which is found in naturally occurring heavy water. No naturally occurring tritium is found on Earth due to its short 12.3 year half-life; however, tritium can be bred on demand by striking lithium-6 with a neutron. Since high energy neutrons are the product of fusion reactors, these can be used to breed tritium on site. The lithium-6 isotope accounts for about 10% of naturally occurring lithium. Since it is an alkaline metal, it is not found in elemental form, but locked into other minerals, such as Li_4SiO_4 , Li_2ZrO_3 , or Li_2TiO_3 . Lithium is found in abundance in Argentina, Chile, Bolivia, and other places. However, it should be noted that due to the popularity of lithium ion batteries, lithium supply may become a concern. Afghanistan is believed to have possibly the world's largest supply, but political issues there could be problematic. The waste products from fusion are not radioactive; however, there are some radioactive concerns. Tritium is a low energy beta emitter. In large quantities, storage and handling must be carefully performed. High energy neutrons can activate other materials. Many materials exposed to these neutrons are unsafe for a period of time, but decay to safe levels within hours, days, or a few years depending on the exposure level. These concerns pale in comparison to fission reactors, and should not be weighed too heavily.



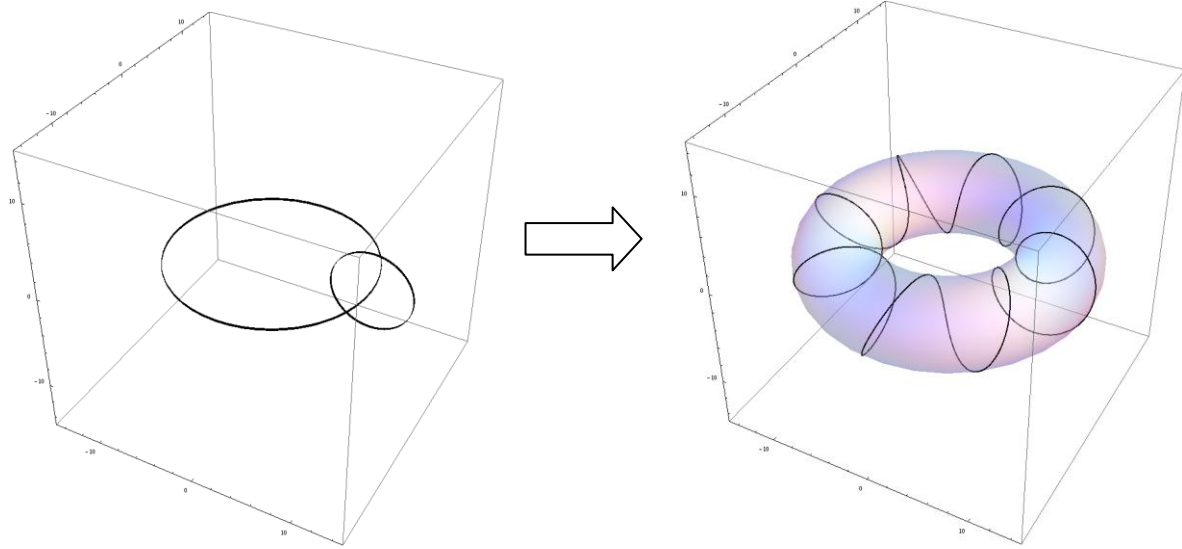
In order to fuse colliding nuclei, the Coulomb barrier must be overcome until they make contact. At very short distances, the nuclear force will dominate Coulomb repulsion and the product atom is formed. To achieve this, the reactants are heated so that they contain sufficient kinetic energy to overcome the Coulomb barrier. Approximately 100 million degrees, or 10 keV, are needed for a D-D reaction [48]. Heating reactants to 100 million degrees generates fully ionized plasma comprised of ions and electrons. Although the gases are ionized, they are quasi-neutral, containing equal numbers of ions and electrons. Containment of gases at these temperatures is non-trivial. The most promising containment technique for a commercial fusion power plant is to employ magnetic fields. Charged particles are confined by

magnetic field lines, and will maintain fusion temperatures and protect the surrounding containment vessel. However, there are many mechanisms that hamper containment, making fusion technology extremely challenging. Failure to contain the plasma will allow the gases to cool and quench the fusion process. There are several magnetic confinement configurations in use around the world. To date, the most successful designs are tokamaks.

I.4 Tokamaks

Among magnetic confinement fusion reactors, the tokamak is a popular configuration [48]. There are several competing magnetic confinement schemes, such as stellarators, reverse field pinches, mirror machines, and others; however, the most successful reactors to date have been tokamaks. Many nations have current fusion research projects using Tokamaks such as: JET and MAST in the United Kingdom, K-STAR in South Korea, EAST and HL-2A in China, ASDEX-U in Germany, DIII-D and NSTX in the United States, and the international cooperation to build ITER in southern France.

Tokamak is a Russian acronym for "тороидальная камера с магнитными катушками", meaning "toroidal magnetic chamber". They consist of a torus shaped vessel to house the fusion fuel. Toroidal field coils generate a strong magnetic field that encircles the torus. Charged particles moving in a magnetic field are subject to the $v \times B$ force; therefore, they are free to move along magnetic field lines, but when moving perpendicular to field lines they will be steered by the $v \times B$ force, resulting in a circular motion about the field lines, and are confined to the torus shape. A toroidal field alone will not contain a plasma; a poloidal magnetic field is also needed. When the toroidal and poloidal fields are combined, the net magnetic field is helical. In a Tokamak, the poloidal field is created by driving the plasma around the torus, creating an electric current. This current will create a poloidal field around it.



Figures 6a and 6b. Diagram of how toroidal and poloidal fields combine to form a helical magnetic containment field in a tokamak. Left: The large ring represents the toroidal field. The plasma current travels around the tokamak along this path, which in turn generates a poloidal field shown with the smaller ring. Right: The two fields combined form a helical field around the tokamak.

To demonstrate why a poloidal field is necessary, consider a torus with only a toroidal field. Electrons and ions can travel around the torus while circling about magnetic field lines at their cyclotron frequency and radius.

$$\text{Cyclotron frequency} \quad \Omega_c = \frac{qB}{m}$$

$$\text{Cyclotron radius} \quad r_c = \frac{\sqrt{k_b T / m}}{\Omega_c}$$

The magnetic field inside a torus falls off with increasing radius proportional to $1/R$. Therefore, as charged particles orbit about the magnetic field lines, the field will vary from slightly stronger to slightly weaker at the inboard and outboard sides, respectively. This causes the cyclotron radius to vary. With

each orbit, the charged particles will drift up or down in the torus, depending on the sign of the charge. Electrons and ions have opposite charge, so they will drift away from each other. This charge separation begins to build an electric field perpendicular to the magnetic field. Other particles caught in the crossed electric and magnetic fields will experience a radial force outward. Electrons and ions will be quickly transported by this $E \times B$ force to the outer radius of the vessel, thereby removing fusion materials from the core and reducing the core temperature, rendering any chance of fusion impossible.

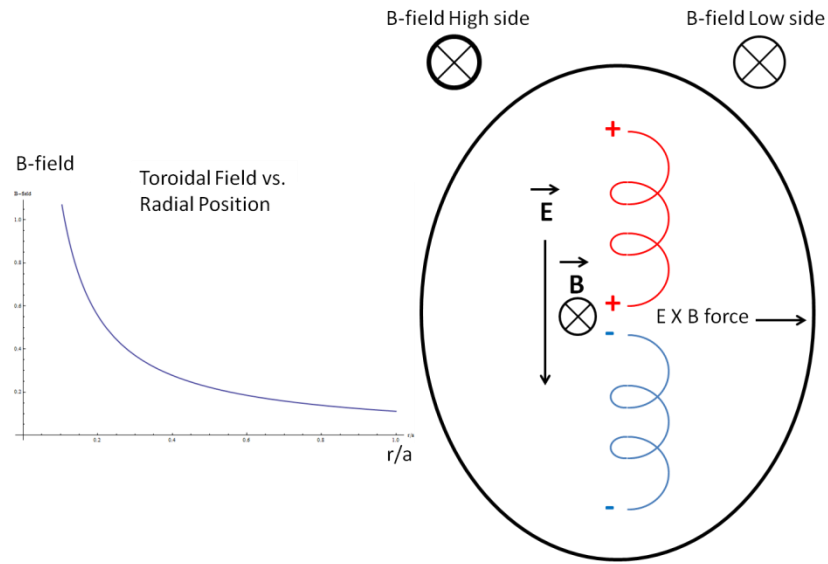


Figure 7. Left: Toroidal magnetic field is proportional to $1/r$ across the cross section of the torus. Right: Torus cross section with a toroidal magnetic field directed into the page. The high field side is on the left, and low field side is on the right. As charged particles orbit about the toroidal field lines their cyclotron radius varies with radial position. In this example, ions will drift upwards, and electrons drift downwards, creating a local electric field. The vertical electric field and toroidal magnetic field create an $E \times B$ force directed to the outer diameter. This will cause the plasma to transport out of the core, demonstrating the need for a poloidal field to reroute particles back to the high field side of the torus.

When a poloidal field is added, the electrons and ions will travel in a helical motion. Particles that experience an outward drift will be redirected back to the interior of the torus. By constantly redirecting

their motion, plasma can be contained. The ratio of how many poloidal turns a magnetic field makes to the number of toroidal turns is called the safety factor “ q ”. In general, the larger q is, the more stable the confinement should be. Magnetic fields in tokamaks are radially dependent; therefore, q will also be radially dependent. Adjusting field strengths and q profiles is one of the ways tokamaks can be tuned for various experimental conditions [55].

There are several methods used to drive the plasma current, and heat the plasma at the same time. Most tokamaks have a solenoid coil in the center of the torus, which when energized will induce a current in the plasma. The ring of plasma acts like a single turn secondary coil in a transformer. This technique is limited, since only a varying magnetic field will induce current. Power is applied to the center coil and systematically increased, but obviously cannot be driven to infinite levels. This technique is limited to pulsed operation; however, the pulse duration can be relatively long with a low dV/dt . This method also heats the plasma through ohmic heating, but this is also limited. As plasmas are heated, their resistance decreases. Ohmic heating can reach a few million degrees, but diminishing returns will limit its effectiveness far below the temperatures needed for fusion. Additional current drive and heating are required. One method is *neutral beam injection* (NBI) [49]. In this case, neutral particles are introduced into the plasma at high energy. Neutral particles can cross field lines and collide with the plasma. Through momentum transfer, the plasma current is increased and heated. Another technique for heating plasmas is *electron cyclotron resonant heating* (ECRH) [49]. Electromagnetic energy is directed into the plasma near the electron cyclotron frequency. Energy transfer from the RF beam to the electrons will heat the plasma. Other plasma resonant frequencies can be exploited through RF heating as well. Through these and other methods, plasma currents can be driven and controlled, and fusion temperatures can be reached.

Plasma density is limited by how hot the plasma is and the strength of the magnetic field. The gas pressure must be balanced by the magnetic containment pressure. The ideal gas law describes the plasma

pressure as the product of density, temperature, and Boltzman's constant, $P=nTk_b$. Magnetic fields also exert a pressure proportional to the field strength squared, $P_m=B^2/2\mu_0$. The ratio of these pressures is the parameter β , which describes the confinement strength. Typical tokamaks operate with β of 0.1 to 0.2.

$$\beta = \frac{nTk_b}{B^2/2\mu_0}$$

Increasing magnetic field strengths creates stronger containment, but practical limits must be realized around a few Tesla. Since high temperatures are required for fusion, and practical field strength limitations exist, the plasma density is restricted to about 10^{14} cm^{-3} .

There are three major factors that will determine how many atoms will actually fuse, and hence, the amount of energy released. First, the atoms must be hot. High kinetic energy will allow colliding atoms to overcome the Coulomb force. Temperature represents an average kinetic energy of the constituent particles. Particles at too low an energy will not overcome the Coulomb barrier. At too high an energy, the collisional cross section of the particles is reduced to a point where collisions are too rare. Therefore, depending on the particles in question there will be an ideal range of temperatures for optimum fusion. Typical fusion temperatures of around 100 million K are needed. The next two factors are related to how many collisions one can expect. The density of reactants and the amount of time the reactor is operating will determine how many atoms actually fuse. Typical fusion plasma densities are on the order of 10^{14} cm^{-3} ($\sim 1/100,000$ of standard atmosphere). Plasma density is limited by the strength of magnetic fields. Typical magnetic confinement ranges from about 1 to 5 T, thereby restricting plasma density to rather low levels. At these temperatures and pressures, plasma confinement must be maintained for several seconds to approach break even power generation, $Q > 1$ [48]. Several minutes of containment, up to an hour or more, with a 50% duty cycle are needed to be commercially viable. Many problems have become apparent that impede confinement times. Chief among these problems is diffusion due to

anomalous transport [54]. Calculations show that classical transport of fusion plasmas across magnetic field lines should be contained for ample periods of time to allow excellent fusion power generation to take place (~ 30 minutes) [56]. However, in practice, current containment times are measured from milliseconds to about a second. There are several competing theories to explain what causes anomalous transport, and how to deal with it. Through the use of plasma diagnostics, plasma properties can be measured and studied. With this information, we can learn how to better confine fusion plasmas, and work towards a commercially viable fusion power plant.

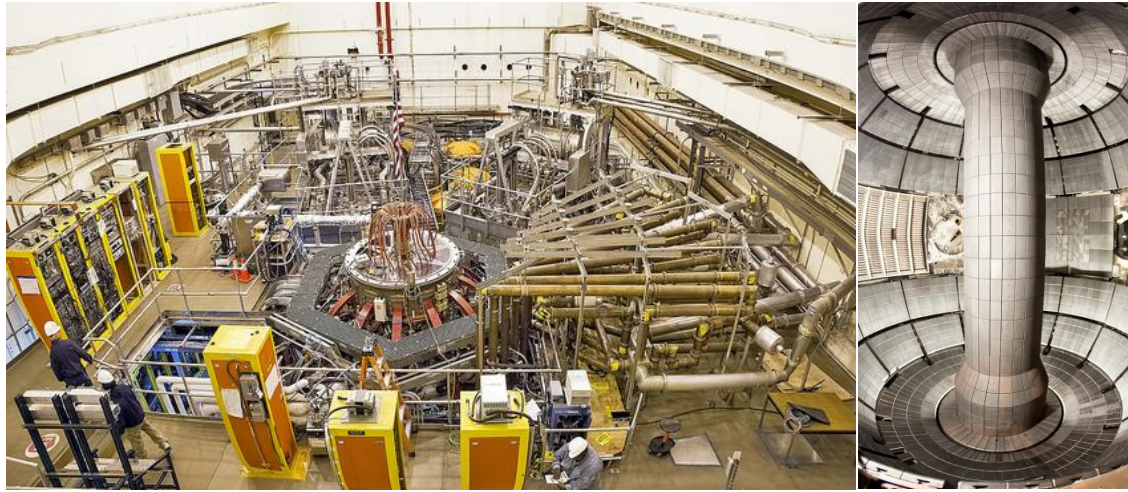
I.5 NSTX-U

NSTX-U is the *National Spherical Torus Experiment Upgrade*, located at the *Princeton Plasma Physics Laboratory* (PPPL). This experimental fusion reactor recently underwent a major upgrade; it was previously known as NSTX. Upgrades to NSTX include a second neutral beam injector (10 MW each), double its previous toroidal magnetic field (from 0.5 to 1.0 T), and double the plasma current (1.0 to 2.0 MA) [53]. The upgrade is expected to provide better confinement and improved power output [53]. Table 2 shows a list of typical NSTX and NSTX-U parameters.

Table 2. NSTX/NSTX-U Parameters [54]

Property	NSTX	NSTX-U
Major Radius (m)	0.86	0.93
Minor Radius (m)	0.57	0.62
Aspect Ratio	1.5	1.5
Toroidal Field (T)	0.45	1.0
Plasma Current (MA)	1.0	2.0
Electron Temperature (KeV)	1.0	1.7
Plasma Density (cm⁻³)	5×10^{13}	1.5×10^{14}
Plasma Frequency (GHz)	64	110
Debye Length (μm)	33	25
Electron Cyclotron Frequency (GHz)	12.6	28
Electron Cyclotron Radius (μm)	170	100

The aspect ratio of a torus is defined as the minor radius divided by the major radius. NSTX-U has a major radius of 0.93 m and a minor radius of 0.62 m, for a ratio of 1.5. Low aspect ratio tokamaks are sometimes referred to as *spherical tokamaks* (STs), as opposed to conventional tokamaks such as DIII-D, with an aspect ratio of 2.7 [53]. NSTX-U does not utilize a central solenoid for initial current drive and ohmic heating due to the small diameter of the center stack. It relies on neutral beam injection (NBI) to initiate plasma heating. Once fusion is initiated, bootstrap currents will sustain the plasma current, and the NBI can be significantly reduced or turned off. Additional plasma heating is provided by Electron Cyclotron Resonant Heating (ECRH). NSTX-U is designed to have improved confinement with less toroidal magnetic fields of comparable conventional Tokamaks. [54]



Figures 8a and 8b. Left: View of the NSTX-U test cell. NSTX-U is circled in red. Right: Interior view of NSTX-U. Photos courtesy of Princeton Plasma Physics Laboratory.

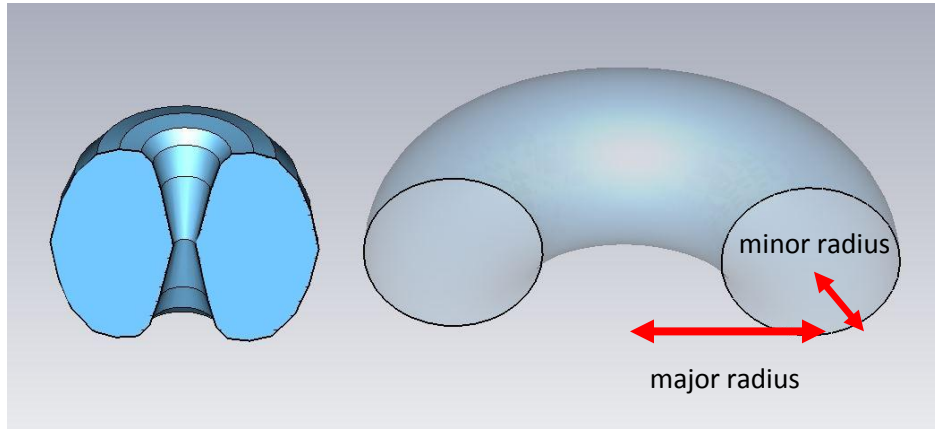


Figure 9. Cutaway view of tokamak interior. The left shows a low aspect ratio (≈ 1.3), spherical tokamak. The right side is a conventional tokamak with an aspect ratio of 3.

Current research at PPPL has theorized that *Electron Temperature Gradient* (ETG) modes could be a major contributor to anomalous transport. Previous work in the low- k region (k is the wavenumber) showed that *Ion Temperature Gradient* (ITG) modes could be suppressed with magnetic shear and safety factor profiles (s/q) [64]. ETG modes are predicted to have similar properties, and may be controlled by

similar manners. ETG mode research is needed to verify the causes of electron scale turbulence, characterize its properties, and suggest how to suppress it. Computer simulations have modeled ETG modes for NSTX [57]. If the computer codes in use can be validated, then research can be further enhanced. NSTX-U offers a unique opportunity to study these phenomena. A vertical rectangular window has been installed to allow the measurements of poloidally scattered signals from a probe beam of 500 GHz to 1 THz. Figure 15 shows a color map of simulated ETG mode k spectrum with the coverage of the *High-k Scattering System* overlaid. The ETG modes measured by this instrument can be compared to computer simulations so that they can be verified and benchmarked.

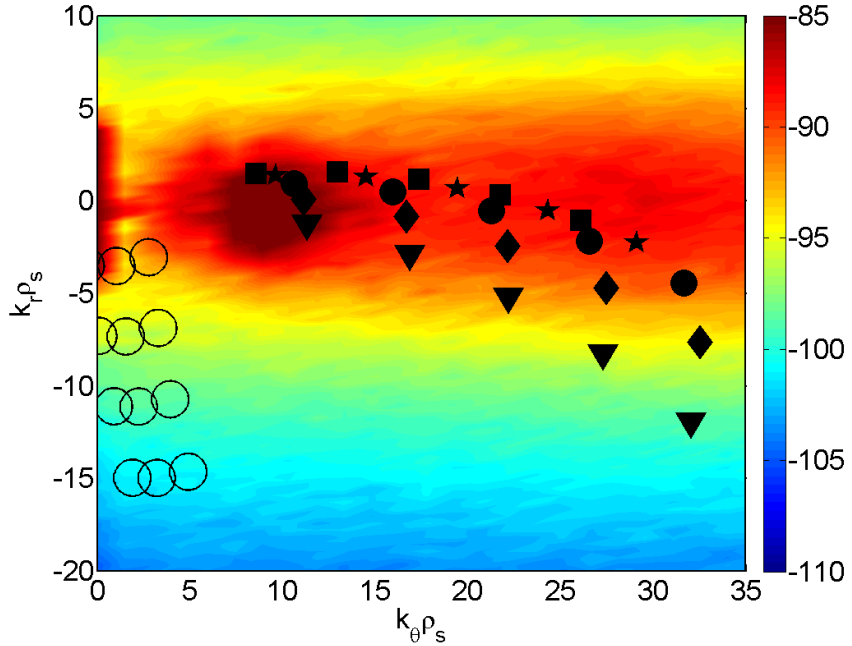


Figure 10. Computer simulation of predicted ETG modes in NSTX-U. The central peak is shown in dark red. The open circles show the coverage of the former *High-k Scattering System*. The black symbols show the coverage of the new *High-k Scattering System* under various conditions. Note: the former *High-k Scattering System* was designed to primarily measure toroidal wavenumbers [65], so its poloidal coverage was incidental. The new *High-k Scattering System* will target poloidal wavenumbers from 7 to 40 cm^{-1} . Image courtesy of Dr. Yang Ren and Dr. Walter Guttenfelder, PPPL.

I.6 Anomalous Transport

Particle and thermal transport describes the ways in which fusion reactors lose confinement, i.e. when particles are transported from the core to the outer edges of a Tokamak, or when their energies are transported out of the core. There are many types of transport that are induced by a variety of conditions [57]. Classical diffusion of plasma shows that through collisions, particles may slowly cross field lines, thereby quenching the fusion process. This type of transport is slow enough to not be a concern for fusion power, but observed confinement times are many orders of magnitude less ($\mu\text{s} < \text{confinement} < \text{s}$). The mechanisms that cause this accelerated transport are not fully understood, therefore referred to as anomalous.

To better understand factors that contribute to anomalous transport, we should first review classical diffusion. Charged particles circling about magnetic lines can cross over field lines through collisions. In an elastic collision, energy and momentum are conserved, but the colliding particles may bounce in new directions. For magnetized plasma, ions and electrons may acquire new guiding centers, and orbit them until their next collision, and so on. [58]

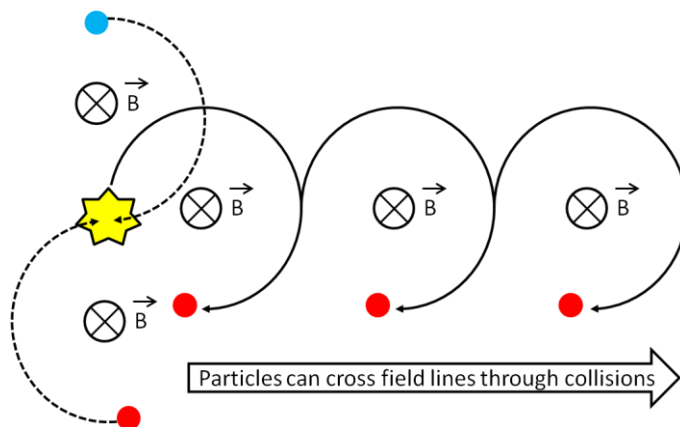


Figure 11. Particles orbiting magnetic field lines may collide, and take on new guiding centers. In the absence of a density gradient, the net drift averages out to a null effect. With a density gradient, the

particles will drift from high concentration to low concentration. The classical diffusion rate is proportional to collision rate and the step size squared. In a magnetized plasma, the step size is effectively the cyclotron radius.

This process of colliding and stepping over is random in direction. If the density of particles is constant, then there is no net diffusion. However, in the presence of a density gradient, particles will diffuse from high concentrations to low. The same phenomenon is seen with heat flow and concentrations of particles in a fluid. The rate of material flux is described by Fick's law.

$$J = -D \nabla \rho$$

where J is the material flux (per area per unit time), ρ is the material density, and D is the diffusion coefficient. The diffusion coefficient depends on the step length squared, divided by the time between steps. In a magnetized plasma, this is the cyclotron radius and collision frequency. In a typical fusion plasma, D^{-1} is roughly the confinement time, which is on the order of 30 minutes. Clearly, there are other mechanisms in fusion plasmas that reduce confinement time dramatically.

Energetic plasmas contain large amounts of free energy, which can drive instabilities. Non-quiescent, non-homogeneous plasmas can experience various types of turbulence depending on the conditions. Turbulent conditions create conditions where particle motion is much greater than cyclotron radii. Since the diffusion constant is proportional to step size squared, this can result in greatly increased transport. If a particular type of transport can be identified and isolated, then its contribution to overall anomalous transport can be quantified. Furthermore, the conditions needed to induce specific types of turbulence, and the remedies to suppress or eliminate them can be identified.

I.7 Drift Waves and ETG Modes

A particular type of turbulence that is of interest in NSTX-U is associated with *electron temperature gradient* (ETG) modes. These modes belong to a class of waves found in tokamaks called drift waves. Drift waves are not necessarily unstable; however, if they become unstable, they can lead to significant transport.

Drift waves are a group of phenomena that can lead to instabilities. If small fluctuations in plasma density become unstable, they will grow. Large fluctuations enable particles to rapidly jump across magnetic field lines. For example, if an electron cyclotron radius of 0.1 mm leads to a diffusion time of 30 minutes, and then turbulent action increased effective electron orbits to 10 mm, the diffusion time would be reduced by a factor of 10,000, or 180 ms. Of the many types of drift waves, the Electron Temperature Gradient (ETG) modes are of particular interest. These modes are believed to be a major source of electron turbulence, and therefore anomalous transport [59].

Drift waves are initiated by a gradient in particle density or temperature. Electrons orbiting their respective magnetic field lines constitute a small local current. Much like surface currents in a magnet, if there is a local imbalance of electron motion, there will be a net diamagnetic current. In a magnetized plasma, the cyclotron radius depends on the electron temperature, with an increased temperature resulting in a larger orbit. Two neighboring electrons will be moving in opposite directions as their orbits pass by each other. Assuming the same magnetic field, they orbit with the same frequency, but the larger orbit will constitute a larger current, and the net electron flow will favor the hotter electron. [58]

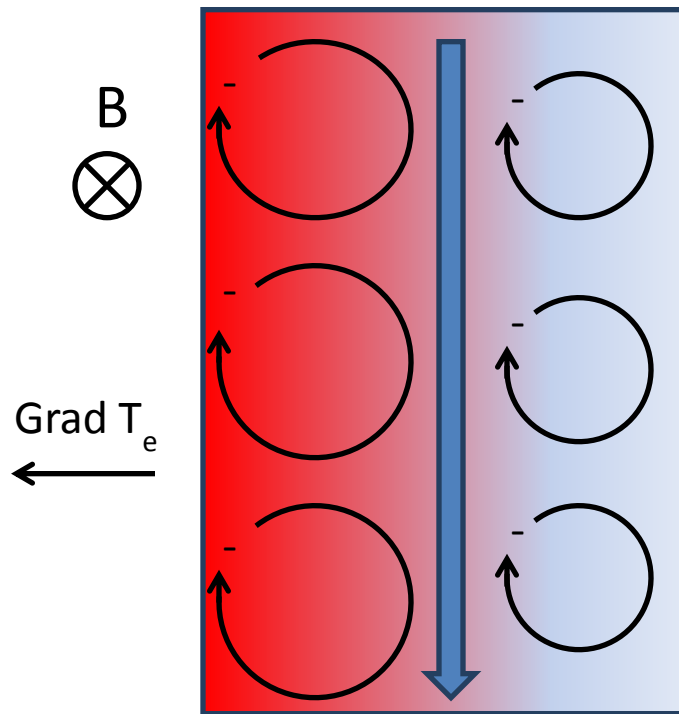


Figure 12. The net flow of electrons due to a temperature gradient in a magnetized plasma, with higher temperatures on the left (red). The blue arrow shows the net effective electron flow.

It should be noted that the electrons do not travel from their initial orbits. The observed diamagnetic current is a net current due to the mismatch of orbital radius. The core plasma is generally the hottest, so these currents travel poloidally around the core, orthogonal to the temperature gradient and magnetic field. Using the conventional current definition, the current travels opposite the net electron flow.

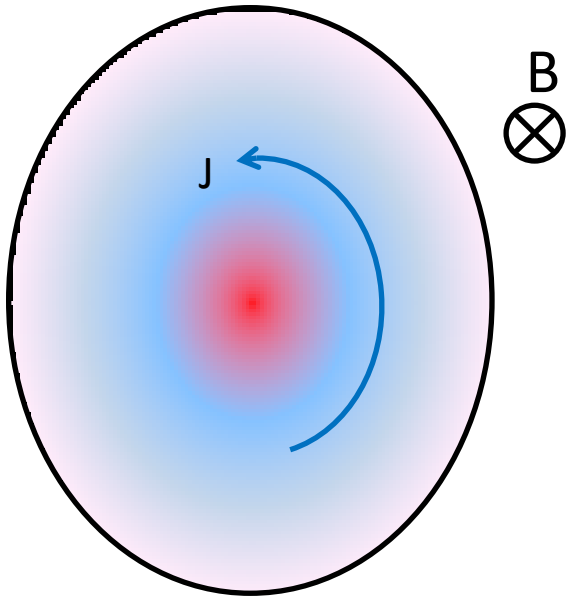


Figure 13. Cross sectional toroidal view of a tokamak, with the hot core plasma at the center. The blue arrow shows the poloidal diamagnetic current caused by temperature gradients in a magnetized plasma.

Initially, these currents do not appear to present a problem. Any inward force ($q(v \times B)$) will be balanced by an equal and opposite pressure from the familiar magnetohydrodynamic (MHD) equilibrium:

$$J \times B = \nabla P$$

Any density perturbations should oscillate in the radial direction, and will travel with the poloidal current as a drift wave. Drift waves can travel at several hundred meters per second, and exhibit a relatively low frequency of < 1 MHz. They will remain stable so long as there are no charge separations between ions and electrons. For the time scale of several μ s, ions are seen to be adiabatic, while electrons are isothermal. Any electric field due to the build-up in ion density will be canceled out by electrons repositioning themselves. However, if there is a phase difference between density and potential fluctuations, then local electric fields will appear due to charge separation. Electric fields oriented along the drift wave propagation will be perpendicular to the magnetic field, resulting in an $E \times B$ force. This force will increase the drift wave amplitude and destabilize it. [58]

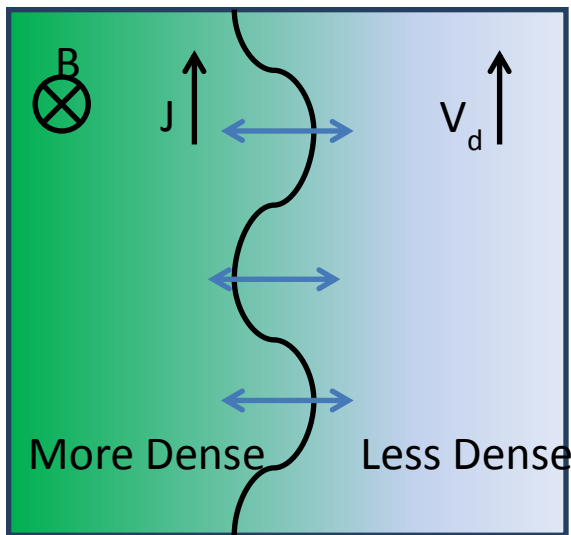


Figure 14. Drift waves perpendicular to magnetic fields and the gradients that caused them. They are seen as plasma material oscillating radially.

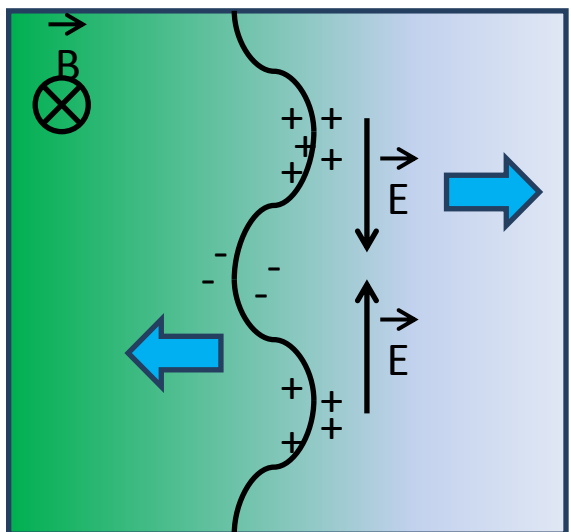


Figure 15. Any phase difference between density and electrostatic waves will create local electric fields. $\mathbf{E} \times \mathbf{B}$ forces will cause the drift wave amplitude to grow, making them unstable. When the amplitude of these waves grow to the point of causing electron transport due to temperature gradients, they are called ETG modes.

Only in an idealized plasma will drift waves be stable. Electron mass and collisions will impede their mobility enough for drift waves to become unstable. Even in a collisionless plasma, Landau damping will have the same effect.

Scientists at PPPL believe ETG modes are a major contributor to anomalous transport in NSTX. Research is needed to study the conditions of how ETG modes form and grow, as well as the types of remedies that

can be employed to suppress or control them [60, 61]. Since this type of instability begins on the electron cyclotron scale, a diagnostic instrument needs to be designed to measure these modes [62, 63].

I.8 Instrumentation

In support of continuing fusion research, it is essential to collect data from experimental reactors. The complexity of plasma physics and scale of physics observed in fusion reactors limit the usefulness of computer simulations. The computer simulations are improving, but can account for only small portions of a fusion reactor [66, 67]. Many theories are untested, and must be verified by experiment to move research forward. It is the development and application of plasma diagnostic instruments that will provide the data needed. This dissertation has focused on two distinct diagnostics for use on the *National Spherical Torus Experiment - Upgrade* (NSTX-U). These systems are the *Far Infrared Tangential Interferometer and Polarimeter* (FIReTIP), and the *High-k Scattering System*. While distinct in their purposes, these instruments have a shared history and have some similarities. Namely, they are both far infrared (FIR) laser based diagnostics, they are both designed for use on NSTX-U, and their laser systems will share the same space at PPPL. It should be understood that both of these systems were developed by UC Davis [68, 69], and were installed on NSTX in 2001/2004, FIReTIP and High-k Scattering respectively. Upgrades to NSTX required the removal and redesign of these instruments, at the same time offering an opportunity to enhance their functionality. These instruments will persist for many years after this dissertation, and will continue to be developed and improved by others. The author's principal contributions to the *FIReTIP* and *High-k Scattering* systems are the redesign, fabrication, and implementation of these plasma diagnostics.

I. References

- [1] "Internation Energy Outlook 2016," *U.S. Energy Information Administration*, DOE/EIA-0484(2016), May 2016.
- [2] "Monthly Energy Review," *U.S. Energy Information Administration*, March, 2015.
- [3] "Clean Air Act," 42 U.S.C. §7401 et seq. (1970).
- [4] A. Liptak and C. Davenport, "Supreme Court Deals Blow to Obama's Efforts to Regulate Coal Emissions," *The New York Times*, Feb. 9th, 2016.
- [5] J. Worland, "Why Trump's Promise to Save the Coal Industry Does More Damage than Good," *Time Magazine*, Aug. 12th, 2016.
- [6] M. Egan, "Why Venezuela's Oil Production Plunged to a 13-Year Low," *CNN Money*, <http://money.cnn.com/2016/07/12/investing/venezuela-crisis-oil-production-plunges/>, accessed Oct. 11, 2012, 1:57 EST, July 12th, 2016.
- [7] "Obama Administration Imposes Five-Year Drilling Ban on Majority of Offshore Areas," *House Committee on Natural Resources*, <http://naturalresources.house.gov/newsroom/documentsingle.aspx?DocumentID=267985>, Press release: Nov. 8th, 2011.
- [8] E. Shogren, "For 30 Years, a Political Battle Over Oil and ANWR," *National Public Radio*, transcript: <http://www.npr.org/templates/transcript/transcript.php?storyId=5007819>, accessed Oct. 11, 2012, 12:00 am EST, Nov. 10th, 2005.
- [9] "Final Supplemental Environmental Impact Statement: Keystone XL Project," United States Dept. of State, <https://keystonepipeline-xl.state.gov/finalseis/index.htm>, January, 2014.
- [10] G. Korte and D. Jackson, "Obama Administration Rejects Keystone Pipeline," *USA Today*, <http://www.usatoday.com/story/news/politics/2015/11/06/obama-reject-keystone-pipeline/75293270/>, 2:30 pm EST, November 6th, 2015.
- [11] D. Kirk, "How Fracking Contributes to Oil Glut, Cheap Fuel for You and Me," *Forbes*, <http://www.forbes.com/sites/donaldkirk/2015/01/26/how-fracking-contributes-to-oil-glut-cheap-fuel-for-you-and-me/#292396ef2699>, Jan. 26th, 2015.
- [12] "Oil and Gas; Hydraulic Fracturing on Federal and Indian Lands; Final Rule," *Dept. of the Interior, Bureau of Land Management, Federal Register*, Vol. 80, No. 50, March 26, 2015.
- [13] S. Ori, "Yes Donald Trump Can Increase U.S. Oil Production," *Forbes*, <https://www.forbes.com/sites/ucenergy/2016/12/15/yes-donald-trump-can-increase-u-s-oil-production/#1e14f9744b4c>, December 15th, 2016.
- [14] "Construction Cost Data for Electrical Generators Installed in 2014," *U.S. Energy Information Administration*, <http://www.eia.gov/electricity/generatorcosts/>, February 25th, 2017.
- [15] "Construction Cost Data for Electrical Generators Installed in 2013," *U.S. Energy Information Administration*, <http://www.eia.gov/electricity/generatorcosts/>, June 3rd, 2016.

- [16] "Levelized Cost and Levelized Avoided Cost of New Generation Resources in the Annual Energy Outlook 2015," *U.S. Energy Information Administration*, Anual Energy Outlook 2105 (AEO 2015), June 2015.
- [17] M. Green, K. Emery, Y. Hishikawa, W. Warta, and E.D. Dunlop, "Solar Cell Efficiency Tables (Version 45)," *Prog. Photovolt: Res. Appl.*, 23: 1-9, Oct. 2014.
- [18] "Space-Based Solar Power," *Energy.gov*, <https://www.energy.gov/articles/space-based-solar-power>, March 6th, 2014.
- [19] R. Gopalswami, "An International Preliminary Feasibility Study on Space Based Solar Power Stations," *Kalam-National Space Society Energy Technology Universal Initiative*, September 12th 2008.
- [20] "Overview of Wind Energy in California," *California Energy Commission*, <http://www.energy.ca.gov/wind/overview.html> accessed Oct. 12, 2016.
- [21] "Wind Power," *National Geographic*, <http://environment.nationalgeographic.com/environment/global-warming/wind-power-profile/>, accessed: Oct. 12th, 2016.
- [22] P. Gilman et al., "National Offshore Wind Strategy," *U.S. Deptarment of Energy and U.S. Department of the Interior*, <http://energy.gov/eere/wind/downloads/national-offshore-wind-strategy-facilitating-development-offshore-wind-industry>, 2016.
- [23] B.C.P. Lau, E.W.M. Ma, "Review of Offshore Wind Turbine Failures and Fault Prognostic Methods," *Prognostics & System Health Management Conference (PHM-2012)*, Beijing, 2012.
- [24] "The first decommission in the World of an Offshore Wind Farm is Now Complete," *Vattenfall*, Press release, Jan. 25th, 2016.
- [25] P. Crawford, "'Hydro' Hindered by Environmentalist Dam," *The New York Times*, December 6th, 1993.
- [26] "California Electrical Energy Generation," *California Energy Commission*, http://www.energy.ca.gov/almanac/electricity_data/electricity_generation.html, July 27th, 2016.
- [27] "Annapolis Tidal Station," *Nova Scotia Power*, <http://www.nspower.ca/en/home/about-us/how-we-make-electricity/renewable-electricity/annapolis-tidal-station.aspx>, accessed Oct. 12th, 2016.
- [28] R. Blackwell, "Bay of Fundy Tidal Power Soon to be Harnessed," *The Globe and Mail*, May 17th, 2015.
- [29] "Where is the highest tide?" *National Oceanic and Atmospheric Administration*, <http://oceanservice.noaa.gov/facts/highesttide.html>, accessed Oct. 12th, 2016.
- [30] "Geothermal," *Orkustofnum: National Energy Authority*, <http://www.nea.is/geothermal/>, Accessed: Oct. 12th, 2016.
- [31] "Monthly Energy Review," *U.S. Energy Information Administration*, September, 2016.

- [32] E. Landau, "Why does 'nuclear' scare us so much?" *CNN*, 2:19 pm EDT, March 28th, 2011.
- [33] "Three Mile Island Accident," *U.S. Nuclear Regulatory Commission*, <http://www.nrc.gov/reading-rm/doc-collections/fact-sheets/3mile-isle.html>, Dec. 12th, 2014.
- [34] Walker, J. Samuel, "Three Mile Island: A Nuclear Crisis in Historical Perspective," *Berkeley: University of California Press*, 2004.
- [35] "Chernobyl Nuclear Power Plant Accident," *U.S. Nuclear Regulatory Commission*, <http://www.nrc.gov/reading-rm/doc-collections/fact-sheets/chernobyl-bg.pdf>, May 2003.
- [36] M. Rahu, "Health Effects of the Chernobyl Accident: Fears, Rumours, and the Truth," *European Journal of Cancer*, Vol. 39, Is. 3, pp. 295-299, Feb. 2003.
- [37] "Chernobyl Accident and its Consequences," *Nuclear Energy Institute*, <http://www.nei.org/master-document-folder/backgrounder/fact-sheets/chernobyl-accident-and-its-consequences>, March 2015.
- [38] M. Grimston, "Fukushima: What happened - and what needs to be done," *BBC News*, <http://www.bbc.com/news/world-asia-pacific-13017282>, April 11th, 2001.
- [39] "Levels and effects of radiation exposure due to the nuclear accident after the 2011 great east-Japan earthquake and tsunami," *UNSCEAR 2013 Report*, Vol. 1, Scientific Annex A, United Nations, New York 2014.
- [40] "Five and a half years after Fukushima, 3 of Japan's 54 nuclear reactors are operating," *U.S. Energy Information Administration*, <http://www.eia.gov/todayinenergy/detail.php?id=27912>, September 13, 2016.
- [41] R. Riffkin, "For First Time, Majority in U.S. Oppose Nuclear Energy," *Gallup Poll*, <http://www.gallup.com/poll/190064/first-time-majority-oppose-nuclear-energy.aspx>, March 18th, 2016.
- [42] K. Muraoka, F. Wagner, Y. Yamagata, and A.J.H. Donne, "Short- and long-range energy strategies for Japan and the world after the Fukushima nuclear accident," *17th International Symposium on Laser-Aided Plasma Diagnostics (LAPD17)*, Journal of Instrumentation, Vol. 11, January 2016.
- [43] K. Muraoka, F. Wagner, and Y. Yamagata, Allowable limit of renewable energy into electricity systems, submitted for publication in J. Elect. Eng. Japan (in Japanese with an English abstract and figure/table captions).
- [44] A. Harder, "Can the U.S. Government Revive Nuclear Power?" *The Wall Street Journal*, <http://www.wsj.com/articles/can-the-u-s-government-revive-nuclear-power-1416777789>, 4:23 pm EST, Nov. 23, 2014.
- [45] C. M. Braams and P. E. Stott, "Nuclear Fusion," Institute of Physics Publishing, Bristol and Philadelphia, 2002.
- [46] K. Hamada, "Anti-nuclear novice wins Japan election, blow to nuclear restarts," *Reuters*, <https://www.yahoo.com/news/japan-antinuclear-candidate-leading-election-key-nuclear-restarts-120246320--finance.html>, October 16, 2016.

- [47] Muraoka K., "Energies in the coming age for Japan", Sangyo-Toshu Publishing, Tokyo, 2012 (a book published in Japanese).
- [48] R. Post, "Controlled Fusion Research - An Application of the Physics of High Temperature Plasmas," *Reviews of Modern Physics*, vol. 28, no. 3, pp. 338-362, 1956.
- [49] M. Peng, "Spherical Torus Pathway to Fusion Power," *Journal of Fusion Energy*, vol. 17, no. 1, pp. 45-59, 1998.
- [50] "ITER, the way to new energy," ITER Organization, 2016. [Online]. Available: <http://www.iter.org/sci/Goals>. [Accessed 10 5 2016].
- [51] I.Ricapito, A. Ciampichetti, R. Laesser, Y. Poitevin, and M. Utili, "Tritium Extraction from Liquid Pb-16Li: A Critical Review of Candidate Technologies for ITER and DEMO Applications," *Fusion Science and Technology*, vol. 60, no. 3, pp. 1159-1162, 2011.
- [52] J.D. Lawson, "Some Criteria for a Useful Thermonuclear Reactor," *Atomic Energy Research Establishment UK*, Harwell, Berks, 1955.
- [53] R.J. La Haye, R.J. Buttery, S.P. Gerhardt, S.A. Sabbagh, and D.P. Brennan, "Aspect ratio effects on neoclassical tearing modes from comparison between DIII-D and National Spherical Torus Experiment," *Physics Of Plasmas*, Vol. 19, 062506, June 2012.
- [54] J.E. Menard et al., "Overview of the Physics and Engineering Design of NSTX Upgrade," *Nuclear Fusion*, vol. 52, no. 083015, 2012.
- [55] J. Citrin, J. Hobrik, M. Schneider, J.F. Artaud, C. Bourdelle, K. Crombe, G.M.D. Hogeweij, F. Imbeaux, E. Joffrin, F. Koechl, J. Stober, the ASDEX Upgrade Team, JET-EFDA contributors, and the ITM-TF ITER Scenario Modelling group, "Predictive Analysis of q-profile Influence on Transport in JET and AUG Hybrid Scenarios", *Plasma Physics and Controlled Fusion* 54, 065008 (2012).
- [56] A. Simon, "Diffusion of Like Particles Across a Magnetic Field," *Physical Review*, vol. 100, no. 6, pp. 1557-1559, 1955.
- [57] W. Guttenfelder, J. Candy, S.M. Kaye, W.M. Nevins, E. Wang, J. Zhang, R.E. Bell, N.A. Crocker, G.W. Hammett, B.P. LeBlanc, D.R. Mikkelsen, Y. Ren, and H. Yuh, "Simulation of Microtearing Turbulence in National Spherical Torus Experiment," *Physics of Plasmas*, vol. 19, no. 056119, 2012.
- [58] F.Chen, *Introduction to Plasma Physics and Controlled Fusion*, New York: Plenum Press, 1984.
- [59] Y. Ren, W. Guttenfelder, S.M. Kaye, E. Mazzucato, R.E. Bell, A. Diallo, C.W. Domier, B.P. LeBlanc, K. C. Lee, D.R. Smith, and H. Yuh, "Experimental Study of Parametric Dependence of Electron-Scale Turbulence in a Spherical Tokamak," *Physics of Plasmas*, vol. 19, no. 056125, 2012.
- [60] D.R. Smith, E. Mazzucato, T. Munsat, H. Park, D.W. Johnson, L. Lin, C.W. Domier, M. Johnson, and N.C. Luhmann Jr., "Microwave Scattering System Design for p_e Scale Turbulence Measurements on NSTX," *Review of Scientific Instruments*, vol. 75, no. 10, pp. 3840-3842, 2004.
- [61] Y. Ren, S.M. Kaye, E. Mazzucato, W. Guttenfelder, R.E. Bell, C.W. Domier, B.P. LeBlanc, K.C. Lee, N.C. Luhmann Jr., D.R. Smith, and H. Yuh, "Density Gradient Stabilization of Electron Temperature

Gradient Driven Turbulence in a Spherical Tokamak," *Physical Review Letters*, vol. 106, no. 165005, 2011.

[62] P. Woskoboinikow, D.R. Chon, and R.J. Temkin, "Application of Advanced Millimeter/Far-Infrared Sources to Collective Thomson Scattering Plasma Diagnostics," *International Journal of Infrared and Millimeter Waves*, vol. 4, no. 2, pp. 205-229, 1983.

[63] S.B. Korsholm, H. Bindslev, V. Furtula, F. Leipold, F. Meo, P.K. Michelsen, D. Moseev, S.K. Nielsen, M. Salewski, and M. Stejner, "Collective Thompson Scattering Capabilities to Diagnose Fusion Plasmas," *Nuclear Instruments and Methods in Physics Research A*, vol. 623, pp. 677-680, 2010.

[64] J. Citrin, J. Hobrik, M. Schneider, J.F. Artaud, C. Bourdelle, K. Crombe, G.M.D. Hogeweij, F. Imbeaux, E. Joffrin, F. Koechl, and J. Stober, "Predictive Analysis of q-profile Influence on Transport in JET and ASDEX Upgrade Hybrid Scenarios," *Plasma Physics and Controlled Fusion*, Vo. 54, No. 6, 23 May 2012.

[65] D.R. Smith, S.M. Kaye, W. Lee, E. Mazzucato, H.K. Park, R.E. Bell, C.W. Domier, B.P. LeBlanc, F.M. Levinton, N.C. Luhmann Jr., J.E. Menard, and H. Yuh, "Electron Gyroscale Fluctuation Measurements in National Spherical Torus Experiment H-Mode Plasmas," *Physics of Plasmas*, Vol. 16, No. 112507, 2009.

[66] W.M. Tang, V.S. Chan, "Advances and Challenges in Computational Plasma Science," *Plasma Phys. Control Fusion*, 47, R1-R34, 2005.

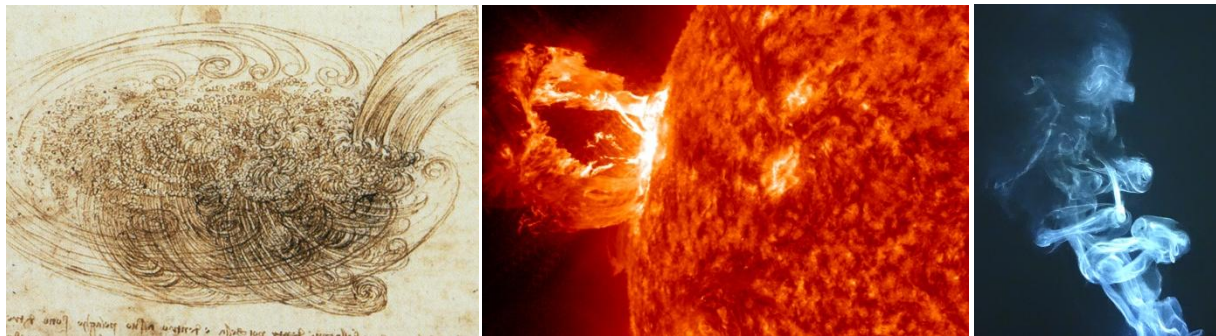
[67] A. Fasoli, S. Brunner, W. A. Cooper, J. P. Graves, P. Ricci, O. Sauter, and L. Villard, "Computational challenges in magnetic-confinement fusion physics," *Nature Physics*, 12, 411–423 (2016).

[68] K.C. Lee, C.W. Domier, M. Johnson, N.C. Luhmann, Jr., and H. Park, "FIR Laser Tangential Interferometry/Polarimetry on NSTX," *IEEE Transactions on Plasma Science*, 32 No. 4, pp. 1721-1726 (2004).

[69] W. Lee, H.K. Park, M.H. Cho, W. Namkung, D.R. Smith, C.W. Domier, and N.C. Luhmann, Jr. "Spatial Resolution Study and Power Calibration of the High-k Scattering System," *Review of Scientific Instruments*, 79, 10E723 (2008).

II. Plasma Diagnostics

Many experts have predicted that a viable fusion power plant is approximately 30 years away [1]. At current funding levels, there are some who are even less optimistic, but agree that the barriers to fusion power can be solved in the coming decades with increased funding [1]. Of the three primary conditions necessary for fusion power to release sufficient energy to be useful (temperature, density, and confinement time), increasing confinement time is the key element. High temperature, confined plasma contains a surfeit of free energy, which can drive instabilities, which in turn lead to loss of confinement. In the case of the aforementioned drift waves, under certain conditions, these waves can create turbulent conditions, allowing particles to jump field lines at a much faster rate than classical diffusion can account for. To better understand this phenomenon, diagnostic instruments are needed to visualize the effects of turbulence. It is difficult to understand turbulence in concise terms. However, imaging systems can help us visualize how they form and grow. Figures 16-18 show examples of how complicated turbulence can be. If plasma physicists and fusion engineers are to solve the enigma of anomalous transport, they first need observational data with which to gauge and validate their theories.



Figures 16, 17, and 18. Images of turbulence. Left: 14th century drawing of turbulent water by Leonardo De Vinci. Center: Solar flare and surface of the sun (Source: NASA / SDO / AIA April 16th, 2012 [2]). Right: Smoke from a recently extinguished candle.

In a tokamak, turbulence can begin at a very small scale, and is essentially invisible to general observation; therefore, instruments must be created to measure these events. The causes of turbulence vary greatly, so instruments must be designed for specific purposes, to explore particular theories of plasma instability. Furthermore, every tokamak has unique geometry and operating conditions; therefore, plasma diagnostic instruments are custom tailored for specific reactors. Apart from collecting scientific research data, diagnostics are also used to collect data on operating conditions, such as plasma temperature, density, and magnetic field strength. These data are essential to basic operations, and can be correlated with other instruments to validate research data. For example, the FIRiTIP system will measure core density in NSTX-U, which can then be used to calibrate the density measurements from the Thomson Scattering system. Real time feedback is also important for dynamic systems control. In addition to collecting the desired data, instruments should also be nonperturbing. If the act of measuring alters the state of the plasma, then the usefulness of a diagnostic is limited. Due to the extreme temperatures of fusion plasmas, many otherwise routine measurements are rendered impractical, such as a simple Langmuir probe [3].

II.1 Types of Plasma Diagnostics

There are many types of plasma diagnostics used world-wide. A few notable instruments are listed below; however, this list is far from complete:

- Electron Cyclotron Emission Imaging (ECEI). Electrons traveling along magnetic field lines will orbit about their field lines at a frequency proportional to the magnetic field strength. They will then emit radiation at the electron cyclotron frequency, with an intensity proportional to electron temperature. An ECEI system is a set of antennae, tuned to the electron cyclotron frequency, or one of its harmonics. A series of optics can focus the antennae on a particular location inside a fusion reactor to passively monitor electron temperature. Furthermore, in a magnetic torus, the

magnetic field strength is inversely proportional to the radial position. Therefore, the electron cyclotron frequency increases with depth. The ECEI instruments are sensitive to a range of frequencies, which can be discriminated in the receiver electronics. A linear array of antennae can then construct a 2D image (radial and poloidal) of electron temperature inside a tokamak.

Examples of this type of instrument are installed on the DIII-D and KSTAR tokamaks [4, 5, 6].

- Thomson Scattering (TS). This instrument uses a high frequency, high power laser beam to pass through fusion plasma. Due to the short wavelength of the probe beam, the beam interacts with individual plasma particles, unlike the High-k Scattering system which uses long wavelength probe beams to collectively interact with many particles at once. Electromagnetic waves will scatter off charged particles, where the bandwidth of scattering signals represents temperature, and amplitude is proportional to density. The intersection of probe beam and receiving optics can localize measurements to any desired location. An example of this instrument was found on NSTX, and has been reinstalled on NSTX-U [7].
- Microwave Imaging Reflectometry (MIR). Electromagnetic waves incident upon a plasma cut-off layer will reflect. An MIR instrument uses this property to transmit certain frequencies into fusion plasma, and then reflected signals are collected. The time of flight (or phase delay) between transmission and reception will provide a radial location for the cut off layer, similar to an active radar system. The cut-off frequency depends on the plasma density; therefore, an array of MIR transmitters / receivers will measure the position of certain plasma density surfaces or surface density fluctuations. Higher frequencies will penetrate deeper into a tokamak; therefore, a multi-frequency MIR system can measure a 2D image of plasma density / density fluctuation with a linear array. Examples of MIR systems are found on DIII-D and KSTAR [8, 9].

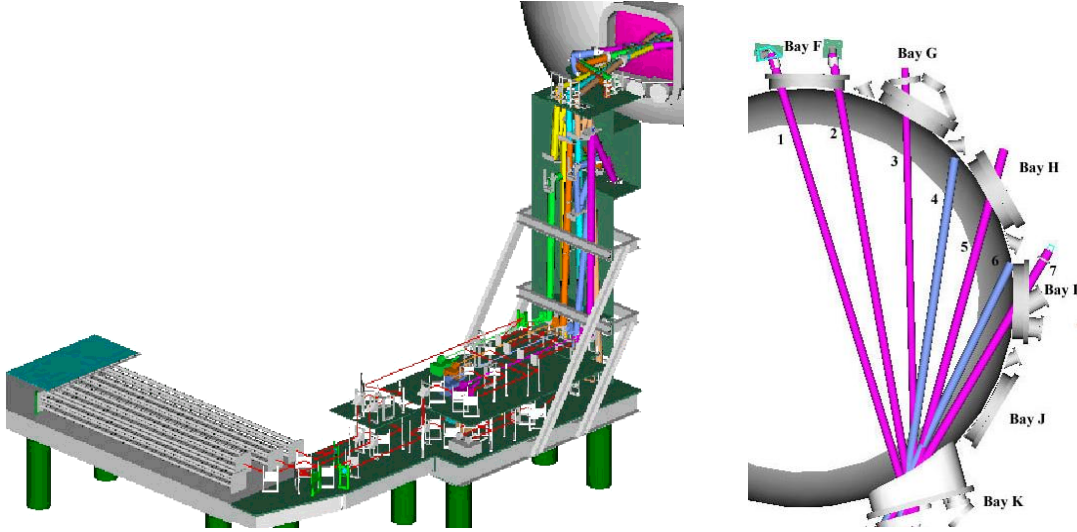
- **Interferometer.** An interferometer can compare differences in optical path length between a signal and reference paths with very high precision. In a tokamak, such an instrument can measure mechanical vibrations or changes in plasma density, since plasma index of refraction varies with density. This instrument differs from MIR in that MIR generally measures surfaces around the outer radial positions. An interferometer can pass a high frequency beam through the plasma core. Density or density fluctuation measurements are possible. Apart from the FIReTIP system detailed in this dissertation, another example was found on the Alcator C-Mod tokamak[10].
- **Collective Thomson Scattering (CTS).** The details of collective Thomson scattering are discussed in this dissertation. In short, a probe beam of wavelength much longer than a plasma Debye length will scatter electromagnetic waves in proportion to the coherent motion of many charged particles. This system is insensitive to plasma temperature or density, but instead scatters strongly from density fluctuations squared. This allows much lower power lasers to be employed than TS systems. In addition to the High-k Scattering System, an example is found for a design for ITER. In their instrument they have designed it to measure the fast ion distribution with a 60 GHz probe beam [11].

Ionized gases confined by magnetic fields are governed by various theories in the realm of plasma physics. Plasma physics in its entirety can be incredibly complicated due to the vast range of scales it must account for. Size scale can range from individual particles to vast nebulae. Time interaction between particles can be described in terms of sub-microseconds to literally astronomic time scales. To focus on a particular application of plasma physics, certain assumptions are made. For example, while studying certain instabilities in a tokamak, magnetohydrodynamic (MHD) approximations can be made [12]. In this case, plasmas are treated as an ionized fluid. MHD equations coincide with observations on a microsecond time scale, which is relevant to instabilities and the formation of turbulence in tokamaks. Since ions are heavier than electrons by a factor of 1800 or more, they can be approximated as adiabatic

particles. Electrons, on the other hand are treated isothermally. Understanding the physical properties of fusion plasmas is crucial to improving fusion power performance. Numerous techniques are used to collect data in fusion reactors to measure properties such as temperature, density, magnetic field strength, and density fluctuations. Data collection can be complicated due to the extreme temperatures of the plasma and the need to collect data in a non-perturbative manner. This section will discuss the theory behind two diagnostic techniques which are employed on NSTX-U: 1) FIReTIP (Far Infrared Tangential Interferometer and Polarimeter, and 2) High- k_0 Scattering System.

II.2 FIReTIP System

The FIReTIP system was first designed by UC Davis, and implemented on NSTX in 2001 [13]. Its primary function was to measure plasma density by way of interferometry. FIReTIP can concurrently operate as a polarimeter to measure the tangential magnetic field strength. The tangential field strength under vacuum is known; however, when a plasma is included there are many conditions that may contribute to localized changes or fluctuations. The FIReTIP polarimeter function can measure these effects to gain insight to the dynamic conditions in the tokamak. Upgrades to NSTX in 2012 required the instrument to be redesigned, although the core of the instrument is unchanged. Namely, the use of far infrared lasers and corner cube mixers to detect the beams for phase comparisons was continued. FIReTIP had been positioned beneath Bay K with up to 7 chords defined through NSTX; however, the most chords ever installed were 6, before NSTX was taken off-line. The various chords could measure plasma density at various radial positions, from core to edge.



Figures 19 and 20. Left: CAD rendering of the original FIRerTIP system. The laser table and optics were located beneath Bay K. A tower rising to midplane at Bay K contains further optics, and up to 7 chords could be directed into the vacuum vessel. Right: The 7 proposed chords of FIRerTIP, originating at Bay K, and focused at retroreflectors from Bays F to I for plasma core to edge coverage. Reproduced from [14], with the permission of AIP Publishing.

The inclusion of a second neutral beam injector (NBI) at Bay K left no space available for FIRerTIP's launch optics or laser systems. The purpose of the instrument was altered as well. For NSTX-U, the new FIRerTIP system will provide a single chord to measure plasma density in real time for machine control feedback [15]. Two additional chords to measure edge density and density fluctuations are optional enhancements should PPPL wish to exercise them. The polarimeter function remains as a secondary purpose. The laser systems have been relocated outside of the NSTX-U test cell, just beyond a 4' thick concrete enclosure to contain excess neutron flux, and act as a firewall in the event of an accident. The same lasers are used in the new system; however, they now share space with the High-k Scattering system which created significant spatial constraints. A new laser table, optics, control, and monitoring systems have been designed to house the FIRerTIP lasers. The laser location in the 'gallery' places them approximately 20 meters from the vacuum vessel; therefore, waveguide was developed to direct the FIR

beams to the launch optics and receiving table. The new chordal path passes between Bays G and B, which required the launching optics to be redesigned. An internal retroreflector is mounted at Bay B, which was designed and fabricated by UC Davis to withstand exposure to the reactor interior. Although the corner cube mixers are unchanged, the receiver table and optics have all been redesigned. The previous FIRiTIP system utilized a homodyne HeNe-based vibration monitor to make phase corrections due to variations in the chord length. The homodyne system required post processing of data to correctly account for path length parity. The new system has an upgraded heterodyne HeNe-based vibration monitor. This, along with a *field programmable gate array* (FPGA) processor will allow real time density feedback to be realized. Reference path equalization, digital filters, and improved spectral analysis should improve performance over the previous installation. The only portion of the previous FIRiTIP system which is unchanged is the IF (intermediate frequency) electronics, which process the signals from the receiving mixers. These electronics were upgraded just prior to the 2012 NSTX shutdown, and still provide good performance for signal processing [16].

II.3 Interferometry

The FIRiTIP interferometer works on the same principle as a Michelson interferometer [17], where a difference in path lengths between measurement and reference beams are observed to interfere with each other. The interference is seen as fringe lines spaced at the wavelength of the light utilized. For FIRiTIP, the path lengths are fixed; however, the plasma in the vacuum vessel will have a variable index of refraction depending on its density. The result is the phase difference observed between a measurement and reference beam is proportional to the chord averaged density of the plasma along the measurement path. The polarimeter portion of the instrument works in a similar manner. The probe beam is comprised of two collinear, circularly polarized beams, one right-handed and other left-handed circularly polarized. In a magnetized plasma, the index of refraction will be different for right handed and left handed polarizations. Right handed and left handed beams combined together will appear as linearly polarized.

When these beams pass through a magnetized plasma, and experience different phase shifts, the observed linear polarization angle will change, known as Faraday rotation [18]. The Faraday rotation angle depends on the path length, plasma density, and magnetic field strength. For the FIReTIP system, the path length is fixed, and the density is known from the interferometer portion of the instrument. The Faraday rotation is determined by measuring the phase difference between the right-handed and left-handed circularly polarized probe beams and is used to infer the toroidal magnetic field strength.

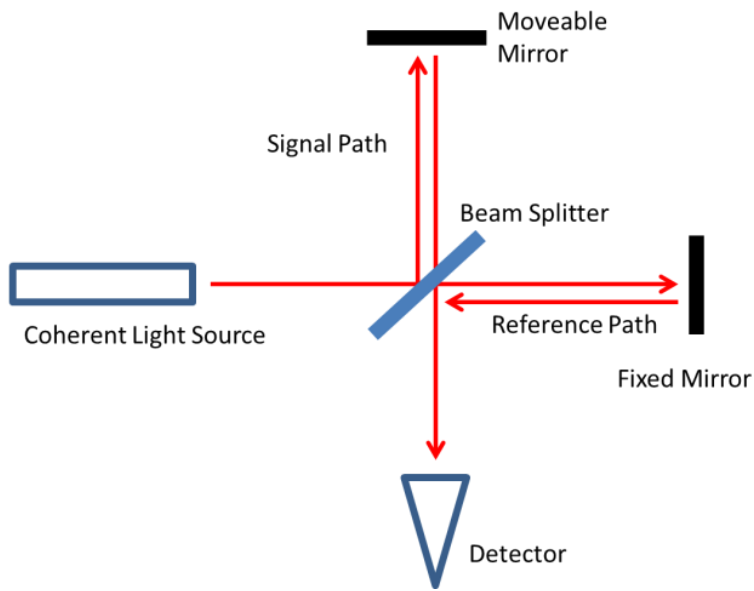


Figure 21. Schematic of a Michelson interferometer. A single coherent light source is split into two beam paths, A and B. These beams are then recombined and observed. Paths A and B will constructively interfere if the difference in path lengths is an integer multiple of a wavelength, and destructively interfere at odd integer half wavelengths. The observer can detect minute changes in the optical path length as light and dark fringes. In the case of FIReTIP, the source is an FIR laser, and the path length difference is measured through fringe counting electronics, and phase comparators.

The choice of wavelength for the system depends on several factors. The frequency should be sufficiently above the plasma frequency to minimize refraction effects of a variable index, and result in a manageable

range of phase shifts. However, too high a frequency will result in very little phase change, and increased sensitivity to mechanical vibrations. In the range of acceptable frequencies, the availability of sources and detectors must also be considered. For FIReTIP, signals in the far infrared are ideal; however, sources and detectors are not plentiful. Gas lasers provide a solution. While developed more than 40 years ago [19], they are still the primary technology used for far infrared sources. FIReTIP employs three optically pumped methanol lasers tuned to 119 μm (2.5 THz). The first methanol laser provides the beams for the interferometer signal and reference, while the second is necessary for the polarimeter. The third laser is a Stark effect laser, which can shift the lasing frequency by several MHz. The Stark laser provides the local oscillator (LO) power to the receiving mixers. The original FIReTIP system reused corner cube mixers originally designed for the MIRI system [20], which was installed on TFTR [21], and they are still in use. Conversion loss at 2.5 THz is ~ -50 dB. This level of performance is acceptable for the FIReTIP system. Developments in THz technologies may provide for improved components in the future; however, for the time being these mixers will be retained. The primary concern for the current corner cube style mixers is the availability for service or repairs should the system experience a breakdown. At present, UC Davis has a supply of the original MIRI mixers that should provide good service for the FIReTIP system for many years. Contained within the mixer housing are a DC bias supply, and low noise amplifier. The RF and LO power are delivered through the same input port. The maximum RF and LO power combined is approximately 10 dBm. To ensure sufficient power can be delivered to the mixers, the FIR lasers should produce about 100 mW at the output coupler. Should these mixers ever be replaced with more sensitive mixers, this would permit either less powerful lasers, or the inclusion of other, less powerful, THz sources to replace the lasers.

Figure 22, below, shows how the FIReTIP lasers are employed for a single chord measurement. The FIR lasers are labeled f_1 , f_2 , and f_{LO} . The cavity lengths for f_1 and f_2 are tuned to slightly alter the laser frequency, by -1 and +1 MHz, respectively. This will allow the right handed and left handed circularly polarized beams to be differentiated on the mixer output. All three lasers emit a Gaussian beam which is

initially vertically linearly polarized. The Stark laser output frequency is shifted by 5 MHz, coupled into waveguide, and then directed to the receiver table in the test cell. Beam splitters divide the Stark output to provide LO power to each of the mixers in use (one for each channel, plus the reference mixer). For FIR lasers #1 and #2, their polarizations are converted to right handed and left handed circularly polarized. First, one laser is passed through a 1/2 wave plate to rotate its polarization from vertical to horizontal linear. Then the beams are combined and passed through a 1/4 wave plate to initiate the right and left handed circular polarizations. From here, the collinear beams are coupled into waveguide and directed to the vacuum vessel. "Tee" intersections in the waveguide will separate the beams to their designated chords, and to the reference mixer. Each channel passes through a series of optics before entering the vacuum vessel. The beams are expanded, and then focused on a retroreflector at the opposite side of the tokamak. The beams are returned along their initial path to make a double pass through NSTX-U, and recoupled back into their waveguide. Beam splitters then direct the signals to the receiver table, where they are combined with the LO signal, and energize their respective mixers.

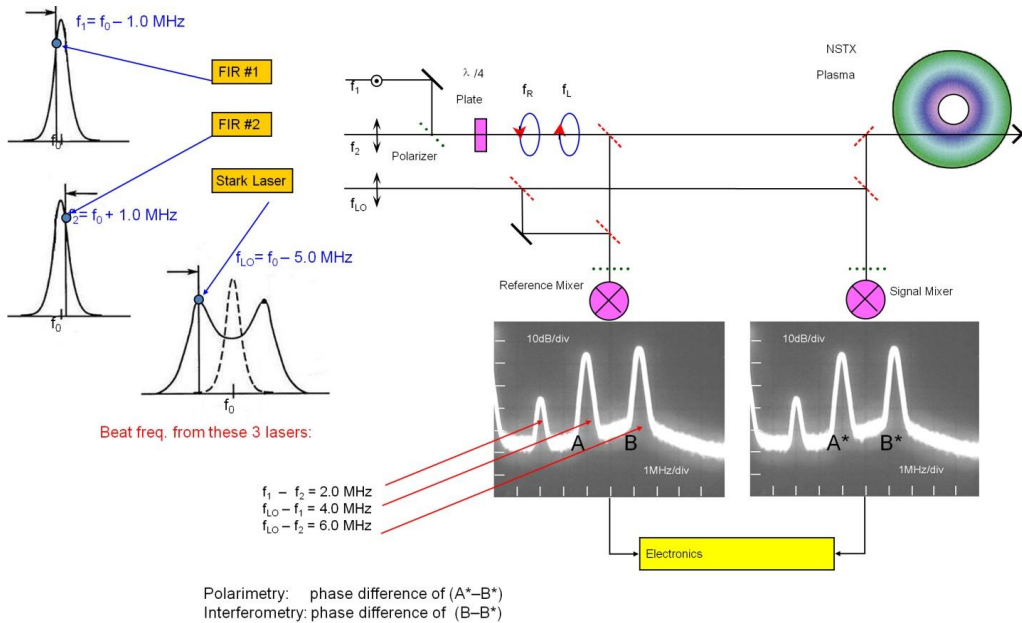


Figure 22. Schematic of the FIR-TIP laser arrangement, laser tuning parameters, and mixer output signals. Reproduced from [14], with the permission of AIP Publishing.

When the mixer output is viewed on a spectrum analyzer, each mixer should show three major peaks: at 2, 4, and 6 MHz. These are the beat frequencies from the three incident lasers. The 2 MHz signal is due to the difference in tuning between FIR lasers #1 and #2. This signal can be disregarded other than to confirm that the two lasers are tuned 2 MHz apart. Peak A (as shown in figure 22) at 4 MHz is the IF output from FIR laser #1 and the LO signal. Peak B, similarly, is the IF output between FIR laser #2 and the LO signal. These mixer outputs are processed by the IF electronics to measure the phase difference between peak B and B* for interferometry, and A* and B* for polarimetry (A and B denote the reference mixer, while A* and B* are from a signal mixer). Note that the polarimeter does not require the reference mixer, because the relevant phase difference is between the right and left handed signal beams. If the interferometer is desired to be run in isolation, then only one FIR and the Stark laser are needed. In this case, the 1/4 wave plate can be removed so that the signal beam remains linearly polarized. The corner cube mixers are arranged so that they receive vertical linearly polarized RF and LO input. Polarizers are included at the mixer input to remove unwanted signals.

In 2011, the IF electronics were significantly upgraded from the original installation. This upgrade improved bandwidth, stability, and signal to noise ratio. The maximum temporal resolution is set by the IF frequency of the mixer output. Similar interferometers have used a two laser FIR system, where the signal and LO are offset by ± 1 MHz, for a 2 MHz maximum bandwidth [15]. By adding a Stark effect laser with an offset of 5 MHz, 4 to 6 MHz bandwidth can be utilized in FIReTIP. The original electronics were limited to 250 kHz [16]. Figure 23 shows the schematic for the new electronics that can operate up to 4 MHz bandwidth [16]. Improved filters, phase locking loops, and phase comparators contribute to the better performance. The zero crossing phase comparators can count fringe lines and utilizes I/Q mixers for phase difference measurements.

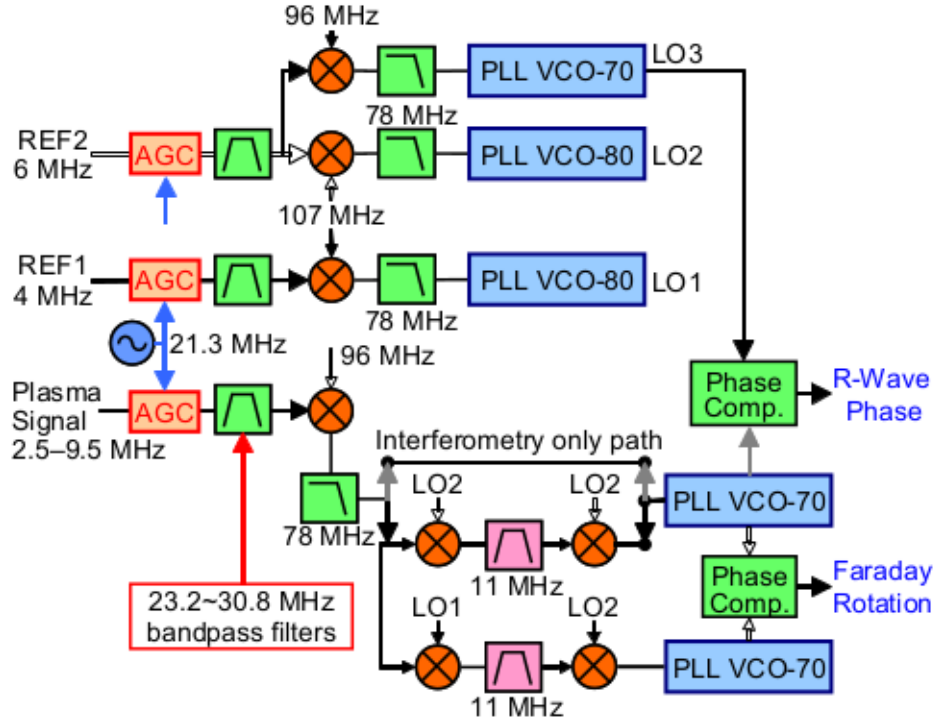


Figure 23. FIReTIP IF electronics schematic. These electronics still provide ample performance for the new installation on NSTX-U with temporal resolution up to 4 MHz. Reproduced from [22], with the permission of AIP Publishing.

Mechanical vibrations will introduce phase noise into the data. Path length variations on the order of 100 μm will not significantly affect the interferometer. Although the beam wavelength is 119 μm , the total phase shift from vacuum to maximum density will be on the order of 200 fringes. The polarimeter, however, measures Faraday rotation on the order of 45 degrees, so it will be much more susceptible to vibration noise. In this installation, the total path length for the reference and signal channels will be equalized in the waveguide runs, thereby ensuring that laser coherence length issues do not contribute to additional phase noise.

The figure below shows example data taken from FIReTIP on NSTX [23]. Each channel has a different chord through the vacuum vessel. The chord averaged density is shown for 12 consecutive shots (#136080 - 91), during the start-up phase of the reactor. The installation on NSTX-U will initially be a single core channel (similar to channel 1 shown below). Similar performance is expected, with some improvement due to equalized path lengths, and additional post-IF-electronics digital filters and processing. The primary improvement in FIReTIP will be to provide real time density feedback for dynamic machine control.

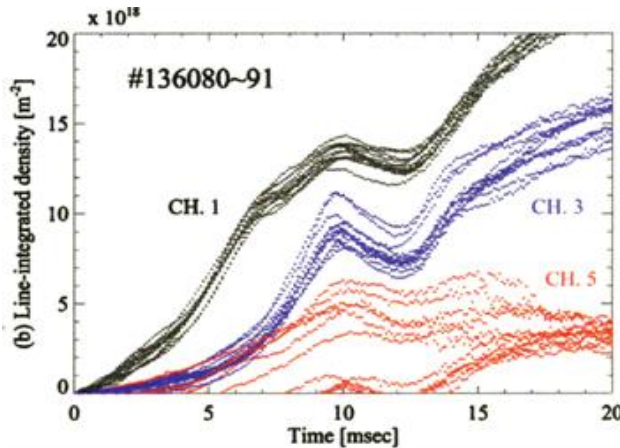
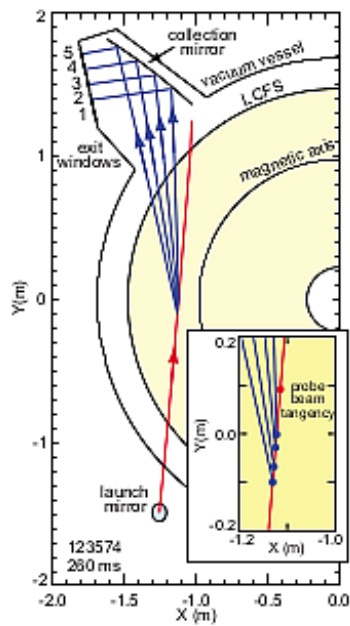
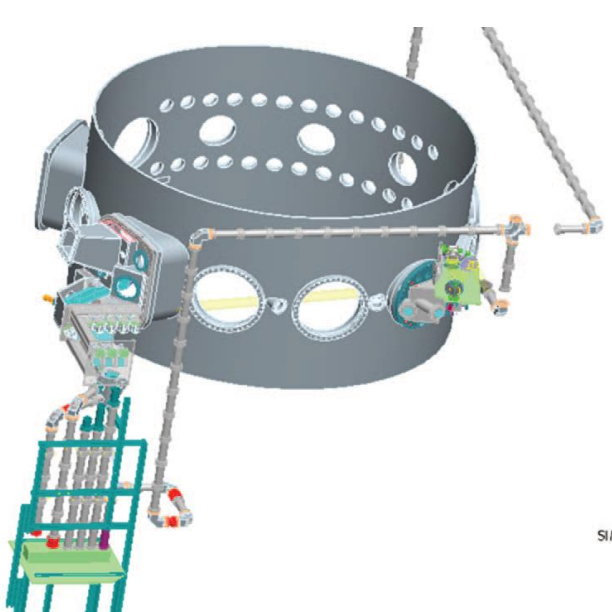


Figure 24. Example data from the previous FIReTIP system on NSTX. Several plots are shown for channels 1, 3, and 5 showing line integrated density during reactor start up. Reproduced from [23], with the permission of AIP Publishing.

II.4 High-k Scattering System

The High-k Scattering System was first developed by UC Davis and installed on NSTX in 2004 [24]. While the upgrades to NSTX required the removal and redesign of the High-k Scattering System, this also provided an opportunity to make substantial changes and improvements to the instrument to better align with current research goals on NSTX-U [25].

The original High-k scattering system was primarily designed to measure electron scale density fluctuation wavenumbers in the radial direction, hereafter referred to as the High-k_r Scattering System. This system used a 280 GHz probe beam to pass through the vacuum vessel, and then scattered signals are detected along a horizontal plane [26]. Initially, a 280 GHz carcinotron provided the probe beam; however, this source was unstable, and was eventually replaced by a 280 GHz, 34 mW solid state source. The source was located outside the NSTX test cell, in the 'gallery' area. 2.5" diameter, corrugated waveguide delivered the probe beam to the vacuum vessel. The beam entered the vacuum vessel through a window at Bay H, and exited on the far side at Bay K. A five channel receiver was positioned beneath the exit window. A curved mirror collected the scattered signals, and then directed them through corrugated waveguide to the receiver table. An additional corrugated waveguide was routed from the launch window, around the tokamak exterior, and to the receiver table to provide a signal for a reference mixer. The receiver table consisted of a system of lenses, beam splitters, mirrors, duplexers, and mixers. The duplexers combined the scattered signals (or reference) with local oscillator power. These signals were focused onto 280 GHz, fundamental Schottky diode mixers [26]. The mixer IF output is then filtered and amplified to digitizers to record the data. Frequency and power of the scattered signal wavenumbers (k) are recorded over time. The frequency of signals varies from the reference channel depending on the Doppler shift of detected density fluctuations, while the scattered power is proportional to the density fluctuations squared via collective Thomson scattering [27].



Figures 25 and 26. Left: Previous High-k Scattering System Set-up. Waveguide enters from the right hand side, and divides between the launch optics at Bay H, and the reference waveguide run. The receiver optics at Bay K direct scattered signals down to the receiver table along with the reference waveguide run. Right: The 280 GHz High-k beam line is shown in red. The blue arrows show the scattered signals that are collected by the receiving optics. Reproduced from [26], with the permission of AIP Publishing.



Figure 27. Interior view of the Bay K port cover. The 280 GHz High- k_r Scattering System receiver optics are circled in red. A long, curved, horizontal mirror is on the right, and five holes are seen on the left. Each hole corresponds to one of five receiver channels. Photo courtesy of Princeton Plasma Physics Laboratory.



Figure 28. 280 GHz High- k_r Scattering receiver system. Waveguides enter the duplexers from above. The right hand side shows the LO source and a series of beam splitters to deliver LO power to each duplexer. The white lenses focus the signals to the mixers of the five channels, plus the reference channel. Photo courtesy of Dr. Calvin Domier, UC Davis.

Figure 29 shows an example of how the High- k_r Scattering System data looks. Data plots from the High- k_r Scattering System are shown. There are five channels, with each channel represented by two windows, the blue background plot above, and the white background plot below. The upper plot shows a color plot of power detected for a range of frequencies over time. The central red line is the reference channel at 280 GHz. The scattered signals are shown at approximately 2 MHz less, due to Doppler shifting inside the tokamak, for 450 ms to 550 ms of a single NSTX plasma shot. There are three thin vertical lines marking the locations of 498, 515, and 532 ms. These lines are time slices within the shot, and are replotted in the lower section in green, black, and magenta, and display the measured power and frequency of scattered signals. The peaks near -2 MHz indicate electron scale turbulence. These plots show that after an ELM event (near 520 ms), the turbulence was repressed [28].

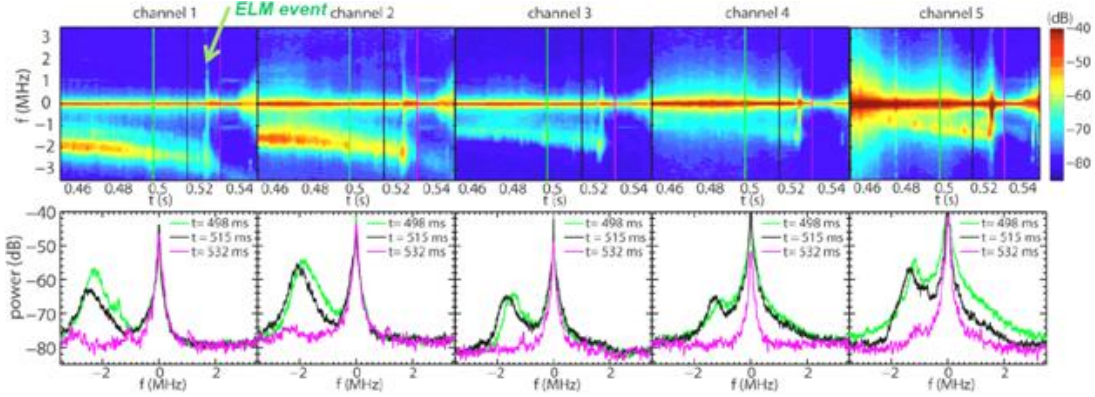


Figure 29. Data plots from the 280 GHz High- k_r Scattering System. Reproduced from [29], with the permission of AIP Publishing.

The measured wavenumbers are not purely radial, but rather a combination of vectors in three dimensions. The wavenumber vectors can be decomposed into their toroidal coordinate system components. By using several channels of various scattering angles focused on a single scattering volume, a broad k spectrum can be developed. New research priorities with NSTX-U outline poloidal wavenumber measurements for electron scale density fluctuations to support electron temperature gradient mode research [30]. The High- k_r Scattering System had insufficient k_θ coverage to meet the research goals. Several major modifications were made to accommodate the new research. To capture poloidal wavenumbers, a vertical scattering plane was needed. A special, 33 cm tall window was installed at Bay L that permits vertical scattering angles up to 15° [31]. The available receiver window allows for a range of probe beam frequencies that will work well to study ETG modes. Sources of ~ 100 mW with frequencies between 500 GHz and 1 THz are suitable. We chose to replace the solid state source with a 693 GHz formic acid laser. There are few choices with adequate power in our frequency range; however, the formic acid laser meets the criteria. The increased frequency provides greater power and increased k resolution. The increased frequency also required the redesign of the corrugated waveguide, new launching and receiving optics, and a 693 GHz subharmonic mixer receiver array. Furthermore, the launching and receiving optics are remote control steerable to move the scattering volume from core to

edge in a variety of scattering schemes for a more complete k spectrum [32]. NSTX-U will exhibit larger density fluctuation Doppler shifts and increased confinement times. These conditions will require broader bandwidth digitizers and increased memory to record scattering data.

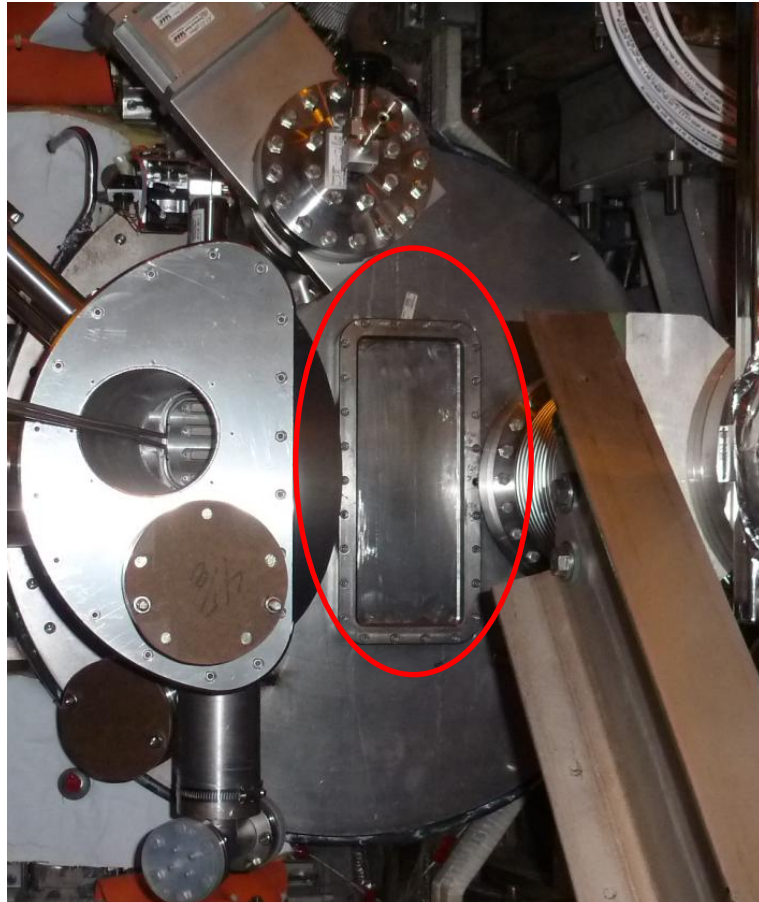


Figure 30. Bay L port cover. The 693 GHz High- k_θ Scattering receiver window is circled in red. This window measures 33 cm tall, and 13 cm wide. It will permit poloidal scattering angles up to 15° . Photo courtesy of Princeton Plasma Physics Laboratory.

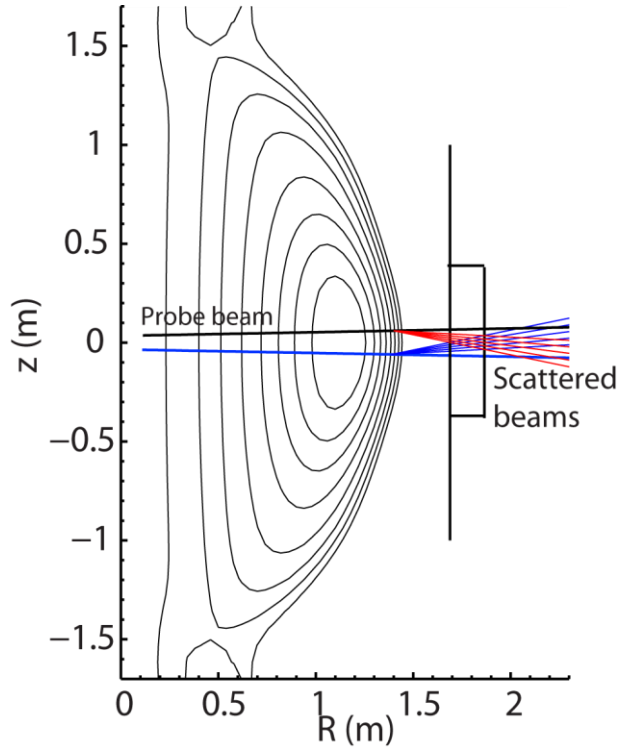


Figure 31. Toroidal cross section showing how the 693 GHz probe beam can pass through the plasma. The launch optics can steer the probe beam up or down by 2.25° . This arrangement allows up or down scattering schemes, shown in red and blue, to provide a more complete k spectrum. Image courtesy of Dr. Yang Ren, PPPL.

II.5 Collective Thomson Scattering

Ordinary Thompson scattering (i.e. not collective) is a phenomenon where charged particles interact with an electromagnetic wave. If an electromagnetic wave is incident on a single charged particle, then the time varying electric field will push and pull on the particle, causing it to oscillate. These oscillations in turn would create dipole radiation. An electromagnetic probe beam passing through a plasma will create this effect when the probe beam wavelength is much shorter than the Debye length. The scattered power is proportional to the density of particles upon which it is incident. Random motion due to thermal energy is also detected by the bandwidth of scattered power, with higher temperatures exhibiting a larger

bandwidth as seen in the TS system on NSTX [7, 33]. With collective Thomson scattering, the wavelength of the probe beam is much longer than the plasma Debye length. The beam will not interact with individual particles, but rather it will interact with the collective motion of many particles. In this arrangement, random motion effectively cancels out; however, the scattering is very sensitive to coherent motion. Therefore, the scattered power is proportional to density fluctuations squared. This permits the use of much lower energy probe beams, both in terms of individual photons, and total beam power. While the TS system on NSTX-U uses a pulsed Nd:Yag laser of 6.7 MW at 1064 nm [7], the High-k Scattering System only needs 100 mW at 432 μm [32].

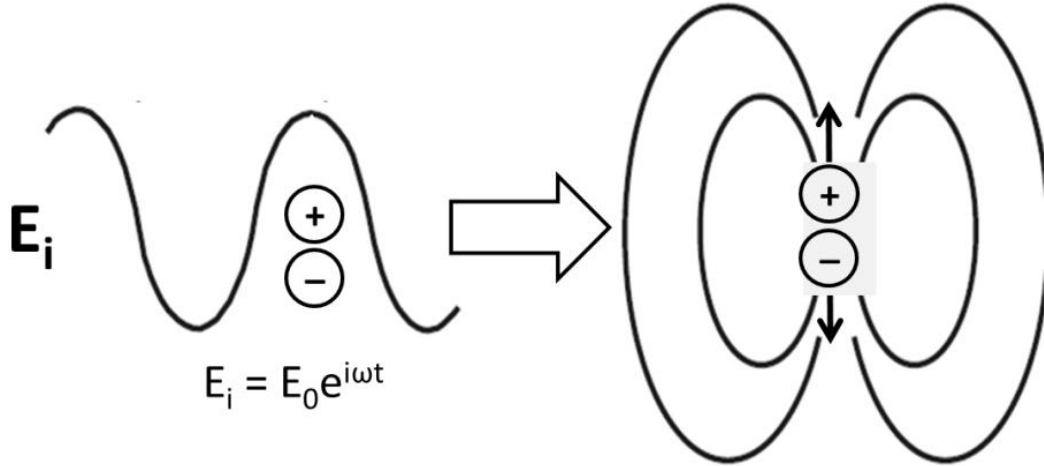


Figure 32. Electromagnetic wave incident on charged particles. The particles oscillate and emit radiation.

The Debye length is a description of how well particles are electrically shielded. A fully ionized plasma consists of electrons and ions; however, since there are equal numbers of each, it is quasi-neutral. The Debye length is how far you would need to be from a particular charged particle to not notice its electric field, due to the numerous surrounding particles of opposite charge. When considering plasma interactions at distances or wavelengths greater than the Debye length, collective behavior will be observed. The Debye length is a function of the square root of the particle temperature and density. [12]

$$\lambda_d = 7.4 \times 10^3 \sqrt{\frac{T}{n_e}} \text{ m}$$

In the event of multiple species shielding a charge, the Debye length squared is the inverse of the sum of the inverse squared species Debye lengths.

$$\frac{1}{\lambda_d^2} = \sum \frac{1}{\lambda_\alpha^2}$$

For a typical NSTX-U plasma ($n \approx 1.5 \times 10^{20} \text{ m}^{-3}$, $T = 1700 \text{ eV}$) the Debye length is about 25 microns.

The FIR laser in the High-k Scattering system emits a 432 micron beam; therefore, it should be well into the collective scattering regime.

Another parameter to determine if collective scattering will be observed is to calculate " α ". When " α " is equal to unity the probe beam wavelength and Debye length are equal. To ensure collective scattering " α " should be much greater than 1.

$$\alpha = \frac{1}{k\lambda_d} \gg 1$$

Energy and momentum must be conserved, such that the scattered frequency must be the sum of the incident probe beam and the density fluctuation frequencies. The vector sum of wavenumbers must also add together in similar fashion. The equations below show this simple constraint, where subscript "i" denotes the incident value of the probe beam, "s" is for the scattered signal value, and the unmarked symbol is the fluctuation value.

$$\omega_i + \omega = \omega_s$$

$$\vec{k}_i + \vec{k} = \vec{k}_s$$

If the fluctuating source has a frequency much lower than the incident frequency ($\omega \ll \omega_i$), then the incident and scattered frequencies must be approximately equal, $\omega_i \approx \omega_s$. Since these are both electromagnetic waves traveling at the speed of light, their wavenumbers will also be the same, $k_i \approx k_s$.

With this approximation, we can solve for the fluctuation wavenumber with the law of cosines, which reduces to the familiar Bragg relation:

$$k = 2k_i \sin\left(\frac{\theta}{2}\right)$$

where θ is the scattering angle, an angle between the probe beam and receiver location. For the *High- k_θ Scattering System*, the fluctuation wavenumber, "k", is a measurement parameter of interest. "k" represents particular types of coherent electron fluctuations (electron scale turbulence). The scattering angle will determine which value wavenumber is being measured. Therefore, to reconstruct a complete k spectrum, multiple scattering channels are needed, each with a different scattering angle. Initially, a 4-channel receiver will be installed which will have scattering angle intervals of $\sim 1.5^\circ$. The receiver will be able to translate through many angles and positions to target a greater range of wavenumbers with scattering angles of $\sim 2^\circ$ to 15° . At a later date, upgrades to the receiver will include an 8-channel receiver array to collect more wavenumbers at a time.

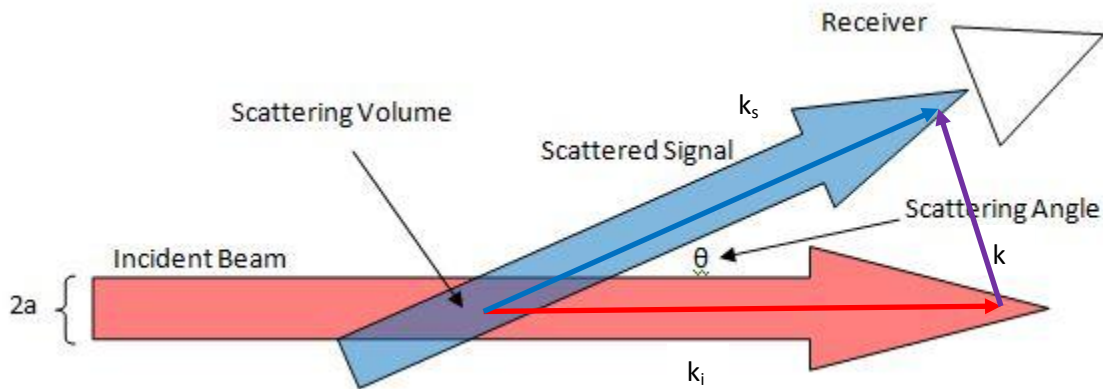


Figure 33. A receiver, at some angle (θ) from the incident beam, will see scattered waves due to fluctuations, k .

Coupled with the Bragg relation, an expression for " α " will depend on the incident wavelength and scattering angle, as compared with the Debye length.

$$\alpha = \frac{\lambda_i}{4\pi\lambda_d \sin(\theta/2)}$$

Collective Thomson scattering can be achieved through a relatively long wavelength probe beam, low scattering angle, or a combination of the two [34]. The parameters given for the High- k_0 Scattering System, α ranges from 10.5 to 78.8, safely in the collective regime.

Scattering resolution will depend on the length of the scattering volume and radius of the probe beam [24]. At low scattering angles, the receiver will be able to view long sections of the probe beam. Larger scattering volumes will yield more scattered power, but at the loss of localization. A larger beam radius will improve k-resolution, but again, at the expense of spatial resolution. With a Gaussian probe beam, k-resolution is approximated by:

$$\Delta k = \frac{2}{a}$$

where “a” is the beam radius, defined to be where the beam intensity is e^{-2} of the central maximum.

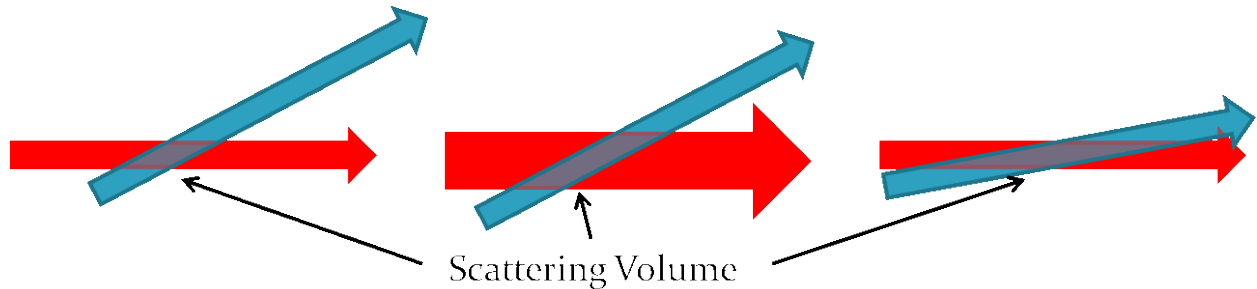


Figure 34. Various examples of how beam size and scattering angle affects spatial and k-resolution.

The power scattered in collective Thomson scattering is given by the following:

$$P_s = \frac{1}{4} r_0^2 |\tilde{n}_e|^2 \lambda_i^2 L^2 P_i$$

where P_s is the scattered power, r_0 is the classical electron radius, \tilde{n} is the density fluctuation, λ_i is the wavelength of the incident beam, L is the scattering length, and P_i is the incident power.

It should be noted that the High- k_r Scattering system utilized a longer wavelength probe beam (280 GHz, 1.07 mm). The increase in frequency to 693 GHz will result in a factor of 4 reduction in scattered power. The formic acid laser will produce approximately 3 times the power, so most of the scattered power is recovered. The design of the receiver will allow the High- k_θ Scattering System to target the predicted ETG mode peaks, which will enhance scattered power, and the increased frequency will improve k resolution. Therefore, the overall performance of the new High- k_θ Scattering System is expected to be improved over the prior system, and the data collected will be of greater interest to PPPL current research priorities.

Collective Thomson scattering is non-perturbing. The incident probe beam is relatively low power at 100 mW, as compared to the NBI systems at 10 MW each. The scattered power is smaller still, in large part due to the incredibly small scattering cross section of electrons at 0.6 barns. Fluctuations in NSTX-U are expected to be on the order of 0.1%. Typical densities are around $1.5 \times 10^{14} \text{ cm}^{-3}$, and \tilde{n} will be about $5 \times 10^{10} \text{ cm}^{-3}$. Furthermore, scattered power is proportional to \tilde{n}^2 ; therefore, a factor of 10^{20} greatly enhances scattered power. Ordinary Thomson scattering is proportional to density, so with collective scattering it is 100 million times more sensitive. With a 693 GHz probe beam at 100 mW, and an approximately 4 cm scattering length, the expected scattered power is on the order of 1.3 μW .

$$P_s = \frac{1}{4} (2.82 \times 10^{-13})^2 (1.5 \times 10^{14} \times 0.001)^2 (0.0432)^2 (4)^2 0.1 = 1.3 \times 10^{-6} \text{ W}$$

At 1.3 μW , reasonably good signal to noise ratios can be expected. More details on this will be covered in the receiver section.

II. References

- [1] K. Muraoka, F. Wagner, Y. Yamagata, and A.J.H. Donne, "Short- and long-range energy strategies for Japan and the world after the Fukushima nuclear accident," *17th International Symposium on Laser-Aided Plasma Diagnostics (LAPD17)*, Journal of Instrumentation, Vol. 11, January 2016.
- [2] "Giant Prominence Erupts," *NASA/SDO/AIA*, http://www.nasa.gov/mission_pages/sunearth/news/News041612-M1.7flare.html, April 16th, 2012.
- [3] M.B. Hopkins, W.G. Graham, " Langmuir probe technique for plasma parameter measurement in a medium density discharge," *Rev. Sci. Instrum.* 57, 2210, 1986.
- [4] L. Yu, C.W. Domier, X. Kong, S. Che, B. Tobias, H. Park, C.X. Yu, N.C. Luhmann, Jr., "Recent Advances in ECE Imaging Performance," *Journal of Instrumentation*, 7, Feb 2012.
- [5] B. Tobias, C.W. Domier, T. Liang, X. Kong, L. Yu, G.S. Yun, H.K. Park, I.G.J. Classen, J.E. Boom, A.J.H. Donne, T.L. Munsat, R. Nazikian, R.L. Boivin, N.C. Luhmann, Jr., "Commissioning of Electron Cyclotron Emission Imaging (ECEI) Instrument on the DIII-D Tokomak and First Data," *Review of Scientific Instruments*, 81, 10D928, 2010.
- [6] G.S. Yun, W. Lee, M.J. Choi, J.B. Kim, H.K. Park, C.W. Domier, B. Tobias, T. Liang, X. Kong, N.C. Luhmann, Jr., A.J.H. Donné, "Development of KSTAR ECE imaging system for measurement of temperature fluctuations and edge density fluctuations," *Review of Scientific Instruments* 81, 10D930, (2010).
- [7] B.P. LeBlanc, R.E. Bell, D.W. Johnson, D.E. Hoffman, D.C. Long, and R.W. Palladino, " Operation of the NSTX Thomson scattering system," *Review of Scientific Instruments*, Vol. 74, No. 3, March 2003.
- [8] B. Tobias, N.C. Luhmann, Jr., C.W. Domier, X. Kong, T. Liang, S. Che, R. Nazikian, L. Chen, G.S. Yun, W. Lee, H.K. Park, I.G.J. Classen, J.E. Boom, A.J.H. Donne, M.A. VanZeeland, R. Boivin, Y. Nagayama, T. Yoshinaga, D. Kuwahara, S. Yamaguchi, Y. Kogi, A. Mase, T. Munsat, "Recent Progress on Microwave Imaging Technology and New Physics Results," *Plasma and Fusion Research*, 6, 2106042, 2011.
- [9] Y. Roh, C.W. Domier, N.C. Luhmann, Jr. "Design of an X-Mode Swept Frequency Modulation Reflectometer for the Measurement of KSTAR Plasma Density Profiles," (Invited) , " *Review of Scientific Instruments*, 75, No. 10, p. 3871-3874, October 2004
- [10] C.P. Kasten, "Two-Color Interferometry as a Fluctuation Diagnostic on Alcator C-Mod," Master of Science Thesis in Nuclear Science and Engineering, Massachusetts Institute of Technology, June 2013.
- [11] F. Meo, H. Bindsley, S.B. Korsholm, E.L. Tsakadze, C.I. Walker, P. Woskov, G. Vayakis, "Design of the collective Thomson scattering diagnostic for International Thermonuclear Experimental Reactor at the 60 GHz frequency range," *Review of Scientific Instruments*, Vol. 75, No. 10, October 2004.
- [12] P.M. Bellan, "Fundamentals of Plasma Physics," *Cambridge University Press*, Cambridge, UK, 2006.
- [13] K.C. Lee, C.W. Domier, M. Johnson, N.C. Luhmann, Jr., and H. Park, "FIR Laser Tangential Interferometry/Polarimetry on NSTX, " *IEEE Transactions on Plasma Science*, 32 No. 4, pp. 1721-1726 (2004).

- [14] B.H. Deng, H.C. Chen, C.W. Domier, M. Johnson, K.C. Lee, N.C. Luhmann, Jr., and B.R. Nathan, "Development of a multichannel far-infrared tangential interferometer/polarimeter for the National Spherical Torus Experiment," *Review of Scientific Instruments*, Vol. 74, No. 3, March 2003.
- [15] R. Barchfeld, E. Scott, C.W. Domier, C.M. Muscatello, P. Riemenscheider, M. Sohrabi, N.C. Luhmann Jr., Y. Ren, R. Kaita, "FIReTIP Design and Installation for NSTX-U," *High Temperature Plasma Diagnostics*, Madison, WI, June 5-9, 2016.
- [16] W.C. Tsai, " High Performance Electronics for Millimeter-Wave-to-Terahertz Plasma Diagnostics Instrumentation and High Power Devices," *Ph.D. Dissertation in Electrical and Computer Engineering*, University of California, Davis, 2011.
- [17] E. Hecht, "Optics," *Addison Wesley*, 4th Ed., San Francisco, CA, 2002.
- [18] F. Chen, "Introduction to Plasma Physics and Controlled Fusion," New York: Plenum Press, 2nd Ed., 1984.
- [19] T.Y. Chang, T.J. Bridges, and E.G. Burkhardt, "CW Submillimeter Laser Action In Optically Pumped Methyl Fluoride, Methyl Alcohol, And Vinyl Chloride Gases," *Applied Physics Letters*, Vol. 17, No. 6, September 15, 1970.
- [20] H. Park, D.K. Mansfield, L.C. Johnson, and C.H. Ma, " MIRI: A multichannel far-infrared interferometer/polarimeter for TFTR," *Rev. Sci. Instrum.* 56, 938, 1985.
- [21] K.M. Young et al., "TFTR Initial operations," *Plasma Phys. Control*, Fusion 26, 11, 1984.
- [22] W.C. Tsai, C.W. Domier, K.C. Lee, N.C. Luhmann Jr., R. Kaita, and H.K. Park, "NSTX far infrared tangential interferometer/polarimeter electronics upgrade," *Review of Scientific Instruments*, Vol. 81, 10D526, October 2010.
- [23] J.W. Juhn, K.C. Lee, Y.S. Hwang, C.W. Domier, N.C. Luhmann, Jr., P.B. LeBlanc, D. Mueller, D.A. Gates, and R. Kaita, "Fringe-jump corrected far infrared tangential interferometer/ polarimeter for a real-time density feedback control system of NSTX plasmas," *Review of Scientific Instruments* 81, 10D540, October 2010.
- [24] W. Lee, H.K. Park, M.H. Cho, W. Namkung, D.R. Smith, C.W. Domier, and N.C. Luhmann, Jr. "Spatial Resolution Study and Power Calibration of the High-k Scattering System," *Review of Scientific Instruments*, 79, 10E723 (2008).
- [25] J. Menard, "Overview of the NSTX-U 5 Year Plan Research Program for 2014-2018," *NSTX-U PAC-33 Meeting*, http://NSTX.PPPL.GOV/DRAGNDROP/PROGRAM_PAC/PAC/PAC-33/PRESENTATIONS/01_MENARD_PROGRAM_NSTXU_PAC33.PDF, February 19-21, 2013.
- [26] D.R. Smith, E. Mazzucato, W. Lee, H.K. Park, C.W. Domier, N.C. Luhmann Jr., "A collective Scattering System for Measuring Electron Gyroscale Fluctuations on the National Spherical Torus Experiment," *Review of Scientific Instruments*, vol. 79, no. 123501, 2008.

- [27] W. Lee, D.R. Smith, E. Mazzucato, H.K. Park, C.W. Domier, and N.C. Luhmann Jr., "Collective Scattering System for Transport Study on NSTX," *14th International Symposium on Laser-Aided Plasma Diagnostics*, Journal of Physics: Conference Series 227, Castelbrando, Treviso, Italy, 2010.
- [28] Y. Ren, S.M. Kaye, E. Mazzucato, W. Guttenfelder, R.E. Bell, C.W. Domier, P.B. LeBlanc, K.C. Lee, N.C. Luhmann, Jr., D.R. Smith, and H. Yuh, "Density Gradient Stabilization of Electron Temperature Gradient Driven Turbulence in a Spherical Tokamak," *Physical Review Letters* 106, 165005 (2011).
- [29] Y. Ren, W. Guttenfelder, S.M. Kaye, E. Mazzucato, R.E. Bell, A. Diallo, C.W. Domier, B.P. LeBlanc, K.C. Lee, D.R. Smith, and H. Yuh, "Experimental study of parametric dependence of electron-scale turbulence in a spherical tokamak," *Physics of Plasmas*, Vol. 19, 056125, May 2012.
- [30] W. Guttenfelder, J. Candy, S.M. Kaye, W.M. Nevins, E. Wang, J. Zhang, R.E. Bell, N.A. Crocker, G.W. Hammett, B.P. LeBlanc, D.R. Mikkelsen, Y. Ren, and H. Yuh, "Simulation of microtearing turbulence in national spherical torus experiment," *Physics of Plasmas* 19, 056119 (2012).
- [31] R. Barchfeld, E. Scott, C.W. Domier, C.M. Muscatello, P. Riemschneider, M. Sohrabi, N.C. Luhmann Jr., Y. Ren, and R. Kaita, "High-k Scattering and FIR TIP Diagnostic Upgrades for NSTX-U," *57th Annual Meeting of the APS Division of Plasma Physics*, Vol. 60, No. 19, Savannah, Georgia, November 16–20, 2015.
- [32] R. Barchfeld, C.W. Domier, R. Kaita, C.M. Muscatello, Y. Ren, C. Robertson, B.C. Stratton, N.C. Luhmann Jr., "High-k poloidal scattering and FIR tangential interferometer/polarimeter diagnostics on NSTX-U", *54th Annual Meeting of the APS Division of Plasma Physics (APS-DPP 2012)*, Volume 57, Number 12, Providence, Rhode Island, October 29–November 2, 2012.
- [33] P. Woskoboinikow, D.R. Cohn, and R.J. Temkin "Application of Advanced Millimeter/Far-Infrared Sources to Collective Thomson Scattering Plasma Diagnostics," *International Journal of Infrared and Millimeter Waves*, vol. 4, no. 2, pp. 205-229, 1983.
- [34] S.B. Korsholm, H. Bindslev, V. Furtula, F. Leipold, F. Meo, P.K. Michelsen, D. Moseev, S.K. Nielsen, M. Salewski, and M. Stejner, "Collective Thompson Scattering Capabilities to Diagnose Fusion Plasmas," *Nuclear Instruments and Methods in Physics Research A*, vol. 623, Is. 2, pp. 677-680, November 2010.

III. FIReTIP Design

The FIReTIP system consists of six major sub-systems. These are: 1) CO₂ and FIR lasers, 2) waveguide, 3) launch optics, 4) receiver, 5) vibration monitor, and 6) electronics. Each sub-system will be discussed in detail, with a focus on the author's contributions. The FIReTIP system is relatively large, with its components distributed over several areas about PPPL's NSTX-U test cell. The NSTX-U test cell is a large laboratory which houses the tokamak, and its supporting equipment, and which measures roughly 80' by 50'. The room is surrounded by a 4' thick concrete barrier to stop any excess neutron flux, and acts as a firewall for the rest of the building. For most of the equipment that interfaces with the tokamak, it is desirable to be physically close to the machine. The nominally available floor space is proportional to r^{-2} ; therefore, the prime locations are in short supply. Due to the size of the FIReTIP laser system, it was not possible to be located beneath the launch window at Bay G. It was deemed necessary to locate the laser system outside of the test cell, and waveguides will be added to deliver the probe beams to the launching optics. The FIReTIP laser system is allocated to a wire enclosed "cage" in the gallery area, which is just beyond the test cell wall. Furthermore, the "cage" enclosure is also the location for the High-k Scattering System lasers. This space is ~20 m from NSTX-U, and quite compact to contain both systems. This created interesting engineering challenges.

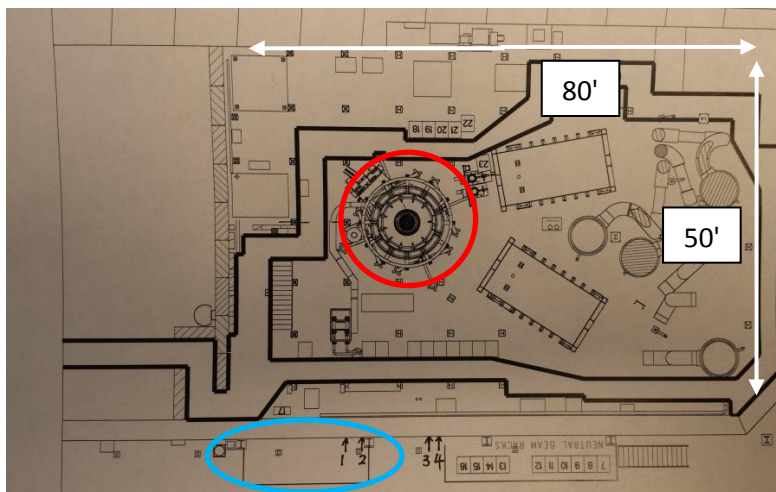


Figure 35. NSTX-U Test Cell. The tokamak is circled in red, and the "cage" for the FIReTIP and High-k Scattering System lasers are circled in blue. A thick concrete wall separates the test cell from the "cage". Source: Princeton Plasma Physics Laboratory.

III.1 FIReTIP Laser System

There are four gas lasers that comprise the source, for all of FIReTIP's measurement ability. Three lasers are far infrared (FIR), methanol lasers. The fourth laser is an infrared (IR) carbon dioxide laser. The methanol lasers provide the probe beams, and local oscillator (LO) power for the receiver mixers. The CO₂ laser is a "pump" laser, which will provide the power to energize the methanol lasers. A single CO₂ laser beam, is divided into three portions to "pump" each FIR laser. Each laser is relatively large at 8 to 9 feet long, and roughly 8 by 12 inches rectangular cross section. Each of these lasers uses a dielectric waveguide for the laser cavity. The waveguides are overmoded, where the diameter is much larger than the wavelength to improve power transmission, yet small enough to suppress excessive transverse modes. The ideal waveguide diameter depends on the wavelength of the laser [1]. The ideal length and diameter for gas lasers is difficult to determine, as it depends on many factors, such as the wavelength, type of gas, pump wavelength, etc... Experimentally, for FIR wavelengths, diameters of 1 - 2 inches, and lengths greater than 2 meters are common [2] Longer lasers can produce more power; however, the lasers will become impractically large. The High-k Scattering System lasers are of comparable size, of which there are two (CO₂ and FIR). All six of these lasers are mounted in the "cage" together.

The "cage" measures 227" wide, by 76" deep, and 85" tall. In addition to mounting six gas lasers in this space, they need adequate space to allow for tuning and maintenance. There are numerous ancillary components to consider as well, such as, optics, power meters, gas supply, vacuum pumps, power supplies, chillers, etc... It is also required that any space with personnel access have sufficient room for emergency egress. To further complicate the matter, there are two vertical structural supports and a water pipe that cannot be altered. The solution to this constraint was to construct a three level table. Each level houses two lasers each. The overall dimension are 144" long, 28" wide, and 84" tall. The lowest level holds the CO₂ lasers (FIReTIP and High-k). The mid level is for the FIReTIP Stark effect methanol laser, and the High-k FIR laser. The upper level supports the remaining two FIReTIP methanol lasers. Also

included on the laser table are power meters, optics, gas controls, motorized laser cavity controls, vacuum gauges, water temperature gauges, water flow meters, and computer DAQ interface. The entire laser table is enclosed in Lexan, and with graphite sheets around the CO₂ laser output area. The enclosure will provide protection to nearby personnel should a beam be misaligned and escape the table. The enclosure also permits the table interior to be filled with dry air to purge any humidity from the beam area. The methanol lasers emit at 119 μm wavelength, which is highly sensitive to attenuation from humidity [3]. The amount of attenuation depends on local conditions; however, nominally -3 dB/m can be expected at 40% R.H. at 70 F. While the table is fully enclosed, the Lexan paneling does not include pliable seals, so some leakage is expected. A small amount of positive pressure (< 1 PSIG) is maintained to ensure the environment stays below 5% R.H.

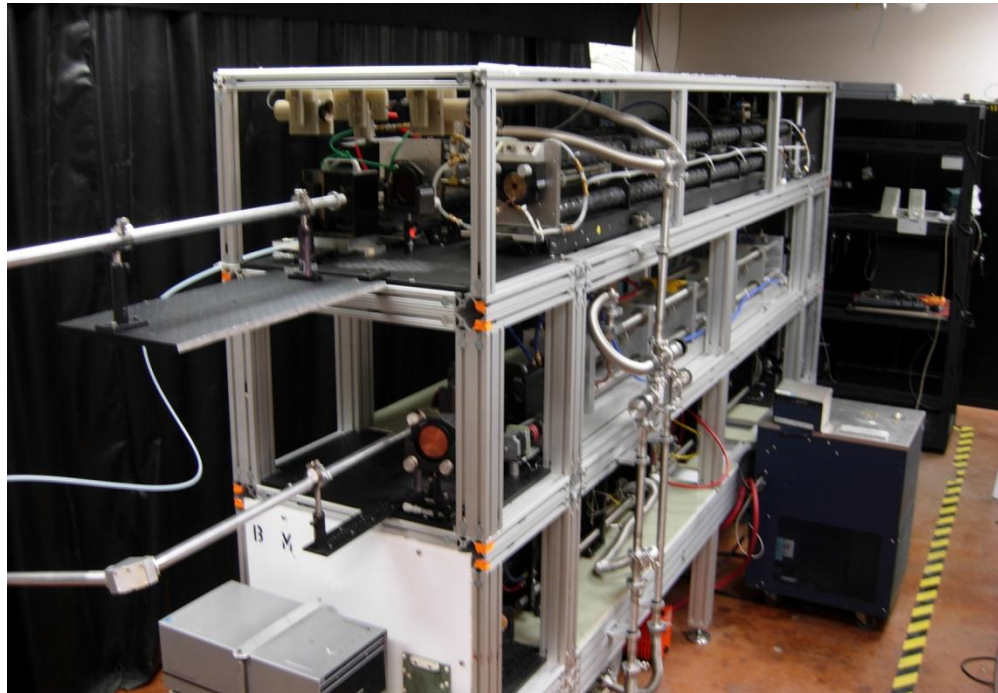


Figure 36. Laser table with Lexan enclosure removed. The overall dimensions are 144" long, 28" wide, and 84" tall. The 4 FIReTIP lasers are installed; however, the High-k Scattering lasers will be installed at a later date.

Additional equipment is needed to operate the lasers that are not enclosed within the table. The CO₂ lasers are powered by high voltage, DC, constant current power supplies. All lasers are water cooled below ambient air temperature, and there are closed loop water chillers connected with water lines. Gas cylinders supply the CO₂ lasing medium to the gas controls. Vacuum pumps beneath the table maintain the proper gas pressures in a free flowing design. An electronics equipment rack connects a computer to the table via a DAQ to monitor/control all laser parameters. Any additional electronic equipment is included in the rack. All the above systems are placed in the "cage" along the perimeter. These systems are discussed in detail in subsequent sections.

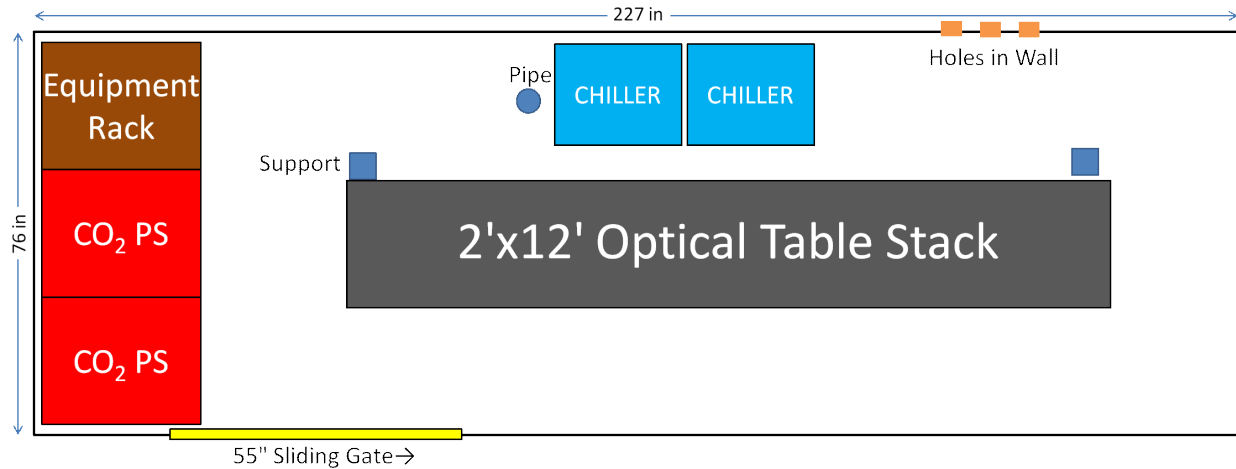


Figure 37. "Cage" layout. The laser table is shown in gray near the center. Two dark blue supports and a pipe are vertical obstructions that run floor to ceiling, and cannot be altered. Additional laser equipment are placed around the perimeter of the "cage".

III.1.1 FIReTIP CO₂ laser

The FIReTIP system uses a single IR CO₂ laser to provide "pump" power to its three FIR lasers. This laser was an original design built by the Plasma Diagnostic Group at UCLA in the mid 80s [1]. It is a grating tunable, free flowing, CO₂ gas laser. It can be tuned between 9 and 11 μm , covering

approximately 100 distinct frequencies. The output mode is TEM_{01} (annulus), with an approximate diameter of 1 cm. CW (continuous wave) power output averages 100 W depending on which spectral line to which it is tuned. The laser chassis measures 8 feet long, and has a rectangular cross section of 12" tall and 8" wide, with a weight of ~ 150 lbs. The chassis is aligned and thermally stabilized by 4 Invar rods. These are heavy metal rods with a low expansion coefficient, $2 \times 10^{-6}/K$ [4]. Lasers similar to this one have been used to "pump" FIR lasers since 1970 [5]. This laser is divided into two lengths with the high voltage cathodes (negative voltage) located at the center of the laser. The high voltage cathodes are enclosed and isolated in the center of the chassis, and the remainder of the chassis is at ground potential. In this arrangement, the high voltage leads are completely enclosed, preventing the risk of accidental exposure [1]. The start up and shut down procedure is covered in Appendix A, along with laser maintenance needs, the alignment process, and common issues to be aware of.

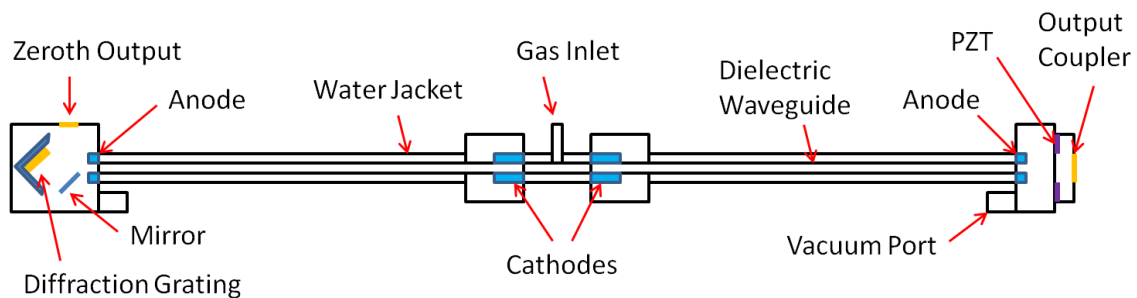


Figure 38. FIReTIP CO₂ laser design. This laser is inherently safe due to the enclosed, oil insulated cathodes. It also does not require custom glass blowing and has no Brewster windows [1].

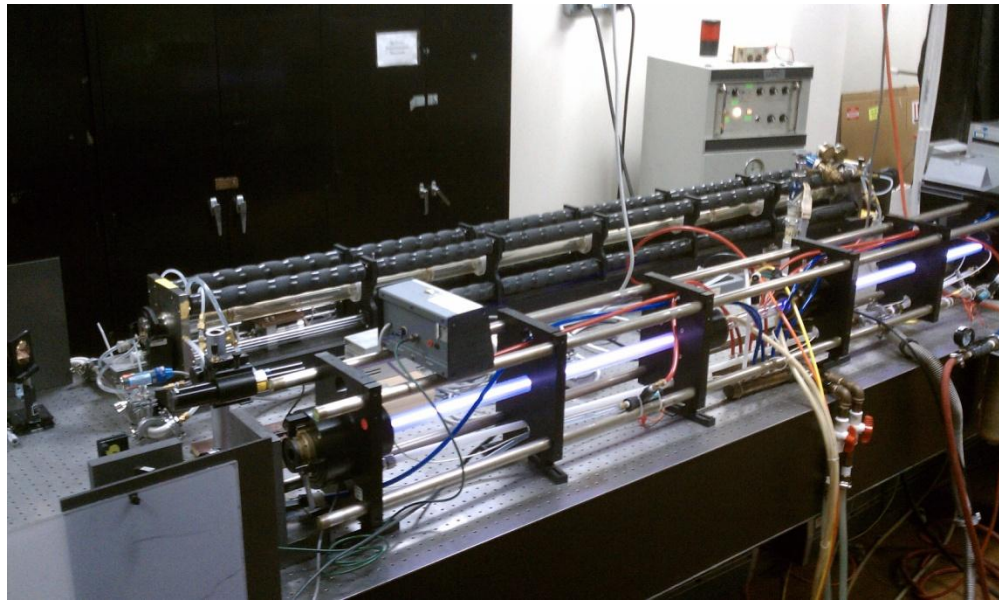


Figure 39. CO₂ and Methanol lasers. The CO₂ laser is in the foreground. The laser is energized as evidenced by the waveguide glowing purple [1].

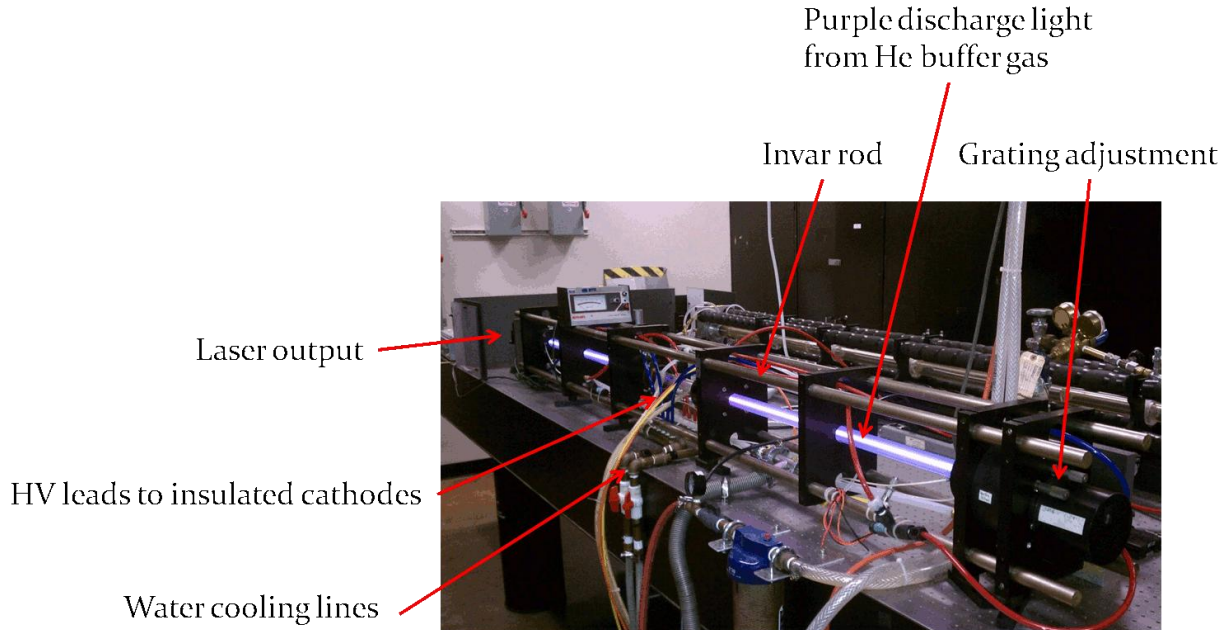


Figure 40. FIReTIP CO₂ Laser. The laser waveguides are observed to glow purple, indicating the laser is operating. This is due to the helium buffer gas in the waveguide. The beam is of course invisible.

This CO₂ laser operates by flowing CO₂ gas at low pressure through a dielectric waveguide. The waveguide is split into two sections, each with its own cathode and anode, in effect, two lasers in series. The waveguides are borosilicate glass with a 10.5 mm inner diameter, and 35" length. The cathodes are located near the center, where the waveguides are closest. They are hollow nickel cylinders to not block the waveguides, and energized around -10 kV during operation. The DC electrical discharge will energize vibrational modes of CO₂ molecules whose transitions are known to emit in the 9 to 11 μm range [6].

Laser power is controlled by a combination of gas pressure and current. 10 to 30 Torr gas mixture and 10 to 100 mA is typical, with larger values producing more power. The cathode housings are filled with dielectric oil to assist with heat transfer to the cooling system. At the outer ends of the waveguide, hollow, nickel disks are the anodes, and are maintained at ground potential. The anode aperture is of selectable size, to limit the number of transverse modes. The smaller the aperture, the lower the cut-off frequency, which can improve mode quality, but can reduce total power output as well. 10 to 11 mm diameter anodes are found to perform well. The main output at the front of the laser is covered with a ZnSe output coupler which is coated for partial reflection at the laser frequency (~80% R at 10 μm). The inner coupler surface is ground with a 20 m concave radius. This helps reflected light to remain collimated in the waveguide.

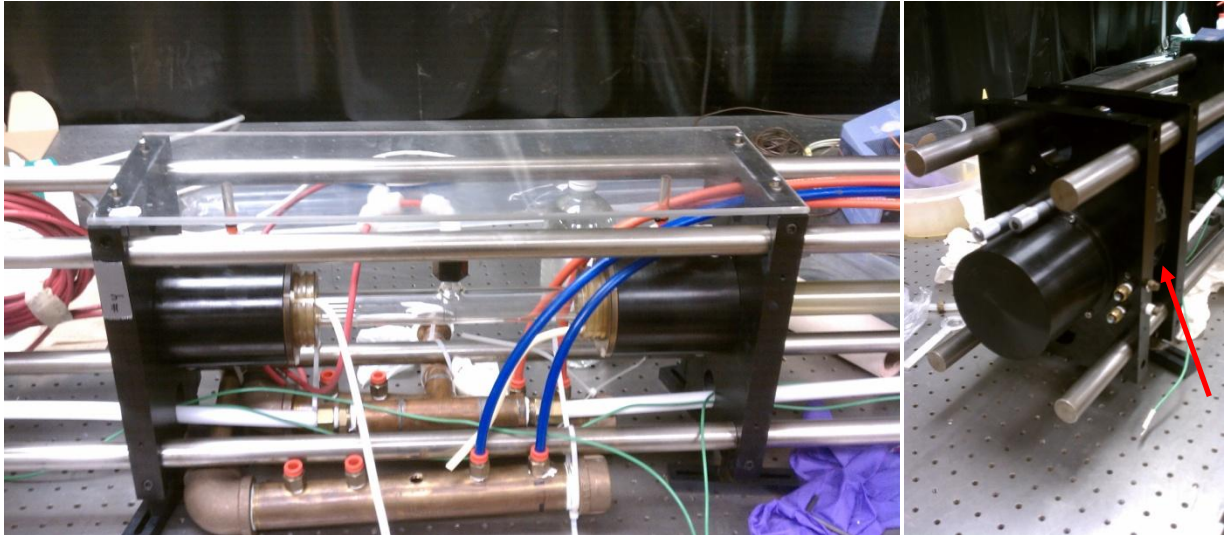
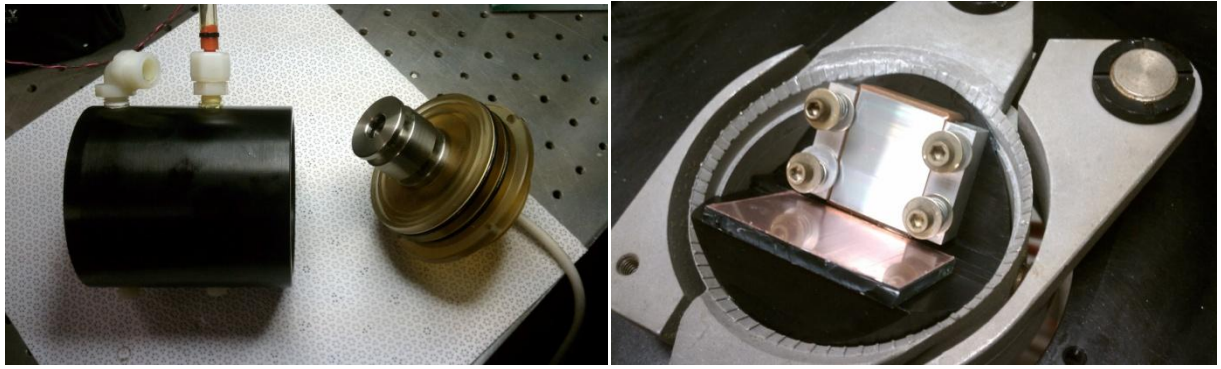
The rear reflector is a diffraction grating. The grating is mounted at 45°; however, it is designed such that first order diffractions are aligned with the waveguide axis. The diffraction angle is frequency dependent; therefore, adjusting the angle of the grating will select which frequency will resonate. The zeroth order diffraction is reflected to a side mounted output window near the rear of the laser. Approximately 1% of the total laser power is directed to the side output, which can be used for power or frequency monitoring.

To allow for frequency fine tuning and thermal variations, the cavity length is adjustable. Since the wavelength is ~10 μm , a very fine adjustment is needed. The output coupler is connected to a piezoelectric crystal. An applied DC voltage of 0 to 1500 V will alter the crystal dimensions to adjust the cavity length by ~ 15 μm ; therefore, there should be two settings that produce maximum power. In practice, adjusting the piezoelectric transducer (PZT) will vary the CO₂ power by about 5%; however, this

fine adjustment is critical for pumping the FIR laser effectively. The waveguides, cathodes, output coupler, and grating are water cooled. A water chiller circulates and cools water flowing around the laser. About 1 kW of cooling capacity is needed to keep the laser from overheating. Furthermore, the laser will produce more power when cooled to near freezing levels [7]. When the CO₂ molecules are energized into a population inversion state, they will emit IR photons when stimulated. Intermolecular collisions will upset the inversion, which limits the gas pressure to ~30 Torr. The cooler the gas, the longer the mean free path will be; therefore, more molecules will retain their energy until stimulated. If the laser is cooled too low, then atmospheric water can condense on the output coupler, absorbing power and interfering with mode quality. The practical limit with 40% R.H. is about 10 C. In a dry air environment colder temperatures may be beneficial.



Figures 41a and 41b. Left: CO₂ laser cathode made from nickel 200. Right: Selective aperture anode made from nickel 200.



Figures 42a, 42b, 42c, and 42d. Top left: Cathode mounted in dielectric cover, with cathode housing. Top right: Diffraction grating mounted in 2-axis adjuster. The mirror opposite the grating reflects zeroth order diffractions to the side output window. Bottom left: Two cathode housing mounted at the center of the laser. Center glass tube supplies gas to each half of the laser. Copper water cooling manifold shown beneath the laser. Bottom right: Rear of laser showing grating cover, grating cooling hook-ups, and micrometer adjusters. Low power side output window shown with arrow.

This laser is powered through a high voltage DC discharge. A constant current, dual DC power supply can deliver 10 kV and 60 mA to each laser half for a total delivered power of 1200 W. The power supply

was originally designed by Apollo Lasers. It uses a pair of tetrode vacuum tube current regulators to maintain the proper power delivery, which is important during laser activation when laser impedance can rapidly vary. These power supplies have been out of production for many years, and many of the components are considered obsolete and in short supply, including some operational amplifiers, zener diodes, and the vacuum tetrodes. UC Davis has a cache of spare parts to keep these lasers operational for several years; however, at some point alternatives may be needed. The power supply automatically adjusts voltage, while the operator chooses the current level. It can operate in CW, single shot, or pulsed mode; although, for the FIReTIP system, CW is always used. Two high voltage leads deliver negative voltage to the laser's two cathodes, and a common ground wire completes the circuit.

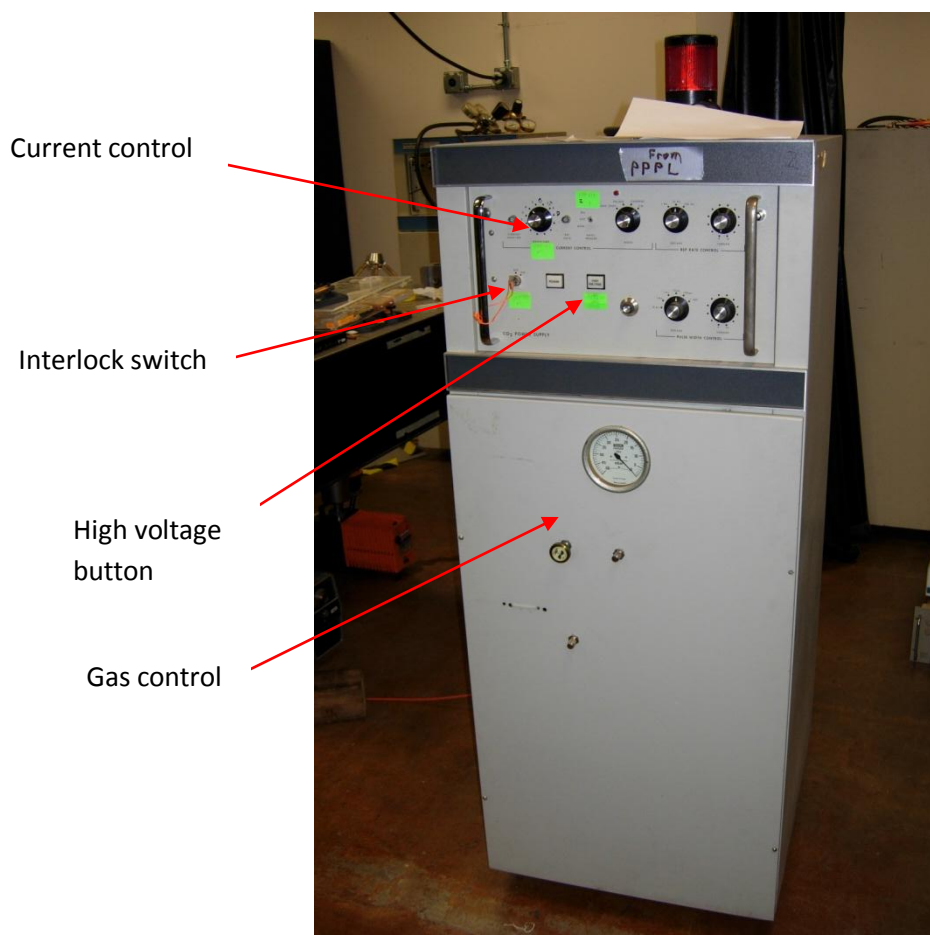


Figure 43. FIReTIP
CO₂ laser power
supply, originally built
by Apollo Lasers.
Note: Not all power
supplies have
integrated gas controls.
The FIReTIP gas
controls are mounted
to the laser table to be
independent of the
specific power supply
in use.

Gas is supplied by a gas cylinder filled with a mixture of carbon dioxide, helium, and nitrogen. While carbon dioxide is the lasing medium, only a few percent of the gas is CO₂. The other gases are buffer gases, which help transfer energy to the CO₂ molecules. Helium molecules travel at higher velocities for a given energy as compared with more massive molecules. This increases their collision frequency, and enables helium to effectively transfer kinetic energy to all species in the gas mixture. Nitrogen gas happens to have a vibration mode that contains the same energy as CO₂ vibration modes. Upon collision with CO₂ it can efficiently activate the desired vibrational modes. Many gas mixture ratios have been tested, and the optimum ratio for power output and gas economy is 6% CO₂, 18% N₂, and 76% He, by moles [1]. A lesser percentage of CO₂ can produce slightly more power; however, the flow rate and operating pressure must be increased. This consumes gas at an accelerated rate, which increases the laser operating costs. Higher portions of CO₂ similarly reduce power output. The free flowing design means that a vacuum pump is continuously running to evacuate the laser cavity. Once free of air or other impurities, the lasing gas is metered into the laser at a rate to reach a dynamic equilibrium of ~30 Torr (for the 6% gas mixture). The pumping rate and gas mixture affect the optimum pressure for highest power. The FIReTIP system uses a dry scroll vacuum pump (Agilent SH-110), which can maintain ~ 6 l/min during laser operation. If a different gas mixture is used, the partial pressure of CO₂ should remain constant, i.e. 1.8 Torr for the FIReTIP system.

Water is circulated by a NesLab HX-75 chiller. The temperature range is selectable from zero to 35 C, and will refrigerate or heat the water as needed. At the lowest setting, water temperatures reach about 8 C in ~ 20 minutes with the laser deactivated. With the laser running at full power, a minimum of 12 to 15 C can be achieved, depending on the ambient temperature. Distilled water is recommended to reduce the possibility of biological growth in the cooling system. A 5% bleach solution can eradicate any growth that occurs; however, bleach should never be left in the system for any length of time. It will corrode brass fittings and other materials over time. Thoroughly flushing the system with clean water is recommended after a bleach treatment. The chiller should not be run with the laser off for any long periods of time,

because the low temperature may cause condensation on the output coupler, disrupting laser functions later.



Figure 44. HX-75 Neslab water circulator and chiller.

Any DC voltage source can power the PZT. FIReTIP uses a Lansing Research lock-in stabilizer model 80.215. In bias mode, it can deliver 0 to 1500 VDC from its high voltage port. High voltage bayonet connectors are used to connect power to the laser. The original laser design used a 7-pin Viking connector for the purpose. This has been modified for use with a coaxial line. The PZT unit has three crystals, each with a positive and negative lead, plus a chassis ground. The positive leads are connected together to the coaxial inner conductor, and the negative leads go to the outer connector. It also has a fast and slow

sweep feature, which can be useful for diagnosing problems, or when setting up the FIR laser for the first time. More details are available in appendix A.



Figures 45a and 45b. Left: Lansing Research lock-in stabilizer to control PZT displacement. Right: CO₂ laser main output. The ZnSe output coupler is shown with the arrow. Vertical and horizontal alignment screws adjust the output coupler position. The bellows and PZT are contained within this housing.

The output coupler is attached by a narrow bellows to allow for two axis adjustment. Fine pitch screws control the position, and once the output coupler is orthogonal to the waveguide axis, it rarely needs adjusting. Care should be taken when adjusting, cleaning, or removing the output coupler. If it falls out of adjustment beyond the ability for the laser to operate, it can become cumbersome to realign it. ZnSe is the preferred material for CO₂ laser windows, couplers, and lenses. It has a very low absorption coefficient at common CO₂ wavelengths, $\alpha = 0.0005 \text{ cm}^{-1}$ at 10.6 μm [8]. Reflection and transmission coefficients are controlled by thin dielectric coatings. There are several vendors who specialize in these products, such as II-VI Infrared and ThorLabs.

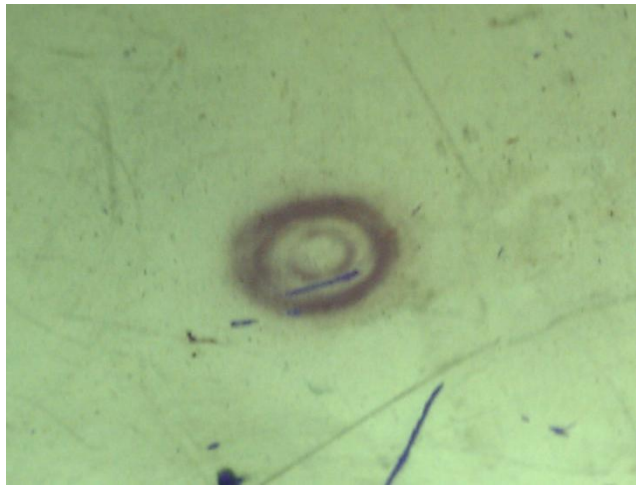


Figure 46. CO₂ laser output mode. The dark ring is an image of the beam cross section. The IR beam is naturally invisible. To observe the beam a fluorescent plate is used. A UV light will illuminate the detector plate, causing it to glow green. When the CO₂ beam also strikes the plate, it casts a shadow in the fluorescence, making a dark spot. The plates are numbered for sensitivity, with #1 being the least sensitive (highest beam power). It is important to use the appropriate plate for the incident power.

The grating is tunable for a range of frequencies; however, there are many factors to consider when choosing a grating depending on the application. The grating groove density should provide sufficient angular dispersion between spectral lines to make their selection distinct, without overlapping resonant lines or causing the angular adjustment too sensitive to be practical. If the groove spacing is too fine, then the range of tunable frequencies will be limited. A single grating generally does not cover the entire 9 to 11 μm range, nor is it desirable to achieve this. A "blazed" grating, designed for the desired wavelength is preferred to maximize efficiency at that wavelength. Groove densities between 135 and 150 g/mm work well. The nominal grating installation is at 45°, relative to the vertical waveguide axis with the grooves horizontal. Sealed micrometers near the rear of the laser provide horizontal and vertical adjustments. It is adjustable by ± 5 degrees in two planes for proper alignment. The grating mount is water cooled, and the grating is clamped in place with vacuum safe, thermal grease assisting in heat transfer. The grating itself

is a copper substrate measuring 1.00" by 0.88" and 0.5" thick. Commercially available gratings typically have their top surface coated in gold, aluminum, or a dielectric, such as aluminum magnesium fluoride (AlMgF_2), to protect the grating from corrosion, and improve power thresholds. The micrometer adjusters are graduated in mils, with 0.0001" precision via a Vernier scale. Repeatability of adjustment is < 1 mil. However, every grating is unique, and each grating will have unique positions for each spectral line. For gratings of different groove densities, blaze angles, or blaze wavelengths, the installed position can be radically different for the same line.

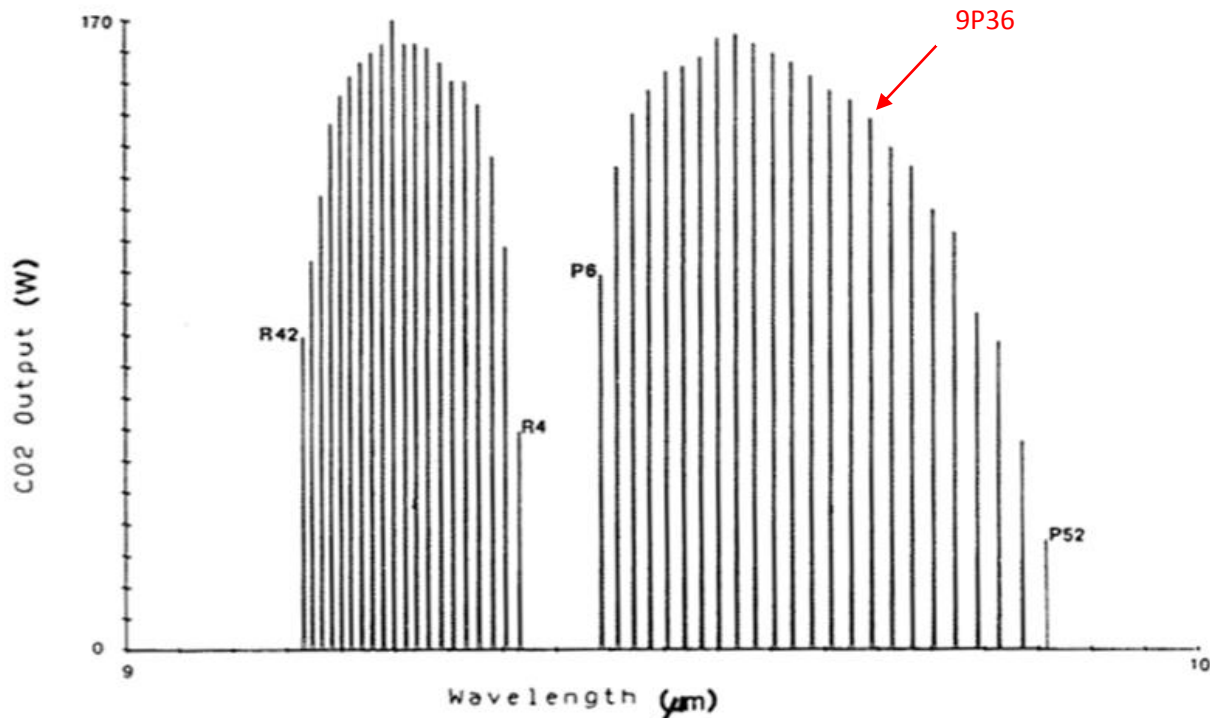


Figure 47. Relative CO₂ laser power output for 9 to 10 μm (9R and 9P series). The methanol lasers require spectral line 9P36 (9.695 μm) to achieve 119 μm output [1].

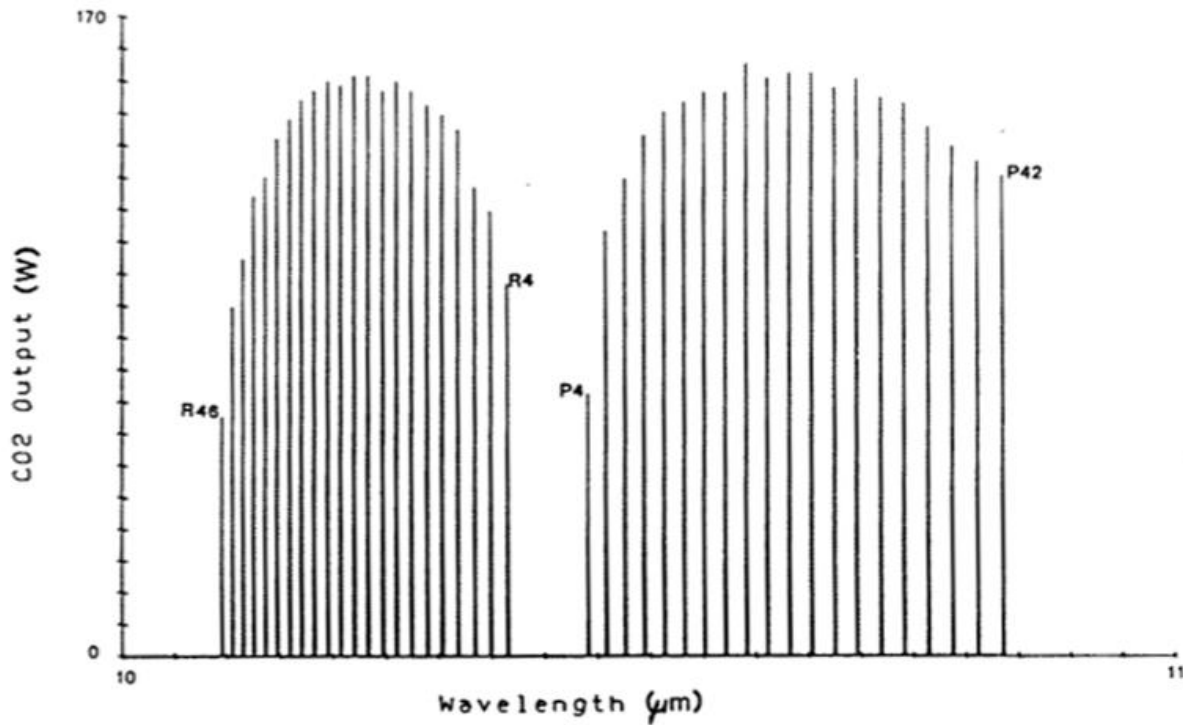


Figure 48. Relative CO₂ laser power output for 10 to 11 μm (10R and 10P series) [1].

A blazed grating has two principle design parameters, blaze angle and wavelength. The purpose of blazing is to maximum efficiency at particular wavelengths, such that the 1st order diffraction provides the most intensity, much more than the zeroth order diffraction. The grating has a sawtooth surface texture. The sawteeth are cut at an angle (blaze angle) and the groove depth is set so that the path length difference between adjacent grooves is $\lambda/2$, where λ is the blaze wavelength. This enables constructive interference at that specific angle and wavelength [9]. Nearby wavelengths will also perform well, but as the grating is tilted more and more, the efficiency is reduced. Equation 15 shows the relation between the blaze wavelength, and the blaze angle and groove density.

$$\lambda_B = \frac{2}{N} \sin(\theta_B)$$

where λ_B is the blaze wavelength. N is the groove density, and θ_B is the blaze angle.

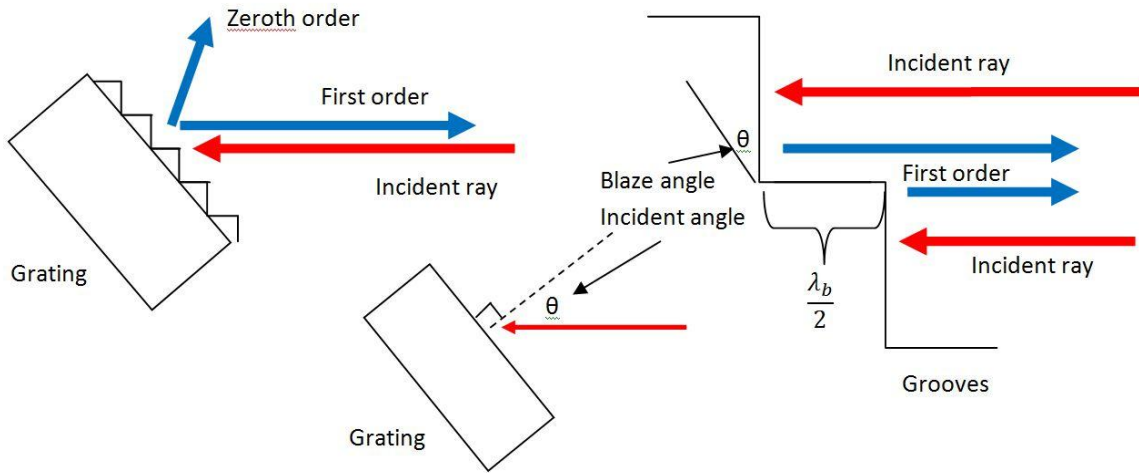


Figure 49. Blazed diffraction grating with special grooves cut so that first order diffractions travel back along the incident path, as shown on the left. In the center, the incident angle of the incoming ray is shown relative to the grating normal. On the right of the grating geometry, 90° grooves are cut so that the blaze angle matches the incident angle. The groove wall parallel to the rays should be $\lambda/2$ of the blaze wavelength.

The energize the methanol lasers for 119 μm output, the CO₂ laser needs to be tuned for spectral line 9P36 (9.695 μm) [10]. These gratings are commercially available; however, UC Davis manufactured custom gratings for FIReTIP. Commercial gratings are typically designed for 10.6 μm , which is generally the most powerful CO₂ laser line for industrial applications, but less useful in scientific applications. Several gratings blazed for 9.695 μm have been machined by the author on the NN1000 "nano-mill" [11]. This machine is a prototype ultra precision CNC mill developed by Digital Technology Laboratory, a subsidiary of Mori-Seiki (now DMG-Mori). The NN1000 was configured for linear scribing using a mono crystal diamond tool. The tool profile is a two edge diamond crystal, ground at 90° from each other. A copper block was carefully surfaced, and then parallel grooves are cut at 150 g/mm. A blaze angle of 47.5° was used. Therefore, the normal scribe depth was 3.22 μm , with a lateral spacing of 6.67 μm . This grating provides tuning from 9 to 10 μm in the FIReTIP CO₂ laser. After machining, the grating was

sputtered with a thin layer of gold to protect the copper from corrosion. The final product works well, generating the same power output as commercial gratings.



Figures 50a and 50b. Nano-machined diffraction gratings. (Left) Close up view of the grooves (6.67 micron peak to peak spacing, 3.22 micron depth), image taken by a Zeta 3-D microscope. (Right) Macro view of the same grating. The surface dimensions are 25 x 22 mm. Total manufacturing time was 12 hours.

The NN1000 "nano machine" is a 5-axis ultra precision CNC mill. Its name derives from its command resolution of 1 nm. While it is not directly related to the FIReTIP or High-k Scattering diagnostics, it has provided ample support to plasma diagnostic and related technologies. This type of machining is a substantial improvement over conventional CNC mills when performing operations that require sub-micron tolerances. A detailed view of this technology, its applications, and a practical guide for its use is found in Appendix B.

III.1.2 FIReTIP FIR Lasers

An optically pumped gas laser is a simpler system in many regards. It has no power supply, no high voltage concerns, and no grating or other tuning mechanism, apart from adjusting the cavity length to account for thermal variations. The FIR output frequency is determined by the type of gas it contains. The

frequency design will then dictate many of the design parameters, including the pumping wavelength, input window, operating pressure, and output coupler. Methanol gas is the lasing medium of choice for FIReTIP. It has a relatively strong output of \sim 300 mW at 119 μ m with 100 W pump power. Methanol also allows for a two level Stark effect broadening [12].

FIReTIP employs three methanol lasers. Two will provide the probe beam power with two different polarizations (right and left handed circularly polarized). The third laser is a Stark effect laser, which allows the output frequency to be shifted by several MHz. This laser provides the local oscillator power to the receiver mixers, and permits improved temporal resolution of 4 to 6 MHz.

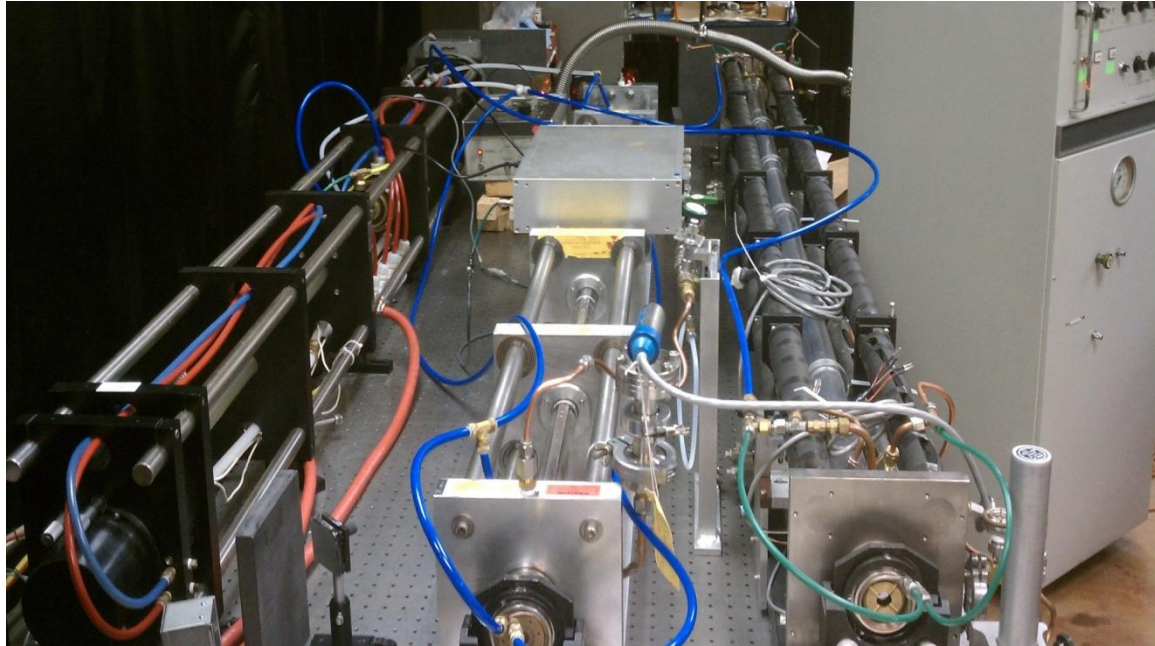


Figure 51. FIReTIP lasers types shown together. From left to right, CO₂ laser, Stark FIR laser, and FIR laser.

The two standard FIR lasers are identical in design. These lasers are 9' long, with a rectangular cross section of 8" wide by 10" tall. Thermal stabilization is provided by neoceram glass tubes. Neoceram is low expansion glass that will tie together the laser chassis to be less susceptible to temperature changes [13]. These lasers were originally designed to be mounted near the tokamak. Invar is paramagnetic, and

external magnetic fields could strain the laser chassis, upsetting the optical alignments. Neoceram was used for its diamagnetism. Each laser weighs about 100 pounds. The laser cavity is a borosilicate round waveguide, measuring 96" long and 1" inside diameter. The input side of the laser has a ZnSe window, anti-reflective coated for the pumping laser. This will reduce any reflected power following the same beam path and disrupting the CO₂ laser. Behind the input coupler window, a copper mirror is installed with a 4 mm hole at its center. The CO₂ laser is focused so that its beam waist is near the mirror aperture, and then expands inside the FIR laser. This feature reduces the amount of CO₂ power inside the FIR laser that can escape back out of the input coupler, and disrupting the CO₂ laser. Some lasers prefer to use an off-axis input hole so that any reflecting or escaping CO₂ photons do not have a path back to the CO₂ laser [14]. The FIReTIP lasers use an on-axis input hole. The output coupler is of a hybrid design. It must reflect 100% of the CO₂ laser power, but act as a partial reflector for FIR wavelengths. To complete the vacuum seal of the laser, the output coupler is covered with a z-cut quartz window. Both input and output couplers are mounted on bellows with two axis micrometer adjusters. The waveguide, input, and output couplers are surrounded by a water jacket for cooling. The cooling system flows in parallel with the same CO₂ water chiller. Cooling the gas to ~10 C also improves power output for the same reasons as the CO₂ laser [7].



Figure 52. FIR methanol laser mounted on top level of laser table. The black tubes running the length of the laser are the neoceram rods wrapped in foam padding.

The laser operates by evacuating the laser cavity, and then maintaining a small pressure of methanol gas, 200 to 300 mTorr is typical depending on conditions [15]. This laser is a free flowing design; however, the consumption rate is very low. Liquid methanol is stored in a 100 ml flask at one end of the laser. At the opposite end, a two stage mechanical oil vacuum pump evacuates the laser to < 2 mTorr. Low pressure in the laser evaporates the methanol, and gas flows through the laser. A needle valve regulates the flow, and the methanol consumption is < 1 ml/day (8 hours continuous operation). The CO₂ laser beam enters the FIR laser through a ZnSe window, and reflects between the end mirrors. 9.695 μm wavelength photons have the correct energy to excite methanol molecules, which in turn can reemit at 119 μm . There are several energy states that can be induced by the CO₂ laser; therefore, it is important that the CO₂ laser is tuned properly. The versatility of CO₂ lasers to energize many different types of

molecules is well known [5]. Energized methanol molecules then reemit when stimulated and reflect between the end mirrors; however, the output mirror is only partially reflective to FIR wavelengths, thus emitting the FIR beam.

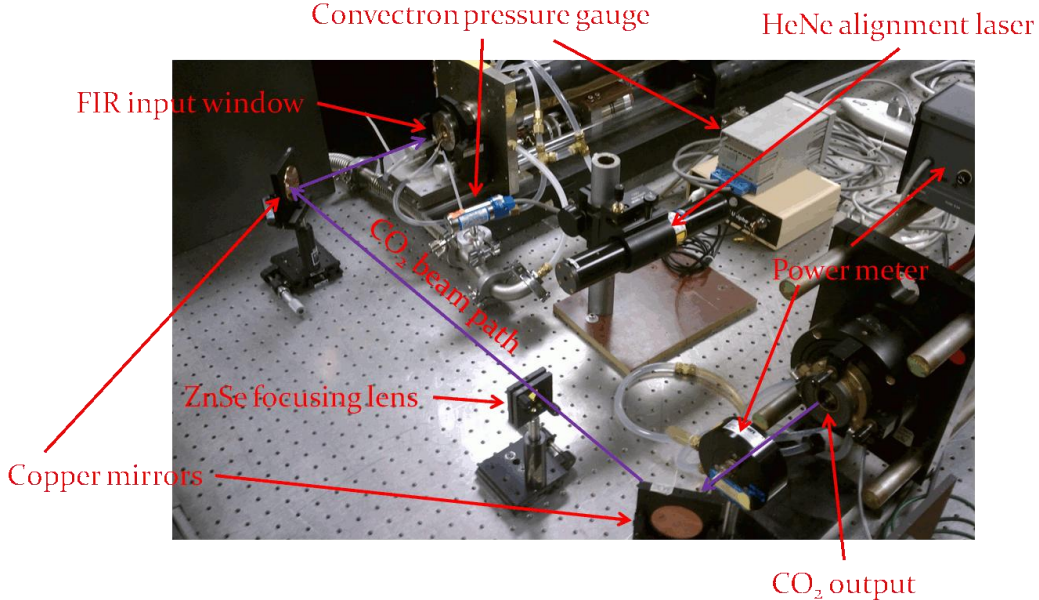


Figure 53. CO₂ pumping configuration. The CO₂ laser on the right side emits a 1 cm diameter annulus beam at 100 W and 9.695 μ m. Copper mirrors reflect the beam to the FIR laser input window. The ZnSe lens focuses the beam down to place the beam waist at the FIR input 75 cm away.

The hybrid output coupler is a design colloquially known as a "Giant Hole Coupler" [16]. It consists of a high impedance ($Z > 1 \text{ M}\Omega/\text{mm}$) silicon substrate. This type of silicon provides very low attenuation in the FIR regime. The silicon wafer is 1.5" diameter and 0.060" thick. The inner surface is coated in gold; however, the center of the coupler has an uncoated portion. Several couplers were fabricated with the uncoated center diameter of 8 to 11 mm. This allows for a selectable reflection/transmission coefficient. These coefficients are roughly determined by the ratio of the coated (visible region i.e. 1" diameter) and uncoated areas. Therefore, 81% to 90% reflection is possible with the couplers on hand. FIR photons will reflect between the end mirrors several times on average, until they happen to find the center of the output coupler. A small amount will also be lost from the 4 mm input mirror hole. The FIReTIP FIR lasers

performed best with a 10 mm giant hole coupler (~85% R, 15% T). It is imperative to reflect all of the CO₂ laser power. The output coupler is coated with thin dielectric layers which are designed for 9-11 μm reflection. At 119 μm , the FIR beam can pass through with low attenuation. Beams exiting the output coupler rapidly diffract, and optics are needed to collimate the beam.

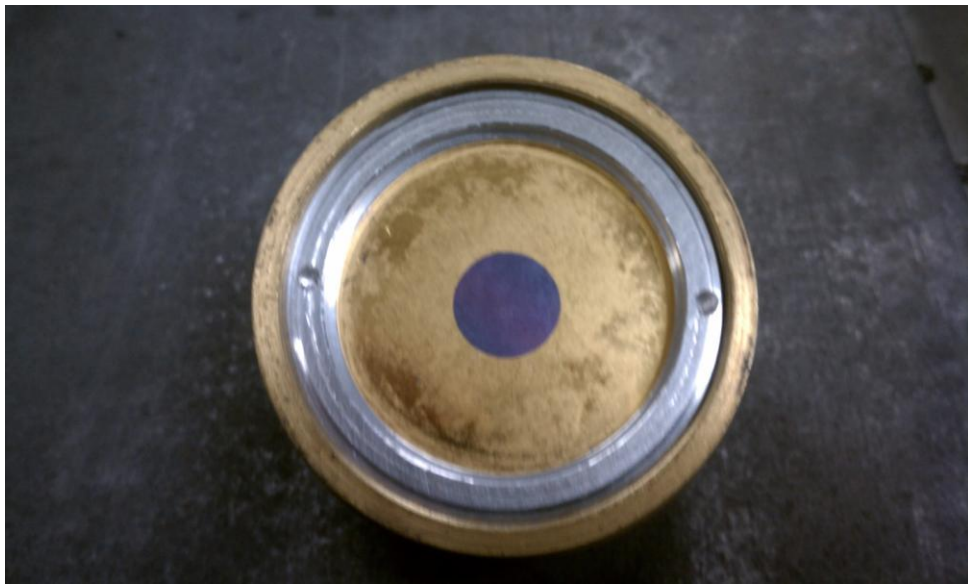


Figure 54. Giant hole coupler. This coupler is retained in its mount by a threaded ring. The gold coating reflects the FIR photons. The dark circle at the center allows FIR photons to pass through. The entire coupler is coated with thin dielectric layers to reflect all CO₂ laser power between 9 and 11 μm .

The output coupler is connected to the laser by a bellows, but it also is mounted to a linear track to adjust the cavity length. A stepper motor controls a micrometer which can extend or retract to control the output coupler position. The low pressure in the laser cavity holds the linear track fast against the micrometer spindle. The stepper motor is controlled through Velmex motor controllers, a computer connection, and a LabView program. A gear reduction in the micrometer allows for ample torque to overcome friction in the system due to the pressure differential, and it provides for sub micron cavity length control. It is essential to tune the cavity length for maximum power output. A few microns too long or short will result

in zero power. Furthermore, different output modes are possible. When a local power maximum is detected, the output mode should be verified. Incorrect modes can be corrected by slight mirror adjustments, or increasing (or decreasing) the cavity length to an adjacent local maximum. Due to the relatively long wavelength, the FIR lasers do not need much adjustment. Once they are thermally stable (~ 1 hr. run time), they typically do not need any further adjustment. The CO₂ laser on the other hand, with its 9.7 μ m wavelength, is much more susceptible to thermal variations. Under start-up conditions, its PZT will need frequent adjustment (~ 1/min). After sufficient warm up time (~ 1hr), it will need readjustment 2 to 3 times per hour. Tuning the CO₂ laser cavity length is critical to FIR laser operation. The PZT will make very fine frequency adjustments to the CO₂ output. The difference of ~100 V (1-2 microns) can mean the difference of full to zero FIR power output.



Figure 55. FIR laser cavity length control. A stepper motor turns a gear reduction micrometer which protrudes through the laser chassis to push against the coupler translation track.

The Stark effect methanol laser is largely similar to the other two FIR lasers. The laser is of similar size at 9' long, and 8" by 10" cross section. It uses invar rods, and has a much heftier chassis; therefore, this laser is much heavier at ~ 200 lbs. The primary difference is in the Stark laser's waveguide. The waveguide is a

borosilicate tube with a rectangular cross section, measuring 22 mm x 11 mm inside dimensions. The two 22 mm wide sides of the waveguide are coated in silver on the inside of the waveguide. These two surfaces are contacted to a high voltage power supply, which can apply a potential of 0 to 500 VDC. When energized, an electric field is applied across the methanol gas. The electric field alters the electronic structure of the methanol atoms, and splits the lasing frequency into two levels, above and below the nominal 119 μ m emission [17]. An applied field of 400 V will split the lasing frequency by \pm 5 MHz. These two frequencies have different ideal cavity lengths; therefore, only one can be tuned for at a time. This is not a problem, and either frequency can be used for the LO source. A computer controlled stepper motor controls a micrometer at the output coupler to tune the cavity length. Other design features are the same. The Stark laser uses a ZnSe input window, and is backed by a copper mirror with an on-axis 4 mm hole. The output coupler is a giant hole design, with a 9 mm aperture; however, due to the smaller waveguide area, the reflection coefficient is \sim 75%. Methanol pressure of \sim 200 mTorr yields relatively good power output [12]. The rectangular waveguide is not an ideal geometry for Gaussian output, nor is the electric field uniform across the lasing medium. Fringing effects between the conductive surfaces cause the electric field strength to vary, and therefore not all of the methanol is perturbed in the same manner. The result is much reduced power output as compared to the circular cross-section, conventional, FIR lasers. With a 100 W CO₂ pump, about 50 mW can be produced. After dividing the power between up to four mixers (3 channels plus 1 reference), several mW can be delivered, which is sufficient LO power.

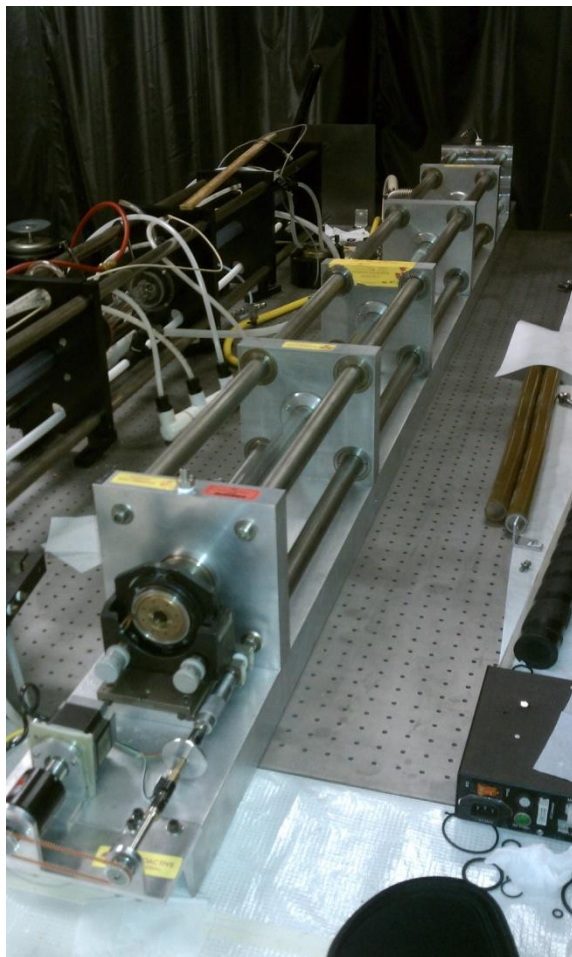


Figure 56. Stark effect FIR methanol laser. The output coupler is seen with two micrometer alignment controls. The cavity length controls are located in front of the coupler.



Figures 57 and 58. Left: Rectangular Stark waveguide. The wide sides (top and bottom) only are coated with silver on the inside of the tube. Right: Stark waveguide installed with the high voltage clips installed.

Unfortunately for the Stark laser, its waveguide suffered damage to one of its ends. It was necessary to shorten the waveguide by 6" (96" down to 90"). This reduction in length also reduced the maximum power output by about 15%. Shortening the waveguide required redesigning parts of the chassis hardware. A new end plate was manufactured to avoid cutting the invar rods. A new bellows mount and vacuum sealed electrical connector for the Stark effect voltage was necessary to replace. The metal coated waveguide is a unique length of glass, so a spare waveguide was manufactured. The original waveguide is a continuous 96" length of borosilicate glass. The glass industry no longer offers this size. 22 mm x 11 mm ID is only available in 48" lengths. UC Davis procured two 48" lengths and fused them together. This technique is not ideal, as it is difficult to fuse the waveguides together with perfect alignment. Furthermore, the inner surface of the waveguide near the joint is prone to ripples, which may perturb the laser mode quality, or affect the quality of the metallic coating. The coating is applied by an electrodeless plating method [18]. It is vital that the coating is applied to the inner surface, otherwise, a static charge can build up, altering the desired electric field. A thin, uniform coating of silver was successfully applied. The coating is quite fragile, and easily scratched. Care should be taken when applying the electrical connector clips. The joint between the waveguide halves does have a minor ripple along the inner surface. It is difficult to judge how severe the surface imperfections are, and how it will affect the laser mode quality without completely assembling and testing the laser. The more troubling part of the spare waveguide is that while the joint is straight, the heat from the fusing process caused a twist along the waveguide axis. When viewed down the length of the waveguide, the two ends are $\sim 20^\circ$ out of alignment. This twist could cause mode quality problems; however, the design of the laser chassis will not permit a twisted waveguide to be installed. The glass would need to be flexed into position, creating significant stress and strain. Due to this problem, the spare waveguide was never tested. It is the author's opinion that only a continuous waveguide should be used, or the laser could be redesigned into two portions similar to the CO₂ laser arrangement.¹

¹The Stark laser spare waveguide development is the original work of UC Davis Graduate student Mohammad Hadi Sohrabi.

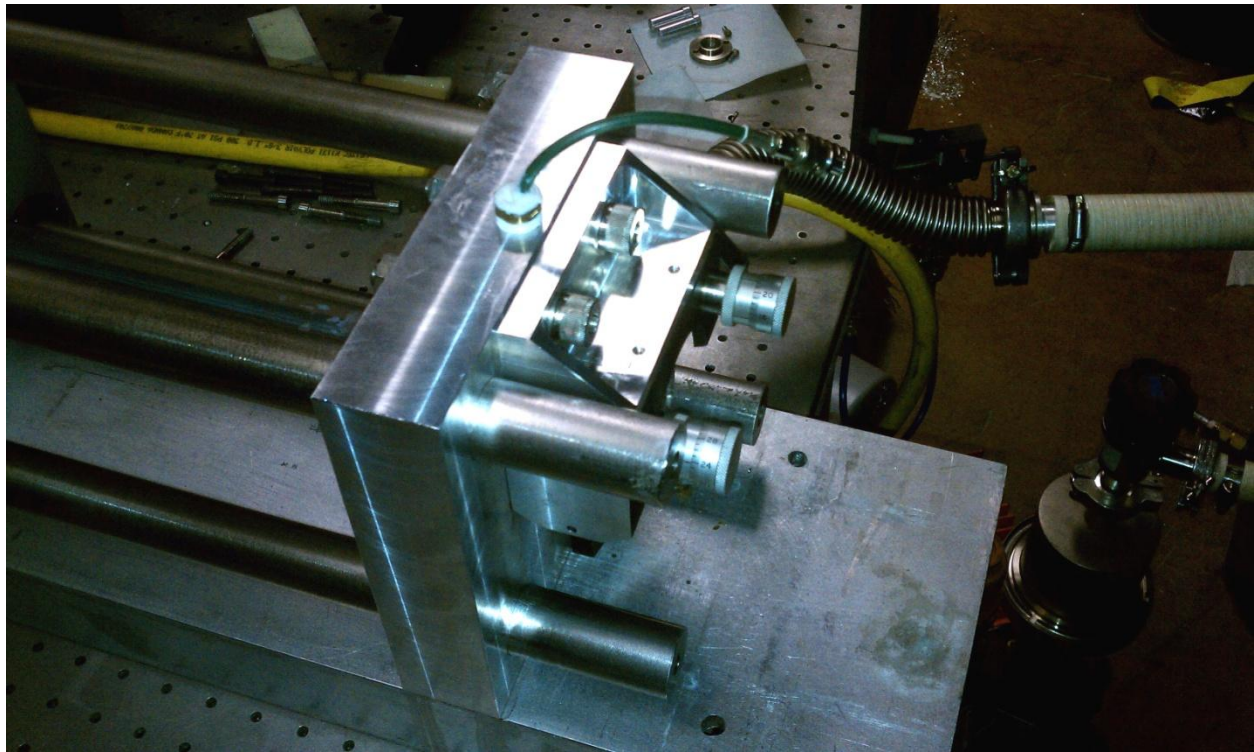


Figure 59. The Stark laser waveguide was trimmed 6" to eliminate a crack in the surface. The vertical end plate was redesigned to allow the laser chassis to be shortened. The invar rods are seen protruding through the plate. The original design mounted the plate to the end of the invar rods.

A single CO₂ laser provides the pumping power for all three methanol FIR lasers. Two ZnSe beam splitters are coated to control the reflection and transmission coefficients. The first beam splitter has 33% reflection, and the second one is 50%. This will divide the CO₂ beam into three equal portions. Nominally, equal power portions are preferred, but not required. For initial FIR laser activation, it is recommended to use the full CO₂ laser power for each FIR laser in turn. It is easier to detect small power levels from an improperly aligned laser using as much pump power as possible. Once the FIR laser is properly aligned and tuned, the applied CO₂ power can be reduced. Maximizing FIR power from a single laser will also assist in aligning the waveguide runs to the vacuum vessel, and adjusting the launch optics. It is also possible to disable the polarimeter function of FIReTIP by energizing one FIR laser and the Stark laser. A two laser system allows each laser to receive proportionally more pump power. In this case,

the FIR laser does not need to be circularly polarized, and a beam splitter on the FIR output can be removed, increasing the delivered laser power further.

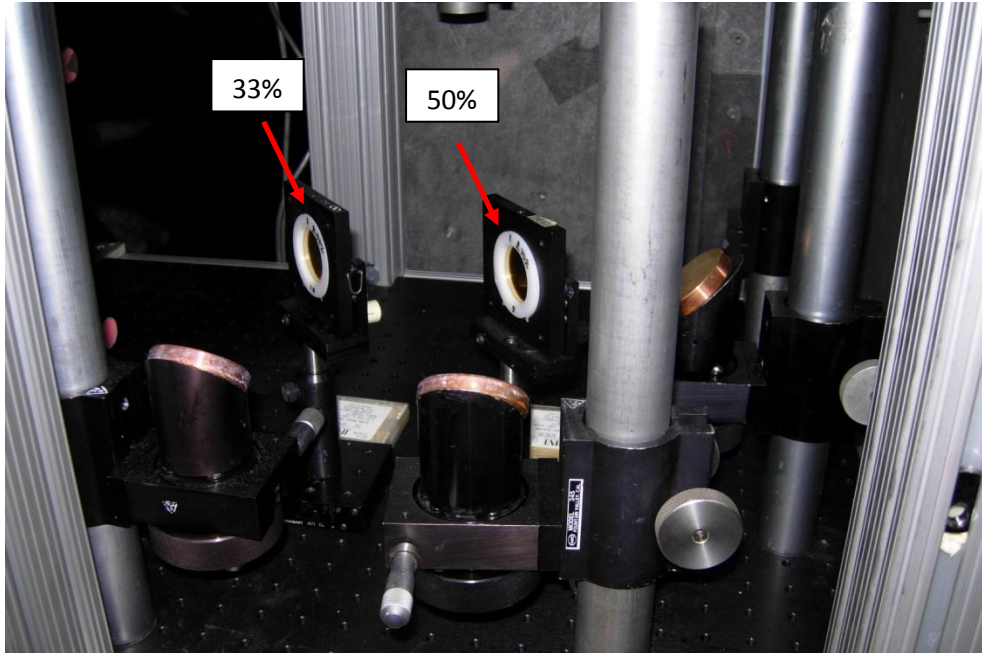
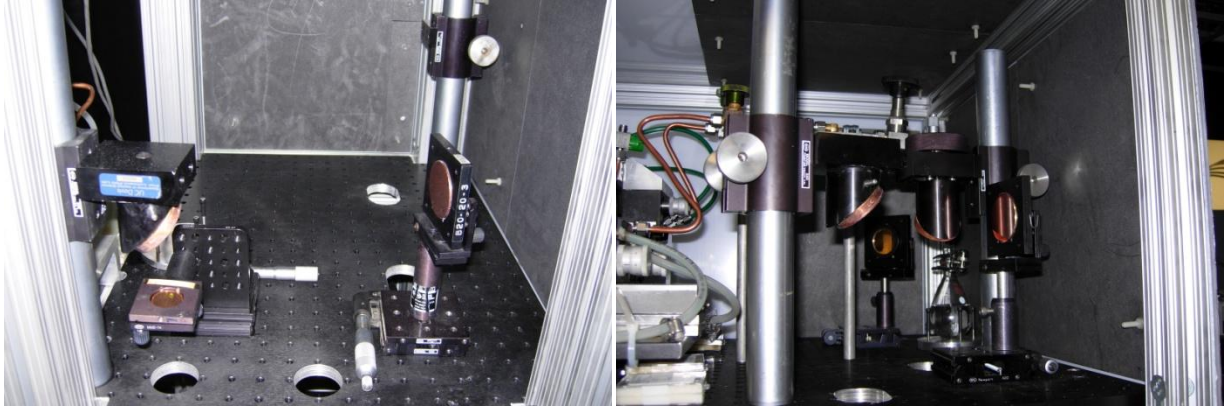


Figure 60. CO₂ laser beam splitters. ZnSe beam splitters are coated for 33% and 50% reflection. Copper mirrors turn all three beams upwards to the upper levels.

After dividing the CO₂ as desired, copper mirrors direct the beams to the upper table levels, one to the mid level for the Stark laser, and the other two to the top level. Each beam path has two more copper mirrors to steer the beams to the input windows of their respective FIR lasers. The beams must be focused down to place the beam waist near the FIR laser rear mirror hole. Upon entering the FIR laser cavity the beam will expand to fill the cavity. Several focusing lenses have been tested to see how best to couple CO₂ power into the FIR laser. The optimum CO₂ beam expansion will expand such that the beam size will equal the waveguide diameter by the time it reaches the output coupler. This equates to using a 75 cm focal length lens. The focusing lens is ZnSe, and anti-reflective coated for 9.7 μ m. The lens is mounted in the CO₂ beam path, 75 cm before the FIR laser input window. This happens to be in the vertical beam

path. This is not a problem, but it is advised to arrange the mounts so that the lenses cannot fall out from gravity.



Figures 61a and 61b. Left: Mid level CO₂ beam path to energize Stark laser. The beam enters vertically from the hole on the left, passes through the focusing lens, and then reflects from two copper mirrors to be directed to the Stark laser input left of the frame. Right: Upper level CO₂ beam path. This arrangement is similar to the Stark configuration; however, there are two CO₂ beams for two FIR lasers. The focusing lenses are just below the frame, mounted to the underside of the level. The 100 ml methanol reservoir flask is seen in the background.

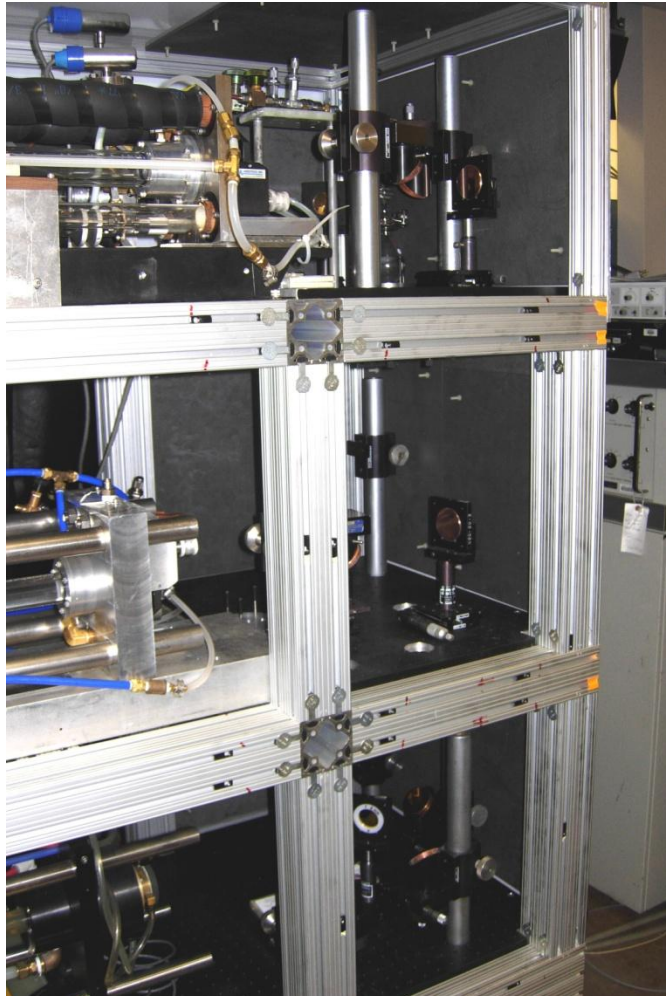
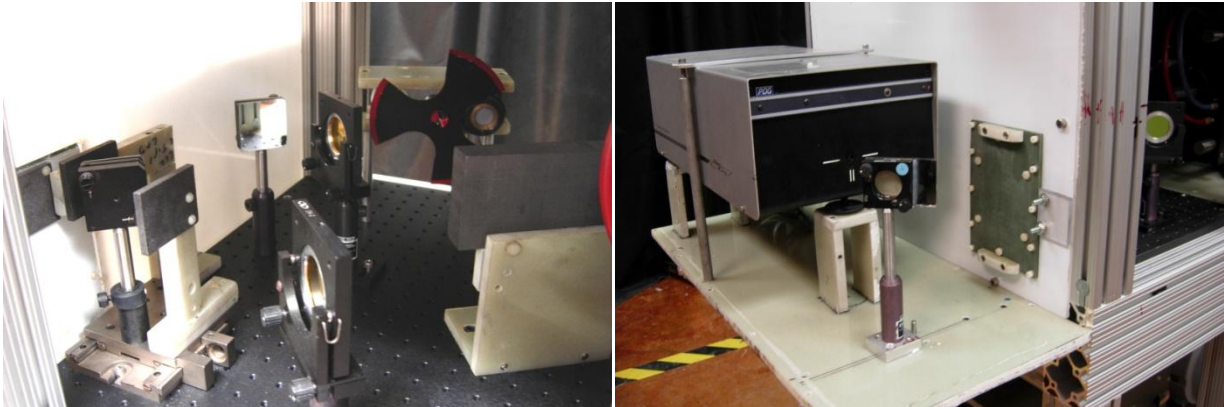


Figure 62. CO₂ beam area. The CO₂ laser on the bottom level is divided into three parts, and then directed to the upper levels to pump the Stark and two FIR lasers. This region of the laser table is lined with graphite for CO₂ laser safety.

The zeroth output from the CO₂ laser is used to monitor laser power, and can be used to verify the spectral line for which it is tuned. Approximately 1% of the main CO₂ output is directed out of the side port located at the right rear of the laser. A first surface mirror reflected the beam rearward to a ZnSe beam splitter. Half of the beam is directed to a power meter. The other half passes to the rear of the table enclosure to a graphite block to absorb the power. This graphite block can be moved out of the beam path to allow the CO₂ power to exit the rear of the table through a removable panel. A mirror then directs the beam to an optical CO₂ spectrum analyzer.



Figures 63a and 63b. Left: CO₂ laser power monitor. A ZnSe beam splitter divides the side port beam between the pyroelectric detector and the spectrum analyzer. The pyroelectric detector is seen at the far side of the table with a chopper, and the spectrum analyzer beam is blocked by a graphite block. The additional optics are for the second CO₂ laser for High-k Scattering with its own power monitor; however, they can share the same spectrum analyzer. Right: Optical Engineering CO₂ laser spectrum analyzer. The spectrum analyzer is mounted outside of the table enclosure, and the green panel can be removed to permit beam access.

The spectrum analyzer is relatively large, and must be mounted outside of the table enclosure. The spectrum analyzer, manufactured by Optical Engineering (now Macken Instruments), uses a diffraction grating and a series of mirrors to shine the sample beam onto a scale. The scale is graduated for spectral line and wavelength for common CO₂ laser wavelengths. The scale uses a fluorescent detection plate, and has a built in UV light to illuminate the scale. Excessive incident power should be avoided, 0.5 to 5 W are recommended. [19]

The CO₂ power meter is a Molelectron P4-42 pyroelectric detector. Pyroelectric detectors have a fast response to changes in temperature. To operate, an incident beam is interrupted by a chopper. The power meter output then produces a square wave, where the wave amplitude is proportional to the laser power. This type of measurement is relative, and must be calibrated against an absolute power meter. For

FIReTIP a Thorlabs CO₂ laser power meter is placed at the main laser output, and correlated to the pyroelectric detector peak to peak output. The pyroelectric detector has a maximum input of about 500 mW before the output is saturated. To reduce the CO₂ incident power, several germanium or silicon wafers are placed before the power meter sensor. These wafers attenuate the incident power to levels reasonable for the power meter. To catch any reflected CO₂ power, a graphite block is mounted. The chopper is a 3-blade, 50% chopper, which rotates at 1000 RPM. A small DC motor turns the chopper, and is powered by a 3 V DC power supply mounted under the laser table. There are many factors that can affect the power meter calibration. The ratio between main laser power, and zeroth power output depends on the spectral line and the grating installed. The beam alignment to the power meter and the incident angle to the beam splitter affect the power meter readings. The chopper RPM can drastically influence the power readings. If any of these parameters are altered, the power meter calibration needs to be redone. The pyroelectric detector output is connected to the control computer, and monitored by the LabView program. Molelectron has since been purchased by Coherent Inc., and these particular models are no longer manufactured. New models are available; however, the FIReTIP units are in good repair and will be retained for the foreseeable future.

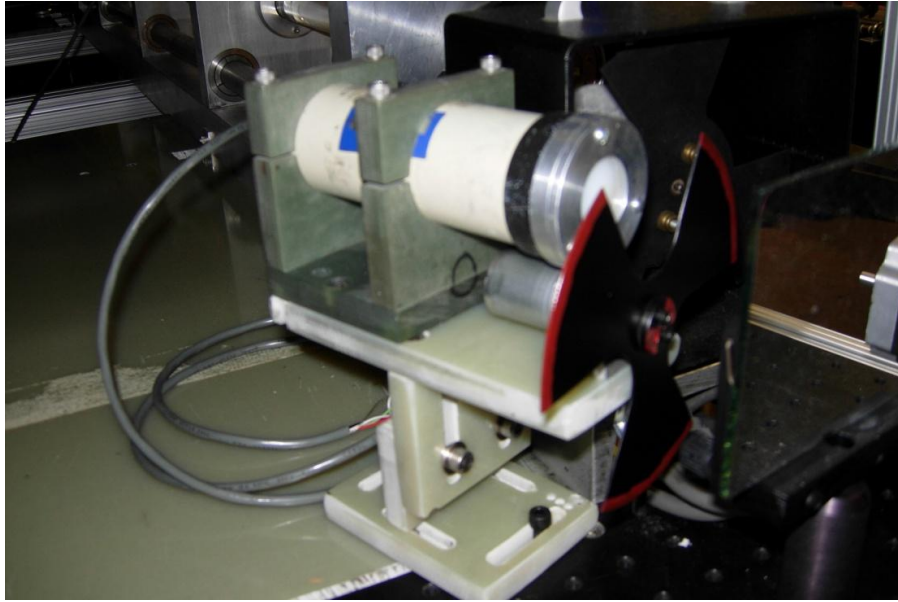


Figure 64. Pyroelectric detector with chopper. The pyroelectric detector is sensitive to small changes in temperature. The measured relative power output is the amplitude of a square wave, which is the difference between the direct laser and interrupted signal. This particular power monitor is assigned to the Stark laser.

The Stark laser output optics are straight forward. A 1 m radius concave mirror collimates the beam, and reflects it to a metallic mesh beam splitter. The beam splitter reflects the beam to the LO waveguide entrance. The transmission side of the beam splitter passes through to a chopper and pyroelectric detector. The power meter is similar to the CO₂ power meter, but calibration is performed by correlating the pyroelectric detector output to a Scientech power meter. The Scientech power meter is sensitive to temperature, but has a long integration time. At low power levels (< 10 mW), it is sensitive to the local environment, including the operator standing too near the power head. While the Scientech power meters are calibrated for absolute power measurements, they are designed for visible or infrared measurements. At longer wavelengths, the reflection coefficient increases causing a systematic reduction in measured power. At 119 μ m, a reduction factor of 0.8 is expected [20]; however, the power reported in this dissertation is the observed power, with no correction given. It should be noted that the various

pyroelectric detectors all have different power sensitivities; therefore, if power meters are ever swapped or replaced, the power calibrations should be performed.

The FIR lasers initially have vertical linear polarizations. A 1/2 waveplate will rotate the polarization of one laser to horizontal. Flat mirrors reflect the beams to a pair of 1 m concave mirrors to collimate the beam. One laser will then intersect a metallic mesh beam splitter. Half the power will be coupled into the FIR waveguide. The other half is directed vertically to a chopper and pyroelectric detector. The second FIR laser is aligned collinearly with the first FIR beam, and coupled at a beam splitter to enter the waveguide together. A portion of the second FIR laser is also directed vertically for power monitoring. Each laser has its own pyroelectric detector for power monitoring; however, they share a common chopper. Before coupling into the waveguide, both beams are passed through a 1/4 waveplate. Since they are vertically and horizontally polarized, they will be converted to right and left handed circularly polarized beams.



Figure 65. Schematic of FIR laser beam paths.

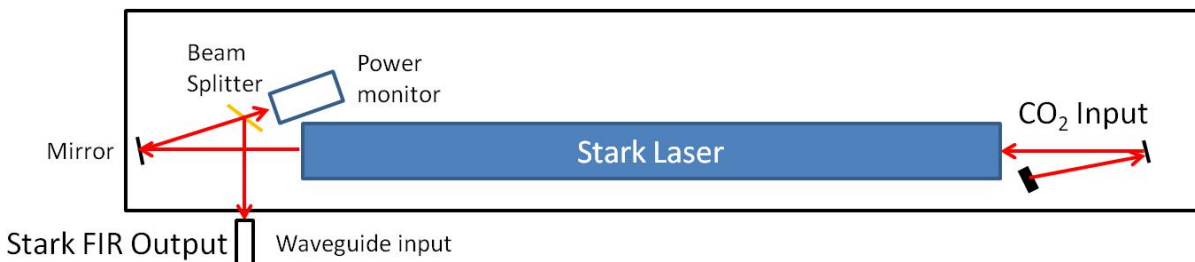


Figure 66. Schematic of Stark laser beam path.

III.1.3 FIR Laser Performance

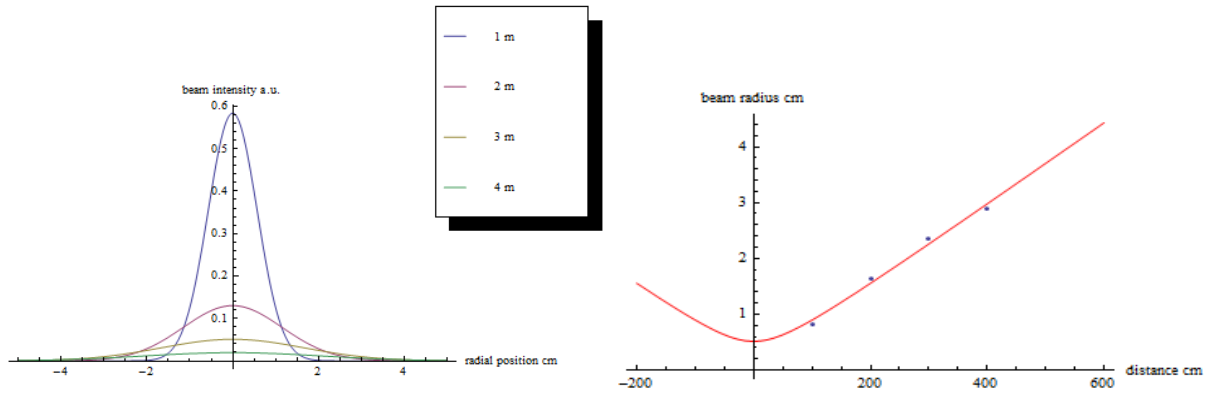
The FIReTIP FIR lasers are capable of up to 300 mW CW power output with a 100 W CO₂ pump laser; however, when the CO₂ laser is divided 3-ways, 100 mW is expected. There are several modes possible, with the most common modes being TEM₀₀, TEM₀₁ (2 degenerate modes), and TEM₀₂. TEM₀₀ is the preferred mode. This mode has a Gaussian profile, which can couple to the HE₁₁ hybrid mode in circular waveguide with high efficiency [21]. The other modes are more difficult to couple into waveguide, which can lead to large insertion losses, and greater attenuation during transmission. It is also possible for these modes with multiple lobes to be multi-frequency. When incident on a receiver mixer, a single beam can mix with itself, causing a beat frequency of a few MHz. Since this frequency is close to the desired IF output, it can confuse the data collected. If the FIR laser mirrors are not perfectly parallel, the cavity length for each lobe will be slightly different, causing a multi-frequency and possibly a lop-sided power distribution. When properly aligned, the Gaussian mode will be accessible.



Figures 67a and 67b. Left: FIR laser output mode, 100 mW, TEM₀₀. Right: FIR laser output, 20 mW, TEM₀₁. Both images were captured with liquid crystal paper. This paper is a thin sheet that is temperature sensitive with blue regions being the hottest, and red regions cooler, and black is the coolest.

Atmospheric water will readily attenuate 119 μm by around -3 dB/m [3]. To eliminate these losses, humid air can be displaced by dry air (< 5% R.H.) or nitrogen gas. Given the internal volume of the laser table,

dry air is preferred so that small leaks are of no concern. This also enables access panels to be removed for laser maintenance with no risk of asphyxiation. A regulated dry air supply is connected to the table, and adjusted to maintain a small positive pressure to expel any moisture. A humidity gauge monitors the table interior.



Figures 68a and 68b. Left: Gaussian fits for beam profiles at distances of 1, 2, 3, and 4 meters from the FIR output coupler. The beam attenuation and divergence can be calculated from these data. The total beam power is proportional to the integral of the Gaussian fit over all space. Attenuation is measured to be -3 dB/m. Right: The Gaussian radius is plotted versus distance, and then fit to a Gaussian beam propagation equation [22]. The beam waist is calculated to be 0.52 cm located at the laser output coupler. Beam divergence is calculated to be 0.43°.

Propagation of a Gaussian beam can be described as:

$$w(z) = w_0 \left[1 + \left(\frac{\lambda z}{\pi w_0^2} \right)^2 \right]^{1/2}$$

where w is the Gaussian radius, w_0 is the beam waist radius, λ is the wavelength, and z is distance.

The FIR beam is roughly the size of the giant hole coupler aperture, in this case 10 mm diameter. The beam diverges rapidly, and optics are needed to control the beam size and collimation. The beam size is

defined by its Gaussian radius. This is the radius where the beam intensity is e^{-2} of the peak intensity. Another definition is the e^{-1} level of the electric field strength, so care should be taken when performing calculations. Beam profile measurements are made with a pyroelectric detector, which responds to beam intensity; therefore, the e^{-2} definition is used in this dissertation. A pyroelectric detector is mounted to a 2-axis translation stage. Stepper motors, controlled via LabView, move the pyroelectric detector in either horizontal or vertical steps. Between steps, Labview samples the peak to peak waveform amplitude. The detector sensor is 2 mm square, and measurement steps are either 0.5 or 1.0 mm each. A 60 Hz, 3-bladed chopper interrupts the beam to establish a waveform on an oscilloscope. By locating the central beam peak, and then scanning across the beam horizontally and vertically, the beam profile can be measured. A few measurements are done with a full raster scan to show the full beam profile; however, the time this type of scan takes makes it impractical for every measurement. The laser would need to be tuned several times, so the total beam power will excessively vary.

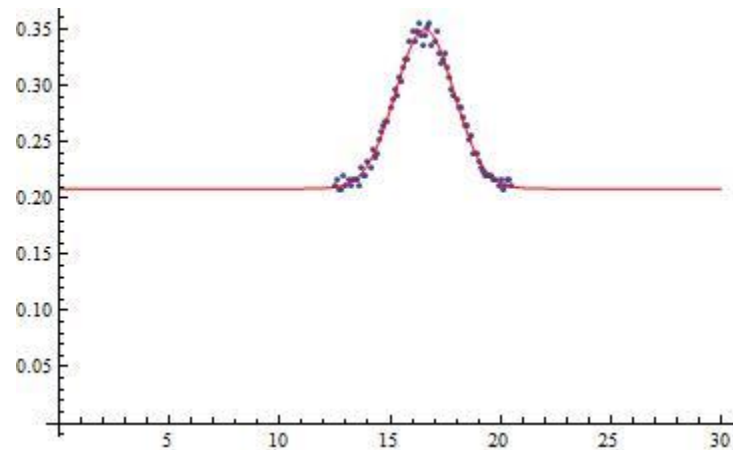


Figure 69. Example of beam profile measurement. The blue dots are peak to peak pyroelectric detector voltage output. The red line is a Gaussian fit for the data.

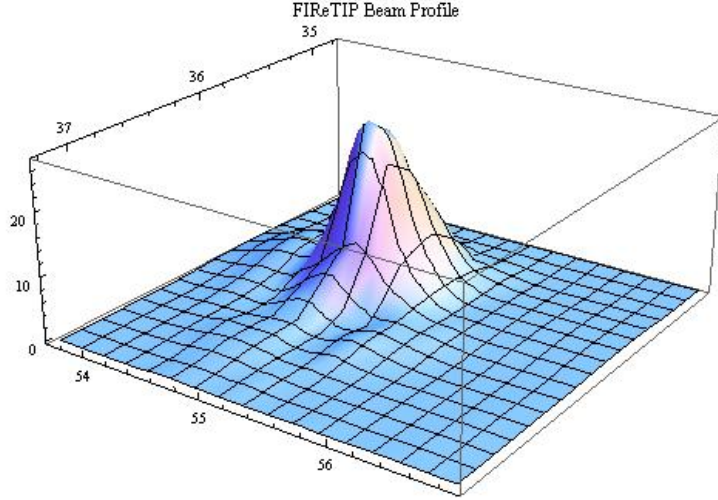


Figure 70. Raster scan of FIR beam. A single peak, round, Gaussian profile is observed when the FIR laser is properly tuned.

To couple into circular waveguide, the beam size should be 60 to 65 % of the waveguide diameter. This will enable coupling to HE_{11} mode with the least insertion loss [23]. Larger beams will be clipped by the waveguide, and some power will be lost. Smaller beams tend to couple to higher order modes. These modes generally have higher losses during waveguide transmission. The waveguide used is 19 mm diameter, so a Gaussian radius of 5.7 to 6.2 mm is desirable. The FIR beam is allowed to diverge for 20 to 24 inches, and then reflected from a 1 m radius concave mirror to collimate the beam. To avoid a beam astigmatism, the incident angle should be as small as practical ($\theta_i < 10^\circ$). Mirrors are preferred over lenses for this frequency due to the high absorption of most dielectric materials. Mirrors were chosen for all FIReTIP FIR optics.

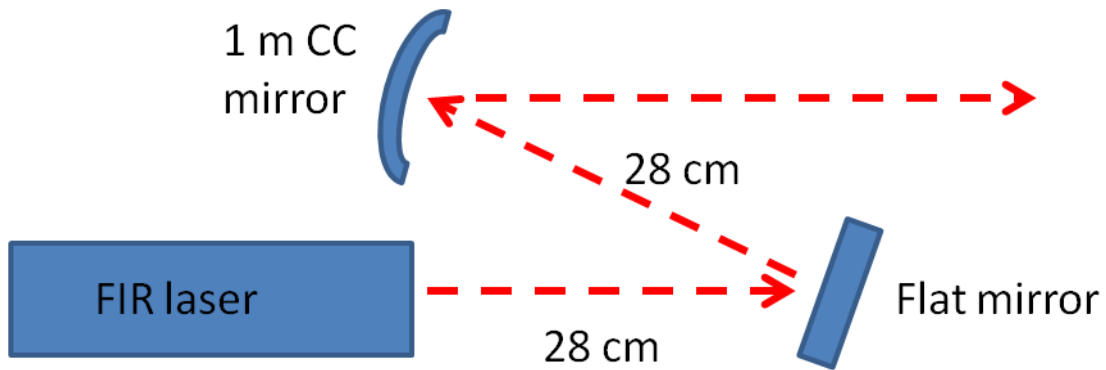


Figure 71. FIR beam collimation for coupling into 19 mm waveguide. The beam is allowed to expand for 56 cm, and is then collimated by a 1 m concave mirror. To avoid introducing an astigmatism, the incident angle should be less than 10°.

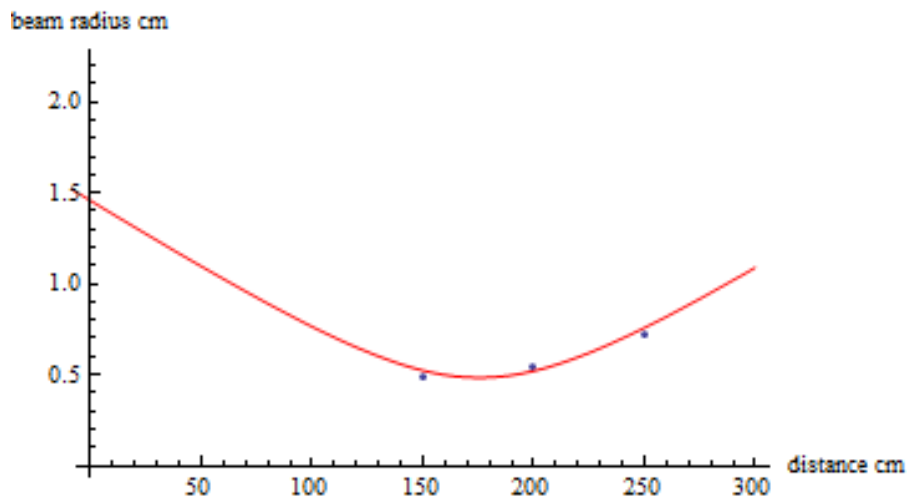


Figure 72. The collimating mirror moves the beam waist out to about 1.75 m from the output coupler. To couple into the waveguide, the waveguide entrance should be placed between 1.5 and 1.75 m from the laser.

FIRETIP uses metallic mesh beam splitters to divide and/or recombine FIR beams. They measure 3" by 5", and have a mesh density of 500 lines per inch (lpi). At 119 μm and 45° incidence, the 500 lpi mesh

has 70% transmission and 30% reflection. The mesh material is commercially available. It is manufactured by electroforming a dielectric square mesh, and then copper coating the surfaces [24].

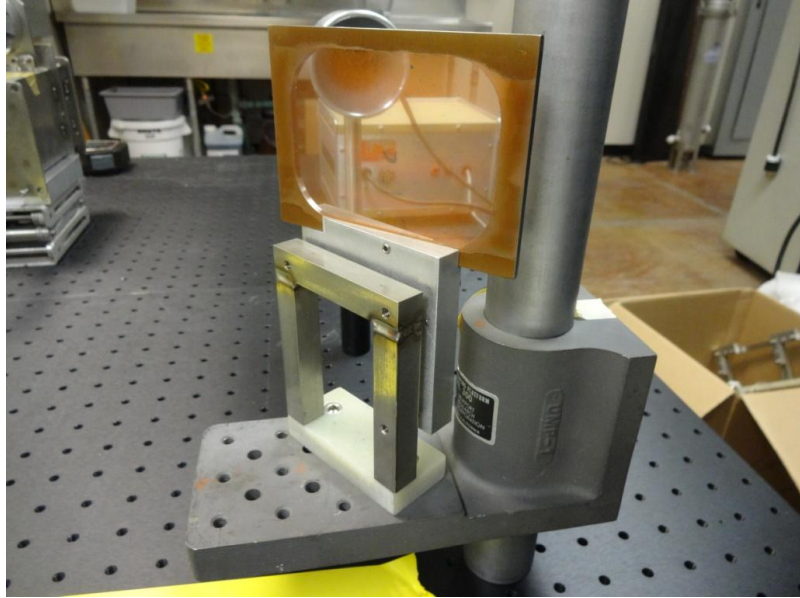


Figure 73. Metallic mesh beam splitter. FIReTIP has two line densities to choose from, 500 and 400 lpi.

The coherence length of the FIR lasers is important to understand for an interferometer. There are several longitudinal modes that can be emitted from the lasers. Each of these modes will have slightly different frequency and phase. Under small perturbations, the modes may change, inducing slight frequency and phase shifts. This can reduce the coherence between the signal and reference beams to a level where the output signal is dominated by phase noise. The coherence length describes the maximum difference between path lengths of reference and signal beams for effective interferometry; however, a shorter path length difference is preferable when possible to reduce concerns for coherence. When an interferometer splits its laser beam into signal and reference beams, each path length should be as equal as possible. If the path length varies by more than the coherence length, then random phase shifts will create enough noise to dominate the instrument. [25]

The FIReTIP FIR laser coherence length was measured to be ~ 10 m. The test setup uses a waveguide to deliver a FIR beam to an optical table. A beam splitter then divides the beam into two parts. One part travels to a pair of mirrors, each at 45° incidence to bounce the beam back in a U-shaped path. These mirrors are mounted to a track to vary the path length [26]. At short distances, two flat mirrors were used; however, when the path length becomes long, the beam divergence can be a problem. Under these circumstances, a concave mirror replaces one flat mirror to help collimate the beam. The return path of this variable length beam intersects a second beam splitter to recombine with the source beam. These collinear beams are then focused into a receiver mixer. A 50% chopper interrupts the beams 10.8 kHz so that the mixer will respond to a single frequency beam. The mixer output is displayed on an oscilloscope, and the observed waveform amplitude will depend on the phase difference between the signal and reference beams. The variable path beam also has a micrometer to make fine adjustments. By sweeping the path length through several wavelengths, the mixer output amplitude is observed to vary between zero and some maximum value, showing that the beams are still coherent. As the path length is increased, the maximum amplitude of the mixer output slowly reduces, until there is no response from small variations in path length. When the beams are observed to have no coherence, the difference in the path lengths is the coherence length. This occurred at approximately 10 m. This number is reasonable because a rough estimate can be made by multiplying the length of the laser by the average number of trips a photon makes between the laser mirrors before being emitted. The FIReTIP lasers are 2.4 m long, and with $\sim 15\%$ transmission from the giant hole coupler, a 17 m coherence length is estimated. This experiment is subject to uncertainty due to beam alignments, focusing, and attenuation; however, to be within a factor of 2 of estimate techniques seems reasonable. To verify that this experiment is not systematically short due to low power at the mixer due to atmospheric attenuation, the path length difference was equalized, but the total path length was increased by 10 meters. The mixer output for this test was sensitive to small changes in path length, showing that the beams are coherent, and the mixers were still sensitive at this reduced power. As a result of this test, the path lengths for FIReTIP's signal and reference beams should be no more than 1 m. It is no extra effort to install the waveguide runs with a path length difference < 1 cm. The

previous FIReTIP system did not have equalized signal and reference paths, which may have contributed to measurement noise.

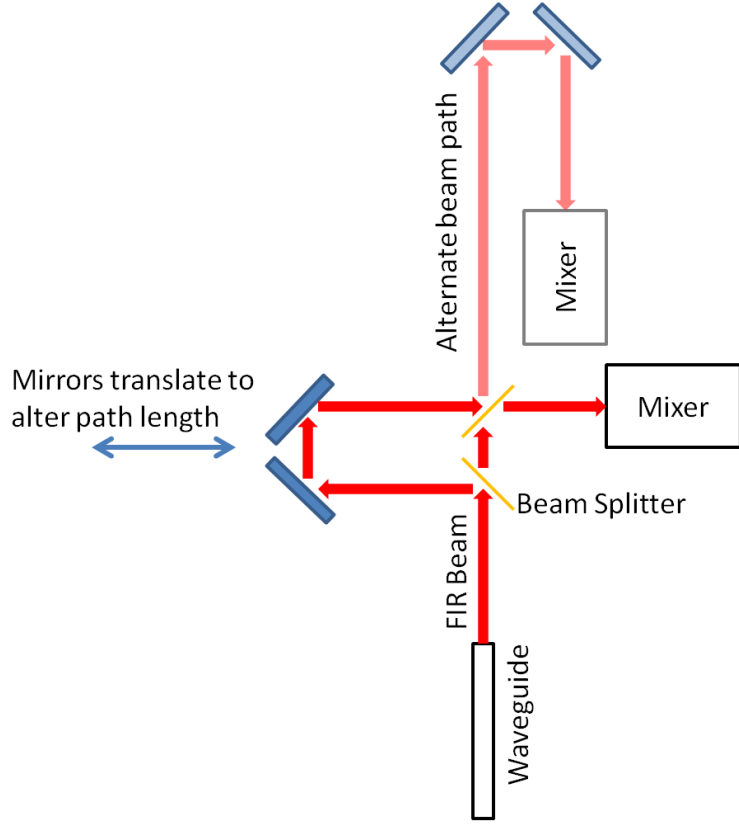


Figure 74. Coherence length set-up. The FIR beam is divided into two parts, and then recombined in a Michelson style set up. One path length can be altered to test for beam coherence at various lengths. An alternate path can be included to increase the path length of both beams as an experiment control.

III.2 FIReTIP Waveguide

The distance between the lasers and NSTX-U is approximately 20 m. To deliver the FIReTIP signals to the tokamak, an overmoded, hollow, dielectric waveguide has been developed. The preferred technique for transmitting electromagnetic waves through waveguide is to use corrugated waveguide [27, 28]. However, this is impractical at 119 μm ; the ideal corrugation depth is nominally $\lambda/4$ ($\sim 30 \mu\text{m}$). This is a difficult machining process to control on the inside diameter of a small tube, and prohibitively expensive.

Due to the tiny corrugations, it is not practical to confirm the machined dimensions without destructive testing. Machining errors can be expected to be on the order of ± 0.5 mil, which is on the order of the corrugations themselves. As an alternative to corrugations, a thin dielectric layer can be used. The dielectric will serve the same function as the corrugations by reducing the electric field in the waveguide walls as much as possible. The dielectric thickness depends on the transmission wavelength and dielectric thickness[28]:

$$kd\sqrt{n^2 - 1} = \frac{\pi}{4}$$

where the transmission wavenumber, $k = 2\pi/\lambda$, and n is the dielectric index of refraction.

The principal source of waveguide loss is due to Ohmic losses due to boundary surface currents. If the electric field strength in the waveguide wall can be minimized, transmission losses can be significantly reduced [29]. Under ideal conditions, the HE_{11} hybrid mode has no boundary electric field, and therefore no surface currents. The HE_{11} hybrid mode is a combination of TE_{11} and TM_{11} modes, resulting in a linearly polarized, near Gaussian profile [30, 31]. A linearly polarized, Gaussian beam can be coupled into waveguide with this mode with great efficiency under the right conditions. The Gaussian radius of the beam should be 60 to 65 % of the waveguide radius, and the beam should be collimated so that the beam waist is located at the waveguide entrance [21]. Under these conditions, the HE_{11} hybrid mode can be achieved with as little as 4% insertion loss [23]. If the beam diameter is too large, insertion losses will increase because the outer radii of the beam will miss the waveguide entrance, and this power cannot be recovered. Too small of a beam diameter will excite higher order modes, which in turn leads to increased attenuation. When the conditions are right to couple to the HE_{11} hybrid mode, the electric field is purely transverse, and Bragg reflections between the waveguide wall and dielectric coating will cancel out electric fields at the boundary, thereby eliminating surface currents. However, the waveguide material is

not a perfect conductor, and the dielectric will have a finite absorption coefficient. When implemented properly, the losses can be very low. Overmoded waveguides are sensitive to beam coupling, waveguide alignment, and mode conversion. At lower frequencies, corrugated waveguide have been used with great success with < -0.01 dB/m possible [33]. At higher frequencies, the waveguide tolerances are increasingly more difficult to satisfy, and small errors can readily compound into large losses. With the proper coating, undesirable modes are suppressed, and the HE_{11} hybrid mode is promoted. Upon exiting a waveguide, the HE_{11} hybrid mode couples back to TEM_{00} Gaussian profiles [32].

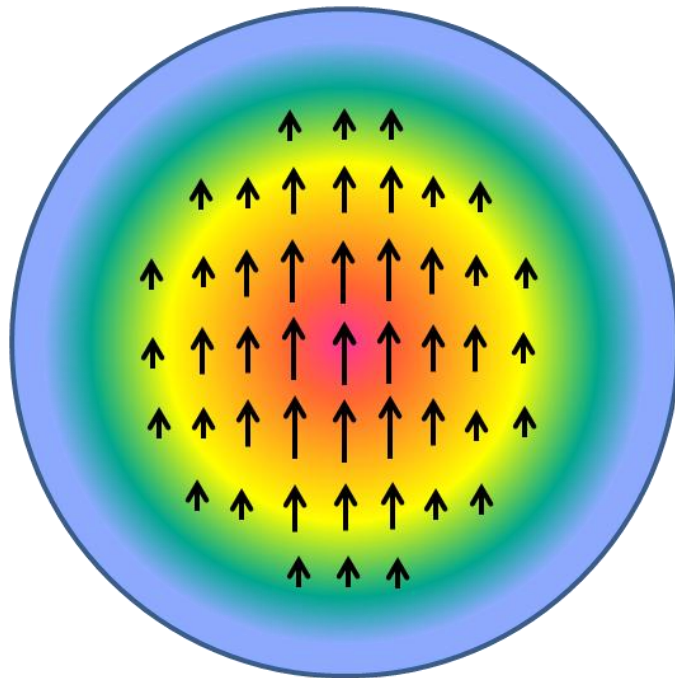
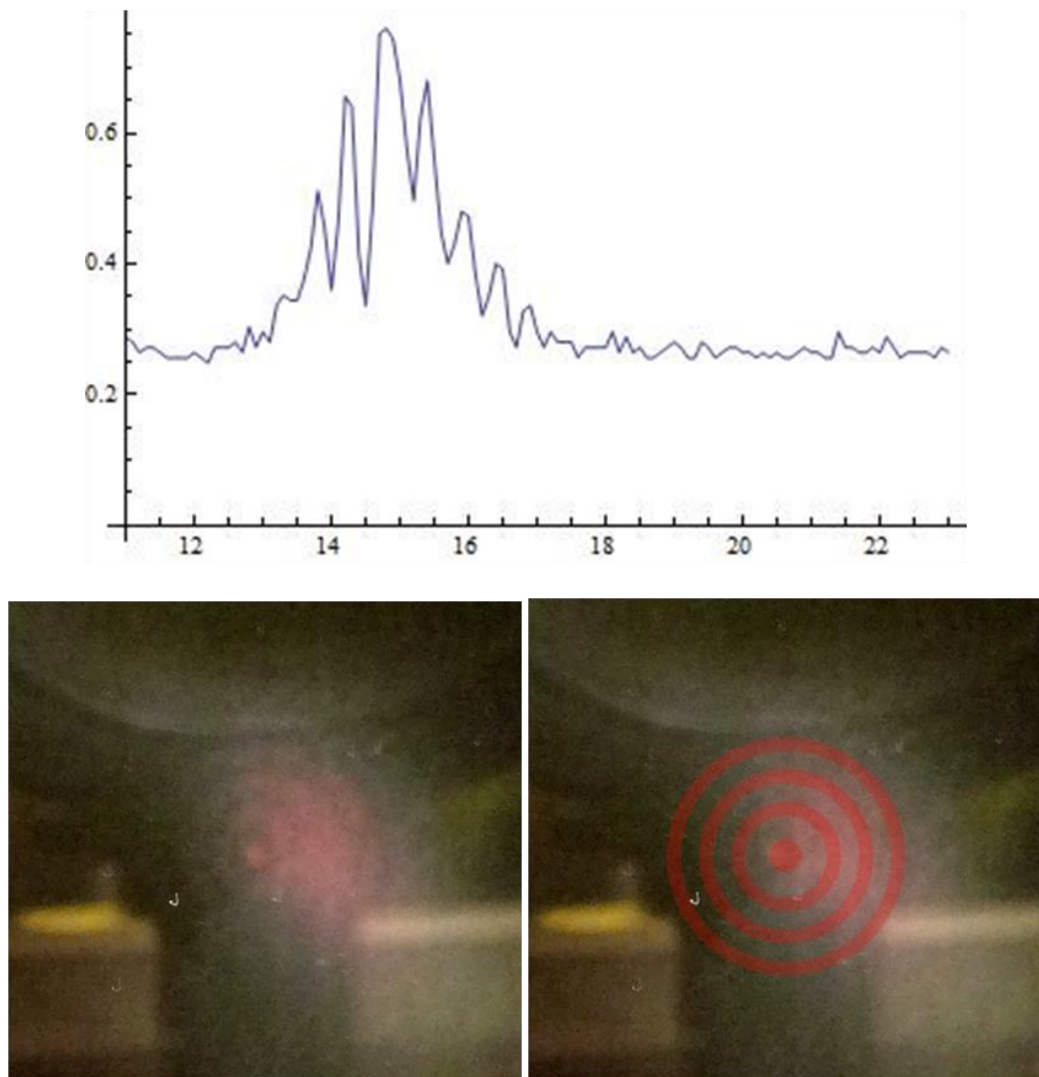
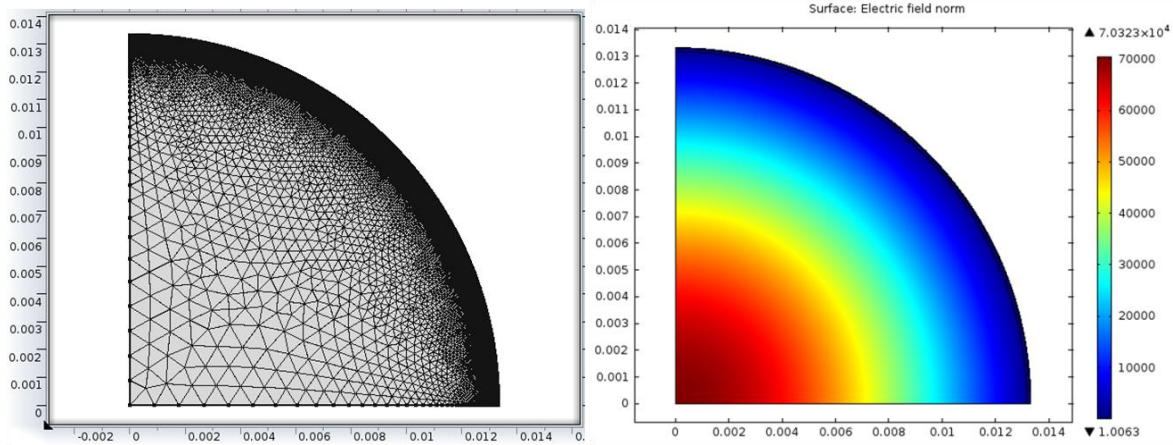


Figure 75. HE_{11} hybrid mode, a combination of TE and TM modes resulting in a linearly polarized, near Gaussian profile.



Figures 76a, 76b, and 76c. Higher order modes coupled into the waveguide. Above: Beam profile after coupling a 12 mm diameter Gaussian beam into a 44 mm diameter aluminum waveguide. Left: Waveguide output HE_{14} observed on liquid crystal paper. Right: Same waveguide output photo with an overlay to help see the mode structure.



Figures 77a and 77b. Simulations of waveguide modes using COMSOL. Symmetry allows 1/4 of the waveguide to be simulated to decrease computation time. Left: Variable mesh structure with large cells near the center of the waveguide, and fine mesh ($\lambda/20$) near the edge where the thin dielectric layer is. Right: Dominant mode is HE_{11} .

The FIReTIP waveguide is constructed of an aluminum waveguide, with a thin dielectric coating on its inner surface. The dielectric material should be a low loss material for the wavelength to be transmitted, and have a refractive index near $\sqrt{2}$ for the greatest power transmission [27]. For 119 μm transmission, a material that satisfies these conditions is polytetrafluoroethylene, PTFE (Teflon). At 119 μm , PTFE has an index of refraction of 1.38 - 1.43, with an absorption coefficient of $\sim 3 \text{ cm}^{-1}$ [34, 35]. PTFE has advantages over other good performing dielectrics, such as TPX, in that is inexpensive, can be applied in thin layers, has excellent adhesion, is widely available, and is a durable coating [36]. The principal challenge to applying PTFE is maintaining an even coating with good thickness tolerance. The waveguide material chosen is 6063, seamless aluminum tubing. The nominal inner diameter is 3/4", with a 0.060" wall thickness. Al-6063 is a high conductivity aluminum at ~55% of copper [37]. Aluminum is light weight, easy to work with, and readily available at low cost. It is rigid, and much more resistant to kinks, dents, and other surface aberrations than similar copper tubing. The tubes are manufactured by extrusion to avoid seams along its surface. Each waveguide section is 3' long, and many sections are joined end to

end to form a waveguide run. Each waveguide section is straight, and turns are accomplished with 90° miter bends. The inside diameter is coated with 1 mil thick PTFE.



Figure 78. FIReTIP waveguide section. 6063 seamless aluminum tubing, 19 mm I.D., 36 inches long each.



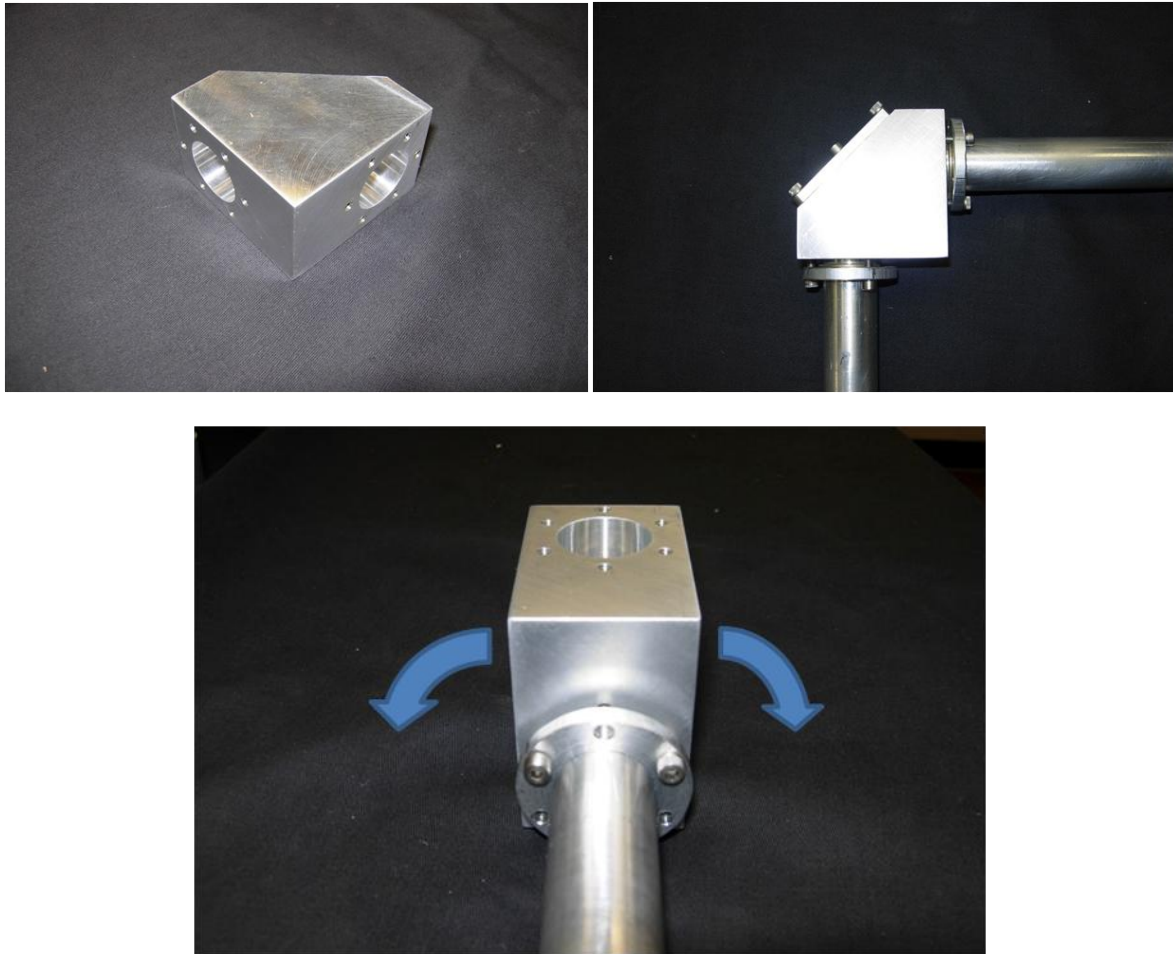
Figure 79. End view of FIReTIP waveguide. Black Teflon coating on interior, 1 mil thick. Flange and retaining ring shown for attaching waveguide sections to other components.

Waveguide sections are joined end to end to extend the length. A 1.5" long sleeve is fit to the waveguide ends to align two sections concentrically. A pair of flanges flank the alignment sleeve, and 2" long stainless steel fasteners secure the joint. The sleeve will keep the waveguides concentric; however, there are a few degrees of adjustment. Differential torque about the flanges will facilitate angular adjustments. Flange adjustments can provide waveguide fine tuning; however, the primary alignment is managed by waveguide mounts, which clamp onto the waveguide body at least every 6'.



Figures 80a and 80b. Waveguide union joint. Left: Each waveguide end is inserted into an alignment sleeve. Right: Assembled union with stainless steel fasteners.

Miter bends have been constructed to provide 90° turns in the waveguide. The in-going and out-going beams are perpendicular; however, the azimuthal angle can be swiveled to any position. This allows some flexibility in how the waveguide run is routed. A first surface mirror is attached to the miter bend at a 45° angle to the two waveguide sections. Anytime the miter bend angle is not aligned with, or perpendicular to the laser polarization angle, there will be a shift in the polarization angle. These angle shifts will propagate through the system. When circularly polarized, this shift is irrelevant; however, since the Stark laser is linearly polarized, consideration is given to the waveguide path to ensure that the final signal is vertically polarized at the receiver mixers. The proposed waveguide route is made entirely with right angles; however, it may become necessary to alter the run to accommodate other needs in the NSTX-U test cell. The receiver mixers are designed for a vertical linear polarization; therefore, if the polarization angle is too far from vertical, a 1/2 waveplate can be added to rotate the polarization. If the polarimeter function is disabled, then only one FIR laser will be used. In this case, the single FIR laser will be linearly polarized, and may need a 1/2 waveplate as well. 1/2 and 1/4 waveplates for 119 μm are commercially available. X-cut quartz is birefringent, and has excellent transmission at this wavelength. Crystal quartz ordinary and extraordinary refractive indices are approximately 2.13 and 2.18, respectively [22].



Figures 81a, 81b, and 81c. Left. Miter bend body. Right: Miter bend with waveguides installed. Bottom: Miter bend attached to waveguide sections with the flange, but the miter bend can swivel about the waveguide axis.

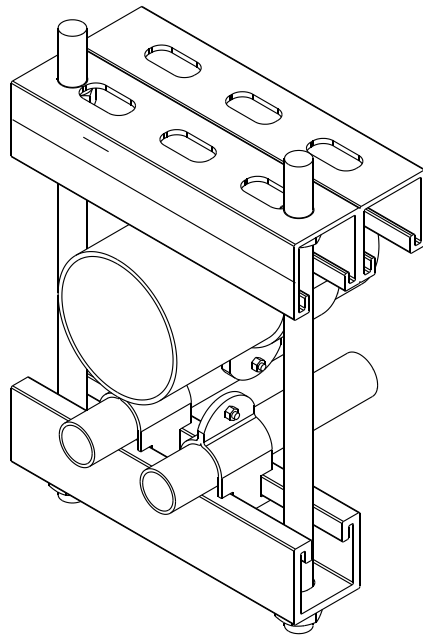
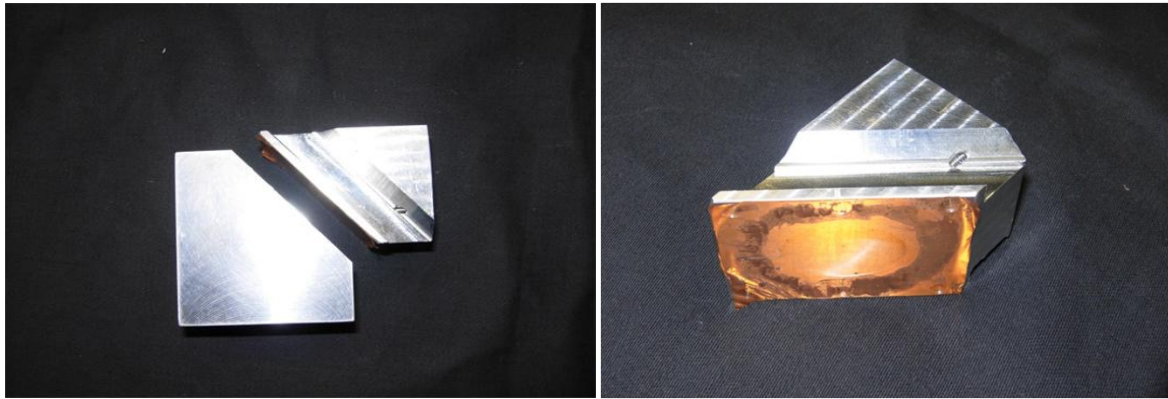


Figure 82. Waveguide mount, with three waveguides shown. The large waveguide is for the High-k Scattering System. The two smaller waveguides are for the FIReTIP signal and LO. Each waveguide in the mount is individually adjustable. Image courtesy of Robert Ellis, PPPL.

A miter Tee, 4-way cross, and U-bend have been fabricated for the FIReTIP waveguide. These components are essentially two miter bends attached together back to back in various arrangements. The 4-way cross is two miter bends with their reflector plates removed, and then attached back to back. A 500 lpi metallic mesh beam splitter is mounted between the miter bodies. This will provide for 70% reflection and 30% transmission. To convert a 4-way cross to a tee, one of the ports is covered with a graphite plate to absorb any power incident upon it. The 180° bend connects the output of one miter bend immediately to the input of another. This compact arrangement can reverse the direction of the waveguide run in a 3" lateral shift.



Figures 83a and 83b. Left: Miter bend with the reflector plate removed. A third port is then attached to the reflector location to fashion a miter tee. Right: Metallic mesh beam splitter attached in place of the reflector plate.

Waveguide output was measured for mode quality and beam divergence. A raster scan of the waveguide output was performed to confirm that it was in the form of a Gaussian beam, and then a wire polarizer is placed at the output and rotated to check for polarization angle. The waveguide output was round, near Gaussian profile, and the polarizer confirmed that the beam was vertically polarized.

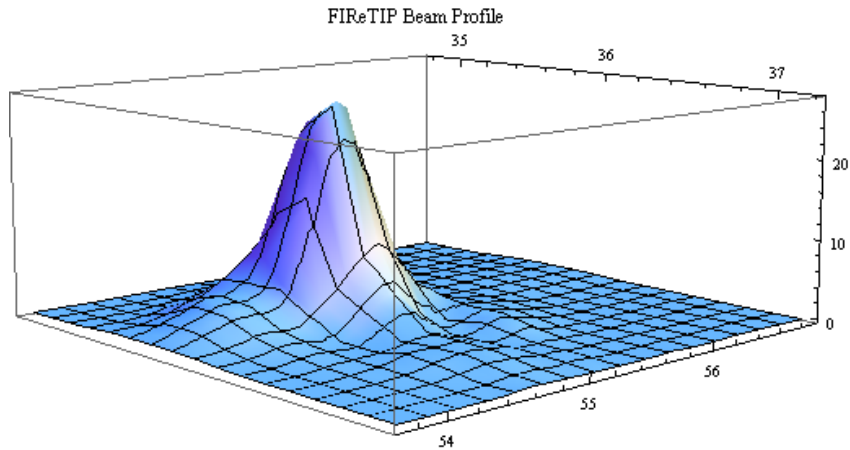


Figure 84. FIReTIP waveguide output. A raster scan provides a three dimensional image of the beam intensity, showing a roughly circular, single peaked profile, similar to a Gaussian beam.

Several beam scans are made at various distances to compare the beam size against Gaussian propagation equations [38], and calculate the beam divergence. The far field measurements indicated a beam waist radius of ~ 5 mm, with a beam divergence of 0.41° .

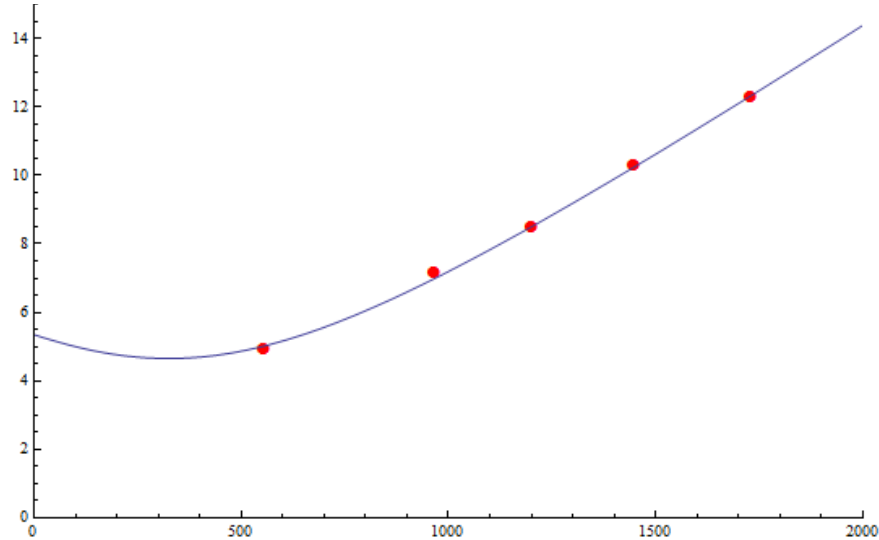


Figure 85. Far field measurements of the FIReTIP waveguide output. The Gaussian beam radii are curve fit to Gaussian propagation equations indicating a beam waist radius of ~ 5 mm, and divergence of 0.41° .

To confirm these beam parameters, a second test was performed. The long distances gave poor signal to noise ratio measurements due to the attenuation in ambient air, and expanding beam size. To offset this problem, the waveguide output beam was reflected from a 76.2 cm focal length, concave mirror. The beam focusing increased the beam intensity for improved measurements. The resulting calculations indicated a beam radius at the waveguide exit of 5.87 mm.

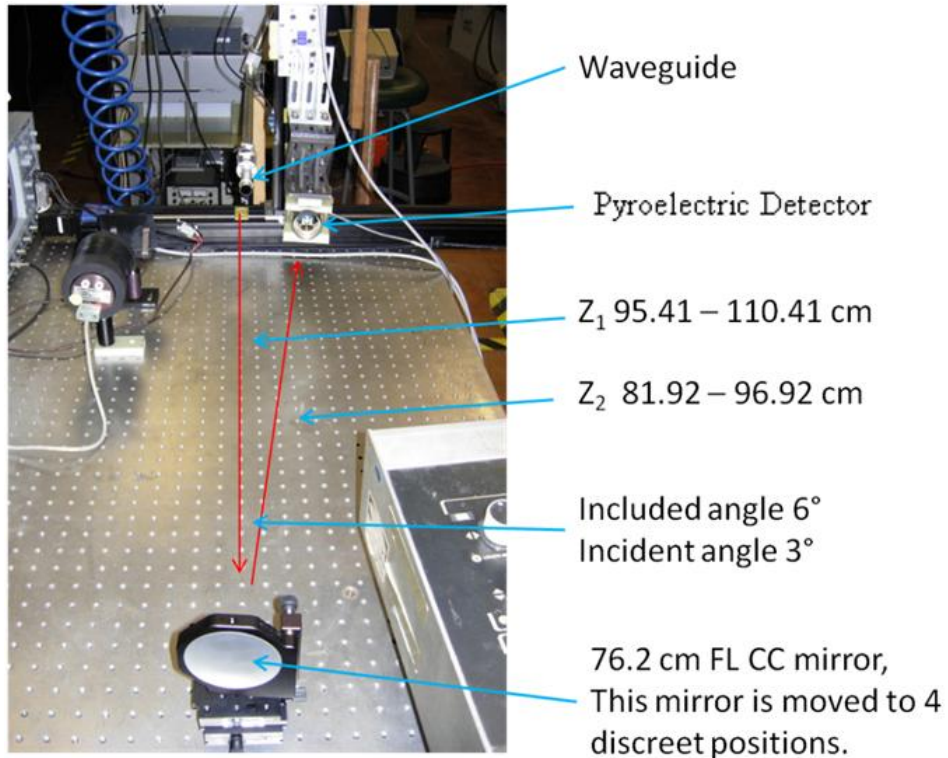


Figure 86. Far field beam measurement set up for second test.

Table 3. FIReTIP Waveguide, Far Field Data, second test

Test	Z ₁ cm	Z ₂ cm	Z _{total} cm	X _{rad} mm	Y _{rad} mm
1	95.41	81.92	177.33	5.19	5.58
2	100.41	86.92	187.33	5.03	5.54
3	105.41	91.92	197.33	4.92	5.26
4	110.41	96.92	207.33	4.44	4.86

The main concern for power transmission is mode conversion. Modes other than HE₁₁ can attenuate signals quickly. Perturbations can cause other modes to become active. The primary sources of perturbations are due to waveguide misalignments. If the waveguide is not straight, the beam can reflect

at angles greater than "glancing". If the beam is off axis near a miter bend, the beam could strike the reflector off 45° , and fail to recouple to the HE_{11} mode at the next waveguide section. In extreme cases, the beam could miss the reflector plate and scatter off of the interior miter bend geometry. To maintain excellent transmission, the waveguide should be aligned to within 0.1° . Since atmospheric water will attenuate $119\text{ }\mu\text{m}$ at $\sim -3\text{dB/m}$, the waveguides must be purged of humidity. A regulated nitrogen line is tapped into the waveguide at a miter bend. At either end of the waveguide run, a valve is opened to allow nitrogen to backfill the waveguide. The ends of the waveguides are capped with a thin film of polyester ($< 5\mu\text{m}$). The polyester has no appreciable attenuation, and can withstand about 7 PSIG before rupturing. A small positive pressure ($\sim 0.5\text{ PSIG}$) is maintained in the waveguide to keep it water free.

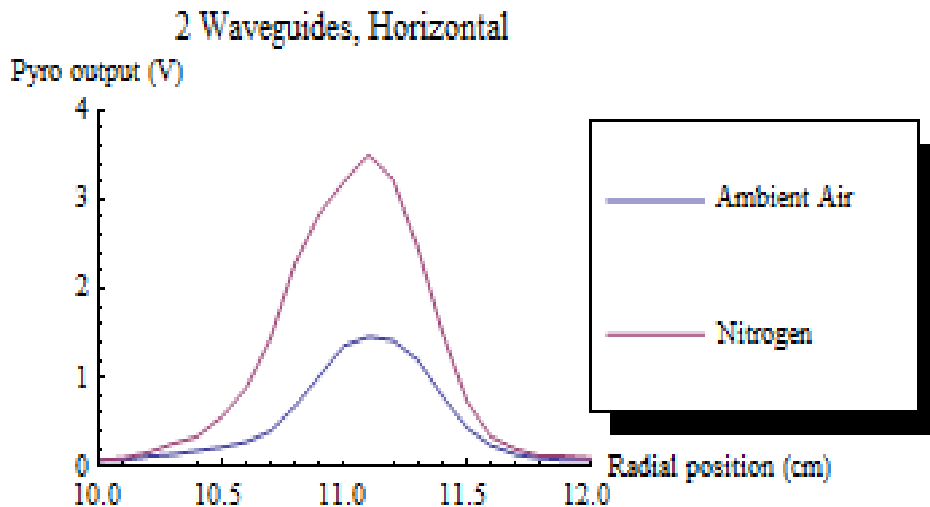
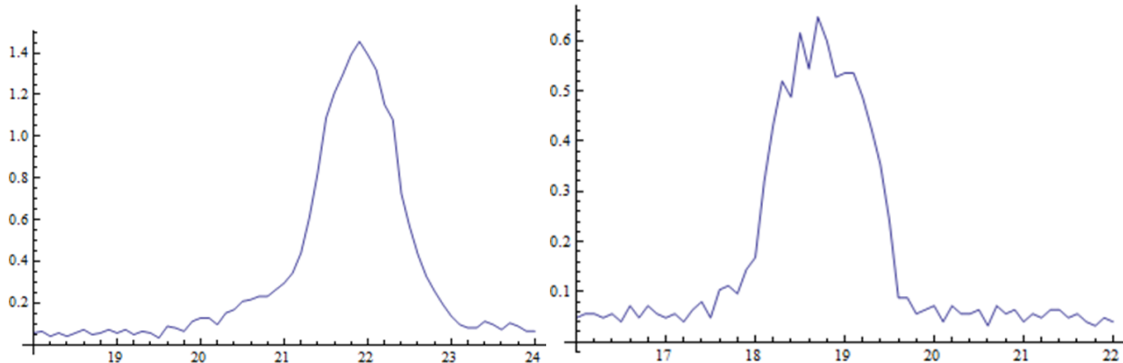


Figure 87. FIReTIP waveguide output beam profile. The FIR laser was coupled into two meters of waveguide. The blue line is the beam profile with ambient air at 50% R.H. The red line is the beam profile when the waveguide is purged with nitrogen.



Figures 88a and 88b. FIReTIP waveguide output modes after passing through two, 3-foot waveguide sections. The incident power coupled into the waveguide for both cases was 30 mW. This test was not conducted in a nitrogen environment; therefore, atmospheric attenuation can account for ~ -3 dB/m. Transmitted power is measured with a Scientech Model 365 power meter, and the mode quality and relative power was measured with a Molelectron pyroelectric detector. Left: Beam profile with waveguides aligned within 0.1° . Right: The joint between two waveguides is intentionally misaligned by 0.5° . Higher order modes are observed in the beam profile, and the pyroelectric detector signal amplitude is reduced from 1.4 V to 0.6 V, which corresponded to 7 and 3 mW absolute power measurements.

The FIReTIP waveguides were tested for repeatability and robustness under path deflection. 21 waveguide sections were setup in the lab with 5 miter bends to form a 63' waveguide representative of the final installation on NSTX-U. The waveguide was aligned, and filled with nitrogen, to establish a base line power and mode. The relative output power and mode is measured with a pyroelectric detector. A two axis translation stage swept the pyroelectric detector horizontally and vertically across the waveguide output to record the beam profile. The resulting beam scans are a measure of the relative power by curve fitting the beam profile to a Gaussian curve and integrated over all space. Near the center of the waveguide run, there is a 21' long, straight section. A micrometer is placed at the center of this section. The micrometer is adjusted to apply pressure to the waveguide to cause a deflection, and the output mode and power are measured. Small deflections of < 2 mm had no appreciable effect. Increasing the deflection

steadily decreases the output power. At 5 mm deflection, mode conversion is observed and total power transmission is approximately -3 dB from the initial setup. Removing the deflection restored the mode quality and power to original levels.



Figure 89. 63' FIReTIP waveguide run. 21 waveguide sections and 5 miter bends comprise this test setup.

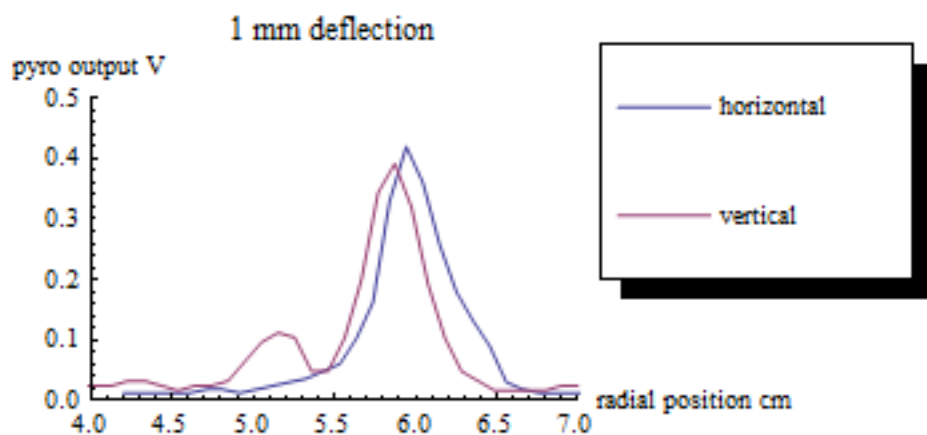


Figure 90. FIReTIP 63' waveguide test. The center of the waveguide is deflected out of alignment by 1 mm ($\sim 0.02^\circ$). The waveguide output is primarily Gaussian with a small side lobe.

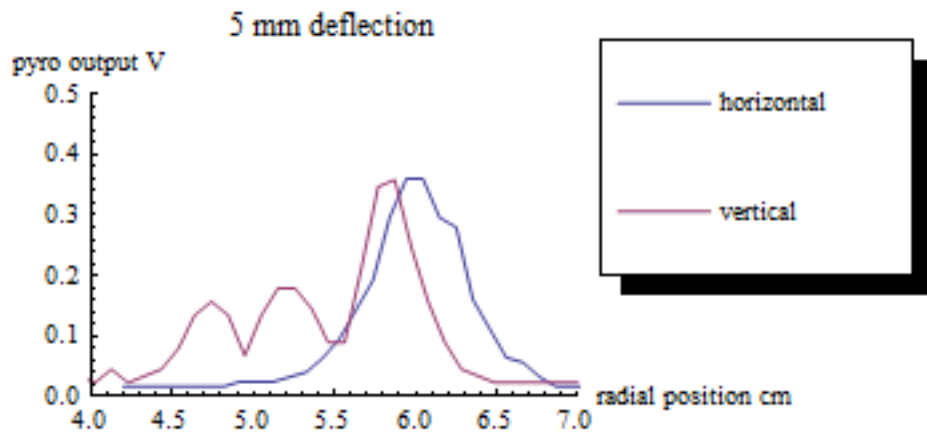


Figure 91. FIReTIP 63' waveguide test. The center of the waveguide is deflected by 5 mm ($\sim 0.1^\circ$). Mode conversion has occurred in the direction of the deflection with a total power drop of -3 dB.

Power transmissions measurements were also made with this 63' waveguide. The FIR beam can be accessed at any miter bend by removing the reflector plate, and connecting the pyroelectric detector at the opening. The relative power is measured at these locations, and the average waveguide performance is assessed. The beam profiles were measured at intervals of 1 m, 7 m, 14 m, and 21 m. The resulting beam profiles were then fit to Gaussian curves, and integrated over all space for a relative power measurement. During this test, the waveguide losses averaged -0.17 dB/m; therefore, total losses for the waveguide were ~ -3.25 dB. Similar losses are expected for NSTX-U depending on the final waveguide lengths

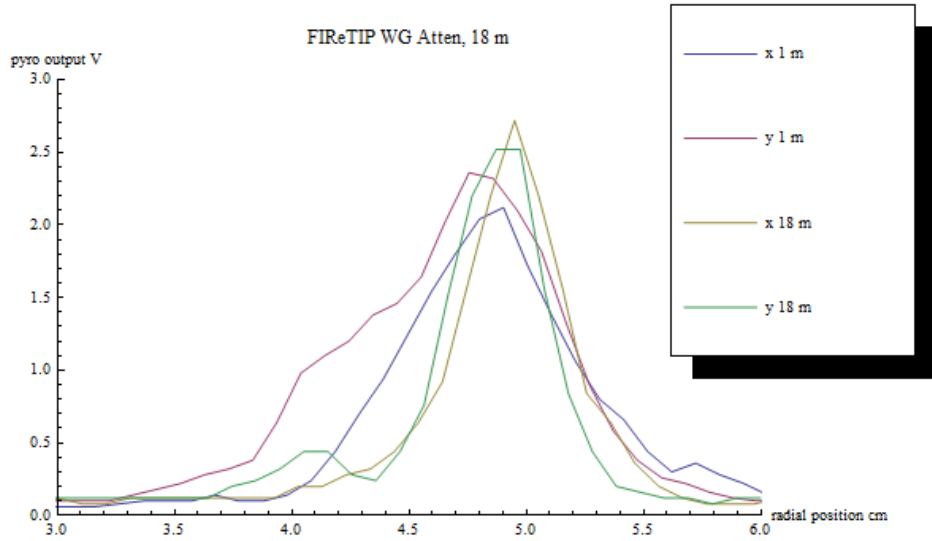


Figure 92. Beam profile comparison of horizontal and vertical measurements after passing through 1 m, and 18 m of waveguide.

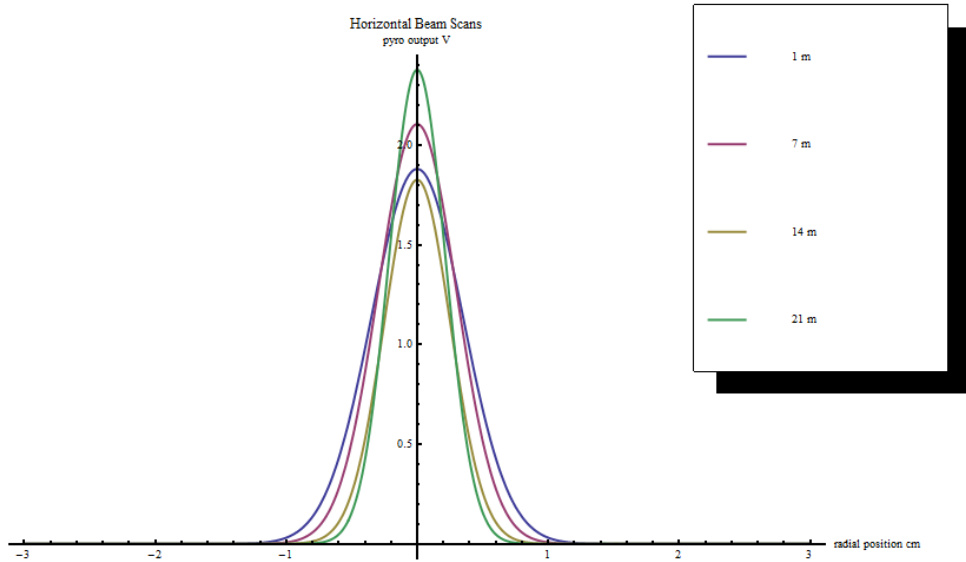


Figure 93. Gaussian fits of beam profiles after 1, 7, 14, and 21 m of waveguide.

There are five waveguide runs to complete the FIReTIP system: 1) the FIR lasers share a waveguide to supply the signal source for each channel and reference signal, 2) the Stark laser supplies LO power with

its own waveguide to the receiver table, 3) a waveguide connects from the source waveguide to the launch optics, 4) a return signal waveguide delivers the measured plasma to the receiver table, and 5) the reference waveguide connects from the source to the receiver table.

The first two waveguide runs originate at the laser table, and pass through the test cell concrete wall. To pass the waveguides through the wall, a single 6" diameter penetration is available. This hole must accommodate two FIReTIP waveguides, plus the High-k Scattering waveguide. The outer diameters are 7/8" and 3"; however, each waveguide has flanges which increase the maximum diameters to 1.5" and 4". To avoid waveguide joints within the wall penetration, two 6' long waveguides were fabricated for FIReTIP. The High-k Scattering waveguide is much more robust; therefore, there are no concerns about misalignments in the wall. Once the waveguides are inserted into the wall penetration, the hole will be packed with fire insulation, making later adjustments problematic.

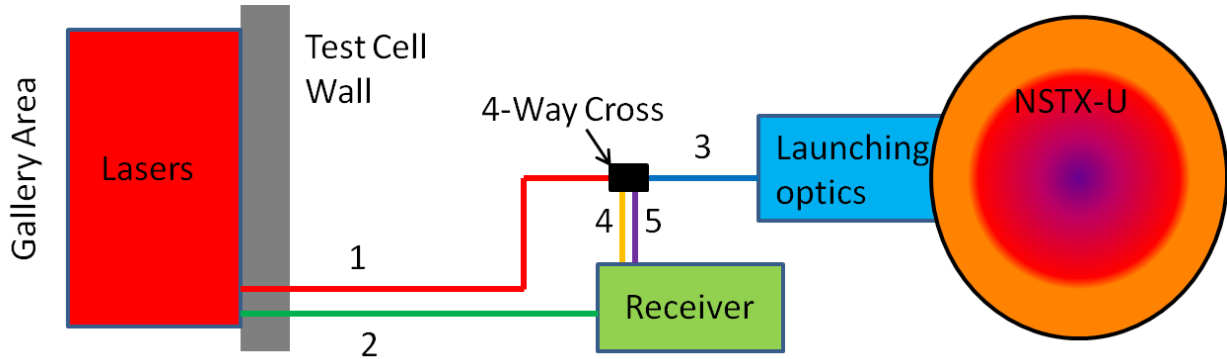


Figure 94. FIReTIP waveguide schematic. There are 5 waveguide runs: 1) Signal waveguide delivers both FIR beams between the laser table and terminates at a 4-way cross, 2) LO waveguide connects the Stark laser to the receiver table, 3) waveguide passes the signal from the 4-way cross to the launch optics, and then returns the signal to the 4-way cross, 4) from the 4-way cross, the return signal is delivered by waveguide to the receiver table, and 5) a reference signal is split from the initial FIR beams, and routed by waveguide to the reference table.

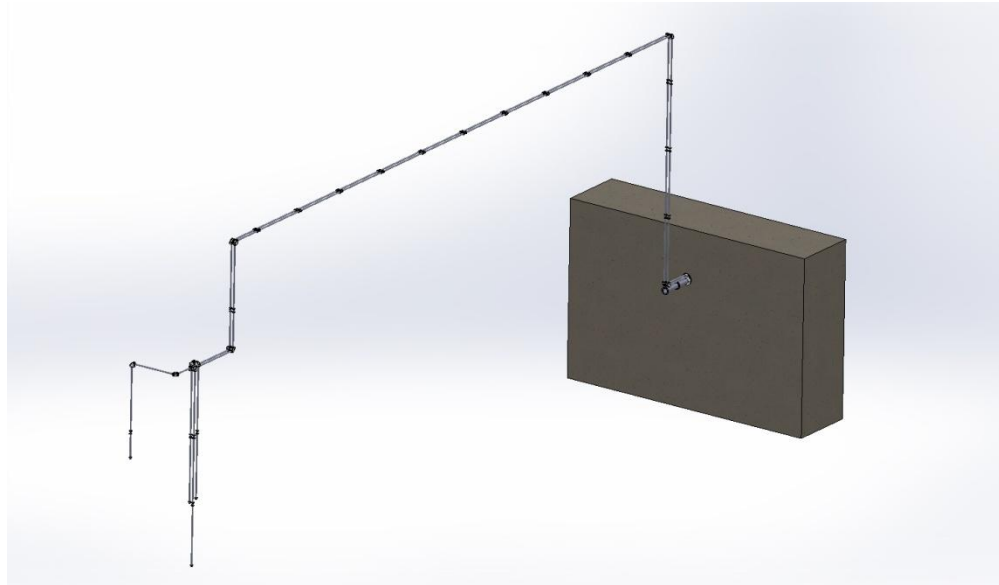


Figure 95. CAD drawing of the FIReTIP waveguide runs. The waveguides pass through the test cell wall seen at the right. The waveguides are then routed upward to pass over equipment around the tokamak, and then are divided at the 4-way cross to route various runs to the launch optics and receiver table.

From the wall penetration, the waveguides turn 90° upward, and then turn horizontal to be routed above the tokamak near bay G. The LO waveguide then turns straight down and enters the receiver table from above. The source waveguide terminates with a 4-way cross. One port connects the reference waveguide to the receiver table, but first it has an ~8 m long, U-shaped run to equalize the reference length to the signal path length, including the double pass through the vacuum vessel. The next port connects the 4-way cross to the launch optics at Bay G. The launch optics then transmits the FIR beam into the vacuum vessel and focuses on a retroreflector at Bay B. The retroreflector returns the signal to the launch optics and recouples it into the same waveguide with the plasma density encoded in its phase data. The return signal travels back to the 4-way cross. The final port sends the return signal down to the receiver table. Equipment in the "cage" must be electrically isolated from the test cell for safety. Since the waveguide passes through the test cell wall, an insulating break rated for 500 VDC is needed. A waveguide union made from G10 was manufactured. A 0.125" partition in the union prevents the ends of the waveguide

from contacting. DC voltage up to 500 V was applied to the DC break, and the resistance was calculated at $\sim 1 \text{ M}\Omega$.

III.3 FIReTIP Launch Optics

The FIReTIP launch optics serves many functions. First, it will aim the FIR beam through a window on Bay G towards a retroreflector at Bay B. The retroreflector will return the beams back along the original beam path. In order for the return beam to recouple back into the same waveguide, the beam waist needs to be located at the retroreflector. Once the launch optics are aligned and calibrated, no further adjustment should be needed. The launch optics will also deliver a collinear HeNe laser to the same retroreflector; therefore, a coupler is needed to add the HeNe beam to the FIR beam path, and then decouple the HeNe laser on the return trip. The HeNe laser is necessary for a second interferometer to measure mechanical vibrations. These vibrations can add phase noise to the FIReTIP system; therefore, it is important to measure these vibrations for phase corrections. The launch optic assembly is enclosed in Lexan panels for dry air environment to reduce attenuation due to humidity.

The distance between the Bay G launch window and Bay B retroreflector is $\sim 4 \text{ m}$. The launch optics needs a focal length of the same length; however, there are more factors to consider. The beam radius for a Gaussian beam is defined at the radius where the beam intensity is e^{-2} of the peak intensity [22]. There is significant power beyond the defined radius that should not be disregarded. A typical rule of thumb is to increase mirror size (or other components) by at least 50% of the beam radius. The retroreflector is a 50 mm diameter target; therefore, the maximum beam waist radius is 16.67 mm. The launch window at Bay G has a viewable diameter of 60.3 mm; therefore, the FIR beam should not exceed a 20.1 mm Gaussian radius. To meet these constraints, three mirrors are used. First, a convex mirror will increase the beam divergence to expand the beam, then a concave mirror focuses the beam, and finally a flat mirror provides beam steering right before the launch window. The space available at Bay G is limited, so a compact

package is necessary. To avoid introducing astigmatism, the incident angles to the spherical mirrors are at 4°. Based on the beam size and divergence from the waveguide, the following curvatures and distances were chosen:

Table 4. FIReTIP Launch Optic Parameters

Element	Distance to next	Focal Length
Waveguide Exit	566 mm	-
Mirror 1	545 mm	-400 mm
Mirror 2	530 mm	762 mm
Mirror 3	-	∞

The launch optic design parameters were developed with the CodeV optical software. Experimental data for the beam size and divergence are programmed into the software.² Once the optimum mirrors were chosen, the launch optics were assembled and tested. The experimental results were then used to adjust the CodeV program. With this iterative process, good agreement between simulation and experiment was achieved. The Gaussian beam radius at the launch window is 18 mm, well short of the 20.1 mm maximum. The distance between the launching mirror and retroreflector is 4150 mm. The measured focal length is 4160 mm with a beam waist radius of 12.9 mm. When installed on NSTX-U, the optics may need to be tuned slightly for beam size and focal length; however, there is ample adjustability to keep the optics true to the design parameters.

²Optical design performed by Dr. Calvin Domier.

Lens Data Manager

Surface #	Surface Name	Surface Type	Y Radius	Thickness	Glass	Refract Mode	Y Semi-Aperture	X Semi-Aperture	
Object	Sphere	Infinity	0.0000			Refract	0	0	
1	Sphere	Infinity	20.0000			Refract	0.0000	0.0000	
2	HeNe Beamsplitter	Sphere	Infinity	-180.0000		Reflect	6.3500	6.3500	Decenter & Bend
3	HeNe Mirror	Sphere	Infinity	15.0000		Reflect	6.3500	6.3500	Decenter & Bend
4	CC lens surface	Sphere	-38.7600	2.5000	NBK7_SCHOTT	Refract	6.3500	6.3500	Decenter & Return
5	CC plano surface	Sphere	Infinity	33.0000		Refract	6.3500	6.3500	Decenter & Return
6	Si Mirror	Sphere	Infinity	-369.5000		Reflect	24.0000	24.0000	Decenter & Bend
7	CV mirror	Sphere	-800.0000	545.0000		Reflect	25.0000	25.0000	Decenter & Bend
8	CC mirror	Sphere	-1524.0000	-530.0000		Reflect	38.1000	38.1000	Decenter & Bend
9	flat mirror	Sphere	Infinity	100.0000		Reflect	40.4100	28.5700	Decenter & Bend
Stop	window	Sphere	Infinity	2.4000	'c_quartz'	Refract	23.8000	23.8000	
11	tube	Sphere	Infinity	400.0000	AIR	Refract	23.8100	23.8100	
12		Sphere	Infinity	3637.0000		Refract	16.8848	16.8848	
Image	Retro Reflector	Sphere	Infinity	0.0000		Refract	18.0000	18.0000	
End Of Data									

Decentered Surfaces

Surface #	Decenter Type	X Decenter	Y Decenter	Z Decenter	Alpha Tilt	Beta Tilt	Gamma Tilt	Non-Centered Data
0 - HeNe Beamsplitter	Decenter and Bend	0.0000	0.0000	0.0000	-42.0000	0.0000	0.0000	Decenter & Bend
1 - HeNe Mirror	Decenter and Bend	0.0000	0.0000	0.0000	42.0000	0.0000	0.0000	Decenter & Bend
2 - CC lens surface	Decenter and Retu	0.0000	0.0000	0.0000	15.0000	0.0000	0.0000	Decenter & Retur
3 - CC plano surface	Decenter and Retu	0.0000	0.0000	0.0000	15.0000	0.0000	0.0000	Decenter & Retur
4 - Si Mirror	Decenter and Bend	0.0000	0.0000	0.0000	-45.0000	0.0000	0.0000	Decenter & Bend
5 - CV mirror	Decenter and Bend	0.0000	0.0000	0.0000	4.0000	0.0000	0.0000	Decenter & Bend
6 - CC mirror	Decenter and Bend	0.0000	0.0000	0.0000	-4.0000	0.0000	0.0000	Decenter & Bend
7 - flat mirror	Decenter and Bend	0.0000	0.0000	0.0000	45.0000	0.0000	0.0000	Decenter & Bend
End Of Data								

Apertures

Surface #	OR	Shape	Type	Label	X Semi-Aperature	Y Semi-Aperature	X Decenter	Y Decenter	Rotation Angle
Object	<input type="checkbox"/>	Circular	Edge		8.0000	8.0000	0.0000	0.0000	0.0000
2 - H	<input type="checkbox"/>	Circular	Clear		6.3500	6.3500	0.0000	0.0000	0.0000
3 - H	<input type="checkbox"/>	Circular	Clear		6.3500	6.3500	0.0000	0.0000	0.0000
4 - C	<input type="checkbox"/>	Circular	Clear		6.3500	6.3500	0.0000	0.0000	0.0000
5 - C	<input type="checkbox"/>	Circular	Clear		6.3500	6.3500	0.0000	0.0000	0.0000
6 - S	<input type="checkbox"/>	Circular	Clear		24.0000	24.0000	0.0000	-7.0000	0.0000
7 - C	<input type="checkbox"/>	Circular	Clear		25.0000	25.0000	0.0000	0.0000	0.0000
8 - C	<input type="checkbox"/>	Circular	Clear		38.1000	38.1000	0.0000	0.0000	0.0000
9 - f	<input type="checkbox"/>	Elliptical	Clear		28.5700	40.4100	0.0000	0.0000	0.0000
Stop - w	<input type="checkbox"/>	Circular	Clear		23.8000	23.8000	0.0000	0.0000	0.0000
11 - t	<input type="checkbox"/>	Circular	Clear		23.8100	23.8100	0.0000	0.0000	0.0000
Image -	<input type="checkbox"/>	Circular	Clear		18.0000	18.0000	0.0000	0.0000	0.0000

Figure 96. CodeV design data for FIReTIP launch optics.

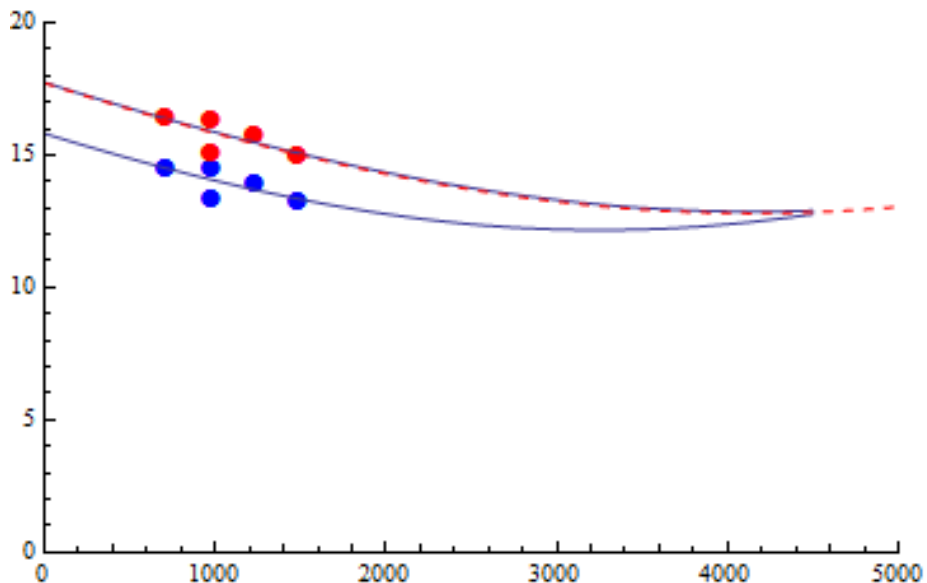


Figure 97. FIReTIP launch optic measurements. The FIR beam radius is measured at several positions far from the beam waist. Gaussian beam propagation equations are fit to the data points to calculate the beam waist size and location. Measuring the beam waist directly is difficult due to measurement noise and low divergence. Measurements in the far field region offer more distinct measurements. The blue markers show measurements from a beam slightly too small. The red dashed line is the ideal beam propagation, and the red markers show experimental results in good agreement.

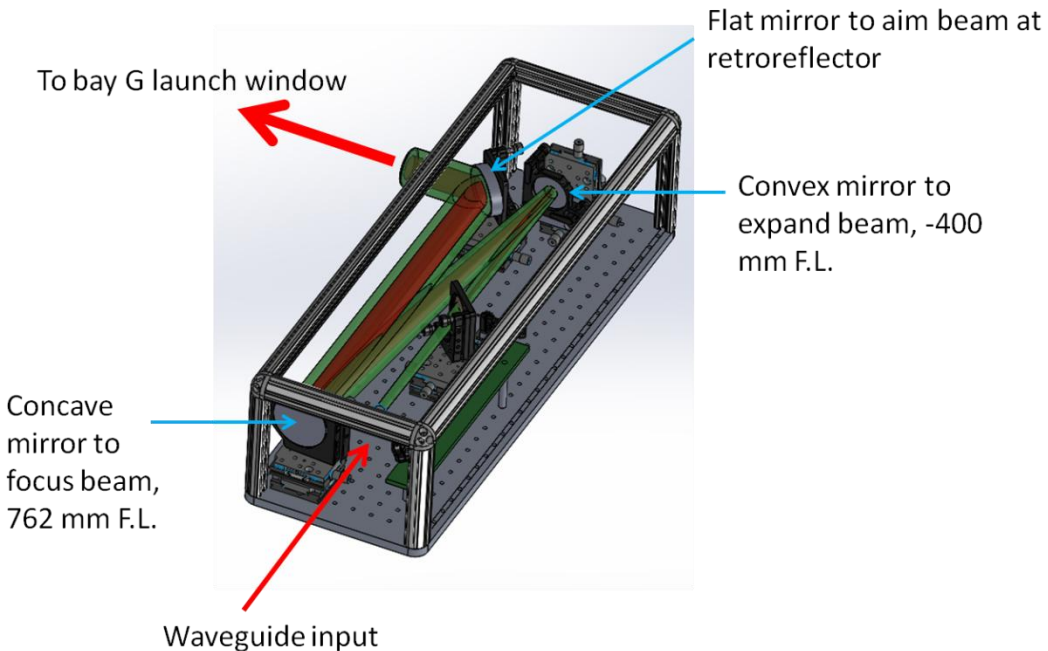


Figure 98. FIReTIP launch optics CAD model. The green trace marks the FIR beam path and size.

The launch optics box is mounted on Bay G such that the waveguide entrance comes in from above, and the launching mirror sends the beam into the vacuum vessel horizontally. The overall dimensions are 76 cm tall, 26 cm deep, and 20 cm wide. Aluminum breadboard forms the base, an extruded aluminum frame surrounds the optics, and Lexan paneling completes the enclosure. All mirrors are mounted on 3-axis translation stages to tune the mirror alignment, and focal length.

The HeNe laser for the vibration monitor is mounted on the receiver table, and fiber optic cables deliver the beam to the launch optics. A separate fiber optic cable returns the HeNe signal to the receiver table. In order to measure the FIR path length variation, the HeNe beam needs to be collinear to the FIR beam, and strike the same retroreflector. A coupler was fabricated to add the HeNe beam to the FIR beam path. A high impedance, 0.5 mm thick, silicon wafer was polished and coated with thin layers of ZnSe and ThF₄. The coupler exhibits low attenuation at 119 μ m, and the FIR beam can pass through with 90% transmission at an incident angle of 18°. The dielectric coatings are designed for high reflectivity at 633

nm for 99+ % HeNe reflection, and low attenuation at FIR wavelengths. The HeNe beam uses the same launch mirrors; however, it is different in size and wavelength. In order to place the HeNe beam waist on the retroreflector additional beam shaping is needed. The incoming fiber optic uses a lens coupler to collimate the emitted beam. The HeNe beam intersects a 50% beam splitter to send the beam to a small silicon mirror, and through a concave lens. The lens has a -19.38 mm focal length to increase the beam divergence. Next, the HeNe beam reflects off the coupler to align with the FIR beam. The HeNe lens adjusts the beam so that the FIR mirrors will have the correct curvature to place the beam waist at the retroreflector. The HeNe system focal length can be adjusted independent of the FIR system by positioning the lens, and/or tuning the fiber optic coupler. The return signal for the HeNe beam follows the same path back, except at the beam splitter; the return signal passes through to a separate coupler and fiber optic cable.

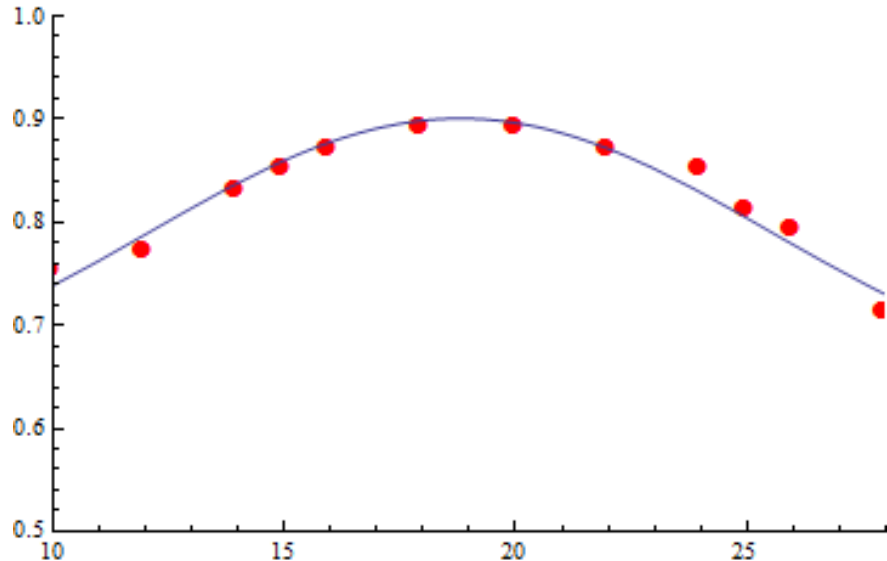


Figure 99. HeNe/FIR coupler transmission versus incident angle. 119 μm transmission is a maximum of 90% at 18° incident angle. The HeNe laser reflects 100% at any angle.

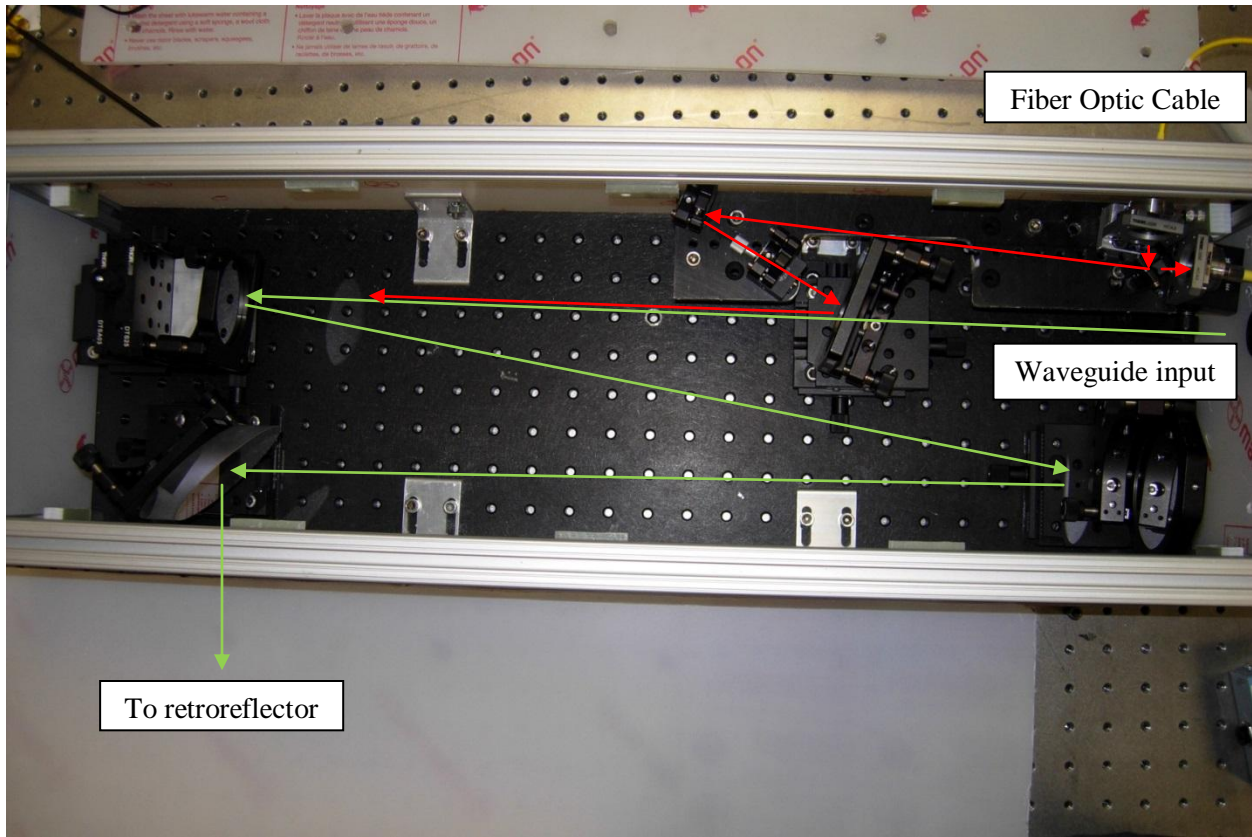


Figure 100. FIReTIP launch optics. The FIR beam (green) enters from a waveguide at the right side, passes through the HeNe coupler to the convex mirror, reflects to the concave mirror, and finally to the launching mirror. The HeNe beam (red) enters from a fiber optic cable at the top of the photo, reflects off a beam splitter, reflects off a mirror, passes through a lens, and reflects off the HeNe coupler. From here, it follows the same path as the FIR beam. When the return HeNe beam gets back to the beam splitter, it passes through the beam splitter to a different fiber optic cable at the right of the photo.



Figure 101. FIReTIP launch optics with one Lexan panel removed. The waveguide input is seen at the bottom with a rubber boot to provide a seal.

The launch window provides a vacuum seal for the tokamak at Bay G, and allows the FIR and HeNe beams to enter/exit the vacuum vessel. The window material is 3.43 mm thick, z-cut crystal quartz to provide low attenuation at FIR and HeNe wavelengths. The window is brazed into a standard ConFlat flange, 2.5° from normal. The small incident angle will cause any reflections from the window to deviate from the beam path, and prevent them from re-entering the waveguide. Window reflections could potentially reach the receiver table and mix with the FIR signals generating significant phase noise. Transmission and reflection coefficients were measured for the FIR and HeNe beams. Transmission measurements are straight forward, and accomplished by aiming the beam at a pyroelectric power meter, and then inserting the window in the beam path. FIR reflected power was quite small, and near the pyroelectric noise level. The pyroelectric detector requires a chopper to interrupt the beam. The measured power level is proportional to the amplitude of the output waveform, where the maximum and minimum

peaks are due to the beam passing through to the pyroelectric detector sensor, or blocked by the chopper blade. To eliminate noise in the pyroelectric detector output, the output signal was phase locked to the chopper frequency; therefore, all frequencies other than the precise chopper frequency are filtered out. A HeNe laser was aimed through the chopper to a diode detector to provide a reference frequency. The reference signal and pyroelectric detector output are connected to a phase lock amplifier, which subsequently produces a DC voltage proportional to the FIR beam intensity.

The z-cut quartz window was measured at 2.5° incidence. The FIR beam was measured to have 82% transmission, 5% reflection, and the remaining 13% are absorbed or scattered. For comparison, a common BK-7 window was tested at 119 μm . Transmission was measured at less than 0.02%, with reflections of 13.8%. The majority of the power was absorbed by the glass. High absorption of IR to FIR wavelengths is common for most types of glass depending on their water content. Quartz has low absorption for visible wavelengths; however, the transmission and reflection coefficients will be different. The HeNe laser was measured to have 87.7% transmission, 12.3% reflection, and no appreciable absorption.



Figure 102. FIReTIP launch window. The window is brazed into a ConFlat™ flange, and then mounted to the Bay G port cover.

At Bay B, a retroreflector is installed inside the vacuum vessel to return the FIR and HeNe beams back along their original beam paths. A retroreflector is comprised of three orthogonal mirrors, with their reflective surfaces on the interior. Any beam incident on the interior will reflect from all three surfaces, and return antiparallel to the incident beam. The return beam may have a lateral shift; however, if directed at the retroreflector center, the return beam will be collinear. A retroreflector is independent of incident angle. Incident angles are typically normal to $\sim 2^\circ$; however, incident angles of 5° or 10° will perform equally well as normal incidence. The previous installation of FIReTIP used retroreflectors mounted outside of the vacuum vessel. This isolated the retroreflectors from vibrations and heat; however, the new installation has mounted a retroreflector on the interior near Bay B. A retroreflector was designed and fabricated for this application. The material must be diamagnetic to avoid interfering with the tokamak magnetic fields. During bake-out procedures, temperatures of ~ 300 C° can be expected. The FIReTIP retroreflector must reflect 119 μm and 633 nm, and be able to handle low to high temperature cycling without going out of alignment.

The FIReTIP retroreflector is constructed of 316 stainless steel. The overall dimensions are a maximum diameter of 50 mm and 50 mm tall. The reflective surfaces were polished with lens grinder/polishing equipment for a mirror surface finish and as flat as possible. Reflection coefficients were measured by reflecting a HeNe laser from the surface, and measuring the beam intensity with a pyroelectric detector. For bare stainless steel, a maximum reflection of 50% was achieved. Since the retroreflector reflects light from three surfaces, the assembled performance is 0.125 reflection coefficient. To improve upon the performance, the retroreflector was sputtered with a thin gold layer. Single surface reflections were improved to 70%, and provided a final performance of 0.343 reflection coefficient at 633 nm.



Figures 103a and 103b. FIReTIP retroreflector. Gold coated, 316 stainless steel, maximum diameter 50 mm, height 50 mm.

Reflections at 119 μm are less of a concern due to the much longer wavelength. FIR performance was measured by aiming the FIR laser at a beam splitter, and measuring the transmitted beam profile for mode quality and power. The retroreflector is then placed in the beam path, and the beam scanner is moved to the reflection side of the beam splitter. The reflection coefficient of the beam splitter is 30%; therefore, the reflected power is expected to be reduced to the same level. The path length for transmitted and reflected signals are equalized to better equate the two measurements. The retroreflector reflection coefficient was found to be near 100%. The beam size and mode quality was unchanged; however, there was increased noise in the beam profile. This is due in part to surface imperfections in the retroreflector, and a reduced signal to noise ratio for the lesser overall power due to the beam splitter.

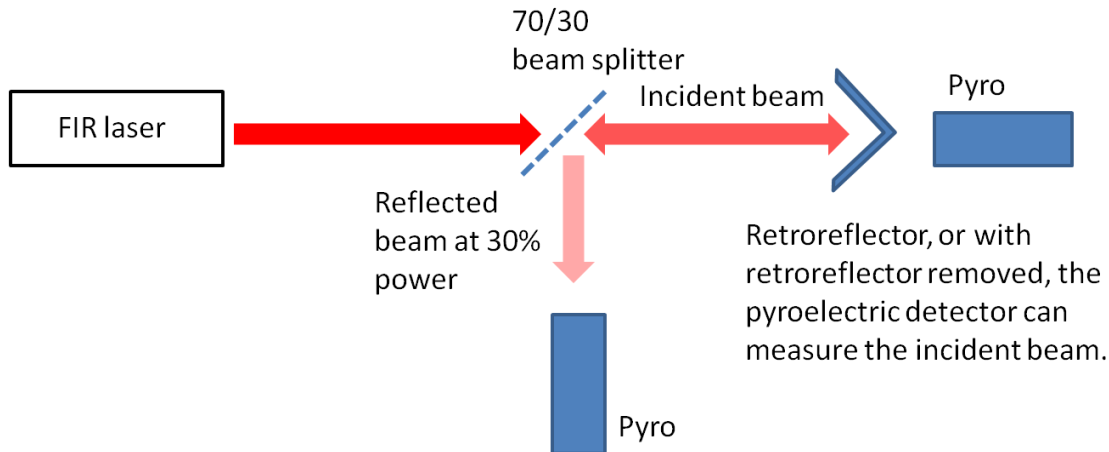
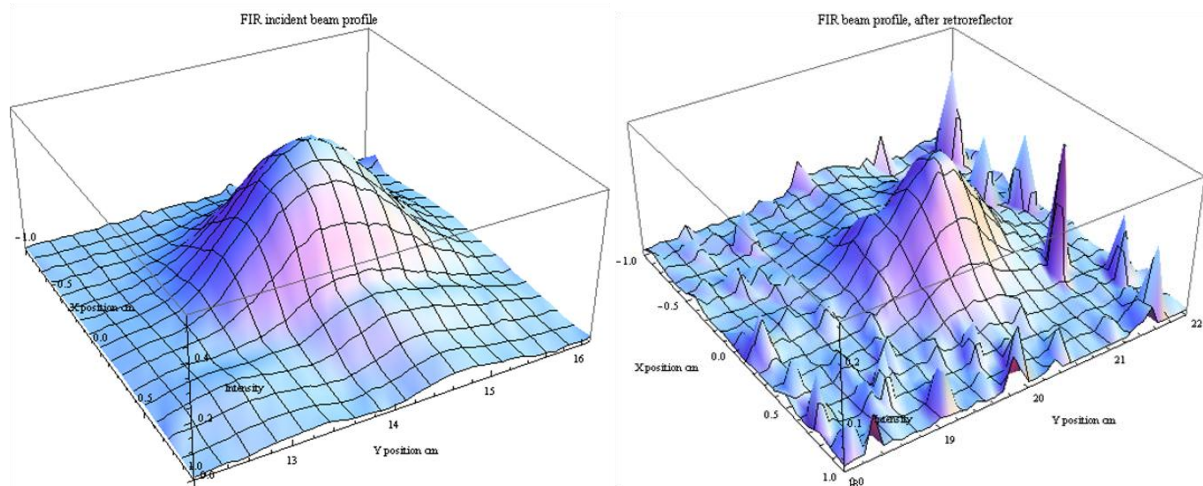


Figure 104. Retroreflector FIR reflection test set-up



Figures 105a and 105b. Raster scan of FIR beam profile. Left: Incident beam profile. Right: Beam profile after reflecting from the retroreflector. The main peak is the same as the incident profile, but reduced in power for the additional passage through the beam splitter. The small peaks are a small amount of scattered power due to surface imperfections and flaws in the mirrors' edges.

The assembly and adjustment of the retroreflector is a delicate process. The three mirrors need to be orthogonal, collectively within ~ 1 arcminute. The maximum allowable deviation of the return beam depends on the ability of the return beam to recouple into the waveguide. The total distance from the end

of the waveguide to the retroreflector is 5.79 m. The return beam alignment should not exceed a maximum of 0.1 degrees from the incident beam, and a lateral shift in beam position up to 2 mm is acceptable. Based on these parameters, when aligning the retroreflector, the return beam was measured to ensure that the deviation from the incident beam does not exceed 1 arcminute. To measure the retroreflector assembly alignment, a HeNe laser was placed 3 m from the retroreflector. A sheet of white paper with a 0.125" aperture is placed at the laser source. Reflections from the retroreflector will be imaged on the paper. When the incident beam crosses the parting line between mirrors, or all three in the case of striking the center, the beam is divided into multiple parts, with each part taking its own path. When properly aligned, the return beam will be round, and centered on the aperture. The parting line between two mirrors should be seamless. If there are any gaps, not only will a portion of the laser power be lost, but diffraction can interfere with mode quality. Aligning the mirrors is a painstaking process, and once all the fasteners are secured, and the alignment confirmed, care should be taken not to disturb the retroreflector.

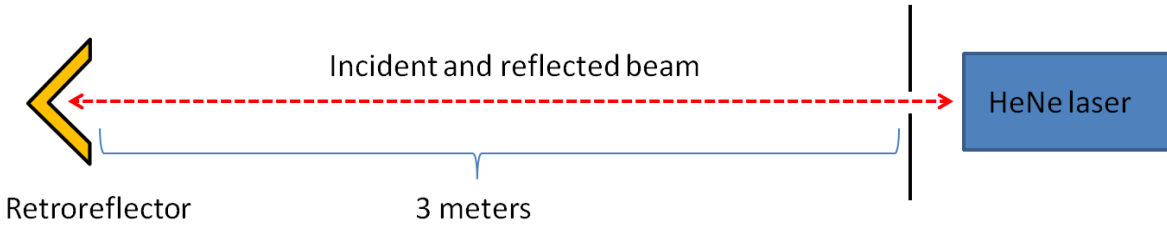
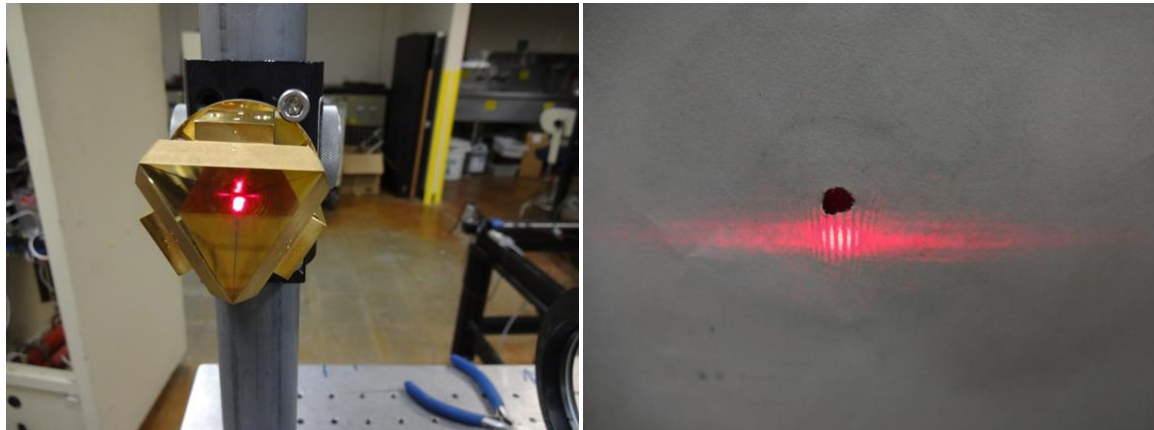


Figure 106. Retroreflector alignment test setup. Altering the incident angle of the HeNe laser should have no effect on the reflected beam. Translating the retroreflector should cause the return beam to translate by the same amount, while remaining parallel to the incident beam. Any other results from this test indicate misaligned mirrors.



Figures 107a and 107b. Retroreflector with misaligned seam. Left: The HeNe laser is aimed just below the center, at a parting line between two mirrors. Right: The reflected signal is reflected below the incident beam; however, a diffraction pattern is observed due to a small gap along the mirror parting line.

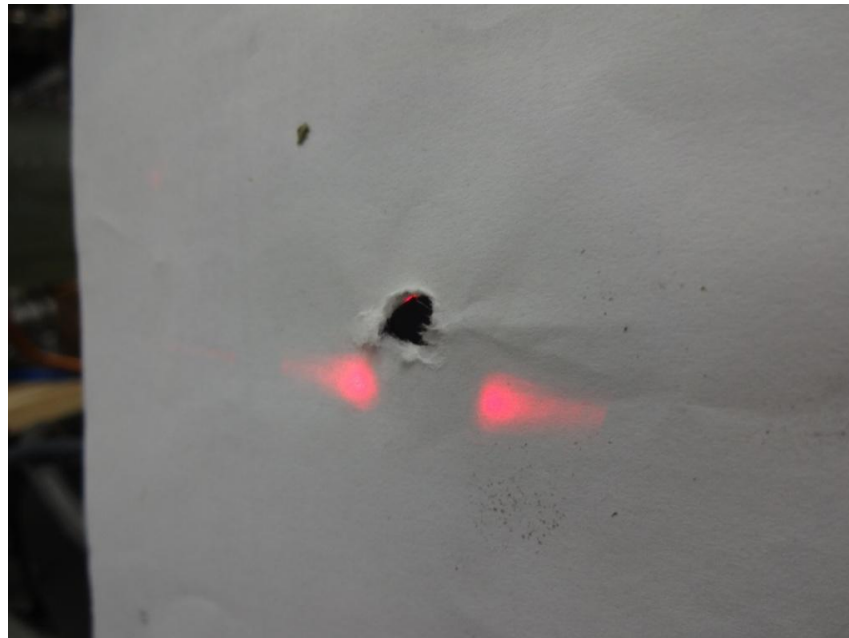


Figure 108. Misaligned retroreflector. The incident beam was directed at a seam between two mirrors, and the return beam is divided into two parts. The separation between reflected beams is due to the mirrors not being orthogonal. Whether the angle between mirrors is too large or too small cannot be determined from this photo. The beams could be divergent, or could have crossed each other first. By translating the retroreflector, and observing the reflection movement, the nature of the misalignment can be discerned.

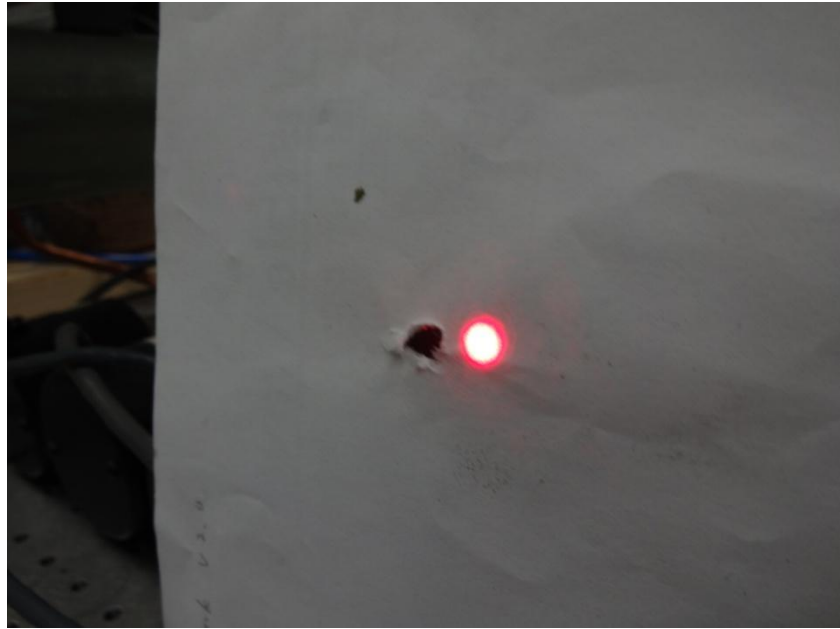


Figure 109. Properly aligned retroreflector. The return beam is observed to be round. The laser is aimed off center so the return image is clear for the photo. Translating the retroreflector shifts the image accordingly. The beam should remain round, and move smoothly, without jumping or reversing directions. Traversing across mirror seams will generally reveal any problems with the alignment.

During bake out procedures, NSTX-U can reach temperatures of ~ 300 $^{\circ}\text{C}$. This is the highest temperature the retroreflector is expected to be exposed to. It is vital that the retroreflector does not fall out of alignment, or that the gold coating blisters. To verify this retroreflector can handle the thermal load, the retroreflector was baked at 300 $^{\circ}\text{C}$ for 30 minutes, and then quickly measured (< 1 minute) while hot. The retroreflector is then allowed to cool to 20 $^{\circ}\text{C}$, and measured again. There was no change in alignment during or after heating. The gold coating showed no signs of blistering or other defects. While it is difficult to measure the retroreflector at high temperature, it is not vital to do so. During plasma operations, NSTX-U is not expected to reach 300 $^{\circ}\text{C}$; it is only during bake out procedures that high temperatures are reached. To ensure good retroreflector performance, it is important that the retroreflector does not change after thermal cycling.

There is some concern that the retroreflector will lose performance over time due to liquid lithium deposits, or high energy particles striking the surface. The location near Bay B is set back from the plasma edge, which should offer some protection. However, the longevity of the retroreflector under real operating conditions is unknown. A second retroreflector has been fabricated, which can be exchanged during any scheduled venting of the tokamak should it become necessary. Replacing the retroreflector is not otherwise difficult, since it is insensitive to the incident angle of the lasers.

III.4 Vibration Monitor

The previous installation of FIReTIP [38] included all externally mounted retroreflectors, which were relatively isolated from machine vibrations. For channel 1 of the new installation, the retroreflector is mounted to the interior of the Bay B port cover. This will be subject to mechanical vibrations, and the subsequent phase noise must be accounted for. Vibrations are expected at low frequencies (< 1 kHz) with amplitudes on the order of 50 μ m. Since the FIReTIP system uses a double pass measurement, the mechanical vibrations are effectively doubled. The interferometer is expected to pass through about 50 fringes during measurements, so the vibrations would only account for 2% of the signal. However, the amplitude is on the order of the FIR wavelength, and care must be taken when considering 2π phase jumps. The IF electronics must be able to account for increasing or decreasing path lengths to work properly. The polarimeter is much more sensitive to vibrations. Faraday rotation is expected to be 5 to 10 degrees, so the mechanical vibrations will dominate the signal unless carefully measured.

The previous FIReTIP system included a HeNe based homodyne interferometer to provide phase corrections; however, it was not possible to distinguish the parity of the phase shift. The vibration data was manually reviewed, and then the proper phase corrections were applied. The new system will include a heterodyne vibration monitor, which will allow the proper phase corrections to be calculated

automatically. This will not only ease the work load of the operator, but more importantly, will be able to provide phase corrections in real time. In this manner, the FIReTIP system will be able to provide real time density feedback for machine control. The major points of the vibration monitor are discussed in this dissertation to complete the understanding of the diagnostic operation; however, the finer details are the work of another graduate student.³

The FIReTIP vibration monitor utilizes a single HeNe laser, which is passed through an acousto-optical modulator (AOM). This device uses a PZT to oscillate a medium at 60 MHz, which acts like a diffraction grating for the HeNe laser. The AOM splits the HeNe beam into two portions, 60 MHz apart, a separated by a small angle ($\sim 1^\circ$). The beams are coupled into fiber optic cables and split into two halves (4 beams total). One pair of beams is sent to a diode detector to act as a reference mixer. The second pair of beams is coupled into another diode detector; however, one of the beams is directed to the FIReTIP launch optics first. This beam is passed through the vacuum vessel to the retroreflector, and returned with phase shifts proportional to the mechanical vibrations. The phase difference between the reference and signal diode detectors is a measure of the vibrations. To calculate these values in real time, the diode detector outputs are sent to an FPGA (Field Programmable Gate Array) processor. The FPGA also accepts input from the FIR mixer outputs, and will apply phase corrections automatically. The FPGA then sends the corrected signals to the IF electronics to calculate the plasma density and toroidal magnetic field.

³ Refer to fellow UC Davis graduate student, Mr. Evan Scott's dissertation for details on the FIReTIP vibration monitor.

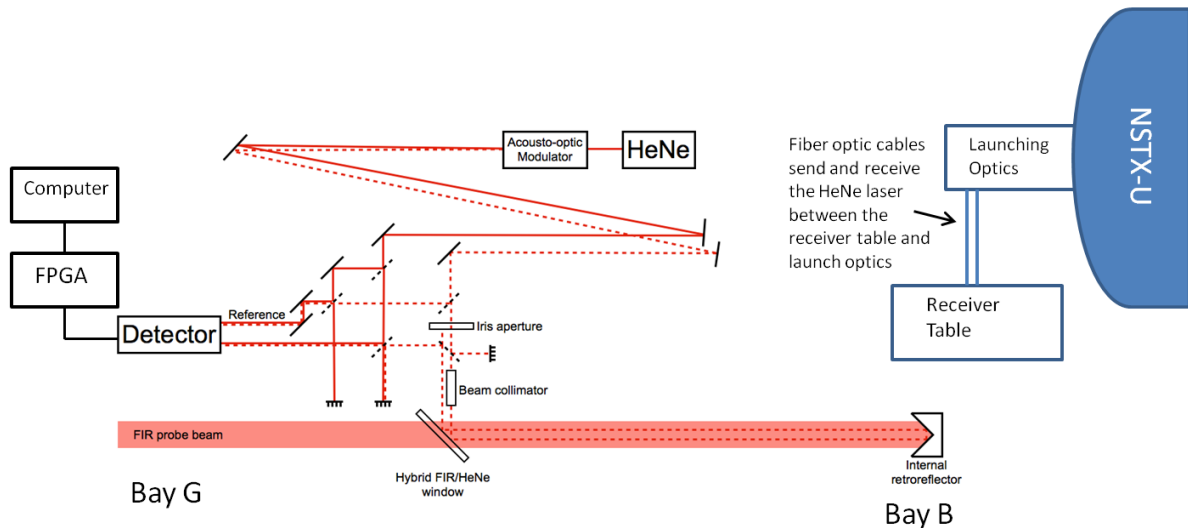


Figure 110. Schematic of FIReTIP vibration monitor. The thin solid red line represents the 60 MHz modulated HeNe beam, and the dotted line is the unmodulated beam. The schematic shows mirrors and beam splitters for clarity; however, in actuality the HeNe beams will be contained in fiber optic cables for most of the system. Equalizing the path lengths between signal and reference is accomplished by adding lengths of fiber optic cable.

The majority of the vibration monitor is contained on the top level of the receiver table. This includes the laser, AOM, fiber optic cables and couplers, and the diode detectors. A fiber optic cable will deliver the signal beam to the launch optics, where it is coupled to free space, and then the return signal is coupled to a separate fiber optic cable and directed to the diode detector.

The HeNe laser produces a Gaussian beam of 1.5 mW CW at 633 nm with a diameter of approximately 3 mm. It is emitted well collimated, and has a long coherence length (> 30 m). This type of laser is desirable for the low beam divergence and long coherence length; however, the low power output can be a concern. The beam is divided up to five times, and also has losses with each coupler, mirror, and window it encounters. Should the retroreflector lose efficiency at 633 nm, it is possible the signal to noise ratio will increase to an unacceptable level. There are many solutions to this issue. Replacing the laser

with a diode laser can greatly increase the power output for little cost; however, the increased divergence will require additional optics to shape the beam, and poor coherence length could make path equalization difficult. There are also concerns for eye protection if the beam power is increased to too high a level. More powerful HeNe lasers are available, but are expensive. The more powerful examples typically allow the propagation of more laser modes, which reduces coherence length, and excessive power brings up eye protection concerns again. Careful consideration is needed before replacing the current laser.



Figure 111. National Instruments cRIO, FPGA.

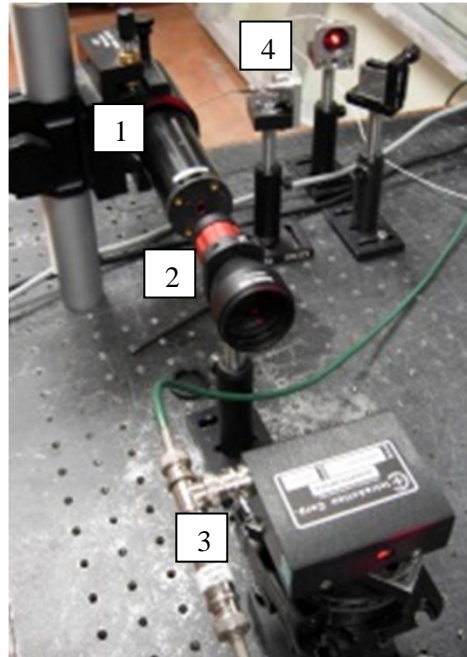


Figure 112. HeNe laser and various components of the vibration monitor. 1) HeNe laser, 2) Beam expander, 3) Acousto-optic Modulator, 4) Fiber optic couplers.

III.5 FIReTIP Receiver Table

The FIReTIP receiver table houses all of the FIR receiver mixers, the vibration monitor, and all related optics. This is the final destination for all laser beams before being converted to electrical signals. It consists of a three level table made from G10 laminate, an aluminum frame, and Lexan paneling to enclose the table for dry air. The top level is reserved for the vibration monitor equipment. The mid and lower levels contain the FIR receiver mixers and related optics. The table is positioned on the test cell floor, beneath Bay G. Up to five waveguides enter the table from above. They will pass through the upper level to access the mid and lower levels. For initial installation, only three waveguides are needed: 1) channel 1 signal, 2) reference channel, and 3) LO power. The two remaining waveguides will be for channels 2 and 3 if they are installed at a later date.



Figure 113. FIReTIP receiver table. A three level table is shown with two sides of Lexan paneling removed. The lower level is for the FIReTIP reference channel and channel 1 signal. The mid level is for channels two and three when they are installed. The upper level is reserved for the HeNe based vibration monitor. Five waveguide inputs are seen at the rear of the table, entering from above.

All FIReTIP receiver mixers use the RF input port for the signal and LO input. These beams are combined with a metallic mesh beam splitter to enter the mixer bodies in a collinear fashion. The LO

beam must be split into four equal portions, and each path length should be equal. For initial operations, the LO beam splitter on the mid level will be removed to allow additional power for the channel 1 and reference mixers. Figures 114 and 115 display the beam paths more clearly.

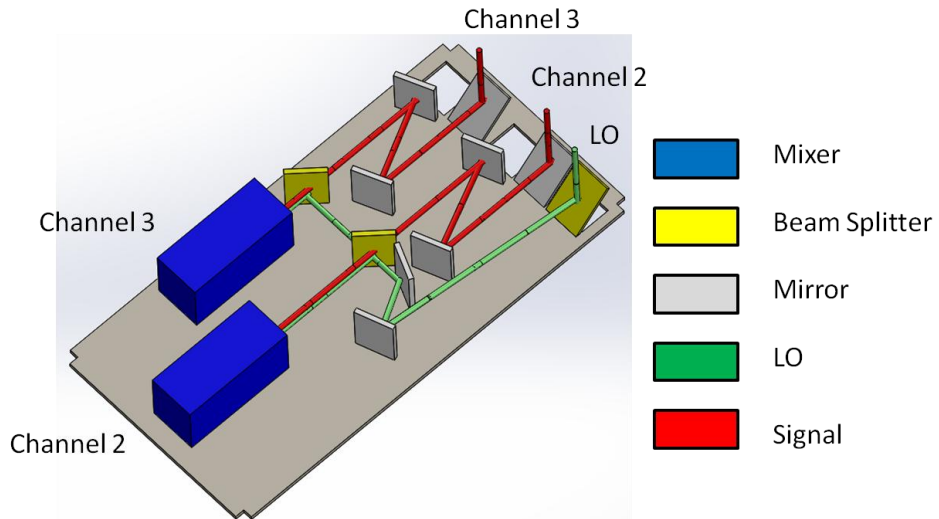


Figure 114. CAD rendering of the FIReTIP mid level receiver table. The LO path (green) uses an extra mirror to increase the path length to equalize the path lengths to the lower level. The receiver mixers (blue) are staggered for the same purpose.

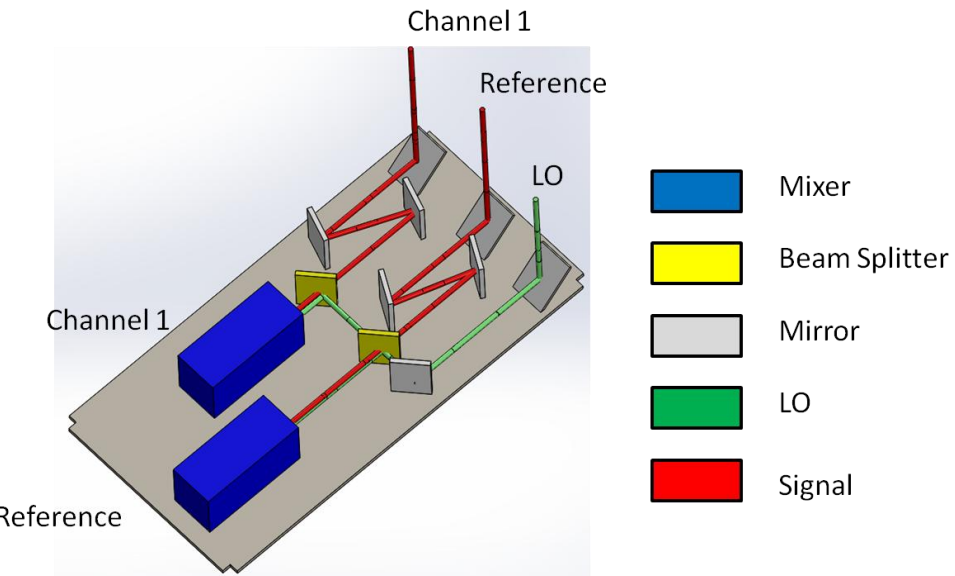


Figure 115. CAD rendering of the FIReTIP lower level receiver table. Each beam path uses multiple mirrors to independently control beam steering for each axis of freedom.

The receiver table will be placed beneath Bay G. Rubber pads will isolate the table from room vibrations. Vibrations can cause the beams to misalign to the receiver mixer input, causing fluctuations in insertion loss. This is generally not a problem so long as it is not severe because it is the phase data that are vital to the diagnostic. However, the size and wavelength of the HeNe system is more susceptible to small vibrations. Should the rubber pads provide insufficient isolation, then an active air isolation system can be installed. Vibration analysis of the test cell is currently being evaluated by colleagues on site at PPPL. They will advise if further isolation is warranted.

The FIReTIP receiver mixers have been recycled from the MIRI system originally installed on TFTR [39]. During the TFTR era, these mixers were among the few options available for operation at 2.5 THz. They are Schottky diode corner cube mixers [40]. The mixer is comprised of a pair of perpendicular reflectors (similar to a retroreflector), with a whisker antenna near their intersection. The antenna receives RF signals and delivers them to a Schottky diode. When the RF and LO signals constructively interfere, the diode is activated to pass the beat frequency to a low noise amplifier. A tunable DC bias circuit can provide additional voltage to the diode to ensure the RF/LO combination is near the “turn-on” point of the diode. The corner cube mixer, DC bias, and LNA are contained in a stainless steel enclosure. A pair of coaxial connectors provide: 1) power for the DC bias and LNA (+15 DCV), and 2) the output signal from the LNA. At the enclosure wall, the coaxial cables are converted to triax cable. The outermost triax conductor is not used directly; it provides additional shielding for the signals to prevent pick-up noise from other equipment in the test cell. A 19 mm hole near the front of the enclosure permits the RF and LO beams to enter. Three mirrors help steer and focus the beams onto the corner cubes. First, a spherical mirror above the enclosure reflects and focuses the beam. The second mirror redirects the beam into the 19 mm opening. At the opening, a wire polarizer rejects non-vertical polarizations. Inside the enclosure, a third spherical mirror focuses the beam further onto the corner cube.

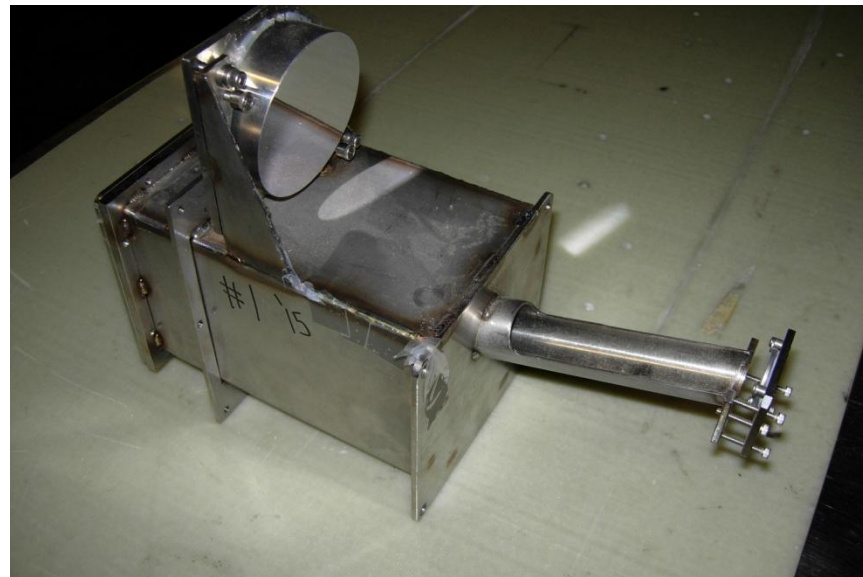


Figure 116. FIReTIP receiver mixer assembly. The large mirror on top focuses the beam towards a small flat mirror at the right, and then the beam enters the receiver mixer enclosure.

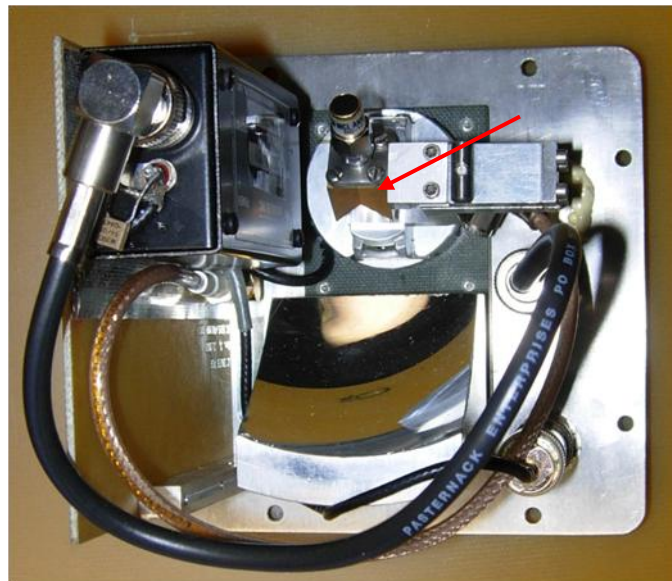


Figure 117. FIReTIP receiver mixer. This photo shows the internal arrangement of the mixer assembly. The arrow points to a V-shaped block, which is the corner cube mixer itself.

The mixer is not particularly efficient at 2.5 THz. The corner cube faces have a relatively large reflection coefficient. The diodes are not designed to operate at 2.5 THz, which is in the fall off region above the

ideal bandwidth. Conversion loss is approximately -50 dB. Since most of the incident power is not coupled into the diode, additional input power can be applied to offset the losses. However, as a practical limit, the RF and LO beams should not exceed 10 mW combined to avoid damage.

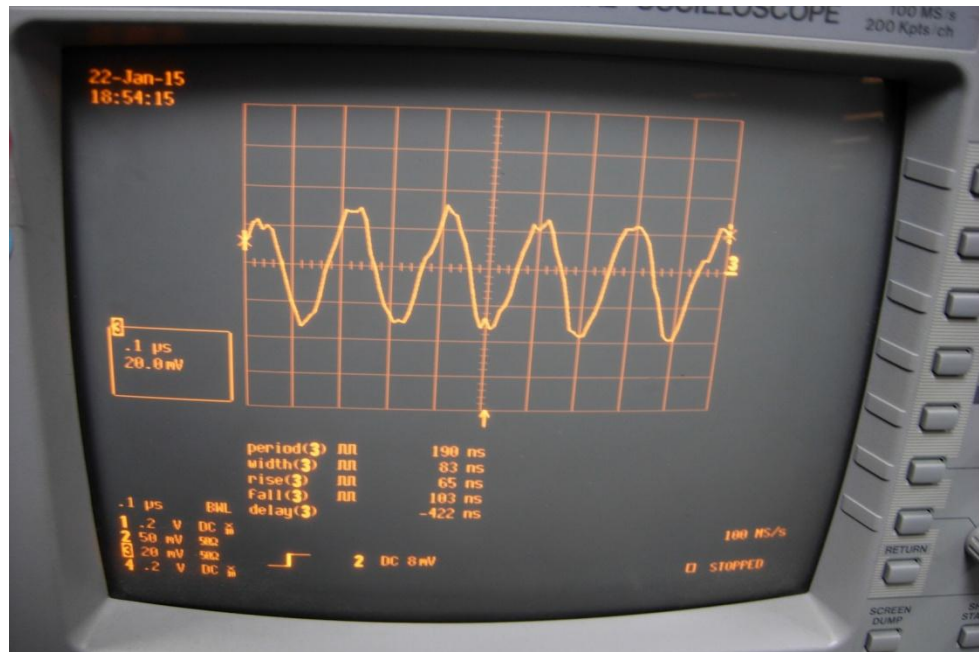


Figure 118. FIRerTIP receiver mixer output. This photo shows a sample of the mixer output. The incident power was 4.5 mW RF, and 5.5 mW LO. With 400 volts applied to the Stark laser, an IF frequency of 5 MHz is observed.

Most laboratory testing is performed with the mixers supplied by a 15 V, DC power supply. However, to reduce signal noise at PPPL, three wet cell batteries will provide power to the mixer electronics. Chemical batteries can produce a much more stable DC voltage. During daytime operations, the batteries will supply 15 to 18 volts to the receiver mixers, and at night time, the batteries will be recharged for the next day's operation.

Of the original MIRI corner cube mixers, only six are still operational. Two are needed for initial FIRerTIP operation, and two more may be added with channels 2 and 3, leaving two spares. This type of

whisker contacted diode mixer has been replaced by mixers employing planar GaAs Schottky barrier diodes [41], and repairing these corner cube mixers is unlikely. Eventually, the corner cubes will need to be replaced with new technology; however, they are expected to operate for several years. The conversion loss is relatively high at ~ -50 dB; however, the overall signal to noise is sufficient for good performance, and there is no need to develop replacement mixers. When the time comes to replace the mixers, there have been many developments in THz mixers that could supply suitable replacements [42, 43]. In addition to the mixers, it may be possible to replace the 2.5 THz LO source at the same time. The availability of high power ($\sim 100+$ mW) sources at 2.5 THz are few; therefore, the methanol lasers are still the preferred source. Furthermore, for heterodyne detection, two sources are needed with similar, but slightly different, frequencies. FIReTIP employs a Stark effect methanol laser to achieve a temporal resolution of ~ 5 MHz. An alternative method may be to utilize a quantum cascade laser (QCL) for the LO source. THz capable QCLs have been improving; however, they are limited in power output, duty cycle, and require low operating temperatures. Recent developments report a ~ 3 THz QCL producing ~ 4 mW at 200 K, with 300 ns pulses at 300 Hz [44]. A similar QCL can produce ~ 200 μ W at room temperature [45]. To employ a QCL as an LO source, only a few mW are needed per channel, depending on the mixer sensitivity and system losses. If the FIReTIP receiver mixers were replaced, then a QCL may be possible to be incorporated into the design at that time.

III.6 FIReTIP IF Electronics

Output signals from the FIReTIP receiver mixers will be routed to the vibration monitor FPGA for real time phase corrections. From there, the signals will be processed by the IF electronics. Ultimately, the IF electronics will measure the phase difference between the various mixer outputs to determine the chord averaged plasma density for the interferometer function. The polarimeter will measure the Faraday rotation to discern the tangential magnetic field strength during plasma operations. This dissertation will

summarize the IF electronics design; however, all of the work is credited to a former graduate student⁴ who developed the electronics in 2011 as an upgrade to the previous FIReTIP system [46]. These electronics are in good working order, still meet the current instrument needs, and there is no reason to alter them.

The original electronics allowed for 7 channels of processing. The new installation will only use 3 channels (1 at initial installation), leaving the balance available for back-up. There are two additional inputs for reference signals at 4 and 6 MHz. All channels pass through automatic gain control modules to equalize the power levels before up converting to \sim 70-80 MHz depending on the channel. Each channel is then connected to a phase locked loop (PLL). In this part of the circuit, a voltage controlled oscillator (VCO) output is mixed with the channel input signal. If the VCO output has a different phase, the mixer will produce an error signal. The electronics tune the VCO to reduce the error signal to zero, establishing a phase locked signal. The final portion of the circuit is the phase comparators. The signals are down converted to \sim 9-10 MHz to improve spatial resolution for phase determination. There are two methods used to measure phase delay. First, a digital fringe counter is used to measure low frequency signals (< 500 kHz). Second, IQ demodulators are used to measure signal phase up to 4 MHz, where the phase is the arctangent of Q/I demodulator outputs. The phase differences between the signals of interest can then be compared, and the final output is recorded by a digitizer to archive the data by computer. [47]

⁴ The current FIReTIP IF electronics were developed by Wen-Ching Tsai as part of her Ph.D. dissertation at UC Davis.

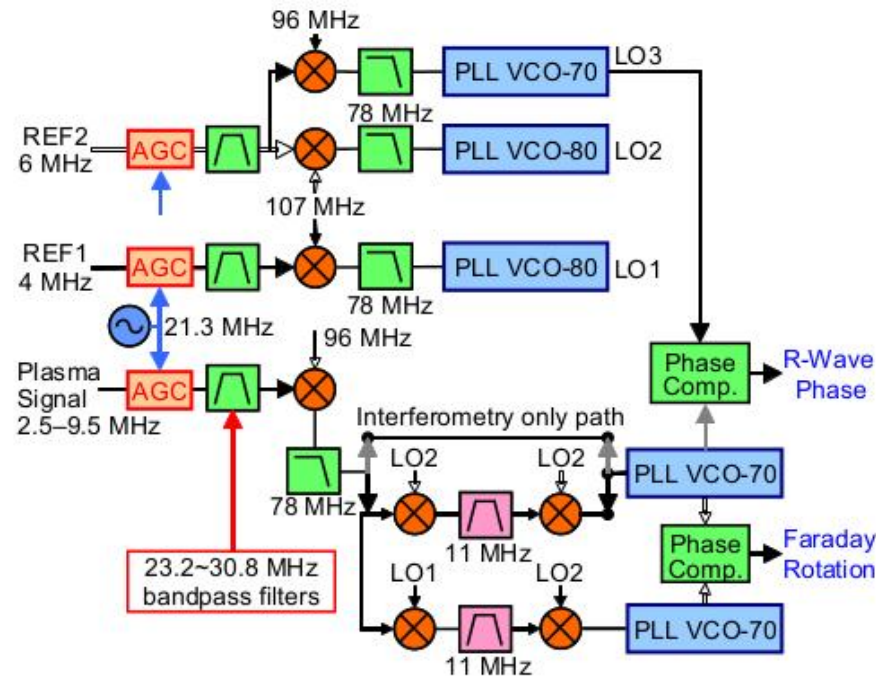


Figure 119. Schematic of FIReTIP IF electronics. Reproduced from [46], with the permission of AIP Publishing.

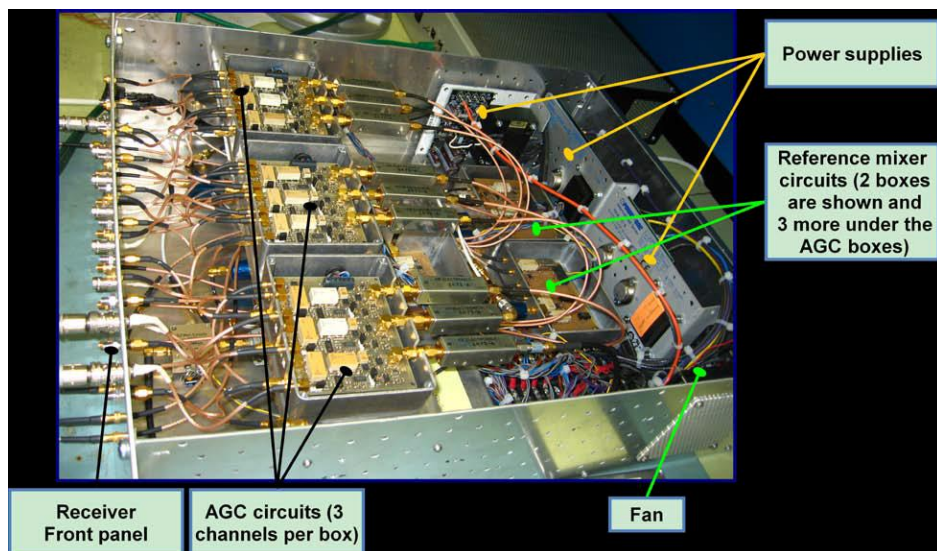


Figure 120. Inside the FIReTIP receiver box. This unit accepts signals from the FIReTIP mixers, and two reference signals. Included are the automatic gain control modules and reference signal phase locking loops. Receiver box outputs then connect to the phase comparator modules [47]. Photograph courtesy of Dr. Wen-Ching Tsai.

7-channel plasma signal I/O		
Label	Function	Connector type
H1 ~ H7	HHFW monitor ports	MCX
M1 ~ M7	Input monitor ports	SMA
I1 ~ I7	Plasma signal inputs	TRIX
O1 ~ O7	AGC & up-conversion circuits outputs	SMA

Reference signal I/O		
Label	Function	Connector type
REF1/ REF2	4 MHz/ 6 MHz inputs	TRIX
MON1/ MON2	Input monitor ports	SMA
LO1	for narrowband polarimetry measurement	MCX
LO2	for narrowband interferometry/polarimetry measurement	MCX
LO3	for wideband interferometry measurement using I-Q mixer	MCX
96 MHz	Up-shift AGC signal output to around 70 MHz	MCX

Figure 121. Receiver box connector assignments [47]. Photograph courtesy of Dr. Wen-Ching Tsai.

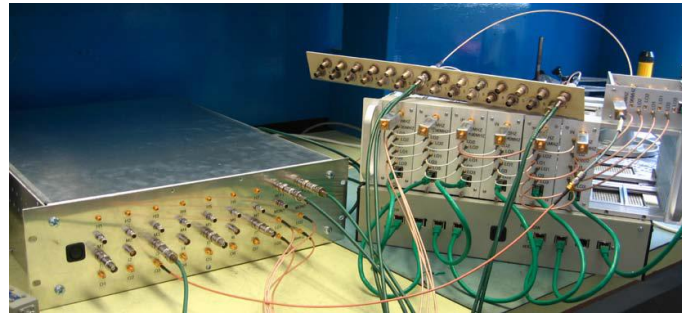


Figure 122. FIReTIP IF electronics. The receiver box is shown on the left. On the right are the phase comparators for each channel, and the phase comparator power supply [47]. Photograph courtesy of Dr. Wen-Ching Tsai.

The FIReTIP IF electronics has a maximum temporal resolution of 4 MHz. The Stark laser offset sets the maximum resolution possible. At 400 V applied potential, the Stark laser offset is about 5 MHz, depending on the cavity length tuning. With the FIR lasers tuned to +1 and -1 MHz, the FIReTIP receiver mixer IF outputs will be 4 and 6 MHz. Before operating the FIReTIP system, these frequencies should be checked and tuned if necessary. The receiver monitor ports can be observed on a spectrum analyzer to verify the current instrument operation. The spectrum analyzer is also useful for diagnosing laser problems, or beam alignments. More in depth details for the IF electronics design, operation, and performance can be found in reference #47.

III. References

- [1] T.M. Lehecka, "Development of High Power Optically Pumped Far Infrared Lasers for Fusion Plasma Diagnostics," *Thesis for a Master of Science degree in Electrical Engineering*, University of California, Los Angeles, 1986.
- [2] D.T. Hodges, "A Review of Advances in Optically Pumped Far-Infrared Lasers," *Infrared Physics*, Vol. 18, pp. 375-384, 1978.
- [3] R.J. Foltynowicz, M.C. Wanke, and M.a. Mangan, "Atmospheric Propagation of THz Radiation," *Sandia Report*, SAND2005-6389, Sandia National Laboratories, October 2005.
- [4] S. Jacobsson, "Review: Optically Pumped Far Infrared Lasers," *Infrared Physics*, Vol. 29, No. 5, October 1989.
- [5] T.Y. Chang, T.J. Bridges, and E.G. Burkhardt, "CW Submillimeter Laser Action in Optically Pumped Methyl Fluoride, Methyl Alcohol, and Vinyl Chloride Gases," *Applied Physics Letters*, Vol. 17, No. 6, September 1970.
- [6] A.G. Maki, C.C. Chou, K.M. Evenson, L.R. Zink, and J.T. Shy, "Improved Molecular Constants and Frequencies for the CO₂ Laser from New High-J Regular and Hot-Band Frequency Measurements," *Journal of Molecular Spectroscopy*, 167, 211-224, 1994.
- [7] N.M. Lawandy, "Temperature Dependence of Optically Pumped Far-Infrared (FIR) Laser Output Power," *Infrared Physics*, Vol. 19, pp. 127-134, January 1978.
- [8] "Zinc Selenide (ZnSe)," <http://www.iiviinfrared.com/Optical-Materials/znse.html>, accessed: November 6th, 2016.
- [9] C. Palmer, "Diffraction Grating Handbook," *Newport Corporation*, 6th Ed., Rochester, New York, 2005.
- [10] J.S. Bakos, A. Lash, Zs. Sorlei, and D.N. Yundev, "Effect of Helium Addition on Output Power of a CW Optically Pumped Far Infrared Methanol Laser," *Infrared Physics*, Vol. 33, No. 2, pp. 141-146, 1992.
- [11] R. Barchfeld, D. Gamzina, Y.M. Shin, J. Kim, C. Alldritt, L.R. Barnett, and N.C. Luhmann Jr., "Microfabrication of Terahertz Vacuum Electronic Devices," 26th Annual Meeting of the American Society of Precision Engineering, Denver, Colorado, November 2011.
- [12] D.K. Mansfield, P.A. Krug, M. Vocaturo, L. Guttadora, M. Rockmore, and K. Micai, "Stark-tuned, Far-Infrared Laser for High-Frequency Plasma Diagnostics," *Applied Optics*, Vol. 31, No. 24, August 1992.
- [13] M. Montazerian, S.P. Singh, and E.D. Zanotto, "An analysis of glass-ceramic research and commercialization," *American Ceramic Society Bulletin*, 94(4): 30-35, May 2015.

- [14] Z.U. Qinxin, W.A. Peebles, C. Jing, L. Cardenas, S. Burns, and N.C. Luhmann Jr., "Experimental Studies of 374 μm NH₃ Optically Pumped Far-Infrared Laser," *Chinese Physics Letters*, Vol. 10, No. 9, 1993.
- [15] D.K. Mansfield, E. Horlbeck, C.L. Bennett, and R. Chouinard, "Enhanced, High Power Operation of the 119 μm Line of Optically Pumped CH₃OH," *International Journal of Infrared and Millimeter Waves*, Vol. 6, No. 9, 1985.
- [16] K.J. Button, "Infrared and Millimeter Waves, Volume 7: Coherent Sources and Applications, Part II," *Academic Press*, New York, 1983.
- [17] M. Inguscio, P. Minguzzi, A. Moretti, F. Strumia, and M. Tonelli, "Stark Effect on CH₃OH and CH₃F FIR Lasers: Large Frequency Tuning and Resolved Structures," *Applied Physics*, Vol. 18, pp. 261-270, 1979.
- [18] H.K. Park, J.K. Yoon, and K. Kim, "Novel Fabrication of Ag Thin Film on Glass for Efficient Surface-Enhanced Raman Scattering," *Langmuir*, 22 (4), pp 1626–1629, January, 2006.
- [19] CO₂ Spectrum Analyzer, *Macken Instruments Inc.*, <https://www.macken.com/collections/spectrum-analyzers/products/16a>, Accessed: November 9th, 2016.
- [20] F.B. Foote, D.T. Hodges, and H.B. Dyson, "Calibration of Power and Energy Meters for the Far Infrared/Near Millimeter Wave Spectral Region," *International Journal of Infrared and Millimeter Waves*, Vol. 2, No. 4, 1981.
- [21] P. Belland, and J.P. Crenn, "Matching of a Gaussian Beam into Hollow Oversized Circular Waveguides," *International Journal of Infrared and Millimeter Waves*, Vol. 10, No. 10, 1989.
- [22] P.F. Goldsmith, "Quasi-Optical Techniques," *Proceedings of the IEEE, Invited Paper*, Vol. 80, No. 11, November 1992.
- [23] R.K. Nubling, J.A. Harrington, "Launch conditions and mode coupling in hollow-glass waveguides," *Optical Engineering*, 37(9), 2454-2458, September 1998.
- [24] "Electroformed Copper Mesh," *Precision Eforming LLC*, <http://www.precisioneforming.com/electroformed-copper-mesh/>, Accessed: November 9th, 2016.
- [25] H.P. Barber, "Coherence Length Extension of HeNe Lasers," *Applied Optics*, Vol. 7, No. 3, March 1968.
- [26] S. Alaruri, "Experimental Method for Determining the Coherence Length of CW Lasers Using a Michelson Interferometer," *Journal of Laser Applications*, Vol. 5, No. 2 & 3, 1993.
- [27] J.P. Crenn, "Optical Propagation of the HE₁₁ Mode and Gaussian Beams in Hollow Circular Waveguides," *International Journal of Infrared and Millimeter Waves*, Vol. 14, No. 10, 1993.
- [28] C. Dragone, "Attenuation and Radiation Characteristics of the HE₁₁ Mode," *IEEE Transactions on Microwave Theory and Techniques*, Vol. 28, No. 7, July 1980.
- [29] B. Bowden, J.A. Harrington, and O. Mitrofanov, "Low-loss modes in hollow metallic terahertz waveguides with dielectric coatings," *Applied Physics Letters*, 93, 181104, 2008.

[30] E.J. Kowalski, D.S. Tax, M.A. Shapiro, J.R. Sirigiri, R.J. Temkin, T.S. Bigelow, D.A. Rasmussen, "Linearly Polarized Modes of a Corrugated Metallic Waveguide," *Plasma Science and Fusion Center Massachusetts Institute of Technology*, PSFC/JA-10-61, Cambridge MA, http://dspace.mit.edu/bitstream/handle/1721.1/94403/10ja061_full.pdf?sequence=1, 2010.

[31] O. Mitrofanov and J.A. Harrington, "Dielectric-lined cylindrical metallic THz waveguides: mode structure and dispersion," *Optical Society of America*, Vol. 18, No. 3, February 2010.

[32] E.A. Nanni, S.K. Jawla, M.A. Shapiro, P.P. Woskov, R.J. Temkin, "Low Loss Transmission Lines for High Power Terahertz Radiation," *Plasma Science and Fusion Center Massachusetts Institute of Technology*, PSFC/JA-11-53, Cambridge, MA, January 2013.

Retroreflector

[33] Y.S. Jin, G.J. Kim, and S.G. Jeon, "Terahertz Dielectric Properties of Polymers," *Journal of the Korean Physical Society*, Vol. 49, No. 2, August 2006.

[34] W.R. Folks, S.K. Pandey, and G. Boreman, "Refractive Index at THz Frequencies of Various Plastics," *Optical Society of America*, 2007.

[35] "Teflon PTFE, fluoropolymer resin," *Dupont Properties Handbook*, http://www.rjchase.com/ptfe_handbook.pdf, Accessed: Nov. 22, 2016.

[36] "Conductivity and Resistivity Values for Aluminum & Alloys," *NDT Education Resource Center*, Iowa State University, https://www.nde-ed.org/GeneralResources/MaterialProperties/ET/Conductivity_Al.pdf, Accessed: Nov. 12th, 2016.

[37] "Crystal quartz," *Boston Piezo Optics Inc.*, <http://bostonpiezo optics.com/crystal-quartz>, accessed: November 12th, 2016.

[38] B.H. Deng, H.C. Chen, C.W. Domier, M. Johnson, K.C. Lee, N.C. Luhmann, Jr., B.R. Nathan, and H. Park, "Development of a multichannel far-infrared tangential interferometer/polarimeter for the National Spherical Torus Experiment," *Review of Scientific Instruments*, Vol. 74, No. 3, March 2003.

[39] D.K. Mansfield, H.K. Park, L.C. Johnson, H.M. Anderson, R. Chouinard, V.S. Foote, C.H. Ma, and B.J. Clifton, "Multichannel far-infrared laser interferometer for electron density measurements on the tokamak fusion test reactor," *Applied Optics*, Vol. 26, No. 20, pp. 4469-4474, 1987.

[40] H. Park, D.K. Mansfield, L. Johnson, C.H. Ma, "MIRI: A multichannel far-infrared interferometer/polarimeter for TFTR," *Review of Scientific Instruments*, Vol. 85, No. 5, May 1985.

[41] S.M. Marazita, W.L. Bishop, T.M. Cunningham, P.J. Koh, T.W. Crowe, and R.M. Weikle II, "Planar GaAs Schottky Barrier Diodes," *Eighth International Symposium on Space Terahertz Technology*, Harvard University, March 1997.

[42] P.H. Siegel, R.P. Smith, M.C. Gaidis, and S.C. Martin, "2.5-THz GaAs Monolithic Membrane-Diode Mixer," *IEEE Transactions on Microwave Theory and Techniques*, Vol. 47, No. 5, May 1999.

[43] F. Boussaha, J. Kawamura, J. Stern, and C. Jung-Kubiak, "2.7 THz Balanced Waveguide HEB Mixer," *IEEE Transactions on Terahertz Science and Technology*, Vol. 4, No. 5, September 2014.

- [44] S. Fathololoumi, E. Dupont, C.W.I. Chan, Z.R. Wasilewski, S.R. Laframboise, D. Ban, A. Matyas, C. Jirauschek, Q. Hu, and H.C. Liu, "Terahertz quantum cascade lasers operating up to ~ 200 K with optimized oscillator strength and improved injection tunneling," *Optics Express*, Vol. 20, No. 4, February 2012.
- [45] K. Fujita, M. Hitaka, A. Ito, M. Yamanishi, T. Dougakiuchi, and T. Edamura, "Ultra-broadband room-temperature terahertz quantum cascade laser sources based on difference frequency generation," *Optics Express*, Vol. 24, No. 15, pp. 16357-16365, 2016.
- [46] W.C. Tsai, C.W. Domier, K.C. Lee, N.C. Luhmann, Jr., R. Kaita, and H.K. Park, "NSTX far infrared tangential interferometer/polarimeter electronics upgrade," *Review of Scientific Instruments*, 81, 10D526, 2010.
- [47] W.C. Tsai, "High Performance Electronics for Millimeter-Wave-to-Terahertz Plasma Diagnostics Instrumentation and High Power Devices," Ph.D. Dissertation in Electrical and Computer Engineering, University of California, Davis, 2011.

IV. High- k_θ Scattering System

The High- k_θ Scattering System is made up of several components. They can be categorized into five major subsections: 1) laser system, 2) quasi-optical waveguide, 3) launch optics, 4) receiver optics, and the 5) receiver and electronics. There are similarities to the FIReTIP system, in that it is an FIR laser-based diagnostic, with a long quasi-optical waveguide to deliver the beam, optics to focus and collect the FIR signals, and a quasi optical receiver to convert the FIR signals to electrical data. The laser system shares the same space as the FIReTIP lasers, so there is some coordination with the physical layout, waveguide paths, and computer controls. After these facts, the similarities end. The High- k Scattering system was first designed and installed on NSTX in 2004 [1]. When NSTX underwent major upgrades in 2012 [2], the High- k Scattering system was removed and redesigned. The fundamental changes to the system include: 1) the solid state 280 GHz source has been replaced with a 693 GHz formic acid laser, 2) the launch and receive optics are remote steerable to position the scattering volume about the plasma, and 3) a tall receiving window is installed to facilitate poloidal wavenumber measurements.

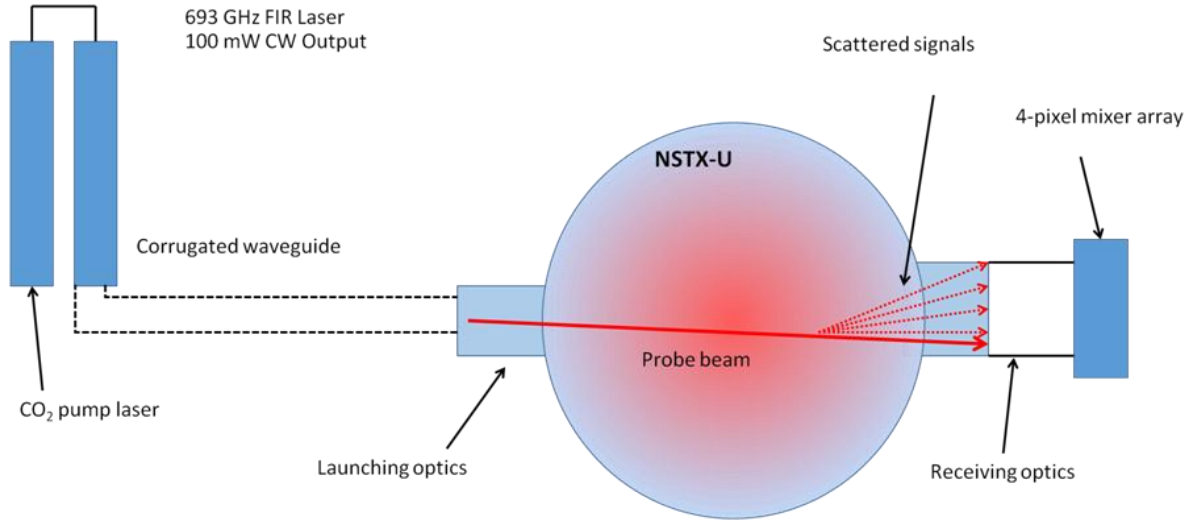


Figure 123. Schematic of the High- k_0 Scattering System. Starting at the left is an optically pumped FIR laser. Corrugated waveguide delivers the beam to the launch optics. The launch optics steer and focus the beam through the vacuum vessel. The receiving optics collect and collimate scattered power, and deliver these signals to the receiver.

IV.1 High- k_0 Scattering Laser System

The High- k_0 Scattering source is an optically pumped FIR laser. A CO_2 laser provides pumping power to excite gas in the FIR laser. The CO_2 laser is tuned to the 9R20 spectral line to excite formic acid molecules for emission at 693 GHz (432 μm) [3]. The FIR laser can produce up to 100 mW CW with a Gaussian profile (TEM_{00}) output, depending on the CO_2 pumping power. Both lasers are housed in the same three level table as the FIReTIP system. The CO_2 laser is on the bottom level, with the FIR laser on the mid level. Additional equipment for laser operation are contained in the laser "cage" area, such as laser power supply, self contained water chiller/circulator, vacuum pumps, gas cylinders, and computer for monitoring and control. The FIR beam couples into a single 2.5" diameter, corrugated waveguide, which passes through the NSTX-U test cell wall to deliver the beam to the launching optics on Bay G.



Figure 124. FIReTIP/High-k laser table in the "cage" area outside the NSTX-U test cell. The tri-level table fills most of the space within the "cage". The FIReTIP lasers are installed on the table; however, the High-k Scattering lasers are awaiting delivery to PPPL.

IV.1.1 PL-6 CO₂ Laser

Similar to the FIReTIP system, a grating tunable CO₂ laser provides pumping power to an FIR laser. In fact, the identical CO₂ laser was originally slated for use; however, supplemental funding has provided for a new CO₂ laser. The new CO₂ laser is a PL-6, manufactured by Edinburgh Instruments [4]. It functions on the same principles. It is a grating tunable laser from 9 to 11 μ m. The most significant differences for the PL-6 laser is that the power output is nearly double at 180 W maximum output, and the power supply uses solid state technology. The older CO₂ laser power supply uses vacuum tetrode current regulators which are no longer available. Several other components are considered obsolete, and difficult to acquire. While the older power supplies function well, repairs and maintenance lead to concerns for reliability and potentially long service times.



Figure 125. PL-6 CO₂ laser from Edinburgh

Instruments with the cover removed. There are two waveguides in a folded beam path. At the far end of the laser, a system of mirrors reflects the beam in a U-shaped path, connecting the waveguides in series.

The PL-6 CO₂ laser can provide up to 180 W output. To increase the waveguide length, it uses two dielectric waveguides side by side, in a folded beam path configuration. The waveguides are custom made glass with an inner gas tube to serve as the waveguide, surrounded by a glass water jacket. The waveguide diameter varies with the inner surface corrugated with a ~ 1 cm period. These corrugations suppress off-axis modes. At either end of both waveguides, electrodes are permanently mounted into the glass. The electrodes are thin (~3 mm) tungsten rods brazed in place. Crocodile clips connect to the electrodes to complete the high voltage circuit with the power supply. The ends of complete waveguide are sealed with ZnSe Brewster windows. The Brewster windows are aligned with the waveguide axis so that only vertically polarized photons are emitted [5]. The windows are mounted in aluminum bodies, with large vanes for air cooling. At the rear of the laser, mirrors are enclosed to reflect the beams between the waveguides. These mirrors are set from the manufacture, and no adjustment should ever be required. At

the front of the laser, one waveguide end has an adjustable diffraction grating. The other waveguide has a ZnSe output coupler for the beam output. Both of these items are outside the low pressure of the waveguides. This permits them to be adjusted or replaced without disturbing any vacuum seals. Also, under vacuum, these items will not be pulled out of alignment due to pressure differentials.

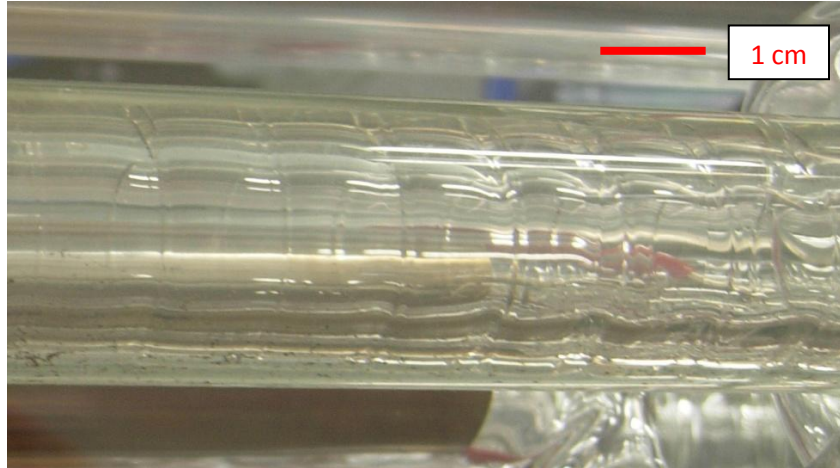


Figure 126. Close up view of the PL-6 waveguide. There are two concentric glass tubes. The outer tube is the water jacket and is smooth. The inner tube with the corrugations visible is the laser cavity waveguide.



Figure 127. PL-6 cathode connection. Red clips connect to the cathodes for ~ -15 kV. Black clips connect to similar anodes at ground potential.

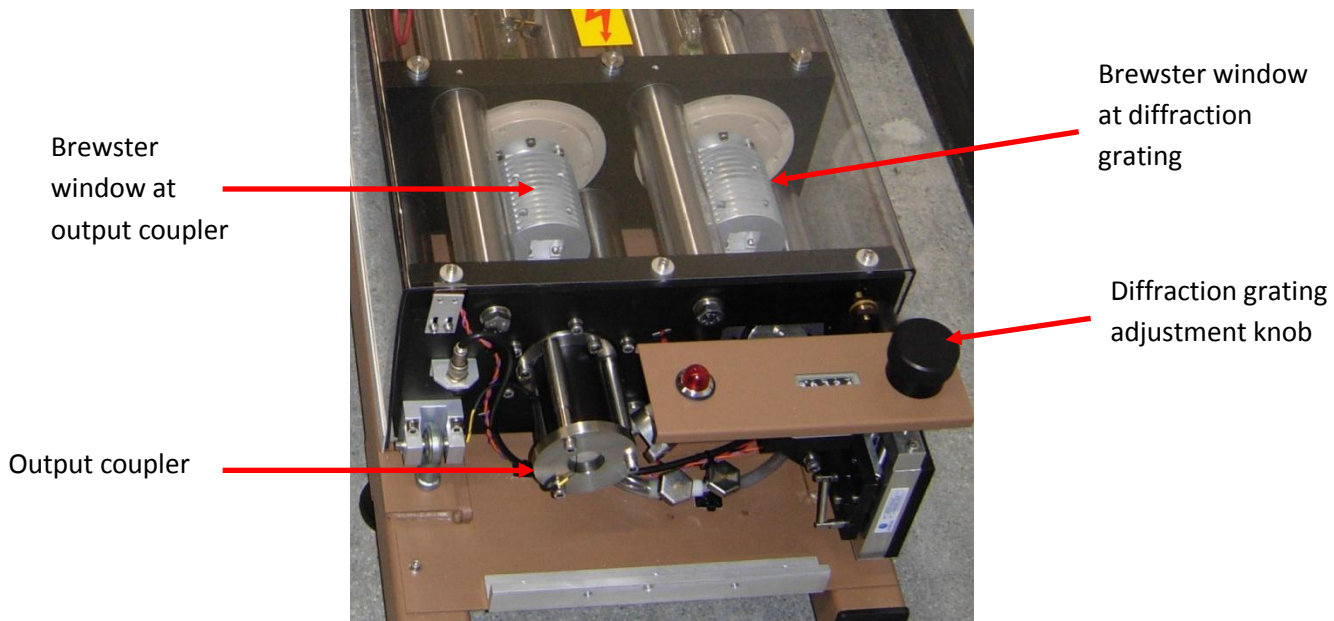


Figure 128. Output end of the PL-6 laser. The Brewster windows, output coupler, and diffraction grating adjustment knob are labeled.

The diffraction grating is a copper substrate, which is ruled at 135 g/mm, and then coated for improved power handling. An adjustment knob controls the angle of the grating to select the lasing frequency. A mechanical counter provides an arbitrary position reference for the grating. Documentation that comes with the laser has a reference table for the grating position (Appendix A), as well as the optimum gas pressure and power supply current, for each spectral line. The output coupler is a ZnSe window, which is coated to control the transmission/reflection coefficients; however, the exact design is proprietary to Edinburgh Instruments. The output coupler is mounted to a ConFlat™ vacuum flange, with a copper gasket. This arrangement does not provide a vacuum seal of any kind. Instead, the copper gasket and knife edge of the ConFlat flange provide a method for aligning the output coupler. Three bolts in a circle can be tightened independently to allow the knife edge to cut into the ductile gasket and alter the flange angle. Once the output power is maximized, the coupler mount will not need any further adjustment. It is important that when adjusting the output coupler that the fasteners only be tightened. Loosening a fastener to tune the laser could result in a loose mount. If the fasteners become too tight, or the mount is adjusted

too many times, the copper gasket can be replaced to begin anew. The laser output has a manually selectable graphite beam block. This beam block should not be used indefinitely. It is designed only for a momentary interruption of the beam to add or remove a power meter or similar component in the beam path. At high power, the beam block can be employed for several seconds; however, eventually it will over heat. The diffraction grating uses the first order diffractions to tune the laser in a manner identical to the FIReTIP CO₂ laser, however, the zeroth output is not accessible. The PL-6 has only the main power output. Five invar rods tie together the laser chassis to keep everything aligned for a range of temperatures. A sheet metal cover encloses the laser to provide protection for its components, and prevents contamination. There are interlock switches to disable the power supply should the cover be removed. During times of maintenance, it may be necessary to operate the laser with the cover removed. In this case, the interlock switch can be bypassed by rearranging the wire connections from the normally open, to the normally closed position. The cavity length of the PL-6 is adjustable by a piezoelectric transducer (PZT) at the output coupler. By applying a DC voltage to the PZT, a crystal will expand or retract to alter the cavity length with submicron precision. Much like the FIReTIP CO₂ laser, this has a small effect on the CO₂ beam power, but allows for precision frequency tuning to energize the FIR laser. For use as a pump laser for the formic acid FIR laser, the PL-6 is tuned to 9R20 (9.27 μm), and can produce up to 170 W at this spectral line.

Each PL-6 waveguide is evacuated from a common Edwards nXDS i15, dry scroll vacuum pump [6]. With the gas supply valve closed, the laser should reach < 1 Torr in a minute or two, while under vacuum, with an ultimate vacuum of 0 Torr displayed on the 0-50 Torr mechanical gauge. The lasing gas used is a mixture of carbon dioxide, nitrogen, and helium. Edinburgh Instruments recommends using 7% CO₂, 18% N₂, and the balance He. This is similar to the FIReTIP CO₂ lasing gas, except it is 7% CO₂ opposed to 6%. Either gas mixture will work adequately; to simplify matters at PPPL, both systems will use the 6% CO₂, 18% N₂, balance He molar mixture. The lesser percentage of CO₂ will require higher gas operating pressure by 14% so that the partial pressure of CO₂ is constant. This will increase the flow rate

of gas through the laser resulting in slightly higher operating costs; however, the laser power will be slightly increased by 1-2 % [7].



Figure 129. Edwards dry scroll vacuum pump. The maximum free flow pumping rate is 250 l/min; however, when operating on the PL-6 laser a 9 l/m pumping rate is expected.

Lasing gas is stored in a standard 200 cu.ft. gas cylinder, and a regulated hose is connected to the laser gas input at 16 PSIG. On the laser control panel, one knob controls the gas supply valve (on/off), and a second dial controls a needle valve to control the gas flow. The actual flow is not measured, rather the gas flow is inferred from the vacuum gauge. The flow control dial is marked with arbitrary numbers for reference only. Laser power is regulated by three things: 1) gas pressure, 2) gas flow, and 3) power supply current. Gas pressure is set by the flow control dial until the vacuum gauge reads the desired setting. More gas generally equates to more power; however, too much gas will upset the population inversion and de-energize the laser due to intermolecular collisions. The laser is always energized at low power / low gas pressure (8-10 Torr). Excessive gas pressure during start up may cause the power supply to momentarily deliver too much current and will trip the power supply's internal circuit breakers. Once the laser is

energized at low power, the gas pressure can be gradually increased to maximum levels. Maximum gas pressure is typically 25 to 30 Torr. Gas flow is determined by the gas supply pressure and the vacuum pump flow rate. The vacuum pump used can achieve up to 9 l/min when the PL-6 is at full power. During start up procedures, the gas pressure is typically set to ~10 Torr before being energized. This prevents the power supply from tripping its breakers upon activation. Once lasing is initiated, the gas pressure/flow can be increased.



Figure 130. Laser head control panel. All laser hook-ups are made through this panel including, electrical, gas, vacuum, and water. The Gas shut off and flow control are located at the upper right. The PZT control is at the upper left.

The PL-6 power supply is an LPS2000 constant current, dual channel power supply, manufactured by Edinburgh Instruments. Each waveguide in the laser has its own anode and cathode, independently adjustable at the power supply. Current control knobs adjust the current flow from 0 to 50 mA for each channel. The high voltage output will automatically scale to keep the current constant. Typical operation at full power is 40 mA and 15 kV DC. At 20 kV, the power supply will automatically shutdown to

prevent internal damage. While each half of the laser is independently adjustable, they are generally run at the same settings. However, if low laser power is desired, either channel can be deactivated by isolation switches on the rear panel. With a single channel energized, the PL-6 will produce 20 to 60 W depending on the settings. With both channels energized, it will produce 90 to 180 W. The power supply has a keyed switch to prevent unintentional activation. There are also optional interlocks, which can be connected to external systems. The external interlock is a loop of wire accessible at the rear power supply panel. To add an interlock, the loop must be cut, and then spliced into the desired systems. The power supply will only function when the circuit is closed. The power supply has an interlock connected to the water chiller. The high voltage (HV) circuit cannot be engaged unless the chiller is activated, and all other interlocks closed. The power supply also provides power to the PZT to control the laser cavity length; however, the PZT control knob is on the laser head control panel. At initial laser activation, the PZT may need to be adjusted frequently for maximum FIR output; however, after 30 minutes of operation, the laser thermally stabilizes, and the PZT only needs slight adjustment every ~60 minutes. Once the current knobs are set for maximum CO₂ power, it is not necessary to adjust them further. The laser may be activated at high current flow; only the gas pressure needs to be reduced for start up.



Figure 131. LPS2000 power supply front panel. Key switch turns on the power supply, but does not activate high voltage. White and blue buttons at the upper left turn the high voltage on and off. Each waveguide has independent current control.



Figure 132. LPS2000 power supply rear panel. All of the electrical connections are made on the rear panel, including: mains power, HV for channels 1 and 2, PZT output, and the laser head controls. The interlock connector is located at the upper right. The two orange rocker switches can activate or isolate the laser channels.

The PL-6 is cooled by a self contained, water chiller manufactured by Betta-Tech Controls [8]. The water temperature can be set by the chiller front panel; 15 °C is the recommended setting. As already stated, cooler temperatures can produce higher power output due to the increased mean free path length of the gas [9]. However, if the laser is cooled too low, condensation on the laser optics can interfere with the beam output. Consequently, 15 °C is a good compromise between power and reliability. The power supply delivers ~1,200 W when the laser is operating at maximum power. The chiller has ample capacity to cool the PL-6, and the FIR laser in parallel. Distilled water is recommended to reduce the chances of contaminates or biological growth in the cooling system. When filling the chiller with water for the first time, the pump may not be primed, and is prone to cavitation. This will cause the coolant to foam; however, after a few minutes the foaming will recede.

The LPS2000 power supply and Betta-Tech Controls chiller are designed for 230 VAC 1-phase, 20 A, 50/60 Hz, electrical input. At PPPL, the available power is 208 VAC 1-phase. To accommodate the electrical connections, two auto transformers are included to convert 208 VAC to 230 VAC. All other electrical needs are standard 110 VAC.



Figure 133. Betta-Tech Controls cu600 chiller.

The High- k_0 Scattering System was originally designed to use the same type of CO₂ laser as the FIReTIP system. The laser table was built to accommodate this laser, including the zeroth output port and the rear of the laser for power and frequency monitoring. The addition of the PL-6 laser required the table to be modified. There were three alterations required to install the PL-6 laser; however, the FIReTIP style CO₂ laser can still be used if the need arises. The first table alteration is due to the PL-6 possessing a larger footprint. This laser measures 88" long, 11" tall, and 18" wide. The width causes the laser to extend beyond the confines of the table. To fit the PL-6, the lower level of the table was expanded by 5". G10 laminate reinforce the table bottom to support the 220 lbs. laser, and Lexan paneling surrounds the expansion to seal the table for dry air. The second issue is that the PL-6 does not have an accessible zeroth output port. In order to retain the capability of constant power monitoring, the power meter was redesigned. A ZnSe mirror is placed in the beam path at 10° incidence. The ZnSe is coated for 99+% reflection; however, the maximum reflection is achieved at 45° incidence. By varying the incident angle, the amount of power transmitted through the window can be altered. At 10° incidence, the transmission is ~0.01 %. This equates to about 10 mW available for power monitoring. A Scientech Model 365, absolute power meter is mounted behind the window, and its recorder output delivers a DC voltage from 0-10 V proportional to the selected scale. Absolute power meters are more susceptible to environmental interference, especially when measuring relatively low power levels. Since the power meter is contained within the table enclosure, it will be stable, once the laser systems reach thermal equilibrium. The Scientech power meter can be replaced with a pyroelectric detector and chopper if power measurements are not sufficiently reliable after installation at PPPL. The final alteration is due to the PL-6 output being in a different location than the original CO₂ laser. The mirrors are relocated to accommodate the new beam path. The new power meter facilitates the new beam path with the ZnSe mirror incorporated into the system.



Figures 134a and 134b. Left: Laser table extension for the PL-6 laser. Right: Inside table view for the High- k_θ Scattering CO₂ laser. The FIReTIP style CO₂ laser is installed; however, the extra width for the PL-6 is shown.



Figure 135. PL-6 power monitor. The red lines show the CO₂ beam path. The white arrow marks the power meter directly behind the ZnSe mirror. Note: This set up photograph was taken during laboratory testing. The laser table uses a similar arrangement, except the beam is directed vertically.

The CO₂ beam is directed to the mid level of the table, to be focused into the High-k₀ Scattering FIR laser. Copper mirrors are used, except for one ZeNe mirror, for high power thresholds for the ~180 W beam. Each mirror mount has multiple axes of adjustment to align the CO₂ beam with the FIR laser waveguide axis. The FIR laser input window has a 4 mm aperture to admit the CO₂ beam. The PL-6 emits a TEM₀₀ beam nominally 11 mm in diameter. A ZnSe lens focuses the beam to pass through the FIR input window and then fill the FIR laser cavity. The best performing lens choice was observed to be when the beam waist is located near the input access aperture, and then expands to the waveguide diameter at the position of the output coupler [10]. The nearest available lens for this application was 75 cm focal length. The 75 cm focal length lens is mounted in the CO₂ beam path 71 cm before the input window. This is due to a separation distance between the FIR input window and rear mirror. The mirror also has a 4 mm hole to pass the CO₂ beam. The mirror and window are spaced by 8 cm, so the beam waist should be placed between these components. The ZnSe lens happens to be mounted in the vertical CO₂ beam path, between the lower and mid levels.

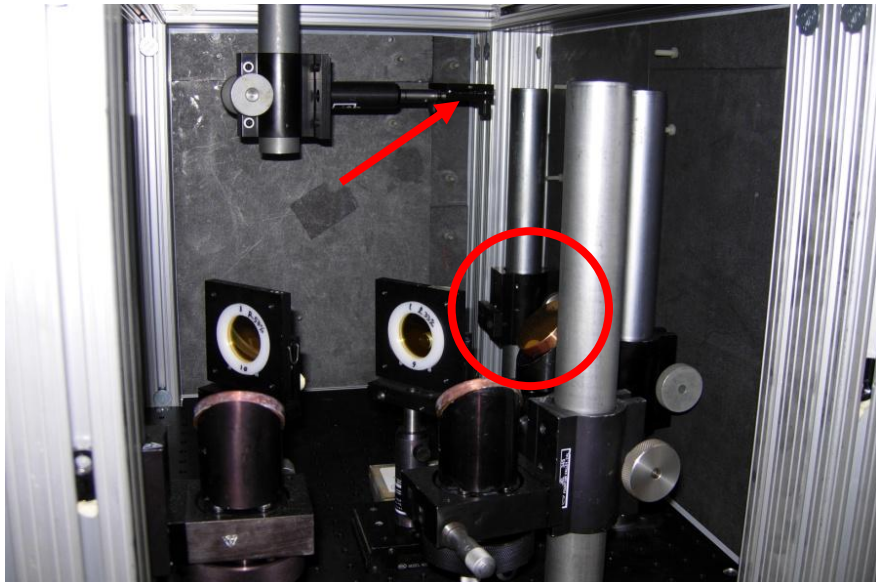


Figure136. Laser table lower level CO₂ laser beam area. The PL-6 vertical copper mirror is circled in the back ground. This area is enclosed with graphite panels for safety. The arrow shows the ZnSn lens.

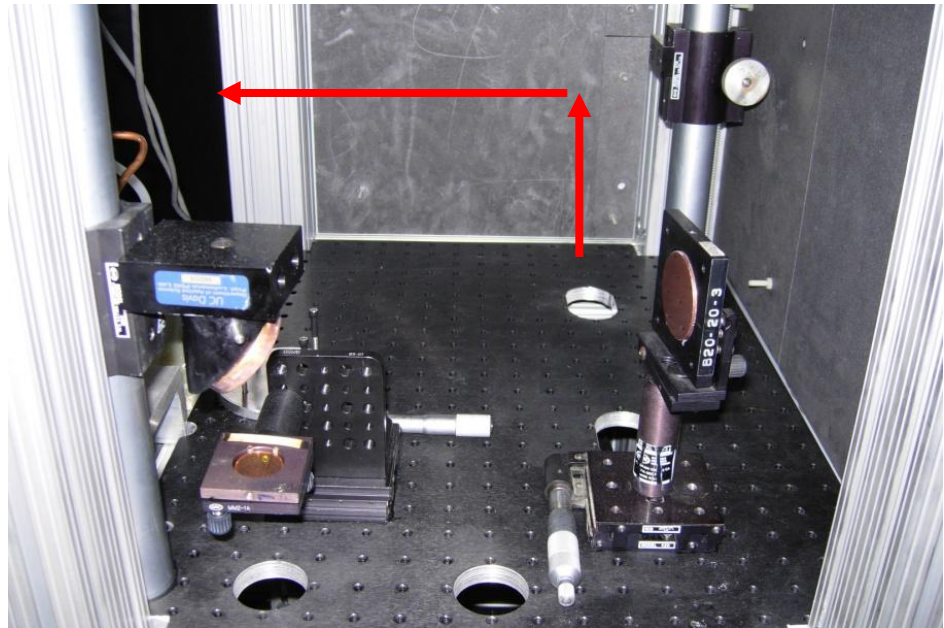


Figure 137. Laser table mid level. The PL-6 beam travels up through the bread board access, and then reflects off a copper mirror (not installed) to the FIR laser input.

IV.1.2 Formic Acid FIR laser

The High- k_0 Scattering probe beam is supplied by an optically pumped formic acid FIR laser. The laser is constructed from several components. There are two end boxes. Each box is an aluminum rectangular cavity measuring 10 x 10 inches, and 8 inches tall. The top of each box is open; however, they are sealed with a slab of plate glass and buna-n seal. The end boxes are secured to the laser table with a 62 inch long waveguide between them, although any reasonable wavelength can be installed. A second concentric tube surrounds the waveguide to serve as a water jacket. The inner waveguide is a 1.5" I.D. borosilicate tube. The outer water tube is a 2.375" I.D. Plexiglass tube, which is connected to the PL-6 chiller in parallel. This laser was originally built as a twin FIR laser [11], with two sets of waveguides connecting the end boxes for parallel laser cavities; however, only one beam is needed for the High- k_0 Scattering System, so one of the waveguides is removed and sealed with HDPE plugs.

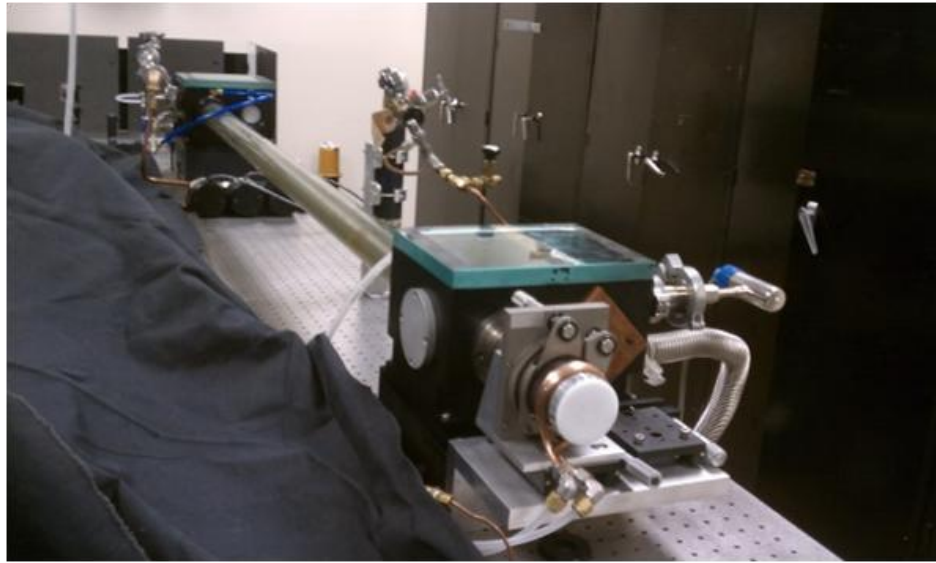


Figure 138. High- k_0 Scattering FIR laser. This laser is an optically pumped formic acid laser tuned to 432 μm output.

One end box houses the CO_2 input window, and rear laser mirror. The input window is ZnSe coated for anti-reflection at 9.27 μm . The window is mounted to a thick copper plate fixed to the end box exterior, with cooling coils soldered around the window location. The window provides a vacuum seal for a 4 mm diameter hole, which admits the CO_2 beam to the laser cavity at the central axis. Inside the end box, the rear mirror is mounted to a remote controlled two-axis mount. Control wires pass through a vacuum sealed fitting to a control box. The mirror is contained in the laser vacuum; therefore, there is never a pressure differential which could cause a misalignment. The mirror mount axis motors are simple DC motorized micrometers. The micrometer translation rate depends on the applied voltage of -9 to +9 VDC. While they are simple to manipulate, repeatability is poor, which can make mirror alignments tedious. However, once the mirror position is set, no further adjustments are necessary. The rear mirror is a 2" diameter flat copper mirror with a 4 mm hole at its center to admit an on-axis CO_2 pump beam. The mirror is backed by a thick copper disk, with a similar central hole, to act as a heat sink. The heat sink has copper cooling tubes soldered to it, which are passed through the end box to connect into the cooling system. The opposite end box mounts a hybrid output coupler. The coupler is designed to reflect 100% of

the CO₂ laser power, while acting as a partial reflector for FIR wavelengths. The output coupler two axis alignment is facilitated by a pair of micrometers; however, the cavity length adjustment utilizes a remotely controlled stepper motor. The motor turns a micrometer to position a linear track which mounts the output coupler assembly. A bellows allows for track movement, as well as alignments. A copper coil wraps around the output coupler housing to connect into the cooling system.

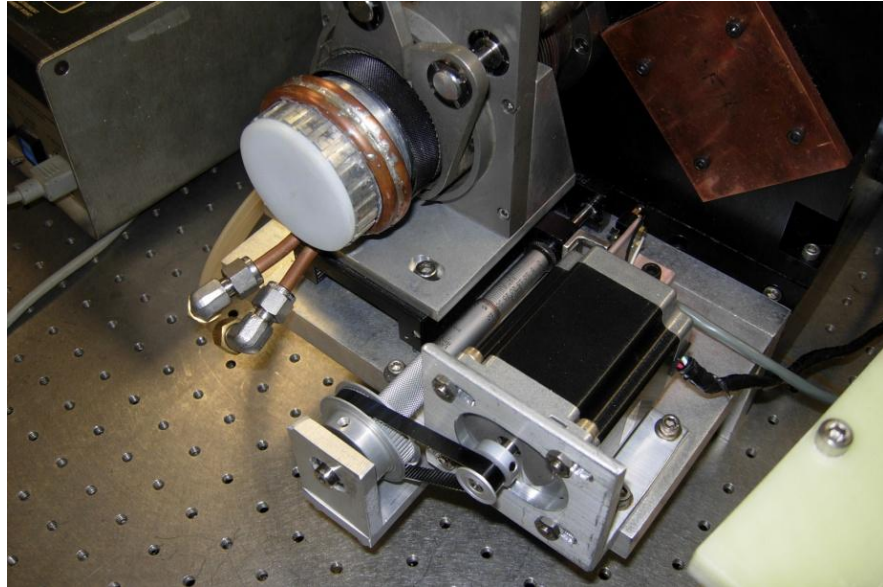


Figure 139. FIR laser output coupler. The white HDPE window forms a vacuum seal, and provides lensing effects for the FIR beam. The stepper motor controls the cavity length via a belt driven micrometer with 0.5 μm resolution.

Formic acid gas was chosen as a lasing medium for operation at 693 GHz. Optically pumped FIR gas lasers have been in use for more than 40 years [12, 13]. There are several output wavelengths that can be excited by CO₂ lasers. There are numerous laser lines for formic acid; however, the four most common wavelengths, and their respective CO₂ spectral lines are listed in Table 5 [3]. A free flowing gas system is employed; therefore, a vacuum pump is used to evacuate the laser, and then to flow formic acid gas at low pressure. Gas pressure in the range of 150 to 200 mTorr works well for this laser[14]. Gas pressure is

measured with a convection gauge. These gauges depend on thermal conduction of the gas measured, and therefore depend on the type of gas measured. The convection gauges employed are calibrated for nitrogen.

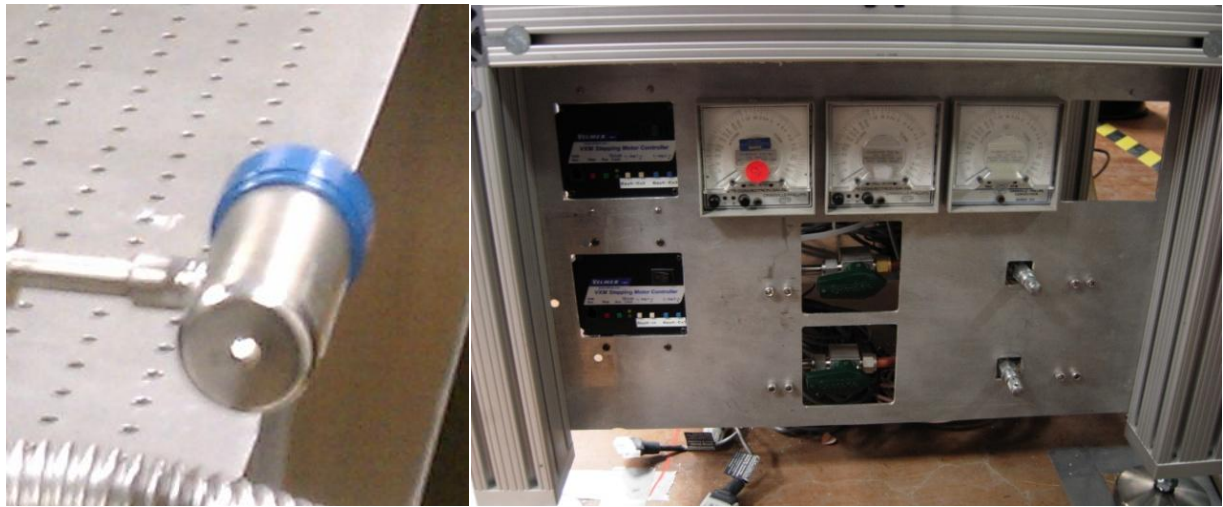
Correction factors are published for many types of gas; however, all pressures cited in this dissertation are uncorrected values. Dry scroll vacuum pumps can achieve ~50 mTorr [15]; however, this is insufficient for the low operating pressures of FIR lasers. A dual stage mechanical oil pump with an ultimate vacuum of 0.1 mTorr is used. Formic acid fumes can be problematic. Formic acid can react with the vacuum pump oil, which shortens the life of hydrocarbon based oils. Synthetic oils, such as Fomblin, are recommended for extended oil life; however, these oils are considerably more expensive [16]. Formic acid vapor will be expelled from the pump exhaust. Typical gas flow is ~0.8 l/hr. To prevent formic acid fumes from accumulating, a blower and vent line are installed at PPPL to exhaust any hazardous fumes outside. The oil vacuum pump is located beneath the laser table; therefore, the vacuum lines have a vertical height of ~44 inches from pump to FIR laser. This extra height to the FIR laser helps prevent oil back streaming into the laser cavity. A foreline trap is also installed on the vacuum pump inlet for the same reason. This FIR laser can require a long time to evacuate from atmospheric pressure (~4 hours); therefore, when not in use the laser should be under vacuum. Continuous use of the oil vacuum pump is undesirable due to the eventual contamination of oil in the laser; therefore, a dry scroll pump is used to maintain vacuum when the laser is not in use. A dry scroll pump will typically maintain ~50 mTorr; however, before activating the laser, the vacuum should be < 5 mTorr before adding formic acid gas.

Switching from the dry scroll pump to oil pump will typically reduce the vacuum to ~2 mTorr in about 45 minutes. At ambient room temperature, formic acid is a liquid. For the High- k_0 Scattering System, liquid laboratory grade (> 99% by weight, 26.5 mol/l) formic acid is stored in a 100 ml Pyrex flask. The flask is connected to the laser through an isolation valve and needle valve. Low pressure in the laser cavity will evaporate the liquid, and the needle valve will regulate the flow to set the desired pressure. It is recommended that high concentration formic acid be stored at low temperature (~ 4 °C). Formic acid will naturally decompose into carbon dioxide and water until it reaches about 88% (23.6 mol/l). At 88%, FIR output power is reduced by 50%; therefore, it is important to keep the formic acid fresh. Storage at cold

temperatures increases the shelf life. Unrefrigerated, the acid will lose its potency in 2 to 4 weeks, depending on the conditions, while refrigerated formic acid can be stored for 6+ months. The typical acid consumption is 10 ml/8 hr. Based on these observations, the laser reservoir is filled with 50 ml for 1 week of operation. The Pyrex reservoir is connected to the laser by stainless steel tubing; however, the glass to metal connection is a short length of Tygon tubing. Tygon material is resistant to formic acid, but over time gas vapors will react with the tubing, and condense and drip back into the reservoir. This condensation turns the colorless acid to a light amber. The reservoir will slowly turn color to amber over about two weeks; therefore, the color of the reservoir can be used to estimate the age of the formic acid. When the acid becomes noticeably colored, it is time to replace it.

Table 5. Formic Acid Laser Emission

Formic Acid λ (μm)	Formic Acid ν (GHz)	CO ₂ Laser Spectral Line
393.9	761.61	9R18
432.9	692.95	9R20
419.0	716.0	9R22
513.7	584.0	9R28



Figures 140a and 140b. Left: Convectron gauge sensor. It is recommended to mount the convectron body horizontal to avoid gravity induced errors. Right: Laser table control panel. Three convectron gauge monitors are located at the top center. Left to right, they are assigned to the Stark laser, FIReTIP FIR #1, FIReTIP FIR #2, and the empty hole is for the High-k FIR laser. On the left side are two stepper motor controllers, and the bottom shows the CO₂ gas control valves.



Figure 141. Four vacuum pumps are located underneath the laser table. The round pumps are dry scroll pumps, and the rectangular pumps are dual stage mechanical oil vacuum pumps.

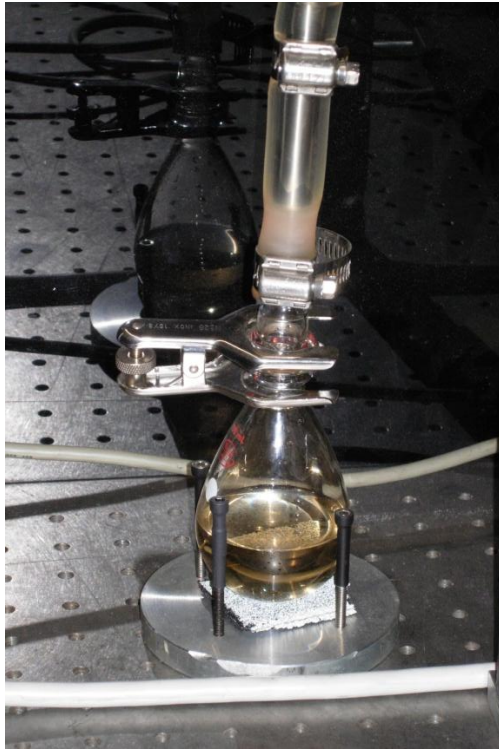


Figure 142. Formic acid reservoir. New formic acid is colorless. In this photograph, the acid is a medium amber hue, indicating it is due for replacement.

The hybrid output coupler was designed specifically for the High- k_0 Scattering System as a mesh backed hybrid coupler [17]. The main body is made from 6061 aluminum, and threads into the laser output bellows. Castle teeth on the outer surface facilitate installation and removal via a custom made spanner wrench. Copper cooling tubes wrap around the outer surface, which tie into the laser water circulation system. There are three elements inside the output coupler body. Inner most to the laser cavity is a high impedance silicon wafer. It is 50.8 mm diameter and 1.52 mm thick. This material has low absorption for FIR wavelengths, and provides a substrate for a reflective coating at 9.27 μm . The silicon wafer is coated with thin layers of germanium and zinc sulfide for a high/low index pair. Thin layers are applied by vapor deposition for maximum reflection between 9 and 10 μm . Experimental results showed that near 100% of the CO_2 beam is reflected with no detectable power transmission. FIR wavelengths can pass through the

wafer with low attenuation. At 432 μm , power transmission was measured at 98%. The next element in the output coupler is a selectable metallic mesh. A metallic mesh is attached to a thin aluminum ring, and retained by a threaded ring. Several mesh densities were tested for transmission and reflection at 432 μm . Several theories predict how a rectangular mesh will transmit or reflect wavelengths of similar dimension to the mesh spacing [18, 19, 20]. Applying these theories for mesh selection offers a range of suitable meshes; however, only particular meshes are commercially available. The High- k_0 Scattering FIR laser was tested with 250, 300, 333, and 500 lpi meshes, detailed in Table 6. The highest FIR power output was achieved with a 300 lpi mesh, which has 80% reflection and 20% transmission. It is also possible to electroplate a metallic mesh directly to the silicon waver [21]. This has an advantage of avoiding the very delicate meshes, and a custom mesh size can be used to maximize performance. However, this technique is expensive, and does not lend itself well to economic experimentation and is beyond the scope of this project. The final element of the output coupler is a 5 mm thick HDPE vacuum seal. HDPE has low absorption ($\sim -0.5 \text{ db/cm}$ [22], depending on the water content) and an index of 1.52 at 432 μm . This element has a concave spherical lens cut into its outer surface to increase the beam expansion. This will facilitate coupling into waveguide as discussed below.

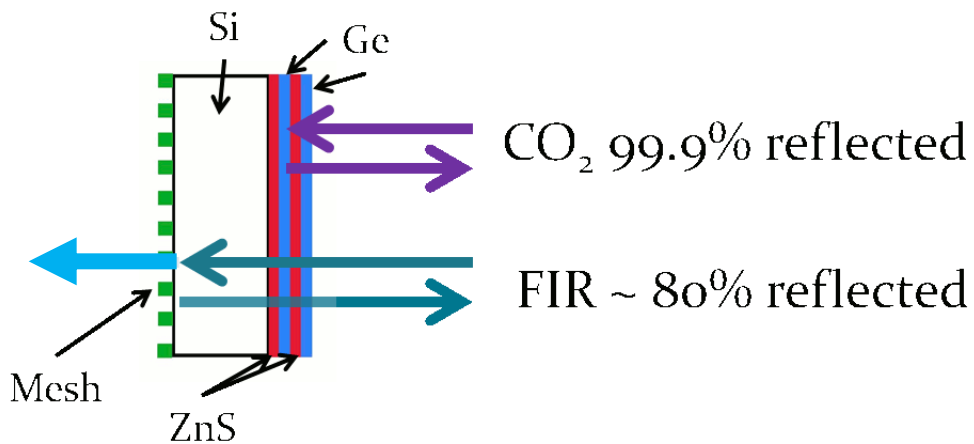


Figure 143. Schematic of hybrid output coupler. A silicon substrate is coated with thin layers of germanium and zinc sulfide to reflect CO₂ laser power. FIR wavelengths pass through the silicon, and then partially reflect off a metallic mesh.

Table 6. Metallic Mesh Properties at 693 GHz and FIR Power with 100 W Pump

Mesh lpi	Reflection	Transmission	FIR Power mW
250	0.83	0.17	16
300	0.90	0.10	42
333	0.92	0.08	30
500	0.98	0.02	8

FIR output of 50 mW at 432 μ m was measured with a Scientech 365 power meter. This power meter is designed for IR and visible wavelengths. At FIR wavelengths, reflections from the power head will reduce the measured power. At 432 μ m, power measurements can be reduced by ~50% [23]. Disregarding reflections, the Scientech power meter is an absolute measurement. The power head has banana socket connectors to a heater element inside. Electrical power can be applied directly while monitoring voltage and current; while comparing the delivered power to the meter reading, this power meter can be calibrated. Two Scientech meters were used in testing, and one was found to be < 1% error in calibration, and the other measured 15% low. This 15% discrepancy was added to power readings so that power measurements between these meters can be equated; however, corrections for reflections are not included. The Scientech meters employed are coated with RF absorbing paint to mitigate reflections; however, the effectiveness at 432 μ m is unknown.



Figure 144. FIR hybrid output coupler. From left to right: retaining ring, dielectric coated silicon wafer, body with cooling tubes, metallic mesh, o-ring, HDPE window, retaining ring.

The FIR beam output profile was measured by a two axis translatable pyroelectric detector. Two motorized translation stages are arranged horizontally, and vertically. LabView software controls stepper motors to position each stage location. Mounted to the two axis stage is a pyroelectric detector with a 2 mm square sensor. The FIR beam is interrupted with a 1000 RPM, 3 blade, 50% chopper. The pyroelectric detector is sensitive to small changes in temperature; therefore, the output signal is a square wave, where the amplitude is proportional to beam intensity. The LabView program will sample the peak to peak pyroelectric detector output between horizontal or vertical movements.

Several FIR modes are possible. Translating the output coupler to vary the cavity length, may alter the output mode for any given local power maximum. Each mode will have a different maximum power associated with it, so they can be discerned without measuring the beam profile. Generally, TEM_{00} will be the most powerful mode when properly tuned. It is possible for the output coupler to shift slightly out of alignment when altering the cavity length. A misaligned output coupler (or rear mirror) can prevent the

TEM₀₀ mode being possible. Anytime the output coupler is traversed through multiple wavelengths, the output couple alignment should be tuned for maximum power output. The FIR beam far field was measured at several distances. The beam profile was measured horizontally and vertically through the central peak to measure the Gaussian beam radius. The beam radius versus distance data are fit to Gaussian propagation equations to measure the beam waist location and radius, and the divergence angle [24]. Raster scans can be used to develop a more detailed image of the beam profile; however, due to the increased demand on resources, a simple two axis scan is usually employed. The FIR beam is vertically, linearly polarized, which is verified by rotating a wire polarizer in the beam path while measuring the transmitted power.

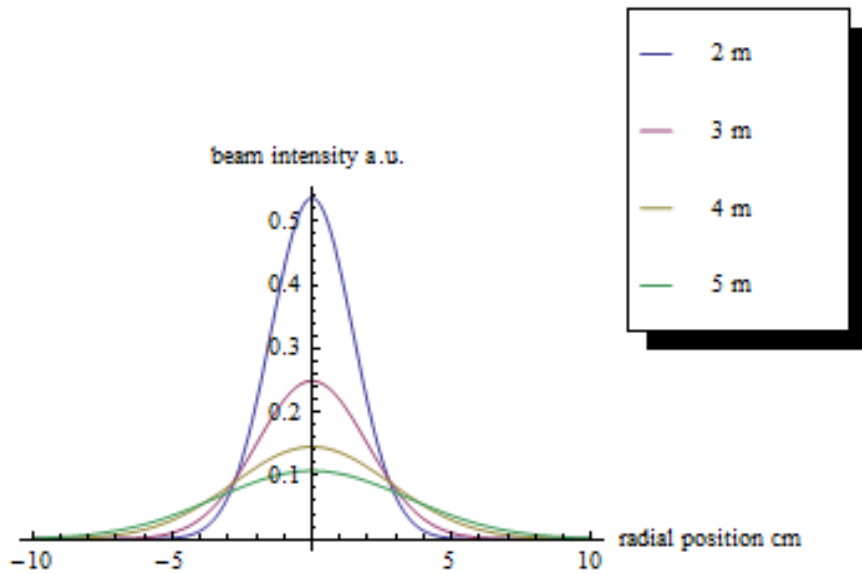


Figure 145. Far field beam profiles at 2 to 5 m. The beam intensity lessens as the beam expands; however, the total power is only slightly diminished due to atmospheric attenuation.

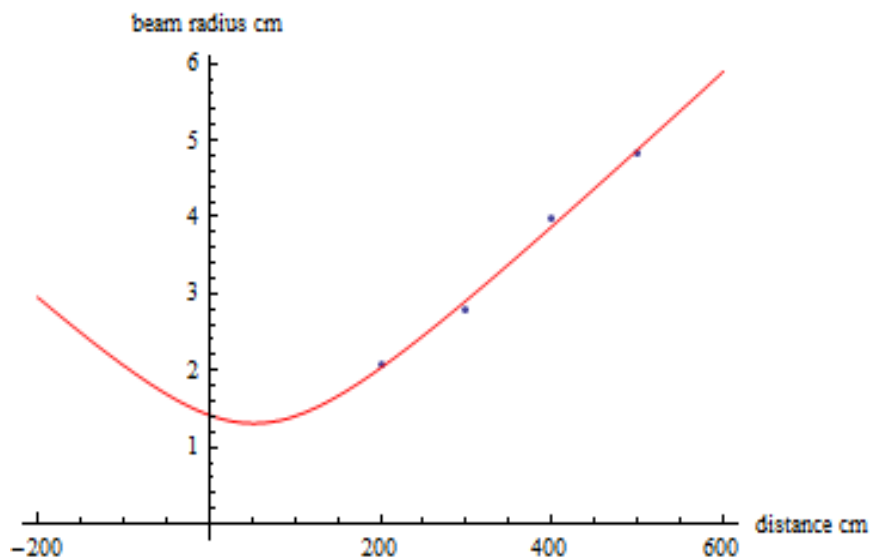


Figure 146. FIR beam size versus distance data are fit to Gaussian propagation equations. The Gaussian beam waist radius is determined to be 1.2 cm with a divergence of 0.5° .

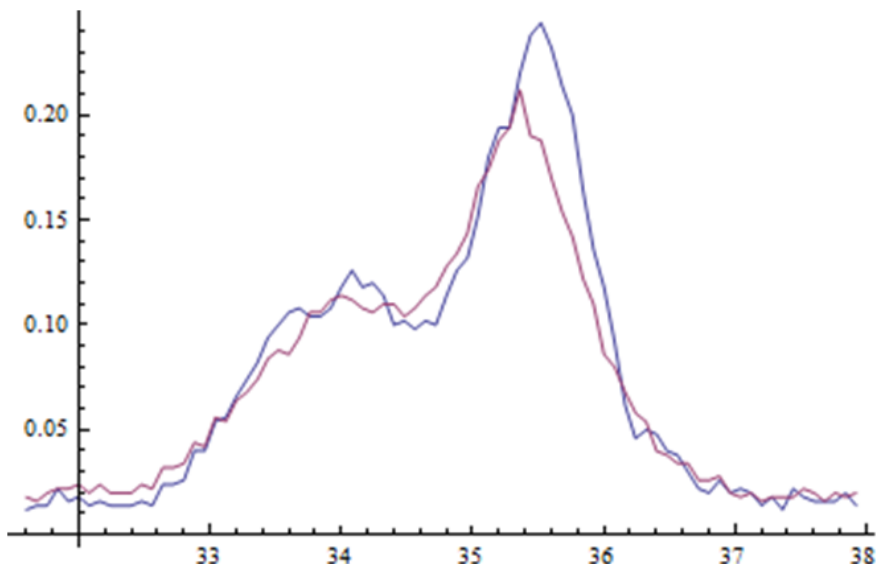


Figure 147. Two beam profiles raw data plots showing an example of poor FIR laser mode quality. Adjusting the cavity length and aligning the output coupler should correct this problem.

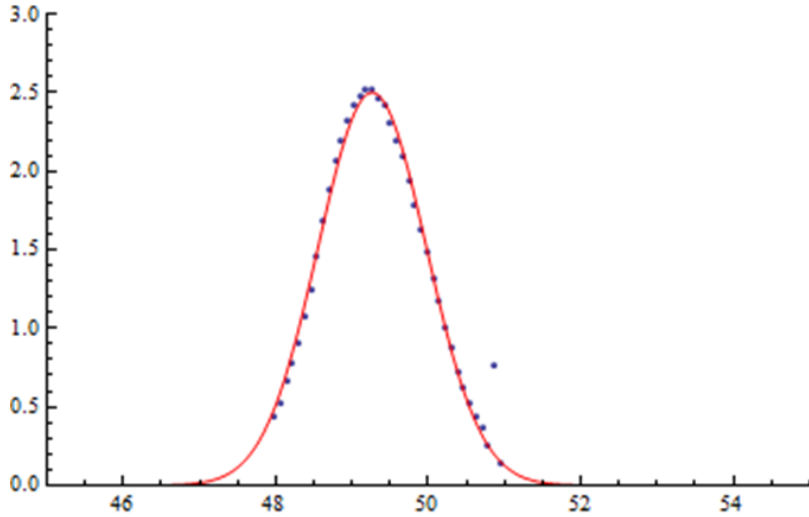


Figure 148. FIR beam profile raw data with Gaussian fit for a properly tuned laser.

IV.2 High- k_0 Scattering Corrugated Waveguide

The remote location of the laser system requires that waveguide be employed to deliver the FIR beam to NSTX-U. Corrugated, overmoded waveguide with a nominal inside diameter of 63 mm is run between the laser table, through the test cell wall, and terminates at the launching optics at Bay G. The waveguide is formed by securing many sections end to end. Each section is 254 mm long. A close fitting brass ring fits around the waveguide outer diameter to locate two sections concentrically. Two sections are secured together by fasteners tightened through flanges on either side of the ring. Miter bends allow the waveguide to be turned 90°. The miter bend body accepts two waveguide sections to be secured to it with their existing flanges. A first surface mirror is mounting inside the miter bend at 45°.

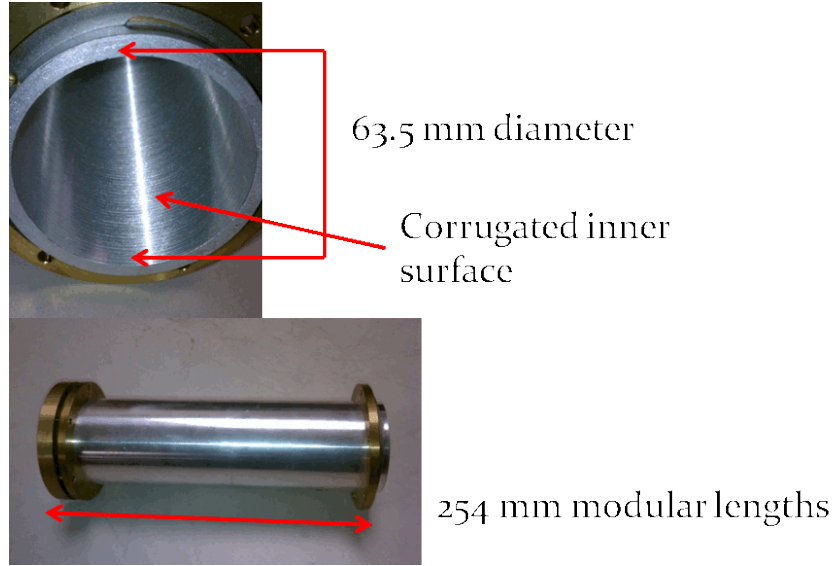


Figure 149. High- k_0 Scattering corrugated waveguide.

The FIR laser emits a Gaussian profile beam, which can couple to the HE₁₁ hybrid mode in the waveguide under the right conditions [25]. The Gaussian beam radius should be 60 - 64 % of the waveguide radius and collimated at the waveguide entrance. Too large a beam and the waveguide boundary can clip beam power, and too small a beam will couple to higher order modes. The FIR beam is emitted at 24 mm diameter, and needs to be expanded and collimated to 40 mm diameter in the space of ~1 m. To properly align the beam to the waveguide, two mirrors are installed on the laser table to control horizontal and vertical axes independently, and a third mirror is needed to steer the beam to the waveguide. A mesh beam splitter in the beam path reflects a small amount of power to a chopper and pyroelectric detector for real time power monitoring. Several meshes, from 30 to 500 lpi, are available to select the amount of power reflected/transmitted. Table 7 lists the mesh properties tested at 693 GHz. The beam path from laser output to waveguide entrance is 1 m. CodeV simulation software was used to design the waveguide coupling optics. Simple ray tracing was used to approximate the needed lens focal lengths and spacing. The lens system is then refined by including the laser output size and divergence, and using CodeV Gaussian analysis. The final design uses two HDPE lens spaced 990 mm apart. First, the laser output vacuum seal was machined for a -400 mm spherical radius to increase the beam divergence. The beam

then expands to 40 mm diameter at the waveguide entrance. A second HDPE lens with an 810 mm spherical radius was fabricated and mounted at the waveguide entrance to collimate the beam.

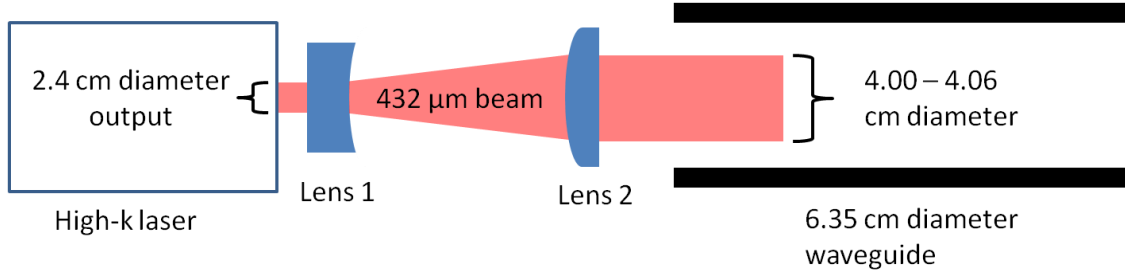


Figure 150. A two HDPE lens system is designed to expand, and then collimate the FIR beam to couple into the corrugated waveguide.

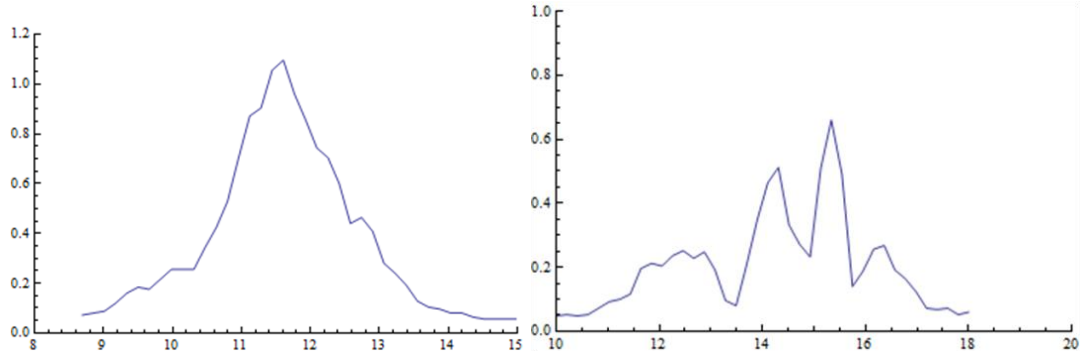
Table 7. Metallic Mesh Performance at 693 GHz

Mesh Ipi	Reflection	Transmission
30	0.05	0.95
45	0.09	0.91
50	0.10	0.90
60	0.20	0.80
100	0.26	0.74
120	0.19	0.81
125	0.30	0.70
200	0.76	0.24
250	0.96	0.04
280	0.85	0.15
333	0.98	0.02
400	0.96	0.04
500	0.97	0.03

Note: The various meshes cannot be compared directly based on the line density. The thickness of the mesh wire varies between samples. Table 7 is an inventory of the meshes on hand at UC Davis.

The High- k_θ Scattering waveguide is overmoded, corrugated, aluminum waveguide. The original High- k_r Scattering System used similar waveguide; however, it was designed for 280 GHz, with a pass band of 75 to 575 GHz [26]. Corrugated waveguide is known for broad bandwidth transmission; however, the new system is 2.5 times higher frequency, so the waveguide needed to be redesigned. The previous waveguide was machined smooth, and then new corrugations were machined into the inner surface.

The HE₁₁ hybrid mode is linearly polarized and similar to a Gaussian profile; therefore, TEM₀₀ can couple with low insertion loss. To propagate the HE₁₁ mode, the waveguide diameter must be much larger than the laser wavelength, and the corrugation depth is nominally $\lambda/4$ [27]. Bragg reflections from the corrugations will eliminate the electric field at the waveguide boundary, which also eliminates surface currents. In the absence of surface currents, the dominant mode should be HE₁₁ [28]. The majority of the waveguide losses are due to ohmic losses from surface currents; therefore, HE₁₁ can propagate with low loss. Imperfections in the corrugations, and misaligned waveguides can lead to mode conversion and increased losses.



Figures 151a and 151b. Left: Waveguide output beam profile when properly coupled and aligned. Right: The same beam purposely misaligned couples to higher order modes and significantly increased attenuation.

The waveguide corrugation parameters were determined by solving the following equation for minimum losses at the frequency of interest [29]:

$$\alpha = \frac{R_s \chi_m^2}{2Z_0 k^2 a^3} \left(\frac{1 - \frac{t}{p} \sin^2(kd) + \frac{d}{p} + \frac{1}{kp} \sin(kd) \cos(kd)}{(1 - t/p)^2 \sin^2(kd)} + 1 \right)$$

where α is the attenuation constant, R_s is surface resistivity, Z_0 is the impedance of free space, χ_m is proportional to the mode index impedance at the waveguide surface, k is the propagation wavenumber, a is the waveguide radius, t is the corrugation vane thickness, p is the corrugation period, and d is the corrugation depth.

Additional considerations are made when calculating the preferred corrugations. Ideally, the corrugations should be a series of concentric rings; however, due to the large waveguide diameter, a helical cut corrugation was permissible. The resulting pitch angle was slight enough that no beam rotation is observed [29]. To successfully machine corrugations on the order of $\lambda/4$ at 432 μm , the aspect ratio of cutting depth to groove width should not exceed 1:1, and the resulting vane thickness should have a thickness at least equal to the corrugation depth to avoid becoming too fragile.

This equation assumes that $ka \gg 1$, the corrugations are rectangular, and that solutions are only valid near the central frequency, ~ 1 octave. In this example, $ka \sim 460$. The solutions are found graphically by programming Mathematica software with the equation and variables, and plotting the result of attenuation versus frequency. The attenuation and bandpass are observed and optimized. In addition to computer simulations, the feasibility of fabricating the waveguide must be considered. Small corrugations are difficult to machine due to the frailty of equally small tooling. A compromise between low attenuation and machinability was determined to be:

Table 8. Corrugation Dimensions

Dimension	Value
Waveguide radius "a"	31.5 mm
Corrugation Depth "d"	127 μm
Corrugation width "w"	188 μm
Corrugation period "p"	300 μm

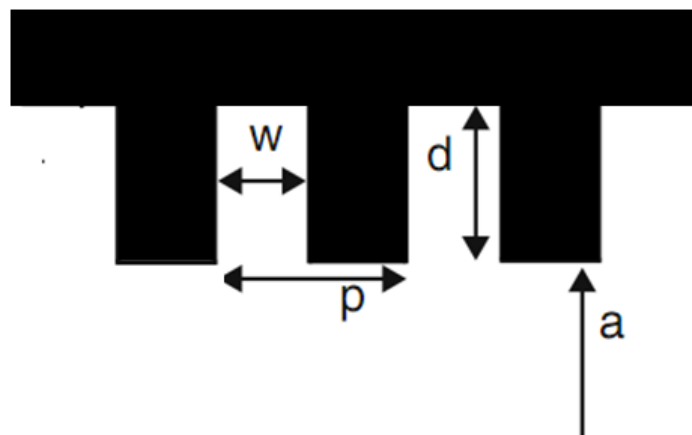


Figure 152. Corrugation dimensions: $a = 31.5 \text{ mm}$, $d = 127 \mu\text{m}$, $w = 188 \mu\text{m}$, and $p = 300 \mu\text{m}$.

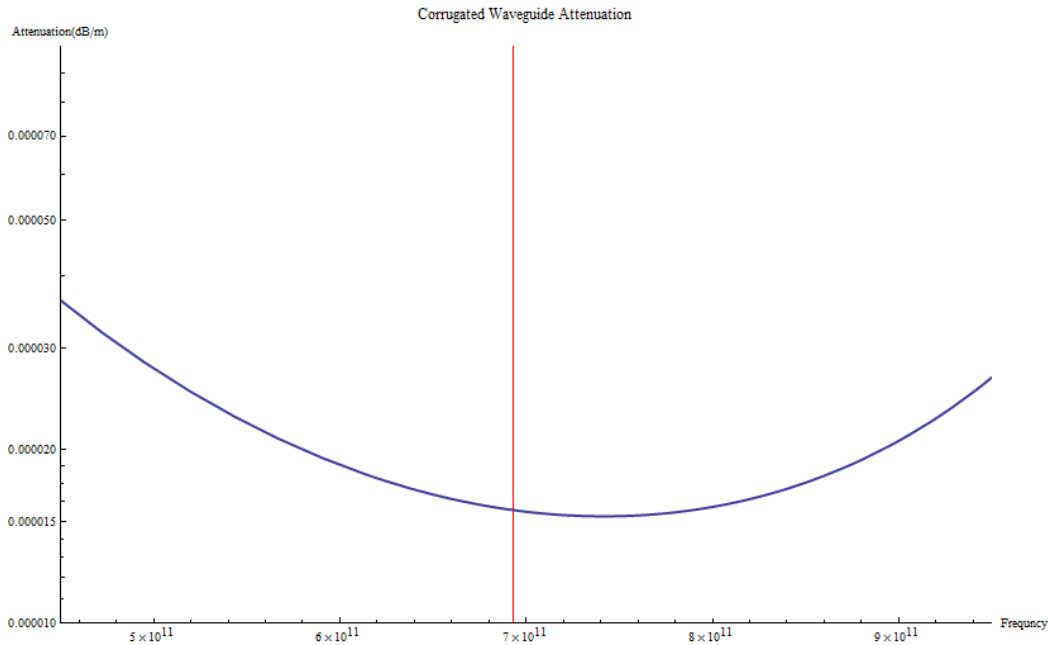
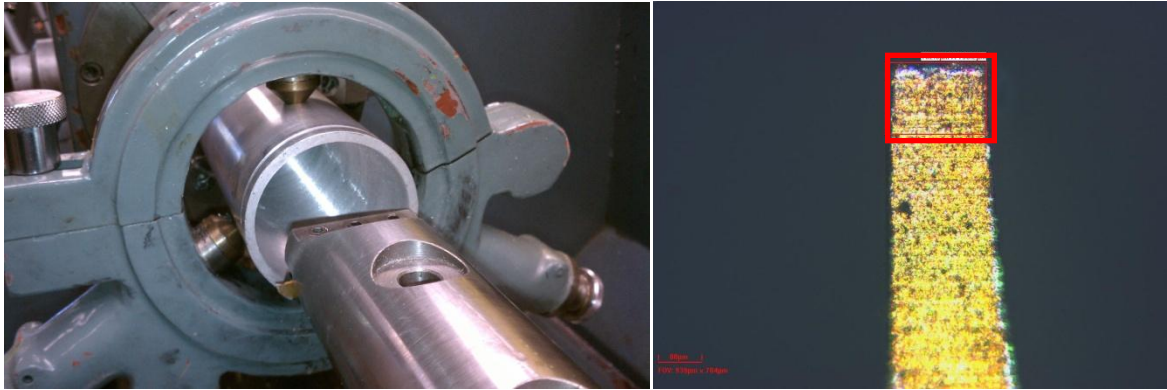


Figure 153. Calculation of corrugated waveguide attenuation (dB/m) versus frequency. The red line marks 693 GHz. The analytical result shows attenuation on the order of -2×10^{-5} dB/m. Actual attenuation will be higher.

Several test samples were machined at UC Davis to verify that HE_{11} mode is supported. Waveguide samples are also needed to measure the FIR beam characteristics on exiting the waveguide, and to test the launching and receiving optics. After the sample performance was verified, the remainder of the waveguide machining was outsourced to local machine shops.



Figures 154a and 154b. Left: Machining process to cut corrugations into the waveguide. Right: Microscope view of the cutting tool. A tungsten carbide tool was ground to 183 μm width and 130 μm microns deep. The red box highlights the cutting portion of the tool.

The measured performance was found to be acceptable with a measured attenuation of -0.1 dB/m. The FIR laser was passed through the input coupling optics, and then through a straight section of up to seven waveguide sections, for a length of 1.78 meters. The output mode was measured with the pyroelectric detector, two axis, beam scanner. Relative power measurements are made by fitting the measured beam to a Gaussian profile and integrating across the curve. Attenuation can be estimated by measuring the transmitted power through different length waveguide runs. The FIR beam power is also measured for the same distances without the waveguide to estimate the attenuation in air. 693 GHz propagates well through ambient air with attenuation of ~ -50 dB/km [30]; however, due to the length of the waveguide run, dry air or nitrogen is recommended to minimize any losses. The waveguide entrance is sealed by the HDPE coupling lens. The waveguide exit has a thin, planar HDPE window. If necessary, the waveguide exit window can be replaced by a lens to alter the launch optics focal length. The laser table already features a dry air environment due to the FIReTIP system. The High- k_0 Scattering System launching and receiver optics are a sufficiently short path length that a low water environment is not warranted. The input coupling optics did permit the HE₁₁ hybrid mode; however, the alignment is sensitive. If the waveguide sections are misaligned, or if the beam is not centered, mode conversion can occur. Higher order modes

will attenuate considerably faster. Additionally, if the beam exits the waveguide in a mode other than Gaussian, it will not focus properly for the launch optics design. The High- k_0 Scattering waveguide is very robust, and self aligns very well. With the flange fasteners secure, the waveguide ends are square to the central axis, and will butt together with less than 0.1 degree deviation. Fine tuning the waveguide alignment is generally not necessary.

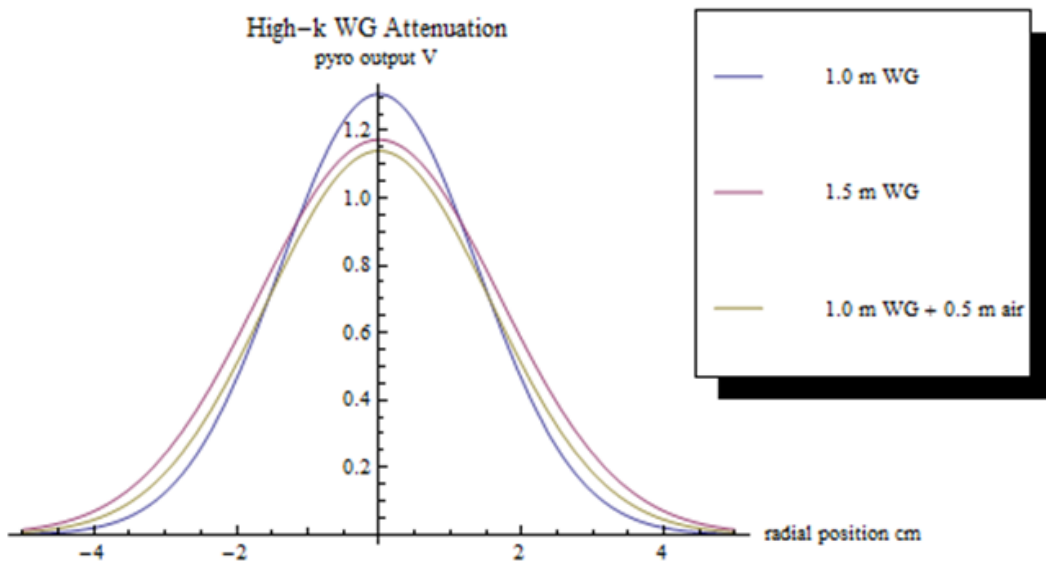
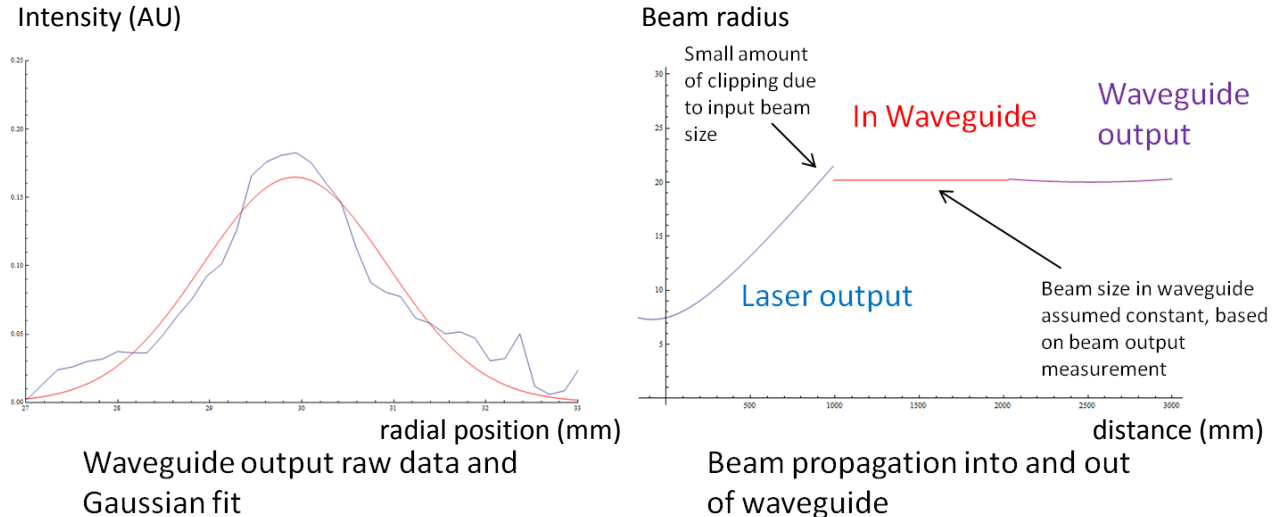


Figure 155. Attenuation measurements for the corrugated waveguide. The blue line is a Gaussian fit for the FIR beam after 1 m of waveguide to establish a baseline mode and power. The red and gold lines show Gaussian fits for an additional 0.5 m of propagation with more waveguide or free space, respectively. Attenuation in air was found to be -0.05 dB/m, and the waveguide accounted for \sim -0.1 dB/m.

The FIR beam output from a 30" section of corrugated waveguide was measured using the pyroelectric detector. A single peaked profile with near-Gaussian properties was observed. The Gaussian beam radius was measured to be 20.1 mm, and nearly colimated, which is 63% of the waveguide radius. The beam radius appeared to be constant for about 0.5 m, before noticeably diverging. This data is then used to

calculate the optimum launching optics to shape the beam, and place the final beam waist at the center of the scattering region in the vacuum vessel.



Figures 156a and 156b. Left. Raw data from the waveguide output fit to a Gaussian profile. The Gaussian radius ($1/e^2$) is measured at 20.1 mm. Right: Beam radius as it progresses through the FIR delivery system. The blue line shows the beam radius emitted from the FIR laser. The -400 mm lens is placed at 0 mm along the abscissa. At \sim 1 m, the 810 mm lens collimates the beam as it is coupled into waveguide. The beam is slightly larger than the waveguide transmission diameter; therefore, a small portion of the beam power may be clipped. The red line shows the presumed beam radius in the waveguide based on the beam radius at output. The purple line is the waveguide output, showing a nearly collimated beam at 20.1 mm.

IV.3 High- k_0 Scattering Launching Optics

The High- k_0 693 GHz Gaussian probe beam is delivered to Bay G via corrugated waveguide. Before the beam passes through the launching window, it will traverse the launch optics assembly to steer and shape the beam. The probe beam then enters the vacuum vessel through a quartz window, and is directed towards Bay L. As the beam passes through the plasma, it will undergo collective Thomson scattering

[31, 32]. Scattering occurs across the length of the beam, in proportion to collective electron density fluctuations, and at a scattering angle dependent on the wavenumber of the fluctuations. To localize a specific scattering volume, the receiver optics are focused on a small portion of the probe beam. The intersection of probe beam and receiver optics view determines the measurement location within the plasma.

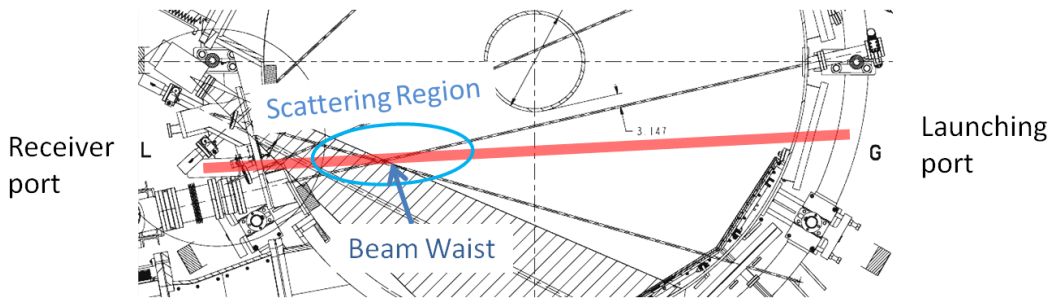


Figure 157. High- k_0 Scattering beam line. The FIR beam travels from Bay G to Bay L. The region circled in blue is the scattering region. The specific scattering volume can be placed anywhere within the scattering region for a localized measurement. Drawing courtesy of Princeton Plasma Physics Laboratory.

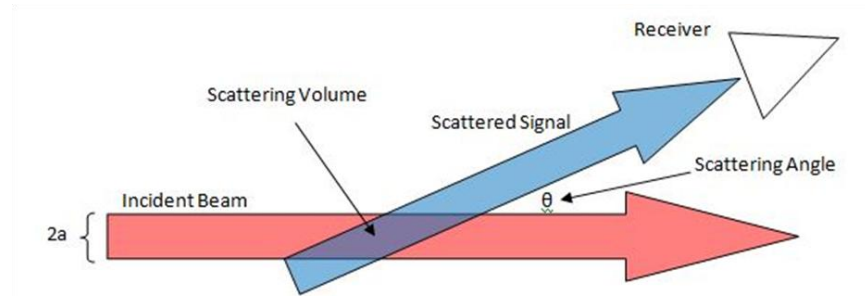


Figure 158. The scattering volume is defined by the intersection of the probe beam and the "view" from the receiver. The receiver optics focuses several channels to a single location along the probe beam.

The beam is remote control steerable up/down and right/left, and the receiver optics can be translated across 5 axes. Correlating the launch and receive systems can move the scattering volume in a variety of locations. The scattering volume can be specified from plasma core to edge. The probe beam can be aimed up/down and right/left. Since the launching mirror is centered at the launching window, but can be tilted in two axes, the possible coverage in the scattering region forms a truncated cone. The average cone diameter at the center of the scattering region is ~10 inches. The probe beam is focused at the center of the scattering region so that the beam is collimated throughout the region. Determining the beam radius at the scattering volume is a compromise between k resolution and spatial resolution.

$$\Delta k = \frac{2}{a}$$

where Δk is the wavenumber resolution, and "a" is the probe beam radius at the scattering volume [33]. The region of interest for scattering ranges from core to edge. This covers a distance of 460 mm, measuring from 290 to 740 mm from the receiver window at Bay L. This places the center of the scattering region 520 mm from the Bay L window and 3356 mm from the Bay G launch window. The launch optics are designed to focus the probe beam to place the beam waist at the center of the scattering region, with a Gaussian radius of ~17-18 mm. This will provide good localization, with a maximum k resolution of 1.16 cm^{-1} . At the extreme ends of the scattering region the probe beam remains reasonably collimated; therefore, the minimal divergence still provides good scattering properties, and it is possible to use a fixed focal length launch optics.

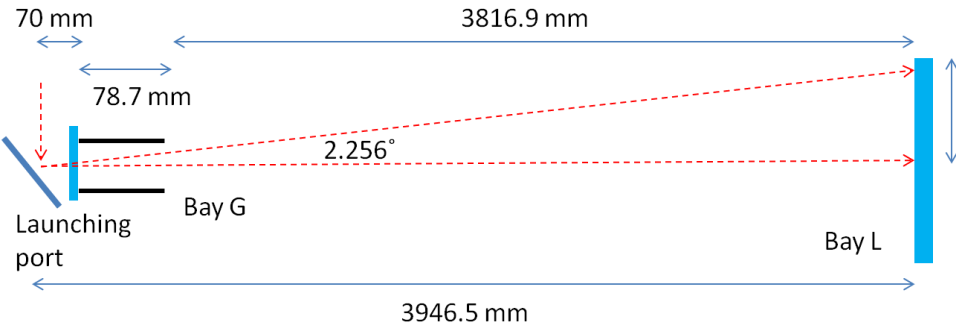


Figure 159. The FIR probe beam can be steered up/down and right/left by $\pm 2.25^\circ$. This permits a greater coverage of k spectra to construct a more complete image of ETG mode fluctuations.

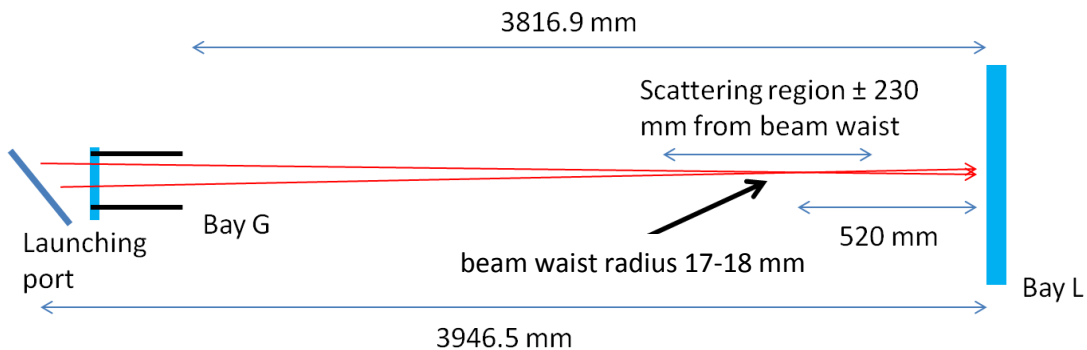


Figure 160. To center the probe beam waist in the scattering region, it should be located 520 mm from the Bay L receiving window.

The Bay G launch window is brazed to a ConFlat™ flange, and mounted to a short launch tube. The launch tube measures 78 mm long and 97 mm I.D. diameter. In order to place the beam waist at the center of the scattering region, the launch tube constraints must be considered when designing the launch optics. Since the Gaussian beam radius is defined as e^{-2} of the peak intensity [24, 34], the minimum aperture size to pass a Gaussian beam is substantially larger than the stated beam size. A rule of thumb is to allow an aperture radius 1.5 times the Gaussian beam radius to avoid clipping the beam and minimize diffraction effects. Smaller apertures can be used; however, the risk of compromising the beam quality increases with smaller dimensions. To best use the available space for steering, the launching mirror should be located as

close to the launch window as practical. A spacing of 70 mm from the center of the mirror to the window surface is chosen to provide sufficient steering angle without risking contact with the window. Setting the maximum allowable aperture to beam radius ratio to 1.3, with 2.25 degrees of steering, the maximum Gaussian beam radius is calculated to be 32.8 mm

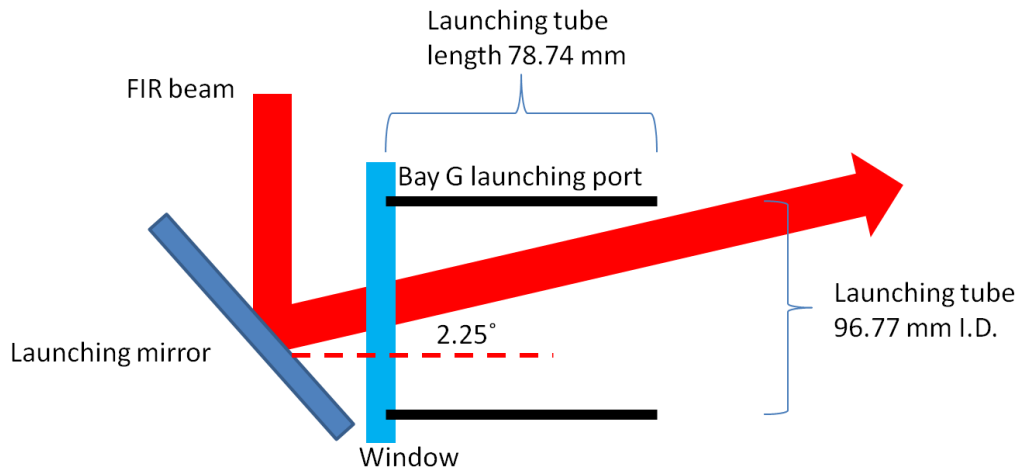


Figure 161. To avoid clipping the FIR beam on the launch tube, the maximum Gaussian radius at the launch mirror should be 32.8 mm. A beam of this size at 432 μm can be focused down to ~ 17 mm beam waist in ~ 3.5 m.

The FIR probe beam design is determined by solving Gaussian beam propagation equations for the constraints above [24]. There are three constraints: 1) maximum Gaussian beam radius at the launch port, 32.8 mm, 2) Gaussian beam waist radius, ~ 17 mm, and 3) the beam waist location should be 3356 mm from the launch window. A solution was found within the design constraints. The solution was then simulated in CodeV optical design software for Gaussian propagation to double-check the calculations. The beam radius at the launch window was determined to be 31.5 mm. The beam waist radius is 17.86 mm, and the beam waist location was within 4 mm of the target location. At the inner edge of the launch tube, the beam radius is 31.0 mm; therefore, the aperture to radius ratio is 1.56 when centered, and drops to 1.37 at the extreme steering angle of 2.25°.

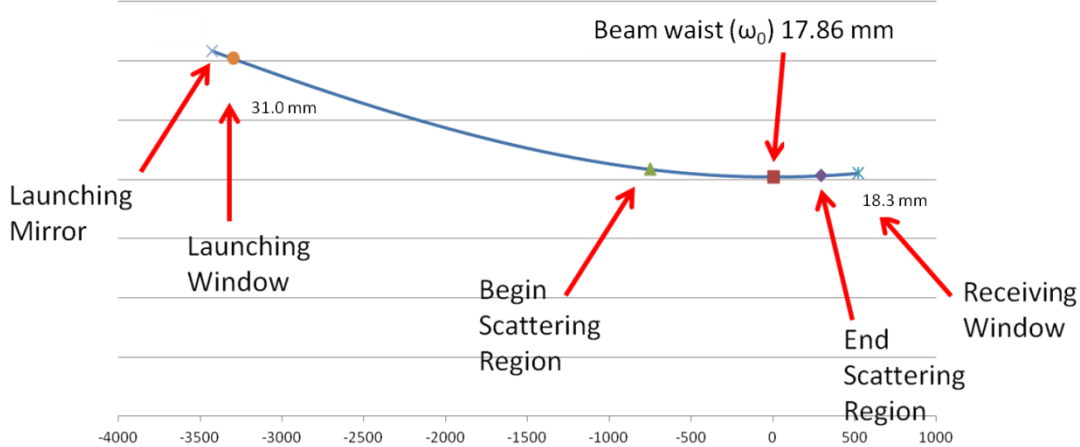


Figure 162. Plot of Gaussian beam propagation calculations. A beam waist of 17.86 mm is determined with a beam radius at the launch window of 31.0 mm.

```
WRX 20.1
WRY 20.1
DIS YES
XZ YES
GO
```

```
GAUSSIAN BEAM PROPAGATION
New lens from CVMACRO:cvnewlens.seq POSITION 1
WAVELENGTH =432000.0 NM DIMENSIONS = MILLIMETERS FIELD POSITION = ( 0.00, 0.00)
PROPAGATION BEAM RADIUS ORIENTATION WAVEFRONT RADIUS PHASE WAIST RADIUS
DISTANCE TO ON SURFACE (DEGREES) OF CURVATURE ORIENTATION BEFORE REFRACTION REFRACTION DISTANCE FROM
SUR NEXT SURFACE X Y X Y X Y X Y X Y X Y
OBJ 100.0000 20.1000 20.1000 0.0 INF INF 0.0 20.1000 20.1000 0.0000 0.0000
1 127.0000 20.1116 20.1116 0.0 -86421.0 -86421.0 0.0 20.1000 20.1000 100.0000 100.0000
2 10.0000 20.1599 20.1599 0.0 -38253.87 -38253.87 0.0 20.1000 20.1000 227.0000 227.0000
3 300.0000 20.3169 20.3169 0.0 -1293.927 -1293.927 0.0 5.5397 5.5397 1197.7285 1197.7285
4 -282.8427 38.9707 27.5564 0.0 -1133.267 -1133.267 0.0 5.5397 5.5397 1087.4680 1087.4680
5 -10.0000 34.4629 34.4629 0.0 1406.6566 1406.6566 0.0 5.5397 5.5397 -1370.311 -1370.311
6 -300.0000 34.6240 34.6240 0.0 2149.2424 2149.2424 0.0 5.5397 5.5397 -2094.225 -2094.225
7 110.3087 46.1971 32.6663 0.0 -5065.331 -5065.331 0.0 17.8555 17.8555 3551.9390 3551.9390
8 -69.9586 45.7592 31.9583 -8.9 5003.5282 5003.5282 0.0 17.8555 17.8555 -3441.63 -3441.63
9 -79.0000 31.5129 31.5129 0.0 -4965.977 -4965.977 0.0 17.8555 17.8555 3371.6717 3371.6717
10 -3066.0 31.0135 31.0135 0.0 -4925.229 -4925.229 0.0 17.8555 17.8555 3292.6717 3292.6717
11 -230.0000 17.9406 17.9406 0.0 -23941.48 -23941.48 0.0 17.8555 17.8555 226.6717 226.6717
12 -230.0000 17.8555 17.8555 0.0 1615071.3 1615071.3 0.0 17.8555 17.8555 -3.3283 -3.3283
13 -290.0000 17.9457 17.9457 0.0 23271.573 23271.573 0.0 17.8555 17.8555 -233.3283 -233.3283
IMG 18.3047 18.3047 0.0 10795.035 10795.035 0.0 17.8555 17.8555 -523.3283 -523.3283
```

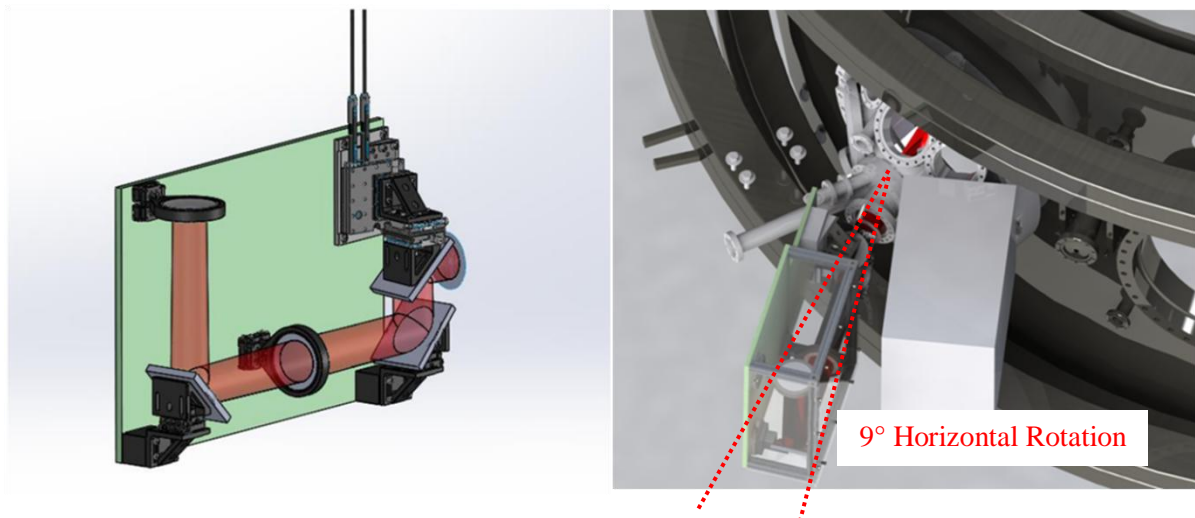
Figure 163. CodeV simulation results for a Gaussian beam propagation. Line 9 shows a beam radius of 31.5 mm at the launching window. Line 10 is the beam radius at the end of the launching tube at 31.0 mm. Line 12 describes the beam waist radius of 17.86 mm at 3.39 mm from the center of the scattering

region. Lines 11 and 13 mark the extreme ends of the scattering region, with a beam radius of 17.94 mm. The slight increase in size from the beam waist indicates the beam is reasonably collimated throughout the scattering region.

The launch optics are designed to match the defined probe beam parameters with a system of mirrors and lenses. Space around Bay G is limited, so it is important the launch optics be compact. The corrugated waveguide terminates at the top of the launch optics enclosure. The beam passes through a concave HDPE lens to expand the beam, and it travels slightly past the launch window vertical location. Then, a mirror turns the beam 90° towards Bay G. A second HDPE lens focuses the beam. A second mirror turns the beam upward. The final optic is the launching mirror to direct the beam through the launching window. A pair of motor controlled goniometer stages position the angle of the launching mirror in two axes for $\pm 2.25^\circ$ of steering. The available space around Bay G is not directly in line with the launch tube axis. The launch optics plane is rotated 9° in the horizontal plane about the launch window, and the angle is compensated by the launching mirror to direct the beam directly into the launching port. The optics spacing and lens curvatures are listed in Table 9. All mirrors are first surface planar mirrors.

Table 9. Launch Optics Components

Component	Distance (mm)	Radius (mm)
Waveguide Exit	-	-
HDPE Lens 1	227	-450
Mirror 1	310	∞
HDPE Lens 2	210	580
Mirror 2	300	∞
Launch Mirror	78	∞



Figures 164a and 164b. Left: CAD model of the optics layout. Right: CAD model illustrating how the launch optics will fit on Bay G. The optics plane is rotated 9° horizontally to the right. CAD model of NSTX-U courtesy of Princeton Plasma Physics Laboratory.

The launch optics components are mounted on manual translation stages for fine tuning, and a single sheet of G11 laminate forms a common base plate. An aluminum framework with Lexan paneling surrounds the first three components. This will protect the optics from dust and debris. The last two optics are exposed. This is due to the limited space at Bay G, and is not of great concern because attenuation at 693 GHz is relatively low [30]. However, after installation, a dust shield can be added above the mirrors for protection. The launching mirror utilizes a compound angle mount to add the 9° horizontal rotation. ThorLabs goniometers provide $\pm 10^\circ$ of steering in 2 axes, ample adjustment to calibrate the alignment, and provide the $\pm 2.25^\circ$ instrument function. "K-cube" servo motor controllers are mounted to the launch optic base board, and are connected to computer controls via USB cables.

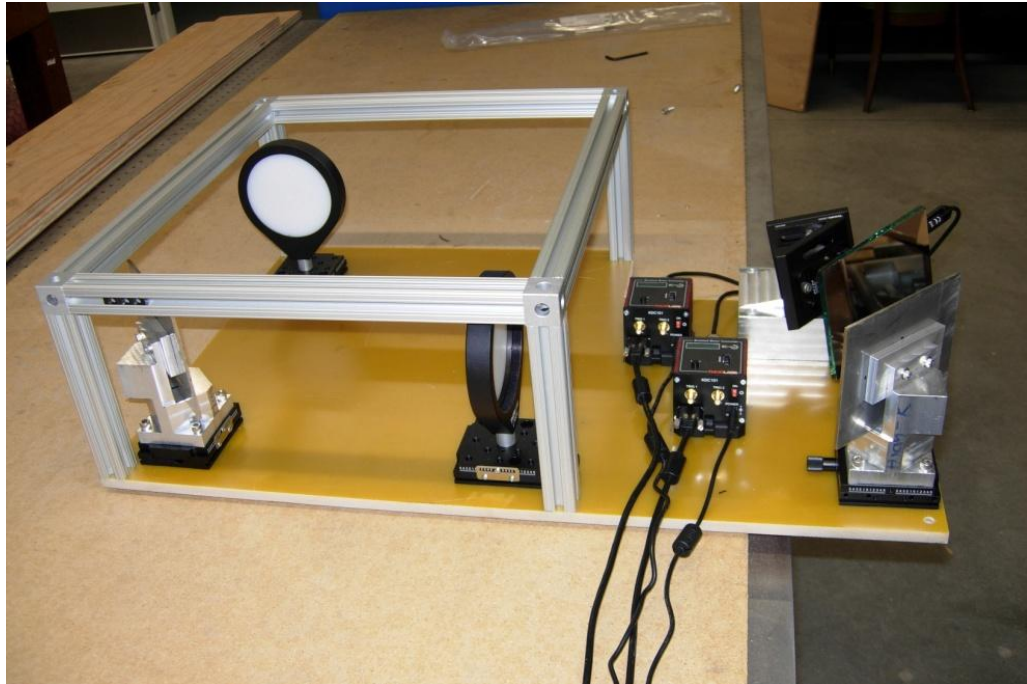


Figure 165. High- k_0 Scattering Launch Optics with Lexan paneling removed.

At 693 GHz, many common window materials are not suitable for transmission [35, 36]. Several materials were analyzed for the best performance for the High- k_0 Scattering System. The windows are nominally 100 mm diameter, and must be safe for vacuum applications. Window thickness of 0.934 cm was chosen to provide a sufficient vacuum safety factor, and minimize reflections to etalon effects. The materials analyzed were fused silica, crystal quartz, and Z-cut crystal quartz. The specifications for window materials varies between vendors, and the water content is critical for FIR transmission. Water molecules trapped in the glass matrix during manufacturing can greatly attenuate FIR signals. More specifically, attenuation is due to the presence of hydroxyl groups, and water content increases the concentration of hydroxide ions (OH^-) [37, 38]. Consequently, it is important to specify low hydroxyl content for FIR compatible windows, which are typically described as “IR grade”. Transmission for windows at normal incidence is:

$$T = \left(\frac{1 - A}{1 - R} \right)^2$$

where R is the reflection from each surface,

$$R = \left(\frac{n - 1}{n + 1} \right)^2$$

and A is the absorption of the material,

$$A = 1 - e^{-(\alpha t)}$$

with α being the absorption coefficient and t is the window thickness [5, 39, 40].

Fused silica provided a maximum transmission of 34%. Crystal quartz is substantially increased with 80% transmission. The best performing material is Z-cut crystal quartz at 95% transmission. Z-cut crystal quartz windows are commercially available, already brazed into standard ConFlat flanges. Z-cut quartz windows were selected for their performance and availability.

IV.4 High- k_0 Scattering Receiver Optics

The High- k_0 Scattering receiving optics are considerably more complicated than the launch optics. In order to receive scattered signals from a broad range of scattering angles, from the probe beam that can be steered in two axes, and for a range of radial positions, the receiving optics need to translate across five axes of motion. The receiver will detect up to eight (four at initial installation) distinct scattering angles in a vertical array at a time. This leads the receiver optics to be relatively large, and the limited space around Bay L further complicates the design. Several optical configurations were examined, including the use of

spherical mirrors and HDPE lenses. Ultimately, the most compact system utilizes two large HDPE lenses to collect and collimate the beams. This solution has a -3 dB impact on the scattered signals compared to similar mirror based systems; however, the spatial constraint prohibited mirror based solutions.

The receiving optics need to collect scattering angles with a $\sim 15^\circ$ spread to provide signals to an 8 x 1 vertical array. The optics can then rotate poloidally about the scattering volume by $\pm 4^\circ$ to further increase the range of scattering angles, and to target the probe beam while in upward or downward scattering configurations. The optics can rotate about a virtual pivot point by using two axes of control. One will raise or lower the optics assembly, and the second will tilt the optics in a vertical plane. The toroidal scattering angle is adjustable as well. A horizontal rotation stage is used to rotate the optics by $\pm 2^\circ$. This is coupled with a horizontal linear stage to keep the optics focus on the desired scattering volume location. The final axis controls the radial position. This will move the scattering volume from core to edge along the probe beam path. The scattering region is 290 to 750 mm from the Receiving window; therefore, the optics require a focal length of ~ 800 mm. When positioned close to the receiving window, plasma core measurements can be made, and when retracted ~ 0.5 m radially, edge measurements are performed. The travel limits for each stage are provided in Table 10.

Table 10. Receiving Optics 5-axis Travel

Axis	Travel Range
Radial	500 mm
Horizontal	76.2 mm
Vertical	76.2 mm
Horizontal Rotation	4° ($\pm 2^\circ$)
Vertical Rotation	8° ($\pm 4^\circ$)

The receiving optics employs two large HDPE lenses, plus a small focusing lens for each receiver channel. HDPE is chosen for its ease of fabrication, and low absorption at 693 GHz [22]. The first lens is a semi-spherical convex lens. This will collect the scattered signals at various angles, and focus them. While the scattered signals are converging, a second HDPE lens will collimate the beams and make the signals parallel to each other. To accomplish this, a meniscus lens has been designed. The collimated signals are then aimed at the receiver mixer array RF input horns. To provide better horn coupling and individual channel tuning, each receiver channel has a 2-axis adjustable, spherical, HDPE lens mounted near the RF input horn of the mixer array.

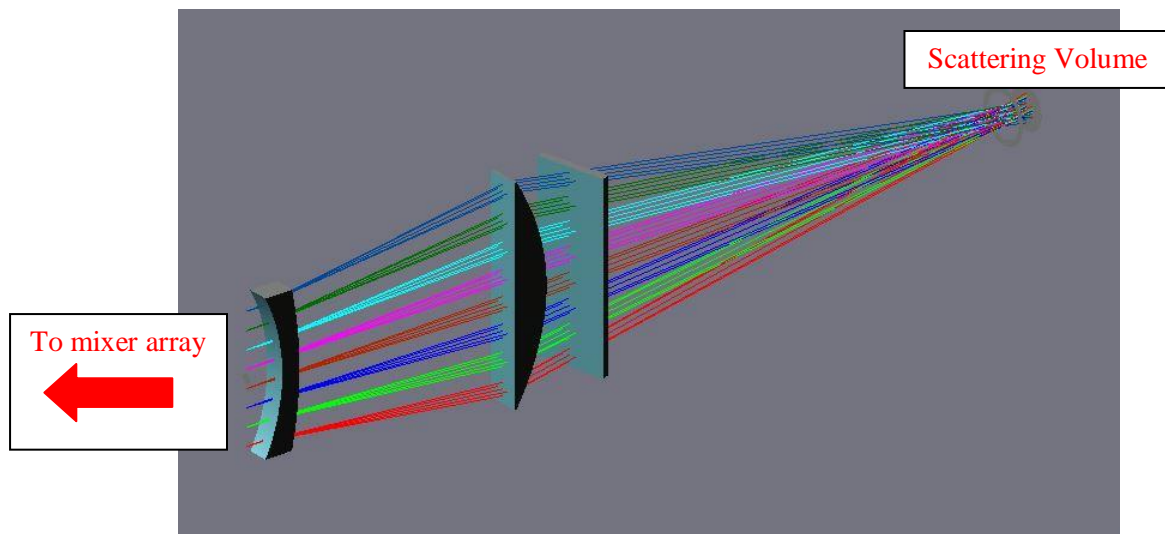


Figure 166. Receiving optics. The focal point at the right represents the scattering volume. Scattered signals at various angles pass through the receiver window, and are then collected by the convex lens. Converging signals then intersect the meniscus lens to collimate the signals.

The lens system was designed with CodeV optical simulation software. The optical design attempts to minimize the lens thickness to reduce attenuation, and to keep the overall size compact. HDPE has an absorption coefficient of $\alpha = 20 \text{ cm}^{-1}$ [41], and index of 1.52 at 693 GHz [41]. The final curvatures are as

follows: 1) Lens 1 is a semi-planar convex lens with a curvature of 290 mm radius, 176 mm tall. 2) Lens 2 is 125 mm tall, with two different curvatures, a concave surface facing the mixer array, and a convex surface facing the plasma, with curvatures of 280 mm and 600 mm radii, respectively. The distance between the lenses is 370 mm.

Surface #	Surface Name	Surface Type	Y Radius	Thickness	Glass	Refract Node	Y Semi-Aperture	X Semi-Aperture	
Object	Minilens	Sphere	Infinity	0.0000		Refract	0	0	
1		Sphere	Infinity	50.0000		Refract	105.0000 O	105.0000 O	
2	Lens A1	Sphere	-280.0000	30.0000	'HDPE'	Refract	125.0000 □	17.0000 □	
3	Lens A2	Sphere	-600.0000	370.0000		Refract	125.0000 □	17.0000 □	
4	Lens B1	Sphere	Infinity	58.0000	'HDPE'	Refract	176.0000 □	27.0000 □	
5	Lens B2	Asphere	-290.0000	60.0000		Refract	176.0000 □	27.0000 □	
6	Window1	Sphere	Infinity	12.7000	'WINDOW'	Refract	155.0000 □	58.0000 □ Decenter & Return	
7	Window2	Sphere	Infinity	750.0000		Refract	155.0000 □	58.0000 □ Decenter & Return	
Stop	Focus	Sphere	Infinity	40.0000		Refract	35.0000 O	35.0000 O	
Image	Center	Sphere	Infinity	0.0000		Refract	35.0000 O	35.0000 O	
							End Of Data		

Figure 167. Receiver optics CodeV lens data.

After the meniscus lens, the scattered signals will be collimated and parallel. Before coupling into the mixer input horns, each horn will have an adjustable spherical, convex lens to fine tune the input. The channel spacing for the mixer array is 30 mm, and each lens is 25.4 mm diameter, with a curvature radius of 35.6 mm. These lenses are placed ~50 mm past the meniscus lens, and are spaced 50 mm from each horn input. Working in reverse from the mixer horn to the plasma, the horn pattern is collimated into a 15 mm diameter signal. The meniscus lens then diverges the channels and increases the signal diameter. The last lens then converges all signals, through the receiving window on Bay L, to a single focus along the probe beam, with a waist radius of ~22 mm, 823 mm from the last lens surface. The main receiver optical lenses, tuning lenses, and mixer array are all fixed in space to each other. They are mounted to a common backboard, and will translate together as a unit.

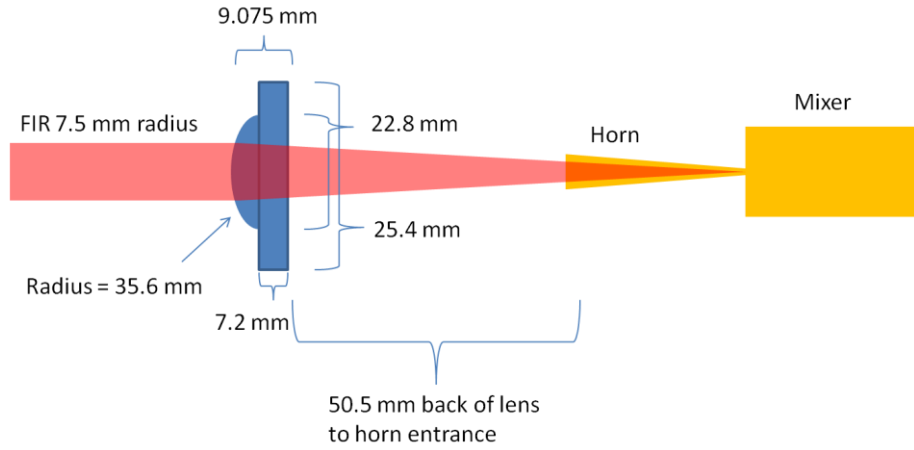


Figure 168. Receiver horn coupling lens design.

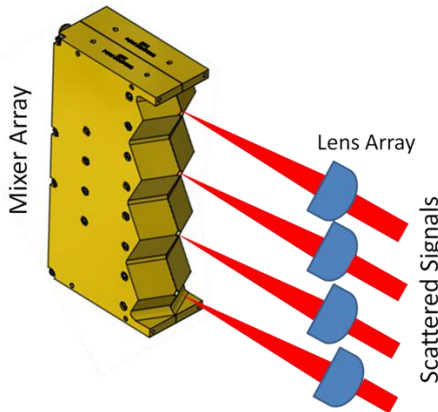
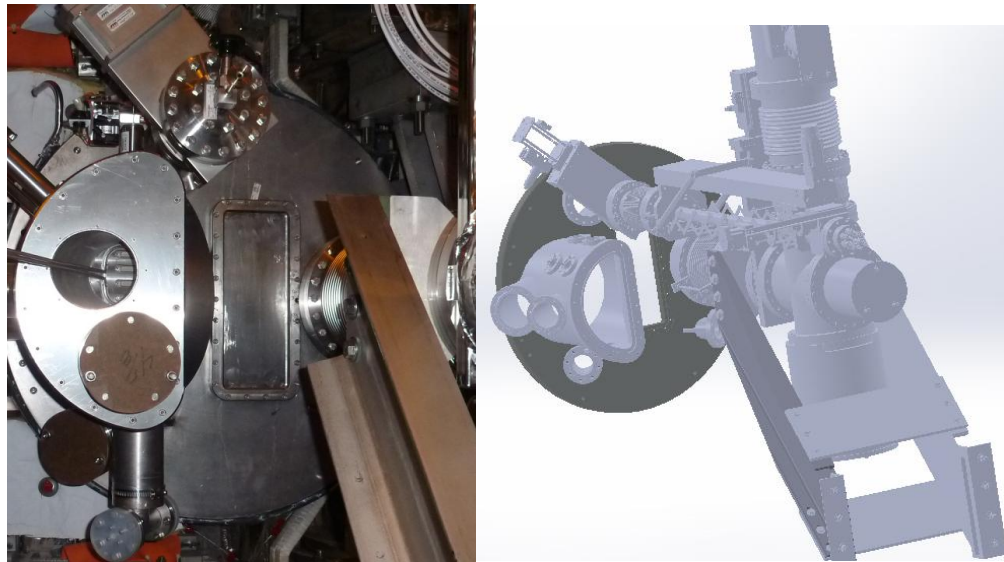


Figure 169. Image of four tuning lenses coupling scattered signals into the four mixer array input horns.

Bay L, on NSTX-U, is located between the NBI systems. There are several installations around the High- k_0 Scattering Receiver window. As viewed from outside the tokamak, there is a large D-shaped port extension to the left. On the right is the Thomson scattering beam dump. Above is the Fusion Products Detector. There are also poloidal field coils above and below the receiver window. The remaining space is adequate to mount the High- k_0 Scattering receiver, but only barely so. There are two areas that need to be addressed: 1) the Thomson scattering support structure, and 2) the fusion products detector. The Thomson scattering system is supported in part by a large length of channel stock. This channel stock interferes

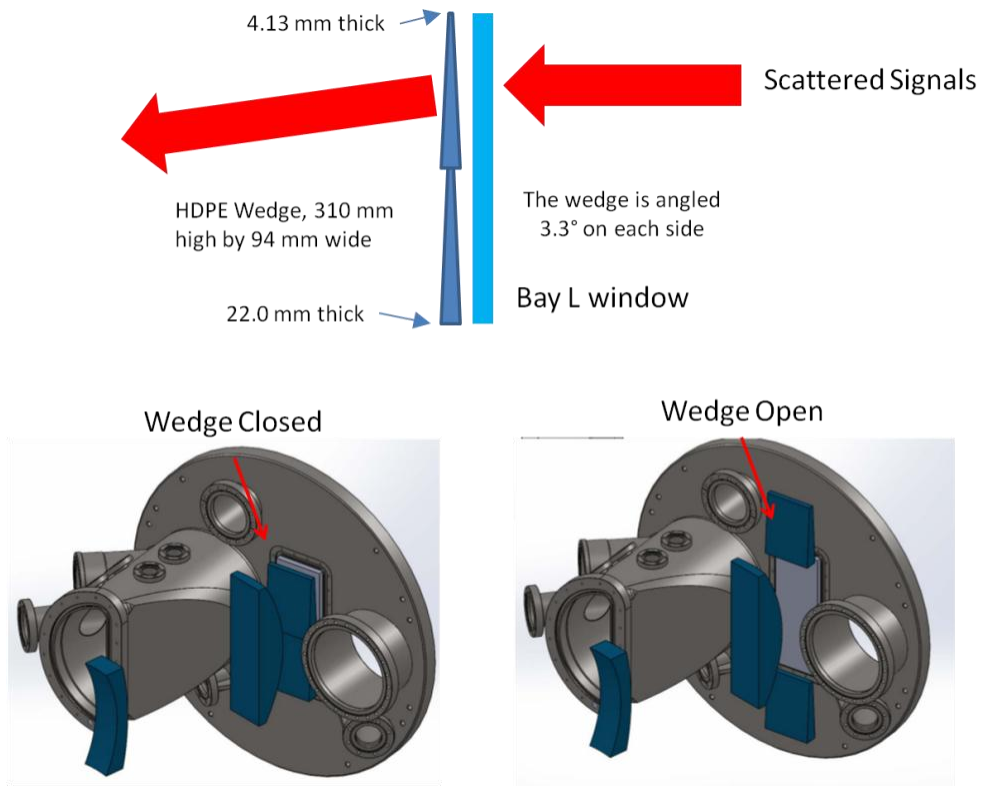
with the receiver when it is retracted away from the receiver window, and translated to the right. This problem is easily remedied by removing material from the channel without compromising the structural support. The fusion product detector required a more involved solution.



Figures 170a and 170b. Left: Bay L port cover. The rectangular receiver window is seen at the center. To the right is a large length of channel stock to support the Thomson scattering system. To the left is a D-shaped port which shrouds the receiver window. Above is a round flange which will mount the fusion products detector. Right: CAD model of the same port cover. The Thomson scattering support beam has a long angled cut to remove its interference. The Fusion Products Detector is seen extending above the window. Photograph and CAD model courtesy of Princeton Plasma Physics Laboratory.

The fusion product detector extends radially from the Bay L port cover, directly above the High- k_θ Scattering receiver. At the closest point, there is about 1" of vertical clearance for the receiver. This prevents the receiver assembly from rising vertically. For upward scattering, the receiver optics need to be raised up to 3" and then tilted down by 4°. To preserve the upward scattering function of the instrument, an optional wedge lens has been designed. The wedge is a slab of HDPE with the leading and trailing

surfaces designed with 6.6° between them. When positioned at the receiving window, between the window and receiver optics, scattered signals will be steered downward 4° . The application of this wedge lens is when downward scattering signals are to be measured, the wedge is removed, and the receiver is positioned normally. When upward scattering is desired, the wedge is installed to introduce a 4° systematic downward shift, thereby enabling the upward scattered signals to be measured with the receiver translating through the downward positions. This system reduces the receiver vertical travel by 50%, and avoids interference with the fusion products detector. The wedge can be installed or removed automatically with remote controlled actuators. It will be mounted to the Bay L port cover, and will slide into or out of position on command. To reduce attenuation from the wedge, and facilitate positioning, the wedge is divided into two halves, split horizontally at the midpoint. Each half has a 6.6° taper, and when installed presents a scalloped surface. The lower half is therefore reduced in thickness by $\sim 50\%$. When positioning the wedge out of position, the upper half slides upward, and the lower half slides downward, leaving the window uncovered. When positioning the wedge in place over the window, the two halves butt together at the center of the window.



Figures 171a, 171b, and 171c. Top: When the wedge lens is in place, traversing scattered signals are steered downward 4°. Bottom left: Wedge lens in place over the receiver window. Bottom right: Wedge lens retracted, exposing the receiver window. CAD models courtesy of Princeton Plasma Physics Laboratory.

The receiver optics are translated in 5 axes by a remote controlled receiver carriage. There are three linear axes, and two rotational. Each translation stage is operated by a stepper motor. A 5-axis motor controller is in turn controlled by a LabView program. The position of the receiving optics is coordinated with the probe beam line to choose the location of the scattering volume. Each axis is positioned individually; simultaneous motion is not necessary. During plasma measurements the scattering volume should not be altered; however, between plasma shots the optics can be repositioned, and there is ample time to accomplish this. Starting at the bottom of the carriage, the first stage is a 20" linear track. This will position the receiver radially from NSTX-U. This moves the scattering volume from core to edge in the

plasma. The next stage is a 5" horizontal, linear track to position the receiver right or left. 5" of travel are available, but only 3" are required. Next is a motorized lab jack to elevate the receiver. To cover the range of $\pm 4^\circ$ of vertical steering, the receiver would need 6" of vertical travel; however, due to the wedge lens addition, only 3" are required. For horizontal rotations, a motorized rotary stage is mounted above the lab jack. Rotary stages generally can rotate 360° ; however, only $\pm 2^\circ$ are needed for this system. The final stage will provide vertical rotation. To minimize the lateral dimension, a slim, linear stage is mounted vertically along the side of the receiver optics. This stage will animate an 11" moment arm to rotate the optics about a pivot point at the optics center of gravity. Again, due to the wedge inclusion, only 50% of the vertical rotation is needed at 0 to 4° . All stages are primarily made from aluminum and stainless steel to minimize magnetic field disturbances due to magnetic induction [42]. The complete receiver optics, mixer array, and carriage weighs ~ 80 lbs. The receiver system is installed at NSTX-U by support brackets from below, and will not directly connect to the Bay L port cover. The wedge, however, does mount to the port cover, and is not included in the weight estimate. The stages employed have ample load capacity to translate the mass of the receiver system. The only concern for load handling is the lab jack for vertical positioning. The upper portion of the receiver assembly load for the lab jack is ~ 35 lbs. This is near the maximum advertised capacity for most scissor type lab jacks, and they are not recommended. A heavy duty, elevation screw lab jack is used, with a maximum capacity of 110 lbs for improved reliability. To avoid interference with the Thomson scattering support and the poloidal field coil below Bay L, the horizontal stage for toroidal positioning is placed at the bottom of the receiver assembly. This is followed by stacking the vertical stage, radial stage, and rotary stage on top of the toroidal stage. When the receiver carriage translates radially to either the extreme "in" or "out" positions, a torque up to ~ 30 ft.lbs. is placed on the vertical and horizontal stages. The vertical stage is very robust, and can handle this load without concern; however, the toroidal stage is prone to binding. This problem is alleviated by adding support bearings on either side of the toroidal stage to carry the load, and keep its motion free. A dry air enclosure is not necessary for 693 GHz operation [43, 44]; however, a dust cover will shield the receiver system from incidental contact and airborne particles.

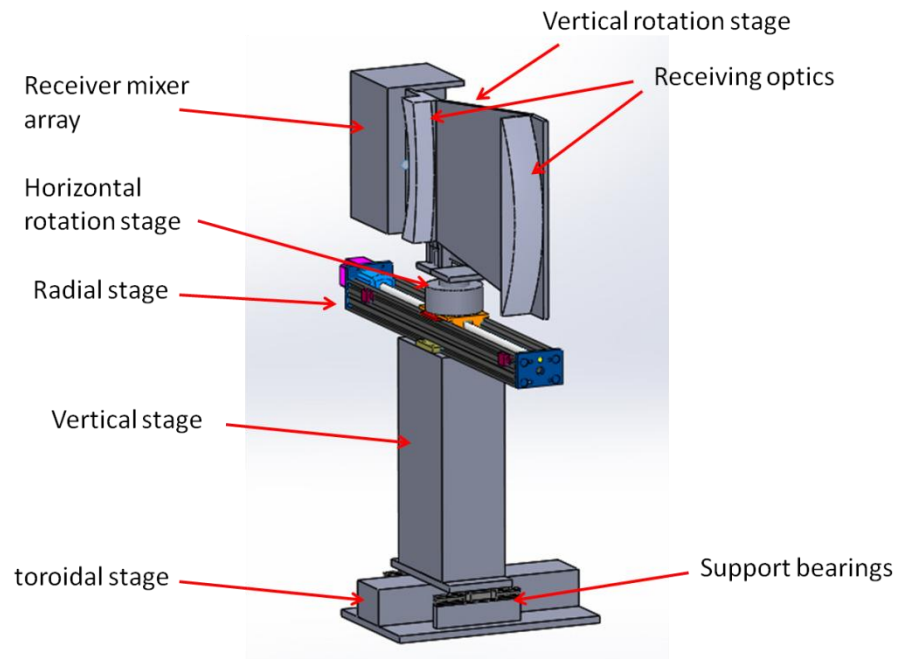
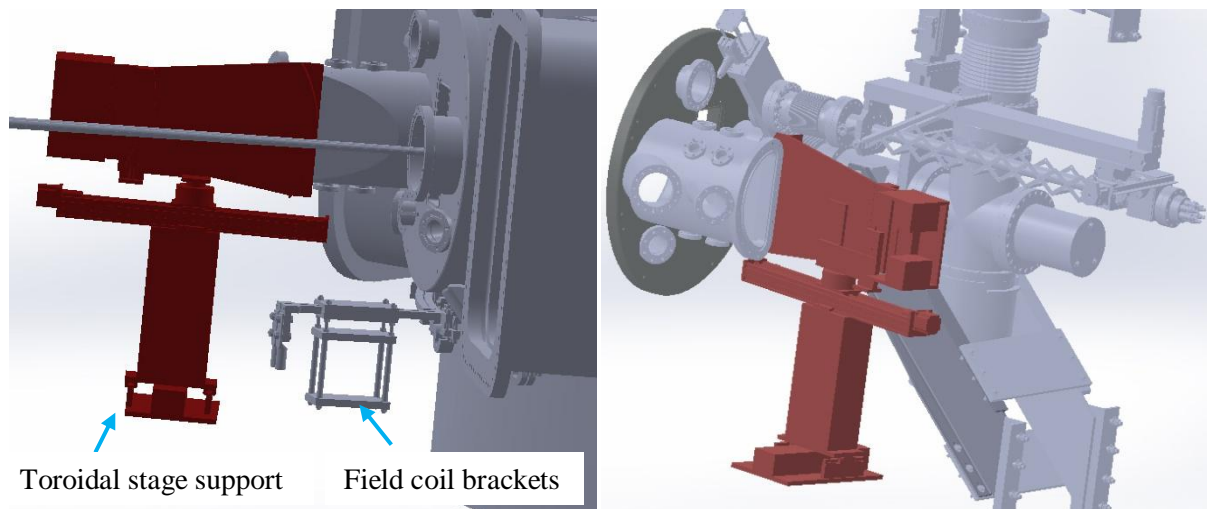
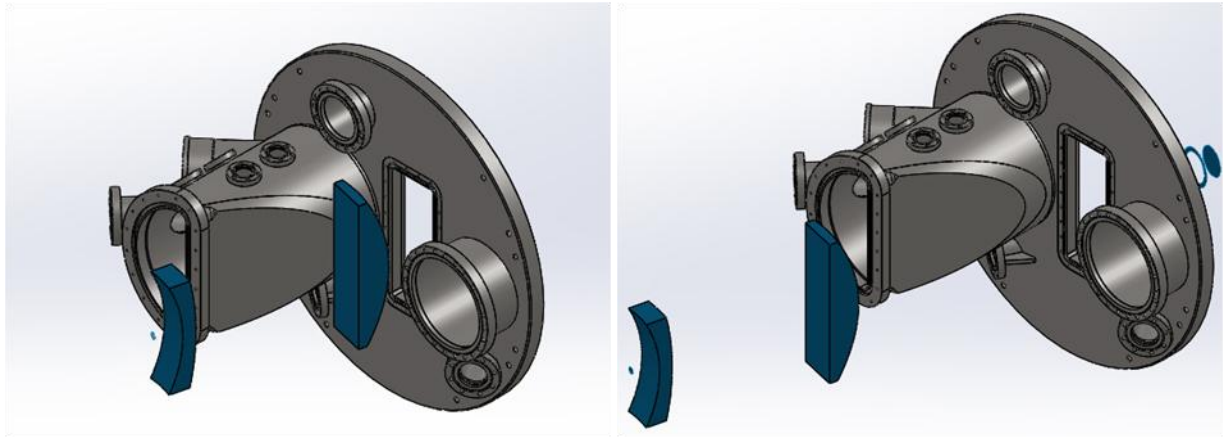


Figure 172. CAD rendering of the receiver assembly. The location of the 5 translation stages are labeled.



Figures 173a and 173b. Receiver system (red) positioned at Bay L. Left: Clearance around poloidal field coil brackets is observed below the radial stage, and before the vertical stage. The toroidal stage support bearings are seen near the bottom of the assembly. Right: The receiver is retracted away from the vacuum vessel at the midway point of radial travel. Bay L CAD Model courtesy of Princeton Plasma Physics Laboratory.



Figures 174a and 174b. Radial position range of receiver optics. Receiver carriage is hidden for clarity.

Receiving optic lenses are shown in blue. Left: Optics close to the window ("in position") for core plasma measurements. Right: Optics retracted 500 mm ("out position") for edge measurements. CAD Models courtesy of Princeton Plasma Physics Laboratory.

The receiver optics and carriage system is fully designed; however, at the time of this writing it has not been fabricated. This portion of the instrument development must be closely coordinated with PPPL engineers. The space allowed around Bay L is very limited. PPPL ensures that installations do not interfere with surrounding equipment, and if modifications are required, they will coordinate communications and modifications with other groups as necessary. Once the High- k_θ Scattering receiver is approved by PPPL, the necessary parts can be purchased, and fabrication can begin. The construction and testing of this system is expected during the spring of 2017.

IV.5 High- k_θ Scattering Receiver

At the core of the High- k_θ Scattering receiver is the mixer array. This is a quasi-optical, subharmonic, 4 x 1 array of mixers designed for RF frequencies at 693 GHz. The mixers will receive RF power scattered from the probe beam, and mix them with a 14.42 GHz LO with a x48 multiplier chain. Nominally, this

produces an IF output at 840 MHz. The precise frequencies utilized may vary slightly due to laser tuning, LO tuning, and Doppler shifts from the scattered signals. The drift waves in the plasma can travel at high poloidal speeds, causing scattered signals to be Doppler shifted by ~10-20 MHz. The mixer array is a self contained system designed by Virginia Diodes Inc. [45] to UC Davis specifications. It consists of a single construction mixer body, which contains the horn antennae, waveguides, IF amplifiers, and mixers for all four channels. There are four SMA IF output ports. A single SMA LO input port is connected to the multiplier chain and 4x power divider. Also included in the assembly are cooling fans, 120 VAC input jack, and DC power supply to power the fans, IF amplifiers, and mixer DC bias. All components are mounted to a 6" by 8" base plate. The only items that are needed to be provided are the LO power, and 120 VAC.

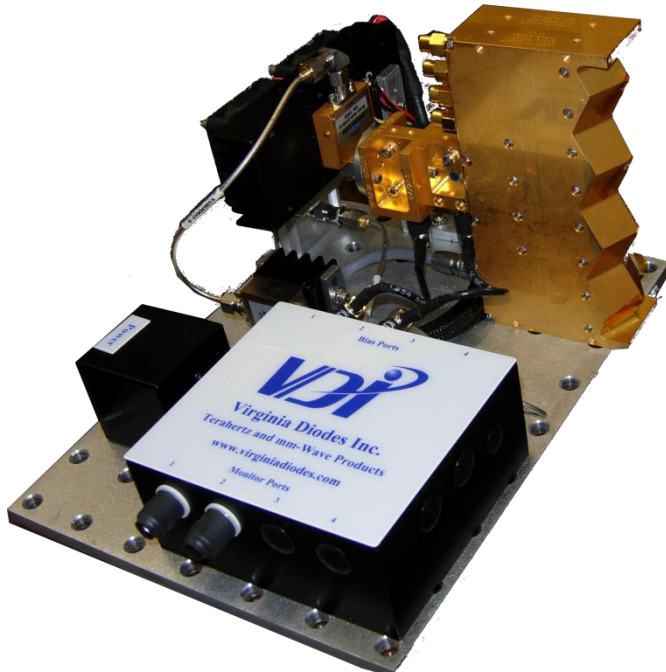


Figure 175. 693 GHz subharmonic 4 x 1 mixer array by VDI.

The mixer body is precision machined from aluminum, and gold plated for corrosion resistance and improved RF performance. The area around each RF horn is heavily relieved to scatter any incident

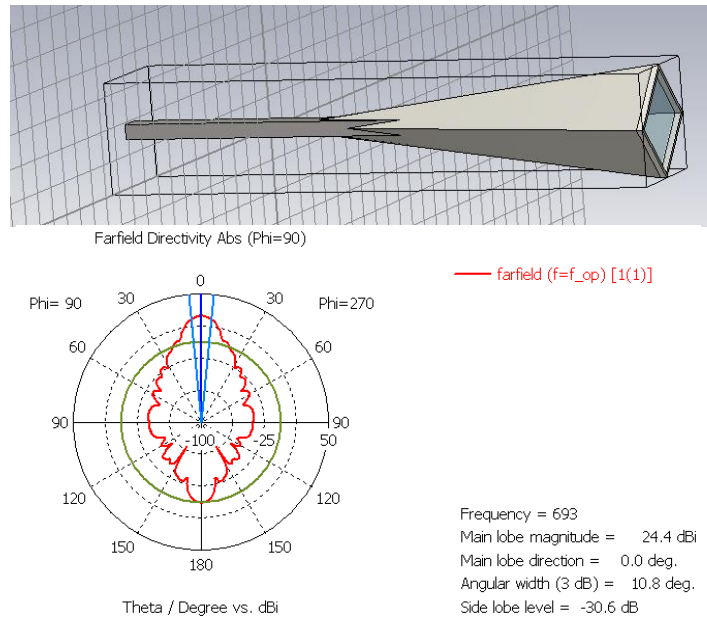
power that is not coupled into the mixer body. The RF horns are a diagonal design, measuring 2 mm along each side, and tapers at 10° down to WR-1.2 waveguide. At either edge of the mixer body are mounting bosses to add components, such as a lens array before the horns. The overall dimensions are 120 mm tall, 30 mm wide, and 60 mm deep. The spacing between channels is 30 mm. The mixer assembly was designed to be expanded to an 8 x 1 array by constructing an identical array, but the mirror image. This will allow one mixer array to be inverted and stacked over the first array, with the RF horn inputs spaced equally at 30 mm for the entire 8 x 1 assembly. The mixer specifications are listed in Table 11.

Table 11. VDI mixer array specifications [45]

Component	Value
RF Input Frequency Bandpass	688-696 GHz
RF Input Power (Typical / Damage)	< -10 dBm / 0 dBm
LO Input Frequency Range	14.33-14.50 GHz
LO Input Power (Typical / Damage)	7-10 dBm / 13 dBm
LO Multiplier Chain	x 48
IF Output Frequency Range	800-1000 MHz
IF Output SSB Conversion Loss	< 13 dB
IF Amplifier Gain	16 dB

The 2 mm diagonal horns were simulated in CST (Computer Simulation Technology [46]) to determine their performance, and to aid in the design of the channel tuning lenses. The far field directivity was found to be 24.4 dBi, with a 3 dB bandwidth of 10.8°. Side lobes were reduced by -30.6 dB. Diagonal horns couple well to Gaussian modes with high directivity [47]. The incoming RF signal is collimated by the meniscus lens with a radius of 7.5 mm. To most efficiently couple the signals into the horns, a

focusing lens is added to provide a convergence angle to match the horn pattern. An HDPE hemispherical lens with a radius of 35.6 mm will provide a 70 mm focal length for the incoming signal. Each lens is positioned ~50 mm from the horn entrances. Each lens has an overall thickness of 9 mm, including a 7 mm thick, 25.4 mm diameter flange for securing the lens in an optical mount. The mount can translate in two axes by miniature, manual, dovetail stages. Several millimeters of translation are available to center the lenses over each horn, and tune the incoming signal for maximum performance. Once the lenses are positioned, no further adjustment should be necessary, and the stages can be locked into position. Each mount and translation stage is staggered in such a way as to avoid conflicts between adjacent positioning knobs.



Figures 176a and 176b. Top: Model of diagonal horn. The opening is 2 mm by 2 mm oriented in a diagonal pattern. Bottom: Far field simulation results. The primary lobe is 24.4 dBi, with a 3 dB angular width of 10.8°.

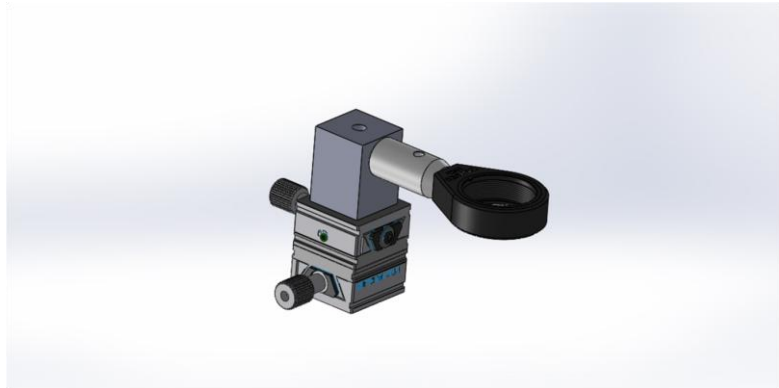


Figure 177. Tuning lens mount. Two miniature stages adjust the position of the spherical lens for coupling signals into the mixer RF input horn. Four mounts are installed for the mixer array with the position knobs arranged so they do not interfere with each other.

The receiving window at Bay L is custom designed for the High- k_0 Scattering System. The window measures 33.48 cm tall by 13.94 cm wide. To maintain a safety factor of greater than 10, the window needs to be much thicker than the launch window. The minimum thickness varies with the type of material used. As with the launching window, the material must be suitable for transmission at 693 GHz. Z-cut quartz provides the best performance; however, for a window this size it would be incredibly expensive. Crystal quartz cannot be considered for the same reason. The material chosen is Corning 7979 IR grade [48]. It is formulated with < 1 ppm hydroxyl content for good FIR performance. To determine the thickness, the following equation can be used for rectangular windows:

$$t = l w \sqrt{\frac{P K SF}{2 M (l^2 + w^2)}}$$

where t is the window thickness, l and w are the window dimensions, P is the pressure differential (14.7 PSI), K is an empirical constant determined by the type of mounting, SF is the desired safety factor, and M is the modulus of rupture [49]. For Corning 7979 IR, the modulus of rupture is 7600 PSI [48]. K is

chosen to be 1.125 based on the mounting flange and recommendations from the manufacturer. The window dimensions calculated are the location of the O-ring contact at 325 mm by 130 mm, rather than the overall dimensions. For this window, the safety factor was set to a minimum of 10, and the thickness of the window was settled at 15.87 mm. The window is expected to attenuate - 3 dB at 693 GHz for this thickness. While not ideal performance, it was a necessary compromise.

IV.6 High- k_0 Scattering Reference Channel

A reference channel is needed for the receiver mixer array. The reference channel will use a subharmonic quasi-optical mixer to sample the laser frequency and power. The FIR signal will be mixed with a \sim 14.42 GHz LO signal from a voltage controlled oscillator (VCO) to produce an IF output near 880 MHz. The IF output is connected to a phase locked loop circuit, where it is compared with an 880 MHz crystal oscillator. The phase lock loop circuit will then adjust the VCO frequency to keep the IF at a steady 880 MHz. With the LO frequency controlled by the reference channel, it is divided into two parts, one for the reference mixer, and the other for the receiver mixer array. Additional ports are included to allow connections to a spectrum analyzer and power monitor to assist in diagnosing potential laser or electronic problems. The reference IF output is sent to the High- k_0 Scattering electronics as a base reference for the laser frequency. The receiver mixer array will then produce IF signals that are slightly shifted (\sim 10 MHz) from 880 MHz depending on the Doppler shift from the poloidal drift wave velocity, and then delivered to the IF electronics.¹

¹ Phase Lock Loop circuitry designed and fabricated by Dr. Calvin Domier.

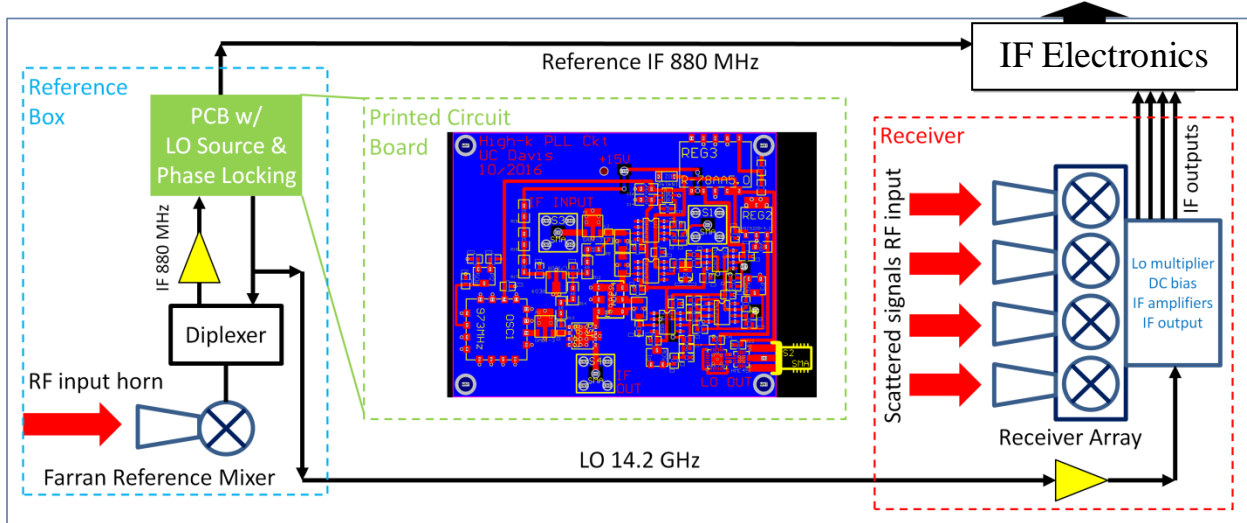


Figure 178. Reference channel schematic.

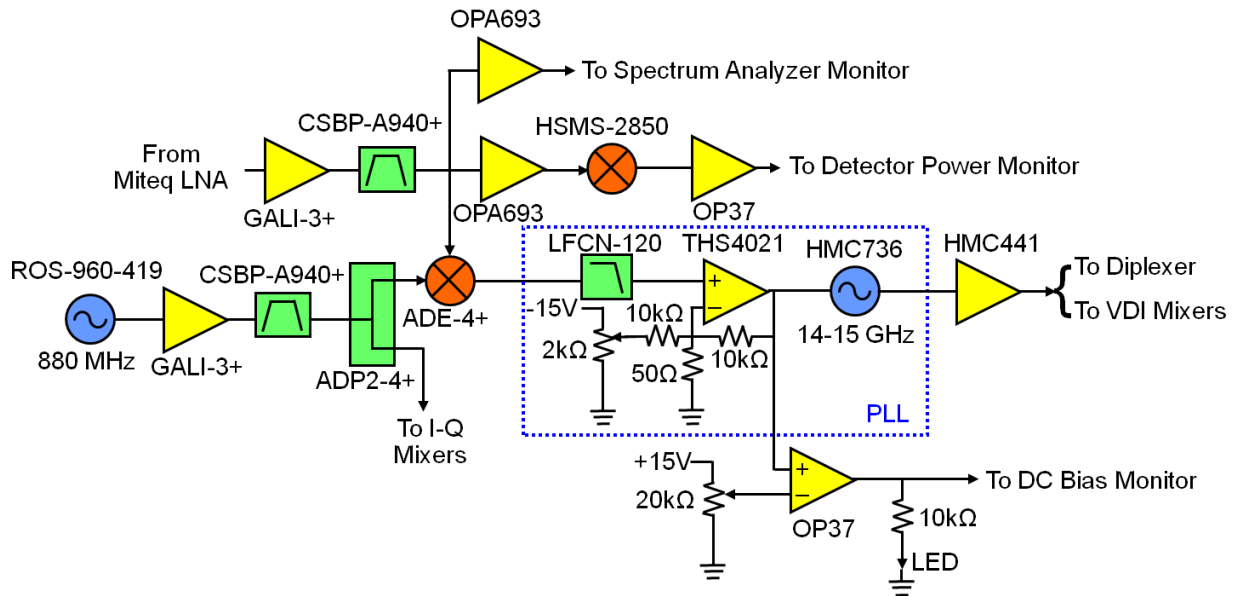


Figure 179. Schematic of phase lock loop circuit.

The reference mixer is a Farran Technology WHMB-2 [50]. Its advertised operational range is 325 to 500 GHz, with a conversion loss of -50 dB throughout the range. The FIR laser operates at 693 GHz; however, the mixer has adequate performance despite being used out of specified limits. With an RF input

level of -8 dBm, a conversion loss of -60 dB was observed. This is about 20 dB above the noise floor, and will allow clear frequency measurements. The mixer output scales with incident power; therefore, it can be used as a power monitor to supplement the pyroelectric detector measuring FIR power at the laser table. The Farran mixer is a compact unit, with the most basic interface. The RF input port is a WR-2.2 waveguide. A conical horn is attached to the RF input port to couple incoming RF signals. The horn was simulated in CST to determine the antenna pattern. It has a directivity of 22.6 dBi with a 3 dB bandwidth of 20°. The input signal is a Gaussian beam delivered from a 63 mm diameter corrugated waveguide. To determine the best method to couple the signal into the horn, CodeV optical simulation software was used to design a focusing lens. The waveguide exit is terminated with an HDPE, double convex lens with a 100 mm focal length. The horn opening is placed 76 mm from the lens center. Experimental results confirmed that the highest mixer output was achieved with a spacing of ~76 mm between the lens and horn. The Farran mixer uses a single SMA connector for the LO input and IF output. A 14/1 GHz diplexer is installed to isolate the LO and IF frequencies. The mixer is sensitive to incident power. The maximum RF power is 0 dBm, but will function at 693 GHz at < -10 dBm. The LO port is designed for 9 - 13.9 GHz, with a narrow power range of 14 - 15 dBm. The High- k_0 Scattering system operates slightly out of specification at 14.42 GHz, but maintains 14.5 dBm. The IF output is quite low at ~ -70 dBm; therefore, a 30 dB gain low noise amplifier is used to before feeding the signal back to the phase lock loop circuit. No DC bias is required. The mixer body, less horn, measures 20 mm x 20 mm x 16 mm.

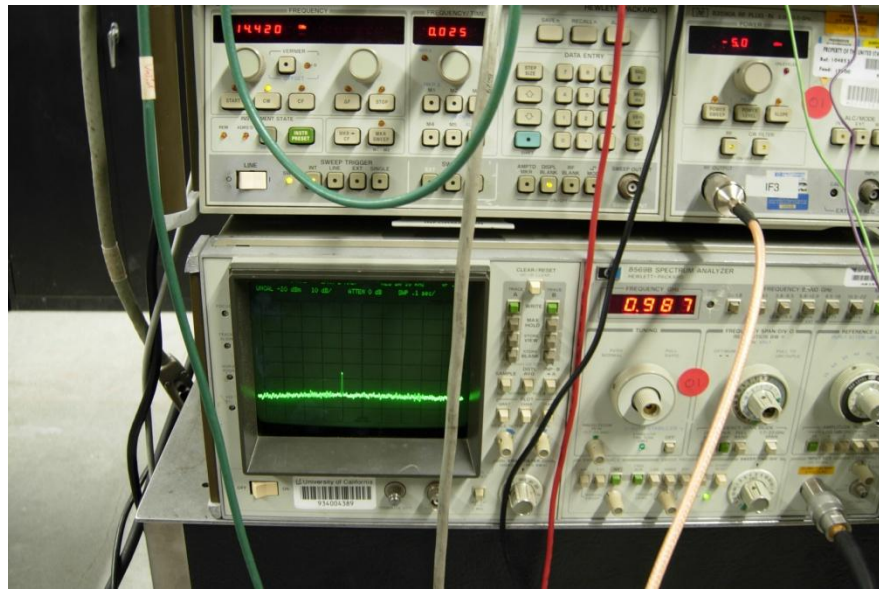
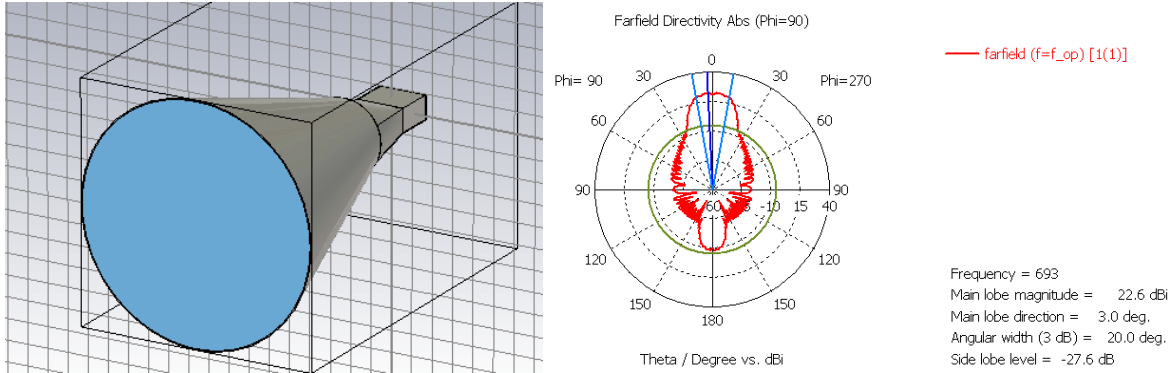


Figure 180. Photo of Farran IF signal. This test verifies that the Farran WHMB-2 mixer will operate outside of specified limits. The FIR laser supplies a 693 GHz RF signal, and a sweep oscillator supplies the LO power at 14.4 GHz. The resulting IF output is observed on a spectrum analyzer near 980 MHz.



Figure 181. Farran subharmonic mixer.



Figures 182a and 182b. Left: Model of conical horn for the WHMB-2 mixer. Right: Simulation results for horn pattern. The main lobe has a gain of 22.6 dBi with a 3 dB width of 20.0°.

The reference signal is split from the FIR beam in the waveguide run prior to the launch optics. This is accomplished by replacing one of the waveguide miter bends with a miter tee. The tee exchanges the regular reflector plate with a high ratio beam splitter. With a 500 lpi beam splitter, 2% of the laser power will be transmitted to the reference mixer box, and the remainder reflects down the waveguide path to the launch optics. Depending on the laser power, and losses prior to the miter tee, the reference signal power is expected to be -3.0 to 3.0 dBm. The reference mixer has a maximum RF power threshold of 0 dBm; therefore, if the delivered power happens to be too high, then an HDPE attenuator can be placed before the mixer RF input horn. The reference mixer, and supporting electronics, are contained within a cast aluminum box, measuring 7" x 9" x 13". The enclosure will protect the components, and provide electromagnetic shielding. To avoid circuit heating, and inconsistent power levels, an AC cooling fan is included in the enclosure. To preserve the RF shielding, air flow holes are 0.125" diameter, providing RF cut off up to 55 GHz. 324 holes are drilled at the fan area, and 400 air exit holes are on the opposite side of the enclosure. A 15 V DC power supply is included to power the various components. Each component has different voltage requirements, such as the fan, LNA, and VCO; therefore, voltage regulators are included to step down the power supply voltage as needed. A 73.5 mm hole is cut into one end of the enclosure to admit the waveguide. The waveguide is securely fastened with flanges and cap screws. The HDPE focusing lens is bolted to the waveguide exit to secure the lens and seal the waveguide for nitrogen

filling. The mixer is mounted to a manual, 3-axis, linear stage. This will allow positioning the mixer for fine tuning adjustments. $\pm 0.5''$ are possible for all three axes.

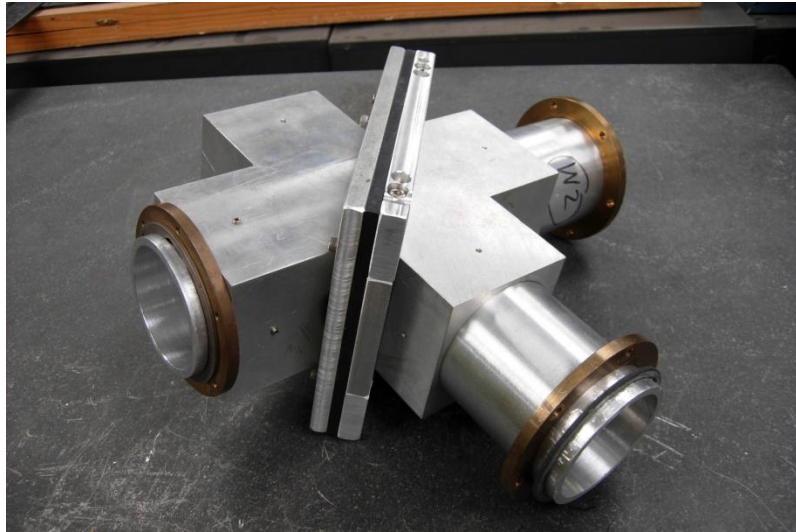


Figure 183. Miter tee. A metallic mesh beam splitter (black partition) is mounted in place of the reflector plate. The transmission and reflection coefficients are determined by the mesh density installed.



Figure 184. Reference box. The reference box is mounted on the transmission port of the miter tee in the waveguide run, prior to the launch optics.

The phase lock loop circuit will set the LO frequency for the reference and receiver mixers. A 14 GHz power divider separates the LO into two parts. A SMA bulkhead connector passes the receiver LO signal through the enclosure, and triax cable delivers the signal to the receiver mixers. Triax cable is used for an extra layer of shielding to reduce pick-up noise. A similar triax line will deliver the reference IF output to the High- k_0 Scattering IF electronics. The receiver mixer has different LO power requirements from the reference mixer, 7-10 dBm, and 14-15 dBm, respectively. Furthermore, coaxial cables can attenuate signals at 14 GHz by ~ -1 dB/foot. The distance between the reference box and receiver mixers is approximately 25 feet. Therefore, an amplifier will be added to the LO cable to set the power to the appropriate level. The exact amount of gain cannot be determined until the cable lengths are finalized during installation on NSTX-U.

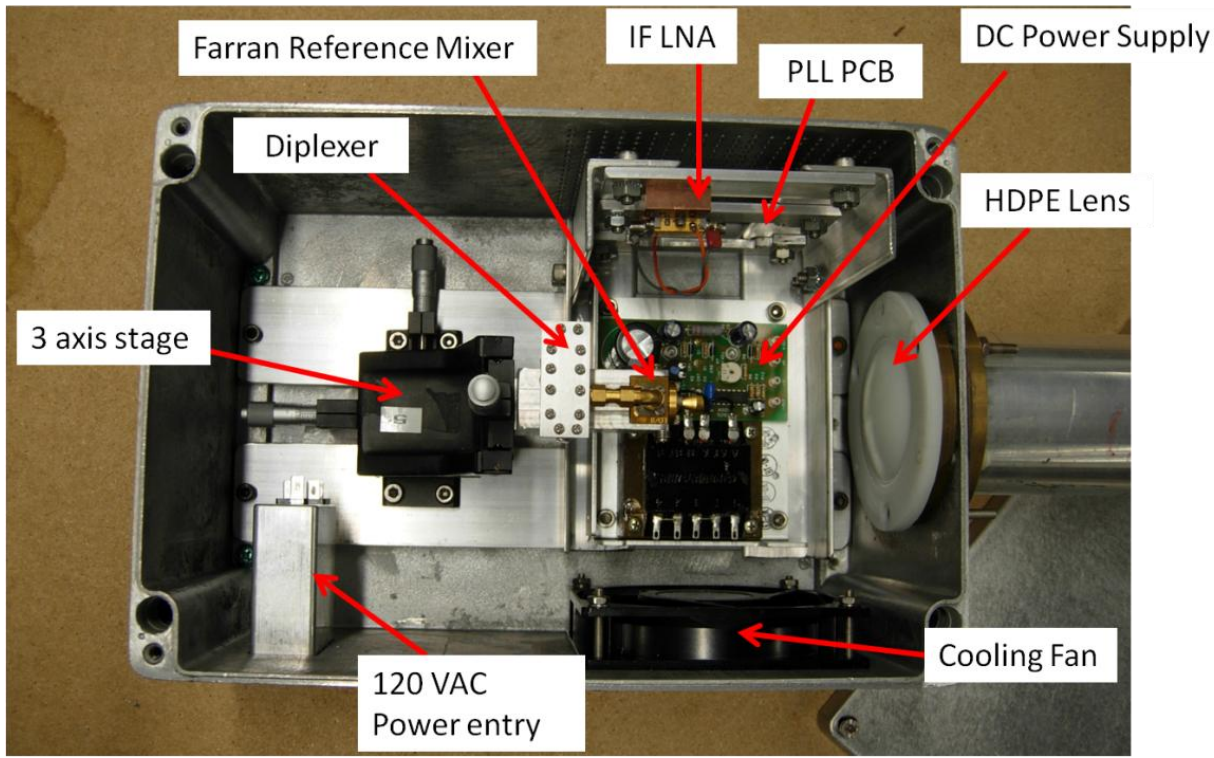


Figure 185. Reference box interior.

IV.7 High- k_0 Scattering IF Electronics

The receiver mixer array and reference channel IF outputs are connected to additional IF electronics before being recorded by digitizers. The signals are demodulated with I/Q mixers to provide amplitude and phase data relative to the reference signal. This information is then used to determine the power level and frequency of the scattered signals. The previous High- k_r Scattering system employed a 5 channel I/Q demodulator for 880 MHz IF input [51]. The new High- k_0 Scattering System retains 880 MHz for the IF outputs; however, the original IF electronics cannot be reused. The increased Doppler shift from NSTX-U will require wider bandpass filters, and eventually the electronics must accommodate up to eight channels. The demodulated data are recorded by digitizers, and then can be accessed by computer for data processing. The original digitizers will be upgraded for the new system. The previous digitizer only required a sampling rate of < 5 MHz; however, due to the increased Doppler shift, sampling rates up to 50 MHz will be needed. Furthermore, the digital memory will be increased to \sim 2 GB due to the expected increase in discharge times up to 5 seconds [2], and increase in receiver channels to 8. The original digitizer will be assigned to FIReTIP data recording.

At the time of this writing, the High- k_0 Scattering IF electronics have not been fabricated. The fundamental design and operation of the IF electronics are unchanged from the previous High- k_r Scattering design; however, the design will be updated for increased band width, higher sampling rate, and four receiving channels. When the second 4 x 1 receiver array is installed, a duplicate set of IF electronics can be fabricated and installed. This development should be completed in 2017; however, it is not strictly needed for instrument testing and calibration. The IF electronics are expected to be finished prior to the High- k_0 Scattering installation schedule on NSTX-U in FY2019.

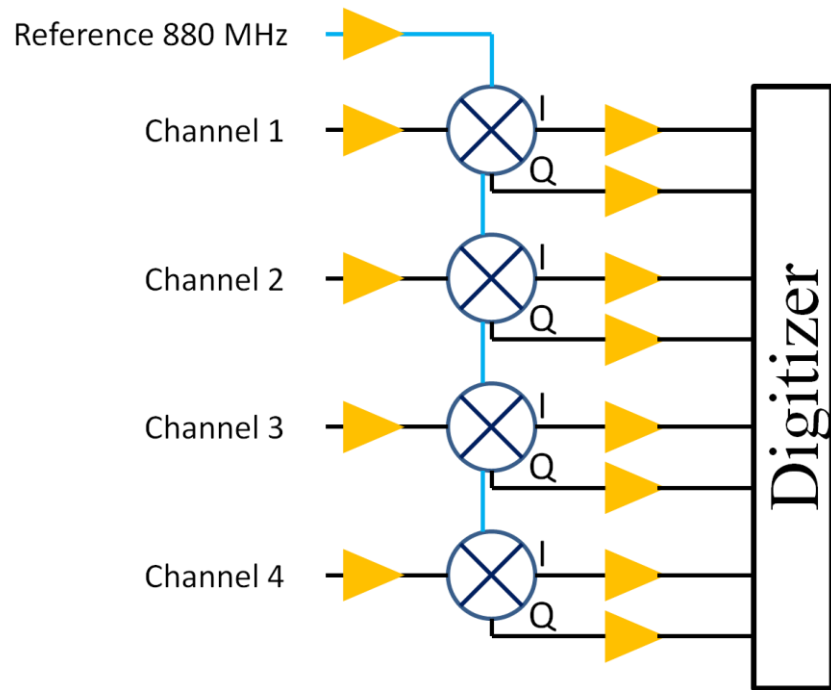


Figure 186. High-k electronics schematic. The reference box delivers a phase locked 880 MHz reference signal to each of four IQ mixers. The receiver mixer array sends one signal for each channel to each of the IQ mixers. The phase and amplitude data for each channel is recorded by a digitizer for later analysis.

IV. References

- [1] D.R. Smith, E. Mazzucato, T. Munsat, H. Park, D. Johnson, L. Lin, C.W. Domier, M. Johnson, N.C. Luhmann, Jr., "Microwave scattering system design for ρ_e scale turbulence measurements on NSTX," *Review of Scientific Instrument*, Vol. 75, No. 10, October 2004.
- [2] J.E. Menard et al., "Overview of the Physics and Engineering Design of NSTX Upgrade," *Nuclear Fusion*, vol. 52, no. 083015, 2012.
- [3] S. Jacobsson, "Review: Optically Pumped Far Infrared Lasers," *Infrared Physics*, Vol. 29, No. 5, pp. 853-874, 1989.
- [4] "CO₂ Lasers 9.1 μm - 10.9 μm ," *Edinburgh Instruments*, <https://www.edinst.com/products/co2-gas-lasers-9-1-%CE%BCm-10-9-%CE%BCm/>, Accessed: November 22nd, 2016.
- [5] E. Hecht, "Optics," *Addison Wesley*, 4th Ed., San Francisco, CA, 2002.
- [6] "Edwards nXDS15i dry scroll vacuum pump," Edwards, subsidiary of Atlas Copco Group, <https://shop.edwardsvacuum.com/products/a73701983/view.aspx>, Accessed: Dec. 12th, 2016.
- [7] T.M. Lehecka, "Development of High Power Optically Pumped Far Infrared Lasers for Fusion Plasma Diagnostics," *Thesis for a Master of Science degree in Electrical Engineering*, University of California, Los Angeles, 1986.
- [8] "Betta-Tech CU Series," Betta-Tech Controls, <http://betta-techcontrols.co.uk/products/>, Accessed: December 12th, 2016.
- [9] N.M. Lawandy, "Temperature Dependence of Optically Pumped Far-Infrared (FIR) Laser Output Power," *Infrared Physics*, Vol. 19, pp. 127-134, January 1978.
- [10] R.K. Nubling, J.A. Harrington, "Launch conditions and mode coupling in hollow-glass waveguides," *Optical Engineering*, 37(9), 2454-2458, September 1998.
- [11] T. Lehecka, R. Savage, R. Dworak, W.A. Peebles, N.C. Luhmann Jr., and A. Semet, "High-power, twin-frequency FIR lasers for plasma diagnostic applications," *Review of Scientific Instruments*, Vol. 57, No. 8, 1986.
- [12] G. Dodel, "On the history of far-infrared (FIR) gas lasers: Thirty-five years of research and application," *Infrared Physics and Technology*, Vol. 40, pp. 127-139, 1999.
- [13] E.J. Danielewicz, T.K. Plant, and T.A. DeTemple, "Hybrid Output Mirror for Optically Pumped Far Infrared Lasers," *Optics Communications*, Vol. 13, No. 4, April 1975.
- [14] L. Lin, W.X. Ding, D.L. Brower, W.F. Bergerson, and T.F. Yates, "Differential interferometry for measurement of density fluctuations and fluctuation-induced transport," *Review of Scientific Instruments (invited)*, Vol. 81, 10D509, October 2010.
- [15] "Dry Scroll Pumps, SH-110," *Agilent*, <http://www.agilent.com/en-us/products/vacuum-technologies/primary-medium-vacuum-pumps/dry-scroll-pumps/sh-110#specifications>, Accessed: November 28th, 2016.

- [16] "Fomblin, PFPE Lubes," *Solvay*, http://www.solvay.com/en/binaries/Fomblin-PFPE-Lubes-for-Vaccum-Applications_EN-220533.pdf, Accessed: December 2nd, 2016.
- [17] R. Densing, A. Erstling, M. Gogolewski, H.P. Gemund, G. Lundershausen, and A. Gatesman, "Effective Far Infrared Laser Operation with Mesh Couplers," *Infrared Physics*, Vol. 33, No. 3, pp. 219-226, 1992.
- [18] R. Ulrich, "Far-Infrared Properties of Metallic Mesh and its Complementary Structure," *Infrared Physics*, Vol. 7, pp. 37-55, 1967.
- [19] M.S. Durschlag and T.A. DeTemple, "Far-IR Optical Properties of Freestanding and Dielectrically Backed Metal Meshes," *Applied Optics*, Vol. 20, No. 7, April 1981.
- [20] R. Ulrich, T.J. Bridges, and M.A. Pollack, "Variable Metal Mesh Coupler for Far Infrared Lasers," *Applied Optics*, Vol. 9, No. 11, November 1970.
- [21] E.J. Danielewicz, Jr., "Far Infrared Guided Wave Optics Experiments Using a Waveguide Laser with a Hybrid Output Mirror," *Dissertation for a Doctor of Philosophy in Electrical Engineering*, University of Illinois at Urbana-Champaign, 1976.
- [22] Y.S. Jin, G.J. Kim, and S.G. Jeon, "Terahertz Dielectric Properties of Polymers," *Journal of the Korean Physical Society*, Vol. 49, No. 2, August 2006.
- [23] F.B. Foote, D.T. Hodges, and H.B. Dyson, "Calibration of Power and Energy Meters for the Far Infrared/Near Millimeter Wave Spectral Region," *International Journal of Infrared and Millimeter Waves*, Vol. 2, No. 4, 1981.
- [24] P.F. Goldsmith, "Quasi-Optical Techniques," *Proceedings of the IEEE, Invited Paper*, Vol. 80, No. 11, November 1992.
- [25] P. Belland and J.P. Crenn, "Matching of a Gaussian Beam into Hollow Oversized Circular Waveguides," *International Journal of Infrared and Millimeter Waves*, Vol. 10, No. 10, 1989.
- [26] A. Cavallo, J. Doane, and R. Cutler, "Low-Loss Broadband Multimode Corrugated Waveguide Performance," *Review of Scientific Instruments*, Vol. 61, 2396, September 1990.
- [27] P.J.B. Clarricoats and P.K. Saha, "Propagation of Radiation Behaviour of Corrugated Feeds," *Proc. IEE*, Vol. 118, No. 9, September 1971.
- [28] C. Dragone, "Attenuation and Radiation Characteristics of the HE₁₁ Mode," *IEEE Transactions on Microwave Theory and Techniques*, Vol. MTT-28, No. 7, July 1980.
- [29] E.A. Nanni, S.K. Jawla, M.A. Shapiro, P.P. Woskov, and R.J. Temkin, "Low-Loss Transmission Lines for High-Power Terahertz Radiation," *J. Infrared Milli Terahz Waves*, Vol. 33, pp. 695-714, February 2012.
- [30] Y. Yang, A. Shutler, and D. Grischkowsky, "Measurement of the Transmission of the Atmosphere from 0.2 to 2 THz," *Optics Express*, Vol. 19, No. 9, April 2011.

- [31] S.B. Korsholm, H. Bindslev, V. Furtula, F. Leipold, F. Meo, P.K. Michelsen, D. Moseev, S.K. Nielsen, M. Salewski, and M. Stejner, "Collective Thomson scattering capabilities to diagnose fusion plasmas," *Nuclear Instruments and Methods in Physics Research A*, Vol. 623, 2010.
- [32] S.L. Prunty. "A Primer on the Theory of Thomson Scattering for High-Temperature Fusion Plasma," *Physica Scripta*, Vol. 89, 2014.
- [33] D.L. Brower, H.K. Park, W.A. Peebles, and N.C. Luhmann Jr., "Topics in Millimeter Wave Technology Vol. 2," Chapter 3: Multichannel Far-Infrared Collective Scattering System for Plasma Wave Studies, Editor: Kenneth J. Button, *Academic Press Inc.*, San Diego, CA, 1988.
- [34] "Gaussian beam optics," *IDEX, Optics and Photonics Marketplace*, https://marketplace.idexop.com/store/SupportDocuments/All_About_Gaussian_Beam_OpticsWEB.pdf, Accessed: Dec. 15th 2016.
- [35] M. Naftaly and R.E. Miles, "Terahertz Time-Domain Spectroscopy for Material Characterization," *Proceedings of the IEEE*, Vol. 95, No. 8, August 2007.
- [36] R. Kitamura, L. Pilon, and M. Jonasz, "Optical constants of silica glass from extreme ultraviolet to far infrared at near room temperature." *Applied Optics*, Vol. 46, No. 33, November 2007.
- [37] T. Ohsaka and S. Oshikawa, "Effect of OH content on the far-infrared absorption and low-energy states in silica glass," *Physical Review B*, Vol. 57, No. 9, March 1998.
- [38] K.W. Hutt, W.A. Phillips, and R.J. Butcher, "Far-infrared properties of dilute hydroxyl groups in and amorphous silica matrix," *J. Phys.: Condens. Matter 1*, March 1989.
- [39] T.J. Parker, J.E. Ford, and W.G. Chambers, "The Optical Constants of Pure Fused Quartz in the Far-Infrared," *Infrared Physics*, Vol. 18, No. 3, 1978.
- [40] M.N. Afsar and K.J. Button, "Precise Millimeter-Wave Measurements of Complex Refractive Index, Complex Dielectric Permittivity and Loss Tangent of GaAs, Si, SiO₂, Al₂O₃, BeO, Macor, and Glass," *IEEE Transactions on Microwave Theory and Techniques*, Vol. MTT-31, No. 2, February 1983.
- [41] P.D. Cunningham, N.N. Valdes, F.A. Vallejo, L.M. Hayden, B. Polishak, X.H. Zhou, J. Luo, A.K.Y. Jen, J.C. Williams, and R.J. Twieg, "Broadband terahertz characterization of the refractive index and absorption of some important polymeric and organic electro-optic materials," *Journal of Applied Physics*, Vol. 109, 043505, 2011.
- [42] J.D. Jackson, "Classical Electrodynamics," *John Wiley and Sons*, 3rd edition, Hoboken, NJ, 1999.
- [43] R.J. Foltynowicz, M.C. Wanke, and M.A. Mangan, "Atmospheric Propagation of THz Radiation," *Sandia Report*, SAND2005-6389, October 2005.
- [44] D.M. Slocum, E.J. Slingerland, R.H. Giles, and T.M. Goyette, "Atmospheric absorption of terahertz radiation and water vapor continuum effects," *Journal of Quantitative Spectroscopy and Radiative Transfer*, Vol. 4, No. 22, 2013.
- [45] "Virginia Diodes Inc.," <http://www.vadiodes.com/>, Accessed: December 17, 2016.
- [46] "Computer Simulation Technology," <https://www.cst.com/>, Accessed: December 17, 2016.

[47] M.I.B. Shams, Z. Jiang, J. Qayyum, S. Rahman, S. Singh, J.L. Hesler, P. Fay, and L. Liu, "Characterizing a WR-1.5 Diagonal Horn Antenna Using Photo-Induced Coded-Aperture Imaging," *39th Int. Conf. on Infrared, Millimeter, and THz Waves*, IRMMW-THz 2014, September 14-19, Tucson, AZ, 2014.

[48] "Corning HPFS 7979, 7980, 8644 Fused Silica," *Corning Inc*, Corning, NY 2014.

[49] "Pressure Windows," *Advanced Glass Industries*, www.advancedglass.net, Rochester, NY, Accessed: December 17, 2016.

[50] "Farran Technology Ltd.," *Farran Technology Ltd.*, www.farran.com, Accessed: December 17, 2016.

[51] L.Y. Lin, "280 GHz Quasi-Optical Millimeter Wave Receiver System for Collective Scattering on NSTX," *Master's Thesis in the Dept. of Electrical and Computer Engineering*, University of California, Davis, 2006.

V. Future work

There are many opportunities to expand or improve the FIReTIP and High- k_θ Scattering systems. Some upgrades for these systems are planned for the next few years, and some are options that can be added to NSTX-U if PPPL chooses to do so. Additionally, there are developing technologies that can greatly improve plasma diagnostics, not only for NSTX-U, but for all tokamaks. Developments in fabrication techniques have allowed vacuum electronics devices to operate at ever higher frequency and power. UC Davis is currently developing vacuum electronics technology to provide improved reliability, at greater power, and in a much smaller package than current FIR lasers. Furthermore, the operation and maintenance is much more simplified than comparable performance lasers, offering significant benefits to plasma diagnostics.

V.1 FIReTIP System Improvements

For initial operation, FIReTIP will employ a single channel (Channel 1). This channel will measure chord averaged core plasma density. With real time feedback, the utility will be for machine control; however, its direct scientific application is limited. Additional channels have been proposed to contribute to anomalous transport research. Passing an FIReTIP probe beam along a chord near the plasma edge can measure plasma density and density fluctuations with time resolutions of \sim 4 MHz. These additional channels are options for PPPL to exercise as funding permits; however, UC Davis has designed FIReTIP to allow for their inclusion to be easily added if desired.

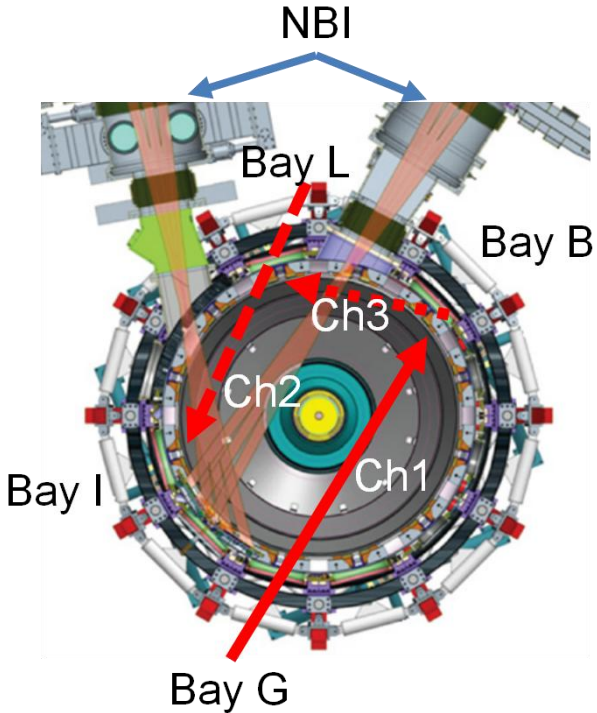


Figure 187. Proposed FIReTIP channel chords. Channel 1 passes between Bay G and B for real time core density feedback. Channel 2 passes between Bay L and I for density fluctuations near $r/a = 0.8$. Channel 3 passes between Bay B and L for density fluctuation measurements near $r/a = 0.9$. Image courtesy of Princeton Plasma Physics Laboratory.

Channel 2 is proposed to pass an FIR beam between Bay L and Bay I. This will target the edge plasma near $r/a = 0.8$ to measure density fluctuations. FIReTIP can access electron scale density fluctuations for $0.1 < k_\theta < 2 \text{ cm}^{-1}$. This would contribute to edge measurements for the lower wavenumber extremity of ETG modes, and cover Trapped Electron Modes (TEM), and Ion Temperature Gradient (ITG) modes [1]. To accomplish this, a portion of the probe beam must be delivered to Bay L. A miter tee is installed in the waveguide run to divide the beam power between Channels 1 and 2. Channel 2 will require launch optics similar to Channel 1; however, the focal length will be different to match the shorter chord length. A retroreflector is mounted at Bay I. The retroreflector differs from that for Channel 1 in that it will be mounted outside the vacuum vessel, and viewed through a quartz window. The external retroreflector is

not subject to vacuum vessel vibrations or bake out temperatures; therefore, a commercial retroreflector can be installed without a vibration monitor. The return signal will be passed through the Channel 2 waveguide, and directed via a beam splitter to the receiver table. Plasma data are measured the same way as for Channel 1, by comparing the phase between the Channel 2 receiver mixer and the reference mixer. IQ demodulated signals are then recorded by digitizers. This channel does not require real time data analysis, as it is not used for machine control.

Channel 3 is similar to Channel 2; however, it will measure k_θ data for the edge plasma near $r/a = 0.9$. The proposed chord passes an FIR beam between Bay B and Bay L. The waveguide is subdivided a second time to route the FIR beam to Bay B. Additional launch optics would be installed at Bay B, and the retroreflector at Bay L would be externally mounted. The return beam is then directed to the receiver table to another receiver mixer.

The receiver table is already fabricated to accommodate Channels 2 and 3 with the necessary optics and receivers installed on the middle level. At present, the middle level is bypassed for Channel 1 operation only. To add one or more channels, the waveguide path needs to be identified, launch optics designed, and retroreflectors installed. This application of FIReTIP could provide k_θ data not covered by existing instrumentation, or provide validation for future diagnostics.



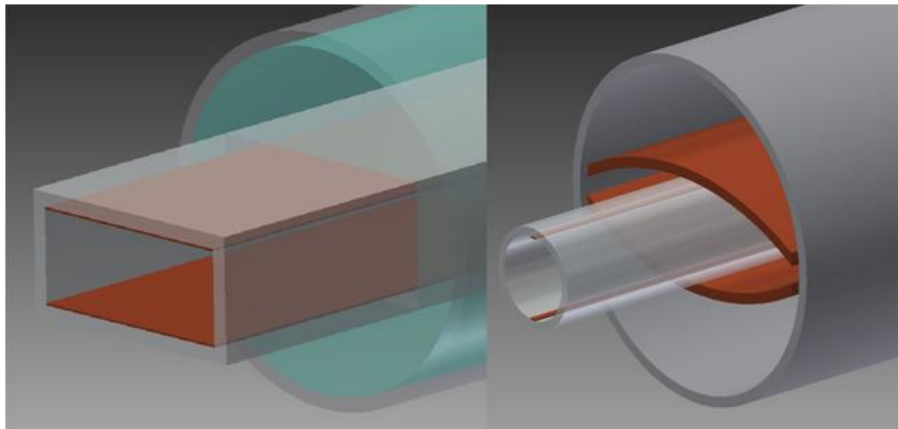
Figure 188. Middle level of the FIReTIP receiver table circled in red. The optics are in place to add Channels 2 and 3. Only the waveguide runs and receiver mixers will need to be installed.

At some point, the aging FIReTIP corner cube mixers may need to be retired given that honeycomb diode chips are no longer available and re-contacting service is no longer offered by vendors. At -50 dB conversion loss, any improvement in performance at 2.5 THz can greatly improve signal to noise ratio. Improved sensitivity allows less incident power, providing the potential for additional channels. A benefit that is less obvious is that there is more leeway for FIR laser performance. Gas lasers require frequent maintenance and tuning to operate at peak efficiency. The better the receiver system, the less demand there is on laser performance, and more time can pass between tuning and overhauls. There are many examples of improved performance for quasi-optical mixers at 2.5 THz [2, 3, 4]. Development of replacement mixers could be investigated. The greater concern is the availability of sources near 2.5 THz. For heterodyne detection, two sources are needed with slightly different frequencies. One technique is to use two methanol lasers that are detuned to shift the resonant frequency by ± 1 MHz. This can provide a

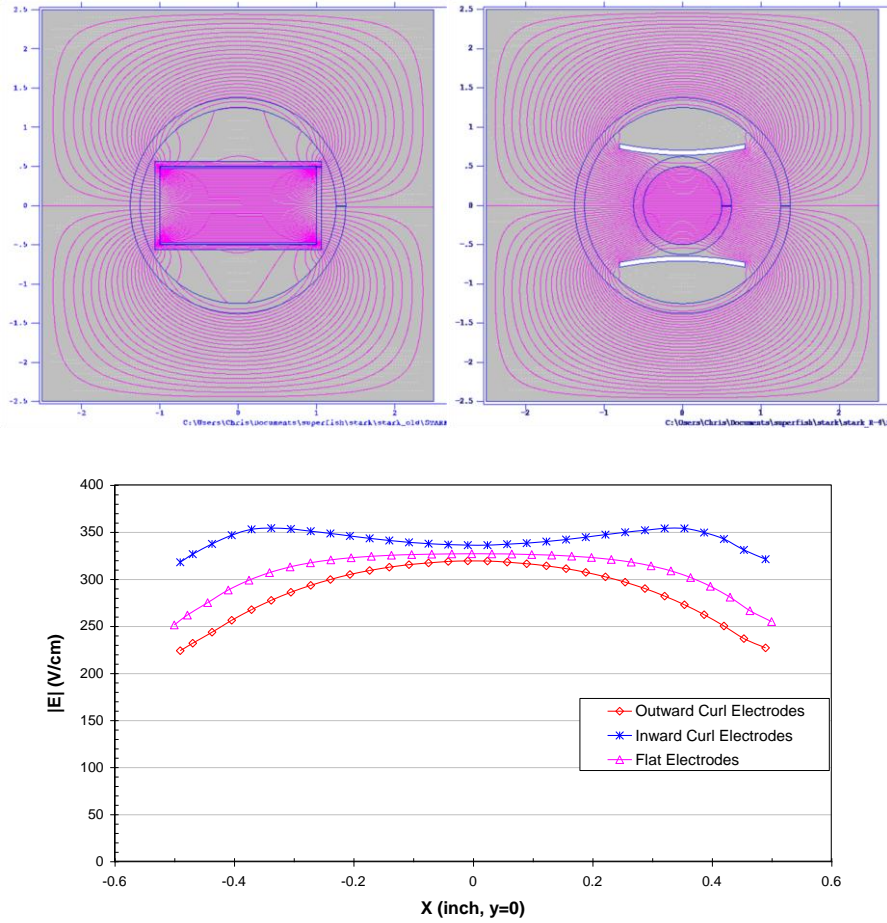
temporal resolution up to 2 MHz. For increased temporal resolution, a Stark effect methanol laser (as employed with FIReTIP) can shift frequencies further for 4 to 6 MHz resolution. Quantum cascade lasers offer a solid state source that can produce frequencies not limited by methanol's electronic structure [5]. They have the potential to be used for an LO source, and possibly replace the FIR lasers for the probe beam; however, they require extensive cooling. Current examples of ~2-3 THz QCL's specify operating temperatures below 100 K [6]. If coupled with more sensitive mixers they may be a viable option [7]; however, at present, this is beyond the scope of the FIReTIP system as currently funded and envisaged.

Improvements can be made to the Stark effect laser to produce a high power (> 50 mW) source at 2.5 THz. The FIReTIP Stark effect laser is limited in power and mode quality due to the waveguide design. It uses a rectangular waveguide, metallized on two surfaces. This essentially makes a parallel plate capacitor. Ideally, the electric field should be uniform across the waveguide interior; however, fringing field effects result in a non-uniform electric field. When tuning the cavity length for a specific frequency offset, only a portion of the methanol molecules will have the appropriate applied electric field. In addition, rectangular waveguide does not couple well to Gaussian modes. The observed dominant output mode is TEM_{10} . TEM_{00} can be achieved; however, it can be difficult to tune for. The resulting power output is about $\frac{1}{4}$ of that of the conventional methanol lasers. The FIReTIP IF electronics currently have a limited bandwidth of 4 MHz. If an improved Stark laser were developed, these would need to be upgraded as well, which is comparatively easy compared to designing a new laser. However, improving the Stark design to produce higher power and better mode quality could be of immediate utility. A round waveguide, similar to the conventional FIR lasers, will improve coupling to the TEM_{00} mode; however, the electrodes will be separated from the waveguide and will follow a Rogowski profile [8]. By curving the edges of the electrodes, the resulting electric field can be controlled to maintain a relatively constant field strength inside the waveguide [9]. The presence of other materials in the vicinity of the electrodes will further shape the field; therefore, these materials should be accounted for during the design process. For example, the material and thickness of the laser waveguide and the water jacket must be included.

These types of electrodes have been designed for similar applications, such as TEA lasers [10, 11]. It can be difficult to design an ideal profile that will also be easy to manufacture. The potential for electrical breakdown must also be avoided. Computer simulations of two dimensional fields are a tremendous asset for designing practical Rogowski electrodes. By separating the electrode from the waveguide surface, virtually any shape can be employed; however, this type of design will necessarily place the electrodes further apart than the current Stark laser. This will require the applied voltage to be increased proportionally for the same field strength. Development of an improved Stark laser design has been conducted, and should additional power be needed to expand the FIReTIP system, an improved Stark laser could be developed.



Figures 189a and 189b. Left: Current Stark laser waveguide design. A rectangular waveguide with two conductive surfaces. Right: New Stark waveguide and electrode design concept. The electrodes are a pair of curved metallic plates on either side of a round waveguide. Note: There are two thin conducting strips on the inside surface of the waveguide. These are required to avoid building a static charge on the waveguide surface [12].



Figures 190a, 190b, and 190c.¹ Top left: Simulation of electric field lines for the current Stark design. The fringing fields are circled in blue. Top right: New Stark electrode design. The curved electrodes produce a uniform electric field across the waveguide cross section. Bottom: Simulation of the electric field strength across the waveguide for different shape electrodes.

V.2 High- k_θ Scattering System Improvements

As mentioned previously, the High- k_θ Scattering System will employ a 4-channel receiver during initial installation. A second 4-channel receiver will be added at a later date to expand the receiver to an 8 x 1 linear array. This will expand the range of k_θ coverage for individual plasma shots as well as the total

¹ Electric field plots provided by Dr. Christopher M. Muscatello.

possible coverage. The receiver optics are already designed to accommodate the 8 x 1 array. All that needs to be done is purchase the new mixer array, and install it on the receiver carriage. The IF electronics currently supports four channels for IQ demodulation; however, a second, identical IF electronics box can be assembled and delivered in short order. The only other component needed will be a second digitizer for additional channels and data storage. These can be purchased commercially.

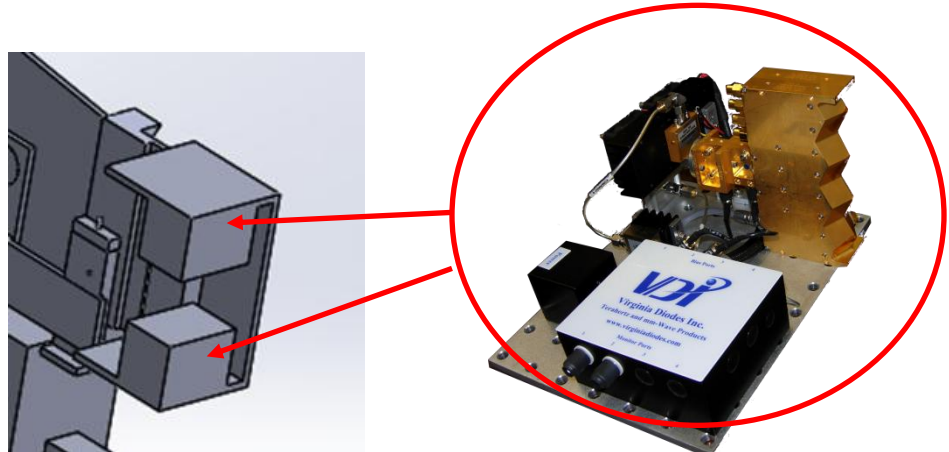


Figure 191. The VDI receiver mixer array is mounted at the rear of the receiving optics. For initial installation, one 4x1 array is installed in the top position. A second 4x1 array will be mounted in the lower position at a later date. Both arrays are identical; however, they will be mirror images of each other so they can be mounted together for a seamless 8x1 array.

UC Davis is developing a vacuum electronics source that can be applied to the High- k_0 Scattering system. At present, the receiver mixer uses a 14 GHz LO source for 48th subharmonic mixing with the 693 GHz RF signal. A 346 GHz Backward Wave Oscillator (BWO) is being developed to allow 1st subharmonic mixing. A BWO is a class of vacuum electronic devices (VED) that is used as a source for high frequency and high power electromagnetic waves [13]. An electron beam is passed through a slow wave structure (SWS) at high power, while being focused by an axial magnetic field. The slow wave structure is designed such that electromagnetic waves propagate at velocities similar to the electron beam. Kinetic energy from the electron beam can then be converted to RF energy. The slow wave structure is designed

with a geometry to be dispersive to a range of transiting RF wave frequencies, where various frequencies will propagate at different velocities. The electron beam velocity is then tuned by varying the electron gun cathode / anode potential difference. This will select which frequency is energized by the beam. In a BWO, the generated RF wave phase and group velocities are in opposite directions; therefore, when energized by the electron beam, the RF wave will travel and grow in the opposite direction. A waveguide coupler connected to the slow wave structure directs RF energy out of the device. Only a small amount of the electron beam energy is converted to RF energy. The bulk of the beam energy passes through the vacuum cavity to a collector. The collector recovers the electron beam to complete the electrical circuit, and disperses any heat generated. High power electron beams (50+ kV) can generate harmful x-rays due to Bremsstrahlung radiation as high energy electrons impact the collector; however, for the devices suggested for use with the High- k_0 Scattering system this is not a concern since the beam energies are in the 10-20 kV range. Depressed collectors can be employed to increase electrical efficiency. A depressed collector uses one or more stages to apply an electric field to slow the spent electron beam. The energy given by the electrons to the field can be recovered and reused, increasing the electrical efficiency and reducing the heat generated [14].

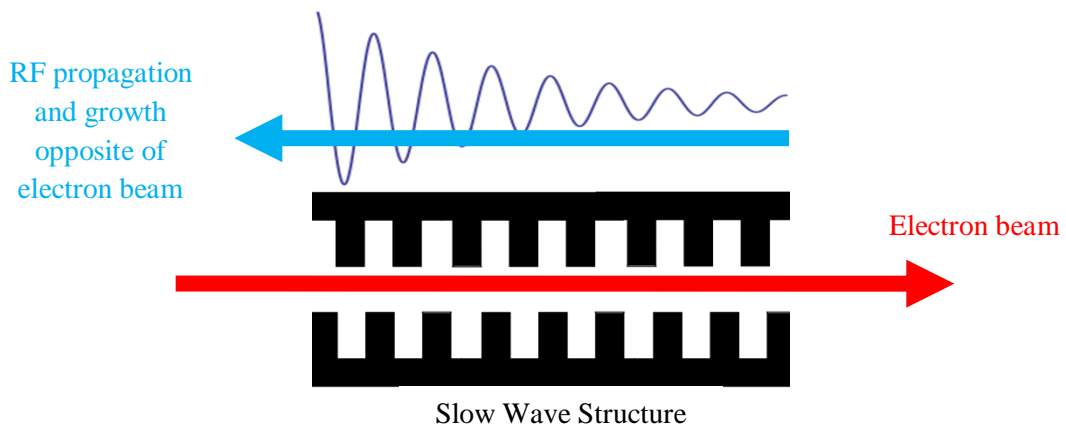


Figure 192. Schematic of BWO operation. The electron beam (red) passes through the slow wave structure from left to right. The RF wave grows and propagates from right to left.

Utilizing this BWO as a LO source can reduce the conversion loss and improve the signal to noise ratio of the receiver. Each receiver mixer generally requires a few mW of LO power, and the expected BWO power output of ~ 1 W will be able to drive many more mixer channels than currently envisioned. BWOs offer a relatively high power, voltage tunable, and compact source, as compared to lasers or solid state sources [15]. If this BWO is successful, it may be possible to scale it down by a factor of two for operation at 693 GHz. Alternatively, a frequency doubler could be developed. At 693 GHz, the optically pumped FIR laser could be replaced entirely. This has enormous benefits to the size, complexity, and hazards of the High- k_0 Scattering System. The CO₂ laser is 8 feet long and weighs 150 lbs. The 160 W CO₂ beam is an obvious danger. The formic acid laser is also large and heavy at 7 feet long and 60 lbs. The additional space for the CO₂ beam coupling, focusing, and shielding also occupies several square feet. All of this equipment could be replaced with a unit less than 12" long and under 50 lbs., the vast majority of which is the collector and cooling system. Both approaches require a water chiller and high voltage power supply; however, there are additional benefits. Storage and handling of formic acid would no longer be a concern. Tuning and maintaining either laser can be a tedious process. The laser system has increased operational costs due to gas and acid consumption. Optical components require periodic inspection and replacement, such as diffraction gratings and output couplers. The size of the lasers requires they be moved outside of the test cell, and long waveguide runs installed. Once constructed, a BWO is simple to operate. It is evacuated to $\sim 10^{-10}$ Torr, the cooling system circulates water, and the high voltage source is activated on demand. The BWO output can be connected to a horn antenna to couple the beam into free space. A true CW source is unlikely due to the power output and small structure features are vulnerable to high thermal loads [16]; however, long pulse should be achievable. Confinement times at NSTX-U are expected to reach ~ 5 seconds [17]; therefore, 5 second BWO pulse lengths can be treated as if the High- k_0 Scattering System were CW.

V.3 Microfabrication Techniques

The most precise components of high frequency vacuum electronic devices are the slow wave structures.

The ability to fabricate these interaction circuits may determine the overall feasibility of a proposed design. Many methods have been used to fabricate high frequency slow wave structures, including: 1) deep reactive ion etching (DRIE) [18, 19], 2) photo lithography (LIGA) [20, 30], 3) electric discharge machining (EDM) [21, 22], and 4) Nano-CNC-machining [23, 24, 38], among others. Each of these have advantages and disadvantages. For the proper applications, each of these methods can perform exceptionally well. For this investigation, they will be evaluated for the fabrication of VED slow wave structures between 200 and 400 GHz.

With increasing frequency, the slow wave structure fabrication is more difficult. Dimensions become smaller, tolerances are tighter, and the surface finish must be smoother. They are enclosed structures, sealed for high vacuum, and allow an electron beam pass through them without intercepting the circuit. They are typically fabricated in two halves to access the interior structure, and then the two halves are fitted and bonded together to make a slow wave structure to pass the electron beam, with the circuit structure surrounding it. Low frequency circuits have long been proven, and can be very large, on the order of several wavelengths designed for [25]. These designs can be scaled down for shorter wavelengths; however, because they are smaller, more fragile circuits, they are prone to overheating much quicker, reducing the power handling capability of higher frequency devices. At very high frequency, the dimensions and tolerances simply exceed the capabilities of current technology. The surface finish of the slow wave structure must be much smoother than the wavelengths designed for. Excessive surface roughness can cause EM scattering, reflections, and increased absorption. A rule of thumb is that the surface finish R_a should be less than the skin depth of EM penetration for the given wavelength and material conductivity [26]. R_a surface finish is defined as the average variation of surface height over a localized area [27].

$$\delta = \sqrt{\frac{2}{\mu\sigma\omega}}$$

where δ is the skin depth, μ is the magnetic permeability, σ is the surface conductivity, and ω is the angular frequency of the RF wave.

For a circuit designed at 346 GHz, the minimum surface finish is \sim 100 nm R_a . Individual circuit features can be expected to measure 50 to 100 μm , with a sub-micron dimensional tolerance. Furthermore the microstructure of the slow wave structure can be expected to possess \sim 3:1 aspect ratios, which makes their fabrication non-trivial.

V.3.1 DRIE

Deep reactive Ion Etching accelerates ions with a strong electric field towards a substrate. A mask of the desired circuit shape will cover portions of the substrate not to be etched. Kinetic energy from the ions can physically displace material, and the ions are chosen to react chemically with the substrate to make the material volatile, and more easily removed. As the etching process cuts deeper into the material, it can undercut the masked area. To keep the sidewalls vertical during high aspect ratio etching, the substrate walls can be pacified to prevent further lateral etching. The result is a slight scalloping of the sidewalls. It is a slow, but accurate process. DRIE can construct high aspect ratio circuits needed for these types of structures up to \sim 0.5 mm deep [28]. Experiments were conducted with silicon, and then gold plated. The dimensional tolerance was good; however, the gold plating was found to have poor adhesion under high thermal loads. There may be short pulse applications where this is an acceptable solution, but any loss of the plating material will become ionized immediately and accelerate towards the negatively charged

cathode. Any contamination on the electron gun emitter cathode will quickly ruin the electron gun. UC Davis determined that DRIE was not suitable under these conditions.

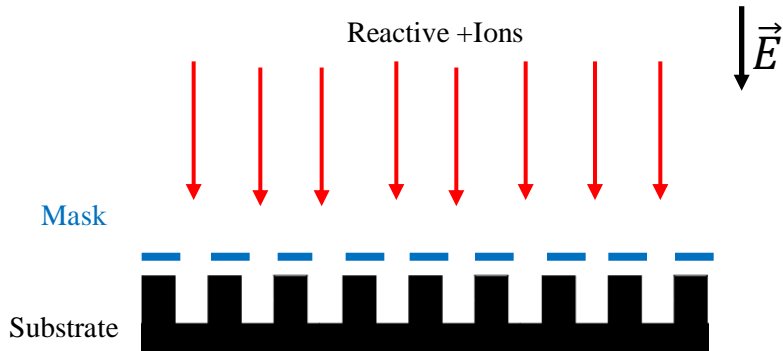


Figure 193. Deep Reactive Ion Etching. Ions are accelerated past a mask to etch a substrate material with both chemical and kinetic energy.

V.3.2 Ultra Violet LIGA (Lithographie Galvanoformung und Abforung)

UV LIGA was performed with some success for the 220 GHz TWT slow wave structure [29]. X-ray LIGA is generally considered superior; however, powerful x-ray sources are in short supply for this type of research. UV LIGA can work in limited circumstances. LIGA is a photo lithography technique [30], where a photo reactive material is applied to a metallic substrate. A mask with the circuit geometry covers the substrate, and it is exposed to UV light. The portion of the photo reactive material that is exposed, will undergo a chemical change. The unexposed portion of the material can then be dissolved away, leaving behind a negative mold of the circuit. The circuit is formed by electroplating on the substrate around the mold, and then the mold is removed. Very fine structures with high aspect ratios can be made this way; however, UV diffraction from the mask limit the depth of the mold. UV exposure tends to broaden with increasing depth, creating side walls that are undercut near the base. For applications at 220 GHz, the circuit feature depth was 385 μm , and side walls averaged about 1° from normal. Efforts at 220

GHz were eventually successfully; however, the difficulties in the process dissuaded experiments for the higher frequency 346 GHz BWO. Limitations for LIGA techniques include the long fabrication preparation times. The UV mask must be custom made, and the formulation of the photo resist has many variables which take a long time for a technician to master. Removing the mold material from delicate circuit structures can be difficult, and it is easy to destroy the part. Each time a different circuit geometry is fabricated a new mask is needed, and long lead times between efforts can be expected. Surface finishes between 50 and 100 nm R_a are possible; therefore, there is promise that this technology can be used in low THz devices. LIGA is typically a two dimensional approach to circuit design because the mold is the same depth across the substrate. It is possible to perform multilayer LIGA [31] structures or a hybrid LIGA / machining approach to make three dimensional structures. This approach greatly increases the complexity of fabrication, and adds significant cost and time to the development process. This level of development is beyond the scope of the research performed so far.

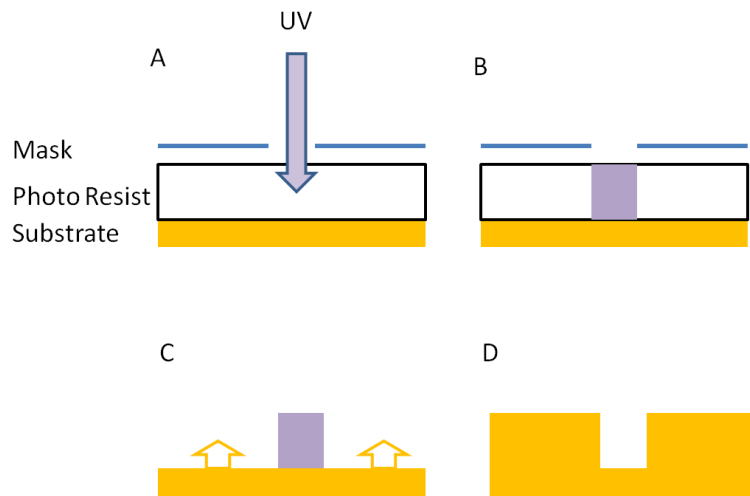
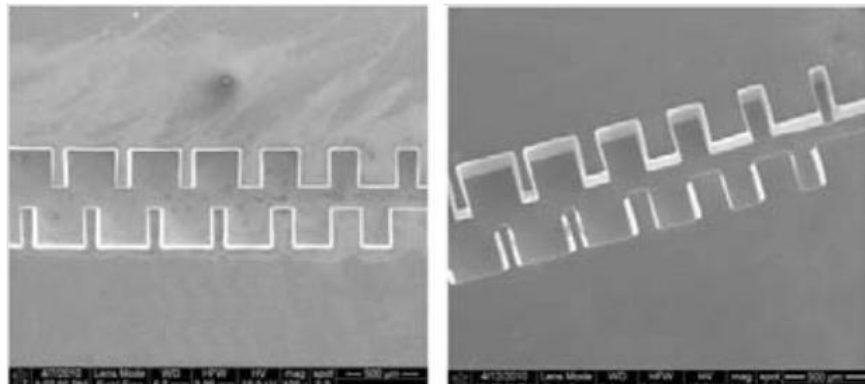


Figure 194. UV LIGA process. A: Photo resist is applied to a copper substrate. A mask covers the top, and UV light is applied to the exposed photo resist. B: The exposed photo resist undergoes a chemical change. C: The mask and unexposed photo resist are removed leaving behind a negative mold. The substrate material is electroplated around the mold. D: The mold is removed, creating a precise circuit matching the dimensions of the mask.

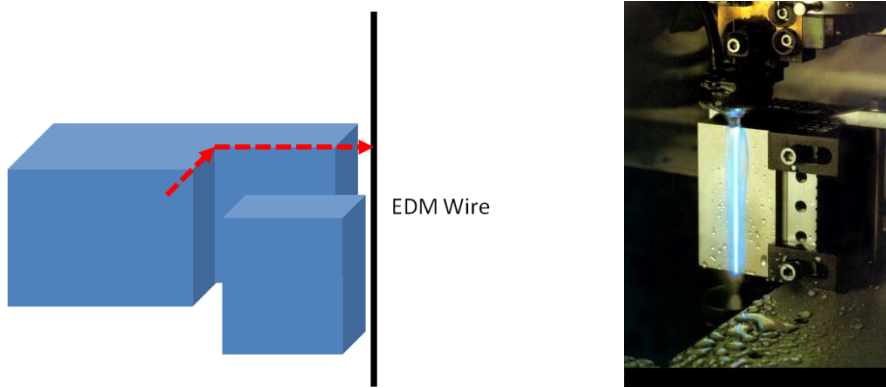


Figures 195 and 196. SEM images of UV LIGA fabricated 220 GHz TWT slow wave structure. Left: Slow wave structure with transition from above. Right: Isometric view of transition portion of the circuit. The vanes get wider, and the space between them are narrower, while maintaining the same period length.

V.3.3 EDM

Electric discharge machining has an advantage for cutting precise structures profiles, or cutting blind holes with variable depths. EDM uses a wire in close proximity to a conductive part, submerged in dielectric oil, with a pulsed high voltage discharge to produce an electric arc to nearby surfaces. The resulting heat at the point of the arc will melt the substrate in a very localized manner. There is no physical contact between the wire and the substrate; therefore, it can cut fine features [32]. Standard wire EDM passes a wire through a material to cut perpendicular to the wire. Sinker style EDM uses a wire probe to cut in line with the wire direction for a finite cutting depth. This method is useful for cutting difficult geometries with variable heights, and for hard materials. Ultimately, the utility of EDM for VEDs is limited by the quality of the surface finish. The overlapping electrical arcs create small craters with typical surface finishes for conventional EDM of ~ 500 nm R_a [33]. New developments in micro-EDM technology is showing vast improvements in surface finish. Experimental EDM machines are reporting surfaces as fine as 10 nm R_a [34]. With dimensional accuracy on the order of ~ 1 μm . This technology may prove to be of great utility. Most research efforts focus on cutting very hard materials,

such as tungsten carbide, and the performance on more ductile, yet highly conductive, materials such as aluminum and copper still need investigating. The advantage over conventional machining is its versatility for more complex geometries, being able to cut near square inside corners, and the ability to cut very hard materials, such as stainless steel, tungsten, or titanium.



Figures 197a and 197b. Left: EDM wire passing through a part taking a "L" shape path, making a well defined inside corner. High voltage pulses arc between the wire and the part to create localized heating to vaporize the material as the wire passes through it. Right: Photo of EDM cutting. The bright blue line is the electrode wire.

V.3.4 Nano-CNC-machining

Conventional CNC machining has been a boon for manufacturing for decades by automating machine controls. Improvements in machine designs and computer controls have made machining processes fast and accurate for most industries. Typical precision of $\pm 0.0005"$ tolerance is readily available, and with skilled operators and specialized equipment $\pm 0.0002"$ can be achieved. This level of precision is suitable for slow wave structures up to ~ 100 GHz for most applications [35]. To manufacture VEDs in the low THz region, more precision is required. Micromachining is a growing market, where high precision machines are available. The term "micromachining" has no set definition, but it generally refers to a

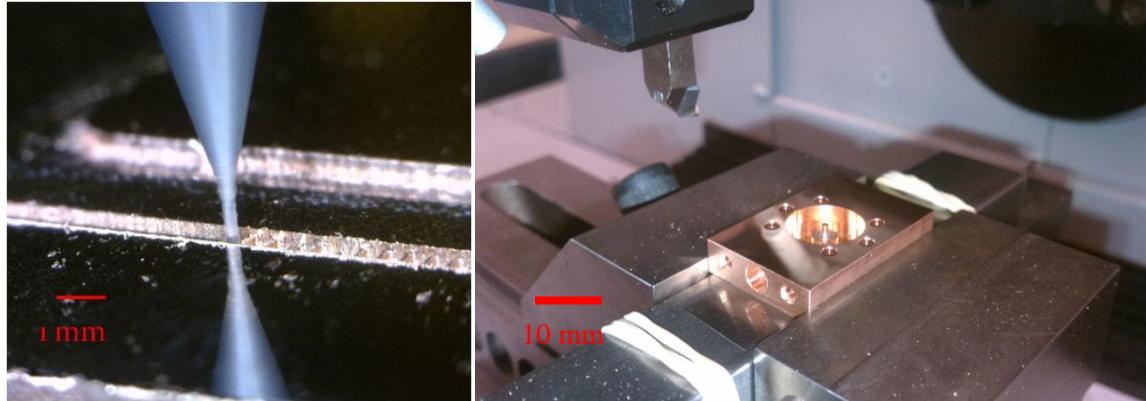
machining process where either the parts to be produced are < 1 mm for major dimensions, or the tolerances to be maintained are on the order of 1 micron.

UC Davis has access to a prototype Nano-CNC-mill called the NN1000. It was developed by Digital Technology Laboratory (DTL), a subsidiary of Mori-Seiki machine tools (now DMG-Mori) [36]. The NN1000 "nano-mill" is not available commercially. The reference to "nano" is a colloquial name, ascribed to the machine because it has nanometer command resolution. The actual precision of the machine depends on the type of operation, material, and tooling used. Some position error is expected in the 10s or 100s of nanometers level. With proper calibration and operation, it is fair to claim sub-micron precision, or $\pm 2 \times 10^{-5}$ inches, when fabricating the TWT and BWO slow wave structures. The NN1000 is a 5-axis (X, Y, Z, A, and C) CNC mill. Its travel limits are 120 mm (X) by 100 mm (Y) by 50 mm (Z). The A axis rotates $\pm 90^\circ$ about the X axis, and the C axis can rotate 360° about the Z axis. The machine features ceramic air bearing guideways, laser scale position sensors, linear drive magnetic servos, a granite foundation, air floating vibration isolation, and a pneumatic spindle capable of 55 kRPM. Alternatively, the spindle can be replaced with a fixed mandrel for linear scribing. The NN1000 is installed on a vibration isolation pad in a room with ± 0.1 C° temperature control.



Figure 198. NN1000 developed by Digital Technology Laboratory.

This machine has proven to be essential to VED development at UC Davis [37, 38]. It accepts standard G-code programming, with only a few minor changes for specialized spindle control. Programs can be written manually, or through the use of commercially available CAM software. Complicated geometries can be programmed for in a matter of minutes. When small changes to circuit dimensions are made, the NN1000 is easily updated. The shortfalls of this technology are it necessarily machines parts one at a time, and micromachining is not a rapid process. This makes the NN1000 very useful for research and development, but not for mass production. Machining processes are limited by the tooling available, which in turn depends on the material to be machined [39]. Most dimensional errors are due to tooling vibration or displacement under load. Tooling wear must also be carefully monitored, and controlled with either programming offsets or tool replacement. This places a large portion of the quality control with the machine operator. For a computer controlled process, it is far from being truly automated.



Figures 199a and 199b. NN1000 machining operations. Left: 254 micron diameter tool milling a 220 GHz TWT slow wave structure. Right: Diamond scribe planes the top surface of a MEMS device.

V.4 Vacuum Electronic Devices

Backward Wave Oscillators are one type of vacuum electronic device (VED). Other types include traveling wave tubes (TWT), klystrons, gyrotrons, and magnetrons [14, 16, 40 - 43]. In general, they all

generate or amplify RF energy by converting energy from electron beams. Vacuum electronics offers high reliability and great efficiency for high frequency and high power electromagnetic waves. The magnetron, first used for radar stations during world war two [44], is now found in every home's microwave oven [45]. Vacuum electronics are used almost exclusively on communication satellites, where electrical power is limited by batteries or solar panels [46]. Furthermore, in space-borne systems waste heat can be extremely problematic. Imaging systems for medical and security applications widely depend on vacuum electronics, where organic materials often have spectral signatures in the millimeter wave region [47]. Radar systems continue to be developed for increased frequency and power, and are manufactured in small, less expensive, and more efficient packages [48]. VEDs are well suited for fusion power research. Many characteristic frequencies of fusion plasmas are in the 10s or 100s of GHz. Many plasma diagnostic instruments utilize these devices. In a slight variation of vacuum electronic principles, fusion plasma heating can be achieved by passing high power electromagnetic waves through a fusion reactor to transfer energy to the electrons and ions within [49]. Power handling capabilities of vacuum electronic devices fall off at $1/f^2$ [50], with few options in the terahertz region. In the infrared and higher frequency spectrum, lasers can provide high power sources; however, lasers are limited to discrete frequencies. The empirical minimum availability and lowest power devices near 1 THz is colloquially known as the THz gap [51]. Applications in THz waves are motivating research to develop various devices to act as sources and amplifiers.

There are three major components to VEDs, an electron gun, slow wave structure, and collector. Furthermore, the electron beam must be focused by an axial magnetic field, and most VEDs require a liquid cooling system to dissipate excess heat generated. The electron gun supplies the electron beam, which will be the source of energy for the slow wave structure. The slow wave structure is the interaction circuit where energy from the electron beam is converted to RF energy. A strong axial magnetic field focuses the electron beam through the slow wave structure. There is typically very little clearance between the beam and interaction circuit, and it is important to eliminate any beam interception. The

collector recovers the electron beam, and helps dissipate any heat generated. The author's primary contribution for UCD's VED development was the microfabrication of the slow wave structure; therefore, this dissertation will focus on that process.

V.4.1 Slow Wave Structures

Slow wave interaction circuits are periodic structures designed to control EM wave propagation over their design range. To exchange energy with a coincident electron beam, the electron beam needs to have a velocity comparable to the effective velocity of the EM wave on the slow wave circuit. In the case of TWTs, a broad range of frequencies will travel near the same phase velocity. This enables a broad range of interaction for a given electron beam velocity. An RF input port will insert a small amount of RF energy within the design bandwidth. As the RF travels through the TWT, it will gain energy from the electron beam, amplifying the signal [52]. An RF port near the opposite end of the circuit will couple the RF power out. Oscillations are undesirable so that only the inserted RF power is amplified. Sometimes an RF sever is included near the center of a TWT interaction circuit by adding RF absorbing material. This RF sever will attenuate RF signals to eliminate oscillation power. However, during interaction with the RF signal, the electron beam will become velocity modulated, which is passed through to the second half of the circuit. RF gain will be achieved in the second half of the interaction circuit resulting in increased stability and gain than could otherwise be achieved. A BWO uses a different approach by dispersing the RF phase velocity within the slow wave structure. Over the designed bandwidth, the electron beam will only interact with a very narrow bandwidth for a given electron beam velocity. Altering the beam voltage will change the beam velocity, which will then interact with different RF frequencies. Oscillations at the resonant frequency will gain power and propagate backwards through the circuit due to the negative group velocity. An RF port near the electron beam entrance will couple RF power out. This device is therefore a voltage tunable source [53].

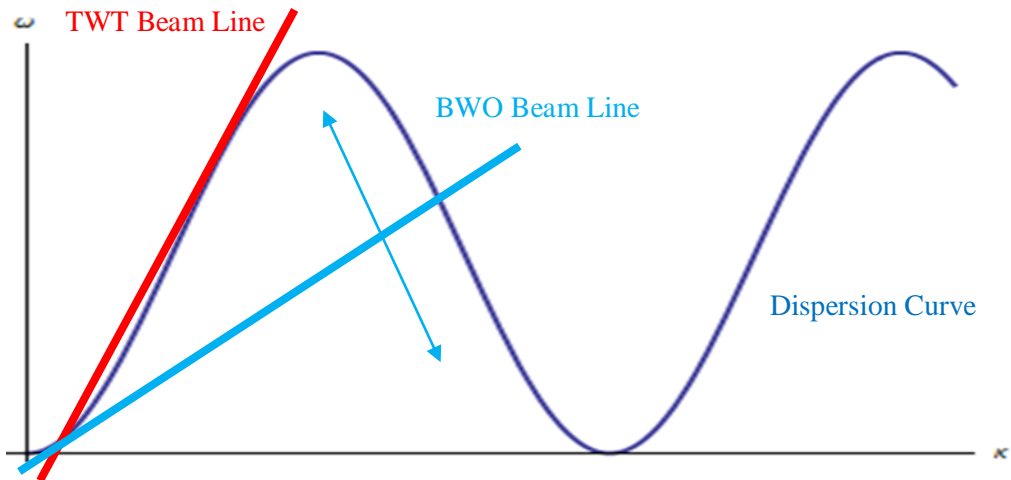


Figure 200. Dispersion plot for a generic slow wave structure. Angular frequency (ω) is plotted versus wavenumber (k). Phase velocity is the slope of the plot position, ω/k , and group velocity is the slope of the dispersion curve at any given point, $\delta\omega/\delta k$. The red line shows the interaction bandwidth for a given beam velocity. A broad range of frequencies can interact with the beam shown by the proximity of the beam line with the dispersion curve. The blue line represents the beam line for a BWO. The interaction between the beam line and dispersion curve is very localized; however, the beam voltage can be altered to change the position of the beam line, thereby changing the interaction frequency. The negative slope of the dispersion curve indicates a backward propagating wave.

V.4.2 Electron Guns

The electron gun consists of an impregnated tungsten cathode heated to high temperatures. A nearby anode at high voltage will cause the electrons to accelerate in the applied electric field; however, an axial magnetic field will steer capture the charged particles, and direct them down the slow wave structure axis. There are many factors to consider for electron gun design: beam current, beam profile, magnetic field profile, beam velocity, and cathode lifetime. The beam current and profile will determine the current density, and the type of cathode material and temperature needed. UC Davis manufactures its own tungsten scandate nano powder cathodes [54], which can deliver exceptionally high current density with

long lifetimes. Conventional dispenser cathodes can deliver ~ 10 A/cm² for up to 1000 hours. Typical applications use a cathode loading of 2 A/cm² with lifetimes up to 10^5 hours. Scandate cathodes offer much higher performance. Short pulse (5 μ s) testing produced ~ 100 A/cm². Lifetime testing is ongoing, and at last check UC Davis scandate cathodes have produced 50 A/cm² consistently for $> 10^4$ hours [54]. The magnetic field profile is critical to ensure that electrons are captured and focused down the beam tunnel for the applied voltage. The applied voltage between anode and cathode determines the beam velocity, which must match the desired RF propagation velocity for the desired output. The magnetic field focuses the beam to maintain current density, and to prevent beam interception along the slow wave structure, which can quickly overheat and destroy the device. The cathode dimensions, spacing, anode surface, and so forth must also be careful not to promote electrical breakdown, thereby shorting and damaging the system. All pieces of a vacuum electronic device are carefully designed to be integrated together. While the process is painstaking, the reward is a simple to operate, reliable source for high frequency and high power emissions.

While conventional round tungsten cathodes are commercially available [55], high performance, nanocomposite, scandate cathodes must be custom fabricated. Using Nano-CNC-machining, UC Davis can fabricate custom cathode emitter profiles. The tungsten scandate nano powder material is fragile, and prone to contamination. Its high current density potential is due to its porous surface structure to increase the available surface area. Shaping cathodes with conventional carbide tooling tends to promote burr formation across the surface pores, thereby filling in the pores, and reducing the cathode performance. Near the edges of the cathode, there is less support for the cutting tool pressure, and edge chipping can occur. Poor cathode edge definition can alter the designed beam emission profile. With the NN1000 precision, and monocrystal diamond tooling, the cathode surface quality and edge dimensions are maintained.

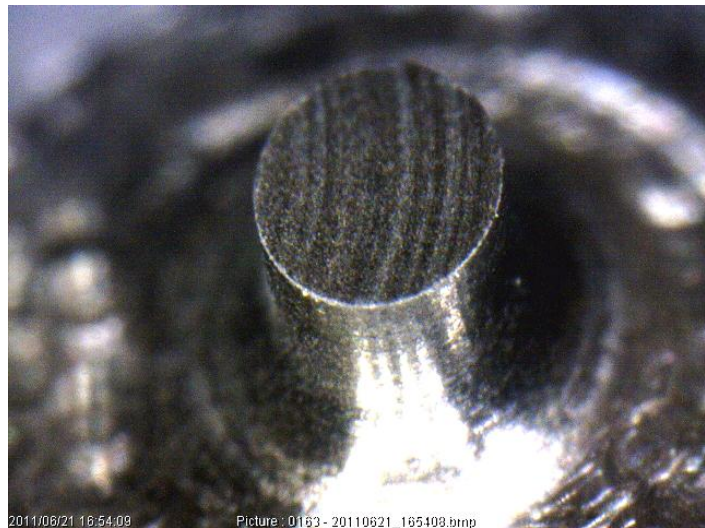


Figure 201. Tungsten scandate nano power cathode machined by the NN1000. The central pedestal top is the emission surface. It is oval shaped, measuring 1.0 mm x 0.8 mm. After machining with diamond tooling, the surface retains its porosity and edge definition.

The electron gun is driven with a high voltage power supply. A heater on the electron gun cathode will supply the desired current; however, it is the anode voltage that will determine the beam velocity. The beam velocity is designed to work with the proper magnetic field at full power. Drops in beam voltage can cause defocusing and severe beam interception. The power supply and device should be designed with safeguards for proper voltage, arc detection, and normal high voltage safety. A properly designed power supply will provide reliable operation, and deviations from the design parameters can cause the VED to fail.

V.4.3 Collector

The collector will receive the spent electron beam to complete the electrical circuit, and can absorb most of the waste heat generated. The axial magnetic field dissipates and diverges at the collector, allowing the electrons to spread across the collector's interior. Baffled structures cause reflected electrons to be

captured within the collector. High energy electrons impacting the surface can introduce ionized material in the slow wave structure, which can quickly damage the cathode. To improve efficiency, reduce heat, and reduce secondary effects due to high energy electrons, depressed collectors are often designed. The collector body is negatively charged to create an electric field opposing the electron velocity. As the electrons work against the field they are slowed to safe velocities and this energy can be reclaimed. The efficiency of a collector design depends on the velocity distribution of the spent electron beam. If the electron energy distribution is broad, multistage depressed collectors can be designed to be more effective [56]. The collector design can increase device efficiency to impressive levels. In satellite applications, space-TWTs are used extensively to amplify communication signals from C band to Ka band [57]. Space applications are highly motivated to operate with high efficiency. Power availability is limited to batteries or solar panels, excess heat can be problematic due to the insulating environment, and higher efficiency directly correlates to increased communication capacity and increased revenues [58]. Overall efficiencies of space-TWTs are routinely above 70%. To achieve these levels, typical component efficiencies are: electronic efficiency 30+ %, circuit efficiency 90+ %, and collector efficiency 80+ % [58, 59]. The proposed BWO for the High- k_0 Scattering System is a terrestrial based VED, and not subject to the stringent demands of space borne systems. Additional power consumption and collector cooling is easily accommodated; therefore, a single stage depressed collector will satisfy the current needs.

V.4.4 Magnetic Focusing

The axial magnetic field is also challenging, not only to design, but to construct and verify. The magnetic field profile must be carefully tailored to capture electrons emitted from the cathode, and focus them through the slow wave structure without any beam interception. High energy electrons impacting the circuit can quickly overheat the material, causing ions to damage the cathode, or simply destroying the device. Too high a magnetic gradient can reflect electrons as a magnetic mirror. Once clear of the interaction circuit, the dispersion of charged particles must be incorporated with the collector design to

avoid localized heating, and maximize efficiency. The magnetic field tolerance is usually very stringent. Individual magnets from commercial sources must be verified for the field applied along the circuit axis. Either additional magnets can be purchased and sampled until a working set is identified, or the magnet mounts can be individually adjustable to tune the field to specifications. Establishing a proper magnetic field can be a sensitive and critical procedure.

V.4.5 Cooling

For all but short pulse, low duty cycle devices, some form of device cooling is required. Depending on the expected thermal loads, many types of cooling systems can be designed. Typical designs circulate water to a chiller or radiator. For high frequencies, thermal expansion could cause a problem with circuit dimensions. Uneven cooling can create thermal stress at vacuum seals. For reliable, long lifetime service, the cooling system should not be overlooked.

V.5 Design and Fabrication of the 346 GHz BWO and 220 GHz TWT

The 346 GHz BWO in development for use with the High- k_0 Scattering System is a collaborative effort between Davis Millimeter Wave Research Center (DMRC) of UC Davis, Lancaster University, and Beijing Vacuum Electronics Research Institute (BVERI). The details below are the result of a team effort, and at the time of this writing, the development is continuing in the absence of the author. While the final product has not yet been delivered, the details will demonstrate the design considerations, and technology employed. As a representative example of the BWO development, details and comparisons of a 220 GHz traveling wave tube are provided. These two devices have very similar circuit features, and manufacturing techniques. The 220 GHz TWT prototype was developed in collaboration with Teledyne Scientific & Imaging and Communications and Power Industries (CPI) as part of the DARPA Hi-FIVE project (grant # G8U543366). The goal was to create a high power amplifier centered at 220 GHz with 50 W output,

and a bandwidth of 60 GHz. This TWT will be incorporated into an all weather millimeter wave imaging system to reduce the effects of fog and rain on visibility. It has been successfully fabricated and tested [60]; however, development and refinement are continuing. The details of the 220 GHz TWT are discussed to show the design and manufacturing techniques proposed for the 346 GHz BWO are valid.

V.5.1 220 GHz TWT

The 220 GHz interaction circuit uses a half period staggered double vane structure with a 12.5:1 electron sheet beam. 80 periodic cells are fabricated with tapering sections at each end for impedance matching to input and output couplers. A sever is included near the center of the interaction circuit by machining an opening over a portion of the circuit and adding lossy material. The interaction circuit is divided into two sections, each with its own input and output couplers [61]. A cold test circuit is manufactured first to measure the RF S-parameters of each circuit half. For cold testing, the sever is omitted. The circuit is connected to 180 - 270 GHz BWO, and the applied RF is swept through the frequency range. A network analyzer will simultaneously measure the transmitted and reflected power. Low reflection and high transmission is desirable. Circuit gain is expected to produce up to 10 dB/cm [62, 63]; therefore, circuit losses must be much less than this value to be useful as an amplifier.

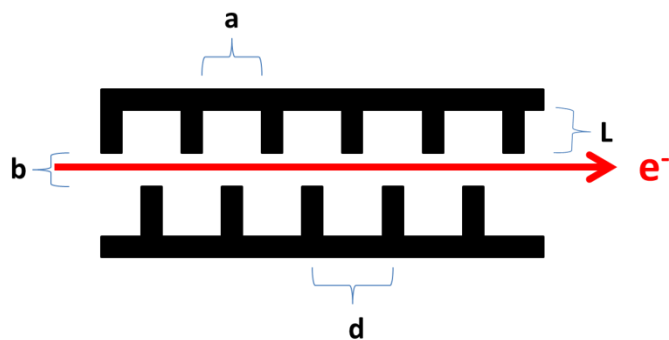


Figure 202. 220 GHz TWT circuit design: $a = 350 \mu\text{m}$, $L = 320 \mu\text{m}$, $b = 150 \mu\text{m}$, $d = 468 \mu\text{m}$, and the width of the circuit is $770 \mu\text{m}$ (distance into the plane of the page). For the LIGA fabrication process each circuit half will be electroplated to a height $\frac{1}{2}$ of the circuit width, $385 \mu\text{m}$.

Several cold test circuits were manufactured. First, UV LIGA was used. The circuit was made in two halves, divided across the beam tunnel center aligned with the electric field plane (E-plane split). The interaction circuit transitions were designed with decreasing slow wave structure dimensions. The interaction cell design alternates between vanes and cavities. The vane thickness is 118 microns, and 350 μm between vanes, for a periodic length of 468 μm . The vane height (SWS depth) is 320 μm . The circuit width across the beam tunnel is 770 microns; however, because the circuit is divided across this dimension, the UV LIGA process will electroplate material to half this value at 385 microns. The sheet beam tunnel measures 770 μm wide and 150 μm tall. The overall length of the circuit is 40 mm. Initial fabricated circuits had alignment issues between the two halves. It was found that if the parts were misaligned by more than 3 μm , standing waves were observed during cold tests. Eventually, improved circuit alignment provided acceptable cold test measurements. The UV LIGA fabricated circuit was found to have a passband from 214 to 266 GHz, with S_{21} at -5 to -10 dB across the bandwidth. S_{11} averaged -7 dB [29, 60].

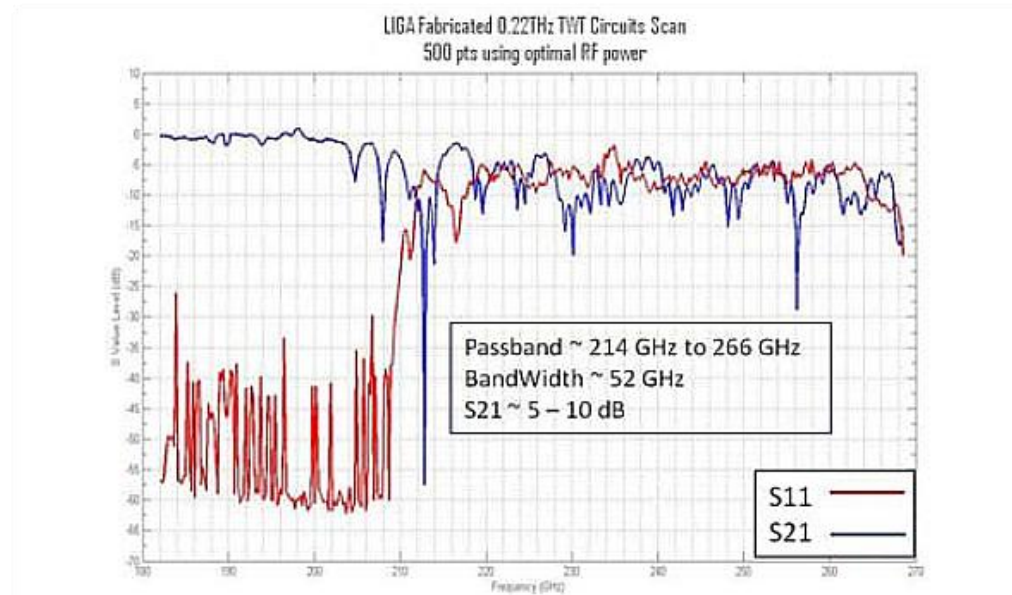
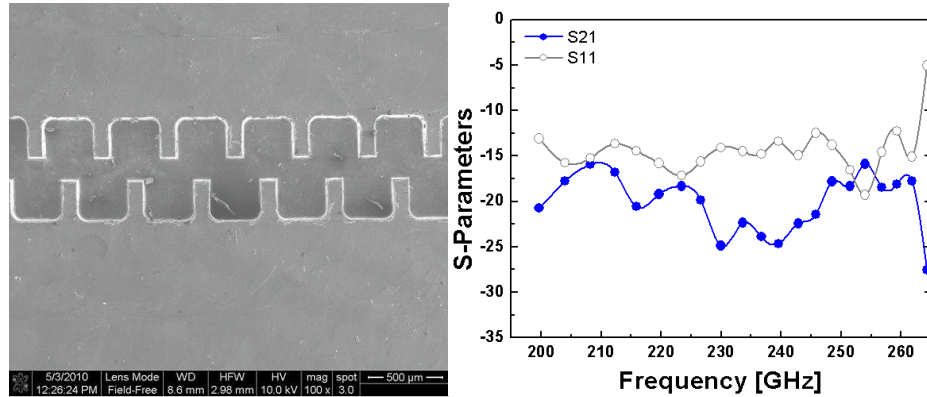


Figure 203. Cold test results for UV LIGA fabricated 220 GHz TWT slow wave structure [60]. Plot courtesy of Dr. Anisullah Baig.

In parallel with LIGA experiments, the NN1000 was first employed to fabricate the same circuit. The narrow beam tunnel and slow wave structure transitions limited the tooling diameter to 127 microns. At 385 microns deep, the machining tool needed a 3:1 aspect ratio. The circuit was first machined in aluminum to test the machine capabilities. The inter-part alignment was solved by including an integrated pocket and island surface feature alongside the interaction circuit. A 1 mm high rectangular protrusion was machined into one circuit half. The other half has a matching rectangular pocket dimensioned to zero μm clearance. When assembled, the circuit halves are positively aligned. Cold test measurements showed immediate results. S-parameters fluctuated across a 60 GHz bandpass; however, the average performance was a transmission of -20 dB, and reflection of -15 dB. Some circuit improvement was needed; therefore, the material was replaced with oxygen free copper. Copper is considerably more difficult to machine due to its ductile nature. If insufficient cutting pressure is applied, the material will be drawn out, rather than cut. Compounding effects will either cause poor surface finish, or increased tool wear and breakage.

Improved surface finish and edge definition was found when using dispersion strengthened materials such as Glidcop. This material uses a small percentage of alumina particles in the copper lattice structure to reduce the grain size of the material. This creates a highly conductive material (92% of oxygen free copper) that is much stronger than pure copper, and it resists annealing to a much greater degree, at high temperatures [64]. For microfabrication, the smaller grain size allows the material to separate easier without drawing long burrs. Alumina particles tend to wear the tooling faster; however, the net result is a better surface finish, and improved dimensional accuracy. Machining improvements were made when rotating the circuit division plane by 90° for an H-plane split. This allows better access for machine tools to cut the cell structure, employing larger diameter tooling with shallower depths of cut. Conventional designs prefer a E-plane circuit split so that there are no surface currents along the parting line between circuit halves. If there is any disruption in the surface currents, the desired EM modes will not be able to propagate along the circuit. The H-plane split will work if the circuit halves are perfectly flat, and fit together so that the two halves appear electrically seamless. Seamless circuits are achieved when the halves surfaced by the NN1000, and are diffusion bonded together. This precludes the ability to

disassemble the circuit for inspection or cleaning; however, the advantages for the machining process make this process worthwhile. The circuit transition couplers were redesigned to accommodate easier machining. Instead of progressively narrower slow wave structure transitions, the transition dimensions maintain a constant length with decreasing depths. The rotary cutting tools will leave a corner radius at any inside corner. Minor changes to the periodic cell for the H-plane split circuit were made to account for the inclusion of inside corner radii of 127 μm . The slow wave structure was then machined with 254 micron diameter, tungsten carbide tooling. Cold test results showed excellent performance with average S-parameters of -15 dB S_{11} and -5 dB S_{21} over a 50 GHz bandwidth [60, 65].



Figures 204a and 204b. Left: SEM image of Nano-CNC-machined 220 GHz TWT slow wave structure. Right: Cold test results, average S_{21} of -20 dB, and average S_{11} of -15 dB.

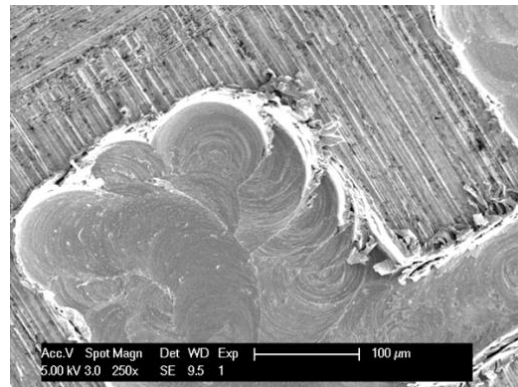
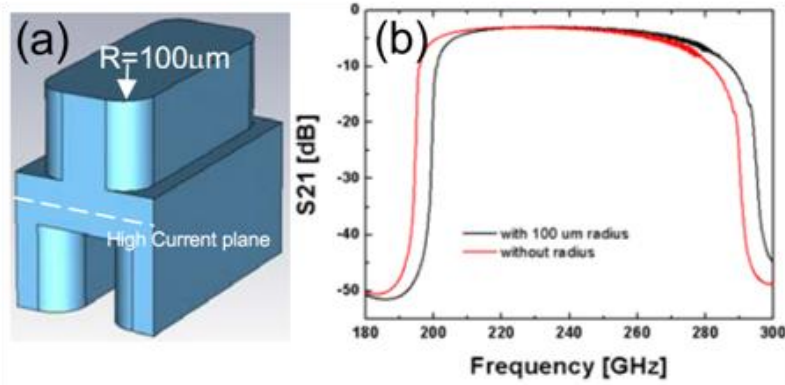


Figure 205. SEM image of micromachined oxygen free copper. The scalloped surface is unacceptable for operation at 220 GHz.



Figures 206a and 206b. Left: Unit cell of the H-plane split 220 GHz TWT slow wave structure. Right: Simulation of the effects of including the corner radii. The bandpass moves up in frequency by about 5 GHz. Images courtesy of Dr. Anisullah Baig.

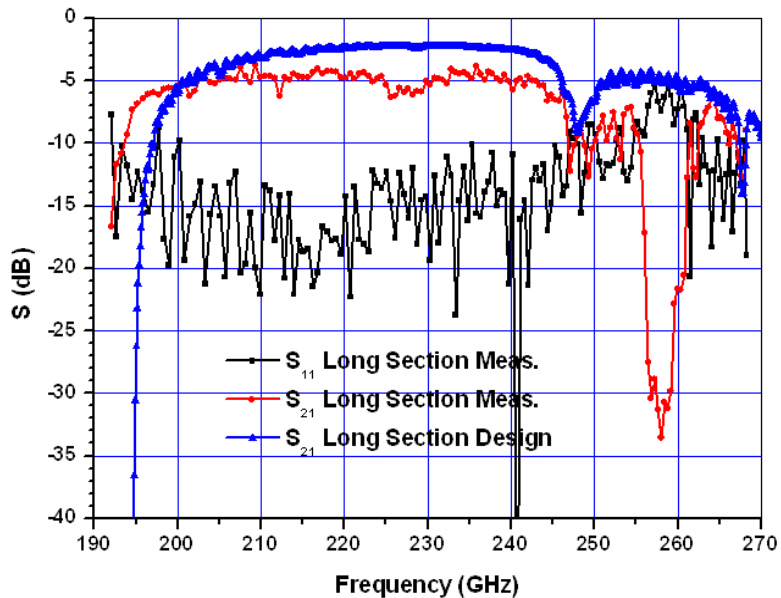
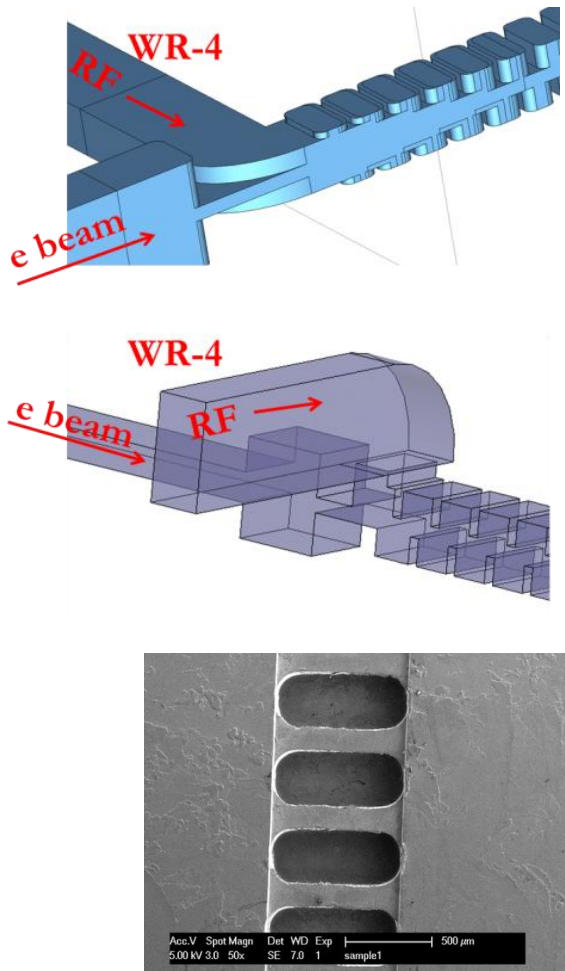


Figure 207. Cold test results for H-plane split 220 GHz TWT slow wave structure [66].

After successful cold test circuits were tested, several hot test circuits were manufactured with the NN1000. Two different RF couplers were fabricated in 2-layer and 3-layer designs. Solenoid and permanent periodic magnet (PPM) designs were employed. Severs were included. The electron gun

provided a 12.5:1 sheet beam at \sim 21 kV. The RF ports are vacuum sealed with diamond windows. 700 ns pulsed hot tests were performed for electron beam voltages of 20.8 and 21.8 kV. For the 20.8 kV beam, average gain of 24 dB was measured for a 14 GHz band width, from 207 to 221 GHz. With the 21.8 kV beam a gain of 30 dB was achieved for a 5 GHz bandwidth, from 197 to 202 GHz. The maximum power output was measured at 110 W at 212.5 GHz [61].



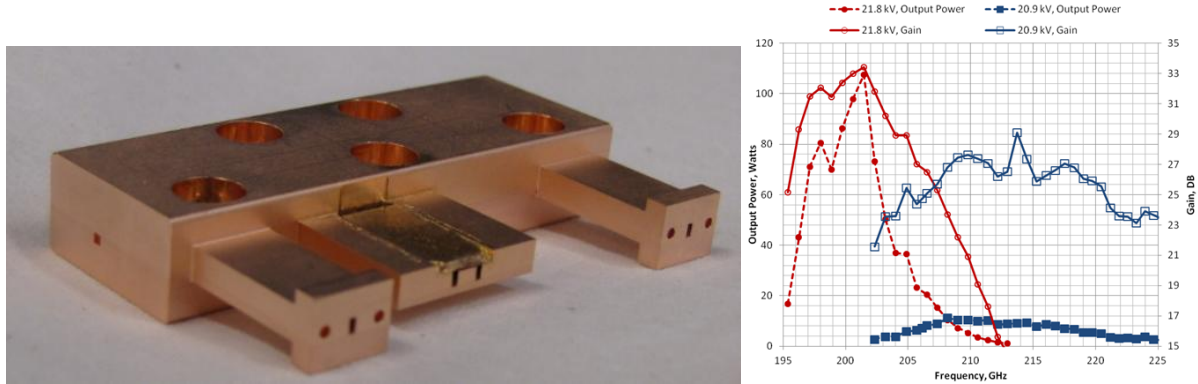
Figures 208a and 208b. Top: Planar coupler design, The RF waveguide intersects the interaction circuit at the same plane. Bottom: Overhead coupler design, the RF coupler is above the interaction circuit.

Figures 209a and 209b. SEM images of H-plane split 220 GHz TWT. Left: Slow wave structure is seen as a series of pockets and vanes. Right: Planar coupler. RF port enters from above, the electron beam tunnel is oriented right and left, and the slow wave structure is seen at the left. The planar coupler allows this design to be made in just two halves.



Figures 210a, 210b, and 210c. Photos of Nano-CNC-machined 220 GHz TWT with overhead couplers.

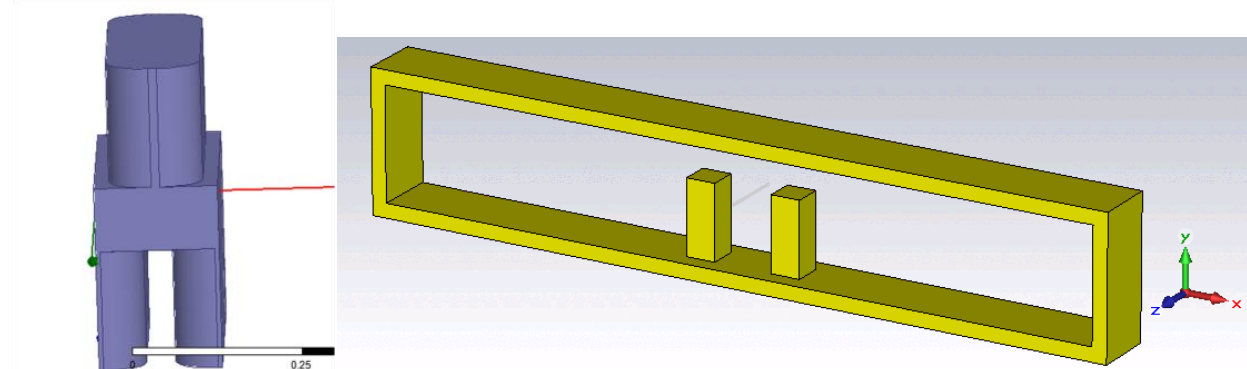
This design requires fabrication in three parts. Left: Slow wave structure lower half. The narrow line near the right side of the part is the interaction circuit. The rectangular feature is the locating island. Center: Mid-plate with upper half of the slow wave structure. This part is 472 μm thick. Right: Waveguide block. The RF coupler waveguides are machined into this block and turn down at each end of the interaction circuits.



Figures 211a and 211b. Left: Completed 220 GHz TWT slow wave structure. This is the overhead coupler, 3-layer design, diffusion bonded together, and the excess material relieved. The small square hole on the left is the electron beam tunnel entrance. Four rectangular waveguides are seen on the protrusions on the right. These correspond to the RF coupler input and exit for each half of the interaction circuit, with the sever material installed along the two center waveguides. Right: Hot test measurements showing gain and power output for two electron beam energies. Peak power was found to be 110 W at 212.5 GHz with a 21.8 kV electron beam for short pulse testing [61]. Images courtesy of Dr. Anisullah Baig.

V.5.2 346 GHz BWO

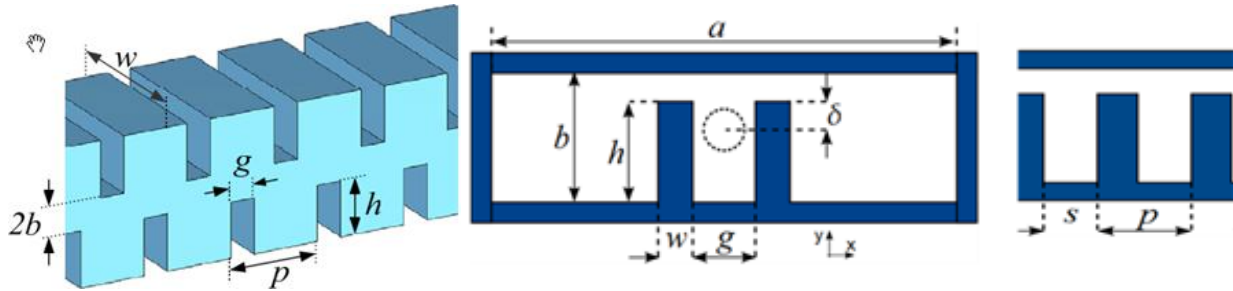
Two 346 GHz BWO slow wave structures have been designed [67]. Cold test circuits are in manufacturing; therefore, the cold test performance is not reported in this dissertation. Design 1 is a half period staggered double vane sheet beam [68]. This is very similar to the 220 GHz TWT; however, it is scaled down for operation at 346 GHz. Furthermore, the interaction circuit is designed for an ~ 15 kV electron beam to interact with the backward wave portion of the RF dispersion curve. The sever is naturally omitted, and there is a single RF coupler port near the electron beam entrance. Design 2 features a double ladder slow wave structure for a round electron beam [69]. The ladder consists of two rows of square pillars in a large cavity, with an electron beam passing between them. The round beam offers advantages in simplicity of gun design, and more readily available cathode emitters.



Figures 212a and 212b. Left: Unit cell for 346 GHz BWO slow wave structure design 1. It features a double vane grating with a half period stagger. Right: Unit cell for design 2. A double ladder structure is formed by two rows of pillars. Image courtesy of Dr. Claudio Paoloni, Lancaster University.

Table 12. 346 GHz BWO Design Specifications

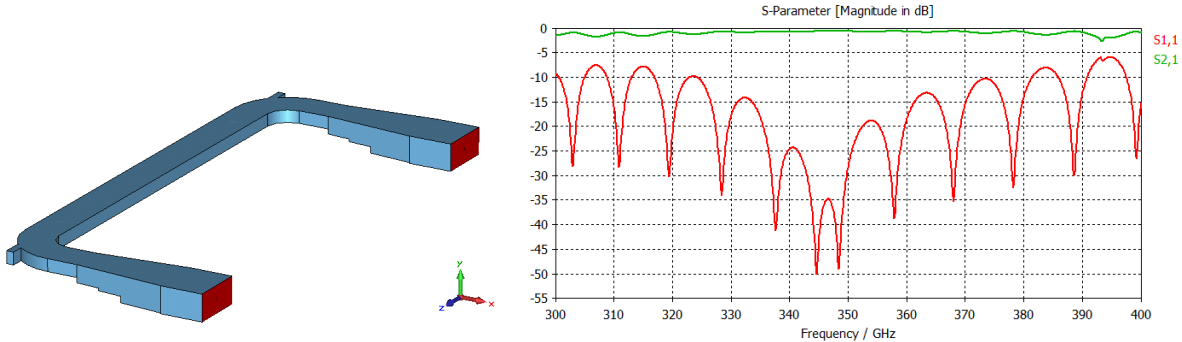
Specification	Design 1	Design 2
Structure	Half period staggered vane	Double pillar rows
Center Frequency	346 GHz	346 GHz
Beam Voltage	16.8 kV	12.8 kV
Beam Current	16 mA	10 mA
Periods	65	116
Power output	1 W	370 mW
Axial B field	0.3 T	0.5 T



Figures 213a and 213b. Slow wave structure dimensions. Left: (Light Blue) Design 1, double vane half period stagger, $p = 185 \mu\text{m}$, $h = 170 \mu\text{m}$, $g = 44 \mu\text{m}$, $b = 45 \mu\text{m}$, $w = 483 \mu\text{m}$. Right: (Dark Blue) Design 2, double pillar row, $a = 2 \text{ mm}$, $b = 200 \mu\text{m}$, $h = 140 \mu\text{m}$, $w = 50 \mu\text{m}$, $g = 120 \mu\text{m}$, $s = 100 \mu\text{m}$, $p = 150 \mu\text{m}$, $\delta = 35 \mu\text{m}$. Images courtesy of Dr. Claudio Paoloni, Lancaster University. [70]

Both interaction circuits will be manufactured for cold test performance. Based on these results and the challenges experienced during fabrication, one will be chosen for hot testing, and final product production. The final interaction circuit will have a single RF output port; however, for cold testing, two RF ports are included to measure circuit attenuation and bandwidth with S-parameters. The RF couplers must be designed and tested first before any determination of the slow wave structure can be evaluated. Two couplers are machined back to back and measured [71]. Once the coupler performance is optimized,

it can be incorporated into the slow wave structure, and the coupler contribution can be subtracted from circuit measurements.



Figures 214a and 214b. Left: Model of the back to back coupler test. WR-3.4 waveguide stair steps down to the beam tunnel size, and then steps back up to WR-3.4. There is no interaction circuit in this test. Right: S-parameters for back to back couplers. Transmission is optimized at 346 GHz with low reflection at -35 dB S₁₁.

Design 1 consists of a slow wave circuit with 65 periodic cells with a period of 185 μm . The cells feature a thin 45 μm wide vane, and 141 μm long cavities. Each bank of vanes are half period staggered. A 90 by 483 μm beam tunnel passes down the center of the slow wave structure. At either end of the slow wave structure, the slow wave structure transition depths are gradually reduced and to match the impedance of WR-2.8 rectangular waveguide. Near the electron beam input side of the circuit, the WR-2.8 waveguide is coupled to WR-3.4 waveguide with a stair step transition. To improve the RF output coupler bandwidth a double ridge waveguide is used at the 90° bend in the coupler. The small dimensions of the circuit cavities require the use of 127 micron diameter end mills. These are commercially available at low cost; however, they are consumed at a rapid rate. Tooling wear must be continuously monitored to make dimensional offsets into the control program, and the tooling must be replaced frequently when wear is excessive or breakage occurs [72]. Tool loading in copper based materials was problematic; therefore, aluminum was chosen for its high conductivity and ease of machining. Even so, dozens of tools were consumed during the fabrication of each circuit. Several test parts will need to be fabricated from

aluminum to optimize the machining process. Supplemental operations such as gold plating or chemical polishing can improve circuit surface finish and performance. Experiments for fabrication techniques for this design are ongoing.

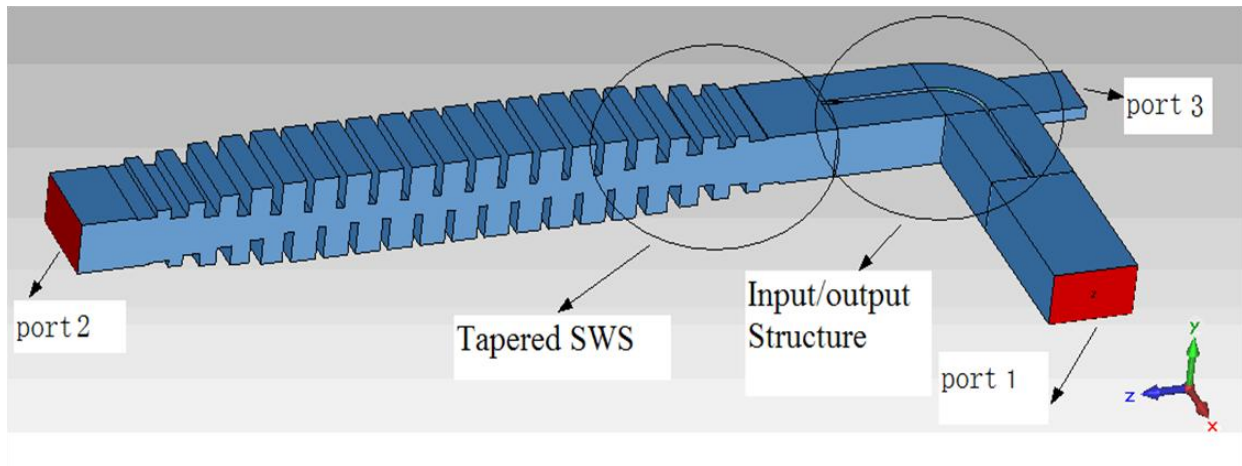
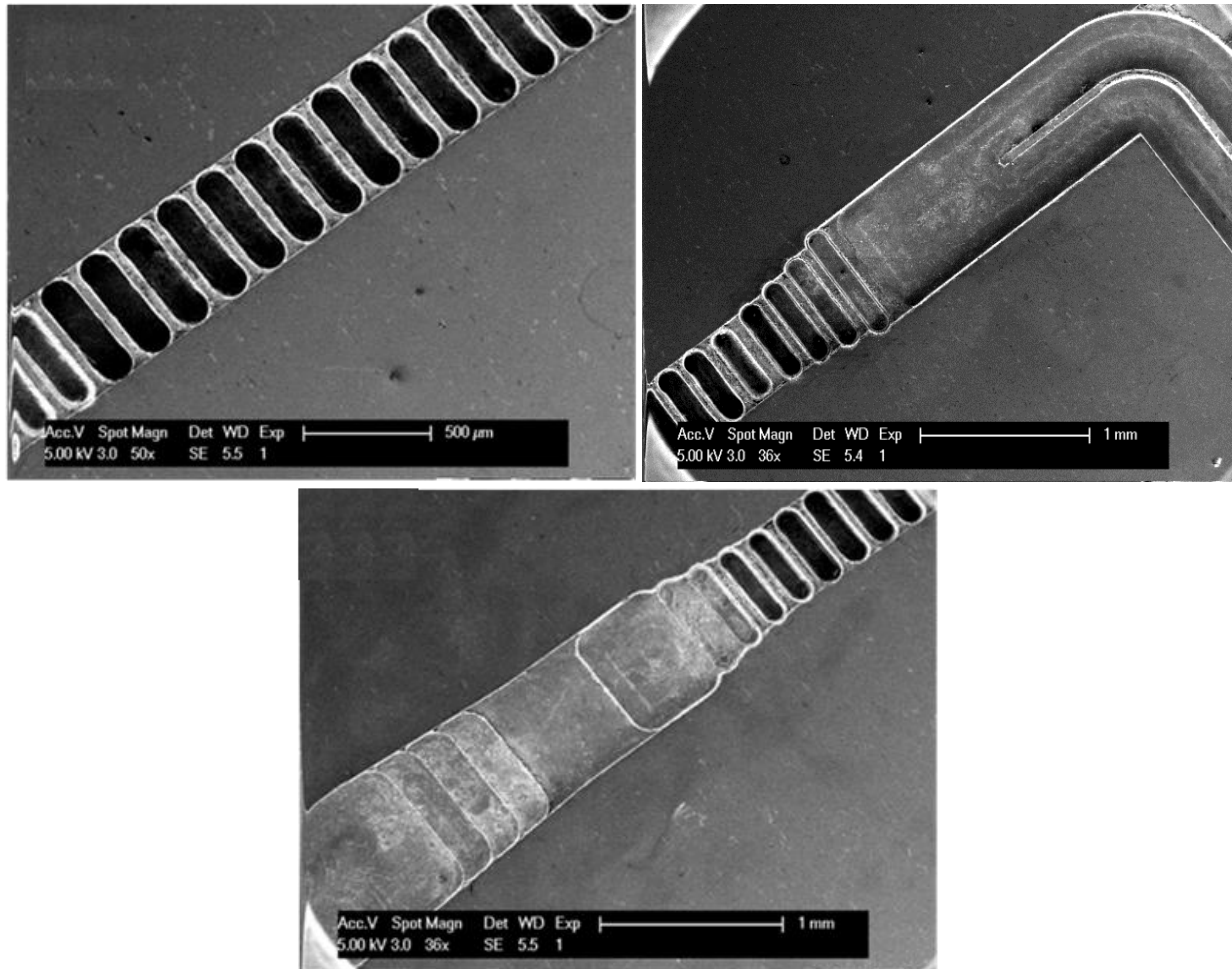


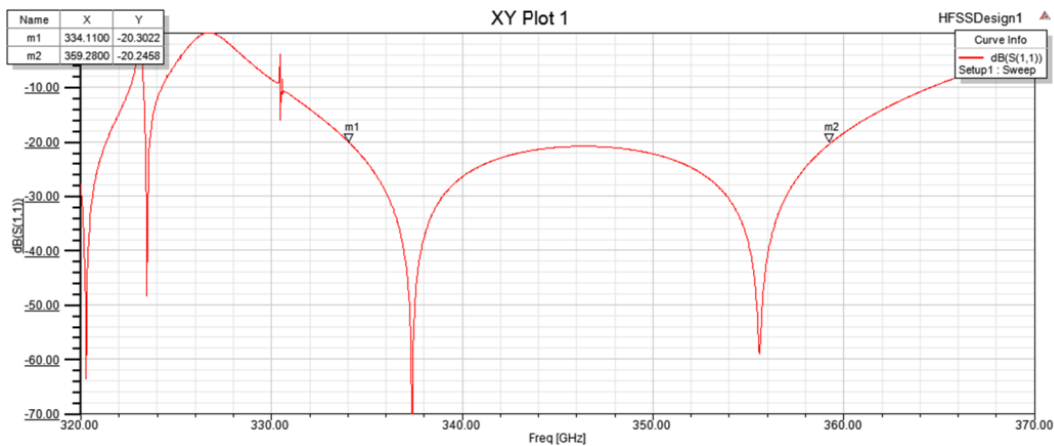
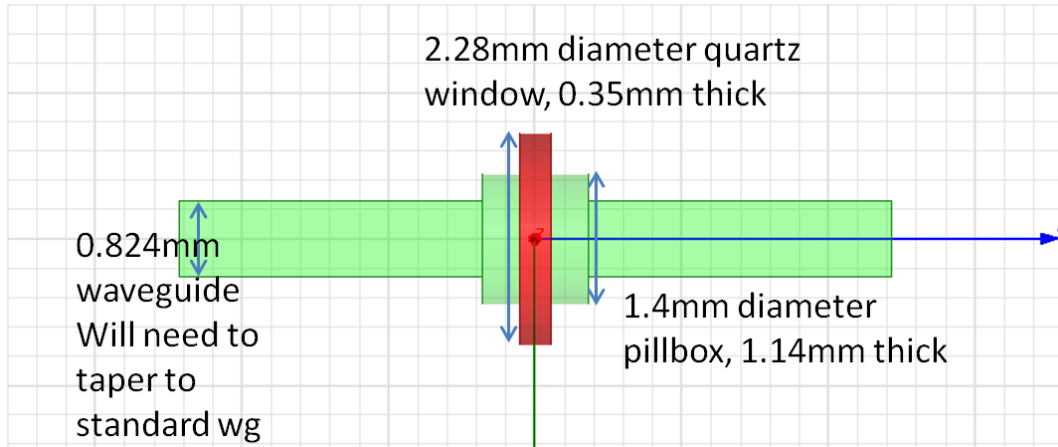
Figure 215. Model of the 346 GHz BWO design 1. Note: This model is truncated for easier viewing. The actual circuit has 65 periods in the slow wave structure. The electron beam travels into port 3 and out port 2 to the collector. RF energy travels from left to right while gaining energy, and is emitted out port 1.



Figures 216a, 216b, and 216c. SEM images of 346 GHz BWO Top left: Several periods of the slow wave structure. Top right: Transition from the slow wave structure to RF output coupler. The cavities are progressively shallower and wider. The ridge at the 90° bend is seen in the waveguide center. Bottom: Example of stair step transition from WR-2.8 to WR-3.4 waveguide.

The output coupler and window for Design 1 provides a vacuum sealed RF port for 346 GHz emission. A coupler connects with the beam tunnel to emit the generated RF signal. The beam tunnel is a non-standard waveguide dimension; therefore, the coupler first transitions to WR-2.8 at the end of the slow wave structure, then it bends 90° with a double ridge waveguide, and finally it stair steps up to WR-3.4 waveguide. The circuit must be able to maintain high vacuum; therefore, a window seals the end of the RF output port. The couplers and window are designed for low reflection at 346 GHz. Diamond offers

excellent performance at this wavelength [73], but is expensive. A single diamond crystal can be grown and polished to high precision to make a low reflection, low attenuation window, as was done with the 220 GHz TWT. Alumina also possesses good transmission properties [74], and is considerably less expensive. However, the dielectric constant at this wavelength is high, which makes its performance very susceptible to dimensional variation. Several windows could be fabricated, with the best performers employed. Crystal quartz is also considered. While less expensive than diamond, and less sensitive than alumina, crystal quartz offers a good performance compromise [75]. A simple pillbox design window has been proposed. A thin window will be placed normal to the waveguide axis, and brazed in place. Its thickness is precisely ground to provide minimum reflection at 346 GHz. A smooth transition from rectangular waveguide tapers up to a 0.824 mm round waveguide, and then steps up to 1.4 mm diameter pillbox. A 2.28 mm diameter quartz window is brazed in place, and then the housing tapers back down to the WR-3.4 waveguide dimensions. The final design is not determined, and several tests are still pending to complete the window dimensions, transitions, and brazing process.



Figures 217a and 217b. Top: Quartz window design for 346 GHz. A 2.28 mm diameter, 0.35 mm thick quartz window is brazed in place to seal the BWO for vacuum. Bottom: Simulation of reflections for this window design. S₁₁ is -20 dB or better for 334 to 359 GHz. Images courtesy of James Do, UC Davis.

Design 2 is designed with two rows of non-staggered pillars with a period length of 140 microns for 116 periods. The pillar dimensions are 50 x 50 microns base, and 140 microns tall. The transition into and out of the slow wave structures are accomplished with gradually decreasing pillar heights. The circuit fabrication is simplified in some ways by not dividing the circuit across the beam tunnel. Instead the entire circuit is to be fabricated in a single piece of bulk material, with a flat plate to complete the vacuum enclosure. The parting line is located at the corner of the rectangular circuit cavity. The small dimensions of the pillars, or more precisely, the small spaces between them create difficulty in fabrication. Nano-

CNC-machining requires 76 μm diameter endmills (which are available) with a 2:1 aspect ratio. This fabrication is more challenging than design 1; therefore, the first cold test circuits are fabricated from aluminum.

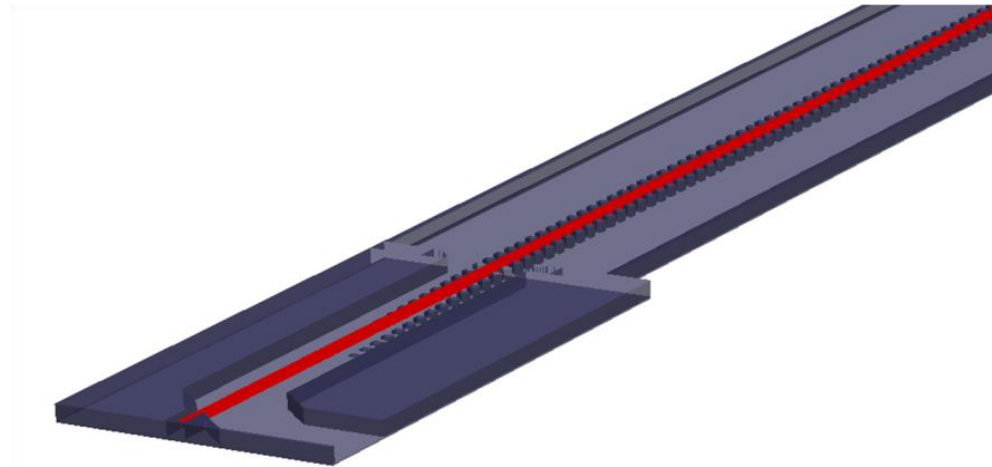
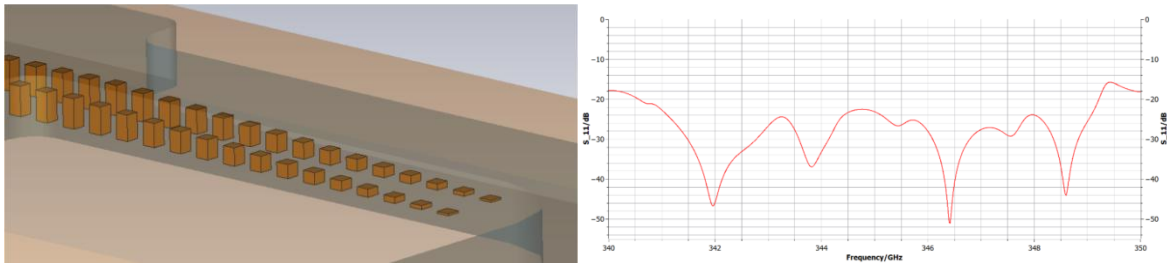


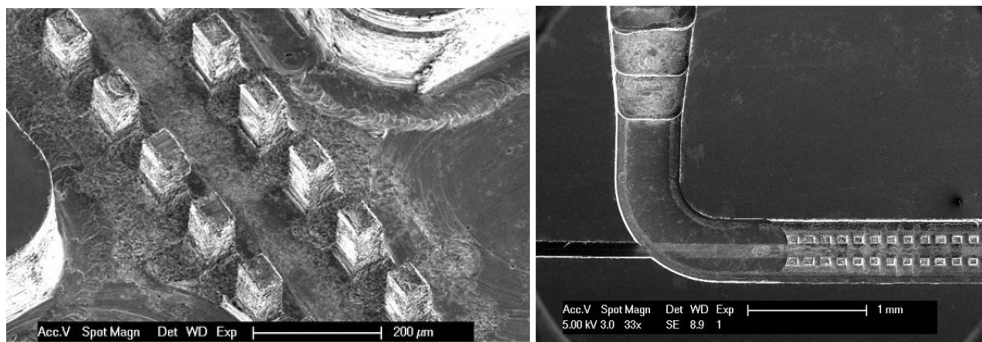
Figure 218. Model of the 346 GHz BWO design 2. Two rows of pillars are machined into large cavity (~2 mm wide) with the electron beam passing between them. Image courtesy of Dr. Claudio Paoloni, Lancaster University.

The transitions at each end of the slow wave structure are formed by gradually decreasing the pillar heights. This type of structure is well suited for nano-CNC-machining to control the pillar heights. The slow wave structure, transitions, and couplers to WR-3.4 have been Nano-CNC-machined; however, they are awaiting cold testing to evaluate their performance. The difficulty of working with 76 μm tools is seen in the SEM images below. Surface roughness and dimensional tolerance vary as the tooling wears [76]. Fabrication was performed using tungsten carbide endmills. Alternatives are being explored to improve the fabrication quality. Poly-crystal diamond, mono crystal diamond, and hybrid LIGA/Nano-CNC-machining are being considered. Poly-crystal diamond tools are made from small diamond grains affixed to the tooling shank. The diamond edges are much harder than the circuit material, and as such remain sharp for extended periods. The primary concern is tool loading causing premature failure or inconsistent performance. Monocrystal diamond tooling uses a single diamond ground to form a single fluted endmill.

These tools are known to perform well for larger sizes; however, at 76 μm diameter with a 2:1 aspect ratio, it is unknown if they will be strong enough to survive. Monocrystal diamond tooling of this size will need to be custom made with long lead times and great expense. A hybrid LIGA/Nano-CNC-machining approach may provide a good solution. The limitations of LIGA fabrication is it is a two dimensional design. However, if a LIGA circuit were fabricated first, then that circuit could be machined afterwards to cut down particular features. This would allow LIGA fabricated circuits to be 3D structures without the tedious repetition of multiple LIGA processes. These options, among others, are in development.



Figures 219a and 219b. Left: Slow wave structure transition. The two rows of pillars are gradually reduced in height. Right: Simulation results of S_{11} for the transition. S_{11} is less than -22 dB across the bandwidth [77]. Image courtesy of Dr. Claudio Paoloni, Lancaster University.



Figures 220a and 220b. SEM images of the 346 GHz BWO slow wave structure design 2. Left: Surface finish inconsistency and dimensional variation is observed with the slow wave structure pillars. Right: Slow wave structure transition to rectangular waveguide. The waveguide bends 90°, and stair steps up to WR-3.4 waveguide. The beam tunnel entrance is seen at the left hand side.

V. References

- [1] S.M. Kaye, F.M. Levinton, D. Stutman, K. Tritz, H. Yuh, M.G. Bell, R.E. Bell, C.W. Domier, D. Gates, W. Horton, J. Kim, B.P. LeBlanc, N.C. Luhmann Jr., R. Maingi, E. Mazzucato, J.E. Menard, D. Mikkelsen, D. Mueller, H. Park, G. Rewoldt, S.A. Sabbagh, D.R. Smith, and W. Wang, "Confinement and local transport in the National Spherical Torus Experiment (NSTX)," *Nuclear Fusion*, Vol. 47, No. 7, June 2007.
- [2] P.H. Siegel, R.P. Smith, M.C. Gaidis, and S.C. Martin, "2.5-THz GaAs Monolithic Membrane-Diode Mixer," *IEEE Transactions on Microwave Theory and Techniques*, Vol. 47, No. 5, May 1999.
- [3] F.M. Boussaha, J.H. Kawamura, J.A. Stern, A. Skalare, and V. White, "A Low Noise 2.7 THz Waveguide-Based Superconducting Mixer," *IEEE Transactions on Terahertz Science and Technology*, Vol. 2, No. 3, May 2012.
- [4] F. Boussaha, J. Kawamura, J. Stern, and C. Jung-Kubiak, "2.7 THz Balanced Waveguide HEB Mixer," *IEEE Transactions on Terahertz Science and Technology*, Vol. 4, No. 5, September 2014.
- [5] H.W. Hubers, S.G. Pavlov, A.D. Semenov, R. Kohler, L. Mahler, A. Tredicucci, H.E. Beere, D.A. Ritchie, and E.H. Linfield, "Terahertz quantum cascade laser as local oscillator in a heterodyne receiver," *Optics Express*, Vol. 13, No. 15, July 2005.
- [6] D. Bachmann, M. Rosch, C. Deutsch, M. Krall, G. Scalari, M. Beck, J. Faist, K. Unterrainer, and J. Darmo, "Spectral gain profile of a multi-stack terahertz quantum cascade laser," *Applied Physics Letters*, Vol. 105, 181118, November 2014.
- [7] F. Boussaha, J. Kawamura, J. Stern, and C. Jung-Kubiak, "2.7 THz Balanced Waveguide HEB Mixer," *IEEE Transactions On Terahertz Science And Technology*, Vol. 4, No. 5, September 2014.
- [8] J.S. Pearson and J.A. Harrison, "A uniform field electrode for use in a discharge chamber of restricted size: design and performance," *Brit. J. Appl. Phys. (J. Phys. D)*, Vol. 2, No. 2, August 1969.
- [9] M.S. Cheon, J.W. Juhn, and Y.S. Hwang, "Design of Stark-tuned far-infrared laser with circular hollow waveguide," *Applied Optics*, Vol. 45, No. 27, September 2006.
- [10] T.Y. Chang, "Improved Uniform-Field Electrode Profiles for TEA Laser and High-Voltage Applications," *Review of Scientific Instruments*, Vol. 44, No. 4, April 1973.
- [11] B. Walter, "Dielectrics for corona preionisation of a TEA laser," *J. Phys. E: Sci. Instrum.*, Vol. 18, December 1984.
- [12] M.S. Cheon, J.W. Juhn, and Y.S. Hwang, "Electric field effect on the optically-pumped far-infrared laser," *Applied Physics B Lasers and Optics*, Vol. 93, September 2008.
- [13] J.H. Booske, R.J. Dobbs, C.D. Joye, C.L. Kory, G.R. Neil, G.S. Park, J. Park, and R.J. Temkin, "Vacuum Electronic High Power Terahertz Sources," *IEEE Transactions On Terahertz Science and Technology*, Vol. 1, No. 1, September 2011.
- [14] Z. Shi, D. Gamzina, L.R. Barnett, A. Baig, and N.C. Luhmann Jr., "3-D Simulations and Design of Multistage Depressed Collectors for Sheet Beam Millimeter Wave Vacuum Electron Devices," *IEEE Transactions of Electron Devices*, Vol. 60, No. 9, September 2013.

- [15] S. Martens, B. Gompf, and M. Dressel, "Characterization of continuous-wave terahertz sources: laser mixing versus backward-wave oscillators," *Applied Optics*, Vol. 48, No. 29, October 2009.
- [16] J.H. Booske, "Plasma physics and related challenges of millimeter-wave-to-terahertz and high power microwave generation," *Physics Of Plasmas*, 15, 055502, 2008.
- [17] J.E. Menard et al., "Overview of the physics and engineering design of NSTX upgrade," *Nuclear Fusion*, Vol. 52, 083015, July 2012.
- [18] A. Muslija and A.D. Lantada, "Deep reactive ion etching of auxetic structures: present capabilities and challenges," *Smart Materials and Structures*, Vol. 23, June 2014.
- [19] B. Lips, and R. Puers, "Three step deep reactive ion etch for high density trench etching," *27th Micromechanics and Microsystems Europe Workshop*, Journal of Physics: Conference Series, Vol. 757, doi:10.1088/1742-6596/757/1/012005, 2016.
- [20] A. Malekabadi and C. Paoloni, "UV-LIGA microfabrication process for sub-terahertz waveguides utilizing multiple layered SU-8 photoresist," *Journal of Micromechanics and Microengineering*, Vol. 26, doi:10.1088/0960-1317/26/9/095010, 2016.
- [21] A. Descoedres, C. Hollenstein, G. Walder, R. Demellier, R. Perez, "Time- and spatially-resolved characterization of electrical discharge machining plasma," *Plasma Sources Science and Technology*, Vol. 17, May 2008.
- [22] B. Ekmekci, A. Sayar, T.T. Opoz and A. Erden, "Geometry and surface damage in micro electrical discharge machining of micro-holes," *Journal of Micromechanics and Microengineering*, Vol. 19, September 2009.
- [23] P. Li, D. Zdebski, H.H. Langen, A.M. Hoogstrate, J.A.J. Oosterling, R.H. Munnig Schmidt and D.M. Allen, "Micromilling of thin ribs with high aspect ratios," *Journal of Micromechanics and Microengineering*, Vol. 20, October 2010.
- [24] Z. Zhu, S. To, K.F. Ehmann, G. Xiao, and W. Zhu, "A novel diamond micro-/nano-machining process for the generation of hierarchical micro-/nano-structures," *Journal of Micromechanics and Microengineering*, Vol. 26, February 2016.
- [25] V.L. Granatstein, R.K. Parker, and C.M. Armstrong, "Scanning the Technology: Vacuum Electronics at the Dawn of the Twenty-First Century," *Proceedings of The IEEE*, Vol. 87, No. 5, May 1999.
- [26] M.P. Kirley, N. Carlsson, B.B. Yang, and J.H. Booske, "Study of the Effect of Surface Roughness and Skin Depth on the Conductivity of Metals at 650 GHz," *Vacuum Electronics Conference (IVEC), 2012 IEEE Thirteenth International*, Monterey, CA, 24-26 April 2012.
- [27] "Surface Roughness Terminology and Parameters," *Precision Devices Inc.*, http://www.predev.com/pdffiles/surface_roughness_terminology_and_parameters.pdf, Accessed: January 3rd, 2017.
- [28] E.H. Klaassen, K. Petersen, J.M. Noworolski, J. Logan, N.I. Maluf, J. Brown, C. Storment, W. McCulley, G.T.A. Kovacs, "Silicon fusion bonding and deep reactive ion etching: a new technology for microstructures," *Sensors and Actuators A*, Vol. 52, pp. 132-139, 1996.

- [29] A. Baig, D. Gamzina, M. Johnson, C.W. Domier, A. Spear, L.R. Barnett, N.C. Luhmann Jr., and Y.M. Shin, "Experimental Characterization of LIGA Fabricated 0.22 THz TWT Circuits," *Vacuum Electronics Conference (IVEC), 2011 IEEE International*, Bangalore, Karnataka, India, 21-24 Feb. 2011.
- [30] R.A. Lawes, "Manufacturing tolerances for UV LIGA using SU-8 resist," *J. Micromech. Microeng.*, Vol. 15, pp. 2198-2203, October 2005.
- [31] D.J. Sadler, S. Gupta, and C.H. Ahn, "Micromachined Spiral Inductors Using UV-LIGA Techniques," *IEEE Transactions on Magnetics*, Vol. 37, No. 4, July 2001.
- [32] K.H. Ho, S.T. Newman, "State of the art electrical discharge machining (EDM)," *International Journal of Machine Tools & Manufacture*, Vol. 43, pp. 1287-1300, June 2003.
- [33] S. Singh, S. Maheshwari, P.C. Pandey, "Some investigations into the electric discharge machining of hardened tool steel using different electrode materials," *Journal of Materials Processing Technology*, Vol. 149, pp. 272-277, November 2004.
- [34] X. Cheng, K. Nakamoto, M. Sugai, S. Matsumoto, Z.G. Wang, K. Yamazaki, "Development of ultra-precision machining system with unique wire EDM tool fabrication system for micro/nano-machining," *CIRP Annals - Manufacturing Technology*, Vol. 57, pp. 415-420, 2008.
- [35] R.L. Ives, "Microfabrication of High-Frequency Vacuum Electron Devices," *IEEE Transactions On Plasma Science*, Vol. 32, No. 3, June 2004.
- [36] "DMG MORI," <http://us.dmgmori.com/>, Accessed: January 4th, 2017.
- [37] R. Barchfeld, D. Gamzina, A. Baig, L.R. Barnett, N.C. Luhmann Jr., "Nano CNC Milling of Two Different Designs of 0.22 THz TWT Circuits," *13th IEEE International Vacuum Electronics Conference (IVEC) and Ninth International Vacuum Electron Sources Conference (IVESC)*, Monterey, CA, April 24-26, 2012.
- [38] R. Barchfeld, D. Gamzina, Y.M. Shin, J. Kim, C. Alldritt, L.R. Barnett, and N.C. Luhmann Jr., "Microfabrication OF Terahertz Vacuum Electronic Devices", *26th Annual Meeting of the American Society for Precision Engineering (ASPE 2011)*, Denver, CO, November 13 – November 18, 2011.
- [39] L. Himes, D. Gamzina, B. Popovic, R. Barchfeld, N.C. Luhmann Jr., "Development of Nano Machining Techniques to Bridge the Terahertz Gap," *17th IEEE International Vacuum Electronics Conference*, Monterey, CA, April 19-21, 2016.
- [40] Y. Zheng, D. Gamzina, B. Popovic, and N.C. Luhmann, Jr., "Electron Beam Transport System for 263-GHz Sheet Beam TWT," *IEEE Transactions on Electron Devices*, Vol. 63, No. 11, November 2016.
- [41] L. Ives, C. Kory, M. Read, J. Neilson, M. Caplan, N. Chubun, R. Wilcox, T. Robinson, S. Schwartzkopf, and R. Witherspoon, "Development of Terahertz Backward Wave Oscillators," *Vacuum Electronics Conference, 2004. IVEC 2004. Fifth IEEE International*, Monterey, CA, 27-29 April 2004
- [42] G. Gaertner, "Historical development and future trends of vacuum electronics," *J. Vac. Sci. Technol. B*, Vol. 30, 060801, 2012.

- [43] R.K. Parker, R.H. Abrams Jr., B.G. Danly, and B. Levush, "Vacuum Electronics," *IEEE Transactions on Microwave Theory and Techniques*, Vol. 50, No. 3, March 2002.
- [44] D.K. Keuren, "Science Goes to War: The Radiation Laboratory, Radar, and Their Technological Consequences," *Reviews in American History*, Vol. 25, No. 4, December 1997.
- [45] J.M. Osepchuk, "A History of Microwave Heating Applications," *IEEE Transactions on Microwave Theory and Techniques*, Vol. 32, No. 9, September 1984.
- [46] M. Cascone, "Vacuum electronics for communications and broadcasting," *Vacuum Electronics Conference, 2008. IVEC 2008. IEEE International*, Monterey, CA, 22-24 April 2008.
- [47] J.F. Federici, B. Schulkin, F. Huang, D. Gary, R. Barat, F. Oliveira, and D. Zimdars, "THz imaging and sensing for security applications—explosives, weapons and drugs," *Semicond. Sci. Technol.*, Vol. 20, June 2005.
- [48] R.W. McMillan, "Terahertz Imaging, Millimeter-Wave Radar," *NATO Advanced Study Institute: Advances in Sensing with Security Applications*, Il Ciocco, Italy, 17-30 July 2005.
- [49] V. Erckmann and U. Gasparino, "Electron cyclotron resonance heating and current drive in toroidal fusion plasmas," *Plasma Phys. Control. Fusion*, Vol. 36, 1994.
- [50] L.S. Nergaard, "Tubes and/or solid-state devices for power generation", *Microwave J.*, Vol. 13, pp. 65-67, April 1970.
- [51] G.P. Williams, "Filling the THz gap—high power sources and applications," *Institute Of Physics Publishing, Rep. Prog. Phys.*, Vol. 69, pp. 301-326, 2006.
- [52] A.S. Gilmour Jr., "Klystrons, Traveling Wave Tubes, Magnetrons, Crossed-Field Amplifiers, and Gyrotrons," *Artech House*, Norwood, MA, 2011.
- [53] J.A. Dayton, V.O. Heinen, N. Stankiewicz, and T.M. Wallett, "Submillimeter Backward Wave Oscillators," *International Journal of Infrared and Millimeter Waves*, Vol. 8, No. 10, 1987.
- [54] J. Zhao, N. Li, J. Li, D. Gamzina, A. Baig, R. Barchfeld, L. Barnett, S. Risbud, and N.C. Luhmann Jr., "Scandia-added Tungsten Dispenser Cathode Fabrication for THz Vacuum Integrated Power Amplifiers", *Invited Paper, Terahertz Science and Technology*, Vol.4, No.4, December 2011.
- [55] "Dispenser Cathodes," *Spectra-Mat, Inc.*, <http://www.spectramat.com/DispenserCathodes-details.html>, Accessed: January 4th, 2017.
- [56] Z. Shi, D. Gamzina, L.R. Barnett, A. Baig, and N.C. Luhmann, Jr., "3-D Simulations and Design of Multistage Depressed Collectors for Sheet Beam Millimeter Wave Vacuum Electron Devices," *IEEE Transactions on Electron Devices*, Vol. 60, No. 9, September 2013.
- [57] N.V. Bijeev, A. Malhotra, V. Kumar, S. Singh, K.S. Dasgupta, R.N. Motta, B. Venugopal, Sandhyarani, O.K. Jinan, and B.K. Jayakumar, "Design and Realization Challenges of Power Supplies for Space TWT," *Vacuum Electronics Conference (IVEC), 2011 IEEE International*, Bangalore, India, 21-24 February 2011.

- [58] D.S. Komm, R.T. Benton, H.C. Limburg, W.L. Menninger, and X. Zhai, "Advances in Space TWT Efficiencies," *IEEE Transactions On Electron Devices*, Vol. 48, No. 1, January 2001.
- [59] V. Srivastava, T.K. Ghosh, M.J. Akhtar, and S.N. Joshi, "Design of a High Efficiency Space TWT," *IETE Technical Review*, Vol. 16, No. 2, pp. 249-254, March-April 1999.
- [60] A. Baig, Y.M. Shin, L.R. Barnett, D. Gamzina, R. Barchfeld, C.W. Domier, J. Wang, and N.C. Luhmann Jr., "Design, Fabrication and RF Testing of Near-THz Sheet Beam TWTA," *Invited Paper, Terahertz Science and Technology*, ISSN 1941-7411, 4, No. 4, December 2011.
- [61] A. Baig, D. Gamzina, T. Kimura, J. Atkinson, C.W. Domier, B. Popovic, L. Himes, R. Barchfeld, M. Field, and N.C. Luhmann Jr., "Performance of a Nano-CNC Machined 220 GHz Travelling Wave Tube Amplifier," *IEEE Transactions on Electron Devices*, submitted 22 December 2016. (Pending publication)
- [62] Y.M. Shin, L.R. Barnett, and N.C. Luhmann Jr., "Phase-Shifted Traveling-Wave-Tube Circuit for Ultrawideband High-Power Submillimeter-Wave Generation," *IEEE Transactions on Electron Devices*, Vol. 56, No. 5, May 2009.
- [63] Y.M. Shin, L.R. Barnett, and N.C. Luhmann Jr., "Strongly confined plasmonic wave propagation through an ultrawideband staggered double grating waveguide," *Applied Physics Letters*, Vol. 93, 221504, December 2008.
- [64] "Glidcop," *SCM Metal Products, Inc.*, http://www.aps.anl.gov/APS_Engineering_Support_Division/Mechanical_Operations_and_Maintenance/Miscellaneous/tech_info/Glidcop/SCM_Glidcop_product_info.pdf, Accessed: January 4th, 2017.
- [65] Y.M. Shin, A. Baig, R. Barchfeld, D. Gamzina, L.R. Barnett, and N.C. Luhmann Jr., "Experimental study of multichromatic terahertz wave propagation through planar micro-channels," *Applied Physics Letters*, Vol. 100, 154103, April 2012.
- [66] R. Barchfeld, D. Gamzina, A. Baig, L.R. Barnett, N.C. Luhmann Jr., "Nano CNC milling of two different designs of 0.22 THz TWT circuits," *13th International Vacuum Electronics Conference (IVEC)*, Monterey, CA, April 24-26, 2012.
- [67] R. Barchfeld, B. Popovic, X. Tang, L. Yue, F. Zhang, M. Mineo, R. Letizia, C. Paoloni, C.W. Domier, N.C. Luhmann Jr., "346 GHz Source for Plasma Diagnostic Applications", *20th Topical Conference on High-Temperature Plasma Diagnostics (HTPD 2014)*, Atlanta, Georgia, June 1st - June 5th, 2014.
- [68] B. Popovic, R. Barchfeld, X. Tang, F. Zhang, L. Yue, M. Mineo, R. Letizia, C. Paoloni, C.W. Domier, and N.C. Luhmann Jr., "346 GHz BWO for Fusion Plasma Diagnostics", *39th Int. Conf. on Infrared, Millimeter, and THz Waves (IRMMW 2014)*, Tucson, AZ, September 14-19, 2014.
- [69] J. Zhang, C. Paoloni, R. Letizia N.C. Luhmann Jr., B. Popovic, L. Himes, R. Barchfeld, D. Gamzina, J. Feng, P. Pan, Y. Tang, F. Zhang, "High Energy Beam THz Backward Wave Oscillator based on Double Corrugated Waveguide," *17th IEEE International Vacuum Electronics Conference*, Monterey, CA, April 19-21, 2016.

- [70] C. Paoloni, L. Yue, X. Tang, F. Zhang, B. Popovic, L. Himes, R. Barchfeld, D. Gamzina, R. Letizia, M. Mineo, and N.C. Luhmann Jr., "High power THz vacuum electron devices for space applications," *Micro- and Millimetre Wave Technology and Techniques Workshop 2014*, ESA-ESTEC, Noordwijk, The Netherland, November 25-27, 2014.
- [71] C. Paoloni, D. Gamzina, L. Himes, B. Popovic, R. Barchfeld, L. Yue, Y. Zheng, X. Tang, Y. Tang, P. Pan, H. Li, R. Letizia, M. Mineo, J. Feng, and N.C. Luhmann Jr., "THz Backward-Wave Oscillators for Plasma Diagnostic in Nuclear Fusion," *IEEE International Conference on Plasma Sciences (ICOPS2015)*, Belek, Antalya, Turkey, May 24-28, 2015.
- [72] D. Gamzina, L.G. Himes, R. Barchfeld, Y. Zheng, B.K. Popovic, C. Paoloni, E.M. Choi, and N.C. Luhmann, Jr., "Nano-CNC Machining of Sub-THz Vacuum Electron Devices," *IEEE Transactions on Electron Devices*, Vol. 63, No. 10, October 2016.
- [73] S. Casalbuoni, B. Schmidt, P. Schmuser, V. Arsov, and S. Wesch, "Ultrabroadband terahertz source and beamline based on coherent transition radiation," *Physical Review Special Topics - Accelerators and Beams*, Vol. 12, 030705, March 2009.
- [74] J.A. Hejase, P.R. Paladhi, and P. Chahal, "Terahertz Characterization of Dielectric Substrates for Component Design and Nondestructive Evaluation of Packages," *IEEE Transactions on Components, Packaging and Manufacturing Technology*, Vol. 1, No. 11, November 2011.
- [75] M. Naftaly, A.P. Foulds, R.E. Miles, and A.G. Davies, "Terahertz Transmission Spectroscopy of Nonpolar Materials and Relationship with Composition and Properties," *International Journal of Infrared and Millimeter Waves*, Vol. 26, No. 1, January 2005.
- [76] D. Gamzina, H. Li, L. Himes, R. Barchfeld, B. Popovic, P. Pan, R. Letizia, M. Mineo, J. Feng, C. Paoloni, N.C. Luhmann Jr., "Nanoscale Surface Roughness Effects on THz Vacuum Electronic Device Performance," *IEEE Transactions on Nanotechnology*, Vol. 15, No. 1, January 2016.
- [77] R. Waring et. al, "Comparison of Couplers for 0.346 THz DCW-BWO," *UCMMT 2016*, Qingdao, China, September 5-7, 2016.

VI. Conclusions

As fusion energy research progresses, and technology improves, new research goals are formed and the instruments needed to facilitate that research are designed. The FIRerTIP and High-k Scattering systems were first introduced on NSTX in the early 2000s [1, 2]. Prior to this, the MIRI system [3] was the predecessor to FIRerTIP on TFTR [4]. These plasma diagnostics are now redesigned and constructed for operation on NSTX-U. Many people have been involved in the development and implementation of these systems over the years and more still will see their use into the future. To ensure the successful usage of these instruments to make meaningful contributions to fusion power research, there are several topics to be discussed regarding the installation and operation of these systems. The author's experience with the design and development of FIRerTIP and High-k₀ Scattering can advise on how to obtain the best performance possible on NSTX-U. The information below should assist future researchers in implementing and operating these plasma diagnostics.

VI.1 Installation

The FIRerTIP and High-k₀ Scattering systems are fully designed, and nearly completed with fabrication and testing. The FIRerTIP system was delivered to PPPL during the summer of 2016, and is in the installation progress. The High-k₀ Scattering System is nearly complete, with only the receiving optics and IF electronics to be finalized before completing fabrication. The installation and commissioning of the High-k₀ Scattering system is scheduled for FY19. Installation prior to the schedule is possible; however, it will depend on the availability of PPPL support. Installation requires cooperation between PPPL engineers and UC Davis personnel. All procedures must be documented and approved by PPPL. UC Davis ensures that the functionality and design of the diagnostics are not compromised. During the integration of the diagnostics onto NSTX-U, it is unavoidable to have conflicts with other systems. Thus, it is important that the design be sufficiently flexible to make minor changes when required. A great deal

of communication between PPPL and UC Davis during the design and review process should ensure that any unforeseen conflicts and/or changes are minimal.

The precise installation schedule cannot be known at this time. NSTX-U has an extended maintenance period for FY17 to redesign and replace multiple poloidal field coils. This requires extensive disassembly of the vacuum vessel, and it is probable that new tasks will be identified during the maintenance period. Access to the test cell and the priority of reassembly/installation must support PPPL's overall plan to restore NSTX-U for operation. As NSTX-U maintenance progresses there will likely be dynamic scheduling for project priorities and personnel assignments.

VI.1.1 FIReTIP Installation

The FIReTIP has been delivered and is undergoing installation procedures. The "cage" area has been prepared for all the laser equipment. These preparations include installing the necessary electrical power for the laser power supply, vacuum pumps, chiller, monitoring equipment, and computer control, as well as test equipment for set up and diagnosis of laser systems. "Cage" preparations for the High- k_0 Scattering System were performed at the same time. The laser table is installed in the "cage" and mounted to the floor for safety. Other "cage" preparations are the required safety equipment, such as laser curtains, laser warning signage, interlocks, and gas cylinder racks. The control computer in the "cage" also needs to be networked to a second computer in the control room. Data cables connect the computer to motor controllers, monitors, and IF electronics in the test cell. Any data cables passing through the test cell wall must be protected from accidental high voltage shorts; therefore, electrical cables are adapted to fiber optics before passing out of the test cell. When the preparations are completed, the CO₂ and FIR lasers will be brought online, and tuned for maximum output power. All of the laser monitors and controls should be installed, and lasers optimized before continuing. The next phase of installation will be mounting the waveguide runs, launching optics, and receiver table.



Figure 221. Laser table installed in the "cage" at PPPL.

FIReTIP waveguide

The waveguides will be installed, starting with the wall penetration. This section of waveguide has no capability to be modified once set. The wall penetration will be packed with fire insulation and sealed; therefore, all other portions of the waveguide will be aligned to the wall penetration. To install the remainder of the waveguide, each section can be added and aligned one at a time. A theodolite will be mounted at one end of the waveguide, and aligned with the waveguide axis. As each section of waveguide

is added, the alignment is verified by observing through the theodolite at a target centered at the waveguide end. As miter bends are added, the theodolite view is maintained by the first surface mirrors. With this technique, the waveguide run can be assembled and verified to within 0.1°. With each waveguide section secured, no further alignment should be necessary; however, the ultimate verification for alignment is determined by the FIR laser transmission. FIR laser power can be measured at the end of any waveguide, or at a miter bend, by installing a pyroelectric detector adapter. The adapter will locate the pyroelectric detector sensor at the waveguide central axis. A chopper mounted on the laser table will interrupt the beam, and the relative power output can be observed on an oscilloscope. This technique is also used to verify that the laser is properly aligned and coupled to the waveguide. For initial FIR beam alignment, maximum FIR power should be used, meaning 100% of the CO₂ laser should be coupled to a single FIR laser. If measuring FIR power transmission for more than a few waveguide sections, atmospheric attenuation will reduce the power below the pyroelectric detector threshold. The nitrogen purging system, and thin film end caps should be in place on the waveguide. Once the entire system is installed and running, the receiver mixers can be used to verify FIR transmission.

Launching optics

The launching optics are to be mounted on Bay G. PPPL engineers have designed the mount to locate the launching optics enclosure to the port cover. Once installed, the mirrors must be aligned so that the FIReTIP beam is centered on the retroreflector at Bay B (already installed). A HeNe laser is introduced to the waveguide at the miter bend nearest the launching optics. The miter bend reflector plate is replaced with a special cover that has a 3 mm diameter hole to admit the HeNe beam at the waveguide axis. The alignment of the beam is verified by centering the beam at the waveguide exit (launch optic input). An iris can be mounted to the end of the waveguide to assist with centering the beam. The HeNe/FIR hybrid coupler must be removed to pass the HeNe laser through the launch optics. The mirrors are then adjusted to aim the beam at the retroreflector, and the return beam should be collinear. The HeNe/FIR hybrid

coupler can then be replaced, the HeNe laser can be removed, and the reflector plate reinstalled. Next, the vibration monitor HeNe beam needs to be aligned. Fiber optic cable delivers a HeNe signal to the launch optics. The fiber optics coupler, beam splitter, mirror, and lens are adjusted so that the HeNe beam follows the same path as the FIR beam. The return signal must be coupled to the return signal fiber optic cable. It is vital that the three FIR mirrors are not adjusted during this process. Only the HeNe specific optics can be used to tune the beam for maximum power returned to the fiber optic cable. When these two procedures are complete, the launch optics should be set, and no further attention is required. The enclosure can then be sealed, and plumbed for dry air.



Figures 222a, 222b, and 222c. Top left: Miter bend HeNe alignment plate. A raised boss locates the plate to the miter body, and the HeNe access hole is drilled on the waveguide centerline. Top right: HeNe access hole seen through the miter bend body. Bottom: Iris adapted to the end of a waveguide.

Receiver table

The receiver table is installed on the test cell floor below Bay G. The waveguide runs for the reference channel, local oscillator, and Channel 1 should be installed and aligned. The receiver optics have a broad range of adjustability; therefore, it is more important for the waveguides to be aligned first, and the table optics can be tuned to accommodate. Each incoming signal needs to be independently aligned with its appropriate receiver mixer. The mixers will respond to a single incident beam if a chopper is placed at the laser source. A 180 Hz or higher frequency chopper is used to modulate the beam. The mixer output at this low frequency is weak and noisy; however, it is sufficient to observe a waveform on an oscilloscope. The next step is to tune the mirrors and/or beam splitters for the maximum amplitude signal. Once a signal beam and LO beam are independently aligned with the appropriate receiver mixer, the chopper can be removed, and both beams run together. With the Stark effect engaged, the FIR and Stark lasers can be tuned for 4 to 6 MHz IF output. The signal amplitude can then be optimized by fine tuning the mirror alignments with the FIR lasers driving the mixers. Once the mixer output is optimized, the receiving optics should not require any further tuning; however, the FIR laser frequencies will require frequent tuning. This will conclude the laser and optics alignment for the FIReTIP system.

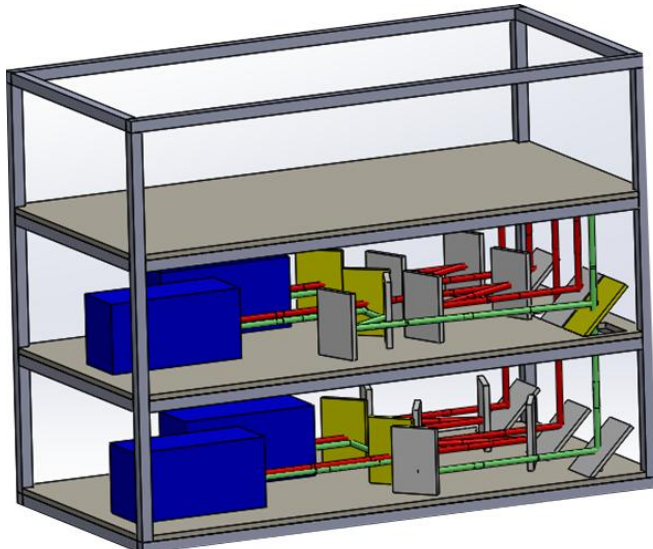
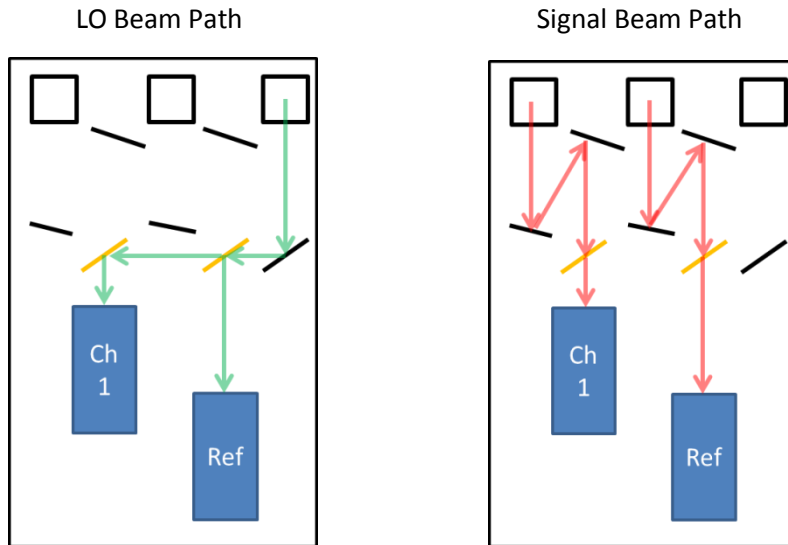


Figure 223. CAD model of FIReTIP receiver table. A system of mirrors (gray) and beam splitters (gold) direct the beams to the receiver mixers (blue). Each mixer has two incident beams, a signal beam (red), and a LO beam (green).

Thermal variation will cause the FIR lasers to drift outside the ideal frequency tuning, and the lasers must be checked and retuned prior to every NSTX-U plasma shot. This tuning should only include varying the laser cavity lengths to fine tune the laser frequencies. Unless disturbed, all of the optical alignments should be static. The optimum tuning for the FIR lasers is to locate the position for maximum power output, and then either increase or decrease the cavity length slightly to adjust the frequency by ± 1 MHz. The Stark effect laser can be tuned for maximum power with the Stark effect turned off. Then the Stark voltage is engaged, and the cavity length tuned to ± 5 MHz. The Stark tuning is verified by mixing with either FIR laser, and the receiver mixer output should be either 4 or 6 MHz. With all three lasers incident on a receiver mixer, there should be three prominent peaks at 2, 4, and 6 MHz. The 4 and 6 MHz signals represent the mixing between the Stark effect laser and the +1 or -1 MHz tuned FIR lasers. The 2 MHz signal is the beat frequency between the +1 and -1 MHz FIR lasers. It may not be obvious which laser is contributing to the spectrum analyzer output; however, it can be inferred by blocking a particular beam or tuning the lasers one at a time and observing the spectrum analyzer display. Through an iterative process, all three lasers can be fine tuned to optimize the receiver mixer output.



Figures 224a and 224b. Layout of the lower level FIReTIP receiver table. Left: The LO beam path is split and delivered to each mixer. The LO alignment can be verified in isolation by chopping the beam, and observing the receiver mixer response. Right: Channel 1 and reference beams are directed to their

respective receiver mixers. Each beam has two independent mirrors (and each mirror / beam splitter has two axes of freedom) to facilitate the alignments without disturbing other alignments.

VI.1.2 High- k_{θ} Scattering Installation

Adding the High- k Scattering lasers to the laser table should be a simple task. The necessary preparations for the "cage" area should already be completed from the FIReTIP installation. The space for the High- k lasers on the laser table are accessible so that the FIReTIP system will not be disturbed. The lasers can be installed, all the monitors and controls connected, and then brought online. The lasers can then be tuned for maximum power output, and all of the monitoring and control systems should be verified. With the laser systems working properly, the FIR beam can be coupled into the waveguide.

High- k waveguide

All of the corrugated waveguide for the High- k_{θ} Scattering System was delivered with the FIReTIP system in 2016. The High- k_{θ} Scattering waveguide and two FIReTIP waveguides need to pass together through the single penetration in the test cell wall. Once all three waveguides are installed in the wall, the penetration will be packed with fire insulation, after which it will be inaccessible. All three waveguides runs share the majority of their paths through the test cell, and a common waveguide bracket is used to secure the waveguides at regular intervals. It makes sense to install them at the same time as much as practical. The theodolite technique will work well to confirm the High- k_{θ} Scattering waveguide alignment. The formic acid laser at 432 μm does not attenuate severely through atmospheric water content; therefore, it may be permissible to align and test the FIR beam without nitrogen filling. However, once the laser is properly aligned and coupled into the waveguide, the waveguide ends should be sealed with HDPE windows and filled with nitrogen to maximize transmission.

High- k reference

The power delivered to the reference channel needs to be verified before exposing the reference mixer to the beam. It has a maximum threshold of 1 mW. A selectable metallic mesh beam splitter in the miter tee can adjust the delivered power. If the delivered power is too high, a dielectric attenuator can be inserted before the mixer input. HDPE has an absorption coefficient of ~ -0.5 dB/cm [5]. The correct thickness attenuator should be designed to deliver between 0.1 to 0.5 mW. The reference channel will supply the LO power to the receiver mixer array. It is vital that the LO power at the receiver mixer input is 7-10 dBm. The SMA cable connecting the reference channel and receiver is long at \sim 20-25 feet, and, at 14 GHz, transmission it can be expected to attenuate the signal ~ -1 dB/ft. An amplifier near the receiver mixer array will boost the power to the appropriate level; however, the power should be verified before connecting. Last minute changes to the cabling route could alter the delivered LO power, and adversely affect the receiver. The LO and IF cables from the reference channel should be shielded from pick-up noise by either using triax cable or metallic conduit, or both.

High-k Launch Optics

The launching optics assembly will be mounted at Bay G. PPPL engineers will design the mounting system to secure the optics assembly. The end of the waveguide is above the assembly, and should be aligned with the center of the optical path. The path can be verified with a HeNe laser. The HDPE lenses are replaced with 4" disks, each with a 3 mm hole at their centers. A HeNe laser can be introduced to the waveguide at a miter bend, aligned with the waveguide axis, and passed through both alignment disks in the launch optics. This will define the beam path through the optics, and can be observed visually. The beam should reflect off each mirror near their centers (± 5 mm), so that the edge of the FIR beam does not fall off the mirrors' edges. The launching mirror position can then be calibrated. Using the HeNe laser to observe the launching mirror alignment, the mirror can be positioned to center the beam for its designed travel limits, and this position is then recorded in the control software. The probe beam alignment controls

can then be tested by computer control, and then the HDPE lenses can be restored, and the HeNe laser removed.

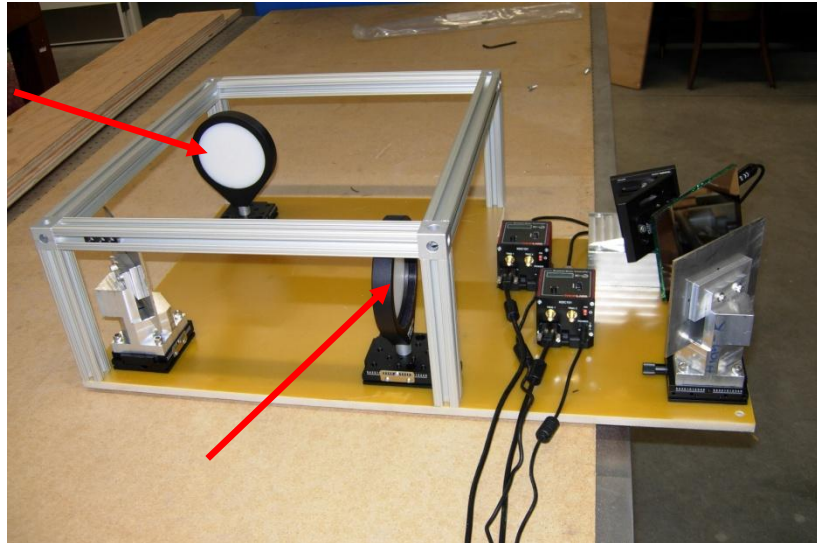


Figure 225. High- k_0 Scattering launching optics. To align the optics, a HeNe laser can be passed through the system. The HDPE lenses (red arrows) should be replaced with 4" disks with a central access hole to pass the HeNe beam.

High-k Receiving Optics and Receiver

The receiving optics and receiver are mounted together as a unit. They will be tested and calibrated at UC Davis before delivery. Testing and calibration is performed by utilizing an acoustic cell [6]. The acoustic cell is a rectangular column constructed of TPX polymer. The column is mounted to a piezoelectric transducer (PZT), which can launch acoustic waves in the cell. Opposite the PZT, the column has an array of tapered structures to eliminate acoustic reflections. To calibrate the High- k_0 Scattering System, the probe beam is directed at the acoustic cell. Acoustic waves are established in the cell by the PZT at a known frequency. The probe beam will scatter off the acoustic cell, and the receiver system can be set up to collect the scattered signals. With the angles of incidence, refraction, and scattering known, the

receiver system function can be confirmed [7]. This will verify the optics design and receiver mixer array functionality. Testing the response from each receiver mixer array channel can be used to calibrate the relative sensitivity of each channel. Each channel's sensitivity may vary slightly, and the incoming scattered signals will vary due to different path lengths through the optics, and different thicknesses of HDPE material to traverse. Once the receiver system design is verified and calibrated, it is ready for installation on NSTX-U.

To properly install the receiver system on NSTX-U, the focal length of the receiver optics, and relative position to the probe beam, must be known. If the receiver needs to be retested/calibrated *in situ*, the acoustic cell can be mounted inside the vacuum vessel during a maintenance period. This should be unnecessary unless a significant change is made to the system. Positioning the receiver system, and calibrating the software to control the receiver translation is critically important. If the receiver focus is not placed along the probe beam, there will be little to no scattered signal. If the focus is placed at the wrong place along the beam, then erroneous data can be collected. All five axes should be tested for their full range of motion. Each translation stage is travel limited to prevent any interference with surrounding equipment. Physical travel limit switches can be adjusted on site, plus the maximum travel should be reflected in the software controls. It may be that there are some intermediate receiver positions that have a conflict with other equipment. If the obstruction cannot be cleared, then these conflicted positions are "blacked-out" in the software. This may require the receiver to travel in multiple axes to move around obstructions. As mentioned above, before connecting the LO power to the receiver mixer array, the delivered power must be verified. If the power level is out of specification, this must be rectified before continuing. The receiver IF cables should be shielded against pick-up noise along their route to the IF electronics.

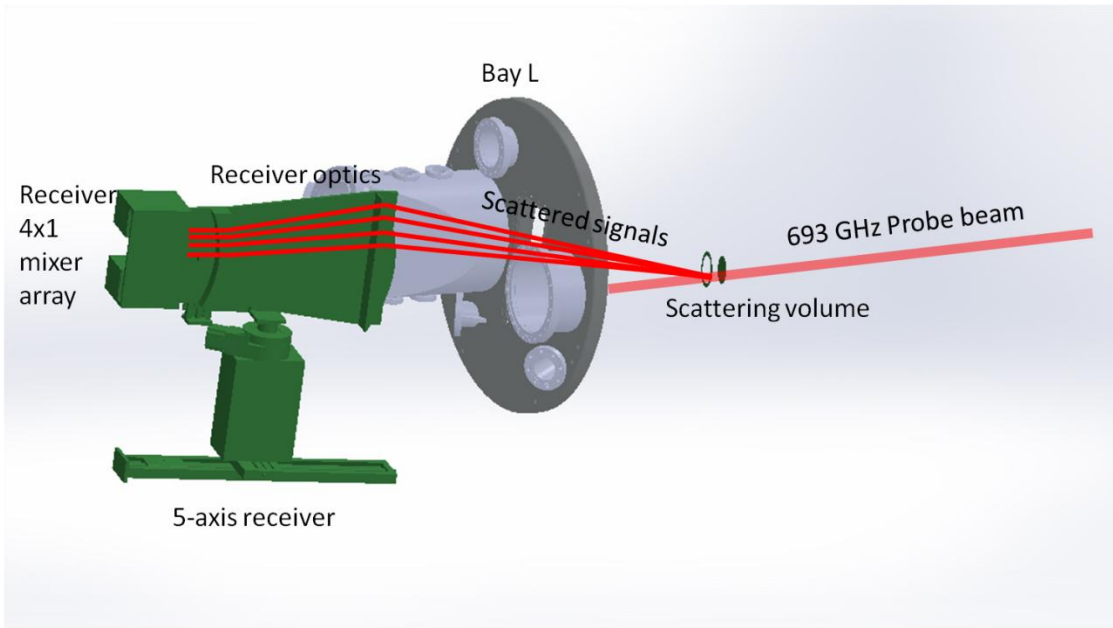


Figure 226. High- k_0 Scattering probe beam and receiver relationship. The scattering volume is the intersection between the probe beam and the receiving optics focus. The launching and receiving optics must be carefully aligned to locate the scattering volume with the desired scattering angles properly.

This concludes the important details when installing the FIReTIP and High- k_0 Scattering systems. These alignment procedures will ensure the instrument will work properly with the best possible signal to noise ratio. Equally important are the procedures to protect the most sensitive components from accidental damage. The FIReTIP receiver mixers, High- k_0 Scattering receiver mixer array and reference mixer, are sensitive and expensive, and considerable caution should be used to ensure they are not damaged.

VI.2 Diagnostic Operation

Once the FIReTIP and High- k_0 Scattering systems are installed and commissioned, they will be ready to collect data from fusion plasmas. There are many safety hazards to observe, such as high power CO₂ laser beams. Inappropriate use could damage critical systems or injure personnel. Only a qualified operator will have the necessary training and understanding to tune the system for maximum efficiency, and safe

operation. The diagnostics' standard operating procedure (SOP) manuals should be referenced for proper operation. FIReTIP and High- k_0 Scattering each have their own SOP manuals. Some of the key points are summarized here for easy reference.

VI.2.1 FIReTIP Operation

When the FIReTIP system is in an inactive state, all electrical equipment should be turned off, except for two items. First, all four FIReTIP lasers are under maintenance vacuum with a dry scroll vacuum pump. This pump should maintain ~ 50 mTorr vacuum to keep the lasers free of contaminants. The High-k FIR laser may also be connected to the same vacuum pump, and it will need to be isolated from the FIReTIP system when either system is operated. Second, a battery charger will maintain the battery voltage for the receiver mixers when not in use; however, during operations the charger should be disconnected to reduce noise in the receiver system. Before initiating the startup procedure, an inspection of all systems should be performed to detect any obvious problems: damaged cables, leaks, missing equipment, etc...

FIReTIP CO₂ Laser Startup

- Turn on laser warning sign
- Notify nearby personnel
- Close laser curtain
- Turn on control computer, run LabView program (details below)
- Isolate CO₂ laser vacuum so that the dry scroll pump is only evacuating the CO₂ laser
- Turn on gas ventilation blower
- Turn on CO₂ gas cylinder
- Turn on laser monitors and controls, CO₂ power meter, chopper, water temperature gauge, water flow sensor, data acquisition interface, and gas pressure gauge

- When CO₂ pressure reaches < 1 Torr, turn on gas valve, adjust gas flow to maintain 8-10 Torr with CO₂ gas mixture
- Turn on water chiller
- Turn on power supply keyed switch
- Turn on PZT power supply
- Put on laser safety glasses
- Safety check equipment and nearby personnel again
- Activate CO₂ laser by pressing “High Voltage” button, the laser tube should glow purple, and the power meter should respond immediately; typical startup power is 10 to 30 W
- Power is increased by increasing gas pressure and power supply current together, maximum power is typically near 30 Torr and 50 mA (the current control knob is labeled in arbitrary units, a setting of “10” is ~50 mA) for 100+ W output

The CO₂ beam should already be aligned with the FIR laser. As the laser reaches thermal equilibrium, it may need frequent tuning to maintain maximum power. It is recommended to allow the laser to run for 30 minutes, and then tune as necessary. The most likely tuning parameter is the diffraction grating alignment. Very small adjustments to the grating position will optimize laser power. Rarely does the output coupler alignment need adjustment. If any laser parameter is abnormal, the process should be stopped, and any potential problems investigated. The shutdown procedure is essentially the reverse process. To deactivate the laser, press the “High Voltage” button, and the laser should immediately turn off. The remaining components can be turned off in any order. It is recommended to reset the CO₂ gas pressure to 8-10 Torr. Make sure the gas cylinder is turned off to avoid losing the laser gas mixture.

To activate the FIR lasers, the CO₂ laser must be active. The CO₂ laser is turned on according to the above procedure, and while it is “warming up”, the FIR laser can be prepared for startup. Ensure that the

laser warning sign is on, safety curtains closed, and nearby personnel are warned. There are no safety glasses for the FIR wavelength; however, due to the CO₂ pump laser, the CO₂ safety glasses must be worn. All three FIR lasers use the same startup procedure. Only the Stark laser has one additional step for activating the Stark effect voltage.

FIReTIP FIR laser startup

- Turn on FIReTIP oil vacuum pump and open valve to evacuate all three FIR lasers
- The control computer and LabView program should already be running(details below)
- Turn on monitoring and control equipment: data acquisition interface, power meters, choppers, water temperature gauge, water flow sensor, motor controllers
- Laser vacuum should be < 7 mTorr before continuing, ~2 mTorr is typical, Note: It can take a long time to reach ultimate vacuum (from 50 mTorr to 2 mTorr can take 45 to 60 minutes, from atmospheric pressure it can be 4+ hours)
- Open gas control valve and allow methanol to circulate, conventional FIR lasers should be set to 500 to 700 mTorr, Stark laser is set to 200 to 300 mTorr
- The chiller should already be activated for the CO₂ laser
- The CO₂ laser beam should already be aligned and coupling into the FIR lasers
- FIR power may not immediately be registered; tune the CO₂ PZT voltage to increase FIR power, if the PZT adjustment yields no result then the FIR cavity length may need adjustment
- Tune the PZT and FIR cavity length for maximum power output, while the lasers are “warming up”; tuning the PZT and cavity length can be frequently needed (up to four times a minute), it is recommended to allow the lasers to reach thermal equilibrium for 30 minutes before tuning for maximum output
- Turn on Stark power supply, ~400 V are needed to shift the laser frequency by 5 MHz; the cavity length may need to be adjusted after Stark voltage is engaged.

- Minor adjustments to the output coupler alignment may be necessary for maximum power output and to control mode quality; however, the majority of laser tuning will be from the PZT and cavity length adjustments; coupler alignments should not be adjusted under normal conditions
- FIR power output depends on the CO₂ pump power. With 100 W pumping power divided into thirds, the conventional FIR lasers should produce 100 mW each, and the Stark laser should produce 25 mW

Deactivating the FIR lasers can be immediately realized by turning off the CO₂ beam by pressing the “High Voltage” button on the CO₂ power supply. Once the lasers are turned off, all the laser components can be turned off in any order. If laser activity is concluded for the day, the lasers should be placed on the maintenance vacuum pump. Turn off the oil vacuum pump and close the valve connected to it. Open the vacuum valves to connect the CO₂ laser, all three FIReTIP FIR lasers, and the High-k FIR laser (if that laser is shut down) to the dry scroll pump. This will reduce the time needed to reactivate the lasers, and it will keep the vacuum cavities clean to reduce laser maintenance and cleaning.

To operate the FIReTIP system for plasma data collection, the following procedure should be used. Turn on and tune the laser systems according to the above directions. The waveguide nitrogen supply, laser table dry air, launching optics dry air, and receiver table dry air supplies should be activated. The ambient humidity should be reduced to < 5% R.H. The vibration monitor HeNe laser, and vibration monitor electronics are turned on. The receiver mixer battery charger is turned off, and the batteries are connected to the mixers. The IF electronics and spectrum analyzer are turned on. At this point, the waveguide shutters can be opened, and the FIR beams will be passed down the waveguide. The lasers may need to be tuned for maximum power output at this time. The receiver mixers will provide an IF signal to the spectrum analyzer. Three signals should be observed (2, 4, and 6 MHz) on the control computer, via the spectrum analyzer output. The laser frequencies are tuned with slight adjustments to the cavity lengths so that the 2, 4, and 6 MHz signals are stable. The control room computer can be remotely logged into the

“cage” computer to observe the FIReTIP system controls. The operator should then verify that the control room computer will adjust the laser output correctly, and the FIReTIP system will be ready to collect data.

When the FIReTIP system is operating and stable, the frequencies will still drift over the course of several minutes. Prior to each plasma shot, the laser output should be checked, and adjusted as necessary to ensure the frequencies are correct. The time it takes to accomplish this task depends on the operator’s experience and skill. The operator will need sufficient warning before the plasma shot to complete the system tuning. If the system is out of specification at the time of the plasma shot, then any data will be erroneous. When used for real time density feedback control, this could affect NSTX-U performance. Furthermore, FIReTIP measurements are used to calibrate the Thomson scattering system; therefore, those operators will need to know anytime the FIReTIP data is deemed unreliable. FIReTIP data are recorded in its digitizers. These data are uploaded to PPPL computers for later retrieval and analysis. If at any time there is a problem with the FIReTIP system (especially with the lasers), the entire system can be shut down with an emergency stop button. This will deactivate the high voltage power supply, and therefore shut down all lasers. To turn off the FIReTIP system for the day, follow the laser shut down procedures above, and all of the additional equipment can be turned off in reverse order. The receiver mixer batteries should be placed back on the battery charger for overnight recharging.

VI.2.2 High- k_θ Scattering operation

The High- k_θ Scattering System has a similar procedure to FIReTIP. First, the laser system will need to be activated, and then the launching and receiving optics must be positioned. The PL-6 CO₂ laser has a few minor changes to the startup procedure as detailed below. The PL-6 laser can be replaced with a FIReTIP style CO₂ if need be, and under these circumstances, the FIReTIP operation instructions would apply.

High-k PL-6 CO₂ laser startup

- Turn on laser warning sign
- Notify nearby personnel
- Close laser curtain
- Turn on control computer, run LabView program (details below)
- Turn on PL-6 dry scroll pump and open vacuum control valves
- Turn on gas ventilation blower
- Turn on CO₂ gas cylinder
- Turn on laser monitors and controls, CO₂ power meter, water temperature gauge, data acquisition interface, and gas pressure gauge
- When CO₂ pressure reaches < 1 Torr, turn on gas valve, adjust gas flow to maintain 8-10 Torr pressure
- Turn on High-k water chiller
- Turn on power supply keyed switch
- Put on laser safety glasses
- Safety check equipment and nearby personnel again
- Activate CO₂ laser by pressing “High Voltage ON” button; the laser tube should glow purple, and the power meter should respond immediately, typical startup power is 70 to 100 W
- Power is increased by increasing gas pressure; maximum power is typically near 28 Torr and a current of 40 mA for each channel for 160+ W output

If the laser does not activate, or if only one side activates, then the high voltage should be turned off. To reset the power supply, the keyed switch must be turned off and then back on. The current control can be left at 40 mA for start-up, and power is controlled solely by the gas pressure. If the laser does not activate, and the fault light comes on, it indicates that the power supply voltage has ramped up too high. Reducing

the gas pressure and current control will typically solve the problem. The PL-6 is more stable than the FIReTIP style CO₂ laser. It generally does not require any tuning to produce maximum power. The diffraction grating is only adjustable in one axis to select the lasing line. The output coupler will not move or need any adjustment under normal conditions. Allowing the laser to operate for 15 minutes should be sufficient to provide a stable pump for the FIR laser, with only infrequent PZT adjustments. To deactivate the laser, press the "High Voltage OFF" button. Note: the PL-6 power supply has two buttons for high voltage control, "ON" and "OFF". This differs from the FIReTIP CO₂ laser power supply, which uses the same button to control the high voltage. When the laser is deactivated, the remaining components can be turned off in any order. Make sure the gas mixture bottle is turned off to ensure no laser gas is lost. It is not necessary to leave on the vacuum pump. Instead, close the vacuum control valves and turn off the pump.

The High-k₀ Scattering FIR laser start up procedure is detailed below. There are some special considerations for formic acid handling. Otherwise, it is similar to the FIReTIP procedure. The CO₂ laser must be activated to pump the FIR laser. Follow the instructions above to turn on the CO₂ laser, and while it is "warming up", the FIR laser can be prepared for operation. The FIR laser should be connected to the FIReTIP dry scroll pump for maintenance vacuum. Before running the High-k FIR laser, it will need to be isolated from the FIReTIP system, and switched to its own oil vacuum pump. Check the formic acid supply before initiating the startup procedure. The FIR laser will consume ~10 ml per 8 hours. If there is insufficient volume, the reservoir should be refilled. Pure formic acid will decompose relatively quickly at room temperature, and the laser will produce less power. If the acid is more than two weeks old, or if it becomes discolored, it should be replaced.

High-k FIR laser startup

- Close the vacuum valve connecting the High-k FIR laser to the FIReTIP system
- Turn on High-k oil vacuum pump and open valve to evacuate the High-k FIR laser
- Turn on the blower for the gas ventilation
- The control computer and LabView program should already be running (details below)
- Turn on monitoring and control equipment: data acquisition interface, power meters, choppers, water temperature gauge, and motor controllers
- Laser vacuum should be < 5 mTorr before continuing; ~2 mTorr is typical, Note: It can take a long time to reach ultimate vacuum (from 50 mTorr to 2 mTorr can take 45 to 60 minutes, from atmospheric pressure it can be 4+ hours)
- Open gas control valve and allow formic acid to circulate, operating pressure should be 150 to 200 mTorr
- The chiller should already be activated for the PL-6 CO₂ laser
- FIR power may not immediately be registered; tune the CO₂ PZT voltage to increase FIR power, if the PZT adjustment yields no result then the FIR cavity length may need adjustment
- Tune the PZT and FIR cavity length for maximum power output; while the lasers are “warming up”, the PZT may need occasional adjustment (every ~5 minutes)
- Minor adjustments to the output coupler alignment may be necessary for maximum power output and to control mode quality; however, the majority of laser tuning will be from the PZT and cavity length adjustments. Never adjust the rear mirror during normal operations.
- FIR power output depends on the CO₂ pump power. With 160 W pumping power, the FIR laser should produce 75-100 mW

Deactivating the FIR laser is accomplished by pressing the "High Voltage OFF" button on the PL-6 power supply. This will turn off the high voltage and all lasers. The remaining laser components can be

turned off in any order. When the formic acid valve is closed, the oil vacuum pump should be allowed to run for ~30 minutes to purge formic acid vapor through the ventilation system. Following this procedure, the oil vacuum pump can be turned off, and the High- k FIR laser can be connected to the FIReTIP dry scroll pump for maintenance vacuum (assuming FIReTIP is not in use).

VI.3 LabView Control program

The FIReTIP and High- k_0 Scattering systems are monitored and controlled by computer. This allows critical functions to be monitored remotely, and many of the diagnostic functions can be remotely controlled. It is important that the operator be in the control room during NSTX-U operations to facilitate communication with PPPL scientists and engineers. If a major problem is detected, the operator can shut down the systems to render them safe. For minor problems, the computer control allows the operator limited ability to tune the system, namely through adjusting the FIR cavity lengths. This will ensure that the lasers are operating at maximum power, and in the case of FIReTIP, tuned to the correct frequencies. There is no access to the test cell during plasma shots; therefore, data must be remotely monitored, and the control systems for the High- k_0 Scattering System must also be remotely controlled. The High- k_0 Scattering launch optics can steer the probe beam by several degrees, and the receiving optics focus must be coordinated with the probe beam for the desired scattering location and scattering angles. The High- k_0 Scattering FIR beam power can be monitored at the laser table, and/or at the reference channel in the waveguide run. The FIReTIP receiver mixer outputs should be continuously monitored on a spectrum analyzer to verify the FIR laser tuning, which is observed and controlled by the control program.

All of these function are controlled by a single LabView program¹ by National Instruments [8]. The computer is located in the “cage” area by the lasers; however, this computer can be remotely accessed

¹The FIReTIP / High- k_0 Scattering LabView control program was developed by UC Davis graduate student, Mohammad Hadi Sohrabi.

from the NSTX-U control room. The various monitors generally produce a DC signal between 0-10 V proportional to the parameter measured. The DC signal is routed to a data acquisition interface (DAQ) to convert the DC analog signal to a digital signal. The DAQ then delivers the signal to the computer, where LabView can interpret and display the signal. Most signals require a correction curve to relate the detected DC voltage to the actual measurement. Many correction curves are not linear; therefore, the correction curves are programmed into the LabView software. For example, each pyroelectric detector has a unique power response. To calibrate these power meters, the pyroelectric detector output is compared with an absolute power meter, and many data points are plotted. These data points are then curve fit to interpolate the data, and the curve equation is programmed into Labview. The following table lists the parameters monitored, and the normal levels.

Table 13. FIReTIP Monitors and Control

Parameter	Normal Range
Water Temp.	10-15 C
CO₂ Gas Press.	10-30 Torr
FIR #1 Gas Press.	500-700 mTorr
FIR #2 Gas Press.	500-700 mTorr
Stark Gas Press.	200-300 mTorr
CO₂ Laser Power	10-120 W
FIR Laser #1 Power	50-150 mW
FIR Laser #2 Power	50-150 mW
Stark Laser Power	10-50 mW
FIR #1 Cavity Length	Δ 0-5 mm
FIR #2 Cavity Length	Δ 0-5 mm
Stark Cavity Length	Δ 0-5 mm
Reference Mixer Output	2, 4, 6 MHz

The reference mixer output is observed on a spectrum analyzer in the IF electronics rack. The spectrum analyzer display is then delivered by a data link to the control computer. This feedback is essential for tuning the system prior to each plasma shot. The cavity length monitor is a relative length reference.

Table 14. High- k_0 Scattering Monitors and Control

Parameter	Normal Range
Water Temp.	12-18 C
CO₂ Gas Press.	10-30 mBarr
FIR Gas Press.	150-200 mTorr
CO₂ Laser Power	20-170 W
FIR Laser Power	10-150 mW
FIR Cavity Length	Δ 0-5 mm
Reference Power	10-150 mW
Probe Beam Angle	± 2.25° (2-axis)
Receiver Position	5-axis control*

The cavity length measurement is a relative length reference. The probe beam angle and receiver position will display 7 axes of control. To set the launching and receiving optics, the radial, vertical, and lateral position of the scattering volume is selected. Then, the nominal scattering angle is selected, and the software will calculate the proper positions for the launching and receiving optics. These 7 axes can then be positioned one at a time. Note: Not all positions are available. If an unreachable position is selected, the software will alert the operator.

There is more information controlled by the software than an operator can reasonably keep track of. To simplify the operation, the LabView program display can be customized. The front panel display is initially blank; however, each of the monitors and controls are represented by a row of virtual buttons along the edge of the display. Selecting any button will cause a particular parameter to be displayed as an inset window or minimized. The displayed windows can be dragged around the screen and arranged to the operator's preference. The normal range of operation and measured parameter are graphically and numerically displayed. If the parameter is normal, a green light is illuminated. If a parameter falls outside of normal, the light will change to yellow to alert the operator. If a parameter differs from normal by a critical amount, the light will turn red. If a measurement indicates there may be danger to the instrument or personnel, it will flash red and immediately shut down the high voltage power supply, thereby shutting down all the lasers at the same time. When the parameter windows are minimized, the virtual buttons will be colored coded in the same way. This allows a cursory inspection of all diagnostic functions at a glance. If all buttons are green, the systems are operating normally. The PL-6 has additional safety controls integrated into its power supply. The PL-6 will automatically shut down if the power supply voltage ever exceeds 20 kV, or if the chiller flow switch registers no water flow. These are not displayed in the LabView program; however, they will cause the laser power to go to zero, which will cause an alarm. If a particular parameter needs to be bypassed, the operator can turn off any monitor or control. It will be colored red to remind the operator the parameter in question is not being monitored.

To access the LabView program:

- Turn on “cage” computer
- Select the control program on the desktop labeled “FIReTIP/High-k Control.vi”, This will load the program; however, it will not be active yet
- Turn on all gauges and sensors to be monitored/controlled, plus the DAQ
- Run the LabView program by pressing the “white arrow” on the task bar

- The program will now monitor all systems; to observe a monitor or activate a control, the desired system button should be pressed to display its window
- The operator may now monitor / interact with the program
- When desired, the “cage” computer can be remotely accessed for remote control
- To shut down the software, the program can be closed at any time
- When not in use, all the system components and computer should be powered down

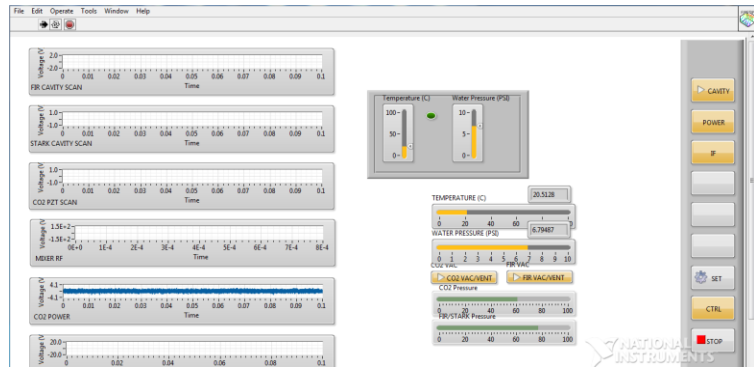


Figure 227. "FIReTIP/High-k Control.vi" LabView control program front panel display. This image displays an example of how the control program display could be configured. The various windows show monitored parameters with graphical and numerical displays. The buttons down the right side will activate or minimize each window. The parameter windows and buttons are color coded to indicate each system's status.

The software can be modified as necessary to the operator's needs. Additional monitors and controls can be added following the modular format of the software. Unneeded or defective systems can be bypassed if the action is warranted.

VI.4 Fusion Power Legacy

It is unknown when fusion power will generate electricity in significant quantities. Experts in the field vary in their estimates; however, a consensus of a few decades is generally accepted [9, 10, 11]. There are many factors which could help or hinder the progress, and debates will continue for the best approach to address future energy demand. Fusion power technology depends on the development of many technical fields. These include: computer simulations, material science, vacuum electronics, microfabrication, quasi-optical electronics, and lasers just to name a few. Even if a commercial fusion power plant is never built, the research is still well worth the effort. So many technologies have been developed in pursuit of fusion, the benefits will be wide spread across science and engineering. There is still considerable work to be done for the foreseeable future. Data collection will be key to fuel fusion research, and in particular the study of plasma instabilities and anomalous transport.

The unique challenges of designing and constructing plasma diagnostics are numerous. The extreme conditions in magnetically confined plasmas require creative solutions. Scientists and engineers must work together to create systems that can collect the data needed to address the current research. The scope of this work is more than any individual can possibly supply. Cooperation among several people is required for even relatively simple projects, and hundreds of people are required for the total effort. It is the author's privilege to make contributions in the area of plasma diagnostics.

The FIReTIP and High- k_θ Scattering systems are fully designed, and largely built and tested. The research goals, design parameters, fabrication, and testing details have been comprehensively discussed. For the tasks to be completed by subsequent personnel, many details have been provided to ensure success. The author has presented experience and advice for future contributors. Cutting edge research is a dynamic environment, and it is important to be flexible. These diagnostics should provide the data required to fulfill the prescribed research; however, they have also been designed for expansion and upgrades for

future research. In addition to the diagnostic designs, details have been provided for related technologies. These include gas lasers, vacuum electronics, and microfabrication. The installation and commissioning of the FIReTIP and High- k_θ Scattering systems is scheduled to be completed in 2017. These plasma diagnostics will provide years of service, and it is the ambition of the author that they make significant contributions to fusion power research.

VI. References

- [1] K.C. Lee, C.W. Domier, M. Johnson, N.C. Luhmann, Jr., and H. Park, "FIR Laser Tangential Interferometry/Polarimetry on NSTX," *IEEE Transactions on Plasma Science*, 32 No. 4, pp. 1721-1726 (2004).
- [2] W. Lee, H.K. Park, M.H. Cho, W. Namkung, D.R. Smith, C.W. Domier, and N.C. Luhmann, Jr. "Spatial Resolution Study and Power Calibration of the High-k Scattering System," *Review of Scientific Instruments*, 79, 10E723 (2008).
- [3] D.K. Mansfield, H.K. Park, L.C. Johnson, H.M. Anderson, R. Chouinard, V.S. Foote, C.H. Ma, and B. J. Clifton, "Multichannel far-infrared laser interferometer for electron density measurements on the tokamak fusion test reactor," *Applied Optics*, Vol. 26, No. 20, October 1987.
- [4] J.D. Strachan et al., "TFTR DT experiments," *Plasma Phys. Control. Fusion*, Vol. 39, June 1997.
- [5] Y.S. Jin, G.J. Kim, and S.G. Jeon, "Terahertz Dielectric Properties of Polymers," *Journal of the Korean Physical Society*, Vol. 49, No. 2, August 2006.
- [6] H. Park, D.L. Brower, W.A. Peebles, N.C. Luhmann Jr., A.L. Savage Jr., and C.X. Yu, "Development and application of multichannel collective scattering systems," *Review of Scientific Instruments*, Vol. 56, 1055, May 1985.
- [7] H. Park, C.X. Yu, W.A. Peebles, N.C. Luhmann Jr., and R. Savage, "Multimixer far-infrared laser Thomson scattering apparatus," *Review of Scientific Instruments*, Vol. 53, 1535, October 1982.
- [8] "LabView System Design Software," *National Instruments*, <http://www.ni.com/labview/>, Accessed: January 13th, 2017.
- [9] "ITER, the way to new energy," ITER Organization, 2016. [Online]. Available: <http://www.ITER.org/sci/Goals>. [Accessed 10 5 2016].
- [10] K. Muraoka, F. Wagner, Y. Yamagata, and A.J.H. Donne, "Short- and long-range energy strategies for Japan and the world after the Fukushima nuclear accident," *17th International Symposium on Laser-Aided Plasma Diagnostics (LAPD17)*, Journal of Instrumentation, Vol. 11, January 2016.
- [11] C. M. Braams and P. E. Stott, "Nuclear Fusion," Institute of Physics Publishing, Bristol and Philadelphia, 2002.

Appendix A Laser Maintenance and Overhauls

The laser systems for the FIReTIP and High- k_0 Scattering systems require maintenance to keep them operating at peak efficiency. Daily operating procedures and frequent laser maintenance, such as laser tuning, and gas consumption, are covered in Chapter 6. This appendix covers the annual maintenance and laser overhaul procedures. Under normal operations, the lasers should run in excess of 1,000 hours without any major maintenance required. This equates to approximately one year's operation at 50% duty cycle. Over time, laser power may fall off slowly. For FIReTIP, if laser power drops below the noise threshold of the detector mixers, then it will be difficult to extract the phase information from the signals. The scattered power from the High- k_0 Scattering probe beam is proportional to the probe beam power; therefore, decreased laser performance can be detrimental to the signal to noise ratio from the receiver array. Before the power drops too low for diagnostic operation, the lasers should be inspected, cleaned, and defective parts replaced as necessary. It is recommended to perform laser inspection and cleaning at least once per year. In the event of laser failure, the cause will need to be investigated, and the appropriate corrective action taken. Annual maintenance may include waveguide cleaning and/or the replacement of optical components, such as couplers or windows. A laser overhaul consists of disassembling the entire laser, inspecting/replacing components, cleaning all parts, and realigning the optics on reassembly.

A.A.1 Laser Maintenance

The following section details the typical annual maintenance needs for the FIReTIP and High- k_0 Scattering lasers. There are many methods to inspect and maintain the various laser components. The recommendations below were found by the author to be the most reliable methods to keep the lasers operating at optimal performance. Anytime the laser performance is less than maximum, the cause should be investigated, and any necessary repairs should be performed as required. If the lasers are running well, then they should be inspected and cleaned at a minimum interval of one year.

A.A.1.1 FIReTIP CO₂ Laser Maintenance

The most common components that need attention for the FIReTIP CO₂ laser are the output coupler and diffraction grating. The exposure to high power IR (~100 W) can lead to compromised optics and coatings. The cooling system circulates water around the mounts for these items to prevent damage; however, they can degrade over time.

Should the output coupler coating become damaged, the transmission and reflection coefficients will become altered, and vary across the surface. This can result in reduced power and/or poor mode quality. This is evidenced by low power meter readings, asymmetrical modes observed on a fluorescent detection plate, and a cloudy appearance across the surface. If the ZnSe substrate fails, it will be obvious due to deep pitting or cracking. A cracked output coupler will not maintain vacuum, and will cause immediate laser failure. Removing/replacing the output coupler is accomplished by first unsealing the vacuum to bring the laser cavity to atmospheric equilibrium. Then, the threaded retaining ring can be unscrewed using a spanner wrench. A small screw driver can be used, but extreme caution must be observed to avoid scratching the output coupler. Then, the tapered spacer, o-ring, and output coupler can be removed. Gloves should always be worn to avoid fingerprints. It is also recommended to place a pad beneath the output coupler housing in case the optic falls upon removal.

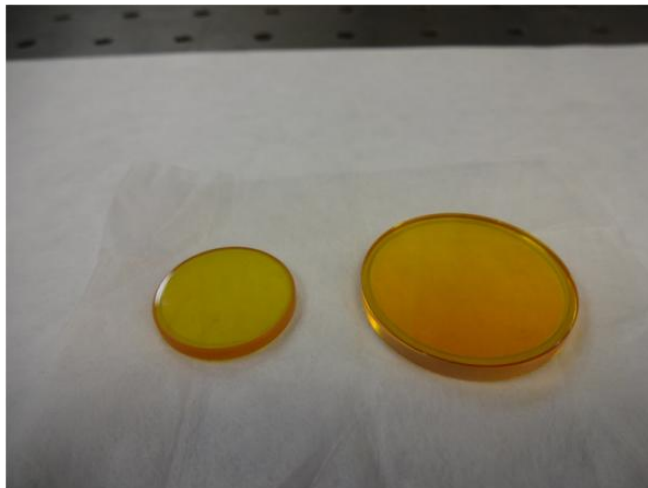


Figure 228. ZnSe optics. Left: CO₂ laser 1" diameter output coupler. Right: Beam Splitter 1.5" diameter.

The output coupler is a 1" diameter, 0.125" thick, ZnSe disk. The outer surface is ground flat; however, the inner surface is concave with a 20 m radius, to help collimate the reflected IR photons in the laser cavity. Thin dielectric coatings on the inner surface are applied to achieve 80% reflection at 9.7 μm . The concave surface is typically labeled on the edge of the optic with a small chevron pointing towards it. The chevron is applied with ink, and is easily washed away; therefore, care should always be taken when handling the optics. The convention for how each side of the optic is identified may vary; therefore, attention to detail is vital. The output coupler should appear as clear, dark amber glass. Sometimes the coating will provide a slight green tint, but the surface should be smooth and free of contaminants.

If the output coupler is visibly dirty, then it can be cleaned by a variety of techniques. These should be applied in the least aggressive to the most aggressive manner as listed below. The least aggressive manner is to gently blow air or inert gas across the surface to remove dust and other particles. If the optic still requires cleaning, then isopropyl alcohol can be applied to dislodge contaminants, followed by gentle drying with an air gun. If this is insufficient, then isopropyl alcohol can be applied and lens quality tissue paper can be gently rubbed across the surface. Only very light pressure should be applied to avoid

damaging the coating. If these techniques cannot clean the optic satisfactorily, then the optic should be replaced.

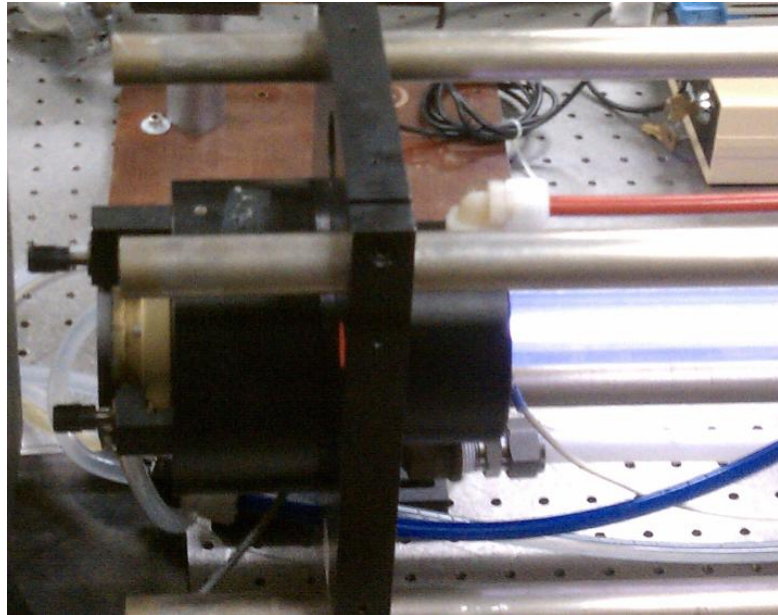


Figure 229. CO₂ laser output. The output coupler housing and PZT are left of the support plate. The anode housing is right of the support plate.

Replacing the output coupler is the reverse order of removal. The optic is set in its housing, concave side in (chevron pointing in). If the o-ring is hard, cracked, cut, or damaged in any way, then a new one should be used. Standard buna-N or nitrile o-rings should be used. The o-ring is placed against the output coupler, and then the tapered space is installed, with the taper towards the o-ring. Finally, the retaining ring is threaded into place. The ring is gently tightened to lightly compress the o-ring. Over tightening will crack the optic. The proper tightening is ~1/8 of a turn past finger tight. This is enough to seal for vacuum, and will not self-loosen. The installation can be tested by evacuating the laser. If the laser pumps down to < 1 Torr in 1-2 minutes, then the optic is sealed correctly.

After reinstalling the output coupler, the optical alignment will not be restored. It may be close enough to register power on the CO₂ power meter if the laser is run. If no power is detected, then adjusting the output coupler alignment by small amounts will likely establish some power. Once a small amount of laser power is measured, the output coupler can be aligned by "walking" the alignment into position. Each alignment axis is adjusted a small amount. If power decreases, reverse the direction. By alternating the alignment of each axis, the output power can be steadily increased until a maximum value is found. When laser power is approaching the expected maximum, the alignment can be improved by alternating between the output coupler and diffraction grating alignments. Tuning the output coupler in this manner depends on the diffraction grating being already aligned. The output coupler and diffraction grating should not be replaced at the same time; otherwise, the combined misalignments could be too much to reasonably establish laser power in a timely manner. In this case, the overhaul alignment technique may be necessary.

The diffraction grating is accessed by removing the three rear laser plate retaining screws, and sliding the plate towards the rear of the laser (without vacuum). The plate should be moved far enough to provide access to the grating. There are two cooling lines attached to the rear plate. If the lines have insufficient slack to move the rear plate, they may need to be removed. Once the grating is visible, it can be inspected. The surface should be clean, and free of burns or debris. Small discoloration may be a sign of reduced performance. The quality of the grating is difficult to determine, and it is a judgment call for the laser operator. If detailed analysis is warranted, the grating can be observed under a microscope. To remove the grating, the zeroth order mirror bracket must be removed. Then, four retaining screws and spring loaded retention clamps are removed. The grating should be labeled with an arrow marking the blaze direction. Note the arrow orientation. It should point away from the laser central axis. The grating can then be gently removed, taking care to never touch the grating surface (gloves required). The grating may appear stuck in place due to thermal grease; however, it should come free with light pressure. The grating is a series of parallel grooves. Under visible light, a spectrum of the visible colors should be observable. If the

spectrum is distorted or spotty, it may indicate a problem with the surface. Any dark spots or disruptions to the grooves will reduce the effectiveness, and reduce laser output. If compromised portions of the surface exceed 50%, the grating should be replaced. Otherwise, the ultimate test for grating performance is to install the grating and run the laser. If laser power and mode quality are sufficient, then the grating is good. Light air can be used to blow dust and debris from the surface; however, no other cleaning method should ever be used. Under no circumstances should anything contact the surface, otherwise, the grating will be damaged.

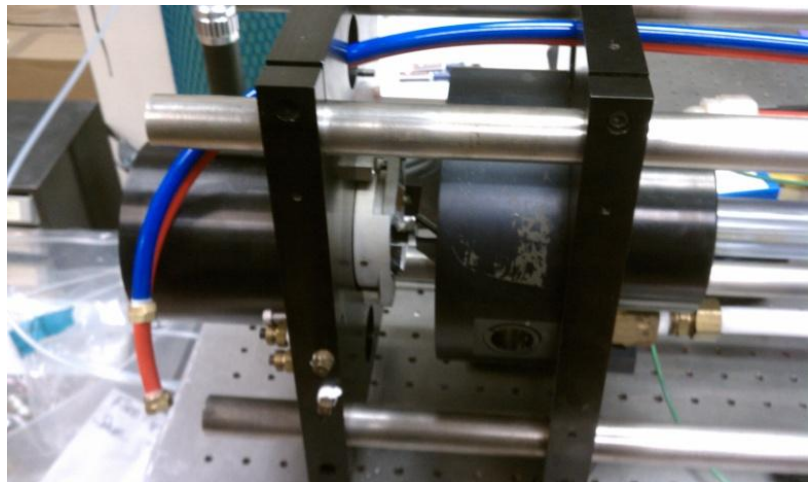


Figure 230. Diffraction grating enclosure in the process of being removed. The red and blue cooling lines are disconnected, and the support plate is slid off the invar rods to the rear of the laser.

To reinstall the grating, the zeroth mirrors should first be inspected. There are two mirrors, one adjacent to the grating location, and the second is attached to an L-shaped bracket that was removed during grating removal. These are first surface mirrors and can be cleaned with isopropyl alcohol and optical tissue paper. They are glued in place; therefore, if they need to be replaced they will likely be broken on removal. The mounting surface can then be scraped clean, and new mirrors glued in place. A thin layer of vacuum safe, thermally conductive grease is applied to the grating mounting surface. If the existing grease is too thick, dirty, or lumpy, then it can be scraped clean, and new grease applied. The grating can

then be set into position, taking care to orient the blaze arrow in the correct direction (away from the laser central axis). A reversed grating will still function; however, the laser tuning and power may be dramatically altered, since the reverse geometry will be blazed for a different wavelength and angle. The retention clamps, springs, and screws are then installed. The clamps will contact just the edge of the grating to locate its position. The screws are tightened to compress the springs to provide the proper tension. The springs should be compressed enough to prevent the grating from moving. Excessive retention can strain the grating surface. The zeroth mirror bracket can be reinstalled. Note: the tolerance of the zeroth mirror bracket screws allows the mirror a few degrees of freedom. This will alter the zeroth output beam alignment slightly. The beam alignment with the spectrum analyzer may need to be verified. The rear laser plate can be slid back into position. Ensure that its o-ring seal is in place, and then the three retaining screws can be tightened, and the water lines reattached if necessary. The reassembly can then be vacuum checked.

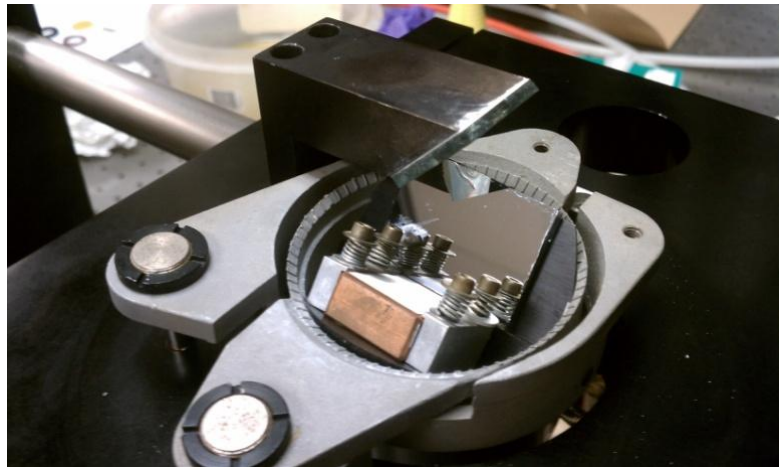


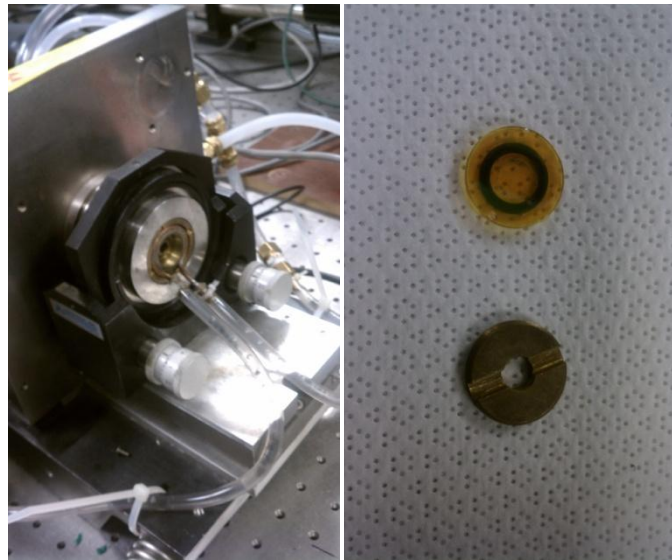
Figure 231. Diffraction grating mount. The copper diffraction grating is seen in its spring loaded clamps. The two zeroth order mirrors are seen. One is adjacent to the diffraction grating; the other is mounted to a bracket above the diffraction grating.

The grating can now be tested by operating the laser. If a used grating is installed, a known position for the alignment micrometers should be adjusted for. The laser may not generate power immediately; however, slight adjustment to the grating alignment should establish power on the laser power meter. Once some power is measured, the grating can be "walked" into position for maximum power in the same manner as the output coupler. Similarly, the output coupler should not be replaced at the same time as the grating to avoid alignment issues. If a new grating is installed (or no known alignment position is available), then the grating can be systematically swept through its positions until some power is established. Setting the power meter for the 3 or 10 W scale will help detect small levels of power. As soon as the power meter registers a CO₂ beam, then the grating can be "walked" into alignment. When sufficient power (> 50 W) is established, the spectral line can be measured with the CO₂ spectrum analyzer. The zeroth output will emit ~ 1% of the main output power. ~0.5 W is about the minimum power required to observe the laser line on the spectrum analyzer. Alternatively, the CO₂ spectrum analyzer can be positioned at the main output; however, no more than 10 W laser power should be directed at it. When the CO₂ beam is aligned with the spectrum analyzer input, a diffraction grating will steer the beam to a fluorescent detection plate according to its wavelength. The detection plate is graduated for the common CO₂ laser lines from 9 to 11 μm . When the CO₂ laser line is determined, the laser can be tuned for the desired line by rotating the grating along the vertical axis. The spectrum analyzer will measure the shifting laser lines by disappearing and reappearing along the graduated scale in discreet increments. The horizontal grating position may need to be tuned as the grating is swept through several spectral lines to maintain laser power. For FIReTIP, the goal is to tune the laser for 9P36 (9.695 μm) to energize the methanol lasers. Every grating will be unique for the position needed for optimum tuning, and not all gratings will have the ability to achieve 9P36 for the given range of adjustment. Most commercial gratings designed for 10.6 μm operation will work; however, better performance can be achieved with a grating blazed for 9.7 μm .

A.A.1.2 FIReTIP FIR Laser Maintenance

The three FIReTIP FIR lasers all have the same optics design, and the same maintenance procedure can be used for all three lasers. Only minor changes to the procedure are made for the Stark laser. The optical components that should be inspected annually are the input window, rear mirror, and giant hole output coupler. These components will rarely need replacing, but should be inspected and cleaned as necessary.

The input window is a 0.75" diameter, 0.125" thick, ZnSe disk. It is ground planar on both sides, and is anti-reflective coated for 9.7 μm . Both sides of the window are identical. The window can be removed (when the laser is not under vacuum) by unscrewing the brass retainer with a broad flat blade screwdriver. The window is removed next. Gloves should be worn when handling the window, and it is recommended to place a pad beneath the window housing in case of accidentally dropping the window. Under the window is the sealing o-ring. This can be left in place; however, it can be removed for inspection if the seal is suspect. The window should be clear, dark amber, glass, free of pits or cracks. If the window is visibly dirty, it can be cleaned in the same manner as the CO₂ laser output coupler: 1) air only, 2) isopropyl alcohol and air, and 3) isopropyl alcohol and gentle rubbing with optical tissue paper. Even though ZnSe has a very low absorption coefficient at 9.7 μm , if the CO₂ laser is focused with the beam waist at the window, the intensity can be high enough to burn a hole through the window. Reinstalling the window is the reverse procedure. The o-ring is installed, then the window is set into place, and the brass retainer is screwed on. The brass retainer will rub directly on the window, which may scratch the surface. This is OK because only the non-visible portions of the window can be scratched. Care should be taken not to over tighten the retainer. The proper retention is just enough to compress the o-ring so that the retainer does not self-loosen. This is $\sim 1/8$ turn past finger tight. The seal can be tested by evacuating the laser. The window mount is inset into the rear mirror retainer and cooling ring.



Figures 232a and 232b. Left: FIR laser input window and two axis mount. Right: ZnSe input window, o-ring, and retainer.

The rear mirror is a 1.5" diameter copper mirror, with a 4 mm hole at its center. It can be removed by unscrewing the rear mirror retainer ring. The input window is inset into the larger rear mirror retainer, and the window does not need to be disturbed to access the mirror. The retainer ring is unthreaded with a spanner wrench. There are two cooling lines attached to the retainer, and these can be left connected. The cooling lines are flexible enough to set the retainer aside. Next, the o-ring is removed, and then the mirror can be removed. Gloves should be worn anytime handling the optics. The inside surface of the mirror is ground flat and is polished. The mirror should be highly reflective in the visible spectrum. If reflections are cloudy, burned, or distorted, the mirror may need to be re-polished or replaced. There is no coating on the mirror; however, copper is soft and care should be taken when cleaning the mirror. Isopropyl alcohol and an air gun are usually sufficient for cleaning the mirror. Installation is in the reverse order. It is important to install the mirror before the o-ring. The laser will seal either way; however, if the o-ring is installed first, the mirror may be tightened in a cocked position. This will alter the alignment of mirror, and it may be out of the tuning limits for the mirror alignment.

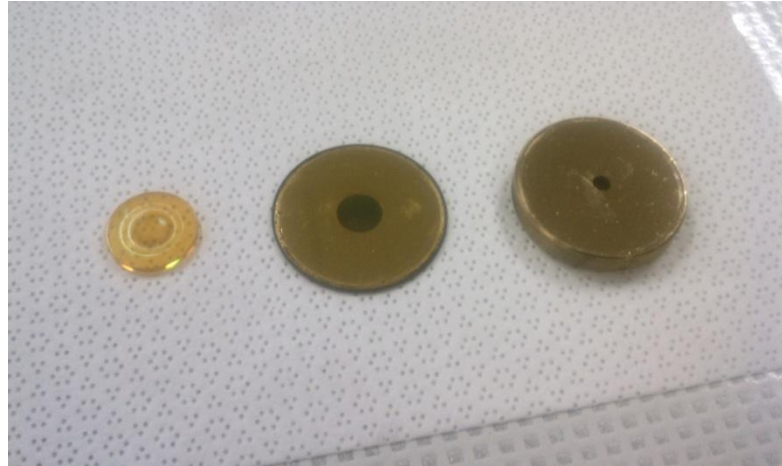
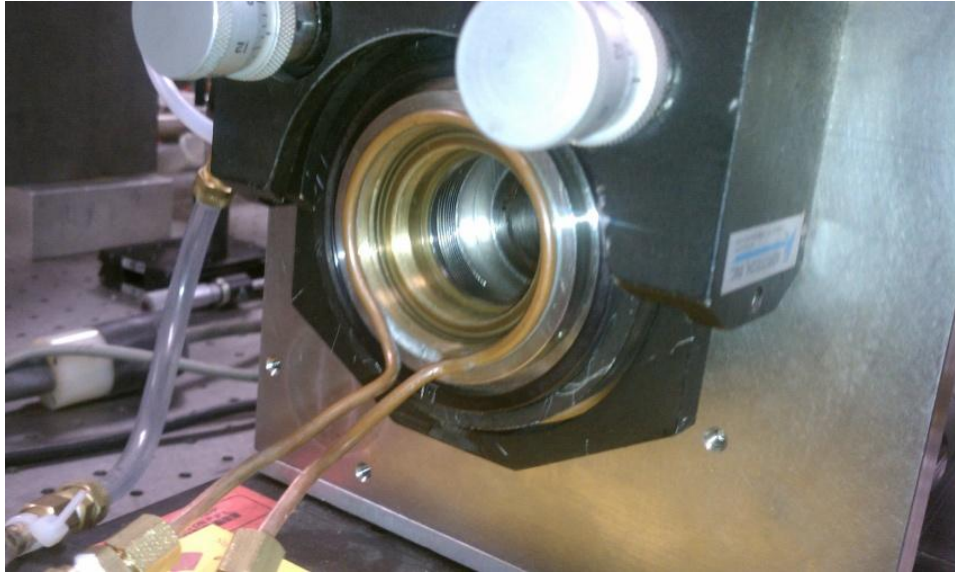


Figure 233. FIReTIP FIR laser optics. From left to right: ZnSe input window, giant hole hybrid output coupler, and rear mirror with 4 mm hole at center.

The output coupler housing is similar to the input window side. The outermost part is a z-cut quartz window. It is retained by a threaded cover, and sealed with an o-ring. This part generally never needs to be removed. Next is the output coupler retainer. This retainer is a thick brass cover. The cooling lines are soldered into a separate structure. The outer retaining ring secures the cooling ring, and does not need to be disturbed. The inner portion is the retainer, and it is removed with a spanner wrench. Behind the retainer is a sealing o-ring. Next is an aluminum retaining ring which secures the hybrid, giant hole output coupler. The aluminum retaining ring is unthreaded, and then the output coupler can be removed. As always, gloves should be worn when handling the optics. Furthermore, the coupler should only be held by its edges.



Figures 234. FIR laser output with coupler retainer and output coupler removed.

The output coupler is fragile and custom made for the FIReTIP application. Extreme care should be taken when handling the optic. These couplers are more than 15 years old, and the coating is beginning to flake around the edges. This portion of the coupler is not exposed to the laser light; therefore, it does not affect performance. When cleaning the output couplers, care should be taken not to accelerate the coating degradation. Isopropyl alcohol and light air pressure is all that is needed to clean the coupler.

Installing the output coupler is the reverse procedure. The coupler is set in place with the "giant hole" facing the interior of the laser. Next, the aluminum retainer ring is threaded into place. This ring does not need to be tight. It is threaded down so that it seats against the optic. Finger tightening is sufficient. Then the retainer o-ring is installed, the finally the retainer is installed and tightened with the spanner wrench. Excessive tightening can damage the retainer threads. It only needs to be tight enough to provide a vacuum seal. Once the retainer is contacting the o-ring, an additional 1/8 turn is needed to establish the seal. The installation can be tested by evacuating the laser.



Figure 235. Exploded layout of the FIR laser output coupler assembly. From left to right: quartz window and retainer, window o-ring, output coupler retainer, o-ring, spacer and retaining ring, giant hole hybrid coupler. Above on the left is the spanner wrench to remove the output coupler retainer. Above to the right is a set screw and allen wrench to help secure the output coupler retainer.

Working with the rear mirror or the output coupler will likely, slightly, alter the laser alignment. Most of the time, the laser will still be sufficiently aligned to generate power, and then the laser can be fine tuned. If the laser does not generate power, small adjustments can be made to the optical alignment until power is established, and then the laser is tuned by "walking" the optics into optimum position. Should the alignment be irrecoverable, then the overhaul alignment procedure will be needed to reestablish laser power.

The interior of the laser is generally exposed only to vacuum, methanol, and light; therefore, it should be a very clean environment. However, over time, oil will back stream from the oil vacuum pump and slowly coat the interior surfaces. This is why the dry scroll pump is preferred for maintenance vacuum. Cleaning the optics as described above will ensure consistent performance for many years. The dielectric waveguide should also be cleaned. The waveguide can be cleaned by removing the rear mirror and output

coupler to see through the laser cavity. An insulated wire is fed through the waveguide. The wire should be stiff enough to not bunch up during insertion. The insulation provides padding to prevent the waveguide from being scratched. With the wire protruding from the end of the waveguide, a loop is fashioned to hold a patch of lint free cloth or optical tissue paper. The cleaning patch is saturated in isopropyl alcohol, and then drawn through the waveguide. Contaminants in the waveguide will be seen on the cleaning patch. The process is repeated as necessary until the waveguide is visually clean, and the cleaning patch is drawn out clean. Gentle air flow will dry the tube, and then the optics can be reinstalled. This procedure requires both the rear mirror and output coupler to be removed. Usually, the alignment is preserved well enough to establish laser power, and then the alignment can be fine tuned.

The Stark laser has one important difference in the waveguide cleaning procedure. The metallic coating is on the inside of the waveguide, and it is fragile. The electrode clips should be carefully removed. The clips should not be allowed to slide along the waveguide surface, as this will scratch off the metallic coating. The clip pressure is relieved by opening the clip spring, and then removing or installing the clip on the waveguide. With the electrode clips removed, an insulated wire can be passed through the waveguide, ensuring that the wire does not bunch up inside the waveguide, which may scratch the inner surface. The rectangular waveguide has a smaller cross section than the conventional FIR lasers. The cleaning patch is carefully sized to fill the waveguide cross section, without exerting too much pressure against the coating. When drawing the patch through the waveguide, the resistance should be barely perceptible. The patch is saturated with isopropyl alcohol, and gently drawn through the waveguide. To preserve the life of the waveguide a long as possible, this waveguide should only be cleaned when it is required to do so.

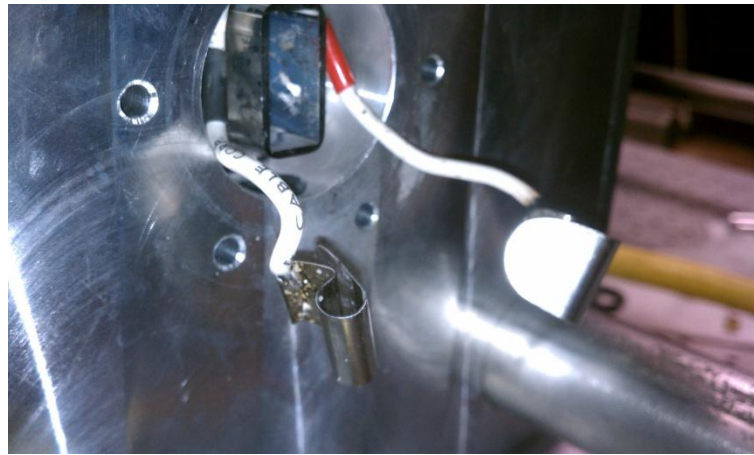


Figure 236. Stark laser clips. The end of the rectangular Stark laser waveguide is seen. The two connections for the Stark potential are removed from the waveguide.

A.A.1.3 High- k_0 Scattering PL-6 Laser Maintenance

The PL-6 is in current production (2017) by Edinburgh Instruments. Any parts that are needed can be purchased through Edinburgh Instruments, and they can make service calls if necessary. Over time, the laser may reduce in power output as the optical components degrade. There are four components that should be inspected on an annual basis: 1) diffraction grating, 2) output coupler, and 3 & 4) two Brewster windows.

If the grating becomes visibly discolored or burned, the laser power will be reduced, and it should be replaced. The grating surface can be cleaned by gently blowing air over the grating surface. No other cleaning technique should be used. Never touch the grating surface with anything. The diffraction grating mount is carefully aligned so that its adjustment is in one axis only. It is critical that a new grating be mounted squarely so that it maintains its alignment for the full range of adjustment. If the grating is askew, or if the mount's alignment is altered, the utility of the PL-6 will be severely compromised. The standard grating from Edinburgh Instruments is grooved at 135 g/mm, and is blazed for 10.6 μm . The

grating mount has sufficient travel to access all spectral lines from 9 to 11 μm . Every grating is unique, and if replaced, the laser calibration reference sheet will become invalid. The laser should then be recalibrated. The output power should be reduced to < 10 W by deactivating one of the discharge tubes with the isolation switch on the rear of the power supply (either channel is OK). The laser can then be activated with the normal start up procedure, and then the gas pressure is reduced to ~5 Torr, and the current control reduced to ~15 mA. At 10 W or less, the beam will be safe to direct at a CO₂ spectrum analyzer. When the spectrum analyzer is aligned, the laser can be tuned for maximum power for each spectral line. The grating position indicator is recorded for each spectral line. The output coupler and diffraction grating should not be replaced at the same time to reduce the number of variables for aligning the optics.

The output coupler is ZnSe, coated for 60% reflection. It should be a dark amber glass, and clear to visible light. If the coupler is discolored or cloudy, it should be replaced. New couplers are available from Edinburgh Instruments. If the output coupler is dirty, then it can be cleaned with the same procedure as the FIRiTIP CO₂ laser output coupler. The output coupler is mounted to a flange, which is attached to the PL-6 chassis with a ConFlatTM flange. If the coupler or the flange gasket is replaced, the coupler will need to be realigned. Assuming the alignment of the coupler is good before removal, the following procedure can be used. Set up a HeNe laser incident on the center of the coupler. The HeNe beam does not need to be aligned with the laser axis; however, the HeNe reflection should be visible in a convenient location. The location of the HeNe reflection should be carefully marked at a reasonable distance from the laser. A longer distance will equate to increased accuracy; six or more feet should be sufficient. Without disturbing the HeNe laser, the coupler can be removed, and replaced. The reflection from the new installation will probably be in a different location. Tune the alignment by tightening the flange adjustment screws as necessary to place the HeNe reflection back to the original location. This will set the coupler alignment very close to optimum. The final alignment is performed with the PL-6 operating on the desired spectral line. The coupler flange can be adjusted with the laser running for maximum power

output. The direction of coupler alignment is determined by applying slight pressure to the coupler flange in various directions, while observing the power output. Tighten the appropriate flange screws in small increments until the laser output is maximized. The flange screws should not be loosened, or the flange may become loose. If loosening a screw is necessary, ensure that the final action is in the tightening direction, and the flange is secure.

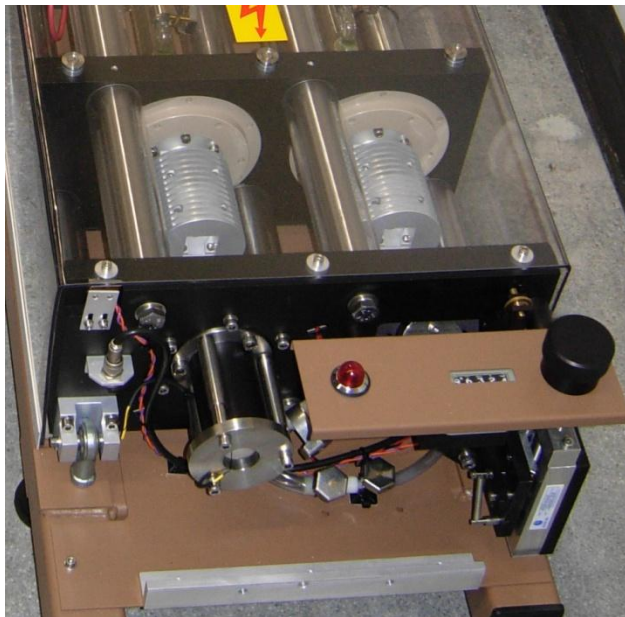


Figure 237. PL-6 CO₂ laser with the cover removed. The finned aluminum housing contains the Brewster windows. The output coupler is on the left, and the diffraction grating is on the right, under the position indicator and knob.

The Brewster windows seal the end of the each waveguide, and pass only vertically polarized laser light. They can be removed by releasing the vacuum from the laser waveguides, and unscrewing the fasteners from the window housings. The housing halves are then separated, and the windows can be removed. Pliable (O-rings style) gaskets seal the windows in the housings, and should be inspected for integrity. Similar to the output coupler, they are made of ZnSe, and can be cleaned with the same techniques. The windows are mounted at the Brewster angle to select the vertical polarization. This angle is integral to the

housing design, and there is no adjustment. The windows are reinstalled in the reverse procedure. After installation, the seals can be checked by evacuating the laser.

A.A.1.4 High- k_0 Scattering FIR Laser Maintenance

The most frequent maintenance for the formic acid laser is replacing the formic acid. The acid reservoir has enough capacity for 40 hours (50 ml) of laser operation; however, if the acid is more than two weeks old, it will probably need to be replaced for maximum power output. Pure formic acid decomposes into CO₂ and water until it reaches about 88% formic acid. Vapors from these contaminates will reduce power output. Anytime, the laser's power is low, the acid should be evaluated and replaced if suspect. When handling formic acid, gloves and eye protection are required, and the reservoir is filled in an acid approved fume hood. When the reservoir is removed and replaced, it will introduce air into the gas delivery system. To purge the air before laser operation, the laser should be evacuated with the oil vacuum pump to < 5 mTorr, and then the gas valve turned on. Allow formic acid to pass through the laser for one hour at normal operating pressure (~150 mTorr). The FIR laser should now be ready to normal operations.

Once per year, the laser optics should be inspected, cleaned, and replaced as necessary. There are four optics that need attention: 1) input window, 2) rear mirror, 3) output coupler CO₂ reflector, and 4) output coupler metallic mesh. In addition to these optics, the dielectric waveguide may need to be cleaned as well.

The input window admits the CO₂ laser beam at the rear of the FIR laser. It is made from ZnSe, and coated for anti-reflection at 9.27 μm . It measures 0.75" diameter, and 0.125" thick. There is no adjustment for this window. It is mounted with an o-ring seal, and a copper threaded retainer. The window is easily removed by releasing the laser vacuum, and then unscrewing the retainer. Gloves should be worn, and a

pad should be placed beneath the window in case it is dropped. The window can be evaluated and cleaned with the same standards as other ZnSe optics above. Replacing this window will not affect the laser alignment.

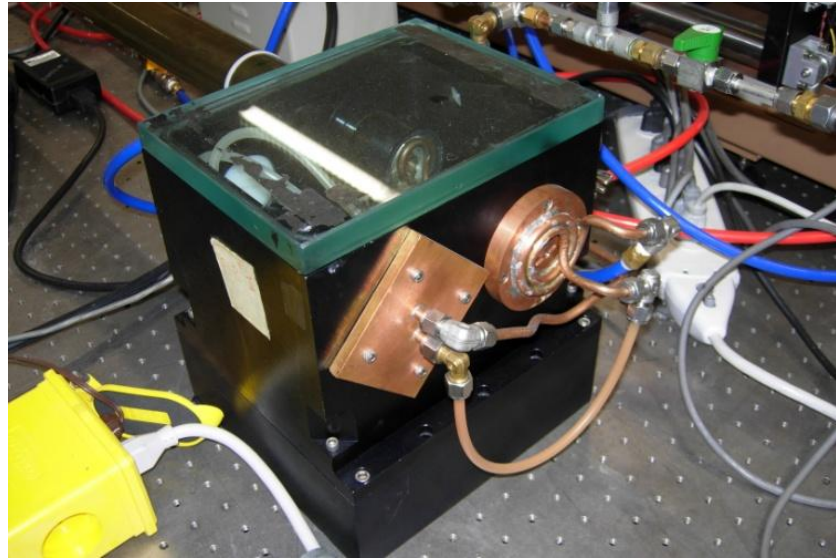


Figure 238. Formic acid FIR laser input end box. The input window is on the right hand side, with copper cooling lines soldered around it. The square plate on the left provides a vacuum seal for the removed second FIR channel, and the mirror cooling lines pass through this plate. The top cover is a slab of plate glass.

The rear mirror can be accessed by releasing the laser vacuum, and removing the top plate glass cover. There are no fasteners of any kind. Only vacuum with a pliable seal retains the glass cover. The mirror can be inspected without removing it from the laser. If the surface is smooth, clean, and reflective at visible wavelengths, then it should be left in place. Light cleaning can be performed in place by gently blowing air across its surface, or applying isopropyl alcohol followed by blowing air. If the mirror needs to be removed, it is highly probable that its alignment will be lost. This mirror is difficult to align; therefore, the following procedure should be used.

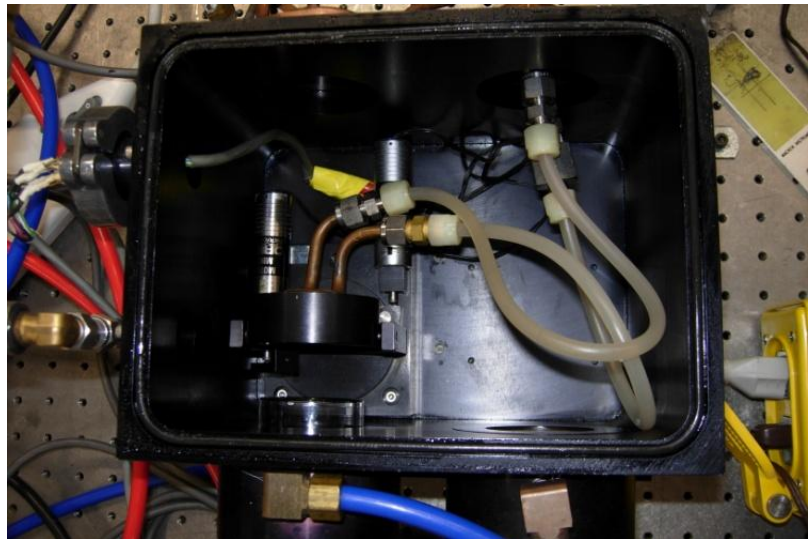
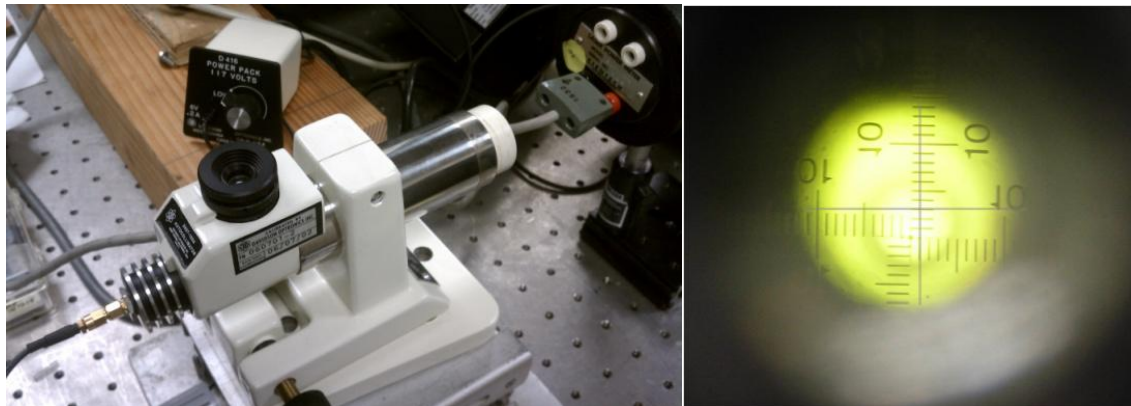


Figure 239. Inside the input end box. The cooling lines are routed to the rear mirror heat sink.

First, release the vacuum from the FIR laser. Remove the output coupler with its spanner wrench by unscrewing it counter clockwise, and set it aside. Place a 1.5" diameter alignment disk with a central hole in place of the output coupler. A spare rear mirror can serve this function. Set up a HeNe laser at the input window to pass the beam through the rear mirror, and through the front alignment tool. The ZnSe window will partially reflect the HeNe laser; however, a sufficient portion will be transmitted. This will identify the laser axis. An auto-collimating telescope is placed at the laser output so that the HeNe laser is incident at the center of the telescope objective lens. The telescope can be aligned so that the HeNe beam exits the telescope through the center of the eye piece. Do not look through the telescope. This approximates the telescope alignment with the laser axis. Turn off the HeNe laser, and turn on the telescope light source, and then observe the rear mirror through the telescope. If the telescope is near orthogonal to the mirror, a set of cross hairs will be visible against a graduated scale. Small adjustments to the telescope alignment may be necessary to observe the cross hairs. Continue to adjust the telescope alignment until the cross hairs center is at zero along both axes. This will establish a reference alignment for the rear mirror. The rear mirror is flat; therefore, it is not critical to observe along the true centerline. The hole at the center of the rear mirror will not affect the cross hairs image. The rear mirror can now be removed by unthreading

the retainer ring at the rear of the mount. The heat sink with cooling lines attached is set aside, and then the mirror can be removed for cleaning or replacement. Installation is in the reverse order. Once the mirror is secure, observe its alignment through the auto-collimating telescope. If the cross hairs are not at zero, adjust the mirror position by translating the mirror mount with the motorized micrometer controller. Keep the telescope in position and reinstall the output coupler. Remove the HDPE window by gently prying it out of the housing with a thin screw driver to expose the metallic mesh and the silicon CO₂ laser reflector. Observe the output coupler through the telescope and align it by adjusting the manual micrometers until the cross hairs are at zero. The cross hairs will be reflected from the polished silicon surface. The metallic mesh will be observed; however, it will not impede the alignment process. The azimuthal angle of the mesh grid makes no difference. The HDPE window can now be reinstalled by pressing it into place. An o-ring will provide a vacuum seal. The laser is now ready to reactivate, but it will need some tuning. Remove the HeNe laser from the input window, but leave the telescope in position. Place a power meter between the output coupler and the telescope. Should there be any problems with the laser alignment, the telescope should still be aligned with the rear mirror. Activate the FIR laser using the standard start up procedure. When the output coupler is installed, and when the HDPE window is set into place, the clearance in the threads and o-ring seal tend to make the alignment inconsistent. If laser power is low, then adjust the output coupler alignment only until power is established. Continue to tune the FIR laser until maximum power is achieved. Do not adjust the rear mirror. This is the one element that should be aligned already, and there is no reference point for its position once the laser is sealed. It is easy to lose track of this alignment, which then requires the entire process to be repeated.



Figures 240a and 240b. Left: Auto collimating telescope. The power supply for the illumination is in the background. Right: The view through the auto collimating telescope. The cross hairs are seen over the graduated reticule. The reticule graduations are 1 arcminute per line.

To inspect the output coupler, a similar procedure will be used as given in the above paragraph. Unthread the output coupler and set up the HeNe laser and auto-collimating telescope as above. The silicon wafer can be removed by first removing its threaded ring retainer. The metallic mesh is removed first, and carefully set aside; then the silicon wafer can be removed. Only one side is coated for CO₂ laser reflection (facing the inside of the laser). The sides of the wafer may not be marked with a chevron, so care must be taken to be certain of its parity. The wafer is 1.5" diameter, 1.52 mm thick, polished high impedance silicon. Its appearance should be a silver colored mirror surface. If it is cracked or discolored, it should be replaced or tested for CO₂ reflection and FIR transmission. The wafer can be cleaned by applying isopropyl alcohol and gently blowing air.

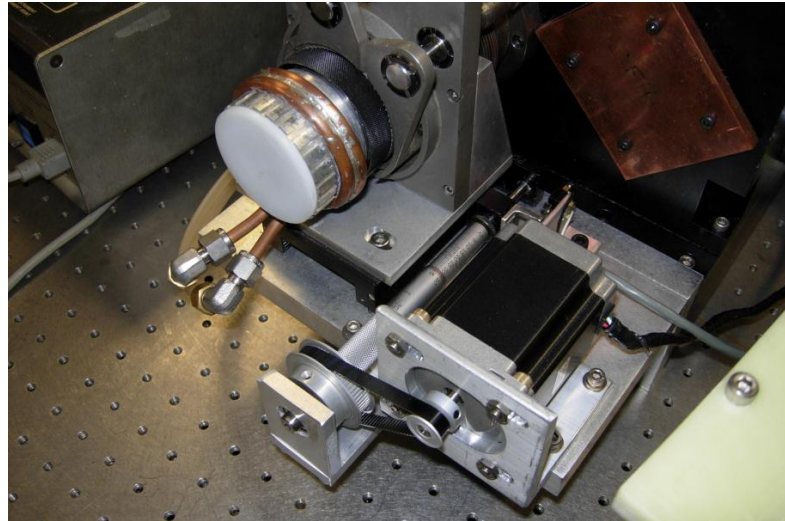


Figure 241. Output end of the formic acid FIR laser. The white disk is the HDPE laser output window.

The cavity length motor control is seen on the right.



Figure 242. High- k_0 Scattering FIR laser output coupler housing and spanner wrench.

The metallic mesh is installed on the outer side of the silicon wafer, with its mounting ring acting as a spacer to the silicon (i.e., the mesh does not contact the silicon surface). The metallic mesh is extremely fragile. It cannot be cleaned in any way. Even a gentle air stream can stretch or tear the mesh. If the mesh is intact, it can be reinstalled. If it has any visible damage, it should be replaced. The mesh specifications are 300 lines per inch, mounted to a 1.5 mm thick aluminum ring.

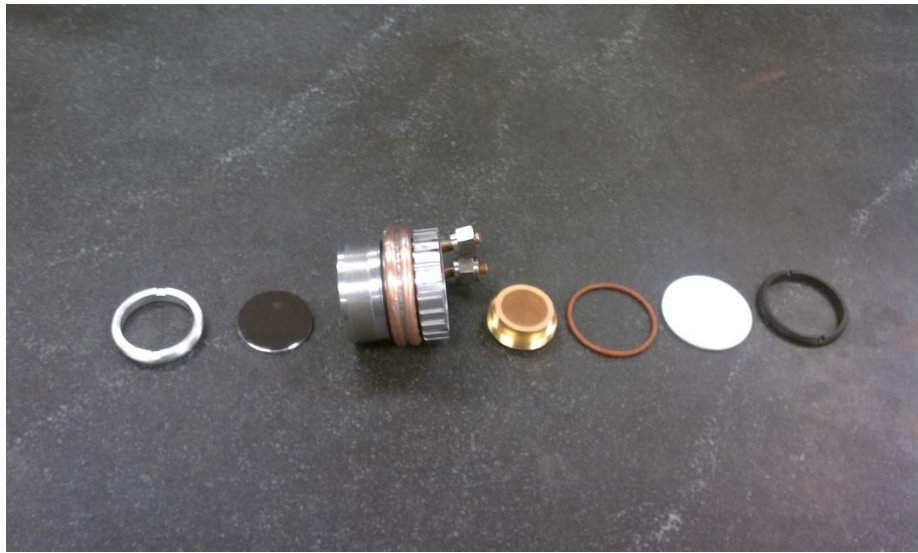


Figure 243. Exploded view of the High- k_0 Scattering FIR laser output coupler. From left to right: retainer ring, silicon CO₂ beam reflector, housing with cooling lines, metallic mesh, o-ring, HDPE window, and retainer ring.

The low pressure requirements of the FIR laser requires a mechanical, oil-based vacuum pump to be used. Over time, oil from the pump can back stream into the laser cavity. This will slowly coat the waveguide, rear mirror, input window, and the silicon CO₂ reflector. The mesh is on the outside of the CO₂ reflector; therefore, it is protected from oil contamination. Contamination will slowly degrade laser performance, and should be cleaned every 1,000 hours, or annually. Each of the optical components can be cleaned according to the above procedures. The waveguide is easiest to clean when the output coupler and rear mirror are removed. An insulated wire is passed through the waveguide. A lint free cleaning patch is attached to the end of the wire, saturated with isopropyl alcohol, and then drawn through the waveguide. Dirt and contaminants will be seen on the patch. This process is repeated until the patch is drawn through clean, and the waveguide is visibly clean. If the output coupler is in place, the wire can be inserted into the waveguide by removing the plate glass cover. When drawing the wire through the waveguide, hold it near the central axis to avoid dragging the wire along the edge of the waveguide. If the rear mirror is in

place, the waveguide can still be cleaned. The rear of the waveguide has about 20 mm clearance to the rear mirror. This is enough room to carefully pull the wire out of the waveguide, and attach a patch. Caution should be used to avoid disturbing or scratching the rear mirror.

A.A.2 Laser Overhauls

Annual maintenance should be sufficient to keep the lasers operating with high power output, and reliability. If there is a catastrophic failure, or if regular maintenance does not restore regular laser power, then an overhaul may be required. In short, the lasers will be completely disassembled, cleaned, inspected, and repaired as necessary. In general, the lasers are disassembled from the outside first, and working towards the inside. Care should be taken when handling the glass waveguides and other fragile components. The basic steps for laser disassembly are listed below, and then the specific concerns or peculiarities for each laser are discussed. Reassembly is the reverse procedure. The procedure is not difficult so long as attention to detail is maintained. The most difficult part will be aligning the optical components, and the techniques for optics alignment are discussed at the end. For all laser overhauls, the electrical connects should be disconnected, vacuum lines disconnected, fluids drained, and gloves are recommended.

A.A.2.1 FIReTIP CO₂ Laser Overhaul

The following procedure can be used to disassemble the FIReTIP CO₂ laser into its subcomponents. Important details are included with each point. There are six plates connected together with four invar rods. Ultimately, the alignment of the laser depends on these rods being straight. The plates are numbered 1 through 7, with 1 being at the front of the laser (main output). When sliding plates along the invar rods, the rod clamps must be loose, and if the feet are bolted down, those bolts must be removed. If a plate is immobile, a soft faced mallet can be used to dislodge a difficult plate. The plates may become cocked on

the rods; therefore, striking the plate in different positions may ease the process. Avoid striking any sealing surfaces or any other laser parts. The plates generally slide without much difficulty. A particularly difficult plate could indicate a bent invar rod.

- Disconnect all electrical lines.
 - H.V. leads at the power supply, ground wire, PZT cable, and any gauge sensors.
- Disconnect water lines and drain as much water as possible.
 - Gently blowing air into a water line will help purge water out the other end. Remove the water drain plugs from the cathode housings (the two outside plugs).
- Remove all water lines and water distribution manifolds.
- Drain oil from cathode enclosures (drain plugs are under the cathode housings, two inner plugs ~1 cup of oil each).
- Remove the gas supply and vacuum lines.
- Remove the rear mounting plate (#7) with the diffraction grating mount attached.
 - The grating assembly can then be disassembled according to the maintenance procedure above.
- Remove the next rear plate (#6) with the anode housing attached.
 - When the anode housing is clear of the water jacket, any remaining water will spill out. After removing the plate, the anode and the anode housing can be removed.
- Carefully remove the rear water jacket and rear waveguide by gently pulling them straight to the rear.
- Plate #5 can remain where it is.
- Mark the location of the next plate (#4) on the invar rod, then slide the plate rearward enough to remove the central glass tube.
- Remove the cathode housings from plates #3 and #4.

-The H.V. leads cannot be removed at this time. The cathode assembly can be removed by unscrewing the four polymer fasteners from the cathode insulating mount and gently prying the insulator mount from the cathode enclosure. This part can be difficult to remove. Use caution when separating the insulator mount. The H.V. lead can then be disconnected from the cathode, and the cathode can be pressed out. An arbor press may be necessary. Do not remove the H.V. lead from the insulator mount.

- Remove the output coupler housing from plate #1

-The output coupler can be disassembled according to the maintenance procedure above. The PZT housing should not be disassembled unless it is not functioning. The output bellows should not be disassembled unless necessary. If it is necessary, then the fasteners for the rear plate on the housing are removed. The rear plate is then unscrewed from the bellows. The bellows must be held stationary, otherwise it will be twisted, stretched, and possibly damaged.

- Remove plate #1 with the anode housing attached.

-When the anode housing clears the water jacket, any remaining water will spill out. The anode and the anode housing can then be removed.

- Plates #2 and #3 can remain where they are
- Carefully remove the forward water jacket and waveguide by gently pulling them straight out.

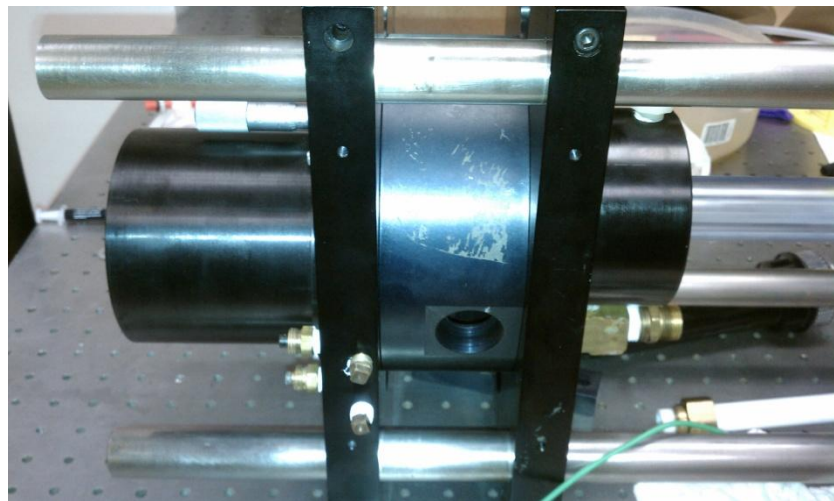


Figure 244. Rear sub-assembly of the FIReTIP CO₂ laser. Two vertical support plates slide over four invar rods. The left plate is slide off to remove the diffraction grating assembly. The zeroth order output window is observed in the center section. The cylinder to the right is the anode housing.

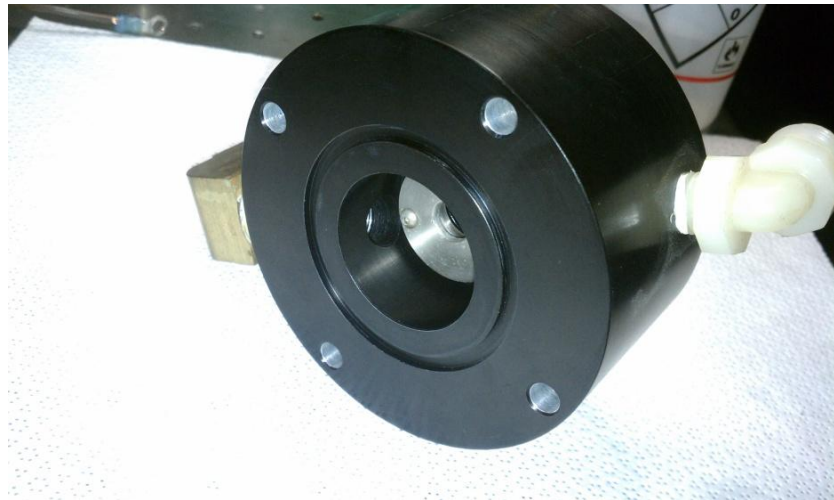


Figure 245. Anode housing removed from the FIReTIP CO₂ laser. The nickel anode is seen at the center.

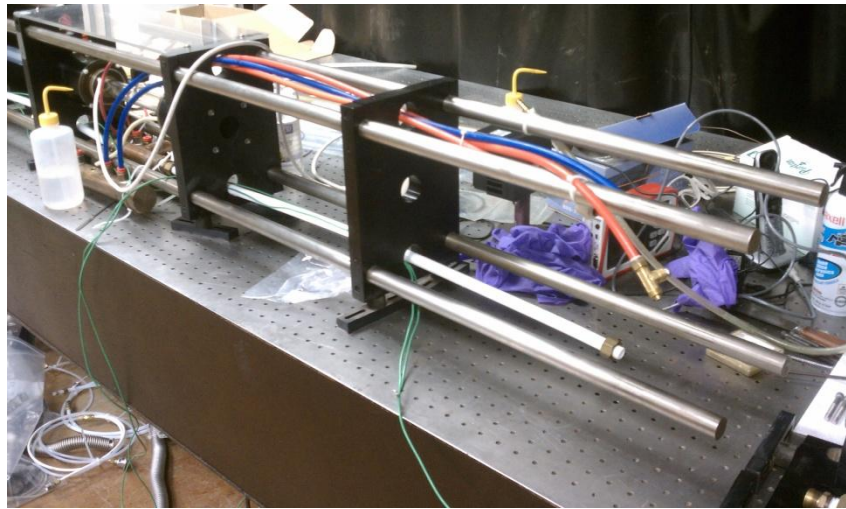


Figure 246. Partially disassembled CO₂ laser. The rear sub-assembly, waveguide, and water jacket are removed.

With the laser completely disassembled, all parts can be inspected and cleaned. Parts can be cleaned with hot soapy water, rinsed with water, and air dried. Any parts that are exposed to vacuum, should then be washed in isopropyl alcohol, and then air dried. The waveguides should have an isopropyl soaked patch drawn through them until they are visibly clean. There are many o-rings between the various laser parts to seal either vacuum or water. Every o-ring should be inspected for pliability, deformation, cracks, or cuts. Replace any o-rings with buna-N or nitrile material as necessary. The anode and cathode surfaces should be bright and smooth. If they are discolored or pitted, they can be polished. If polishing will not restore the surface, they should be replaced. The ends of the waveguides may be burnt. This is not necessary bad, unless the burnt surface will prevent o-ring sealing or if it extends to the inner surface of the waveguide. If the waveguide condition is uncertain, replace the waveguides. Various inner diameters are available, this laser works best with a 10.5 mm inner diameter. The water jackets often have a curvature to them. They can be flexed into position when installing; however, if they are bent severely enough to complicate the installation, or possibly break the waveguides, then they should be replaced. The various pipe thread fittings should be checked to ensure they are tight. If they are loose, then remove them, reapply Teflon tape sealer, and retighten.

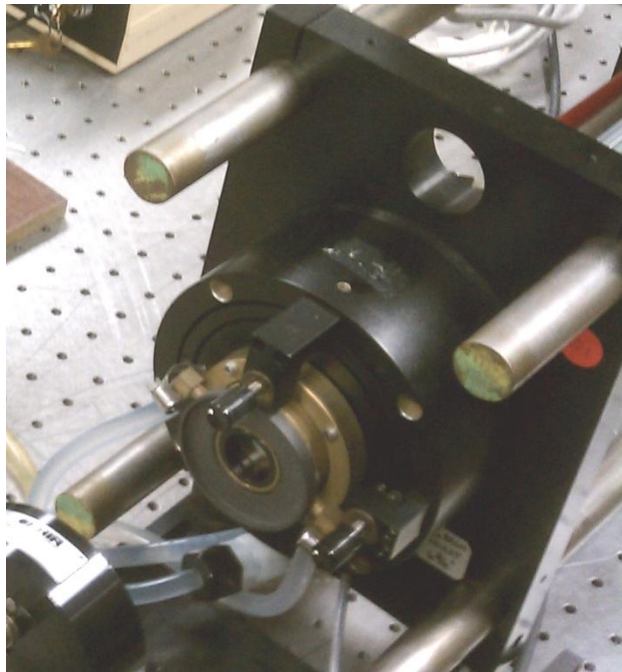
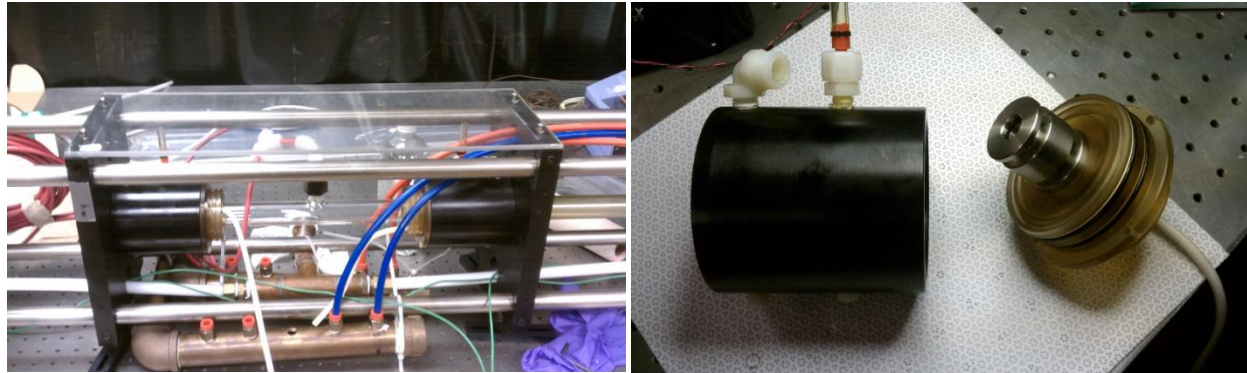


Figure 247. FIReTIP CO₂ laser output coupler housing. Opposite the support plate is the forward anode housing.

Assembly is the reverse procedure. There are a few items to be aware of to be successful. A light coating of vacuum safe grease will help slide parts past o-ring seals. Each component that bolts to the support plates must be concentric with the central hole of each plate. When each component is bolted to a plate, the bolts should only be lightly tightened, and then loosened so that the parts can be moved independent of the plates. An alignment cylinder is inserted into the component and the central hole of each plate to position the component concentrically. The bolts are then tightened, and the alignment cylinder removed. The central glass tube is positioned between plates #3 and #4. It should have about 1/16" of clearance so that it is free to rotate. If the plates are too close together, there is a risk of damaging the glass. The reference mark for plate #4 on disassembly should help position the plates for the correct spacing. When installing the waveguides into the cathodes, there are two o-ring seals for each waveguide. Make sure the waveguide is inserted into both o-rings. The anode housing can be installed before plates #1 and #6;

however, it is best to leave the anodes off at this time. Install the plates by sliding them over the invar rods. The water jacket and waveguide will be inserted into the anode housing at nearly the same time. Take care not to damage the waveguide. A thin tool can be used to elevate the waveguide to help guide it into the anode housing. With plates #1 and #6 in position, the end of the waveguides will be protruding from their o-ring seals. The anodes can now be installed, ensuring that the end of the anode does not apply pressure to the waveguide. If the waveguide is not fully seated, it may contact the anode, and could break when tightening the fasteners. Do not drop the fasteners down the vacuum port. The output coupler housing can now be installed. Make sure the bellows are straight, or laser performance can be affected. There is no alignment cylinder for the output coupler housing. It will be aligned later, so for now, simply bolt it on. There is no alignment necessary for the diffraction grating housing. The grating has sufficient area to cover the waveguide opening, and it is adjustable in two axes. Complete the assembly by reconnecting all the electrical, vacuum, and water lines. Check the laser assembly by first evacuating the laser. Then, water can be circulated to check for water leaks. After the laser passes vacuum and water tests, the cathode enclosures should be filled with dielectric oil. Never operate the laser without oil. This will cause the cathodes to overheat and damage them. Oil is added through the vent on top of each cathode enclosure. Approximately 1 cup of oil is needed for each side. The oil level should completely cover the cathode, and be roughly half way between the top of the cathode and the bottom of the vent hole. If the oil is overfilled, it will expand with heat and overflow from the vent. The last remaining task is to align the output coupler before energizing the laser.



Figures 248a and 248b. Left: FIR-TIP CO₂ laser center sub-assembly. The two cathode housings are seen, with a glass vacuum tube between them. Right: Cathode assembly. The cathode housing is on the left. To the right is the nickel cathode and insulator mount.

It is difficult to pre-align the diffraction grating. If the grating was used previously, the alignment micrometers should be set to a known good position. A new grating should be set to a known good position for a similar used grating to approximate the alignment. The output coupler can be aligned by the following procedure. Remove the diffraction grating assembly, and the output coupler housing, so that the waveguides can be viewed all the way through the laser. Insert an alignment cylinder with a central hole into each end of the laser. Align a HeNe laser so that it passes through both alignment cylinders from rear to front. This will establish the center axis of the laser. The HeNe laser is best placed at a fairly long distance from the laser; 6 to 10 feet is recommended. Remove the alignment cylinders, and replace the output coupler housing. The HeNe beam will be visible on the output coupler. Center the beam on the output coupler and tighten the mounting bolts. The HeNe beam is split by the ZnSe output coupler. Adjust the output coupler alignment so that the reflected HeNe beam is returned along its incident path. The coupler is now normal to the laser axis. The transmitted HeNe beam will approximate the CO₂ laser beam path. This can be used to align the mirrors to the FIR input window as discussed below. With the output coupler aligned, the diffraction grating housing can be reinstalled, and the laser energized according to the standard start up procedure. The waveguide should glow purple due to the helium buffer gas; however, the laser may not produce power immediately. Do not adjust the output coupler; it will be close enough to

establish some power on the power meter. Systematically adjust the diffraction grating until some laser power is registered. If necessary, increase the gas pressure and power supply current, and set the power meter for the 3 or 10 W scale. When power is detected, the grating can be tuned for maximum power, and then the output coupler is adjusted. Alternate between the diffraction grating and output coupler alignments until no further improvements are made. The PZT can be adjusted as well; however, it will only make a few percent difference in power output. With the laser producing power, the wavelength can be measured and adjusted with the CO₂ spectrum analyzer.

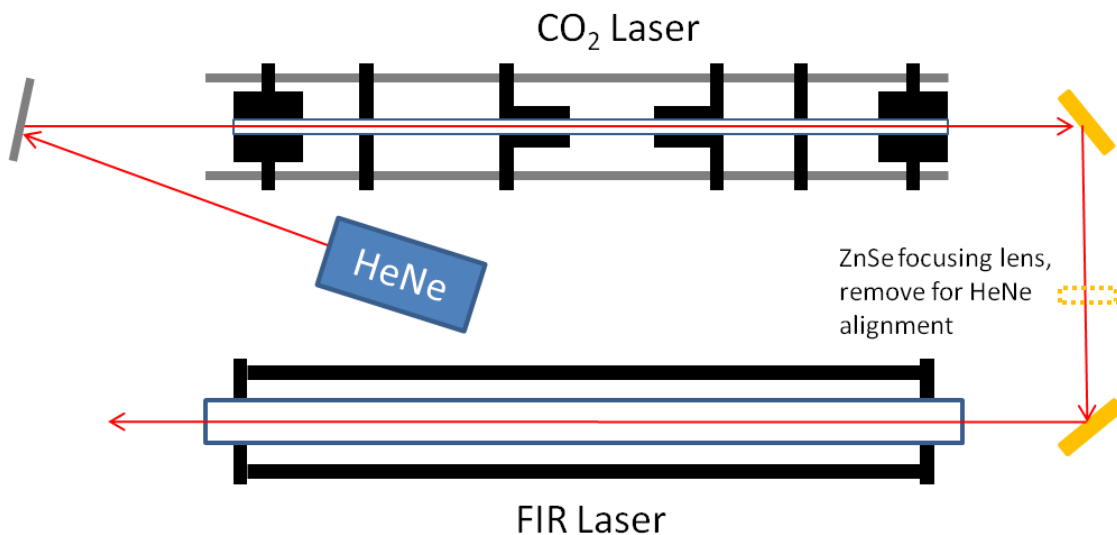


Figure 249. HeNe laser alignment technique. An axial HeNe laser is passed through the CO₂ and FIR lasers. The HeNe beam can be used to align the CO₂ laser output coupler, and the CO₂ laser beam path through the FIR laser. The ZnSe focusing lens should be removed for this procedure.

During a CO₂ laser overhaul, it is often convenient to align the beam to the FIR laser at the same time. To do this the FIR laser in question should have its output coupler removed, and replaced with an alignment disk (a 1.5" diameter disk with a 3 mm hole at its center). The input coupler and rear mirror can remain installed. The HeNe laser alignment beam should be emitted from the center of the CO₂ laser output coupler as described above. The 75 cm focusing lens is removed. The HeNe beam is then aligned with the various mirrors in the CO₂ laser beam path so that it passes through the FIR input window, through the

FIR laser, and out of the center of the output alignment disk. The CO₂ beam should now be concentric to the FIR laser cavity; however, it may not be perfect, so the CO₂ beam must be checked afterward. The 75 cm focusing lens can be reinstalled and aligned. The lens should be square to the HeNe beam; therefore, align the lens so that the HeNe reflection is returned along its incident path. To double check the CO₂ beam alignment, block the CO₂ beam with a graphite beam block, remove the FIR laser output alignment disk, and place a CO₂ power meter at the output end of the FIR laser. Energize the CO₂ laser, and set the power for 5-10 W. Using a fluorescent CO₂ beam detector plate and black light, carefully trace the CO₂ laser beam through the optical system all the way to the FIR input window. The beam should be incident on the center of the input window. If not, adjust the alignment so that it is. Once the beam is passing through the FIR input window, the output transmission can be measured by the CO₂ power meter. Use a fluorescent detector plate to observe the CO₂ beam at the FIR laser output. It may be necessary to increase the laser power to observe the beam since the beam is expanded to ~1 inch diameter at the FIR output. Align the CO₂ beam mirrors so that it is centered on the input window and centered at the laser output. The CO₂ power meter can also be used to judge the alignment, by aligning the CO₂ beam for the greatest power transmission. The beam should be aligned with the FIR laser axis for the highest power and best mode quality. Typical power measured at the FIR output is 60 to 70 % of the power emitted from the CO₂ laser. Note: if the FIR laser optics were aligned prior to this procedure, the output coupler alignment can be preserved by setting up an auto-collimating telescope at the output coupler. The rear of the giant hole output coupler is polished and observable through the quartz vacuum window. When the output coupler is reinstalled, and power meter removed, the output coupler can be easily reestablished.

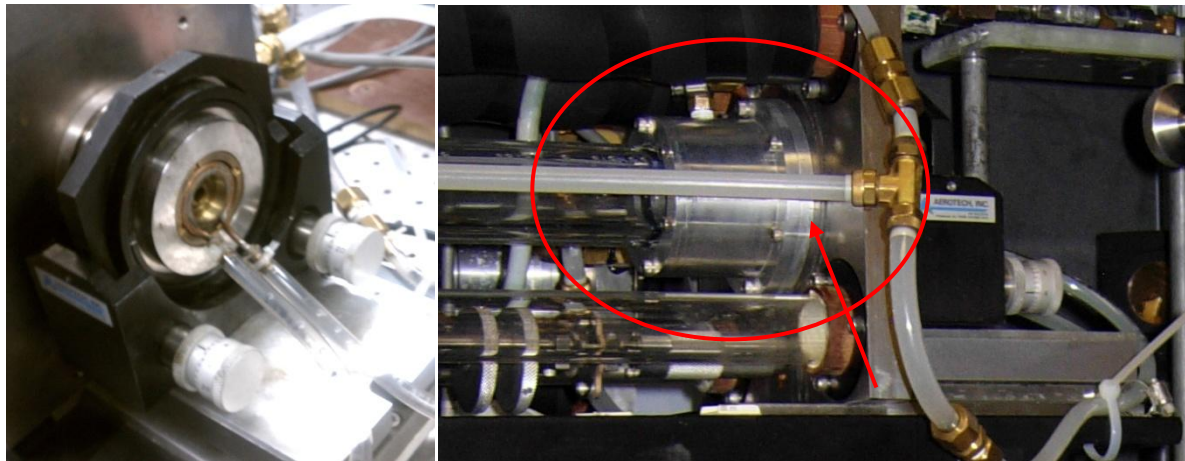
A.A.2.2 FIRETIP FIR Laser Overhaul

The FIR lasers are much simpler than the CO₂ pump laser. There are few electrical components, just the optical components, waveguide, and cooling system. The annual maintenance is all that is usually needed. Any time the front and rear optics are removed, the waveguide should be cleaned with isopropyl alcohol.

Aligning the optics can be challenging, and a procedure for the conventional methanol and Stark laser is discussed below. If the lasers need to be disassembled, the following procedure can be used.

FIReTIP Conventional FIR Laser Overhaul

- Disconnect electrical connections.
 - motor connection, and any gauge sensors.
- Drain water from the cooling system.
 - Gently blowing air into a cooling line will encourage water to come out of other exposed lines.
- Disconnect all cooling lines.
- Disconnect all gas feed and vacuum lines.
- Remove the input window housing.
- Remove the rear mirror.
- Remove the output coupler housing.
- Remove the output coupler.
- Unbolt the water jacket mounts, and slide them inward.
 - These mounts provide sealing for the vacuum and cooling systems. Any water remaining in the system will be released when these mounts are loosened. Note: within the mounts the water jacket has a hole to admit water into the water jacket. This hole can be positioned anywhere azimuthally; however, it must be completely between the mount o-rings. The outermost portion of the mount is a thin aluminum ring, which is bolted to the laser end plates with recessed fasteners. In inner portion of the mount must be slid away to expose the fasteners.
- Unbolt the bellows fasteners and two axis alignment mounts.
 - The bellows fasteners are covered by the water jacket mounts, which must be removed first.
- Unbolt either end plate and remove it from the laser chassis
- Remove the waveguide and water jacket by lifting them out of the chassis



Figures 250a and 250b. Left: FIReTIP FIR laser input assembly, including the input window, rear mirror, bellows, and two axis mount. Right: FIR laser water jacket mount circled in red. The right most flange (arrow) has hidden fasteners beneath the water jacket mount. This flange also covers the bellows fasteners.

Assembly is in the reverse order. All parts can be cleaned with hot, soapy water, and rinsed. Any parts exposed to vacuum should be cleaned with isopropyl alcohol and air dried. All o-rings should be inspected for pliability, deformation, cuts, and cracks. Replace any defective o-rings with buna-N or nitrile. The FIR lasers should be completely assembled, then tested for vacuum, then water leaks, before aligning the optics.

FIReTIP Stark Laser Overhaul

- Disconnect electrical connections.
 - motor connection, Stark potential, and any gauge sensors.
- Drain water from the cooling system.
 - Gently blowing air into a cooling line will encourage water to come out of other exposed lines.
- Disconnect all cooling lines.
- Disconnect all gas feed and vacuum lines.
- Remove the input window housing.

- Remove the rear mirror.
- Remove the output coupler housing.
- Remove the output coupler.
- Unbolt the water jacket mounts, and slide them inward.

-These mounts provide sealing for the vacuum and cooling systems. Any water remaining in the system will be released when these mounts are loosened. Note: within the mounts the water jacket has a hole to admit water into the water jacket. This hole can be positioned anywhere azimuthally however, it must be completely between the mount o-rings.
- Unbolt the bellows fasteners and two axis alignment mounts.

-The bellows fasteners are covered by the water jacket mounts, which must be removed first.
- Remove the electrical clips from the waveguide end.

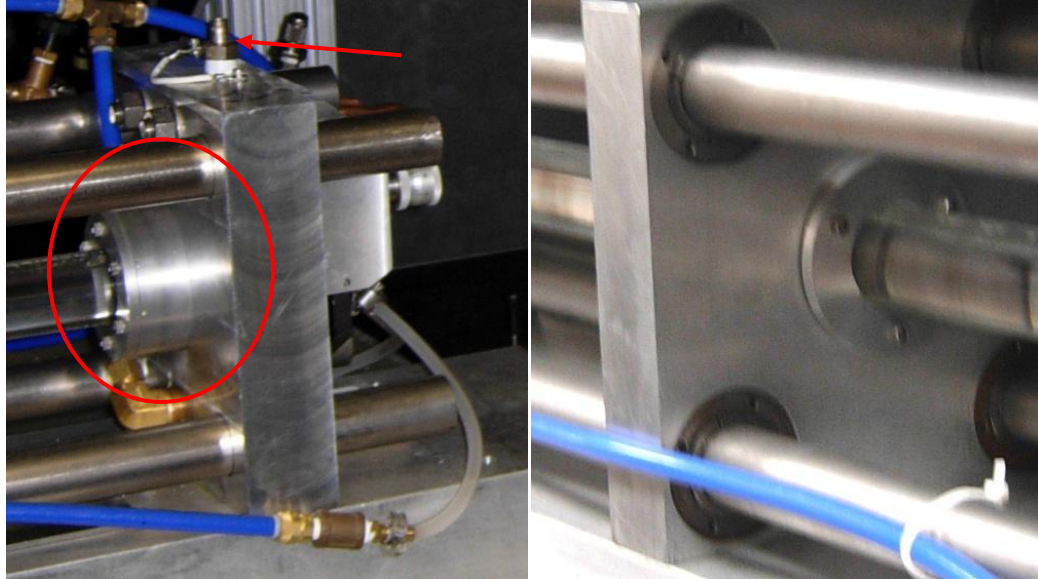
-The metallic coating is very fragile, and the clips should be gently pried open to relieve pressure on the waveguide before removing.
- Remove the woodruff keys from both end plates near the waveguide ends.

-The keys prevent the waveguide from walking laterally out of the water jacket, and they located the waveguide so that it is installed with its longer dimension vertical.
- Remove the waveguide to water jacket seals from both ends.

-Special seals are designed to seal the rectangular waveguide to the inside of a round water jacket. Loosening the seal fasteners will relieve pressure on the inner o-ring, allowing it to be removed easier. The rectangular o-ring is a round o-ring that conforms to the rectangular seal design.
- With extreme caution, slide the waveguide out of the water jacket.

-If the water jacket does not need to be cleaned or replaced, then the waveguide can be left inside it, and the water jacket and waveguide can be removed together to better protect the waveguide.
- Loosen the water jacket retainers at each support plate.

- The water jacket is retained by slotted polymer sleeves. These sleeves are retained by a pair of flanges, and when tightened, the sleeves buckle to apply pressure between the water jacket and support plates. When tightening the flanges, they should not be flush with the support plates; they are tightened just enough to support the water jacket, and prevent it from easily sliding. Excessive pressure can damage the waveguide.
- Remove the water jacket by sliding it out of the support plates.



Figures 251a and 251b. Left: FIReTIP Stark laser input end. The water jacket mount is circled in red. The arrow points to the H.V. Stark potential connection. Right: Stark laser water jacket clamp flange.

Assembly is in the reverse order. All parts can be cleaned with hot, soapy water, and rinsed. Any parts exposed to vacuum should be cleaned with isopropyl alcohol and air dried. All o-rings should be inspected for pliability, deformation, cuts, and cracks. Replace any defective o-rings with buna-N or nitrile. The Stark laser should be completely assembled, then tested for vacuum, then water leaks before aligning the optics.



Figures 252a and 252b. Left: Stark laser waveguide with electrode clips attached. Right: Stark laser waveguide to water jacket seal.

A.A.2.3 FIReTIP FIR Laser Alignment

Aligning the FIR optics can be a challenging task. There are several techniques that can be used; however, the author recommends the following procedure for the most consistent results. This procedure works for both the conventional and Stark FIR lasers. It is convenient to align the CO₂ laser beam to the FIR central axis first. Follow the CO₂ beam alignment procedure in the previous section.

Remove the output coupler and input window from the laser. Place an alignment disk in place of the output coupler. The alignment disk is 1.5" diameter with a 3 mm hole at its center. A spare rear mirror can serve this purpose. Leave the laser's rear mirror in place to act as the rear alignment disk. Set up a HeNe laser to pass through the center of each alignment disk to establish the central axis of the FIR laser. This procedure is more accurate if the HeNe laser is relatively distant at 6 to 10 feet from the laser. The HeNe beam passing out of the FIR input will propagate back to the CO₂ laser, and it can be used to align the CO₂ beam optics. Replace the rear mirror with a flat mirror with no central hole. Align the mirror so that the reflected beam is returned along the incident path. Replace the input window and correct the mirror alignment should it be altered. Replace the front alignment disk with the output coupler. The HeNe beam will now be incident on the polished surface of the output coupler. Align the output coupler to

return the reflected beam along the incident beam path. When vacuum is applied to the laser, the rear mirror and output coupler will be pulled out of alignment. This effect can be measured and corrected for. Place a second HeNe laser so that the beam is incident on the center of the input window. If a second HeNe laser is unavailable, the first HeNe laser can be replaced with an auto-collimating telescope. If using a telescope, align the telescope with the center of the output coupler so that the return image places the cross hairs center at the center of the telescope reticle. The HeNe laser incident on the input window will reflect off the ZnSe material. The beam does not need to be normal to the window; however, the location of the reflected beam should be noted. Evacuate the laser, and observe the location of the reflected HeNe beams, or telescope image. As the optics are moved out of alignment, the reflected images will move. When the laser vacuum reaches < 500 mT, adjust the optical alignment to restore the position of the reflected HeNe beams, or telescope cross hairs. The FIR laser will now be aligned well enough to generate power. Follow the standard laser start up procedures and operate the CO₂ laser at full power. The FIR laser power output may be low, but it should register on a power meter. Alternate between aligning the front and rear optics to increase the power output. The CO₂ PZT may need to be adjusted as well. The PZT can be placed into fast sweep mode, which will vary the PZT potential from 0 to 1500 V at a rate of 2 Hz. FIR output is reduced by about 50% with this technique; however, it eliminates a variable for initial tuning. If no power is detected with the PZT in fast sweep mode, adjust the FIR laser cavity length through several wavelengths. If no FIR power is detected, then the optical alignment procedure may need to be repeated with more scrutiny. The Stark laser follows the same procedure; however, the metalized waveguide can complicate the HeNe alignment. When aligning the rear mirror, the return beam cannot always be seen. Reflections from the metalized sides may interfere with the HeNe beam. The HeNe alignment can be inferred by observed the reflected image. Typically, the reflected image is a swirling pattern, and as the mirror is adjusted the pattern will appear to either be diverging from the center, or converging to the center. During alignment, when the beam is approaching normal, the pattern will be converging, and when the pattern changes direction and begins to diverge, the mirror has been adjusted

too far. This is the most difficult process of the FIReTIP system, and may take several attempts to gain proficiency.

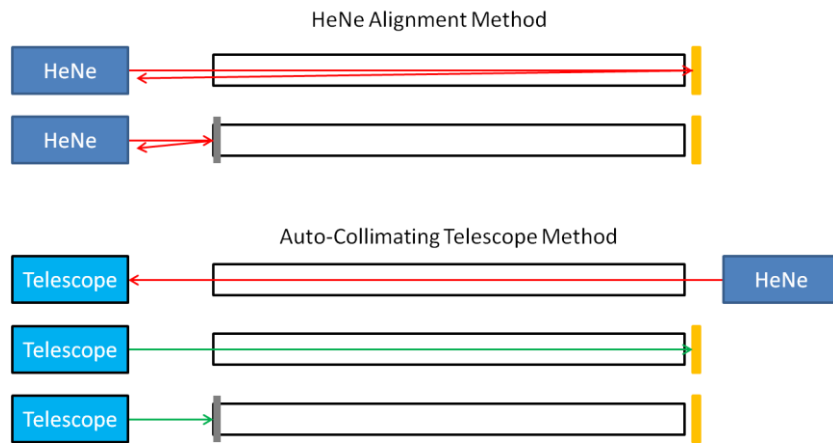


Figure 253. Above: HeNe alignment method. A HeNe laser is aligned with the waveguide axis. The reflected beam from the rear mirror and output coupler are used to align the optics. Below: Auto-collimating telescope method. First, a HeNe laser assists in setting up the telescope on axis. The rear mirror and output coupler alignments are observed through the telescope.

A.A.2.4 High- k_0 Scattering PL-6 Laser Overhaul

The PL-6 CO₂ laser is in current (2017) production, and parts are available from Edinburgh Instruments. Service calls are also available. The laser head does not require frequent overhauls. The anodes and cathodes are brazed in place in the waveguide assemblies. If any failure occurs in the laser head, either the output coupler, diffraction grating, or Brewster windows will need to be replaced. The only other repair that may be required is replacing one or both waveguide assemblies. Cleaning the waveguide is not recommended to avoid contamination of the anodes and cathodes. The waveguides should remain clean while installed in the laser. If the waveguides are removed for any reason, then each end should be covered to prevent contamination. The folding mirrors to couple the two waveguides in series are contained under a vacuum sealed cover. These mirrors should not be disturbed. However, if they need to be realigned, special brackets are mounted at the front of the laser. These brackets have a small aperture

to pass a HeNe beam into the laser through the first bracket, through the center of the first waveguide, through the folding mirrors, out of the second waveguide center, and through the aperture of second bracket. With these brackets in place, the folding mirrors can be aligned or verified. To replace one or both waveguides, the following procedure can be used.

PL-6 Waveguide Replacement

- Disconnect the H.V. leads and electrical connector from the back of the power supply.
- Drain the water from the laser.

-Disconnecting the return water line from the chiller, and directing the water into a bucket will drain most of the water.
- Remove the laser chassis cover.
- Remove the plastic H.V. shield.
- Disconnect the water lines from the waveguide.

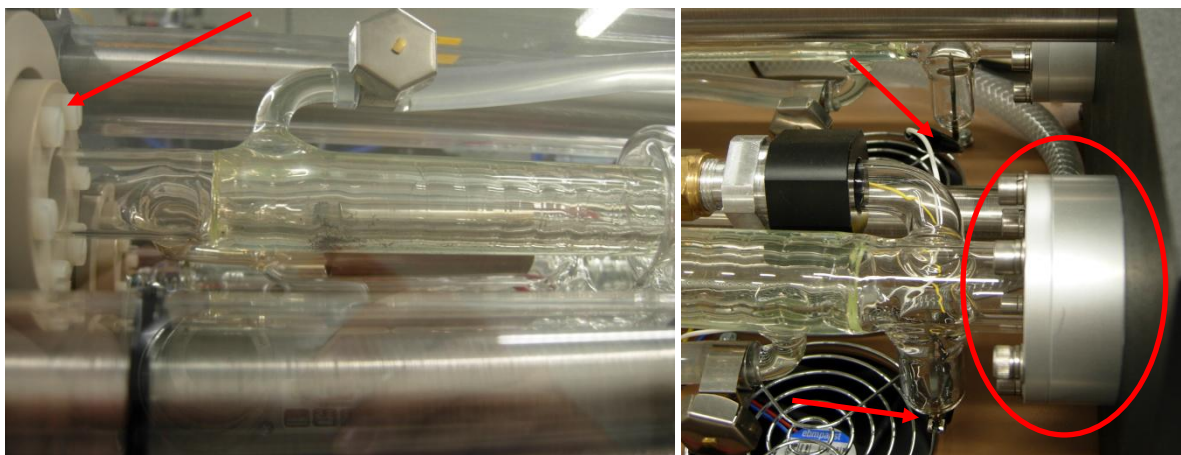
-Any remaining water may spill out at this time.
- Disconnect the vacuum and gas lines from the waveguide.
- Unclip the alligator clips from the anode (black) and cathode (red).

-Keep track of which connectors are connected to which terminals. They should be replaced in the same positions; however, reversing the channels, or cross circuiting the connections can be done to diagnose certain problems with the power supply, or to determine if a problem exists in the laser head or power supply.
- Disconnect the vacuum lines above the waveguide, if they obstruct the removal.
- Remove the top half of the central waveguide support.

-This support has four adjustments to tune the waveguide alignment. During operation, the waveguide can be gently deflected to see if output power increases or decreases. The adjusters are then calibrated for maximum power output.

- Remove the waveguide retainers at either end of the waveguide, and carefully lift the waveguide out of the chassis.

-The retainers at the rear of the laser (near the folding mirrors) are fixed in place. The retainers at the front of the laser can float to adjust the alignment of the waveguide. In conjunction with the central waveguide support, the front retainers can be adjusted for maximum power output and optimum mode quality.



Figures 254a and 254b. Left: Floating waveguide mount for PL-6 laser (arrow). Right: Fixed waveguide mount for PL-6 laser (circled). The black anode crocodile clips are also seen (arrows).

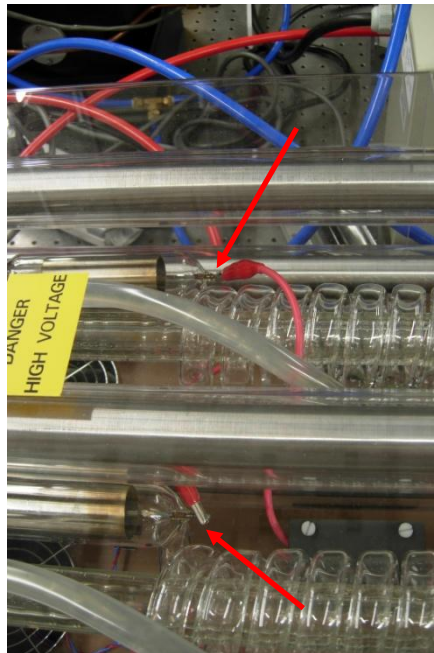


Figure 255. PL-6 laser cathodes and red alligator clips (arrows).

Assembly is the reverse procedure. The waveguide alignment should be perturbed to determine if it needs to be better aligned to optimize laser performance. Once the laser is functioning normally, the diffraction grating calibration should be checked. Several spectral lines should be tuned for using a spectrum analyzer. The laser is then brought up to maximum power, and compared to the calibration sheet. If the laser performance matches the previous performance, then no further calibration is necessary. If the laser under performs, then the cause should be discovered and repaired. If the laser is performing well, but the no longer matches the calibration reference sheet, then a new calibration reference sheet should be made.

A.A.2.5 High- k_θ Scattering FIR Laser Overhaul

The High- k_θ Scattering FIR laser is different from the other lasers discussed. It has no chassis to connect all of its components together with. It must be bolted down to a flat surface to maintain its integrity. This laser rarely needs to be overhauled. The annual maintenance is sufficient to keep the laser operating at maximum power output. However, due to the lack of a chassis, any time the laser is moved, it must be

disassembled and set up again. This is in effect, a de facto overhaul. The optical alignment will positively be disrupted. Anytime the laser is disassembled, the opportunity should be taken to inspect and clean all of its components.

High- k_θ Scattering FIR Laser Overhaul

- Disconnect all electrical connections.
 - Cavity length controls, rear mirror controls, and any gauge sensors.
- Drain the water from the cooling system.
 - Blowing air through an open line will help push water out of any other exposed lines.
- Disconnect all cooling lines.
 - Also disconnect the water transfer line connecting the input coupler and output coupler cooling. There is a union fitting in this line that allows it to be separated, otherwise, the end boxes cannot be removed.
- Disconnect the gas and vacuum lines.
- Remove the plate glass covers from each end box.
 - There are no fasteners for these cover plates. They are held in place by vacuum only.
- Unbolt the output end box from its base plate.
 - There are two rows of bolts near the bottom at the front and rear of the end box.
- Unbolt the output coupler bracket from the base plate.
 - There are three bolts underneath the bracket, screwed into the front of the base plate.
- Slide the output end box away from the waveguide and water jacket, set the end box aside.
 - When the water jacket clears the end box, any remaining water will spill out.
- Remove the waveguide and water jacket together.
- If the laser is to be moved, unbolt and remove the base plate, otherwise, it can remain in place.

- The bolts pass through the top of the base plate. When the end box is installed, the bolts will be covered. When moving the laser, measure the distance between the base plates so that they can be properly mounted in the lasers new location.
- Unbolt the input end box from the base plate, and set aside.
- If the laser is to be moved, unbolt and remove the base plate, otherwise, it can remain in place.



Figure 256. High- k_0 Scattering FIR laser end boxes. Note: Both laser channels are observed in this photograph. For the High- k_0 Scattering system, one of the laser channels has been removed.

Assembly is the reverse order; however, both base plates should be bolted down first. The spacing for these plates is determined by the waveguide and water jacket lengths. The waveguide needs to protrude through the vacuum o-rings at each end box. The water jacket is slightly shorter so that it passes through the water sealing o-rings; however, it should not touch the end boxes. The water jacket should be free to rotate, and have 1/16 to 1/8 inch end play. Once the FIR laser is completely assembled, it can be vacuum and water tested. After passing these tests, the optics can be aligned.



Figures 257a, 257b, and 257c. Photographs of the High- k_0 Scattering hybrid output coupler. Above left: Complete assembly with HDPE window and copper cooling lines installed. Above right: Coupler housing with HDPE window removed. The mesh FIR output coupler is seen. Below: Reverse image of the output coupler housing. The silicon CO₂ laser reflector is seen.

The alignment procedure is similar to the FIReTIP system; however, due to the rear mirror being enclosed in the input box, and the PL-6 laser design there are a few differences. First, the CO₂ beam should be aligned with the FIR laser axis. The HeNe laser cannot be easily set up to pass through the PL-6 laser; therefore, the HeNe laser will be set up in the reversed direction, from the FIR output to the PL-6. Remove the output coupler assembly from the FIR laser and replace it with an alignment disk. The disk is 1.5" diameter with a 3 mm hole at its center. Set up a HeNe laser 6 to 10 feet from the FIR laser, and align the beam to pass through the alignment disk, rear mirror, and input window. This beam will propagate

through the CO₂ beam optics. Remove the 75 cm focusing lens, and align the CO₂ optics so that the beam strikes the center of the PL-6 output coupler. Continue to align the HeNe beam so that it passes through both PL-6 waveguides and is incident on the diffraction grating. The diffraction grating is visible to the operator if the PL-6 cover is removed. It may be necessary to dim the room lights to see the HeNe laser on the diffraction grating. When the HeNe beam is visible on the grating surface, it can be steered to ensure it is centered. When centered, the HeNe beam will be round. As it is steered, the beam will be clipped, creating a shadow over a portion of the HeNe spot. The 75 cm focusing lens can be reinstalled. The lens is aligned normal to the HeNe beam by observing the location of the reflected beam. This will approximate the CO₂ beam path; however, the CO₂ beam alignment will need to be verified. Set up a CO₂ laser power meter at the FIR output. Energize the PL-6, and set the power to ~ 10 W. Trace the CO₂ beam to the FIR input window with fluorescent detection plates. Fine tune the CO₂ beam alignment so that it is centered at the FIR input window, and centered at the FIR output. The beam position can be verified by observing the CO₂ beam with fluorescent detection plates. It may be necessary to increase the PL-6 power to observe the beam location at the FIR output. Alternatively, the CO₂ beam position can be inferred by the CO₂ power meter. If the power meter is centered at the output, the beam will be centered when the power is maximized. Typical power measurements are 60 to 75 % of the power measured at the PL-6 output. Once the CO₂ beam alignment is verified, the PL-6 can be de-energized and HeNe laser removed, and then the FIR optics can be aligned.

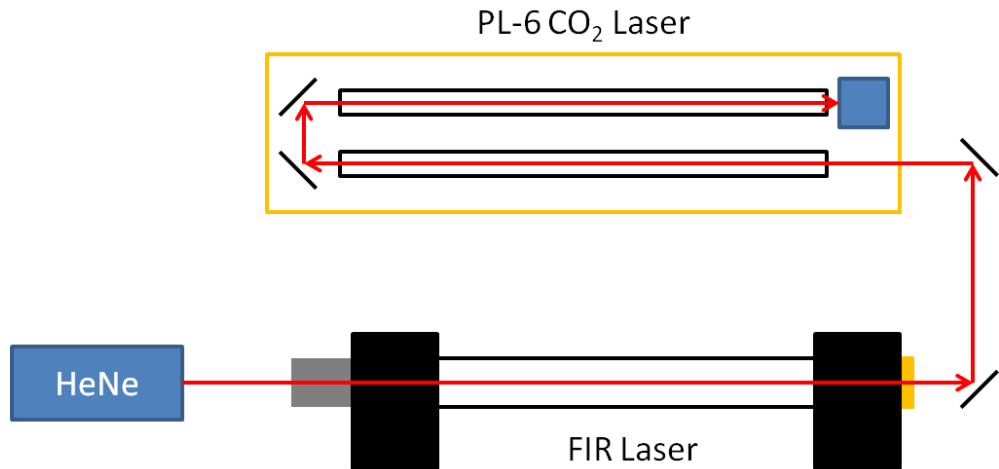


Figure 258. HeNe method for initially aligning the CO₂ laser beam.

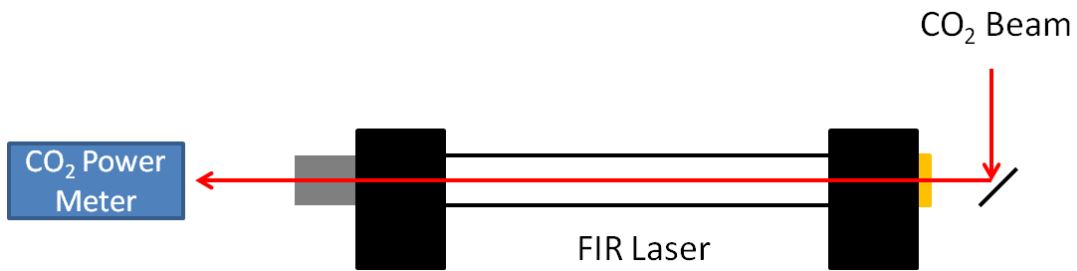
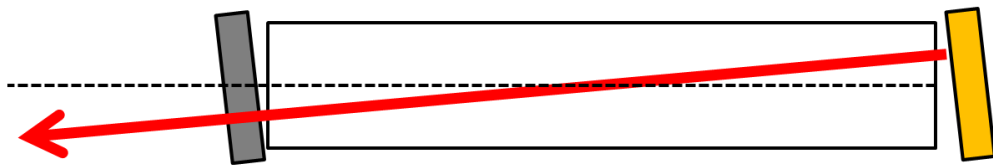


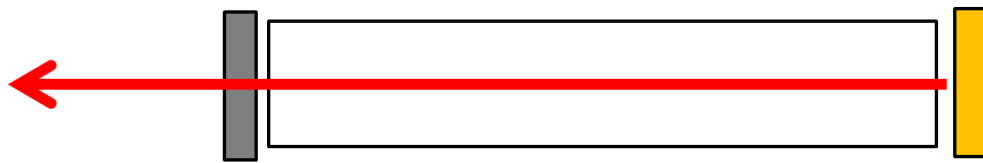
Figure 259. The CO₂ beam should be aligned with the FIR laser axis. The beam location can be verified by using a fluorescent detection plate and black light. Alternatively, the CO₂ power meter can be set up at the center of the FIR laser output. The beam should be centered when the detected power is highest.

Nearly the same procedure can be used to align the High- k_0 Scattering FIR laser and the FIReTIP FIR lasers. Refer to the FIReTIP section for the details, and additional procedures are included at the end of this paragraph. In summary, replace the rear mirror with a solid mirror. Remove the alignment disk from the output coupler location. Align the rear mirror with the motor controls so the HeNe beam returns on itself. Reinstall the rear mirror, and then install the output coupler assembly, less the HDPE output window. Align the output coupler by observing the HeNe beam reflection. Install the HDPE output window, and replace the end box glass covers. Evacuate the FIR laser, and energize the laser according to

the normal procedure. Since the rear mirror is completely enclosed in vacuum, its position will not be disturbed under vacuum. The output coupler may shift slightly under vacuum; however, it should be close enough to produce FIR power. Align the output coupler only to maximize FIR power. It may be necessary to adjust the PL-6 PZT control, and adjust the FIR laser cavity length; however, do not adjust the rear mirror position. When the FIR beam power is maximized, the beam position and mode quality should be checked. It is probable that at maximum power the rear mirror and output coupler are parallel, but not normal to the laser axis. This can cause the beam to be emitted at some angle, and the mode may not be TEM_{00} . To measure the beam position and mode quality, the pyroelectric detector can be set up on a motorized translation stage. The FIR beam is interrupted with a chopper, and the pyroelectric detector will output a waveform proportional to the beam intensity with a period equal to the chopper speed. The pyroelectric detector sensor is 2 mm square; therefore, it will only detect a small portion of the beam. Translating the beam scanner across the FIR beam in two axes will map out the beam profile and center location. If the FIR beam is not straight, it will likely be TEM_{01} as well. Using small adjustments, steer the rear mirror in the direction needed to align the beam with the laser axis. Ensure that the mirror is not moved so far that the power drops to zero. Should the alignment be off enough to emit zero FIR power, it will be very easy to lose track of the rear mirror position. If this happens, it may be necessary to repeat the entire alignment process. With the rear mirror adjusted, align the output coupler for maximum power. Then measure the FIR beam position and mode. Repeat this procedure until the beam is aligned with the laser axis. With the optics normal to the axis, and the CO_2 beam centered down the FIR laser, the mode should be TEM_{00} .

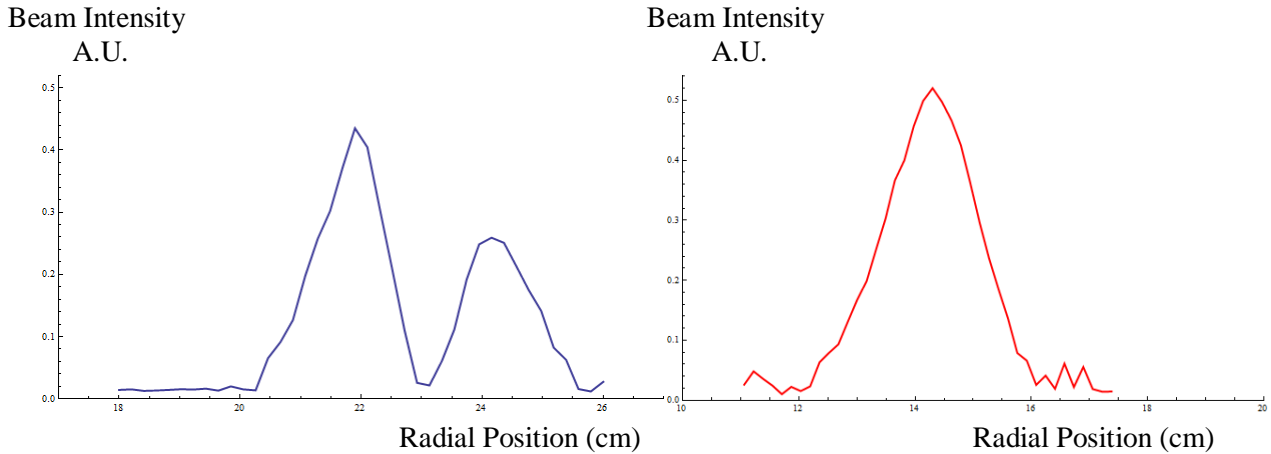


Laser optics form a parallelogram, steering the beam off axis, and couples to higher order modes.

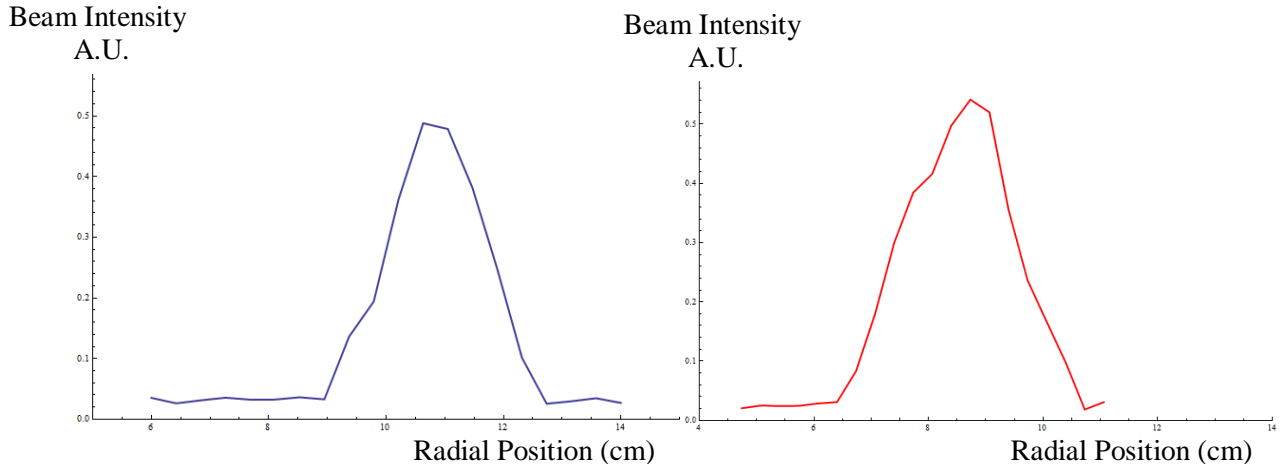


Laser optics parallel and normal to the laser axis, and couples to TEM_{00} , Gaussian mode.

Figure 260. Laser optics alignments. Above: The output coupler (gray) and rear mirror (orange) are parallel; however, they are not normal to the laser axis (exaggerated). This results in the beam being emitted at an angle to the central axis, and promotes coupling to higher order modes; TEM_{01} is the most common mode to couple to with this situation. Below: The laser optics are parallel and normal to the waveguide axis. The beam will be emitted straight, with a Gaussian mode. Walking the optics alignment from a parallelogram to normal must be done slowly and carefully. It is very easy to lose track of the rear mirror position in the High- k_θ Scattering FIR laser.



Figures 261a and 261b. FIR laser beam profile, mode TEM_{01} is observed. In this case, the center of the beam profile was measured to veer from the laser axis low and left by 0.4 degrees Left: Horizontal beam profile shows two distinct peaks. Right: Vertical scan shows one peak. This peak was centered at the maximum beam intensity of the left peak of the horizontal scan.



Figures 262a and 262b. The FIR laser optics alignment has been corrected to align the beam with the laser axis. The observed mode is now TEM_{00} . Left: Horizontal profile of the FIR laser beam. Right: Vertical profile of the FIR laser beam.

Appendix B. Nano-CNC-Machining

Microfabrication utilizing Nano-CNC-machining is a versatile approach to meet the needs of many applications. It has many advantages and limitations as discussed earlier including the capability of being quickly programmed and edited as designs are updated during development; however, it can only produce one part at a time, which limits production capability for parts with long cycle times. Depending on the geometry and material for parts, high aspect ratio structures can be fabricated. To be successful with Nano-CNC-machining, certain techniques should be employed, and the operator requires experience and skill in machining. CNC (computer numerically controlled) machine tools are controlled by computer; however, the computer only follows the instructions from the operator. CAM (computer aided machining) software does not replace the skill and experience of a machinist, any more than simulation software can make someone a software engineer. Microfabrication with nano-CNC-machining has many factors to consider: 1) dimensional tolerance, 2) surface finish, 3) edge definition, 4) fragile micro structures, 5) tool life, 6) production time, and 7) the properties of the material to be machined. The techniques discussed below address these issues. However, good technique alone is not sufficient for success, especially when developing new parts. A machinist's experience is essential when analyzing the quality of parts, especially when the quality of the parts does not meet initial expectations. Improvements to surface finish, reducing tool wear, and decreasing cycle times are enhanced with machining experience. The following information will convey the techniques and advice developed by the author while operating the ultra precision *NN1000* CNC-mill, developed by Digital Technology Laboratory.

A.B.1 Machining Fundamentals

The information discussed in this chapter is best utilized by those with a background in machining; however, to make the information relevant for the uninitiated, the basic machining definitions, jargon,

and operations are discussed below. This information should assist in communication between machinists and other members of a design team. For example, most designs for vacuum electronics will begin with computer simulations. If the simulation expert is not familiar with manufacturing techniques, then it is possible that a part that is impossible to fabricated could be designed. A familiarity with fabrication techniques, and a common language, is essential for efficient development. Furthermore, for high frequency (>100 GHz) vacuum electronics, the fabrication of the slow wave structure is often one of the primary challenges. It may be beneficial to accommodate the manufacturing technique to produce a higher quality part, rather than to optimize the simulation results. Understanding how parts are made, and the limitations of particular technique, can accelerate the development process, and ultimately produce a higher performance device.

Micromachining is not a well defined term. There are several ways to apply this terminology, all of which are correct in their context. One definition is the machining of parts that have dimensions, or features within a part, that are less than 1 mm. Another definition is to fabricate parts whose tolerances are finer than conventional machines. Typical, conventional machine tools (mills, lathes, and other machines) can maintain dimensional tolerances of ± 0.0005 inches ($\sim 13 \mu\text{m}$). With careful preparation and workmanship, it is possible to achieve perhaps ± 0.0002 inches ($\sim 5 \mu\text{m}$); however, this level of precision is exceptional. If tolerances can be reliably held to better than ± 0.0002 inches, then this is in the realm of micromachining. A third definition describes the interaction between the tooling (the cutting implement) and material at the μm scale. Conventional machining assumes that materials are isotropic, with grain structures much smaller than the cutting surfaces of the tools, or the chip loads machined. When the machining process approaches dimensions on the order of the grain structure of the material, then conventional machining parameters may no longer be valid. For the machining operations discussed by the author in this dissertation, the first and second definitions are true. As such, conventional machining

techniques provide an excellent guide for initial machining operations; however, the small dimensions, tight tolerances, and surface finish requirements do alter standard techniques somewhat.

A.B.1.1 Conventional Machining

Conventional machining is well documented for a variety of materials and tools. When using miniature end mills (diameters less than 1 mm), standard cutting parameters, colloquially known as "speeds and feeds", are applicable. For milling operations, the conventions to describe cutting parameters are *surface cutting speed* and *chip load per tooth*. These are the speed of the leading cutting edge relative to the material, and the radial depth of the cut per tool engagement.

$$\text{Surface cutting speed} = RPM \cdot \pi D$$

$$\text{Chip load per tooth} = \frac{Feed}{RPM \cdot T}$$

In the above, *RPM* is the rotational rate of the spindle, *D* is the tool diameter, *Feed* is the speed of the tool advance, and *T* is the number of teeth on the tooling. There is also the *length of cut*, which is the axial engagement of the tooling. For various material and tooling combinations, there are recommended machining parameter recommendations found in any machinist's handbook. As the tooling diameter becomes smaller, the spindle RPM must increase. The *chip load per tooth* and *length of cut* will affect the surface quality, and the cutting force applied by the tooling. The recommended parameters often offer a range of values to account for the variety of tooling and variations of materials. The material that is to be machined is often referred to as the "work". In milling operations, the work is held in the machine, and the tooling spins to perform the cutting action. The work can be translated in three Cartesian axes (X, Y, and Z) to make parts that have flat, perpendicular faces. Additional axes of freedom may be defined by

making rotations about Cartesian axes, where axis-A rotates about axis-X, axis-B rotates about axis-Y, and axis-C rotates about axis-Z. With computer controls, these axes can be moved in coordination to fabricate curves and abstract shapes. Lathes have a different configuration, where the work is held in a spindle and spins. The tooling is fixed to a carriage to move in two axes, Y and Z. Axis-Y is the radial position of the tooling to the spindle centerline, and axis-Z is the lateral position along the spindle axis. Lathes are primarily used for fabricating round parts, threads, or other helical structures. Non-round parts are also possible through a variety of techniques, such as computer controls or off axis cutting, such as Blanchard lathes. Free form machines combine the features of mills and lathes to create very complicated geometries, such as turbines and propellers with a single machining operation. These categories make up the basic elements of machine tools; however, the varieties of configurations that exist are inexhaustible. Many machines are special purpose built to fill a particular need. What these machines have in common is that the cutting process is done by the mechanical engagement of tooling and material to physically cut away material. Alternative machining methods may include EDM (electric discharge machining), laser cutting, sonic machining, and precision grinding.

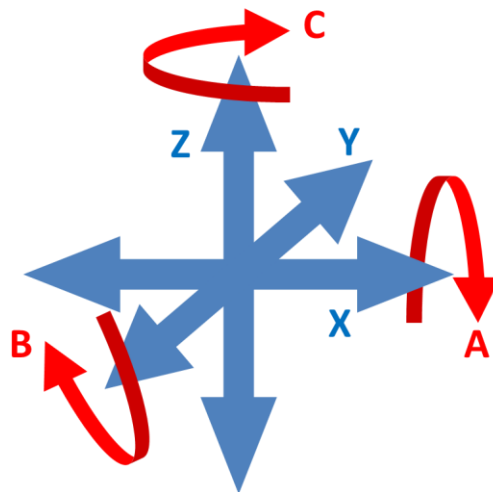


Figure 263. Machine tool milling axes. Linear translations are performed along right-handed Cartesian axes in blue. Rotations about the Cartesian axes are shown in red.

A.B.1.2 Nano-CNC-Machining

Nano-machining is a term ascribed to using ultra-precision CNC mills, lathes, and freeform machines.

The terms "Nano-Machining" and "ultra-precision" are colloquial expressions to describe machine tools that have significantly better precision than conventional machines. The advertised precision is typically given as the command resolution, meaning the resolution to which the CNC controls can be programmed. The true machine position may possess some error, thereby reducing the accuracy of the programmed dimensions.

The *NN1000* is a "nano-mill" developed by *Digital Technology Laboratory* (DTL, a subsidiary of Mori Seiki, now DMG-Mori). This machine tool features a command resolution of 1 nm; therefore, it has been dubbed the "nano-mill". The machine is a 5-axis (X, Y, Z, A, and C) CNC mill. Its 1 nm command resolution is supported by laser scale position sensors with a resolution of 34 pm. Air bearing guide ways, linear drive magnetic motors, and anti-vibration technology provide a smooth and accurate platform for this machine. The pneumatic spindle has a range of 38,000 to 55,000 RPM, with options expanding the top speed to 160,000 RPM. Alternatively, the spindle can be replaced by a fixed mandrel for linear scribing. The *NN1000* can feed tooling between 1 and 500 mm/min, except for the X-axis, which is capable of 3000 mm/min. The typical cutting force is a few Newtons, with 20 Newtons as a practical upper limit. The Cartesian axes can travel 120, 150, and 50 mm for X, Y, and Z, respectively. The A-axis rotates about the X-axis $\pm 90^\circ$, and the C-axis has 360° capability. The working accuracy of this machine depends on the type of operation, tooling, material, etc... Linear scribing is the most stable machine operation because the tool fixture and tooling are robustly mounted. Linear scribing is limited to planing topmost surfaces, grooving, or cutting regular patterns in a surface with form tools, such as pyramid arrays, or diffraction gratings. The *NN1000* excels with scribing operations with typical position errors less than 50 nm. Using mono-crystal diamond scribes on copper or Ni-P, the *NN1000* has machined surface finishes better than 5 nm R_a . Rotating tools via the pneumatic spindle greatly increases the

versatility of the machine, but some performance loss will be realized. Small diameter tooling is prone to flex and vibrate, and the spindle itself floats on air bearings that may allow for small deflections under cutting loads or vibrate if not properly balanced. Performance is still impressive with position errors up to a few hundred nm. Under ideal conditions, the surface roughness has been measured at 10 nm R_a , using diamond end mills on copper. With conventional tungsten carbide tools performance varies, but 50 to 200 nm R_a are typical results on copper. To maintain this level of precision, the machine must be installed on an vibration isolation pad, and the room it's in should be temperature controlled to ± 0.1 C. The *NN1000* is a prototype machine. The information in this chapter will concern the *NN1000* No. 2 specifically; however, many of the principles will apply to any nano-machine platform. As a prototype, the *NN1000* has some peculiar attributes which will be addressed below.



Figure 264. *NN1000* No.2, developed by Digital Technology Laboratory.

Things to consider when nano-machining is what material is to be used, the scale of the features to be machined, and what tolerances are truly required for a part to perform as expected. This information will affect tool selection and machining strategies. If the material, tooling, or scale is new to the machine operator, then it is recommended to experiment first. Fabricating simplified versions of the desired parts allows the operator to fine tune the machining parameters in less time than making complete parts. The

finer the tolerance, the more painstaking the processes will become. 10 μm is of little consequence, but at less than 3 μm the effort to make a part increases substantially. Sub-micron tolerances are possible with tungsten carbide tooling; however, extreme care must be taken to achieve this level of precision. The chip load is proportional to the cutting force, and the maximum chip load is limited by the strength of the tooling and power of the machine. With small diameter tooling, the chip load can easily deflect the tool. Tool deflection and vibrations limit the ability to achieve finer precision and reduces surface quality. Diamond tooling can improve the part quality; however, diamond tooling is very expensive, and cycle times are significantly increased. If the quality of tungsten carbide tooling will suffice, then it is generally recommended.

Understanding burr formation is critical to successful nano-machining. As material is removed from a work piece, the parts that are cut and break away are chips, but near the edges of a feature some chips will remain attached to the part, making a burr. Since nano-machined parts typically have small features (< 1 mm) with sensitive tolerances, it is not advisable to mechanically remove burrs. Many features may simply be too fragile to touch. Chemical processes may reduce burrs and improve surface finish, but there are limits. Chemical polishing tends to focus on places where the surface area to volume ratio is large and on sharp edges. While burrs will be reduced, other desirable features may be adversely affected, such as sharp corners may become rounded or smooth surfaces may become pitted. Therefore, every effort should be made to reduce or eliminate burrs during the machining process. The inherent shear strength of a material provides support against the cutting force of machining. In bulk, the material is well supported, and the tooling can cut through with few burrs created. However, near the edges of a part, the material is thinner, and at some point there is insufficient support, and it becomes easier to bend the material out of the path of the tool, rather than cut it. The greater the cutting force, and the more ductile the material, the more likely a burr will form. To minimize this effect, cutting pressure and chip load should be reduced when near the edges of a machined feature. Increasing the spindle RPM and/or decreasing the feed rate

can reduce the burr size. Climb milling (tool rotation at the point of contact is opposite of the tool advance) is usually preferred over conventional milling (tool rotation at the point of contact is in the direction of tool advance) since the chip profile tapers down as the tool advances. This naturally reduces the cutting pressure as a chip is cut free. The axial and radial depth of the cut will define the maximum size of a burr. In practice, rough machining is performed to remove material in an efficient manner, but as the final dimensions approach, the depth of cut and feed rate are reduced.

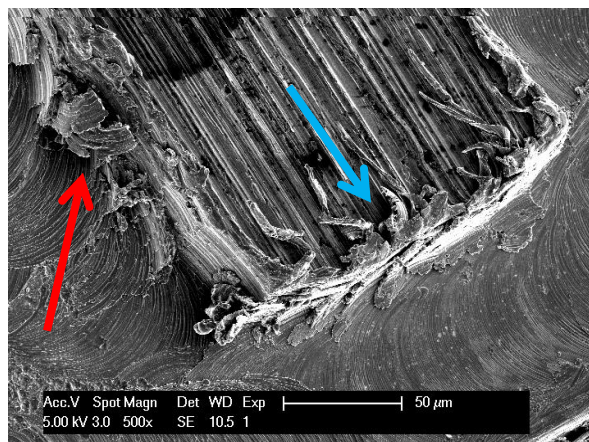


Figure 265. SEM photograph of micro machined oxygen free copper. Copper is a ductile material, and it is easily drawn away from the bulk stock. The side walls of this part are seen to have large burrs from the clockwise turning end mill (red arrow). There are also burrs along the top edge of the part (blue arrow).

A.B.2 Machining Techniques

Nano-CNC-machining is not a rapid process. Small chip loads and feed rates equate to long cycle times; therefore, efforts should be made to reduce cycle times. This will save time and money. The time spent on a nano-CNC-machine should be minimized by preparing parts on a conventional mill, and creating the proper jigs to hold parts. Bulk material is cut to size using conventional machining techniques. Most features on a part can be pre-cut, but undersized, with 50 to 100 μm stock allowance for nano-CNC-machining. When transferring a part into the *NN1000* (part setting), the location and alignment of the part

can be determined to within 25 to 50 μm with little effort from the operator. Greater precision in alignment can take several hours, and alignment better than 10 μm is a difficult task. Allowing 50 to 100 μm of material to be finished with nano-CNC-machining should permit the part to be installed in the machine with little effort, and allows the part to be finished with ultra precision and excellent surface finish in less time. This is especially true for surfacing operations. The first step in most nano-CNC-machining is to plane the top surface of the part parallel to the machine X-Y plane. Casually installing a part on to the machine can easily be off by 100 μm of elevation per 50 mm. Surfacing several square cm by 100 μm , can take an exceptionally long time, 24 hours or longer is common. This is not a good use of the machine, and the tool wear and expense compound the issue. Leveling the part as much as possible before machining is highly recommended. Leveling within 25 μm over 50 mm is not a difficult task, but even finer leveling is recommended. Achieving a level surface within 10 μm is recommended. A quality jig can ease part setting tremendously. A jig is a device that is designed to secure work into a machine that automatically aligns and locates the part, or at least simplifies the alignment procedure. A generic fixture, such as a precision vise is not recommended. When the vise clamps onto the part, it applies stress that could be detrimental to fragile parts. They also tend to shift a part's position as they are tightened beyond the acceptable limits for nano-CNC-machining. Repeatability with a precision vise is poor; therefore, if the work needed to be removed and reinstalled in the machine, the operator would essentially have to start the alignment process over. Jigs should be designed to mount into conventional machines and *NN1000*, so that when transferring the jig between machines, the work can remain affixed to the jig. For most applications, the work is located with alignment pins, and is bolted from underneath. This technique is accurate, very secure, provides access to all sides of the work, and minimizes strain on the part.

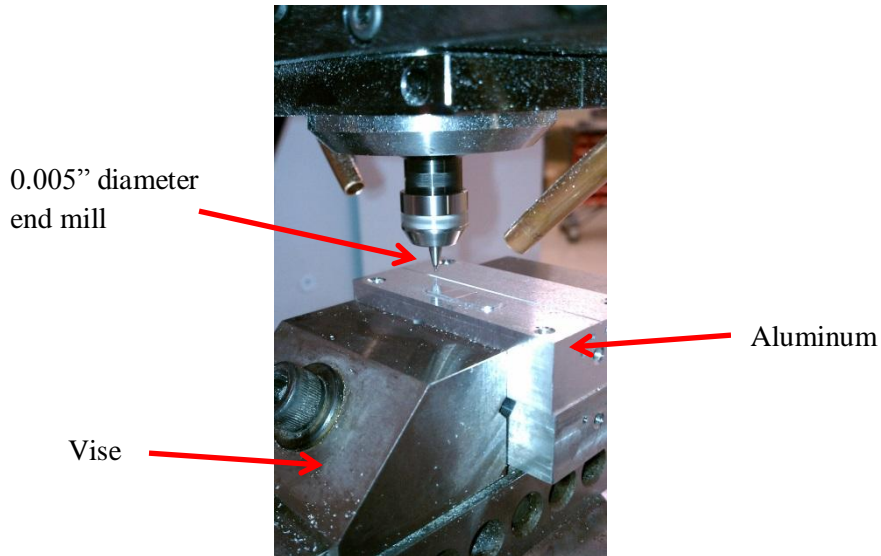


Figure 266. *NN1000* milling aluminum mounted in a precision vise. When vises such as this are tightened, there is a tendency for the part to shift, bringing the material out of level by several microns. The material can be surfaced flat; however, the repeatability of mounts like this is insufficient for nano-CNC-machining tolerances. The tooling in use is a 0.005 inch diameter end mill.

Machining strategies can further decrease the propensity for burrs to form along the edges of parts. Burrs created upon tool entry into a work piece are much smaller than those created on tool exit. When possible, tool paths can be programmed to eliminate exit burrs by ensuring the tooling enters a work piece from the edges, but disengages the part somewhere in the middle. When first engaging a tool into a work piece, a minimal depth of cut should be used, on the order of the dimensional tolerance. Additional cuts along the same path will gradually increase in depth until a maximum roughing cut chip load is established. The bulk of the material can now be removed with more aggressive roughing parameters. However, as the final part dimensions are approached, the chip load and depth of cut should be reduced. The final finish pass should have a depth of cut on the order of the dimensional tolerance. Since there is usually some tool deflection, additional spring passes (repeating a machining action with the identical tool path of a previous operation) will make for extremely light cuts, and can remove existing burrs and improve surface finish. This may increase the cycle time by a factor of ~2; however, the reduction of burrs on

microstructures is worth the effort. In some cases it may be possible to tilt the tooling at an angle so that the flute pitch is parallel, or angled down into the part along the upper edges. This will discourage burr formation, but it is not always possible since there must be sufficient room to angle the tooling, and it complicates the tool path, and machine set-up.

Once the basic machining strategy is laid out, and tooling and cutting parameters are selected, the process of fine tuning can begin. Even small parts can have excessively long cycle times since miniature tooling uses slow feed rates and tiny chip loads. Most programs when initially written have inefficient tool movement that can be edited to reduce cycle time. CAM software can be a great aid for writing programs for complicated geometries, and for quickly altering programs, but they are not necessarily the best programs to run. CAM software often creates very large programs, where megabytes of data could be replaced with a simple “while loop”. It is important not to rely on CAM software. Programming bugs can have catastrophic results if not carefully checked. CNC programs (often called G-code) should be simulated by computer to verify the program works as expected without risking actual material, tooling, or the machine tools. Programs can also perform dry runs on machine tools, where no tool engagement ever occurs. Once a program is “proofed”, it should be safe to make parts; however, new programs or set ups should be carefully monitored to prevent accidents. In general, CNC machine tools will do exactly as they are programmed to do. There are no real safe guards from crashing the machine, and potentially causing significant damage. Care should be taken when evaluating the most efficient speeds, feeds, and tool paths. Material removal is usually inversely proportion to tool life. While high material removal saves time, it may require additional tools, which also takes time to change and set. Optimizing time, quality, and budgets is often a relevant challenge.

A.B.2.1 Materials

Vacuum electronic device, slow wave structures are constructed from high conductivity materials. Copper is a common choice; however, copper has some peculiar machining properties because it is so ductile. On a casual observation, machining copper may seem like an easy task, but there is a narrow window of cutting parameters where results are good. Being too aggressive with copper will increase tool loads, tool wear, burrs, and ultimately break tools. Problems with cutting too slow are less obvious. If the cutting edge does not take a definitive “bite” into the material it may swedge material instead of cutting into it. The tooling cutting surfaces may displace material without cutting. “Plowing” through the material will increase tool loads, temperature, and cause large burrs, tool wear, poor surfaces, and poor edge definition. Finding the ideal speed and feed is a matter of experimentation. For copper, the ideal chip load is relatively heavy, however, for very small tools the ideal feed rates may be beyond the strength of the tooling. For example, Harvey Tools recommends surface cutting speeds of 225 feet/minute with a chip load of 4 to 5 microns for miniature endmills on copper. For a 0.020 inch diameter tool, this equates to a spindle RPM of ~43 kRPM, and a feed rate of ~400 mm/minute. This can be achieved for long, linear cutting movements with good results; however, the microstructure of the parts often have small features that limit tool movement. The machine must slow down feed rates to follow curved paths or change direction with high precision. This results in feed rates frequently dropping below 100 mm/minute. This accelerates tool wear, and causes concerns for part quality. Smaller diameter tooling requires higher spindle speeds to maintain proper cutting speeds, and feed rates are proportionally increased. The ideal material removal rate exceeds the strength of the tooling below 0.010 inch diameter tools, and tool breakage increases significantly. During the author’s experience with the *NN1000*, it was configured with a spindle with a maximum speed of 55 kRPM. Therefore, for tooling less than 0.015 inch diameter, machining was below recommended surface cutting speeds. Even though these conditions are not ideal, it is still possible to get good results. As tooling size is reduced, and cutting parameters are less ideal, tool wear and tool breakage increases. This is compensated with more frequent tool changes. Diamond tools

offer a possible solution for this problem. They typically use very small chip loads, and also use slower feed rates. When used properly, diamond tooling maintains its cutting edge, and consistent performance is observed for the tool lifetime. Diamond tooling does not require changing, or programming offsets. Since they require little attention from the machine operator it is possible to allow the machine to run unattended or overnight, thus offsetting the increased cycle times. However, diamond tools are not always practical or possible.

Aluminum is also a popular material for millimeter wave devices. It is much easier to machine than copper. It is a rigid material that is easy to cut. It is more forgiving for machining parameters, and good surface finish and low burr formation is easier to achieve to comparable copper machining. The principal drawback is the tooling must be kept clean. Aluminum chips easily stick to hot cutting tools, and can clog tooling flutes, or obstruct the cutting edge. Chip evacuation is of paramount importance in avoiding these problems. Nano-CNC-machining does not generate much heat, but using an air stream to clear chips from the cutting area is recommended.



Figure 267. End mill failure due to extreme aluminum loading. This end mill had insufficient lubrication, and aluminum chips loaded the flutes. This completely blocks the flutes, preventing any additional chips from being evacuated from the cutting area, and compounding the problem.

An alternative to copper or aluminum is dispersion strengthened copper, Glidcop. This material adds a small amount of alumina particles to a copper matrix. This controls the grain size of the material, and strengthens the material while maintaining high conductivity. Glidcop is much more resistant to annealing under heat than oxygen free copper. This property is beneficial for diffusion bonding slow wave structures together. For H-plane split slow wave structures, fasteners and clamps are insufficient to provide the necessary electrical contact between part halves. Brazing is discouraged because it is difficult to guarantee that no braze material enters the slow wave structure. Diffusion bonding allows a seamless bond. To accomplish this, the slow wave structure halves are assembled, placed in an oven, and weights are applied to increase the pressure between the parts. The assembly is heated to ~ 1000 C, and then allowed to cool over a period of time. Using oxygen free copper is a concern because it will anneal with temperature, and the circuit may become distorted under the applied weight. Glidcop can withstand the pressure at temperature with little concern. For nano-CNC-machining, Glidcop offers some advantages as well. The small grain structure limits the property for the material to be drawn out of the bulk material. This improves the surface finish, and decreases burr formation. However, the inclusion of alumina can increase tool wear. Alumina is very hard, and it will chip tooling and degrade coatings. Increased wear rate is offset by higher quality parts. Using diamond tools on Glidcop is a greater concern. It will cause chips and microfractures in diamond crystals. The expense of diamond tooling cautions against the use of diamond on Glidcop.

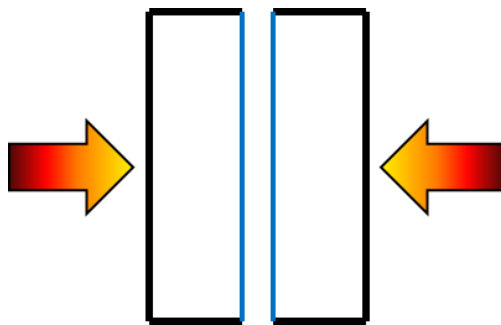


Figure 268. Diffusion bonding process. Two flat parts are pressed together and high heat is applied. Over time the parts will exchange material and become bonded to each other. To be electrically seamless, the

parts need to be as flat as possible, so there are no gaps. The recommended surface finish is a minimum of 200 nm R_a .

A.B.2.2 Tooling

Tool wear with tungsten carbide is the primary cause for dimensional errors and poor surface finish. Miniature end mills will axially wear down during milling. As the tooling becomes shorter, it will not reach the intended tool depth. Furthermore, the face of the tooling will lose its cutting edge, which can lead to increased tool loads, deflection, heat, and poor surface finish. The tooling length must be periodically measured, and then the CNC program can be offset to compensate. In copper milling with 0.010 - 0.020 inch diameter, axial tool wear of $\sim 50 \mu\text{m}/\text{hour}$ is typical. Cutting fluids were found not to be beneficial. With oil based cutting fluids, tool wear was found to increase. The purpose of cutting fluids is to cool the tooling and material, flush away chips, and keep the tooling flutes clear. Spinning the tooling at 55 kRPM in cutting fluid, without cutting any material, was found to cause tool wear. The cutting loads are so small, and chip loads so light, that cooling the tooling and material, and keeping the tooling flutes clear are unnecessary. However, when machining high aspect ratio structures, evacuating the chips is critical. A buildup of chips can cause tool deflection, wear, and, in extreme cases, tool breakage. To keep the parts clear of chip build up, ambient air jets are used to blow chips away from the machining action. Cold air guns are not recommended due to the temperature sensitivity of the *NN1000*. A large temperature gradient would cause energy transport throughout the machine, and it is unknown how the machine would react. Most miniature end mills can tolerate about 100 μm of axial wear before needing replacement. Radial wear is minimal over the same period, except on the corners of square ended tooling, where sharp, square edges are rounded off to about a 30 micron radius. The increased corner radius can be acceptable for roughing tools, where the machined part has not been cut to final dimensions yet. However, for final machining a fresh tool is recommended for the best accuracy. Tool coatings to

improve the surface hardness are recommended. Common coatings such as AlTiN (aluminum titanium nitride) will increase tooling cost by ~30%; however, tooling lifespan can be increased by 50%. Miniature tungsten carbide end mills are inexpensive at \$10 - \$20 each; however, at ~2 hour lifespan, the cost can accumulate for parts with long cycle times. Micrograin tooling material is also recommended. When tooling wears and chips away, the tool degradation is typically gain by gain. This is not important for macro-machining, where the chip size is much larger than tooling grain sizes; however, for micro-machining, the tooling grain size should be smaller than the chip size to keep an edge longer. It is not always obvious how dull a tool may be. Even relatively large burrs are difficult to see un-aided. Nano-machining is virtually silent with sharp tools and light cuts. Should the cutting process become audible, it is a sure sign that the tooling has lost its edge. Monitoring motor loads is a reliable method of judging tool life. The time to change a tool will depend on the needs of the part, but a tool used overlong will certainly cause issues with part quality.

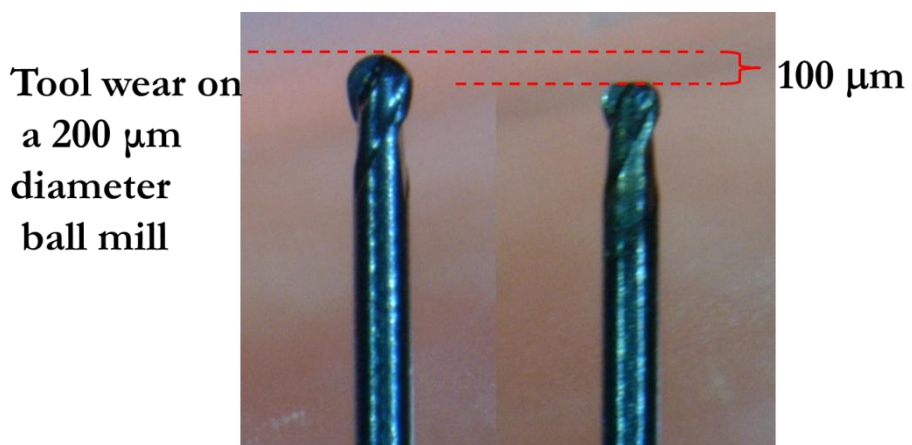


Figure 269. Tool wear on a 200 μm diameter ball mill. 100 μm of axial wear is measured, while the diameter of the ball mill is virtually unchanged.

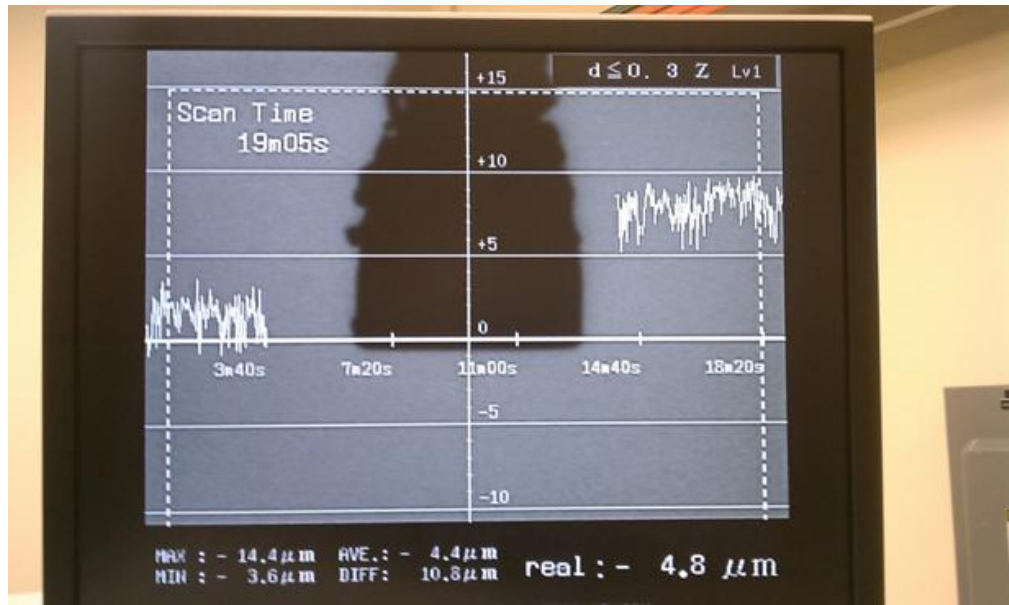
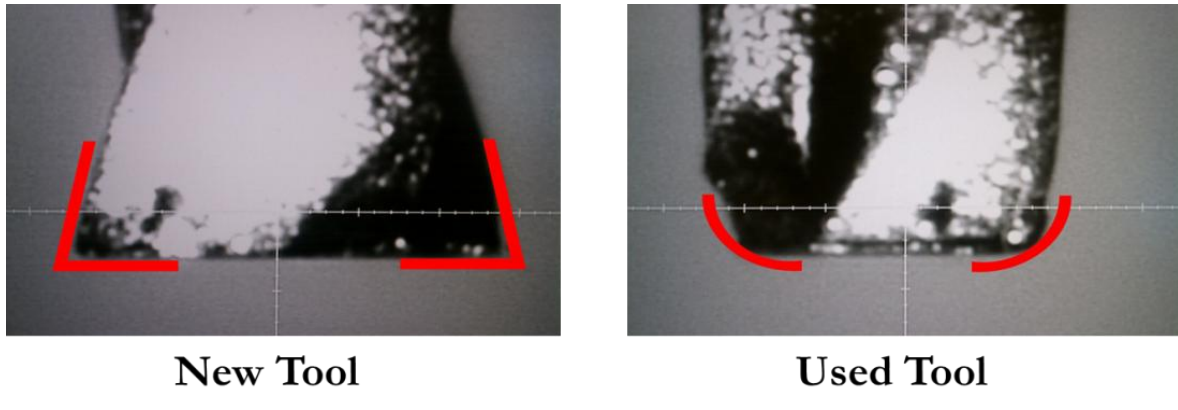


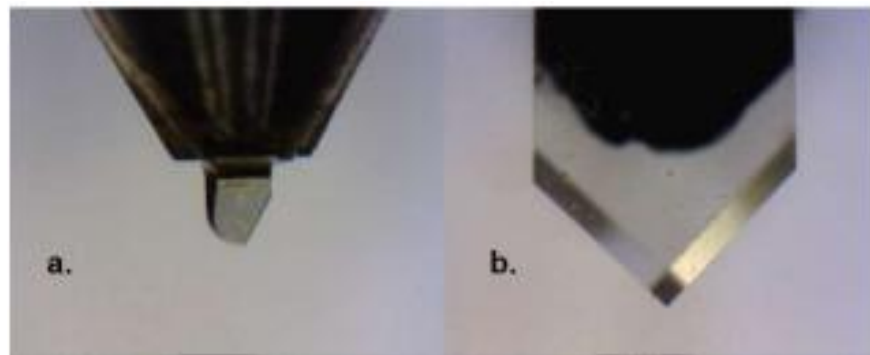
Figure 270. Tool wear measurements using a DynaVision optical tool setter. The central shadow is an image of a 0.010 inch diameter end mill as viewed from the side. The DynaVision optical tool setter analyzes this image to measure the tooling length and diameter. The plot overlaid in white are relative length measurements. The abscissa represents time, covering a span of 19 minutes. The ordinate is length, measured in microns. On the left side is a plot of length measurements up to the 4 minute mark, averaging $\sim +2 \mu\text{m}$. From 4 minutes to 14 minutes, the tooling was used to machine, and then at 14 minutes the tooling was returned to the DynaVision where the length was measured at $\sim +8 \mu\text{m}$. This shows $6 \mu\text{m}$ of wear over a 10 minute period. The actual time between measurements spent machining was ~ 7 minutes, giving a wear rate of $50 \mu\text{m}/\text{hour}$.



Figures 271a and 271b. Left: Side view image of a new, 2-flute, miniature end mill. The tips of the end mill are sharp, and when spinning this tool will cut square channels. Right: The same tool after two hours of use. The corners are rounded off to a radius of $\sim 30 \mu\text{m}$.

Diamond tooling is recommended for extremely exacting tolerance applications, since they essentially do not wear. However, diamonds are not appropriate in many applications. Diamonds react poorly with ferrous materials, and are not recommended for many hard materials such as titanium where high cutting temperatures can be expected. Diamonds are also quite brittle, and in miniature sizes they can be extremely fragile. Tool aspect ratios of length of cut to diameter are typically 1.5:1 to 3:1, but for very small diameters, such as $10 \mu\text{m}$, the aspect ratios are 1:1. There is also a concern for cost and availability. Miniature diamond end mills may cost \$1000 to \$2000 each, and they are typically custom ground to size, which makes for a few months lead time. Under appropriate applications, diamond tools can be expected to last more than 1000 hours. Ultimately, they will perform better, and represent an overall economy compared to tungsten carbide; however, cycle times will increase by a factor of 4 to 10. Diamond tooling uses very small chip loads, of $0.5 - 1 \mu\text{m}$, and are typically single flute tools. Comparable tungsten carbide tools are two flute tools with chip loads of $1 - 5 \mu\text{m}$. For example, using a 0.010 inch diameter tool at 50,000 RPM will call for feed rates of 25 - 50 mm/minute for diamond, and 100 - 500 mm/minute for tungsten carbide. Cutting fluids are recommended for diamond tooling. There are special formulations recommended for diamond tools available from tooling suppliers. Excessive cutting fluids are not

beneficial; therefore, these fluids can be applied in a very fine mist, or occasionally added 1 drop at a time between machining operations. If the part in question requires surface finishes better than $50 \text{ nm } R_a$, or tolerances less than 1 micron, then diamond tooling may become necessary, but other factors (not the least of which is economics) may lend towards conventional tooling. A hybrid approach of roughing with tungsten carbide tooling, and finishing with diamond tooling can take advantage of both types of tools. Choosing the best tooling for an application can be an involved process, especially if there is little documentation available. An experienced machinist can be a great asset in the planning and design phases of a project.



Figures 272a and 272b. Left: Single flute, 1 mm diameter, diamond ball mill. Right: 90° diamond scribe. Photographs courtesy of Logan Himes.

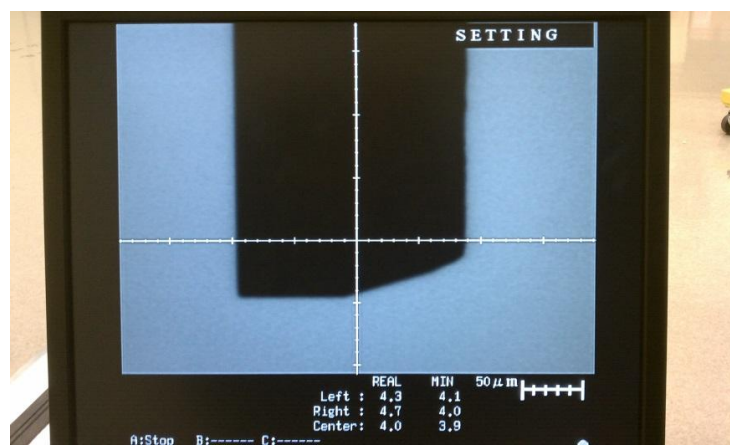


Figure 273. Single flute, $200 \mu\text{m}$ diameter, diamond end mill profile. Image from the DynaVision optical tool setter.

When selecting tooling, the largest tool that will fit is generally a good approach, since they will last longer and remove material faster. Tool strength is roughly proportional to the radius squared. Since larger tools are stronger, they can handle greater chip loads, and therefore greater material removal rates. However, part specifications may dictate smaller diameters, particularly when machining an inside corner radius. Always use larger tooling to machine rough features, and then smaller tooling can provide the finish work if necessary. Since miniature end mills wear axially quite readily, they lose their ability to plunge in the Z direction. Engaging a part with the side of a tool is preferred, but with a closed pocket there is no choice but to feed in the Z direction. Ramping down into a part will greatly reduce tool load in the Z direction. Tool ramping should be programmed to use all the available lateral space to minimize the slope of the ramp.

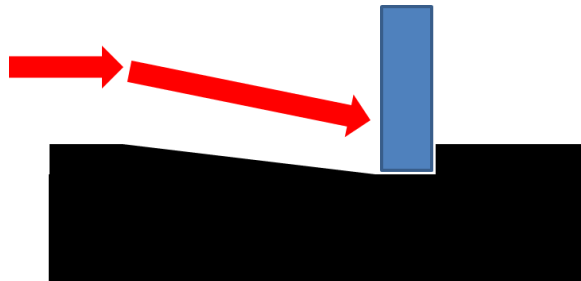
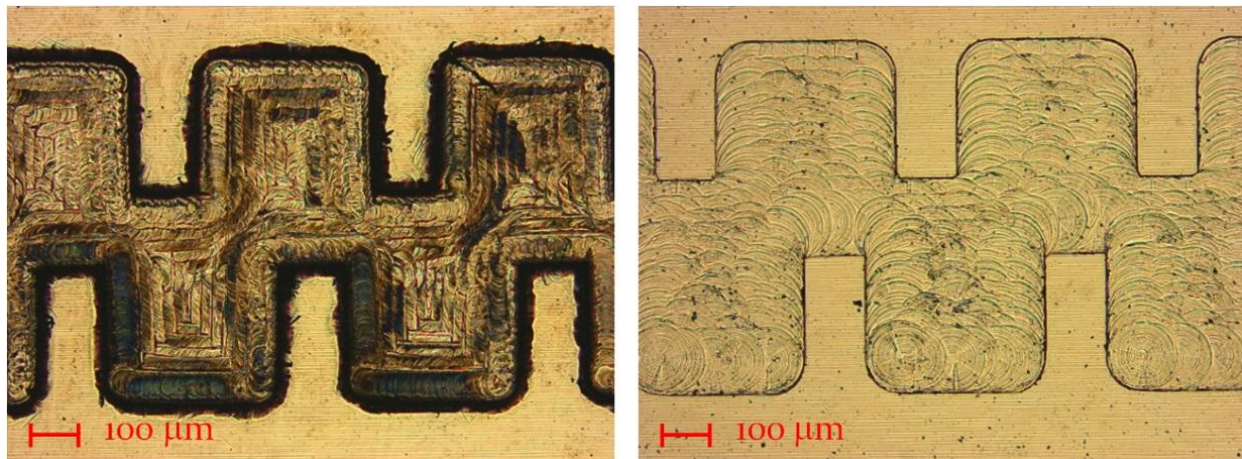


Figure 274. Ramping tool path to avoid Z-axis plunging. The arrows show an end mill engaging material with a shallow ramp.

Square ended, center cutting, two-fluted, tungsten carbide end mills are the standard tooling recommended. Tungsten carbide tooling with AlTiN coating will work for most applications with copper, aluminum, steels, and stainless steels. If parts possess surfaces sloped in the Z direction, then it may be prudent to use bull-nose tooling profiles. These tools have a corner radius ground into their cutting profile. This will help smooth surface finishes when tool paths travel diagonally in the Z direction. Square end mills tend to stair step these types of faces, and additional spring passes are needed to smooth out the surface. An alternative is to rotate the A-axis so that the tooling axis is square to the face. This can be a

difficult procedure on the *NN1000* because there is no tool setter to determine the length the tooling protrudes from the spindle. When rotating the A-axis, the tip of the tool, or center of a ball mill, should be located at the axis of rotation. Otherwise, the location of the end of the tooling will shift in the Y-Z plane, and this shift must be measured to properly offset the coordinate system. Ball mills are used when the tool radius is needed to provide a fillet between two part faces. They are not recommended for machining flat surfaces. They essentially make point contact with the work, and it will be difficult to achieve a fine surface finish across a plane. Single fluted mono-crystal diamond end mills are recommended for non-ferrous materials when sub-micron tolerances or surface finishes finer than 50 nm R_a are required.

Diamond scribing can provide the best surface finish for topmost planes or channels. The machine must have room to linearly translate a scribe across a part without obstructions at relatively high feed rates. It is often the case that a scribe cannot access the tool path it would need; however, for the top most surface of a part it is an excellent method to employ. An alternative method for surfacing is a diamond face mill. A relatively large diameter (~4 mm) diamond face mill can efficiently surface large surfaces, and pass around protrusions. There are numerous material/tooling combinations that have yet to be tried. More development in tool coatings and exotic materials is encouraged.



Figures 275a and 275b. Comparison of tungsten carbide versus diamond tooling on copper. Left: Double grating structure machined into copper 50 μm deep. The dark spots indicate burrs and relatively rough surfaces. Right: The same operation performed with diamond tooling. The improvements in edge definition and surface quality are clear.

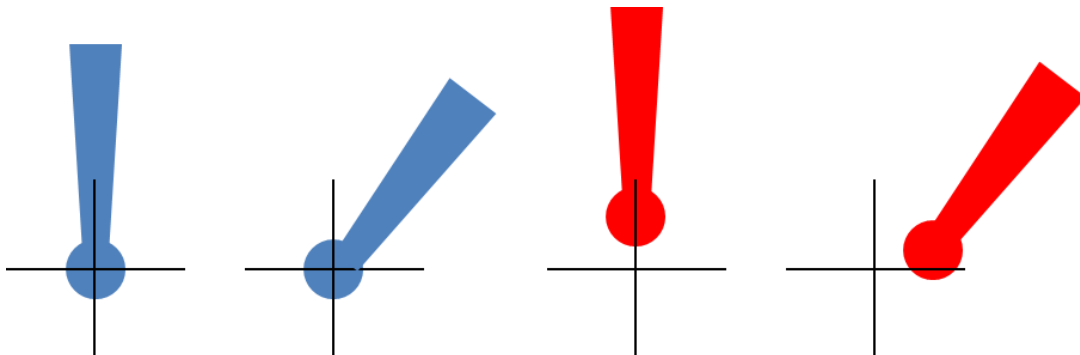


Figure 276. Two examples are shown to demonstrate how A-axis movements are affected by the tool length. The cross hairs mark the location of the A-axis center of rotation. Left: In blue, a ball mill is centered on the A-axis, and rotations have no effect on the tool position. Right: In red, the same tool is installed too high so that the tool center is above the A-axis. When rotated, the center of the tool will shift in the Z and Y positions. To maintain accurate machining, this shift in position must be measured.

A.B.2.3 Tool Setting

Setting the tool length and measuring tool wear is an important process for nano-CNC-machining. The tools are held in the *NN1000* spindle by selectable collets, 3 mm, 4, mm, and 0.125 inch diameters are the most common. The tooling should extend out of the bottom of the spindle ~10 mm. Using a depth gauge or hollow tube setter will not provide micron accuracy. The tip of the tool must be measured relative to the top surface of the part. First, the spindle must be running at cutting speed. The spindle uses air bearings, and when first activated the spindle rotor will raise up by ~ 20 μm , and over the next 10 minutes it will settle down about half the distance (10 μm above the rest position). The A-axis must be perpendicular to the top surface of the reference plane. The top of the part can be used, or a separate surface can be used to avoid scratching the part. Whichever surface is used for reference, it should be surfaced first so it is level. The spindle is then slowly lowered until the tooling makes contact with the reference plane. With small diameter tooling, it can be difficult to tell when the tooling first makes contact. Alternating between translating the tool laterally, and lowering it 1 μm at a time on a surface that has been surfaced will make tool contact obvious. As soon as chips appear, or a scratch is made, then the Z-axis position can be noted, and the machine can be calibrated to define the Z=0 plane. Performing this test will scratch the reference plane. If there is no suitable location (or if scratches are not permitted) on the part, then a sacrificial reference plane can be used. A separate piece of material can be installed near the part, and surfaced. The relative height difference between the sacrificial plane and top of the part will need to be measured, so at least one small scratch is necessary. After using the tool for 10 to 20 minutes, its wear should be measured by repeating the scratch test. The tooling will likely be shorter by several μm , and the Z=0 plane can be offset as necessary. This procedure is repeated as often as desired, or anytime the tooling is replaced. During roughing operations, the depth is not as critical, and any undetected wear will cause the machine to under-machine, so there is little risk to the parts. When the part dimensions approach the final size, the tool length should be checked more frequently. The depth of

machined features is confirmed when the tool length is set, the machine makes a spring pass at the final depth, and then it is measured with no wear.

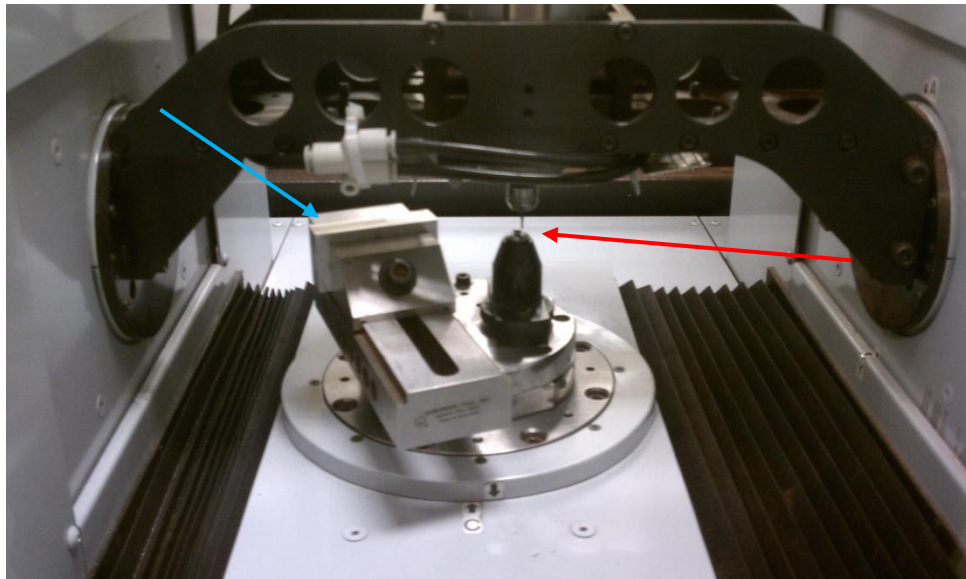


Figure 277. Tool height measurements. The part being machined is a tungsten scandate cathode mounted in the vertical collet (red arrow). The cathode is quite small at 3 mm diameter, and there is no suitable location to perform a scratch test. The vise on the left holds an aluminum block. Tool height measurements are performed on the aluminum (blue arrow), and the difference in height between the aluminum block and cathode were previously measured.

A variation to this method is to use an optical tool setter, such as ones produced by DynaVision. The optical tool setter is mounted to the machine, where the tooling can access it. It uses a camera and monochromatic light source, and when the tooling is positioned in front of the camera, it will measure the tool silhouette. The spindle must be spinning to make accurate measurements. This technique still requires a scratch test to measure the relative position of the part surface to the optical tool setter measurement position. This technique is accurate and easy, and it can measure tool length and tool run out (to provide the effective tool diameter) at the same time. Tool run out is due to the tooling spinning off axis due to being installed off center, bent tooling, or vibrations. Corner radius wear, or ball mill

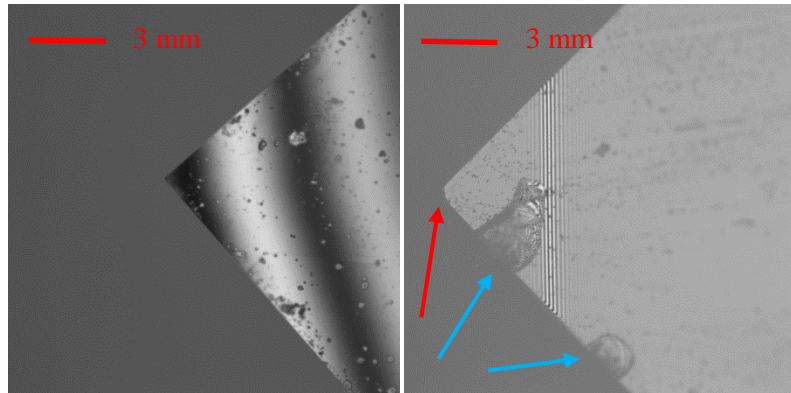
profiles, are easily observed as well. The negative attribute of the DynaVision is that it is large. There is little room inside the *NN1000*; therefore, sometimes the optical tool setter cannot be installed. The scratch test or the optical tool setter can provide 1 μm accuracy for tool lengths equally well.



Figure 278. DynaVision optical tool setter mounted on the *NN1000* table. The tool setter is large, occupying about half of the table. Often times there is insufficient space to utilize it.

When setting diamond tools, the same procedures can be used. The initial tool contact can be difficult because the diamond is nearly clear. It is difficult to judge how close the tooling is to the part. Lowering the tool 1 μm at a time can take a long time to set the part. With experience, it becomes easier to judge the distance. When the reference surface is cut to a mirror finish, the tool image is reflected from the surface. Contact will be made when the tooling and its reflection touch. Setting a diamond scribe works the same way. It can be helpful to write a short program that will translate the tool over the surface of the part, and lowering it 1 μm at a time between passes. An "optional stop" (G-code, M1) in the program will allow the program to run continuously, or pause after each pass, at the operator's command. The diamond tooling generally does not wear for most applications; however, at the end of the machining process its length

should be measured to verify the tool length. Once diamond tool operations are complete, and the tooling is removed from the machine, it is recommended to inspect the tool under a microscope to check its condition.



Figures 279a and 279b. Grooves up to 1 mm deep were scribed into quartz with diamond tooling. Left: New 90° diamond scribe. Right: After scribing quartz the tip is rounded off to $\sim 250 \mu\text{m}$ radius (red arrow). Fractures developed in the diamond crystal (blue arrows) along the leading edge of the tool. Diamond is harder than quartz, and it will cut the material; however, it will grind down diamond tooling, and the stress may fracture the material.

A.B.2.4 Surfacing

Consider a surfacing operation for a 50 by 50 mm copper plate using a diamond scribe with a 1.5 mm nose radius. To perform this operation, the material must be mounted and leveled in the machine. Any tilt in the part will result in additional depth the machine must cut and multiplies the cycle time. It is recommended to level the part to within 10 μm to minimize the surfacing time. A reasonably square material casually mounted in the machine can easily be off by 100+ μm . Improving the alignment to within 25 μm can be accomplished by inserting shims under the part or mount. The part alignment is sensitive to the torque applied to mounting clamps and fasteners. Differential tightening can be used to

fine tune the alignment, provided the part is secure. Leveling within 25 μm may take several hours, and leveling better than 10 μm is possible with experience, patience, and some luck. Serious consideration should be given to the time spent setting up a part. Special fixtures, vacuum chucks, and other aids may be a worthwhile investment.

Most diamond scribes designed for surfacing are constructed from a single diamond crystal, whose cutting edge is ground with a radius. This will prevent the corners of an otherwise flat scribe from leaving scratches at the edges of each tool path. Each pass of the scribe will make a shallow, curved cut in the surface of a part. With each pass the tool will step over a small distance so that adjacent cuts overlap. The final surface will have a ripple that depends on the tool nose radius and step over distance. This height variance can be prescribed, depending on the surface finish requirements of the part, and can be calculated as follows.

$$h = r(1 - \cos \alpha)$$

$$\alpha = \sin^{-1} \left(\frac{d}{2r} \right)$$

where h is the maximum ripple height, r is the tool radius, and d is the step over distance. For example, using the aforementioned 1.5 mm radius tool and a step over of 30 microns will leave a maximum height of 75 nm between cuts. Large radius tools make for flatter surfaces, but since they cut more material, their depths of cut are limited. A good starting point for this type of operation is 5 to 10 micron depth of cut. Deeper cuts are possible, but the extra tool load may prematurely wear out the tooling. For the most accurate cuts, the load should be minimized to reduce tool flexing and chatter. Since scribes are fixed in place, they must be translated at high feed rates to achieve the correct surface cutting speed. Feed rates are typically between 2000 and 3000 mm/min. This is far less than recommended surface cutting speeds for milling operations; however, for diamond scribes this will provide excellent results so long as the tooling is in good condition. The *NN1000* is designed to scribe along the X-axis only. This axis is more robust

than other axes, and it has a maximum feed rate of 3000 mm/minute. For comparison, the Y-axis is limited to 1000 mm/minute. Some extra distance should be given for the leading edge of the part, to allow the machine to accelerate to full speed before engaging the part. 20 mm is typically enough space to get feed rates to 3000 mm/min. Once the tool crosses the part, it must stop, rise up a small amount, return back to its starting location, move over the desired step over distance, and then lower to the depth of cut and repeat until the entire part is surfaced. The resulting surface can be extremely flat, with mirror quality surface finish; however, this process can take a long time. The surfacing cycle time is calculated using the above example. A 50 x 50 mm part is surfaced using a 1.5 mm radius diamond scribe with a 30 μm step over. Each pass over the part will travel 70 mm at 2000 mm/min, with a return trip at 500 mm/min. Accounting for the step over and Z-axis movements, it takes about 30 seconds for each pass. To cover the entire part, we need 1667 passes, which is just less than 14 hours to surface. Now if the part is 20 microns out of level, and we want to use a depth of cut of 5 microns, it will take four complete surfacing operations totaling 56 hours. Even though this is a long time just to surface a small part, it is critical that the part be surfaced in the *NN1000* so that the surface is parallel to the machine axes. Once an operator is confident that the programming is correct, and the surfacing operation is progressing well, the machine can be left unattended. Allowing the machine to operate overnight, or over a weekend can greatly offset the long cycle time.

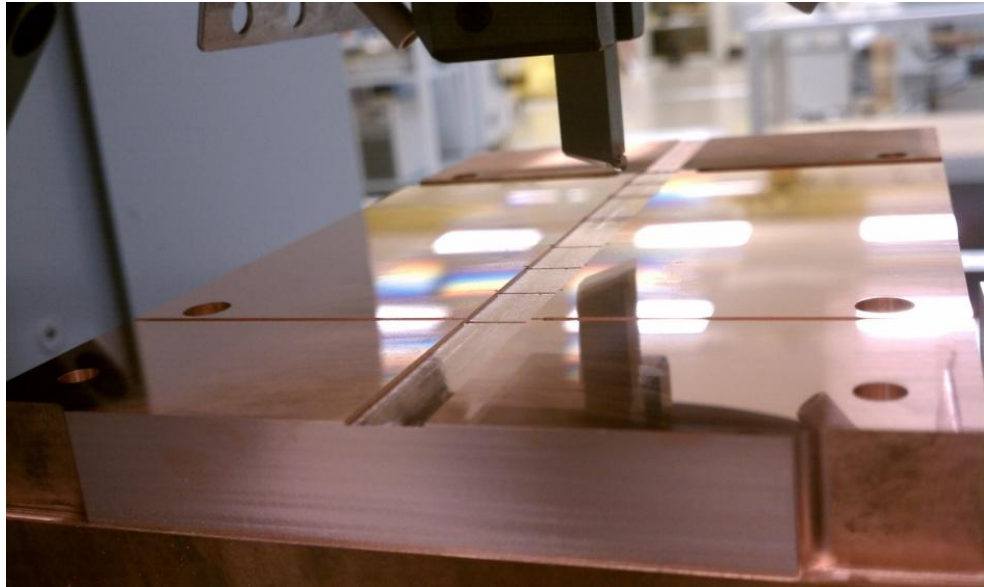


Figure 280. Surfacing a 95 GHz sheet beam klystron with diamond tooling. The scribe is reflected from the copper surface. Note the dispersion from the room lighting diffracting from the surface in a rainbow spectrum.

When the surface finish needs to be better than $50 \text{ nm } R_a$ (better than $10 \text{ nm } R_a$ is possible) the scribing technique is preferred whenever possible. An alternative is to use a diamond face mill. This can save time, and still provides $50 \text{ nm } R_a$ surface finish. Either method will provide a suitable surface for diffusion bonding. The diamond face mill employed on the *NN1000* is a single flute, 4 mm diameter tool. It is designed to sweep out a large area for shallow depths. Cutting depths of 1 to $5 \mu\text{m}$ are recommended with $1 \mu\text{m}$ radial chip loads, turning at 50,000 RPM. If a significant amount of material ($> 20 \mu\text{m}$) needs to be surfaced, then it is recommended to cut down the bulk of the material with 0.125 inch diameter tungsten carbide tools. This will save unnecessary wear on the face mill.

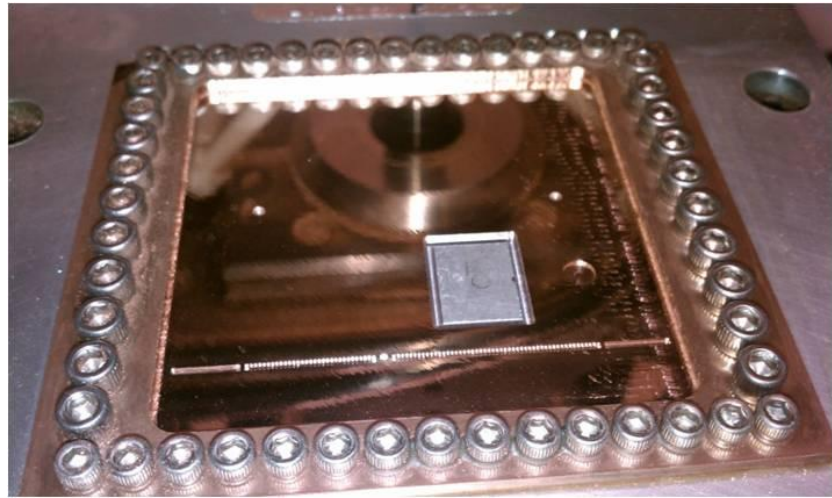


Figure 281. Part of a 220 GHz TWT assembly. The center section is depressed by 2.5 mm; therefore, it is inaccessible for scribing. A 4 mm diameter diamond face mill machines the final surface. The bottom of the *NN1000* spindle is seen in the reflection.

A.B.2.5 Milling

Most machine operations involve slotting, facing, pocketing, side milling, drilling, or some combination of these. Each type of operation has its own concerns and cutting parameters. Any machinist's handbook will provide a starting place for the machining parameters; however, optimization through experimentation is often warranted. Under the right conditions, the *NN1000* performs exceptionally well, with submicron precision, and surface finishes as fine as 50 nm R_a , with standard tungsten carbide tooling. Performance is further enhanced with diamond tooling. However, nano-CNC-machining is not fast. It is quick to set up, and to program; however, the actual fabrication process can be lengthy depending on the specific geometry and tooling used. For the 220 GHz TWT slow wave structure (Chapter 5) mentioned earlier, ~80 hours cycle time was typical for a complete circuit. This time does not including the surfacing time, which was typically done overnight. Cycle times refer to the actual time spent machining. It does not include part preparation, set-up, or measuring.

To understand why the cycle times are so long, consider an example using a 2-flute, 250 μm diameter end mill to cut a 40 mm long, 1 mm wide, and 0.5 mm deep slot into copper. The concept is to feed the tool down the slot multiple times until it is the proper width, and then repeat the process with increasing depth until the slot is finished. A good chip load for a tool this size is about 2 microns. Since this tool is exceptionally fragile, a relatively low RPM and slow feed rate will be used, namely 38,000 RPM and 150 mm/min. The surface speed of the tooling will be less than ideal, but it will be necessary to avoid breaking the tool. A step over distance of 20% of the tool diameter, and a depth of cut of 10 μm , will be about as much as this tool can handle, especially once it gets dull. This arrangement will cut away chips that are about 1 cubic nanometer each, for a removal rate of 0.076 mm^3 per minute. Under ideal conditions, the cycle time is about 4 hours; however, the actual time will be longer. In order to decrease burrs along the edge, the step over rate should decrease as the slot approaches its full width. Initially stepping over 0.050 mm, but then leaving a decreasing stock allowance of 0.025, 0.005, 0.001, and finally a finish pass to size, will require 16 trips through the slot. At 150 mm/min, this is 4.27 minutes, but only at a depth of 0.010 mm. To reach the depth of 0.5 mm, 50 such passes will need to be made. Also, to further reduce burrs, the first cut should be very shallow, say 1 micron deep. Subsequent passes can slowly increase the depth of cut to 1.5, 2.5, and 5 microns, and then maintain 10 micron depths. In order to achieve good surface finish at the bottom of the slot, and similar reduction of depth of cut should be made. Therefore, 6 additional passes will be necessary. During this time, upwards of 200 microns of tool wear can be expected, so additional passes must be made to reach a 0.5 mm depth. Instead of 50 passes, this feature will require 76 passes at 5.5 hours. This estimate excludes the time spent measuring and changing the tooling, which adds another 30 minutes, as well as additional tool movements to step over, overshoot the slot length, accelerate and decelerate, Z movements, and lead in and lead out times, which can be significant if the part geometry is complicated. When using "exact stop mode" (G-code, G61, highly recommended for maintaining micron tolerances), cycle times can be as much as double. To make matters worse, when features are on the order of a mm or less, there is not enough room for the machine

to accelerate to ideal feed rates; therefore, the average feed rate is much less than the programmed rate.

Slower than ideal feed rates also increases tool wear. This simple slot will take between 6 and 7 hours to complete. Complicated microstructures of similar volume could easily take 24 hours to complete.

Pocketing is an operation where a hole (of any geometry) is cut into a surface. The only access for the tooling is to be fed into the material in the Z direction before cutting in the X-Y plane, known as "plunging". The cutting edges on the face of a tool are the first to wear away, which will greatly impede Z direction feeds, and plunging straight down should be avoided. Instead, the dimensions of the pocket define an area where the tooling can be ramped into the material at some angle. The ramping angle should be as small as practical to minimize machine loading, and axial tool wear. Tooling can be fed in a helical manner, or a linear ramp, using as much area as the pocket will allow. Consider a pocket in copper with the dimensions 800 by 375 microns, and 320 microns deep using the same tooling, and machining parameters, as above. Positioning the tool at one end of the pocket, and ramping down at 0.25° , will lower the tool by 5 μm per pass. Machining out the pocket at a depth of 5 μm , and then ramping down another 5 μm , and repeating the cycle until the full depth is machined should take about 1.5 minutes under ideal conditions. However, several factors will increase the time. This pocket is small enough that a feed rate of 150 mm/min will almost never be realized. An average feed rate of 75 mm/min is more realistic. To maintain a 1 μm tolerance, "exact stop mode" (G61) will be necessary. "Exact stop mode" is a CNC programming option that translates the tooling to the exact specified coordinates for each tool movement, and momentarily stopping before continuing to the next line of code. Without this feature activated, CNC machines will try to blend tool direction changes together to make them smoother; however, it is less precise, and can lead to small errors near the corners of features within a part. Slower than expected feed rates, increased tool wear, and exact stop mode will increase the cycle time of this example by a factor of 10. Adding in some extra time for checking the tooling for wear and occasionally replacing the tooling

can make a seemingly 1.5 minute feature take 20 minutes to complete. The 220 GHz TWT slow wave structure has 160 of these pockets to machine, contributing 50 hours to the fabrication time.

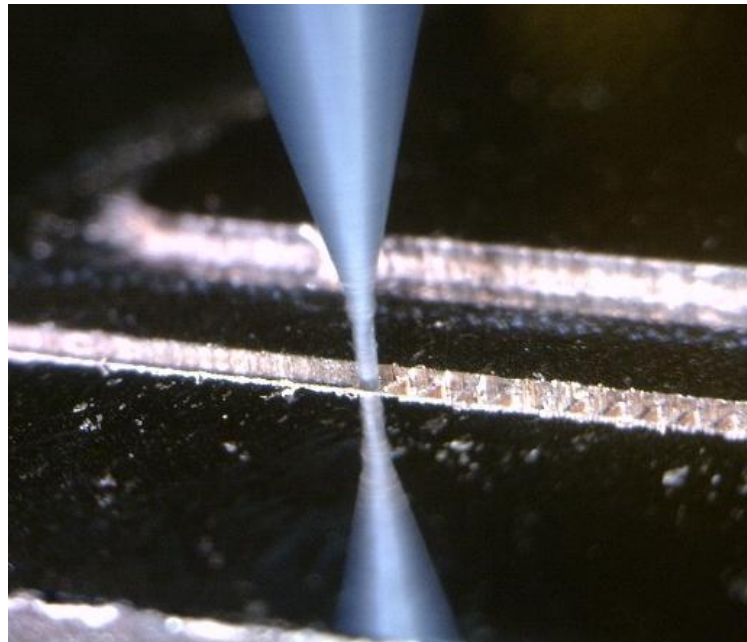


Figure 282. Pocketing operation on a 220 GHz TWT. The tooling is a 254 μm diameter tungsten carbide end mill. The pockets measure 800 x 350 μm , and 320 μm deep. Several 118 μm wide vanes are observed to the right of the end mill.

Diamond tooling of similar dimensions of the above examples typically employs a 1 μm chip load, which will reduce the feed rate. Also, they are single tooth cutters, so the feed rate must be reduced by a further factor of 2. Spindle speed can be increased to 50,000 RPMs; however the final feed rate is reduced to 50 mm/min. The depth of cut is usually more modest at around 5 microns for most operations. This makes for chips that are about 0.25 cubic nm, and an ideal removal rate of 0.0125 mm^3 per minute. This makes diamond tool operations slower by a factor of 6. However, they do eliminate the tool wear problem, and can be run unattended. The improvement in surface finish and tolerance makes diamond tooling an

attractive choice, but the needs of the project must be considered before committing to the use of diamond tooling.

Drilling and reaming can be problematic for the *NN1000*. Drills are designed to remove large amounts of material in short order. The *NN1000* spindle is not designed to handle high axial loads. Z-axis cutting force should remain below 20 N to avoid problems. The load is approximated on the *NN1000* load meter, where 1% of load equates to ~1 N. At 40 N or higher, the machine may trip a safety alarm, and shut down, to protect the spindle. The nature of drilling is not a precise operation; however, if it must be done, it is possible. To avoid overloading the machine, drills should not exceed 1.5 mm diameter, and hole depths less than 10 mm are recommended for aluminum. For copper, only a few mm are possible before the material heats the bit, and seizes it during drilling. High chip loads from drill bits can easily clog drill flutes, which can lead to breaking drill bits. When drilling aluminum, there is additional concern for chips sticking to the drill face. Peck cycles help, where the machine periodically retracts from the hole to clear away the chips. Reaming will make precision holes; however, it is not recommended with the *NN1000*. Reaming is best done at low RPMs; however, with a minimum speed of 38,000 RPM, even small diameter reams are short lived. To make precision holes, end mills are recommended with a helical tool path. This allows for chip clearance around the edges of the tooling, and most of the cutting can be done as a side milling operation. Holes for dowel pins can be machined with excellent control on the pin fit. The maximum depth of a hole depends on the length of cut for the end mill. Most miniature end mills are available in a 3:1 length to diameter aspect ratio, but some extended reach tooling is also available.

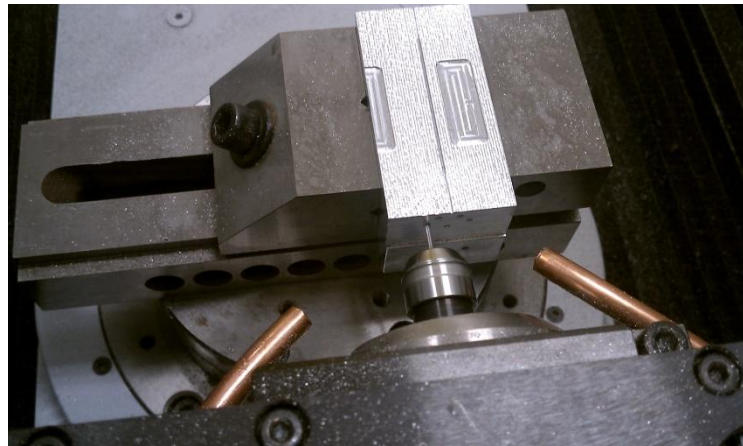
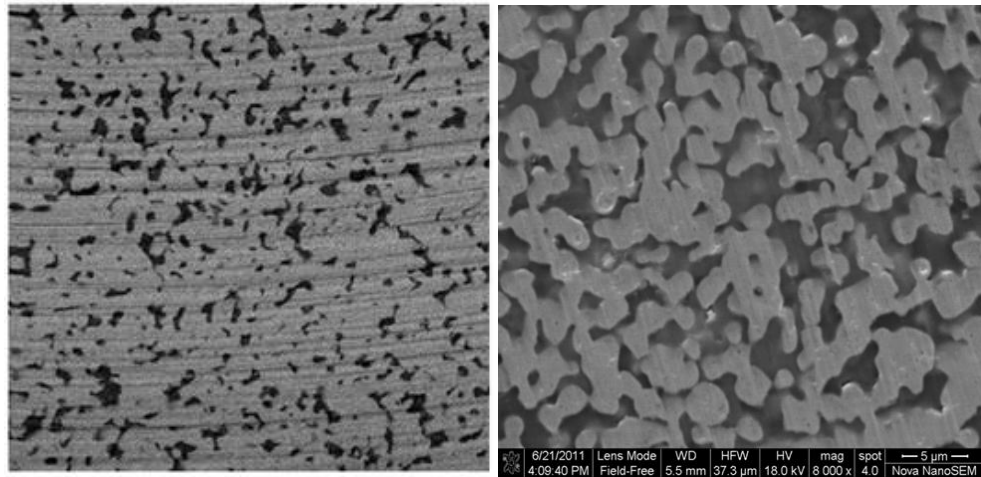


Figure 283. Drilling pin pilot holes with the *NN1000*. The A-axis is rotated -90° to access the end of the part to machine a flange mount centered on the beam tunnel of a 220 GHz TWT.

Milling tungsten scandate cathodes can be difficult. This material is a sintered structure, made from micron or submicron particles. It is very porous, which increases the emission surface area, and is very fragile. The lack of structural support in the cathode matrix makes it prone to chipping near the edges, and micro burrs across the surface, which are observed as the pores being filled in. This will reduce the surface area, and is detrimental to cathode performance. This material is very sensitive to contaminants. The cathode must be kept absolutely clean during the entire process.

The cathode blank is a small cylinder, 2 - 3 mm diameter, and 4 - 5 mm long. A small collet mount is installed in the *NN1000*, so that the cylinder axis is vertical. Tungsten carbide tools tend to generate micro burrs. While the top surface must be burr free, emission is not desirable from the sides of the cathode; therefore, cathode roughing is performed with tungsten carbide tooling. The cathode profile is machined with a 1 mm diameter ball mill at ~50,000 RPM with a 2 μm chip load. However, the emission surface is left extra high by ~150 μm . The edges of the emission surface will be heavily chipped as much as 100 μm deep. A diamond face mill is installed in the spindle, and the top of the cathode is slowly machined down. The diamond face mill is run at 50,000 RPM with a 1 μm chip load. For the first several passes, a 10 μm

depth of cut can be used. The edge chipping will be dramatically reduced. When there are about 20 μm remaining before the final emission surface is machined, the depth of cut should be reduced to 1 μm . The 4 mm diamond face mill can cover the entire cathode surface with a single pass. The leading edge of the face mill should only cut each part of the cathode only once. There are no spring passes in this operation. This will reduce the chance of disrupting the porous surface.



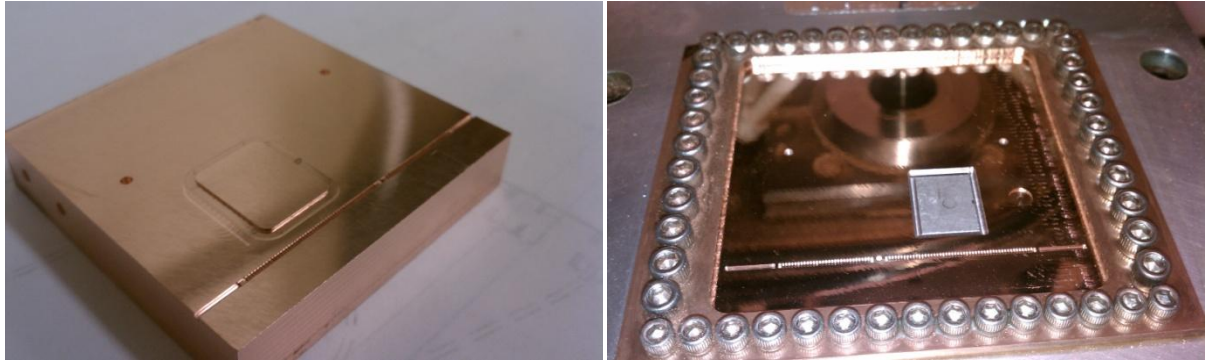
Figures 284a and 284b. SEM images of tungsten scandate cathode emission surfaces. Left: Cathode emission surface machined with tungsten carbide tooling. The surface pores are largely filled in, reducing the effective surface area. Right: Cathode emission surface machined with a diamond face mill. The microstructure is preserved, yielding a higher performance cathode.

A.B.2.6 Part Assembly Alignments

Whenever possible, parts should be made with as few pieces as possible. This eliminates the need to assemble and align parts, and eliminates the fasteners holding them together. However, sometimes this is not possible. For example, to access the interior of the slow wave structures for vacuum electronic devices, the slow wave structure must be divided into two or more pieces. When these pieces are assembled, it is critical to align them with exacting standards. The 220 GHz TWT was found to reflect

certain frequencies within its bandpass, observed as standing waves, if the circuit halves were misaligned by more than 3 μm . The common practice for precision alignment is to employ dowel pins. Precision holes are cut into each part, and fitted for precision ground dowel pins. "Slip fit" clearance is typically 5 μm ; however, for the 220 GHz TWT application, 2 μm was used. With the *NN1000*, pin holes are machined with end mills on a helical path (as described above). The diameter of the helix sets the hole diameter, and can very accurately create pin holes with any fit desired. Tighter pins should improve the alignment; however, the parts become difficult to handle when the clearance is reduced to an interference fit. Even with 2 μm clearance, the parts can be difficult to handle due to pins becoming cocked in their bores. The cumulative effect of small clearances, and possibly cocked pins, can create some variation in inter-part alignment.

To achieve a more reliable, and precise fit, alignment features can be machined directly into the parts. This is accomplished by machining a large protrusion (island) in one part, and its corresponding part had a matching depression (pocket). The island and pocket are machined to the same dimensions so that they precisely fit into each other. A $0 \pm 2 \mu\text{m}$ fit is recommended, where the dimensions are as identical as possible. Too loose a fit has obvious consequences. A slight interference fit will assemble without any problems; however, there is a risk that the material will deform, and create burrs that will perturb the alignment. The alignment features are rectangular in shape because straight lines are more accurate in the milling process. The corners of the rectangular are machined with two different radii so that the rounded portions of the island and pocket do not contact. The flat sides align in the X-Y plane, and mating surfaces keep the parts parallel. The pocket should be deeper than the island is tall to ensure that only the mating surfaces contact. Islands 0.5 mm tall should provide sufficient engagement. It is recommended that the alignment features be as large as practical in the X-Y plane to provide consistent assembly. A few square centimeters should be sufficient.



Figures 285a and 285b. Upper and lower circuit halves for a 220 GHz TWT. Left: Lower block, the thin channel is the TWT slow wave structure. The rectangular island protruding from the surface will locate the circuit halves together. Right: Mid-plate, the rectangular hole is the receiving pocket for the alignment island on the lower block. This pocket extends all the way through the mid-plate because the plate is only 0.5 mm thick. A third part (not shown) is the waveguide block, which connects four waveguides to four overhead couplers in the slow wave structure. It mounts on top of the TWT to sandwich the mid-plate between the lower block and waveguide block to complete the assembly.

A.B.3 NN1000 Details

The *NN1000* is a prototype machine. Several prototypes were built before the program was discontinued; however, The Davis Millimeter-Wave Research Center at UC Davis retains access for their use. This section will address information specifically for the *NN1000* No. 2, the second prototype built, that an operator should be aware of. The details below discuss some of the unique features this machine has, some quirks it possess and how to circumvent them, and some general recommendations of machine operation. Much of this information is only useful for an experienced machinist using the *NN1000* No. 2. The *NN1000* is a 5-axis machine (X, Y, Z, A, and C). The maximum travel for each axis is 120, 150, and 50 mm for X, Y, and Z respectively. A-axis can rotate $\pm 90^\circ$ from vertical, and the C-axis can turn 360° any number of times. The pneumatic spindle is mounted in a bridge that spans the work table. The table is 150 mm diameter, has a radial bolt pattern for mounting work in the machine, and has a capacity of 15 kg.

X and C motions are controlled by moving the table, and Y, Z, and A motions are controlled by moving the spindle bridge.

The *NN1000 No. 2* uses a Fanuc control system. The Fanuc brand is a popular control system for machine tool. One item to note is that the on-board memory is quite small by today's standards, with less than 1 MB RAM available for program storage. This is sufficient for numerous hand-coded programs; however, complicated structures coded with CAM software can easily exceed 1 MB. For larger programs, the machine should be run in DNC (Distributed Numerical Control) mode. In this mode, programs can be stored on a flash drive, memory card, or accessed through a network. Small parts of the program are "drip" fed into the machine a few lines of code at a time.

The master power switch is color coded red and green, where red is on, and green is off. "Green" is used for "off" because "green" is associated with "safe". When the machine is first activated, all five axes will be unlocked, and floating on air bearings. The center bridge must be in static equilibrium before pressing the "on" button on the control panel, which is green. Then, the axes will engage and lock into place. The servo motors will initiate a series of pulse tests, and if it passes these tests the machine will be ready to calibrate. If it fails, then it must be powered down to try again. On occasion, it will fail this test, usually after a machine crash. Two or three attempts to start are sometimes required. Once the machine is successfully turned on, the controller will have no reference point to its current position; therefore, the machine must be calibrated to its "home" position. This is performed one axis at a time by jogging each axis position from negative to positive, back to negative, and then pressing the home button. Home position is considered zero, and it is roughly at the midway point for each axis. When all five axes are in the home position, the machine is ready to use. Note: when the machine automatically travels to the home position it will translate slowly, over several seconds. However, if the C-axis has already been calibrated, and it is given a home command a second time, it will spin very rapidly. If there happens to be considerable mass in the C-axis table, its moment of inertia could be enough to trip a machine alarm,

therefore requiring a restart. Also, the x-axis travels opposite the convention for most mills. Most machines use a right handed Cartesian coordinate system, with $-x$ on the left and $+x$ on the right. Translating the X-axis will move the table left for minus, and right for plus; however, the spindle is fixed in place. Therefore, when the table moves left, the tooling is moved to the right of the work. Most machines use the orientation of the tooling to define the coordinates, and the *NN1000* is opposite.

When the machine is idle, the load meters should be $< 3\%$ for all motors. Many axes have two displays, such as X1 and X2. This is because these axes use two motors to position the table. The spindle bridge is supported by pneumatic actuators to offset the weight of the assembly versus gravity. The air pressure to the regulators can be adjusted to minimize the load on the Z-axis motors. If the A-axis is tilted beyond $\pm 45^\circ$, the torque on the Z-axis motors may create a load to maintain position. Adjusting the air actuators can compensate for this torque. Whatever position the bridge may be in, it should float freely with $< 3\%$ load when not in use. The air spindle uses air bearings to support its rotor. If the air bearings are turned off, the rotor should not be handled. Turning the rotor by hand can damage the bearings. Normal air bearing pressure is 0.5 MPa. If the line pressure drops below 0.35 MPa, the machine will automatically shut down. When the machine shuts down due to low air pressure, the Z-axis should lock in place so that the bridge does not fall. The bridge breaks are not quite strong enough to hold it, and it will slowly descend over a few minutes. It is important not to let tooling descend into the work, or tool damage, or unintentional machining may occur. If the spindle was running before an alarm, it takes considerable time to spin down, and can do significant damage to parts, fixtures, or the machine. If the load meters exceed 100% (40% for the Z-axis), then the machine will automatically shutdown. Dull tooling or aggressive cutting are the most likely causes for machine overload. For the axes that have two motors (X, Y, Z, and A), each motor control and position sensor must agree, or the motors may start working against each other. This is observed by a pair of motor load meters increasing in load, and fluctuating. Depending on the severity, this can result in greater position errors as well. Under these circumstances, the servo controllers and position sensors need to be recalibrated. This can be done through the control interface

panel; however, it is a delicate process, and should only be performed by a fully qualified operator. Refer to the Fanuc control manual to learn the process. If the *NN1000* experiences an overload alarm, or other system fault, that automatically shuts down the machine, then all of the servo motors will be disengaged. The intent is to protect the machine servos and bearings from damage. This results in all five axes becoming free to float on their air bearings. Depending on what the machine was performing at the time of the shut down, the axes may drift with disastrous effects. The spindle is disengaged, but it may be rotating at high speed, and will continue to cut anything it contacts. It is possible the incidental motion will destroy the parts in progress, break the tooling, and possibly damage any mounting fixtures, or the machine table. The serious consequences of this action caution the operator from contributing to this result.

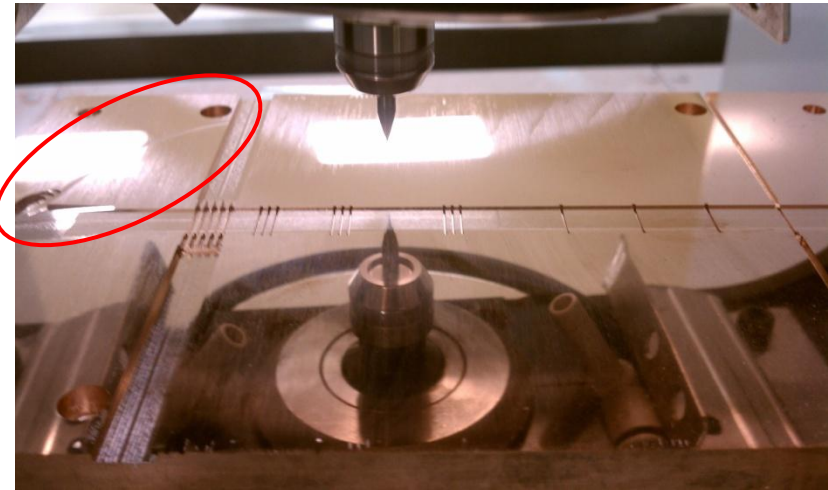


Figure 286. 95 GHz sheet beam klystron. The results from a machine shut down are observed on the left side of the circuit, circled in red. At this point the sheet beam tunnel tapers outward as the beam disperses into the collector. While machining the exit taper, the end mill failed, resulting in the sudden loading and shut down of the *NN1000*. With the tooling engaged in cutting, it was pulled into, and along, the top surface. A deep notch is cut into the taper sidewall, and an arced groove is cut along the surface to one of the RF output ports. The location of this error happened to not adversely affect the klystron performance; however, in any other location it could easily have destroyed a 100 hour fabrication effort.

When changing tools on the machine, the large, red, emergency stop button should be depressed. This will cause all the motors to disengage and float freely. If the machine is handled by hand when it is running will most likely trip the motor overload alarm, which has the same effect as the emergency stop button. Gently pushing against any axis is readily seen on the load monitor screen. With the bridge floating freely, and the air bearings on, the A-axis should be rotated horizontally to point the tooling at the operator. The collet is loosened with a pair of wrenches, the tool replaced, and then retightened. Do not over tighten the collet; ~20 ft.lbs. of torque is ample for tool retention. Positioning the spindle in a horizontal position lessens the risk of dropping a tool out of the spindle before it is secure. Restarting the controller by pressing the green "on" button will reactivate all the servo motors. If the controller is reset in this manner, the machine will not need to be recalibrated. If the machine shuts down due to an alarm, or if the master switch is turned off, then a full axis calibration will need to be repeated.

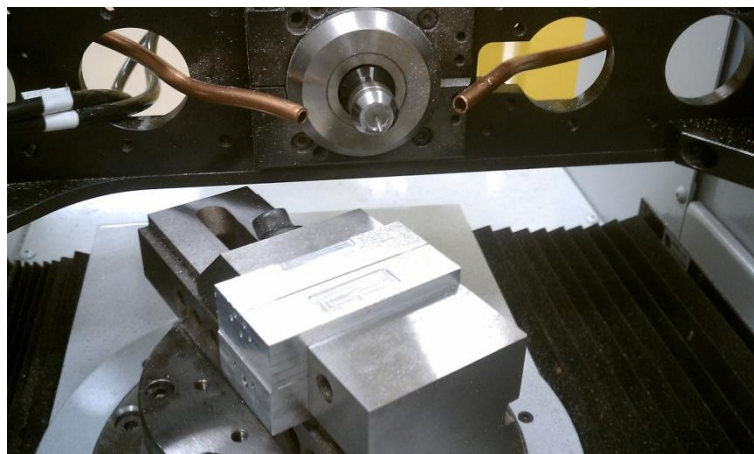


Figure 287. The *NN1000* bridge is rotated to +90° to provide access to the spindle collet. The copper lines are a modification to bypass the oil mist system in favor for air jets to clear chips from the cutting area.

The foundation of the *NN1000* is a thick granite slab. Granite is used for its thermal stability. All the air bearing guideways, servo motors, and position sensors are mounted directly to the granite. The granite slab is then suspended on air isolation mounts. The granite slab should auto level anytime it is disturbed;

however, there are limits. The machine should always be installed on a level floor, and the chassis leveled, before the granite air mounts can be expected to work properly. If necessary, the air mounts can be deactivated by turning off its air regulator. The *NN1000* will run fine without them; however, this will eliminate one of the vibration isolation barriers.

With the *NN1000*, a quirk related to tooling wear was discovered. When tooling becomes dull, the position error steadily increases as tool deflection pushes against the positioning servos. This can be observed with the motor load monitors, which measure the current delivered to each axis. Typical loads are observed as a percent of the machine design maximum, and 10 to 20 % load is normal. Dull tooling will cause the load meters to increase and fluctuate. The computer controls are programmed to provide a target coordinate for the machine to travel to. The machine will not proceed to the next line of code until the position sensors have indicated that the machine has reached its target position. There is some allowance for position error, which is typically ~50 - 100 nm for X and Y axes. With dull tooling, sometimes the tool deflection will be severe enough to prevent the machine from reaching its target position. The displayed position will be static; however, the actual position will vary by a few hundred nm, as it bounces around the target until it happens upon the target position within tolerance, and then it will continue with the program. The net effect is the machine will occasionally pause when machining with dull tooling. At first, this is only observed with slightly increased cycle times. In extreme cases, the machine may pause at a single position for ~10 minutes. If the *NN1000* appears to be stuck, then it is likely time to change the tooling.

Most of the time, air jets are used to evacuate chips from the work piece during machine. The *NN1000* was modified to bypass its oil mister, and the air regulator for this system is routed to a pair of air nozzles located under the bridge. Turning the air regulator knob will adjust the air flow. A gentle air stream is enough to clear the chips. Excessive air flow will be noisy, and could deplete the air supply needed for other systems. Just enough air to keep the chips away from the cutter is sufficient.

When programming the *NN1000*, there are several G-code commands that should be used. First, the spindle does not respond to normal speed commands. M3 (clockwise rotation) turns on the air to the spindle turbine, and M5 (spindle stop) deactivates the air. M4 (counter clockwise rotation) is deactivated. The pneumatic spindle turns clockwise only, as viewed from above. The speed commands do not set the RPM directly. Instead, commands S0 through S10 set the air pressure to the spindle turbine. S0 turns the spindle off. S1 is the slowest setting at ~38,000 RPM, and the air pressure increases systematically to the maximum at S10, ~55,000 RPM. The air bearings remain on, so long as there is air pressure and the master switch is on. The spindle will spin for a long time after the turbine is disengaged. It may take upwards of 15 minutes to come to a complete stop. It is not recommended to assist the spindle stopping with any assisted braking. G61 (exact stop mode) is recommended for most operations. The only time this feature can be omitted is if the tool path is linear all the way through a part, such as slotting for a electron beam tunnel, or grooving a diffraction grating with a scribe. If the machine needs to travel to specific locations, and change directions within a part, then G61 will help maintain precision and accuracy. When G61 is active, it is also recommended to active G5.1 (look ahead). This command allows the controller to interpret the CNC code several lines in advance. The controller will automatically adjust the feed rate (by slowing the feed rate) of the machine to more precisely follow the upcoming commands. When small movements are required, such as small radius turns, this will vastly improve the accuracy and precision of the machine. Without this command, the machine will move too quickly, and overshoot target locations, and cause arcing tool paths to be irregular.

A.B.4 Nano-CNC-Machining Conclusion

Nano-machining is a versatile process that can compete with, and outperform, other microfabrication methods in many areas. As a research and development tool, it can provide excellent parts on short notice. Design changes can be readily programmed into the machine in a few minutes, while other methods could

take months to realize. The only down side to nano-CNC-machining is that parts must be made one at a time. Therefore, it may not be suitable for mass production. Cycle times tend to be long, so careful consideration should be given to nano-CNC-machining processes to minimize this issue. Precutting features on a conventional mill could greatly speed up nano-CNC-machine production, but the amount of stock allowance to leave on a part will depend on the quality of the roughing machine, and the confidence with which a machinist can install a precut part and still be within tolerance. Any part preparation should always be done with as much care and precision as possible. If a part is even slightly out of square it could result in hours and hours of otherwise unnecessary nano-CNC-machining. Choices of materials and tooling are critical to success. Experimenting with cutting parameters is likely time well spent. Parts often take too long to afford a mistake that could have been identified with a few simple tests. When designing parts, consider what the true needs for performance are, and choose a fabrication process that is well suited to deliver the most critical aspects. Sometimes it may be necessary to alter the part design to ease the fabrication. It is better to have a part that is well made, then to have a great design that is poorly made. Initial machine performance may not provide the results desired, but have patience and address the issues one at a time. Small changes can make a big difference. For many applications, nano-CNC-machining provides an excellent fabrication platform. It is the author's hope that this information will serve as a guide for future machinists to make significant contributions to science.